Meiotic chromosome dynamics: a structural characterisation

James Dunce

Thesis presented for the degree of Doctor of Philosophy

Institute for Cell and Molecular Biosciences
Newcastle University

May 2019

Abstract

Meiotic chromosomes are bound in architecturally enforced synapsis during the first meiotic division by a proteinaceous megastructure known as the synaptonemal complex (SC). This molecular scaffold is built between paired homologues, providing a unique three-dimensional environment in which to form genetic crossovers, physical inter-homologue connections critical in ensuring equational segregation at metaphase. The SC structure represents the hallmark of meiotic division, with a striking tripartite appearance, conserved across evolution, in which chromosomally associated lateral elements are connected to a midline central element via transversal filaments.

Such that the SC installs between correctly identified maternal-paternal pairs, a genome-wide, sequence-based, homology search is facilitated by rapid chromosomal movements. Cytoskeletal forces power these movements, transmitted through the nuclear envelope (NE) to the chromosome's telomeric ends via the LINC (**Li**nker of **N**ucleoskeleton and **C**ytoskeleton). Importantly, NE recruitment and tethering is mediated by the meiotic telomere complex, consisting of MAJIN, TERB1, and TERB2, without which meiotic progression is stalled.

The works herein reveal the structural basis of synapsis in the human SC and chromosome tethering to the nuclear envelope by the meiotic telomere complex. Specifically, I report a complete biophysical characterisation of SYCP1, the transversal filament protein of the human SC, and present crystal structures which represent mechanisms of its assembly within the SC mediated by sequences at both its N-termini (which mediate midline, head-to-head, associations) and C-termini (which undergo pH dependent, back-to-back assembly on the chromosome axis). Further, we solved the crystal structure of the MAJIN-TERB2 complex and characterised its mode of DNA association providing key insights into how NE tethering is achieved. Our findings are discussed within the context of the existing molecular understanding of meiotic chromosome dynamics.

Acknowledgements

For giving me the position in the first place, I thank Dr Owen Davies. You took me on as your PhD student and worked me hard! You brought me from the ground up and I wouldn't be the biochemist I am today without your guidance. I think we've achieved a lot since 2014. However, you made one fatal error on September 23rd 2016 when you emailed to ask if I would like to work with a laboratory assistant. My acceptance eventually led to my marriage with said assistant, Natalija Stepurko, with whom I spent the best year of my life. Owen, I must thank you for making that mistake, and Natalija, your friendship has been incredible since the beginning, with your fiery nature fuelling my imagination and inspiring my own critical thinking. There's only so much I can write here but I'm looking forward to entering a new era with you as I set foot outside of Newcastle for the first time!

I'd like to thank all of our lab members, past and present, with whom I shared good, great, and downright frustrating days in the lab. Particularly, I extend gratitude to Gurusaran Manickam, fellow PhD student and flatmate of the past year, for his friendship and many advices. Not to mention our collaboration whilst working with Amy Milburn on the meiotic telomere complex project. Stressful though it was, we made it out the other end alive, just about. Special thanks also to Lucy Salmon and Dr Orla Dunne – some crazy parties were experienced! I hope everyone has successful futures!

Despite not having seen them very much, I thank my family and the few but close friends I have. You appear to have dealt well with my silence, though that assertion shall be tested when and if we meet again!

Now, I hope you enjoy reading the rest of this book. There's no turning back now.

Declaration of originality

The work presented within this thesis was performed in order to characterise the molecular structure and function of key protein assemblies of the meiotic cell cycle. The work presented within the third chapter details my work focusing on the role of SYCP1 within the synaptonemal complex. I performed all biochemical and biophysical experiments relating to SYCP1 except those in reference to the N-terminus of SYCP1 which was mostly performed by Matthew Ratcliff with contributions from myself. I grew crystals of the SYCP1 C-terminus whilst Matthew Ratcliff grew crystals of the N-terminus. X-ray diffraction data were analysed by Dr Owen Davies and he solved all structures. SEC-SAXS data were collected and analysed by Dr Orla Dunne and Dr Owen Davies. The fourth chapter details my contributions towards a highly collaborative project between myself and PhD students Gurusaran Manickam and Amy Milburn, working towards the structural characterisation of the meiotic telomere complex which mediates nuclear envelope tethering of meiotic chromosomes. The work I present here on MAJIN-TERB2 was joint between myself and Gurusaran Manickam and his contributions are highlighted. I crystallised native MAJIN-TERB2 and Gurusaran Manickam crystallised the seleno-methionine derivative of MAJIN-TERB2 which was used to solve the structure by Dr Owen Davies. SEC-SAXS data in this chapter were analysed by Dr Owen Davies.

Unless otherwise stated, all figures are of my own creation.

Table of Contents

Abstract i

Acknowledgements iii

Declaration of originality v

List of figures xii

List of tables xvii

Abbreviations xvii

Amino acid codes xxi

Chapter 1 1

INTRODUCTION 1

- 1.1.1 Meiosis – a myriad of molecularly-mediated motions 2
- 1.1.2 The first meiotic division in mammals 5
- 1.1.3 Nuclear architecture, dynamics and premeiotic DNA replication 7
- 1.1.4 Premeiotic/early leptotene homologue pairing 10
- 1.1.5 Formation of the axial elements 12
- 1.1.6 Self-inflicted DSBs and homologous strand invasion reinforce homologue association. 15
- 1.1.7 Rapid prophase movement of chromosomes facilitates pairing 20
- 1.1.8 Formation of the synaptonemal complex in mammals 20
- 1.1.9 Components of the mammalian SC central region 23
- 1.1.10 The SC central element proteins – building a model for the mammalian SC 25
- 1.1.11 The SC central element: a molecular understanding 25
- 1.1.12 Conservation of SC components across phyla 29
- 1.1.13 Physical interactions between the transverse filaments and the central element 29
- 1.1.14 A 3-dimensional model of the synaptonemal complex 29
- 1.1.15 The SC and the formation of crossovers 31
- 1.1.16 Defects in SC formation and physiological consequences in humans 32
- 1.1.17 Disassembly of the SC 32
- 1.1.18 Aims and objectives 34

Chapter 2 37

METHODS 37

- 2.1.1 Protein sequences analysed in this study 38
- 2.1.2 Bioinformatic analyses 38
- 2.1.3 Preparation of plasmids for recombinant protein expression 38
- 2.1.4 Purification of soluble recombinant proteins 39
- 2.1.5 Expression of seleno-methionine derivative SYCP1$_{676-770}$ 41
- 2.1.6 Expression of seleno-methionine derivative MAJIN$_{1-112}$-TERB2$_{168-220}$ 41
- 2.1.7 Purification of SYCP1$_{1-976}$ and SYCP1$_{1-783}$ by refolding from inclusion bodies 41

2.1.8 Circular dichroism (CD) spectroscopy 43
2.1.9 Size-exclusion chromatography multi-angle light scattering (SEC-MALS) 44
2.1.10 Size-exclusion chromatography small-angle x-ray scattering (SEC-SAXS) 46
2.1.11 Modelling coiled-coil structures using ROSETTA 48
2.1.12 Transmission Electron microscopy (TEM) 49
2.1.13 Electrophoretic mobility shift assay (EMSA) 49
2.1.14 Determination of apparent K_D by EMSA 50
2.1.15 Assay for the determination of zinc content 50
2.1.16 Oxidation assay using Ellman's reagent (DTNB) 51
2.1.17 Protein crystallisation, X-ray data collection, and structure solution. 52
2.1.19 X-ray diffraction data collection for solved crystal structures 54
2.1.18 Notes of interest in the solution of crystal structures 57
2.1.19 Mammalian cell transfection and imaging 58
2.1.20 Thin slice preparation for Transmission EM (TEM) 59
Chapter 3 .... **61**
The molecular basis of meiotic chromosome synapsis through SYCP1 self-assembly **61**
INTRODUCTION **63**
3.1.1 The transverse filament proteins and human SYCP1 63
3.1.2 Mammalian SYCP1 63
3.1.3 Bioinformatic analysis of SYCP1 65
3.1.4 SYCP1 bi-orients within the mammalian SC 67
3.1.5 Unrelated proteins Zip1 and C(3)G localise to the SC, form TFs and share domain structure with SYCP1 70
3.1.6 Zip1 and C(3)G orientate as SYCP1 within the SC 73
3.1.7 The central coiled-coil domain of the TFs defines the inter-chromosomal distance 73
3.1.8 The role of the C-terminus of TFs in chromosomal recruitment 74
3.1.9 The unknown role of the N-termini of TFs and CE association 74
3.1.10 A link to the central element 75
3.1.11 The TF proteins of the *Caenorhabditis elegans* SC 76
3.1.12 Polycomplex formation provides a clue for the assembly mechanism of TFs 76
3.1.13 TF-mediated synapsis is required for proper DNA repair 80
3.1.14 Functions of the TF proteins in centromeric pairing 81
3.1.15 SYCP1 in cancer 82
3.1.16 Uncovering the molecular structure and mechanism of assembly of SYCP1 within the SC 83
3.1.17 Coiled-coil proteins: structure and function relationships 84
3.1.18 Techniques suited for the study of coiled-coil molecules 85
RESULTS **89**

Part I **89**

- 3.2.1 The purification and refolding of full-length SYCP1 from inclusion bodies 89
- 3.2.2 Optimised purification of His$_6$-SYCP1$_{1-976}$ 93
- 3.2.3 SYCP1 is helical and forms large assemblies in solution 95
- 3.2.4 Purification and characterisation of SYCP1$_{1-783}$ 95
- 3.2.5 The unstructured C-terminus of SYCP1 binds DNA 97
- 3.2.6 Human SYCP1 also forms polycomplexes upon heterologous expression 99
- 3.2.7 Truncation or mutation of the SYCP1 C-terminus blocks filamentous network formation 103
- 3.2.8 The SYCP1 helical core possesses intrinsic self-assembly capacity 104
- 3.2.9 Deletion of the SYCP1 αN-tip permits biophysical characterisation of obligate SYCP1 106
- 3.2.10 Size and shape determination of the SYCP1 structured core by X-ray scattering 108
- 3.2.11 A stable parallel coiled-coil caps the C-terminus of the SYCP1 helical core 109
- 3.2.12 Determining the orientation of helices within SYCP1$_{640-783}$ 113
- 3.2.13 Modelling the SYCP1$_{640-783}$ coiled-coil structure *in silico* 113
- 3.2.14 Dissecting the core structure of SYCP1 116
- 3.2.15 Biophysical characterisation of the SYCP1$_{206-362}$ and SYCP1$_{358-783}$ 116
- 3.2.16 Determining the orientation of helices within SYCP1 reveals its overall geometry 120
- 3.2.17 Initial recruitment of SYCP1 to the chromosome axis 125

Part II **133**

- 3.3.1 SYCP1 N-terminal self-assembly is mediated by the αN-tip 133
- 3.3.2 Crystallisation and data collection of SYCP1$_{101-206}$ and SYCP1$_{101-175}$ 135
- 3.3.3 Solution of SYCP1$_{101-175}$ crystal structure 136
- 3.3.4 Differentiating physiologically relevant interactions and crystallographic artefacts within the crystal lattice 139
- 3.3.5 The C-terminal tail-to-tail contact appears to be induced by the crystal lattice 142
- 3.3.6 Solution of the SYCP1$_{101-206}$ crystal structure 143
- 3.3.7 Midline assembly of SYCP1 through homotypic association of the αN-tip 146
- 3.3.8 The SYCP1 N-termini stabilise long range extension of synapsis 149

Part III **151**

- 3.4.1 Role of the stable, extended, dimeric coiled-coil SYCP1$_{640-783}$ 151
- 3.4.2 Attempts to solve the SYCP1$_{640-783}$ crystal structure 151
- 3.4.3 Construct optimisation identifies SYCP1$_{676-770}$ as a new crystal target 153
- 3.4.4 SYCP1$_{676-770}$ crystals have pathologies which inhibit structure solution 159
- 3.4.5 Patterson Function reveals translational symmetry 161
- 3.4.6 Experimental phasing strategies 162
- 3.4.7 Iodide soaking 162

3.4.8 Seleno-methionine incorporation 165
3.4.9 SYCP1$_{676-770}$ crystallisation 167
3.4.10 Structure solution of SYCP1$_{676-770}$ in spacegroup I4$_1$22 168
3.4.11 The SYCP1$_{676-770}$ I4$_1$22 crystal lattice 169
3.4.12 Structure solution of SYCP1$_{676-770}$ in spacegroup C2 171
3.4.13 An analysis of the SYCP1$_{676-770}$ crystal structures 173
3.4.14 The SYCP1$_{676-770}$ tetrameric interface 176
3.4.15 The SYCP1$_{676-770}$ lateral interfaces 178
3.4.16 Identification of the solution conditions required for assembly 179
3.4.17 The SYCP1$_{676-770}$ undergoes dynamic remodelling in response to pH changes 179
3.4.18 Mutagenesis of SYCP1$_{676-770}$ central tetrameric interface 187
3.4.19 What is the role of the C703 pinch points? 189
3.4.20 DNA binding of SYCP1$_{676-770}$ and chromosomal assembly 192
3.4.21 Back-to-back assembly might play a role in polycomplex formation 194
DISCUSSION 199
3.5.1 The structure of SYCP1 and its role in SC formation 199
3.5.2 Self-assembly is a recurrent feature of SC proteins 201
3.5.3 The sexually dimorphic structure of the SC – length and width. 202
3.5.3 Long-range synapsis is dependent upon other SC proteins 203
3.5.2 Are the structure of SYCP1 and its mechanisms of self-assembly conserved across phyla? 203
3.5.2 The unknown function of the SYCP1 N-terminal unstructured region 205
3.5.2 DNA-binding constitutes the only known link to the chromosome axis 206
3.4.5 SYCP1 polycomplexes represent misunderstood entities 206
3.4.5 What is the structure of an SYCP1 polycomplex? 208
3.5.6 Controlling chromosomal recruitment and stability of SYCP1 211
3.5.7 Another structure of the SYCP1$_{676-770}$ region 213
3.5.8 SYCP1 as the basis for the synapsis of meiotic chromosomes 213
Chapter 4 207
The MAJIN-TERB2 structure scaffolds the meiotic telomere complex and telomeric DNA 207
INTRODUCTION 209
4.1.1 Homologue pairing is facilitated by rapid prophase movements of chromosomes 209
4.1.2 The generation of rapid prophase movements 210
4.1.3 Transmission of cytoskeletal forces through the nuclear envelope by the LINC complex 211
4.1.4 Connecting telomeres with the LINC complex 215
4.1.5 The meiotic telomere complex: MAJIN and TERB2 219
4.1.6 Bioinformatic and structural analysis of meiotic telomere complex components 220

4.1.7 Connecting components: a meiotic collaboration 222
4.1.8 Interplay between the meiotic telomere complex and the Shelterin complex 223
4.1.9 Uncovering the structural basis for telomere tethering to the nuclear envelope by the meiotic telomere complex 224
RESULTS 225
4.2.1 Initial purification and crystallisation of the MAJIN-TERB2 complex 225
4.2.2 Unstructured termini of MAJIN and TERB2 inhibit crystal growth 228
4.2.3 Construct boundary optimisation 228
4.2.4 Crystallisation of the MAJIN-TERB2 complex 230
4.2.5 Crystal structure solution of the MAJIN-TERB2 complex 230
4.2.6 Analysis of the MAJIN-TERB2 crystal structure 231
4.2.7 Comparison of the high-resolution native, seleno-methionine and a competitor's structure 235
4.2.8 The solution structure of the MAJIN-TERB2 core complex 237
4.2.9 The MAJIN C-terminus is unstructured and extended 239
4.2.10 Disruption of the dimerization interface between MAJIN-TERB2 protomers 244
4.2.11 The MAJIN-TERB2 complex binds dsDNA and does so in a cooperative manner 244
4.2.12 Method for measuring the affinity of MAJIN-TERB2 for dsDNA 246
4.2.13 Quantification of DNA-binding affinities 246
4.2.14 The basic surface of MAJIN is essential for DNA binding 246
4.2.15 The unstructured MAJIN C-termini enhance DNA-binding 248
DISCUSSION 253
4.3.1 MAJIN-TERB2 structure confers 2-fold symmetry to the wider meiotic telomere complex 253
4.3.2 What is the functional significance of a long unstructured MAJIN C-terminus? 254
4.3.3 DNA binding by MAJIN-TERB2 and its incorporation within the attachment plate? .. 255
4.3.4 The dynamics of DNA binding at the meiotic telomere complex 256
4.3.5 The spatial displacement of Shelterin – a consequence of structural rearrangement? ... 257
4.3.6 Higher order assembly to create the telomere attachment plate 261
4.3.7 MAJIN-TERB2: the structural basis for meiotic telomere attachment 261
Concluding remarks: Towards a molecular understanding of mammalian meiosis 263
Publications resulting from this work 263
REFERENCES 265
Appendix 1 – SYCP1 amino acid sequence alignment 280
Appendix 2 – Purification and analysis of C-terminal SYCP1 constructs 282
Appendix 3 – SEC-MALS analysis of SYCP1 C-terminal constructs 284

List of figures

Chapter 1

Figure 1.1.1| Cellular division for replication, growth, and repair.

Figure 1.1.2| The stages of meiosis.

Figure 1.1.3| Chromosome morphology during cell division.

Figure 1.1.4| SYCP2 and SYCP3 are structural components of the mammalian lateral elements.

Figure 1.1.5| The catalytic mechanism of Spo11-mediated DNA double-strand break induction.

Figure 1.1.6| Meiotic recombination.

Figure 1.1.7| Recombinase-mediated strand invasion.

Figure 1.1.8| The evolutionary conservation of the synaptonemal complex.

Figure 1.1.9| Protein components of the mammalian SC.

Figure 1.1.10| Disruption of the mammalian SC central element.

Figure 1.1.11| The self-assembly properties of SYCE3.

Figure 1.1.12| Filamentous assembly of SYCE2-TEX12.

Figure 1.1.13| Model for the localisation of SC components within the mammalian SC.

Chapter 2

Figure 2.1.1| Multi-angle light scattering.

Figure 2.1.2| The study of biomolecules using small angle X-ray scattering.

Figure 2.1.3| Ellman's reagent reacts with free thiols to release stoichiometric quantities of detectable TNB.

Chapter 3

Introduction

Figure 3.1.1| The transverse filaments of the SC.

Figure 3.1.2| Domain structure of the mammalian transverse filaments.

Figure 3.1.3| Bioinformatic analysis of SYCP1.

Figure 3.1.4| SYCP1 within the SC.

Figure 3.1.5| SYCP1 within the SC.

Figure 3.1.6| Bioinformatic analysis of Zip1.

Figure 3.1.7| Bioinformatic analysis of *Drosophila melanogaster* C(3)G.

Figure 3.1.8| Polycomplex formation in *Saccharomyces cerevisiae* ZIP1 and *Drosophila melanogaster* C(3)G.

Figure 3.1.9| Polycomplex formation upon heterologous mammalian expression.

Figure 3.1.10| SCP1 is required for synapsis but not homologue pairing.

Results Part I

Figure 3.2.1| Full-length SYCP1 is insoluble in *E. coli.*

Figure 3.2.2| Refolding SYCP1 from solubilised inclusion bodies.

Figure 3.2.3| Electron microscopy analysis of SYCP1 samples.

Figure 3.2.4| Optimised purification of SYCP1.

Figure 3.2.5| His$_6$-SYCP1 forms helical assemblies and binds DNA via its C-terminus

Figure 3.2.6| Purification of SYCP1$_{1\text{-}783}$.

Figure 3.2.7| SYCP1 forms polycomplexes when heterologously expressed in COS-7 cells.

Figure 3.2.8| Blocking filamentous assembly of SYCP1 by C-terminal truncation.

Figure 3.2.9| Blocking filamentous assembly of SYCP1 by mutation of T859.

Figure 3.2.10| Purification and biophysical characterisation of SYCP$_{101\text{-}783}$.

Figure 3.2.11| Purification and biophysical characterisation of SYCP1$_{112\text{-}783}$.

Figure 3.2.12| SYCP1$_{112\text{-}783}$ is elongated.

Figure 3.2.13| SYCP1$_{640\text{-}783}$ forms stable, helical domain capping the SYCP1 helical core.

Figure 3.2.14| SEC-SAXS analysis of SYCP1$_{640\text{-}783}$.

Figure 3.2.15| Modelling the SYCP1$_{640\text{-}783}$ extended, parallel, coiled-coil.

Figure 3.2.16| Dissecting the SYCP1 core.

Figure 3.2.17| Purification of SYCP1$_{358\text{-}783}$, SYCP1$_{112\text{-}362}$, and SYCP1$_{206\text{-}362}$.

Figure 3.2.18| Biophysical characterisation of SYCP1$_{358\text{-}783}$, SYCP1$_{112\text{-}362}$, and SYCP1$_{206\text{-}362}$.

Figure 3.2.19| Determining helical orientation through SEC-SAXS analysis of MBP-fusions.

Figure 3.2.20| Orienting helices within SYCP1.

Figure 3.2.21| The molecular structure of obligate SYCP1.

Figure 3.2.22| The unstructured C-terminus of SYCP1 is highly unstable.

Figure 3.2.23| Purification and oligomeric state determination of MBP-SYCP1 constructs containing the unstructured C-terminus.

Figure 3.2.24| Purification of SYCP3.

Figure 3.2.25| A model for the chromosomal recruitment and assembly of SYCP1.

Results Part II

Figure 3.3.1| The N-terminus of SYCP1 is helical and monomeric in solution.

Figure 3.3.2| Crystallisation and X-ray diffraction data collection for $SYCP1_{101-206}$ and $SYCP1_{101-175}$.

Figure 3.3.3| The crystal structure of $SYCP1_{101-175}$.

Figure 3.3.4| Coiled-coil stabilising associations between $SYCP1_{101-175}$ chains.

Figure 3.3.5| N-terminal contacts within the $SYCP1_{101-175}$ crystal lattice.

Figure 3.3.6| $SYCP1_{206-362}$ scaffolds head-to-head N-terminal associations to drive assembly.

Figure 3.3.7| C-terminal contacts within the $SYCP1_{101-175}$ crystal lattice.

Figure 3.3.8| The crystal structure of $SYCP1_{101-206}$.

Figure 3.3.9| N-terminal contacts within the $SYCP1_{101-206}$ crystal lattice.

Figure 3.3.10| N-terminal head-to-head contacts drive lattice-like assembly of SYCP1 molecules.

Figure 3.3.11| Remodelling of the SC midline through dynamic and cooperative self-association.

Figure 3.3.12| The N-terminus of SYCP1 stabilises long range assembly.

Results Part III

Figure 3.4.1| Crystallographic trials of $SYCP1_{640-783}$.

Figure 3.4.2| Identification of $SYCP_{676-770}$.

Figure 3.4.3| Biophysical characterisation of $SYCP1_{676-770}$.

Figure 3.4.4| The $SYCP1_{676-770}$ dimeric coiled-coil is parallel.

Figure 3.4.5| Purification and characterisation of GST-fused $SYCP1_{676-770}$.

Figure 3.4.6| Initial crystallisation of $SYCP_{676-770}$.

Figure 3.4.7| Native Patterson map generated for $SYCP1_{676-770}$.

Figure 3.4.8| Soaking $SYCP1_{676-770}$ crystals in sodium iodide solution to gain phasing information.

Figure 3.4.9| Anomalous data collection for $SYCP1_{676-770}$ iodide derivative.

Figure 3.4.10| Seleno-methionine derivate $SYCP1_{676-770}$ crystals.

Figure 3.4.11| Crystallisation and X-ray diffraction analysis of $SYCP1_{676-770}$.

Figure 3.4.12| The $SYCP1_{676-770}$ crystal structure ($I4_122$) reveals an anti-parallel association of parallel chains.

Figure 3.4.13| The details of the $SYCP1_{676-770}$ $I4_122$ crystal lattice.

Figure 3.4.14| The almost identical structure of $SYCP1_{676-770}$ in spacegroup C2.

Figure 3.4.15| Oxidation of C703 decreases chain flexibility.

Figure 3.4.16| Comparison of $SYCP1_{676-770}$ in spacegroups $I4_122$ and C2.

Figure 3.4.17| A hydrogen bonding network and aromatic stacking stabilised the tetrameric interface.

Figure 3.4.18| The lateral interface of the $SYCP1_{676-770}$ tetramer is stabilised by coiled-coil type interactions.

Figure 3.4.19| A reduction in pH triggers SYCP1 assembly.

Figure 3.4.20| A reduction in pH triggers $SYCP1_{676-770}$ assembly.

Figure 3.4.21| A reduction in pH triggers SYCP1$_{676\text{-}783}$ assembly.

Figure 3.4.22| The dimer-tetramer shifts results in increased stability.

Figure 3.4.23| A high salt concentration elicits higher oligomer formation.

Figure 3.4.24| Analysis of a tethered SYCP1$_{676\text{-}770}$ construct confirms tetrameric assembly.

Figure 3.4.25| SEC-SAXS analysis of MBP-SYCP1$_{676\text{-}770}$ confirms anti-parallel helical assembly.

Figure 3.4.26| Mutational analysis of SYCP$_{676\text{-}783}$.

Figure 3.4.27| Oxidation within SYCP$_{676\text{-}770}$.

Figure 3.4.28| The tetrameric form of SYCP1$_{676\text{-}770}$ at pH 5.5 binds DNA.

Figure 3.4.29| Mutation L756P destabilises the second coiled-coil sequence of SYCP1$_{640\text{-}783}$.

Figure 3.4.30| Polycomplex formation upon C-terminal disruption.

Discussion

Figure 3.5.1| A model for the obligate structure of SYCP1.

Figure 3.5.2| A model for SYCP1-mediated synapsis of meiotic chromosomes.

Figure 3.5.3| SYCE3 dynamically remodels the SYCP1 lattice.

Figure 3.5.4| SYCP1 geometry facilitates changes in SC width.

Figure 3.5.5| Electrostatic surface of SYCP1$_{101\text{-}175}$.

Figure 3.5.6| Uncertainty surrounding the nature of SYCP1 polycomplexes.

Figure 3.5.7| Polycomplex formation in *Ascaris suum* and a 2-dimensional model for polycomplex structure.

Figure 3.5.8| Geometric analysis of the polycomplex structure.

Figure 3.5.9| Chromosomal association through SYCP1$_{676\text{-}770}$ assembly.

Chapter 4

Introduction

Figure 4.1.1| The meiotic bouquet.

Figure 4.1.2| The telomeric attachment plate.

Figure 4.1.3| The structure of the SUN-KASH complex.

Figure 4.1.4| Cytoskeletal forces drive rapid prophase movements of meiotic chromosomes.

Figure 4.1.5| Cytoskeletal force transmission in fission yeast.

Figure 4.1.6| Bioinformatic analysis of TRF1.

Figure 4.1.7| The TRF1-TERB1 association.

Figure 4.1.8| The telomeric attachment plate structure in mouse knockouts of the meiotic telomere complex components.

Figure 4.1.9| Bioinformatic analysis of meiotic telomere complex components.

Figure 4.1.10| Mapping the interactions between meiotic telomere complex components.

Figure 4.1.11| Structure of the human TERB1$_{590-649}$-TERB2$_{4-110}$ complex.

Figure 4.1.12| Displacement of TRF1 during the zygotene to pachytene transition.

Results

Figure 4.2.1| Initial purification and crystallisation of a MAJIN-TERB2 complex.

Figure 4.2.2| SEC-SAXS data analysis of MAJIN$_{1-147}$ TERB2$_{147-220}$.

Figure 4.2.3| Optimised the MAJIN-TERB2 construct amino acid boundaries.

Figure 4.2.4| Purification and crystallisation of MAJIN-TERB2 complexes.

Figure 4.2.5| The MAJIN-TERB2 structure.

Figure 4.2.6| Side-chain contribution to the MAJIN-TERB2 β-grasp structure.

Figure 4.2.7| TERB2 side-chain contributions to the MAJIN-TERB2 interface.

Figure 4.2.8| Structure comparison.

Figure 4.2.9| The solution structure of MAJIN-TERB2.

Figure 4.2.10| SAXS-derived molecular envelopes for MAJIN-TERB2.

Figure 4.2.11| The MAJIN C-terminus is unstructured and extended.

Figure 4.2.12| Mutational disruption of the MAJIN-TERB2 dimer interface.

Figure 4.2.13| The MAJIN-TERB2 core binds DNA.

Figure 4.2.14| Method to quantify MAJIN-TERB2-dsDNA binding affinities.

Figure 4.2.15| Quantification of MAJIN-TERB2 core DNA-binding.

Figure 4.2.16| The basic surface of the MAJIN core is essential for DNA binding.

Figure 4.2.17| Design of the basic surface mutant.

Figure 4.2.18| The unstructured C-terminus of MAJIN binds DNA.

Discussion

Figure 4.3.1| Model for molecular architecture of the Meiotic telomere complex.

Figure 4.3.2| Model for the DNA binding mode of the MAJIN-TERB2 complex.

Figure 4.3.3| The telomere bound structure of the meiotic telomere complex during zygotene.

Figure 4.3.4| The meiotic telomere complex during pachytene.

Figure 4.3.5| Super-resolution fluorescence imaging of telomeric ends to visualise MAJIN-TERB2 localisation.

Figure 4.3.6| Recursive assembly of MAJIN-TERB2 at the nuclear envelope.

List of tables

Table 2.1| Vectors utilised in this study.

Table 2.2| Summary of initial and optimised crystallisation conditions.

Table 2.3| Summary of data collections (unsolved crystals).

Table 2.4| Summary of data collections (solved structures).

Table 2.5| Summary of data processing for the unsolved crystals.

Table 2.6| Summary of data processing for the solved crystal structures.

Table 2.7| Summary of structure solution strategies and statistics for the crystal structures.

Table 3.1| X-ray crystallographic statistics for SYCP1$_{101\text{-}175}$.

Table 3.2| X-ray crystallographic statistics for SYCP1$_{101\text{-}206}$.

Table 3.3| X-ray crystallographic statistics for SYCP1$_{640\text{-}783}$.

Table 3.4| X-ray crystallographic statistics for SYCP1$_{676\text{-}770}$.

Table 3.5| X-ray crystallographic statistics for iodide derivative SYCP1$_{676\text{-}770}$.

Table 3.6| X-ray crystallographic statistics for seleno-methionine SYCP1$_{676\text{-}770}$.

Table 3.7| X-ray crystallographic statistics for SYCP1$_{676\text{-}770}$ (I4$_1$22).

Table 3.8| X-ray crystallographic statistics for SYCP1$_{676\text{-}770}$ (C2).

Table 3.9| Summary of SEC-MALS analysis for SYCP1$_{676\text{-}783}$ mutants.

Table 4.1| X-ray crystallographic statistics for MAJIN-TERB2 structures.

Abbreviations

2xYT	
6-FAM	Fluorescein amidite
Å	Ångström
AE	Axial element
APC/C	Anaphase promoting complex / cyclosome
ASU	Asymmetric unit
ATP	Adenosine triphosphate
A$_{xxx}$	Absorbance at xxx nm
BLM	Bloom Syndrome protein
bp	Base pairs
Bqt1	Telomere bouquet protein 1
Bqt2	Telomere bouquet protein 2
C-terminus	Carboxyl terminus
C. elegans	*Caenoorhabditis elegans*
CC	Coiled-coil
CCD	Charge-coupled device
CD	Circular dichroism
CDK	Cyclin-dependent kinase
cDNA	Complementary DNA
CE	Central element
CENP	Centromere protein

CO	Crossover
CtIP	C-terminal-binding protein interacting protein
D. melanogaster	*Drosophila melanogaster*
Da	Daltons
DTT	Dithiothreitol
dH_2O	De-ionised water
dHJ	Double Holliday Junction
D_{max}	Maximum inter-atomic distance
DMC1	DNA Meiotic Recombinase 1
DMEM	Dulbecco's Modified Eagle's Medium
d*n*/d*c*	Refractive index increment
DNA	Deoxyribonucleic acid
DNA2	DNA replication ATP-dependent helicase/nuclease 2
DTNB	5,5'-dithiobis-(2-nitrobenzoic acid)
dRI	Differential refractive index
Drosophila	*Drosophila melanogaster*
DSB	Double-strand break
dsDNA	Double-stranded DNA
E. coli	*Escherichia coli*
EDTA	Ethylenediaminetetraacetic acid
eGFP	Enhanced green fluorescent protein
EM	Electron microscopy
EMSA	Electrophoretic mobility shift assay
EXO1	Exonuclease 1
g	Standard gravity
GABA	gamma-Aminobutyric acid
GE	General Electric
H_2O	Water
HEI10	Human enhancer of invasion 10
His_6	6x histidine affinity tag
HPLC	High performance liquid chromatography
HSP70-2	Heat shock protein 70-2
INCENP	Inner centromere protein
INM	Inner nuclear membrane
IPTG	Isopropyl β-D-1-thiogalactopyranoside
K	Kelvin
KASH	Klarsicht, ANC-1, Syne homology
K_D	Equilibrium dissociation constant
kDa	Kilodalton
keV	Kiloelectron volt
Kms1	Meiotic spindle pole body KASH domain protein
L	Litre
LB	Luria broth
LE	Lateral element
LINC	Linker of Nucleoskeleton and Cytoskeleton
LS	Light scattering
M	Molar
m	Metre
MALS	Multi-angle light scattering
MBP	Maltose-binding protein
MEIOB	Meiosis Specific With OB-Fold
Meiosis I	The first meiotic division
Meiosis II	The second meiotic division

MES	2-ethanesulfonic acid
mg	Milligram
MIP	Methylation-induced pre-meiotically
ml	Millilitre
MLH	MutL homolog
mM	Millimolar
MPD	2-Methyl-2,4-pentanediol
MR	Molecular replacement
MRE	Mean residue ellipticity
MRN	Mre11, Rad50, Nbs1 complex in eukaryotes
ms	Millisecond
MSH	MutS homolog
Mw	Molecular weight
MWCO	Molecular weight cut-off
N-terminus	Amino terminus
NCO	Non-crossover
NE	Nuclear envelope
NEB	New England Biolabs
NEBD	Nuclear envelope breakdown
Ni-NTA	Nickel-nitrilotriacetic acid
nm	Nanometres
NPC	Nuclear pore complex
O.D._{600}	Optical density at 600 nm
ONM	Outer nuclear membrane
P(r)	Inter-atomic distance distribution
PAR	4-(2-pyridylazo)resorcinol
PC	Polycomplex
PCR	Polymerase chain reaction
PDB	Protein Data Bank
PGE	Triethylene glycol
pH	Hydrogen potential
pI	Isoelectric potential
PNS	Perinuclear space
Q	Scattering angle
RAD51	DNA repair and recombination protein 51
RadA	DNA repair and recombination protein A
Rap1	Ras-related protein 1
Rc	Radius of gyration of the cross-section
REC8	Meiotic recombination protein REC8
Rg	Radius of gyration
RIP	Repeat-induced point mutation
RMSD	Root mean squared deviation
RN	Recombination nodule
RNA	Ribonucleic acid
RPA	Replicative protein A
RPM	Rapid prophase movement
rpm	Rotations per minute
s	Seconds
S phase	Synthesis phase
S. cerevisiae	*Saccharomyces cerevisiae*
SAD	Single-wavelength anomalous dispersion
Sad1	Spindle pole body-associated protein 1
SAXS	Small-angle X-ray scattering
SC	Synaptonemal complex
SCC1	Sister chromatid cohesion protein 1

SDS-PAGE	Sodium Dodecyl Sulfate Polyacrylamide Gel Electrophoresis.
SEC	Size exclusion chromatography
SEC-MALS	Size exclusion chromatography multi-angle light scattering
SEC-SAXS	Size exclusion chromatography small-angle X-ray scattering
SfGFP	Superfolder green fluorescent protein
SIX6OS1	Six6 opposite strand transcript 1
SLIC	Sequence- and ligation-independent cloning
SMC	Structural maintenance of proteins
SPATA22	Spermatogenesis-associated protein 22
SPB	Spindle pole body
SPO11	SPO11 initiator of meiotic double stranded breaks
STAG3	Stromal antigen 3
SUN1	Sad1 and UNC84 containing 1
SYCE1	Synaptonemal complex central element protein 1
SYCE2	Synaptonemal complex central element protein 2
SYCE3	Synaptonemal complex central element protein 3
SYCP1	Synaptonemal complex protein 1
SYCP2	Synaptonemal complex protein 2
SYCP3	Synaptonemal complex protein 3
TAAB	TAAB Laboratories Equipment
Taz1	Telomere length regulator 1
TBE	Tris-Borate-EDTA
TEM	Transmission electron microscopy
TERB1	Telomere Repeat Binding Bouquet Formation Protein 1
TERB2	Telomere Repeat Binding Bouquet Formation Protein 2
TEV	Tobacco Etch Virus
TEX12	Testis-expressed 12
TF	Transverse filament
Tm	Melting temperature
TNB	2-nitro-5-thiobenzoate
TRF1	Telomeric repeat binding factor 1
Tris	Tris(hydroxymethyl)aminomethane
μg	Microgram
μl	Microlitre
μM	Micromolar
μm	Micrometre
UV	Ultra-violet
V	Volts
v/v	Volume per volume
w/v	Weight per volume
WT	Wildtype
Zip1	Synaptonemal complex protein Zip1
Zip2	Synaptonemal complex protein Zip2
Zip3	Synaptonemal complex protein Zip3
α-helix	Alpha-helix
β-sheet	Beta-sheet
Δ	Deletion

Amino acid codes

Alanine	Ala	A
Arginine	Arg	R
Asparagine	Asn	N
Aspartic acid	Asp	D
Cysteine	Cys	C
Glutamine	Gln	Q
Glutamic acid	Glu	E
Glycine	Gly	G
Histidine	His	H
Isoleucine	Ile	I
Leucine	Leu	L
Lysine	Lys	K
Methionine	Met	M
Phenylalanine	Phe	F
Proline	Pro	P
Serine	Ser	S
Threonine	Thr	T
Tryptophan	Trp	W
Tyrosine	Tyr	Y
Valine	Val	V

Chapter 1

INTRODUCTION

1.1.1 Meiosis – a myriad of molecularly-mediated motions

The key to the success of a species lies in its ability to reproduce, generation after generation, in an ever-changing environment. There are two determinants which dictate the success of a species in this respect. 1) A species must be able to survive within its environment for long enough to reproduce and 2) a species must harbour an efficient mechanism to produce viable offspring.

Some of the most successful organisms alive are the prokaryotes which multiply by a process of binary fission, a conservative process in which division is preceded by cellular growth and genome duplication (Figure 1.1.1a) (Whitman *et al.*, 1998; Jensen *et al.*, 2002). An outwardly similar process, mitosis, underpins the multiplication of simple eukaryotic organisms, such as *Saccharomyces cerevisiae*, and cellular division during growth of higher organisms (Wieser and Pines, 2015). However, unlike prokaryotes, eukaryotes package their genetic material within chromosomes and utilise compartmentalisation to organise and segregate intracellular processes. This added complexity necessitates additional measures to facilitate and ensure accurate duplication. Thus, mitosis represents an intricate series of molecular events including the breakdown of the nuclear envelope, the assembly of the mitotic apparatus, alignment of chromosomes on the metaphase plate and their subsequent equational segregation forming two genetically identical progeny (Figure 1.1.1b).

However, multicellular eukaryotic organisms, from plants to mammals, replicate through sexual reproduction. Although exceptions exist, such as in the haploid (i.e. containing half the usual chromosome complement) males of the *Hymenoptera* order and in plant species which alternate between diploid and haploid generations, the majority of higher-order eukaryotic species are diploid with sexual reproduction culminating in the fusion of one male and one female haploid gamete, restoring the full chromosome complement within the resultant zygote (Maruyama *et al.*, 2016; Branstetter *et al.*, 2018). The zygote, through successive mitotic divisions, ultimately develops into a sexually mature adult which can reproduce once more. So long as each organism gives rise to at least one sexually successful progeny, on average, the population of a species can persist over generations.

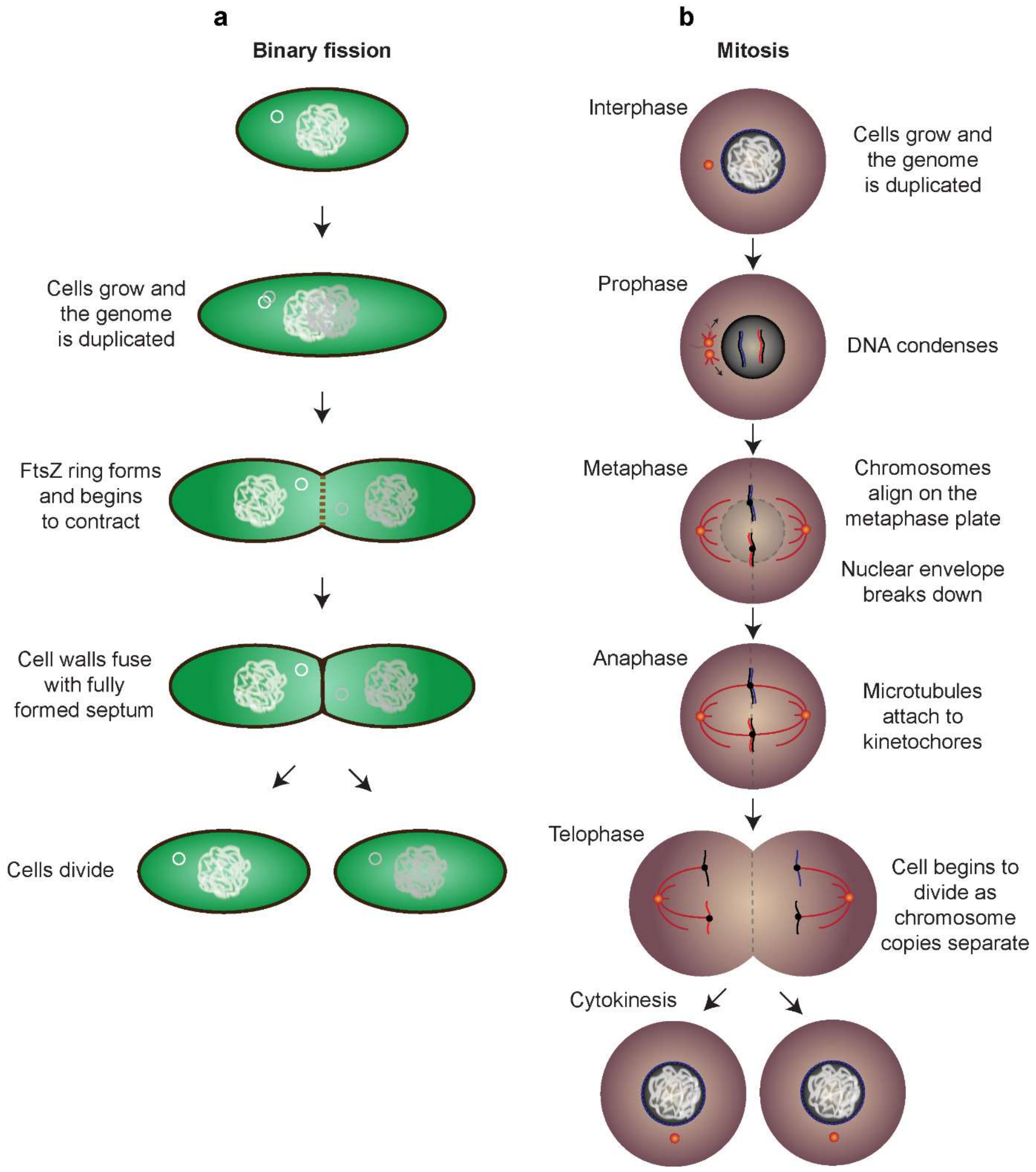
a
Binary fission
Cells grow and the genome is duplicated
FtsZ ring forms and begins to contract
Cell walls fuse with fully formed septum
Cells divide
b
Mitosis
Interphase
Cells grow and the genome is duplicated
Prophase
DNA condenses
Metaphase
Chromosomes align on the metaphase plate
Nuclear envelope breaks down
Anaphase
Microtubules attach to kinetochores
Telophase
Cell begins to divide as chromosome copies separate
Cytokinesis

Figure 1.1.1| Cellular division for replication, growth, and repair. a) The multiplication of prokaryotes occurs through the process of binary fission in which the genome and organelles are duplicated in a growing cell and segregated upon division. **b)** Eukaryotic organisms package their DNA within the nucleus as chromosomes. Chromosomes must undergo a phase of DNA compaction and duplication whilst the cellular architecture undergoes major reconstruction as the nuclear envelope is degraded. Microtubules attach to the kinetochore and exert tension to segregate copied chromosomes into dividing cells.

The production of haploid gametes requires a specialised form of cellular division, named meiosis, in which diploid progenitor cells undergo two rounds of cellular division without an intermediate phase of genome duplication to form four haploid cells (Figure 1.1.2). The first meiotic division (meiosis I) is preceded, as per mitosis, by interphase during which DNA is replicated in S "synthesis" phase resulting in a doubling of the usual chromosome complement. Replicated chromosomes are retained in association as sister chromatid pairs by cohesion complexes (Klein *et al.*, 1999; Onn *et al.*, 2008), discussed later. In *Homo sapiens*, 46 chromosomes (of which 23 are maternally inherited and 23 are paternally inherited) are duplicated to give 46 pairs of sister chromatids. During the onset of meiosis I, homologous chromosomes form maternal-paternal pairs and exchange genetic material through recombinatorial processes before segregating into diploid progeny. Without further replication of the genome, a second round of division, meiosis II, results in the formation of four, genetically distinct, haploid progeny. Here, the generation of genetic variation through exchange of maternal and paternal DNA, alongside spontaneous mutagenesis, provides the underlying basis for diversity within a species. An important consequence of this process is that genetic modifications which confer a selective advantage by improving sexual success are preferably inherited. The theory of evolution of species is founded upon this principal of natural selection and, therefore, ensuring the fidelity of equational chromosome segregation whilst permitting genetic exchange is key to the success of an organism over millennia.

The mechanisms by which cells ensure the faithful and accurate segregation of chromosomes into the progeny of meiosis I are highly controlled and involve the fine orchestration of numerous cellular processes. Both mitosis and meiosis I are defined by a reduction in chromosome number from 2n to n (i.e. 92 to 46 chromosomes in humans). However, they differ in that, in mitotically dividing cells, division is coupled with the separation of sister chromatids, whereas during meiosis I, chromosomes firstly locate and align with their cognate, homologous counterpart (i.e. a maternally-derived sister chromatid pair partners with its homologous, paternally-derived, sister chromatid pair) prior to division in which it is the homologous chromosome pairs which are separated. Therefore, whilst mitosis is a conservative process, the progeny of meiosis I are genetically non-identical, containing a mixture of maternally and paternally derived chromosomes. Meiosis I is followed by meiosis II, a mitosis-like division in which sister chromatids are separated into haploid progeny.

Whilst many features of the mitotic cycle are retained, the described distinction between mitosis and meiosis I originates through the execution of a highly specialised, meiosis-specific molecular program involving the action of countless meiosis-specific factors and protein assemblies. The successful passage through meiosis I is dependent upon the following: 1) The correct pairing of homologous chromosomes, 2) the exchange of genetic material by chromosomal crossover events and 3) the segregation of homologous pairs into the progeny. Each of these are dependent upon specific protein-protein and protein-DNA interactions and the formation of key proteinaceous assemblies and it is these which provide the basis for the following discussion and subsequent study. The meiotic process of the mammalian species will constitute the core of the discussion although comparisons to other organisms will be drawn upon throughout.

1.1.2 The first meiotic division in mammals

Meiosis I, as per mitosis, is composed of four stages: prophase, metaphase, anaphase and telophase. Homologous chromosome pairs are aligned during meiotic prophase I and subsequently localise to the cellular midline and bi-orientate through attachment of the mitotic apparatus during metaphase. In anaphase, chromosome pairs are separated by tension forces generated by microtubule-associated motor proteins with telophase being characterised by the segregation of half of replicated components in each of the progeny. Meiotic prophase I can be further divided into the stages known as leptotene, zygotene, pachytene, diplotene, and diakinesis, each being defined by distinct cellular and chromosomal architectures. Though, as meiosis entails a continuous flow of events and morphological states, rather than occurring in a basic step-wise manner, there is no absolute distinction between the sequential phases and, hence, cells are frequently referred to as being, for example, “early-leptotene”, “late zygotene”, or “mid-pachytene”. The events occurring within the meiotic prophase I are particularly ornate and form the basis for the following discussion. An overview of the mammalian meiotic prophase I is outlined below and depicted in Figure 1.1.2a. It should be noted that, although overarchingly recognisable across evolution, there exist species-specific alterations to the meiotic program of which key and/or interesting differences are highlighted in the subsequent detailing of the individual component processes.

1. Post-genome replication, chromosomes begin to condense, forming thin threads by the leptotene stage of meiotic prophase I. During this period, an array of 200-400 double-strand breaks

(DSBs) are induced across the genome (Barlow *et al.*, 1997; Lenzi *et al.*, 2005; Oliver-Bonet *et al.*, 2005; Baudat and de Massy, 2007).

2. Zygotene follows in which physical connections between homologous chromosomes are established through the formation of inter-homologue DSB-intermediates (Hunter, 2015). DSB-dependent pairing is facilitated by telomere-led rapid prophase movements driven through the connection of chromosome ends to the nuclear envelope and cytoskeleton (Lee *et al.*, 2015) culminating in the formation of the characteristic meiotic bouquet, a polarised, horse-shoe shaped chromosome structure in which all telomeric ends are spatially clustered (Zickler and Kleckner, 1998).

3. Upon the initial tethering of chromosomes, the synaptonemal complex (SC), a ladder-like proteinaceous scaffold begins to assemble between opposing axial elements, now termed lateral elements (Page and Hawley, 2004). During pachytene, this tripartite structure enforces a three-dimensional architecture seemingly required for the processing of double-strand breaks by non-crossover (NCO) and crossover (CO) recombination. CO maturation is mediated by a number of protein complexes and CO frequency and spacing is regulated by CO interference, with as few as one to two forming per chromosome in humans (Hunter, 2015). COs physically manifest as chiasmata, direct linkages between homologue pairs which persist after SC disassembly (Petronczki *et al.*, 2003). The disassembly of the SC marks the end of meiotic prophase I and is followed by metaphase in which homologues are separated and segregated to alternate progeny during diplotene (Barlow *et al.*, 1997).

1.1.3 Nuclear architecture, dynamics and premeiotic DNA replication

Eukaryotic chromosomes are enclosed within the nucleus, a cellular compartment encapsulated by the double-membraned nuclear envelope. The outer-membrane is continuous with the endoplasmic reticulum whilst the inner-membrane is associated with the nuclear lamina. The two meet at the sites of nuclear pore complexes (NPCs) which facilitate cytoplasmic-nuclear transport and tethering of the nuclear lamina to the cytoskeleton (Goldberg and Allen, 1996; Hoelz *et al.*, 2011; Goldberg, 2017). Throughout the early stages of meiotic prophase I, the nuclear membrane provides a fluid two-dimensional plane through which telomeric ends glide under a cytoskeletal driving force (Lee *et al.*, 2015). In mammalian species, the nucleus protects chromosomes from the microtubule-organising centres, the centrosomes - intricate structures with eight-fold symmetry (Fu *et al.*, 2015). This precludes precocious spindle association allowing time for the processes of chromosome alignment and synapsis to complete. The timely onset of chromosome segregation is thus triggered by the breakdown of the nuclear envelop (NEBD). In this, the nucleus is disassembled through tubulation into the endoplasmic reticulum (De Magistris and Antonin, 2018) allowing for microtubule attachment to the chromosome kinetochores. In other organisms, such as yeast, division occurs fully within the context of the nucleus and is dependent upon nuclear expansion and division (Kutay and Hetzer, 2008; Takemoto *et al.*, 2016). This species difference is congruent with the localisation of the microtubule-organising centres; human centrosomes are cytoplasmic whilst the spindle pole body of *Saccharomyces pombe* is fixed within the nuclear envelope (Ding *et al.*, 1997) whereas in S*accharomyces cerevisiae* it is inserted into the nuclear envelope prior to metaphase (Jaspersen and Winey, 2004).

During the premeiotic S-phase, as in mitosis, chromosomes are replicated and remain bound in pairs of sister chromatids. Unusually, premeiotic S-phase is extended in comparison to the mitotic S-phase, for unknown reasons. However, it is postulated that differences in chromosome dynamics and repair procedures between meiosis and mitosis which, respectively, affect and correct errors during the replicative process could be responsible (Forsburg, 2002). Accordingly, the replicative phase length appears to be governed by key meiosis-specific factors which play independent roles early in meiotic progression (Cha *et al.*, 2000). Upon replication, cohesion is quickly established through cohesion

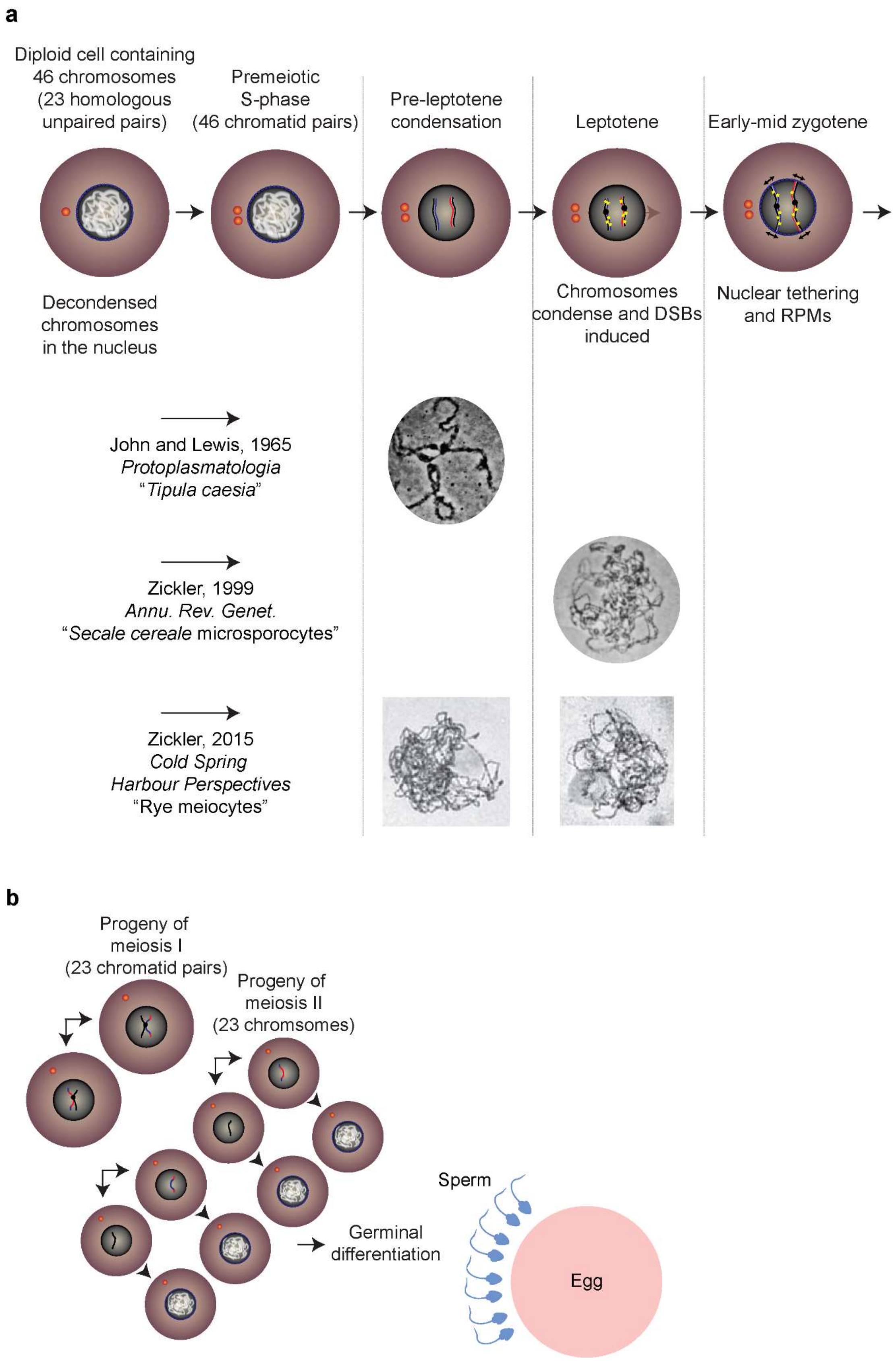
a
Diploid cell containing 46 chromosomes (23 homologous unpaired pairs)
Premeiotic S-phase (46 chromatid pairs)
Pre-leptotene condensation
Leptotene
Early-mid zygotene
Decondensed chromosomes in the nucleus
Chromosomes condense and DSBs induced
Nuclear tethering and RPMs
John and Lewis, 1965
Protoplasmatologia
"*Tipula caesia*"
Zickler, 1999
Annu. Rev. Genet.
"*Secale cereale* microsporocytes"
Zickler, 2015
Cold Spring Harbour Perspectives
"Rye meiocytes"
b
Progeny of meiosis I (23 chromatid pairs)
Progeny of meiosis II (23 chromsomes)
Germinal differentiation
Sperm
Egg

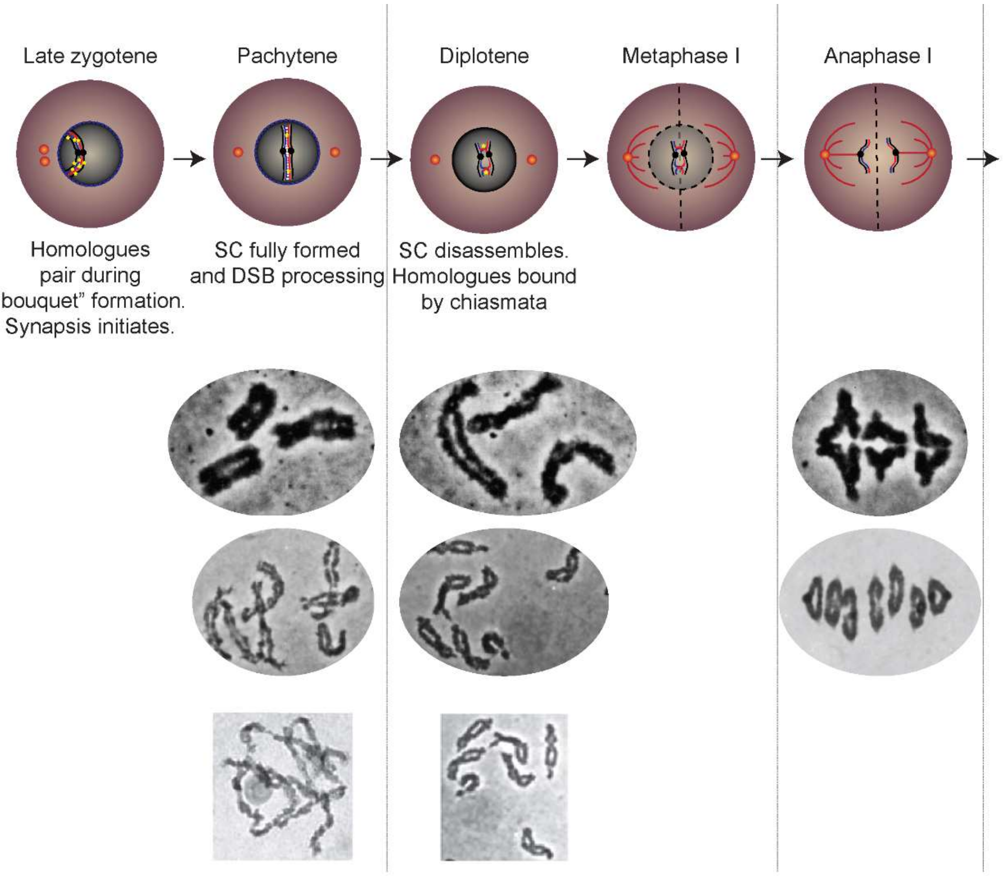
Late zygotene
Pachytene
Diplotene
Metaphase I
Anaphase I
Homologues pair during "bouquet" formation. Synapsis initiates.
SC fully formed and DSB processing
SC disassembles. Homologues bound by chiasmata

Figure 1.1.2| The stages of meiosis. a) During interphase, DNA is in a decondensed state and is replicated, concurrent with centrosome (orange dots) duplication, during a pre-meiotic S phase. Prior to the onset of the first meiotic division, replicated chromosomes (bound by cohesins as sister-chromatid pairs) begin to condense and initiate pre-meiotic pairing (not depicted in this schematic). During leptotene, double strand breaks are induced across the genome (indicated by stars) which are processed to create single-stranded search probes. During a phase of rapid prophase movements (indicated by black, double-headed arrows) homologous chromosomes locate their partners and begin to synapse during zygotene. Fully synapsed chromosomes are visible in pachytene, bound by the synaptonemal complex within which DSB repair intermediates are processed to create one crossover per chromosome arm. Subsequently, the SC disintegrates leaving chromosomes in association through chiasmata. The nuclear envelope breaks down allowing attachment of microtubules to the kinetochores, allowing chromosome segregation during anaphase, thus concluding meiosis I. **b)** Meiosis II follows and consists of a mitotic-like division in which sister-chromatids are released from their cohesin-mediated binding and segregated into haploid progeny. These then further differentiate into either sperm or eggs.

complexes (discussed later) and undergo compaction to produce linear arrays of chromatin loops through the action of condensing complexes utilising an ATP-dependent "loop extrusion" mechanism (Nasmyth, 2001; Goloborodko *et al.*, 2016). However, at this stage there is no discernible distinction between bound sister chromatids (image of pre-leptotene chromatid pair presented in Figure 1.1.3a,b) (Sumner, 1991).

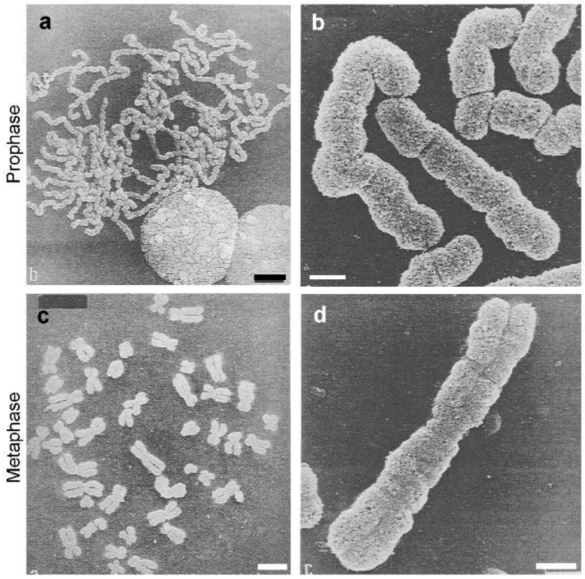

Figure 1.1.3| Chromosome morphology during cell division. a,b) Upon initial condensation, during early prophase (i.e. leptotene in meiosis), no distinction between replicated chromosomes is visible, with bound sister chromatids appearing as a single, segmented entity (scale bars represent 5 and 1 µm, respectively). **c,d)** During metaphase, a clear furrow is visible, slightly separating bound sister chromatids during mitotic metaphase (scale bars represent 5 and 1 µm, respectively).

1.1.4 Premeiotic/early leptotene homologue pairing

During the premeiotic S-phase, replicated chromosomes, which cannot be distinguished as two individual sister chromatids, already undergo partial condensation, forming fine, elongated fibres by early-leptotene (Figure 1.1.2a). At this stage, there is already evidence of early pairing between homologous chromosomes driven by numerous DSB-independent mechanisms, both homology-dependent and homology-independent (Zickler and Kleckner, 2015). It is the exception that these mechanisms constitute the sole mechanism of homologue-pairing during the meiotic cycle, with most organisms establishing pairing through further double-strand break (DSB)-dependent mechanisms which shall be discussed later in this chapter (Zickler and Kleckner, 2015). However, it was these organisms which do not utilise DSB-dependent pairing mechanisms that allowed for early/alternative mechanisms of pairing to become apparent.

The clustering of homologues through homologous sequences, such as those within centromeric and telomeric regions, is evidenced in multiple organisms. In *Caenorhabditis elegans* (Christophorou *et al.*, 2013) and *Zea mays* (Zhang *et al.*, 2013), premeiotic and early-leptotene centromeric associations facilitate relative positioning of homologues whilst in *Arabidopsis thaliana* (Armstrong *et al.*, 2001) and *Mus musculus* (Boateng *et al.*, 2013) clustering of telomeres functions to achieve similar results. In mice, telomeric clustering is dependent upon the DNA topoisomerase SPO11-β which is responsible for DSB-induction during leptotene (SPO11-α is expressed post-pachytene), but independent of DNA cleavage, as evidenced through retention of premeiotic pairing in knock-in mice expressing a catalytic-dead mutant of SPO11-β whilst premeiotic pairing is lost in the homozygous knockout (Bellani *et al.*, 2010; Boateng *et al.*, 2013).

Organisms, including *Mus musculus* (Krueger *et al.*, 2012) and *Saccharomyces cerevisiae* (Weiner and Kleckner, 1994) exhibit homologous pairing in somatic cells, termed somatic pairing, in which homologues remain in association through the premeiotic growth and synthesis phases. Although somatic pairing is not observed within somatic cells of *Drosophila melanogaster*, the mechanism is activated five cycles prior to the meiotic division allowing for pairing establishment (Joyce *et al.*, 2013). Alternatively, in *Caenorhabditis elegans*, homologous pairing initiates at pairing centres, regions containing arrays of repetitive DNA sequences, primarily proximal to the telomeres (MacQueen *et al.*, 2005; Bhalla and Dernburg, 2008). Pairing in this manner appears to be dependent upon the local recruitment of a family of zinc-finger containing proteins (Phillips and Dernburg, 2006).

Interestingly, in *Saccharomyces pombe*, a meiosis-specific non-coding RNA in coordination with Mei2 and Mmi1, which associates within specific loci within chromosomes act as nuclei for homologue pairing (Ding *et al.*, 2013). In some fungi, the mechanistically-unclear phenomena of repeat-induced point mutation (RIP) and methylation-induced premeiotically (MIP) appear to mediate the alignment of short repeat sequences between homologous DNA sequences (Selker, 1990; Gladyshev and Kleckner, 2014).

1.1.5 Formation of the axial elements

During leptotene, the sister chromatids of each replicated chromosome remain tightly bound (Klein *et al.*, 1999; Onn *et al.*, 2008) and undergo further organisation and compaction by the formation of axial elements (AEs) (Page and Hawley, 2004). These represent a protein core from which emanate evenly spaced chromatin loops (a spacing of 20 loops per µm is evolutionarily conserved (Kleckner, 2006)). The frequency, however, of meiotic loops is species- and sex-specific, elegantly demonstrated in humans in which the chromosomes of male are twice as short as their female counterparts and, correspondingly, harbour longer chromatin loops (Tease and Hulten, 2004). This difference appears to not be related to the underlying DNA sequence, as demonstrated through the adoption of host loop spacing upon placement of heterologous chromosomes within a non-native host cell (Loidl *et al.*, 1995).

The underlying protein core of the axial element consists of two protein groups: the cohesins (Klein *et al.*, 1999) and the axial element proteins, synaptonemal complexes proteins 2 and 3 (SYCP2/3) (Kouznetsova *et al.*, 2005). Cohesins are ubiquitously expressed, yet undergo meiosis-specific alterations (Watanabe, 2004). Cohesins form trimeric ring-shaped protein complexes consisting of two SMC proteins which together constitute a coiled-coil/hinge/coiled-coil, V-shaped heterodimer, with the ends being connected by a linking "α-kleisin" molecule. Cohesins are thought to entrap DNA, bind sister chromatid pairs, and facilitate chromatin looping (Nasmyth and Haering, 2009). In mitosis, cohesin complexes are formed by SMC1, SMC3 and the α-kleisin, SCC1 (Nasmyth and Haering, 2005). During mitotic onset, in prophase, most of the cohesion between sisters is lost (Sumara *et al.*, 2002) whilst centromeric cohesion persists to maintain sister chromatid association. Centromeric cohesion is ultimately removed through proteasome-mediated cleavage of SCC1 in a separase-dependent manner in response to APC/C-mediated ubiquitylation upon bivalent biorientation to allow for chromosome segregation (Nasmyth and Haering, 2009). However, despite also containing the mitotic SMC1 and SMC3 (Eijpe *et al.*, 2000), the cohesins of the meiotic chromosome axis are altered and incorporate meiosis-specific components including the α-kleisins REC8 and RAD21L (Ishiguro *et al.*, 2014), SMC1β (Watanabe, 2004) and accumulate STAG3 through leptotene (Prieto *et al.*, 2001; Biswas *et al.*, 2016). Unlike mitotic SCC1, both REC8 and RAD21L avoid depletion during prophase and remain associated with the chromosome arms with REC8 overtly preventing sister-chromatid disjunction and untimely recruitment of SC proteins (Xu *et al.*, 2005; Agostinho and Hoog, 2016; Agostinho *et al.*, 2016). Additionally, like SPO11, meiotic cohesin Rec8 plays an additional role in premeiotic homology pairing (Ishiguro *et al.*, 2014). These alternative mechanisms ensure sister-chromatid attachment during metaphase, allowing only for the separation of homologous chromosomes.

The integrity of the axial element is further maintained by both the axial element proteins, SYCP2 and SYCP3. SYCP3 was first identified in rat as a meiosis-specific axial element component through screening a testis cDNA expression library using antibodies raised against purified synaptonemal complexes (Lammers *et al.*, 1994). The SYCP3 core (residues 66-230 of 236 total) constitutes a four-helical bundle of which the crystal structure was solved revealing an anti-parallel organisation from which unstructured N-termini emanate (PDB 4CPC; Figure 1.1.4a) (Syrjanen *et al.*, 2014). The structure of murine SYCP3 (PDBs 6DD8 and 6DD9) was also solved demonstrating an equivalent fold as its human homologue (West *et al.*, 2019). The N-termini are capable of associating with DNA whilst collaborating with the C-termini to mediate end-to-end association, forming striated, fibrous structures both *in vivo* (Yuan *et al.*, 1998) and *in vitro* (Syrjanen *et al.*, 2014), observable by electron microscopy (Figure 1.1.4b). The formation of these structures can be completely abrogated through the deletion of 6 residues at the extreme C-terminus of SYCP3, implicating these residues in SYCP3 self-assembly (Syrjanen *et al.*, 2014).

SYCP2 was identified during the same screening procedure that identified SYCP3 (Offenberg *et al.*, 1998). Sequence analysis of SYCP2 (1530 residues in total) reveals the presence of two domains separated by a flexible linker (Offenberg *et al.*, 1998). An N-terminal structured domain consists of two elements (a super-helical, armadillo-like fold followed by a twisted β-sheet) whilst a C-terminal domain (residues 1356-1523) is predicted to be helical (Figure 1.1.4c) (Feng *et al.*, 2017). The C-terminal helical region of SYCP2 interacts with the helical domain of SYCP3 (West *et al.*, 2019) with its deletion blocking the recruitment of SYCP3 to the chromosome axis (Yang *et al.*, 2006).

Both components localise along the entire length of the axial elements (Schalk *et al.*, 1998). Single molecule DNA experiments have shown that the association of SYCP3 with DNA induces DNA compaction, suggesting its role in the shortening of leptotene chromosomes (Syrjanen *et al.*, 2017). Correspondingly, the homozygous knockout of SYCP3 results a doubling of chromosome axis length and, in keeping with the inverse relationship between chromosome length and loop size, a halving of the loop size (Novak *et al.*, 2008). Despite being essential for meiotic progression and fertility (Yuan *et al.*, 2000; Yang *et al.*, 2006), recruitment of neither of these protein components is essential for the formation of a partially functional chromosome axis and the recruitment of DNA repair factors such as DMC1 and MSH4 (Pelttari *et al.*, 2001).

Although the overall chromatin status of homologous chromosomes is known to be dynamic, the chromatin status directly proximal to the chromosome axis is unknown (Zickler and Kleckner, 1999). Chromatin status describes whether or not, and in what manner, chromosomal DNA is packaged by histone complexes known as nucleosomes. During interphase, genetically active regions of the chromosome (euchromatin) are loosely packaged, exhibiting a "beads on the string" organisation (in which beads are nucleosomes and the string is DNA) whilst genetically inactive regions (heterochromatin) are highly condensed and associate with the nuclear lamina, exhibiting a tightly wound super-helix in which nucleosomes condense to form a 30 nm fibre (Olins and Olins, 2003; Garcia-Saez *et al.*, 2018). During meiotic division, chromosomes are packaged as heterochromatin though how the regions which make direct contacts with the synaptonemal complex are packaged is unknown. This is relevant when considering the mode by which proteins responsible for forming the axial elements are recruited and further in understanding its overall architecture such that we might build a molecular model for how axial elements of homologous chromosomes juxtapose and mature through meiotic progression.

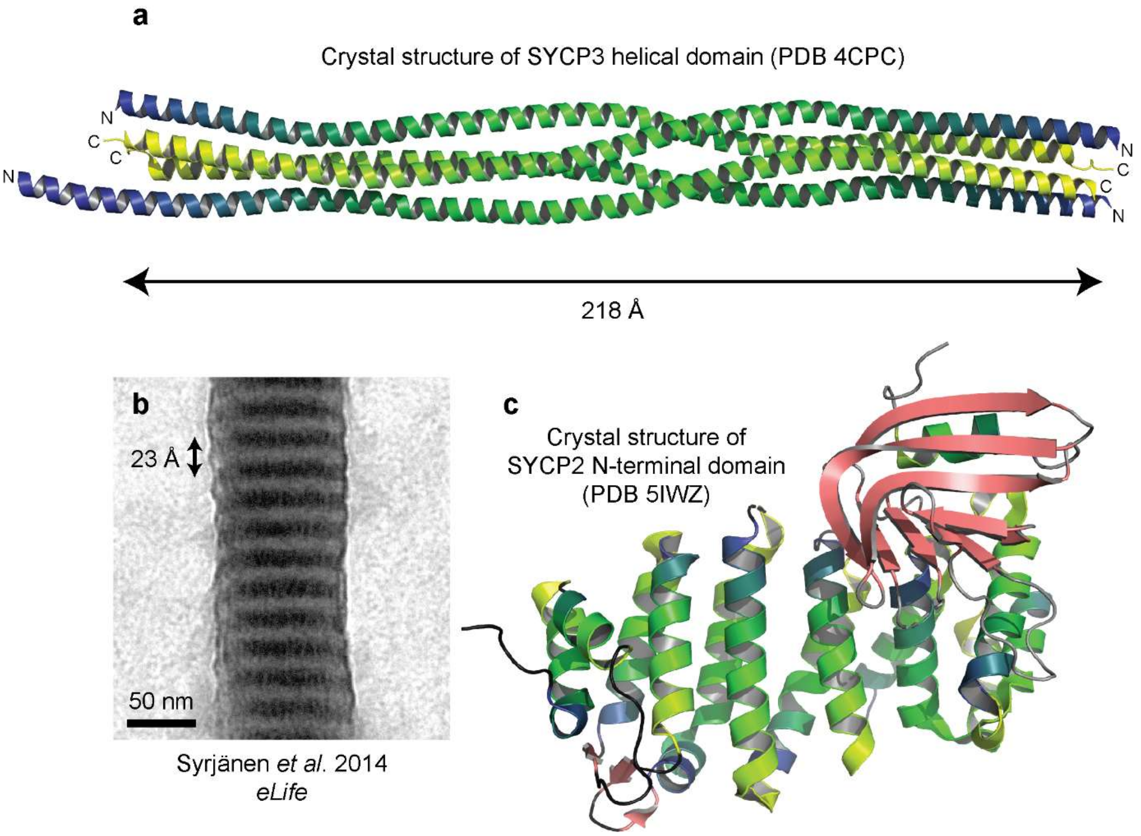

Figure 1.1.4| SYCP2 and SYCP3 are structural components of the mammalian lateral elements. a) SYCP3 forms an anti-parallel four-helical bundle measuring 218 Å in length. **b)** Electron micrograph displaying an SYCP3 assembly reminiscent of those formed upon overexpression *in vivo* and the lateral element structures of the SC. The repeat measures 23 Å. **c)** The crystal structure of the SYCP2 N-terminal domain with helices of the armadillo-like fold coloured in blue/green/yellow and a globular, twisted β-sheet in salmon pink (PDB 5IWZ).

1.1.6 Self-inflicted DSBs and homologous strand invasion reinforce homologue association

In humans, during leptotene, 200-400 DSBs are induced through the action of SPO11, described previously as having, independent of its catalytic activity, a role in homologous chromosome pairing (Barlow *et al.*, 1997; Lenzi *et al.*, 2005; Oliver-Bonet *et al.*, 2005; Baudat and de Massy, 2007; Bellani *et al.*, 2010). SPO11 is a dimeric evolutionarily conserved type II topoisomerase which cleaves both strands of double-stranded DNA through the concerted action of each subunit (Keeney, 2008). It utilises a transesterification mechanism dependent upon catalytic tyrosine residues (Y137 and Y138 in SPO11-α and SPO11-β, respectively) (Klapholz *et al.*, 1985; Keeney *et al.*, 1997; Roeder, 1997; Boateng *et al.*, 2013). The mechanism of cleavage is detailed in Figure 1.1.5 (Krogh and Shuman, 2000). The sites designated for cleavage by SPO11 occur within the looped sequences rather than axis-associated sequences and appear, at least in fission yeast, to be determined by underlying DNA sequence (Blat *et* *al.*, 2002; Ito *et al.*, 2014). Downstream chromosome synapsis, aberrant in the SPO11 knockout, can be restored through the exogenous induction of double-strand breaks by cis-platin (Romanienko and Camerini-Otero, 2000) or radiation (Carofiglio *et al.*, 2018).

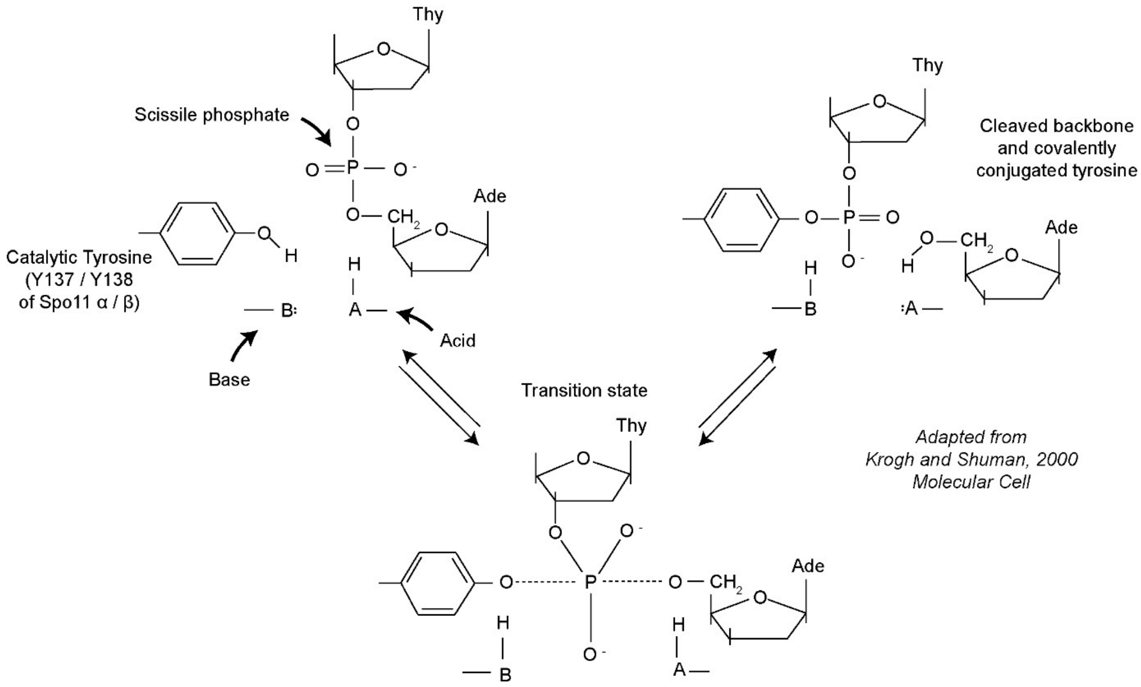
Thy
Scissile phosphate
Ade
Catalytic Tyrosine
(Y137 / Y138
of Spo11 α / β)
Base
Acid
Thy
Cleaved backbone
and covalently
conjugated tyrosine
Ade
Transition state
Thy
Ade
Adapted from
Krogh and Shuman, 2000
Molecular Cell

Figure 1.1.5| The catalytic mechanism of Spo11-mediated DNA double-strand break induction. SPO11 is responsible for the introduction of hundreds of double-strand breaks across the genome. It cleaves DNA through a transesterification mechanism involving a general base and acid and the hydroxyl group of a tyrosine residue. The figure above was adapted from (Krogh and Shuman, 2000).

The resultant double-stranded breaks are subsequently processed through 5’-3’ end-resection to create long, single-stranded DNA extensions. Assuming similarity with the mitotic machinery which process DSBs in preparation for homologous recombination, end-resection is mediated jointly by the MRN complex, CtIP, EXO1, BLM helicase, DNA2, and RPA (Nimonkar *et al.*, 2011; Davies *et al.*, 2015). The single-stranded extensions subsequently act as search probes which, through strand invasion in which one strand of the target double-stranded DNA is displaced to allow base pair-base pair interactions between the probe and target to find homologous regions within chromosomes (Figure 1.1.6).

Mediating the process of strand invasion are the recombinase proteins, RAD51 and its meiosis-specific counterpart DMC1, which displaces RPA (in addition to MEIOB/SPATA22 is meiosis) to coat the single-stranded DNA extensions to create a nucleoprotein filament. RAD51 presents a helical association of subunits whilst DMC1 organises as stacked rings on a thread (Figure 1.1.7a,b) (Baumann and West, 1998; Passy *et al.*, 1999; Luo *et al.*, 2013). The nucleoprotein filament subsequently invades the homologous chromosome to create a single-end invasion intermediate, a D-loop structure which undergoes downstream processing to eventually be repaired by crossover or non-crossover homologous recombination, a process and decision discussed later in this chapter (Figure 1.1.6) (Hunter and Kleckner, 2001). RAD51 and DMC1 were found to localise to axial associations between homologous chromosomes by immuno-gold localisation electron microscopy suggesting that strand invasion mediates close contacts between homologues (Figure 1.1.7c) (Tarsounas *et al.*, 1999). In SPO11 knock-out mice, in which DSBs are not induced, RAD51 and DMC1 are not recruited, resulting in meiotic stallage (Baudat *et al.*, 2000).

Although RAD51 and DMC1 co-localise, they have not been shown, biochemically, to interact. RAD51 and DMC1 are both structural and functional homologues of the archaeal recombinase RadA of which multiple crystal structures are available, adopting both helical and ring-like assemblies reminiscent of the structures coating DNA by electron microscopy (Figure 1.1.7d) (Bishop, 1994). For example, *Pyrococcus furiosus* RadA oligomerises as a heptameric ring (PDB entry 1PZN) whilst *Methanococcus voltae* RadA undergoes recursive self-associations within the crystal lattice to create a helix of indefinite length (PDB entry 2F1H). This is despite sharing an almost identical subunit fold, containing an N-terminal domain and a C-terminal ATPase domain (Figure 1.1.7e). The sequence which mediates its oligomerisation is an FxxA/G motif (indicated in red in all presented structures) which is shared by RAD51 and DMC1 of sexually reproducing organisms.

The structure of both filamentous RAD51 (PDB 5NWL) and ring-like DMC1 (PDB 6R3P) are known (Figure 1.1.7d) (Du and Luo, 2013; Brouwer *et al.*, 2018). Both adopt a similar fold to RadA (Figure 1.1.7e). However, DMC1 forms an octameric ring, whilst RAD51 forms helical filaments (Figure 1.1.7d). The functional relevance of this distinction is unknown though it appears that RAD51 and DMC1 have slightly different functions, with RAD51 being required for the recruitment of DMC1 and DMC1 being required for the disassembly of RAD51 (Bishop, 1994). Both RAD51 and DMC1 may be mediated by BRCA2, promoting their loading/unloading onto single-stranded DNA. This may be achieved through the concerted action of several recombinase-interacting sequences within BRCA2. For example, the BRC repeat sequences (encoded within the BRCA2 exon 11) are known to disrupt the oligomerisation of both recombinases by mimicking the self-association motif (Figure 1.1.7f) whilst a sequence (encoded within the BRCA2 exon 27) stabilises higher-order RAD51 oligomers (Pellegrini *et al.*, 2002; Davies and Pellegrini, 2007; Martinez *et al.*, 2016).

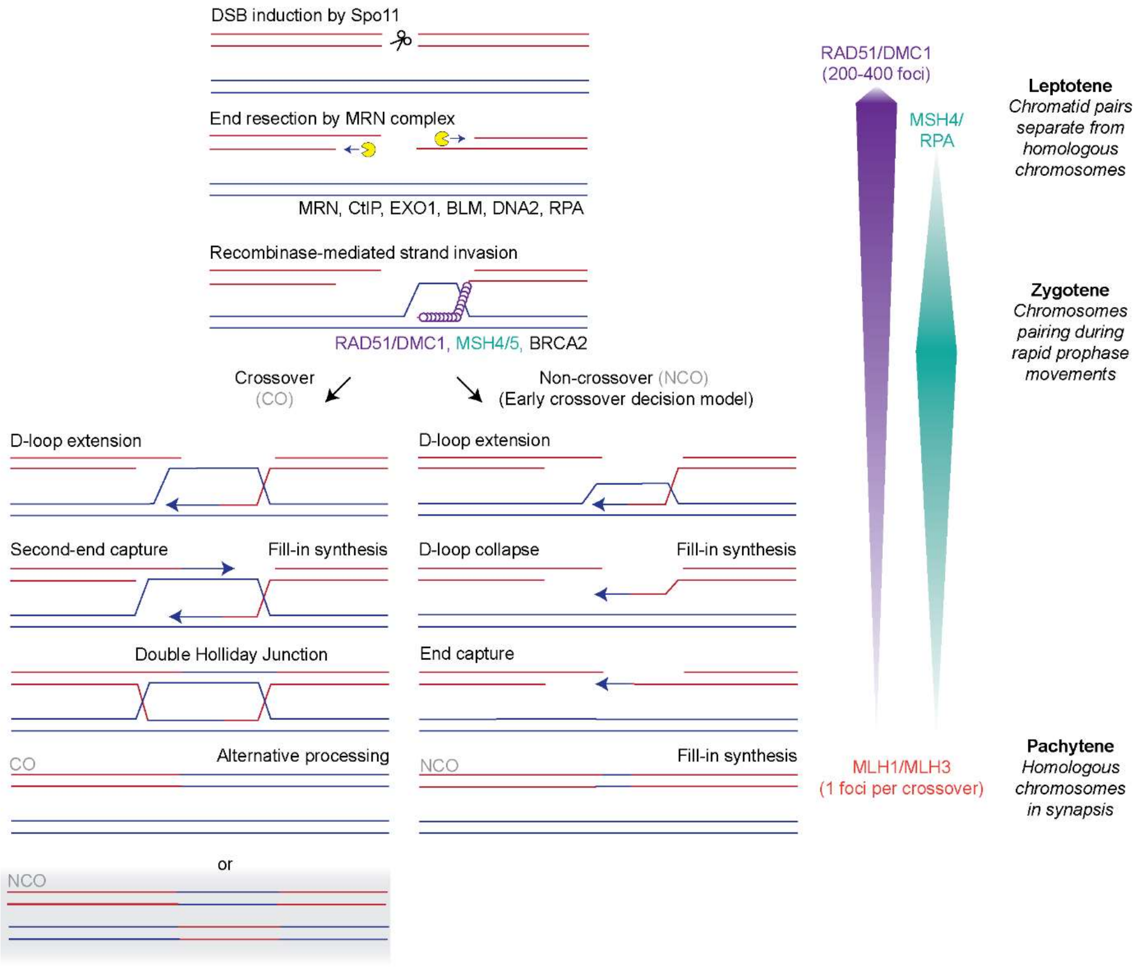
DSB induction by Spo11
End resection by MRN complex
MRN, CtIP, EXO1, BLM, DNA2, RPA
Recombinase-mediated strand invasion
RAD51/DMC1, MSH4/5, BRCA2
Crossover
(CO)
Non-crossover (NCO)
(Early crossover decision model)
D-loop extension
Second-end capture
Fill-in synthesis
Double Holliday Junction
CO
Alternative processing
or
NCO
D-loop extension
D-loop collapse
Fill-in synthesis
End capture
NCO
Fill-in synthesis
RAD51/DMC1
(200-400 foci)
MSH4/
RPA
MLH1/MLH3
(1 foci per crossover)
Leptotene
Chromatid pairs separate from homologous chromosomes
Zygotene
Chromosomes pairing during rapid prophase movements
Pachytene
Homologous chromosomes in synapsis

Figure 1.1.6| Meiotic recombination. Homologous recombination in mammalian meiosis indispensable for homologue pairing. It is initiated through a programmed series of double-strand breaks which are subsequently processed to create single-stranded probes which enact a homology search to tether the homologue and form a D-loop. These DNA repair intermediates are processed and are directed for either crossover or non-crossover repair.

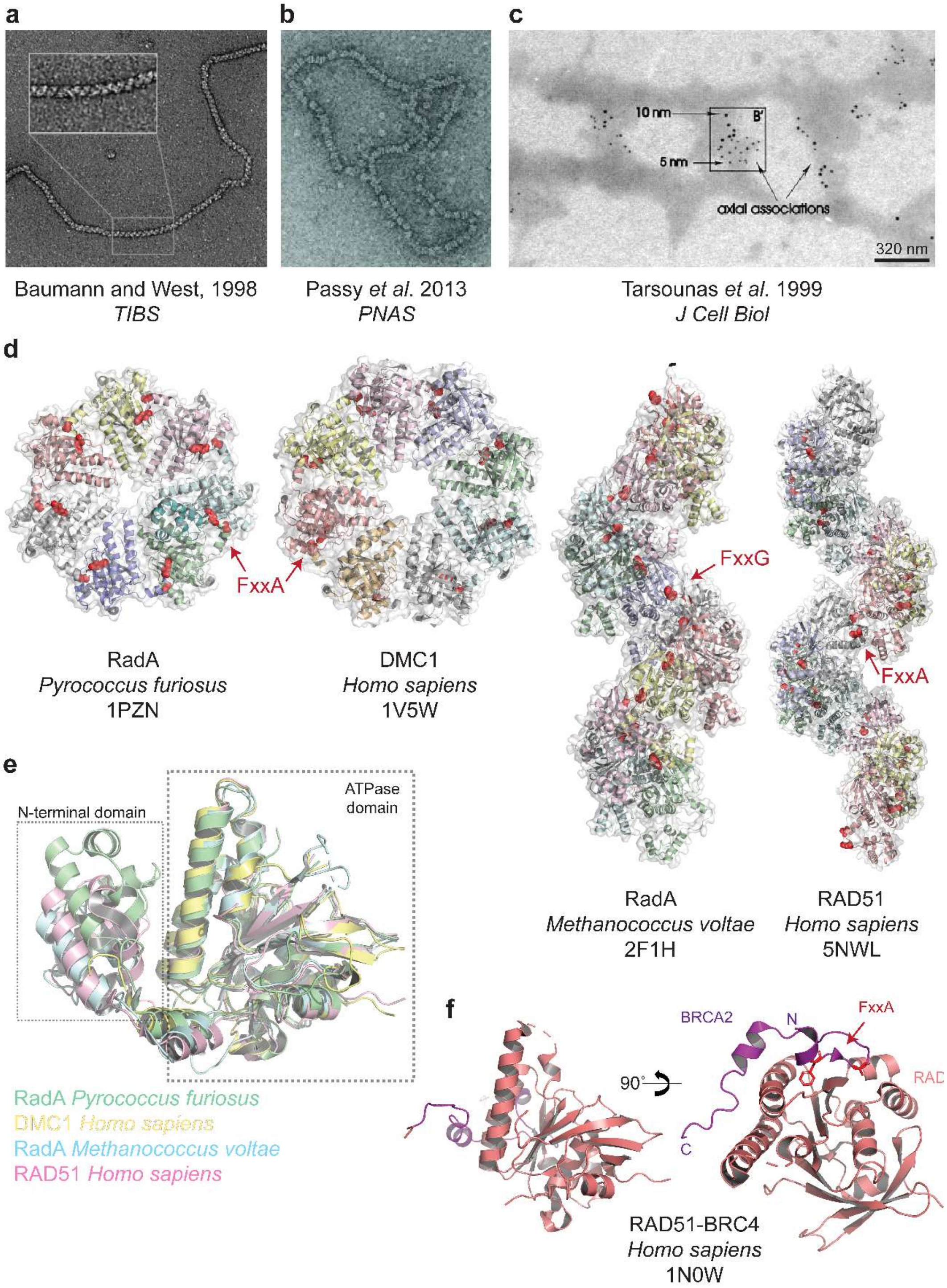
a
b
c
10 nm
B'
5 nm
axial associations
320 nm
Baumann and West, 1998
TIBS
Passy *et al.* 2013
PNAS
Tarsounas *et al.* 1999
J Cell Biol
d
FxxA
FxxG
FxxA
RadA
Pyrococcus furiosus
1PZN
DMC1
Homo sapiens
1V5W
RadA
Methanococcus voltae
2F1H
RAD51
Homo sapiens
5NWL
e
N-terminal domain
ATPase domain
RadA *Pyrococcus furiosus*
DMC1 *Homo sapiens*
RadA *Methanococcus voltae*
RAD51 *Homo sapiens*
f
BRCA2
N
FxxA
RAD
90°
C
RAD51-BRC4
Homo sapiens
1N0W

Figure 1.1.7| Recombinase-mediated strand invasion. a,b) Nucleoprotein filaments formed by **a)** RAD51 and **b)** DMC1 on double-stranded DNA and partially duplex ΦX174 virion DNA, respectively. **c)** Electron microscopy visualisation of RAD51 and DMC1 associated axial associations of mouse chromosomes formed by strand invasion (Tarsounas *et al.*, 1999). 10 nm particles = DMC1, 5 nm particles = RAD51. **d)** Crystal structure of ring-like RadA (*Pyrococcus furiosus*), ring-like DMC1 (*Homo sapiens*), filamentous RadA (*Methanococcus voltae*) and filamentous RAD51 (*Homo sapiens*). **e)** Superimposition of a single subunit from 1PZN, 1V5W, 2F1H and 5NWL demonstrating the similarity of the ATPase domain fold. The crystal structure of DMC1 does not contain the N-terminal domain **f)** Crystal structure of DMC1 ATPase domain (PDB 1V5W). **f)** The crystal structure of the RAD51 (red)-BRCA2 BRC repeat 4 (purple) complex in which the FxxA motif (red) is highlighted demonstrating the docking of the phenylalanine into a hydrophobic cleft (Pellegrini *et al.*, 2002).

1.1.7 Rapid prophase movement of chromosomes facilitates pairing

To facilitate the process of homology searching by strand invasion, during zygotene, chromosomes undergo a period of highly dynamic movements. After the formation of thin, thread-like, axial cores, chromosomes undergo further compaction and embark upon potentially the most dynamic phase of the entire cycle (Zickler and Kleckner, 1998). In this, the telomeric ends of the chromosomes are tethered to the nuclear envelope and, through the transmission of cytoskeletal forces, are quickly moved about the nucleus in what are known as rapid prophase movements (RPMs) (Zickler and Kleckner, 2015). These are thought to both facilitate homology searching by the single-stranded DNA extensions, allowing quick searching of the genome, whilst breaking unwanted inter-chromosomal associations (Koszul and Kleckner, 2009). RPMs appear to be a conserved feature of the meiotic cycle, having been observed in diverse organisms such as *Saccharomyces cerevisiae* (Bhalla and Dernburg, 2008), *Saccharomyces pombe* (Chikashige *et al.*, 1994), mice (Lee *et al.*, 2015), and *Caenorhabditis elegans* (Woglar and Jantsch, 2014). Although there are key differences in RPM dynamics between organisms, such as in telomere-clustering density and movement in relation to the location of the microtubule-organising centre, functionally conserved protein complexes drive this process across evolution. These complexes include Shelterin (responsible for preventing the DNA damage response at telomeres), the LINC complex (which connects the cytoskeleton with the nucleoskeleton), and the meiotic telomere complex (which contains newly discovered components and is responsible for recruitment of telomeres to the nuclear envelope). These complexes, and research performed as part of this study, shall be discussed thoroughly in Chapter 4.

1.1.8 Formation of the synaptonemal complex in mammals

Upon proper pairing, the synaptonemal complex forms, a proteinaceous super-structure which assembles between paired homologous chromosomes. The SC comprises a tripartite organisation, consisting of a central midline element, chromosome-associated lateral elements and transverse filaments connecting the two (Figure 1.1.8) (Page and Hawley, 2004). The SC is critical for meiotic progression with the knockout of any individual component resulting in infertility, embryonic death due to aneuploidy, or recurrent miscarriage (Yuan *et al.*, 2000; Matzuk and Lamb, 2002; de Vries *et al.*, 2005; Bolcun-Filas *et al.*, 2007; Hamer *et al.*, 2008; Bolcun-Filas *et al.*, 2009; Bolor *et al.*, 2009; Kouznetsova *et al.*, 2011; Schramm *et al.*, 2011; Page and Silver, 2016).

The length of the SC is chromosome dependent and varies across organisms. Human SCs have a maximum length of 24 µm and an average length of 11.7 µm (Solari, 1980). The SCs of females are approximately 60 % longer, with 60 % increase in crossover frequency (Jones and Croft, 1989; Wallace and Wallace, 2003; Tease and Hulten, 2004). The width of the central region is conserved across evolution at approximately 100 nm (Figure 1.1.8) (von Wettstein *et al.*, 1984). However, this is also sex-dependent with the inter-lateral element (inter-LE) distance (a value measured as being wider than the width of the SC) being 210.0 ± 3.7 nm in males and 143.0 ± 2.8 nm in females, with similar observations being made in *Bombyx mori* and insects (Rasmussen, 1979; von Wettstein *et al.*, 1984; Agostinho *et al.*, 2018). In addition to inter-LE distance, the width of the central element (CE) displays similar disparity between the sexes, measuring 24.6 ± 0.5 nm in males and 22.1 ± 0.6 nm in females (Agostinho *et al.*, 2018). Synaptonemal complexes were first identified in crayfish by Montrose K. Moses in 1956 and although these initial structures were not quite as striking as some which have been visualised since, this discovery paved the way for a whole new field of biological research focusing upon the role of the SC in meiotic division (Moses, 1956). Presented within Figure 1.1.8 are SC structures from multiple organisms, from fungi to humans, including model organisms such as *Caenorhabditis elegans* and *Drosophila melanogaster* demonstrating their overt evolutionary conservation (Solari and Tres, 1970; Westergaard and von Wettstein, 1972; von Wettstein *et al.*, 1984; McKim *et al.*, 2002; Schramm *et al.*, 2011; De Muyt *et al.*, 2014; Schucker *et al.*, 2015; Cahoon *et al.*, 2017). Some of the central element structures are lattice-like, such as those of insects, *C. elegans*, and some plants, though most are amorphous (Westergaard and von Wettstein, 1972). Despite having been studied extensively cytologically, SCs have up until recently eluded structural characterisation at the protein level.

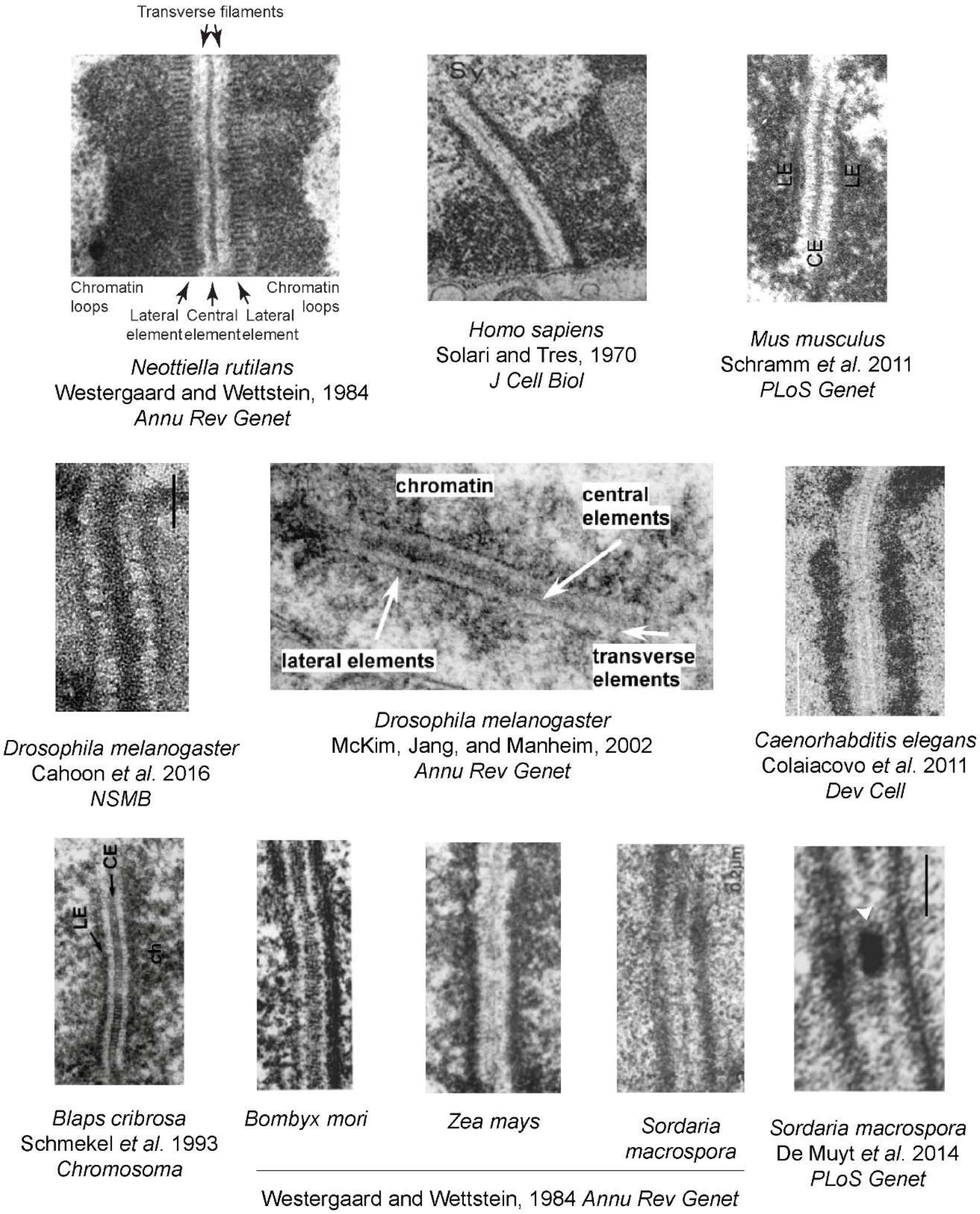
Transverse filaments
Chromatin loops
Lateral element
Central element
Lateral element
Chromatin loops
Sy
LE
LE
CE
chromatin
central elements
lateral elements
transverse elements
CE
LE
ch
0.2µm

Neottiella rutilans
Westergaard and Wettstein, 1984
Annu Rev Genet

Homo sapiens
Solari and Tres, 1970
J Cell Biol

Mus musculus
Schramm *et al.* 2011
PLoS Genet

Drosophila melanogaster
Cahoon *et al.* 2016
NSMB

Drosophila melanogaster
McKim, Jang, and Manheim, 2002
Annu Rev Genet

Caenorhabditis elegans
Colaiacovo *et al.* 2011
Dev Cell

Blaps cribrosa
Schmekel *et al.* 1993
Chromosoma

Bombyx mori

Zea mays

Sordaria macrospora

Westergaard and Wettstein, 1984 *Annu Rev Genet*

Sordaria macrospora
De Muyt *et al.* 2014
PLoS Genet

Figure 1.1.8| The evolutionary conservation of the synaptonemal complex. The synaptonemal complex demonstrates an overtly similar architecture in all known sexually reproducing organisms which utilise an SC.

1.1.9 Components of the mammalian SC central region

The central region of the SC is defined as being the region between, and not including, the lateral elements (axial elements become known as lateral elements upon synapsis by the SC). The first component of the mammalian SC central region to be identified was SYCP1, the transverse filament protein which spans between the lateral elements and the central element (Meuwissen *et al.*, 1992). This protein, and its functional homologues of distinct phyla, are discussed thoroughly in Chapter 3. Briefly, SYCP1 contains a large central helical domain, predicted to fold as a coiled-coil (Meuwissen *et al.*, 1992). As demonstrated by immuno-gold localisation of the SYCP1 termini it was found that SYCP1 is orientated within the SC such that its C-terminus is anchored within the lateral elements and its N-termini are situated within the central midline element, bridging the two elements (Liu *et al.*, 1996; Schmekel *et al.*, 1996). It is proposed to contain DNA binding sites within its unstructured C-terminal tail, a statement which currently lacks experimental evidence.

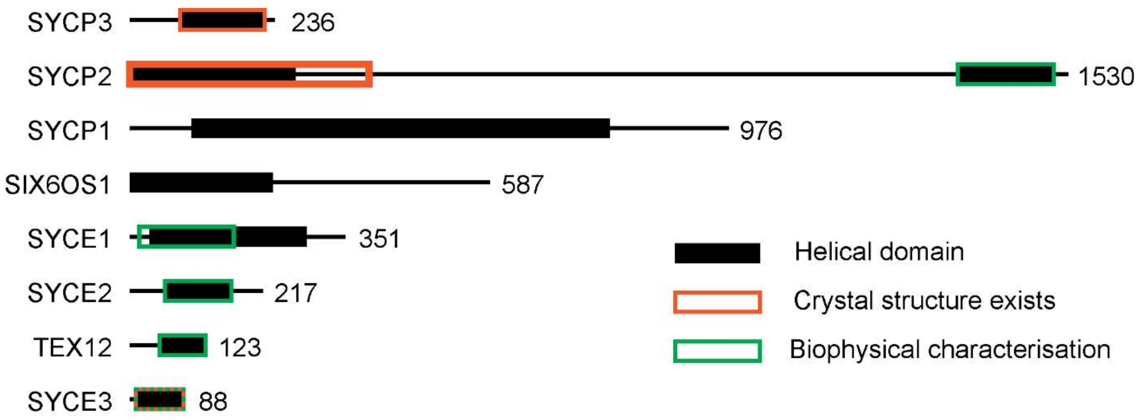
SYCP3
236
SYCP2
1530
SYCP1
976
SIX6OS1
587
SYCE1
351
SYCE2
217
TEX12
123
SYCE3
88
Helical domain
Crystal structure exists
Biophysical characterisation

Figure 1.1.9| Protein components of the mammalian SC. a) To scale schematic of the SC proteins of the mammalian SC annotated with helical regions, domains with structures solved by crystallography and regions characterised through biophysical methods.

Many SC proteins have been localised to the central element of the SC including SYCE1, SYCE2, SYCE3, TEX12 and SIX6OS1 (Costa *et al.*, 2005; Hamer *et al.*, 2006; Schramm *et al.*, 2011; Gomez *et al.*, 2016). In similarity with SYCP1, SYCP2 and SYCP3, all central element proteins contain helical domains with predicted propensity to fold as coiled-coils (Figure 1.1.9). On the basis of their individual knockouts and the effect of each upon synapsis by SYCP1, the central element proteins have been divided into two groups: the initiators and the extensors. Deletion of SYCE1 or SYCE3 results in the ablation of central element formation and allows for only short axial associations (Figure 1.1.10) (Bolcun-Filas *et al.*, 2009; Schramm *et al.*, 2011). In contrast, deletion of SYCE2 or TEX12 does not preclude central element formation but inhibits long-range extension of synapsis (Figure 1.1.10) (Bolcun-Filas *et al.*, 2007; Hamer *et al.*, 2008). Critically, the deletion of any SC protein results in complete meiotic blockage, demonstrating the absolute requirement for correct assembly of the SC. Within the subdivisions of central element proteins, interactions have been identified such as that between SYCE1 and SIX6OS1 and that between SYCE2 and TEX12 (Davies *et al.*, 2012; Gomez *et al.*, 2016). The mechanisms behind the recruitment of these proteins to, and their assembly within, the SC has only recently started to be understood from a molecular perspective due to recent structural and biochemical analyses.

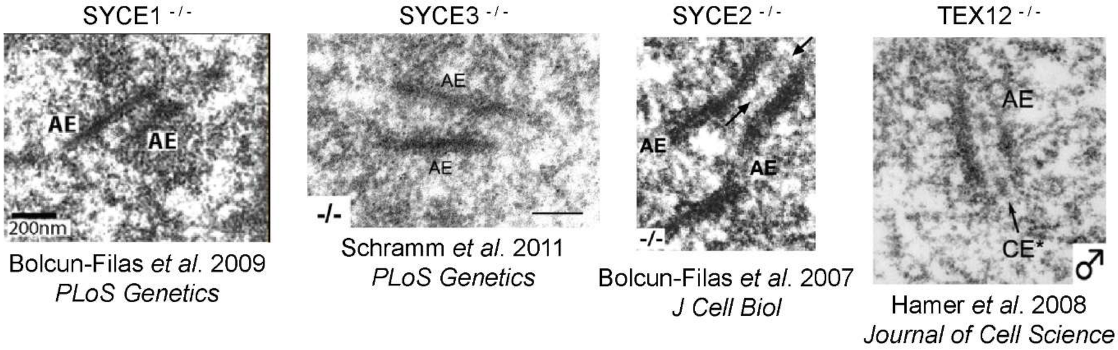

Bolcun-Filas *et al.* 2009 *PLoS Genetics*

Schramm *et al.* 2011 *PLoS Genetics*

Bolcun-Filas *et al.* 2007 *J Cell Biol*

Hamer *et al.* 2008 *Journal of Cell Science*

Figure 1.1.10| Disruption of the mammalian SC central element. Knockout mice demonstrating the contribution of central element components SYCE1, SYCE2, SYCE3 and TEX12 to chromosome synapsis.

1.1.10 The SC central element proteins – building a model for the mammalian SC

Although immuno-gold electron microscopy, the prevailing technique for the localisation of proteins within the SC, proved effect in determining central or lateral localisation, high resolution localisation of protein components was only possible upon the advert of super-resolution fluorescence microscopy techniques. In the high-resolution study of Schücker *et al*, photo-switchable Alexa Fluor® dyes were utilised in conjugation with F(ab)2 fragments as secondary antibodies to improve resolution (Schucker *et al.*, 2015). From bubble-like structures within visualisations of spread chromosomes, which they suggested represented lateral views of SC structure, they proposed a bimodal distribution of SYCE1, SYCE2, SYCE3 and the SYCP1 N-terminus. A contrasting study published the following year, once again utilising immuno-gold localisation, argued against their conclusions suggesting the "bubbles" are artefacts of the preparation technique (Hernandez-Hernandez *et al.*, 2016). They also suggested bimodal distributions of central element proteins, but for only SYCE3 and the SYCP1 N-terminus. However, these suggestions, by inspection of their presented electron micrographs, appear to be based upon relatively few gold particles. Therefore, both studies have aspects to be questioned. The study of Hernandez-Hernandez did, however, interestingly find that SYCE1 and SYCP1 N-termini are randomly localised within the SC central region in TEX12 null mice suggesting the requirement for TEX12 for central region organisation (Hernandez-Hernandez *et al.*, 2016).

From these studies, however, it is eminently clear that the SC is a three-dimensional structure which a depth of almost 100 nm as well as being 100 nm wide. It is therefore almost certainly a structure of multiple layers. The described studies suggest that the SC central region is bi-layered though exactly which components exhibit a bimodal distribution is disputed. Schücker *et al* found that the lateral elements, in association with the SYCP1 C-terminus, demonstrate a monomodal distribution (Schucker *et al.*, 2015).

1.1.11 The SC central element: a molecular understanding

According to published research and unpublished data of the Davies group (Dr Orla Dunne, Dr Lucy Salmon, Dr Owen Davies) (not shown), SYCE3 is the sole and crucial link between SYCP1 and the central element (Hernandez-Hernandez *et al.*, 2016). The crystal structure of SYCE3 was solved, revealing that it forms a stable dimer in which two interlocking chains fold to form a globular four-helical bundle (Lu *et al.*, 2014). The structure was re-refined in a separate study, revealing the organisation of the looped sequences (Figure 1.1.11a) (Dunne and Davies, 2019a). This study further revealed the propensity of SYCE3 to undergo higher-order oligomerisation, mediated through end-on, domain-swapping and lateral associations by surface-exposed aromatic residues (Figure 1.1.11b) (Dunne and Davies, 2019a).

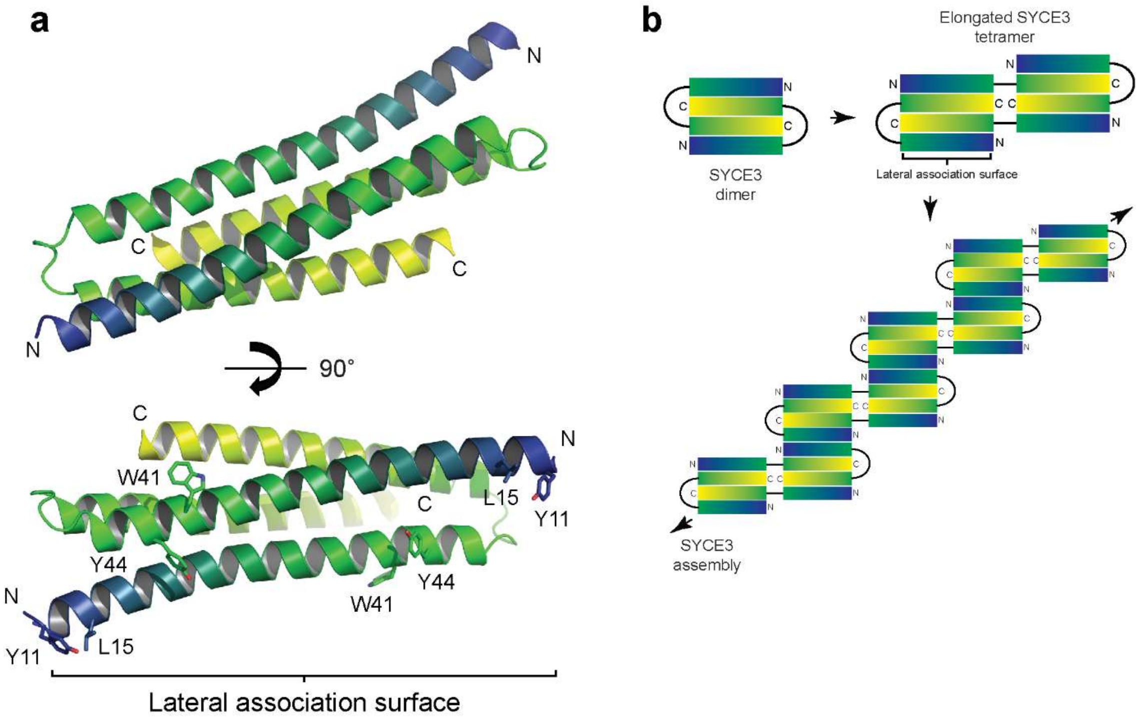

Figure 1.1.11| The self-assembly properties of SYCE3. a) The re-refined crystal structure of SYCE3 (PDB: 6H86) demonstrating a compact, four-helical dimeric fold. Each chain is coloured blue through green to yellow from N to C-terminus. A 90˚ rotation reveals the lateral association surface highlighting key residues Y11, L15, W41 and Y44. **b)** Schematic depicting SYCE3 assembly. SYCE3 is a dimer which can undergo domain-swap or end-on association to create an elongated SYCE3 tetramer. Further oligomerisation is then mediated by lateral associations.

Unlike SYCE3, another initiation factor, SYCE1, does not have propensity for self-assembly and although its crystal structure has not been solved, a complete biophysical characterisation revealed that it adopts an extended, anti-parallel dimeric coiled-coil fold (Dunne and Davies, 2019b). In this study, circular dichroism was utilised to demonstrate the almost total α-helicity of the SYCE1 structural core (residues 25-179) and size-exclusion chromatography multi-angle light scattering (SEC-MALS) utilised to demonstrate its dimeric state. Small-angle x-ray scattering (SAXS) was used to show that the length of the structural core matches that of a theoretical extended coiled-coil (containing an equivalent number of amino acids) with a small folding-back event at one terminus (most likely the N-terminus on the basis of sequence analysis). Further, SAXS was used to analyse MBP-fusions of the SYCE1 structural core to find that SYCE1 adopts an anti-parallel arrangement of chains within the coiled-coil. This method allows for the determination of chain orientation by inspection of the inter-atomic distance distribution profile (a plot representing the frequency of each inter-atomic distance within the proteins structure). Its anti-parallel arrangement, which imposes symmetry, and lack of self-assembly properties suggests that SYCE1 may play a structural role within the SC, perhaps in connecting two layers.

The extension factors, SYCE2 and TEX12, colocalise within the central element (Hamer *et al.*, 2006; Bolcun-Filas *et al.*, 2007). Whether they demonstrate a bimodal or monomodal distribution is debateable (Schucker *et al.*, 2015; Hernandez-Hernandez *et al.*, 2016). These proteins form an equimolar complex and exhibit drastic self-assembly in solution (Davies *et al.*, 2012). The minimal structural unit of the SYCE2-TEX12 complex comprises a 2:2 hetero-tetrameric complex which, through tessellation of the SYCE2 chains and association of both the SYCE2 and TEX12 C-termini, forms a 4:4 complex (Figure 1.1.12a,b). Mutagenesis studies have shown that these C-terminal associations are dependent upon coiled-coil forming residues L110, F114, I117, and L121 in the TEX12 C-termini and V149, V153, V156, and L160 in the SYCE2 C-termini. Further mutagenesis studies have found that this 4:4 building block forms fibrous assemblies through the hydrophobic association of surface-exposed residues F102, F109, and V116 of the TEX12 C-termini. These assemblies are visible by electron microscopy demonstrating a width similar to that of the amorphous central element of the mammalian SC (Figure 1.1.12c) (Davies *et al.*, 2012). These findings are based upon unpublished research of myself and Dr Lucy Salmon, Davies group. A model for SYCE2-TEX12 fibrous assembly is depicted in Figure 1.1.12d.

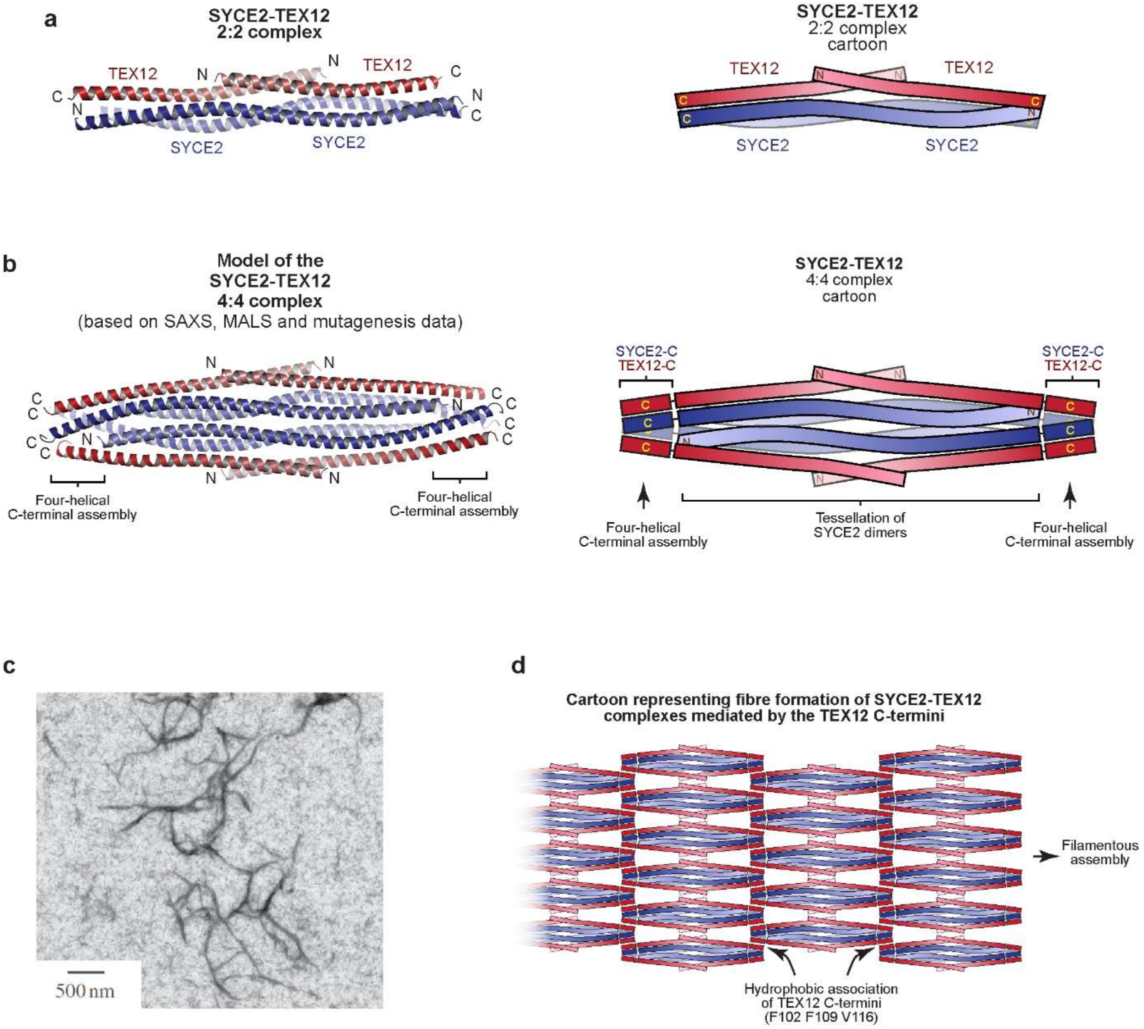
a
SYCE2-TEX12
2:2 complex
TEX12
N
N
TEX12
C
C
N
N
C
SYCE2
SYCE2
SYCE2-TEX12
2:2 complex
cartoon
TEX12
TEX12
SYCE2
SYCE2
b
Model of the
SYCE2-TEX12
4:4 complex
(based on SAXS, MALS and mutagenesis data)
Four-helical
C-terminal assembly
Four-helical
C-terminal assembly
SYCE2-TEX12
4:4 complex
cartoon
SYCE2-C
TEX12-C
SYCE2-C
TEX12-C
Four-helical
C-terminal assembly
Tessellation of
SYCE2 dimers
Four-helical
C-terminal assembly
c
500 nm
d
Cartoon representing fibre formation of SYCE2-TEX12
complexes mediated by the TEX12 C-termini
Filamentous
assembly
Hydrophobic association
of TEX12 C-termini
(F102 F109 V116)

SYCE2-TEX12 filamentous assembly
Davies et al., 2012
Open Biology

Figure 1.1.12| Filamentous assembly of SYCE2-TEX12. a) The crystal structure of the minimal structural unit of SYCE2-TEX12 reveals a 2:2 hetero-tetrameric complex in which complexation is stabilised in four-helical arrangement at the central tetrameric interface whilst lateral interfaces are formed of three-helical associations. This has been cartoonized for simplicity. **b)** Inclusion of additional C-terminal residues flanking the SYCE2-TEX12 structural core allows for the formation of a 4:4 hetero-octameric complex. SAXS and mutagenesis directed modelling suggests the tessellation of two 2:2 complexes. A cartoon demonstrating these C-terminal associations and main chain tessellation is depicted. **c)** Electron micrograph of SYCE2$_{57\text{-}165}$-TEX12$_{49\text{-}123}$ demonstrating the formation of fibres of approximately 40 nm thickness. **d)** A model for assembly of SYCE2-TEX12 to form extended filamentous structures, dependent upon surface-exposed residues F102 F109 V116 within the TEX12 C-termini which flank a 4:4 hetero-octameric core structure.

1.1.12 Conservation of SC components across phyla

Despite the striking architectural conservation of the SC, across phyla the components do not bear any sequence similarity, bearing at most similarities between the domain structures of functionally related components. Sequence conservation of SC components is observable across metazoans down to Cnidaria (Fraune *et al.*, 2014). However, the SC components of yeast, *C. elegans* and *Drosophila* bear no sequence similarity. Despite this, the protein of the transverse filament demonstrates a similar domain structure from humans, to yeast, to *Drosophila*, a feature discussed in Chapter 3. This raises the question of whether the SC evolved through divergent evolution or convergent evolution.

1.1.13 Physical interactions between the transverse filaments and the central element

SYCE3 was proposed as being the sole SC interactor of SYCP1 on the basis of a recruitment assay in an *ex vivo* setup in which SC proteins are overexpressed in the heterologous system, COS-7 cells (Hernandez-Hernandez *et al.*, 2016). Within this system, SYCP1 and SYCP3 both form cytoplasmic networks, named polycomplexes, which were thought to represent their ability to self-assemble. The findings of Hernandez-Hernandez *et al.* found that SYCE1, SYCE2 and TEX12 would not themselves form cytoplasmic networks, nor be recruited to networks formed of SYCP1 unless co-expressed with SYCE3, thus suggesting the role of SYCE3 as being a linker between the transverse filaments and the central element (Hernandez-Hernandez *et al.*, 2016). However, these findings are contrary to those published upon the discovery of SYCE1 and SYCE2 which found that these proteins would be recruited to SYCP1 networks in the absence of SYCE3 (Costa *et al.*, 2005). Direct interactions between SYCP1 and SYCE1 or SYCE2 have not been observed by yeast-two hybrid (Davies *et al.*, 2012). Unpublished findings of the Davies group (Dr Orla Dunne, Dr Lucy Salmon, myself) have confirmed that SYCE3 constitutes the sole SC protein which associates with SYCP1 and is able to mediate further interactions with both SYCE2 and SYCE1.

1.1.14 A 3-dimensional model of the synaptonemal complex

Localisation studies and the described molecular findings regarding the structural and assembly properties of the SC components can be combined to produce an overall model for the structure of the SC. Figure 1.1.13 depicts a model for the SC in which the central region is bi-layered with SYCP1 dimers connecting the central element to the lateral elements, with a bimodal distribution at the midline and converging at the lateral elements. As discussed, the localisations and placement within this model are based on both localisation studies and the structural properties of the proteins derived through biophysical experiments. Firstly, SYCP1 is presented as dimeric coiled-coils (ascribed on the basis of sequence analysis (Meuwissen *et al.*, 1992)) orientated such that the C-termini are localised within the lateral elements in a single plane whilst the N-termini interdigitate at the central element in two spatially separated planes (Liu *et al.*, 1996; Schmekel *et al.*, 1996; Schucker *et al.*, 2015). These aspects of SYCP1 structure and localisation are described in full during the introduction to Chapter 3. From the frontal view, SYCE3 can be seen as making the sole link between SYCP1 and central element proteins SYCE2-TEX12 and SYCE1 (on the basis of unpublished findings of the Davies group: myself, Dr Orla Dunne and Dr Lucy Salmon). SYCE3 is also depicted as forming extensive assemblies on the basis of it forming large assemblies *in vitro* (Dunne and Davies, 2019a). SYCE2-TEX12 are shown together as forming an extensive fibrillar central element structure, only forming direct associations with SYCE3 (Davies *et al.*, 2012). Finally, SYCE1 is shown as forming anti-parallel dimeric structures, only interacting with SYCE3, which form a vertical strut like structure connecting the vertically separated planes of SYCP1 N-termini (Dunne and Davies, 2019b). Remembering to consider the 3-dimensional structure of the SC is key in modelling how any single component of the SC might assemble within the structure.

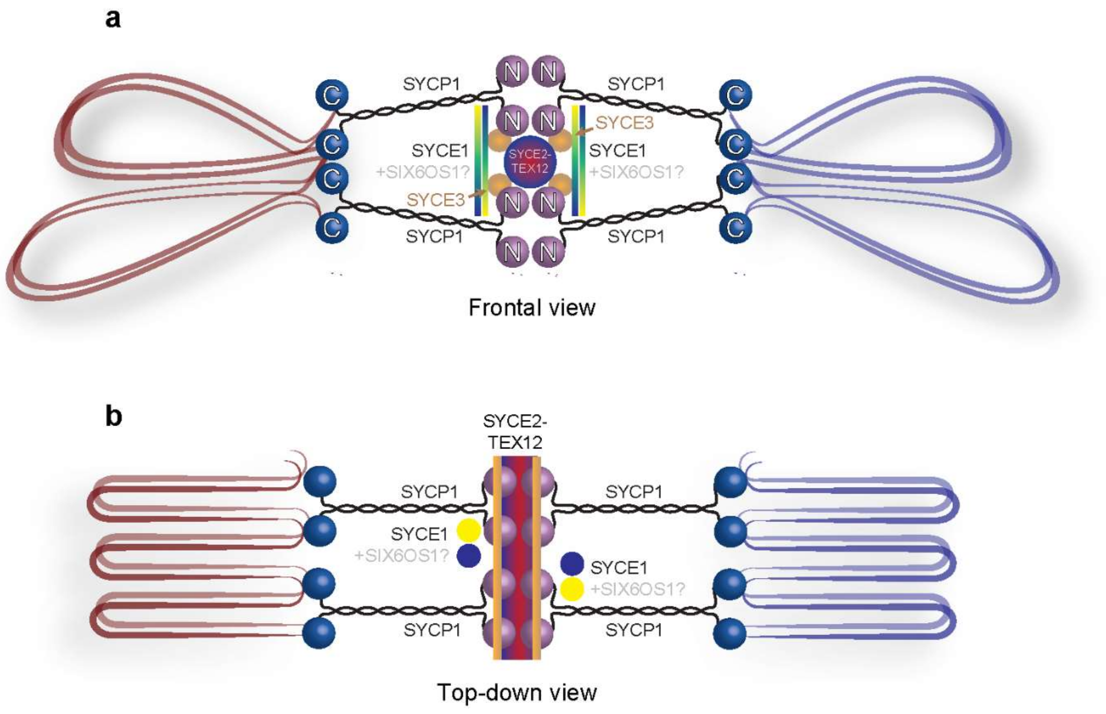

Figure 1.1.13| Model for the localisation of SC components within the mammalian SC. a) Frontal and **b)** top-down views of the SC showing the bi-layered organisation of the central region.

1.1.15 The SC and the formation of crossovers

What is the functional role of the SC? The evolutionarily conserved ladder-like structure enforces a rigid three dimensional architecture unto meiotic chromosomes and its formation appears to be critical for the resolution of DSBs (Colaiacovo *et al.*, 2003). Within the mammalian SC, if components of the SC central element are not present crossovers do not form, demonstrating its critical role (Kouznetsova *et al.*, 2011). Despite this, factors responsible for the early stages of recombination, such as RAD51, DMC1, MSH4/5 are still recruited to form early recombination nodules (de Vries *et al.*, 2005). However, their levels persist rather than decline as in wild-type meiosis. Therefore, the structure of the SC might be required for the maturation of early recombination nodules to late recombination nodules. An example recombination nodule is depicted docked atop the SC of *Sordaria macrospora* in the final panel of Figure 1.1.8 (De Muyt *et al.*, 2014). Whilst the levels of recombinases RAD51and DMC1 peak during leptotene, the levels of MSH4 peak during zygotene, the period of rapid prophase movements and the establishment of inter-homologue axial associations (Figure 1.1.6a) (Kneitz *et al.*, 2000). Levels subsequently decline until late pachytene during which they localise to a couple of discrete foci, alongside other factors essential for meiotic recombination such as RNF212 (Holloway *et al.*, 2014). It is thought that MSH4 forms a complex with MSH5 to specifically stabilise double-Holliday junctions and further associate and cooperate with MLH1 and MLH3 to form crossovers (Santucci-Darmanin *et al.*, 2000; Santucci-Darmanin *et al.*, 2002; Snowden *et al.*, 2004).

It appears that the decision whether a DSB intermediate will be directed towards crossover or non-crossover repair pathways is made early during the meiotic cycle, prior to or during the formation of single-end invasions (Bishop and Zickler, 2004). How this decision is conveyed is unknown, though it could be achieved through interplay between RAD51 and DMC1 – RAD51 D-loops are readily dissolved whilst DMC1 D-loops are more stable (Bugreev *et al.*, 2011). DMC1 is ubiquitously localised across meiotic DSBs suggesting that any effect may be due to recruitment levels or regulation (Tarsounas *et al.*, 1999). However, an additional layer of control in regulating the number of crossovers exists, named “crossover interference”, an effect most drastic in the chromosomes of *Caenorhabditis elegans* in which each chromosome receives one, and only one, crossover (rarely receiving zero) despite a huge disparity in the sizes of each chromosome (Hillers and Villeneuve, 2003). This suggests that a feedback mechanism exists such that the formation of one crossover inhibits another on the same chromosome. It is eminently possible, therefore, that the SC might be involved in the transmission of signals to prevent further crossover formation. Further, crossovers are not frequently present at the kinetochore as observed by electron microscopy of spread chromosomes of *Zea mays* in which the locations of recombination nodules (markers for sites of DSB processing) were analysed (Anderson *et al.*, 2003). In mice, the protein PRDM9 appears to be a major determinant of hotspot location (chromosomal locations with a propensity for crossover formation) (Baudat *et al.*, 2010). Its binding to DNA is dependent upon a zinc finger array at its C-terminus and is proposed to association with histone-modulating proteins early in prophase though exactly how hotspots are marked by this protein remains to be elucidated (Parvanov *et al.*, 2017).

1.1.16 Defects in SC formation and physiological consequences in humans

Defective SC formation results in meiotic arrest, resulting, in males, in the inability to produce sperm, rendering the individual sterile (Judis *et al.*, 2004). Females defective for SC formation are also infertile, often due to embryonic death through aneuploidy, and frequently experience recurrent miscarriage (Hassold and Hunt, 2001). SYCP3 appears to be the SC component most commonly implicated with fertility issues. Introduction of a premature stop codon within the C-terminal coiled-coil results in infertility in males (Miyamoto *et al.*, 2003). In females experiencing miscarriage, mutations predominantly affecting the extreme C-terminus of SYCP3 were identified (Bolor *et al.*, 2009). Both of these mutations/truncations likely interfere with fibrillization and the formation of recursive lateral element structures during meiosis, precluding meiotic progression.

1.1.17 Disassembly of the SC

The mechanisms by which the SC is disassembled involve both modification by phosphorylation of central region proteins and proteasomal degradation dependent upon ubiquitylation (Cahoon and Hawley, 2016). As SC proteins are constantly renewed within the dynamic SC structure, it could be that modifications inhibit self-assembly mechanisms, therefore favouring a decline in protein density and resulting in an eventual disintegration of the SC structure. In mammals, two key drivers of SC disassembly are PLK1 (in association with Aurora B and INCENP), and CDK1 (in association with CyclinB). During pachytene, PLK1, Aurora B and INCENP localise within the central region of the SC and are required for the phosphorylation of SYCP1 and TEX12 (Parra *et al.*, 2003; Jordan *et al.*, 2012).

Additionally, disruption of CDK1 activation through knockout of HSP70-2, a heat shock protein required for CDK1 activation, inhibits SC disassembly, likely through blocking its interaction with CyclinB, with meiosis stalling during mid- to late-pachytene (Allen *et al.*, 1996; Dix *et al.*, 1997; Zhu *et al.*, 1997). Interestingly an interaction between HEI10 and Cyclin B was identified (Toby *et al.*, 2003). HEI10 is an E3 ubiquitin ligase known to negatively regulate levels of pro-mitotic factors, likely doing so through mediating their proteasomal degradation (Singh *et al.*, 2007). Mutations of HEI10 result in the ablation of crossover formation highlighting its mediating role in their formation (Ward *et al.*, 2007). A key role may be in preventing premature meiotic progression through delaying desynapsis at sites designated for the formation of crossovers.

After the SC is disassembled, not all SC components are lost and in fact they are retained at specific places. SYCP2 is retained at the centromeres (Schalk *et al.*, 1998). These proteins may play a role in kinetochore orientation during metaphase I in which microtubules attach and exert tension to segregation homologous chromosome pairs.

Some strange organisms differ in their utilisation of an SC, or forgo its utilisation at all, removing the requirement for similar disassembly pathways (Zickler and Kleckner, 2015). For example, *Saccharomyces pombe* and the fungus *Aspergillus nidulans* do not form an SC, pairing and recombining their DNA in its absence (Egel-Mitani *et al.*, 1982) (Bahler *et al.*, 1993). In *Bombyx mori*, the SC is not disassembled so much as being converted in chromatin state to an elimination chromatin which can be visualised prior to separation and retains form during metaphase (Rasmussen, 1977).

After the SC is disassembled, genetic crossovers physically manifest as chiasmata, additional physical linkages between homologues chromosomes. Homologous chromosomes are then segregated during metaphase, breaking these bonds, completing the first meiotic division whilst facilitating the exchange of genetic information.

1.1.18 Aims and objectives

Despite much headway being made within the past 5 years, an atomistic understanding of the proteinaceous structures present during meiosis is still relatively incomplete precluding our ability to understand the molecular mechanisms which drive chromosome dynamics and facilitate meiotic progression. The following thesis is dedicated towards the biochemical, biophysical and crystallographic characterisation of two key protein megastructures essential to meiotic fidelity: the synaptonemal complex, with a particular focus on the human transversal filament protein, SYCP1 (Chapter 3); and the meiotic telomere complex, responsible for mediating telomeric attachment to the nuclear envelope (Chapter 4). These two assemblies cooperate to mediate chromosome dynamics and are indispensable for meiotic progression. Our understanding of their function is thus-far largely derived from localisation studies with limited functional or structural details. Uncovering their molecular mechanisms through structure solution, biophysical, and biochemical characterisation is therefore important for understanding how meiosis proceeds through the concerted action of cooperative protein assemblies. Within Chapter 3, I worked to characterise the molecular structure and mechanisms of assembly within the SC of SYCP1. Full-length SYCP1 is highly insoluble and unstable, a barrier overcome through truncation of unstructured tails and the identification and removal of 11 key residues which mediate higher-order assembly. This allowed for the discovery that the SYCP1 core is tetrameric, stabilised at its N-terminus as a four helical bundle which splays at its C-terminus into two long dimeric coiled-coils. Chapter 4 focuses on the crystal structure solution of MAJIN-TERB2, a complex formed between two essential components of the meiotic telomere complex. Its symmetrical dimeric architecture and the presence of a large basic surface allowed for the orientation of two further basic patches localised within unstructured regions of the wider complex to create a seamless continuous DNA binding interface. Biophysical characterisation of such a complex, and comparisons between the affinity for DNA of various constructs, provided the basis for a model for the mode of DNA binding of the MAJIN-TERB2 complex in which DNA is looped over the MAJIN dimer. The results presented within these chapters represent the underpinning structural knowledge required for building up an atomistic model for the assembly of the synaptonemal complex and the dynamic movement of chromosomes during meiosis.

Chapter 2

METHODS

2.1.1 Protein sequences analysed in this study

The SYCP1 sequence utilised relates to the canonical human isoform with Uniprot accession code Q15431-1. The MAJIN sequence utilised relates to the human MAJIN isoform X1 (254 amino acids; accession number XP_024304215.1), selected as it most closely matches the canonical isoforms conserved across mammals. TERB1, TERB2 and TRF1 sequences relate to their canonical human isoforms (accession codes Q8NA31, Q8NHR7 and P54274, respectively).

2.1.2 Bioinformatic analyses

Here I shall describe the bioinformatic strategy applied for SYCP1. The same was applied for proteins MAJIN, TERB1, TERB2 and TRF1. An alignment containing 62 SYCP1 sequences compiled by ensembl and verified by manual inspection to contain only vertebrate species (including mammals, birds and fish) was utilised to predict secondary structure using JPred4 and presented using Jalview in Appendix 1 or plotted graphically in Figure 3.1.3 (Waterhouse *et al.*, 2009; Drozdetskiy *et al.*, 2015; Zerbino *et al.*, 2018). An alignment containing 343 sequences compiled by ConSurf and manually edited to remove low quality and non-SYCP1 sequences was utilised to calculate conservation scores per residue (Berezin *et al.*, 2004; Ashkenazy *et al.*, 2016). Coiled-coil propensity was predicted by COILS (Parry, 1982; Lupas *et al.*, 1991; Lupas, 1997). The application charge from the EMBOSS suite was used to demonstrate the gross distribution of electrochemical potential across the SYCP1 sequence (Rice *et al.*, 2000). Using a window size of 5, the application calculates the charge of each residue as an average of the following 5 residues (Lys, Arg and His score +1; Glu and Asp score -1; non-charged residues score 0). The charge of each residue was then plotted graphically as an average of the surrounding 98 residues (10 % the total number of residues).

2.1.3 Preparation of plasmids for recombinant protein expression

Integral to this study was the expression of recombinant proteins in *Escherichia coli*, and occasionally in mammalian cells (COS-7). For bacterial expression, constructs encoding protein sequences of interest were incorporated into pHAT4 and pMAT11 plasmids (Peranen *et al.*, 1996). In the study of MAJIN and TERB2, co-expression was achieved by incorporating the coding sequence for one complex component within the pRSF-Duet1 plasmid (Novagen) which could be co-transformed with a pMAT11 plasmid containing the coding sequence for the second complex component. Coding sequences were amplified by PCR catalysed by KOD DNA polymerase (Novagen) (at 2.5 U/μl) in solution containing magnesium chloride (1 mM), dNTPs (0.2 mM), 1x "KOD DNA Polymerase buffer 2" (Novagen), the template DNA and primers (0.4 µM). Thermocycling was achieved using a TPersonal Thermocycler (Biometra). Primers were purchased from Sigma Aldrich. Amplified products were purified through agarose gel electrophoresis and gel extraction (GeneJET Gel Extraction Kit, ThermoScientific). Plasmids were linearised using NcoI (NEB). PCR products were incorporated within linearised plasmids using one-step sequence- and ligation-independent cloning (SLIC) according to protocol (Li and Elledge, 2012). Successful clones were selected by growth on LB agar containing either 100 µg/ml ampicillin (for pHAT4 or pMAT11) or 50 µg/ml kanamycin (for pRSF-Duet1), cultured overnight in 5 ml LB broth, and DNA isolated using the GeneJET Plasmid Miniprep Kit (ThermoScientific). Correct insertion and coding sequence were confirmed by Sanger sequencing (Source Bioscience).

Vector	Enzyme	Antibiotic resistance	µg/ml
pHAT4	NcoI (NEB)	Ampicillin (Melford)	100
pMAT11	NcoI	Ampicillin	100
pRSF-Duet1	NcoI	Kanamycin (Melford)	50
pEGFP	EcoRI (NEB)	Kanamycin	50
pRARE	N/A	Chloramphenicol (Melford)	34

Table 2.1| Vectors utilised in this study. The restriction endonuclease enzymes used for linearization and the antibiotic resistance they confer to transformed *E. coli*.

2.1.4 Purification of soluble recombinant proteins

BL21 (DE3) *E. coli* harbouring the pRARE plasmid isolated from Rosetta (DE3) *E. coli* (Novagen), henceforth referred to as BL21 (DE3) pRARE *E. coli*, were transformed using plasmids encoding the protein of interest and plated onto LB agar plates containing a suitable antibiotic (as detailed in Table 2.1) to select for successfully transformed clones. Colonies were cultured in 2xYT media (Formedium) at 37 ˚C, 180 rpm to an optical density at 600 nm of approximately 0.8. Induction of protein expression was achieved through the addition of 1M isopropyl β-D-1-thiogalactopyranoside (IPTG) to a final concentration of 500 µM. Cultures expressing SYCP1 constructs were incubated for 16 hours at 25 ˚C, 180 rpm prior to harvesting by centrifugation at 4200 rpm. Cultures expressing MAJIN-TERB2 complexes were incubated at 15 ˚C. The supernatant was discarded, and the bacterial pellets resuspended in lysis buffer containing 20 mM Tris pH 8.0, 500 mM KCl. Cell suspensions were stored at -80 °C prior to further processing. Protein purification was initiated with lysis of the cells by sonication prior to centrifugation at 40,000 g for 30 minutes to remove cellular debris.

Although minor modifications exist across protein constructs, described within the text of the results sections, all purifications approximately conform to the following protocol. Initial purification was achieved via affinity chromatography in which the bacterial lysate was applied to Ni-NTA agarose (Qiagen) equilibrated in 20 mM Tris pH 8.0, 500 mM KCl at 1 ml/min. Post-loading, the resin was washed with equilibration buffer then 20 mM Tris pH 8.0, 500 mM KCl, 20 mM imidazole pH 8.0. The protein was eluted in 20 mM Tris pH 8.0, 500 mM KCl, 200 mM imidazole pH 8.0. The Ni-NTA elution of constructs or complexes including a His_6-MBP-tag were applied to amylose resin (NEB) equilibrated in 20 mM Tris pH 8.0, 150 mM KCl, 2 mM DTT. The resin was washed with equilibration buffer before elution with 20 mM Tris pH 8.0, 150 mM KCl, 2 mM DTT, 30 mM D-Maltose. Non-degraded material was then separated from products of proteolysis by anion exchange using a HiTrap Q column (GE Healthcare) equilibrated in 20 mM Tris pH 8.0, 100 mM KCl, 2 mM DTT, eluted across a gradient in which the concentration of KCl was increased from 100 mM to 1 M over 50 ml.

Affinity-tag cleavage was achieved by incubating the eluate with sfGFP-TEV protease (prepared as per (Wu *et al.*, 2009)) at room temperature overnight prior to removing both the protease and the affinity-tag from solution during a second round of anion exchange chromatography using the HiTrap Q column. For constructs with basic patches, mentioned in text, the HiTrap SP column was utilised. Final purification by size exclusion chromatography was performed using HiLoad® 16/600 Superdex® 200 pg (GE Healthcare) equilibrated in 20 mM Tris pH 8.0, 150 mM KCl, 2 mM DTT at 1 ml/min. Protein concentration was achieved using Amicon Ultra-4 10 kDa MWCO (Millipore).

Protein samples were analysed by SDS-PAGE using the Novex Bolt Bis-Tris gel system (Invitrogen) and stained using SimplyBlue Safestain (Invitrogen). Sample concentration was determined by UV spectroscopy using a Cary 60 UV spectrophotometer (Agilent) with extinction coefficients and molecular weights calculated by ProtParam (http://web. expasy.org/protparam/). Samples were flash-frozen using liquid nitrogen and stored at -80 °C.

2.1.5 Expression of seleno-methionine derivative SYCP1$_{676\text{-}770}$

As a means of gaining phasing information, seleno-methionine incorporated SYCP1$_{676\text{-}770}$ was purified. *Escherichia coli* strain Rosetta DE3 were cultured in 2xYT to an O.D. at 600 nm of approximately 0.6 at which they were harvested by centrifugation. 10 L of culture were used. The bacterial pellets were resuspended in 150 mM NaCl and re-centrifuged. 10 L of M9 minimal media (Formedium) was prepared and supplemented with 5 nM $FeCl_3$, 2 µM $MgCl_2$, 5 nM $Zn(OAc)_2$, 0.4 % w/v D-glucose. The bacterial pellets were resuspended in 200 ml M9 before being added to the rest of the media. After a 1-hour incubation at 25 ˚C, 250 rpm, metabolite poisoning of methionine biosynthesis was induced by the addition of L-amino acids (100 mg/L lysine, 100 mg/L phenylalanine, 100 mg/L threonine, 50 mg/L isoleucine, 50 mg/L leucine, 50 mg/L valine). After a further 1-hour incubation, L(+)-seleno-methionine (Acros Organics, Fisher Scientific) was added to a final concentration of 50 mg/L. After another 30 minutes, protein expression was induced by the addition of 0.5 mM IPTG and incubated at 25 ˚C for 16 hours before harvesting.

2.1.6 Expression of seleno-methionine derivative MAJIN$_{1\text{-}112}$-TERB2$_{168\text{-}220}$

Minor modifications to the protocol utilised for SYCP1$_{676\text{-}770}$ were made, as detailed in the following. Transformed BL21 (DE3) *E. coli* were cultured in 2xYT media (Formedium) and harvested at an O.D.$_{600}$ of 0.6, washed in 150 mM NaCl and resuspended in M9 media (Formedium) supplemented with trace elements (2.5 mg/L $CoCl_2.6H_2O$, 15 mg/L $MnCl_2.4H_2O$, 1.5 mg/L $CuCl_2.2H_2O$, 3 mg/L H_3BO_3, 33.8 mg/L $Zn(CH_3COO)_2.2H_2O$ and 14.10 mg/L TitriplexIII) and 5 µM $Zn(OAc)_2$. After a 1 hour incubation at 25˚C, 250 rpm, methionine biosynthesis was inhibited by addition of 100 mg/L lysine, 100 mg/L phenylalanine, 100 mg/L threonine, 50 mg/L isoleucine, 50 mg/L leucine, 50 mg/L valine. After a further 1 hour at 25 °C, 250 rpm, the cultures were supplemented with 50 mg/L seleno-methionine. Expression was induced after 30 minutes by 0.5 mM IPTG and incubated overnight at 15 °C, 250 rpm.

2.1.7 Purification of SYCP1$_{1\text{-}976}$ and SYCP1$_{1\text{-}783}$ by refolding from inclusion bodies

BL21 (DE3) pRARE *E. coli* were transformed using pHAT4-SYCP1$_{1\text{-}976}$ or pHAT4-SYCP1$_{1\text{-}783}$. Transformants were selected by plating on agar containing ampicillin (100 µg/ml) and chloramphenicol (34 µg/ml). After 16 hours, bacterial colonies were resuspended in 2x 1 L volumes 2xYT media (Formedium) and cultured by shaking at 180 rpm at 37 ˚C. At an O.D.$_{600}$ of 0.8, IPTG was added to a final concentration of 0.5 mM to induce protein expression. Cultures were incubated for 3 hrs at 37 ˚C, shaking at 180 rpm. Bacterial cells were harvested by centrifugation at 4200 rpm for 30 minutes and resuspended in 30 ml 20 mM Tris, pH 8.0, 500 mM NaCl, 50 mM EDTA, pH 8.0, 50 mM DTT, 5 mM $MgCl_2$ with cOmplete Protease Inhibitor Tablets (Roche) and DNase I at 0.1 mg/ml (Roche) per litre culture, frozen, and stored at -20 ˚C.

Here I outline the optimised protocol for the refolding and purification of His_6-$SYCP1_{1\text{-}976}$ and His_6-$SYCP1_{1\text{-}783}$ from inclusion bodies (Fang and Huang, 2001). Cells were defrosted and lysed by sonication on ice. Inclusion bodies and cellular debris were pelleted through centrifugation at 40,000 g for 30 minutes. The supernatant was discarded, and the pellet washed thoroughly by resuspension to homogeneity in buffer containing 20 mM Tris, pH 8.0, 500 mM NaCl, 50 mM EDTA, pH 8.0, 50 mM DTT and 1.5 % Triton X-100 (Sigma Aldrich) to solubilise membranes. Inclusion bodies were pelleted by centrifugation and washed in 20 mM Tris pH 8.0, 1 M NaCl, 50 mM DTT, 50 mM EDTA pH 8.0, 5 mM $MgCl_2$, 0.1 mg/ml DNase I followed by a further wash in 20 mM Tris, pH 8.0, 100 mM NaCl, 50 mM DTT, 50 mM EDTA pH 8.0. Inclusion bodies were then solubilised in deionised 20 mM Tris pH 8.0, 100 mM NaCl, 50 mM DTT, 50 mM EDTA pH 8.0, 8 M urea and stirred on ice for 30 minutes. Urea-containing buffers were deionised by 3 rounds of gravity flow through AG® 501-X8 resin (Bio-Rad) following the manufacturers "Column Method". Remaining debris were removed by centrifugation at 40,000 g for 30 minutes and the supernatant retained.

The supernatant was flowed through a HiTrap Q ion exchange column (GE Healthcare) equilibrated in deionised 20 mM Tris pH 8.0, 100 mM NaCl, 10 mM DTT, 0.5 mM EDTA pH 8.0, 8 M urea at 2 ml/min to bind remaining DNA. The flow-through was then loaded to HiTrap SP HP ion exchange column (GE Healthcare) equilibrated in deionised 20 mM Tris pH 8.0, 100 mM NaCl, 10 mM DTT, 0.5 mM EDTA pH 8.0, 8 M urea at 2 ml/min and eluted by increasing the concentration of KCl to 1 M over 50 ml. Elution fractions containing suitably pure His_6-$SYCP1_{1\text{-}976}$ (2 ml) were dialysed in 1.5 L 20 mM Tris, pH 8.0, 500 mM NaCl, 500 mM L-arginine pH 8.0, 10 mM DTT by stirring overnight at 4 ˚C using a 10 kDa MWCO Slide-A-Lyzer™ dialysis cassette (Thermo Fisher). The protein-containing cassette was then transferred to 1.5 L 20 mM Tris pH 8.0, 500 mM NaCl, 10 mM DTT and stirred for 6 hrs at 4 ˚C. The buffer-exchanged sample was centrifuged at 16600 g for 30 minutes to remove precipitates. The sample was then concentrated using an Amicon Ultra® 10,000 MWCO centrifugal filter unit (Millipore), flash frozen in liquid nitrogen and stored at -80 ˚C. Protein purity was assessed by SDS-PAGE visualised by Coomassie staining and the protein concentration was determined by UV spectroscopy using a Cary 60 UV spectrophotometer (Agilent Technologies) with molecular weights and extinction coefficients calculated by ProtParam (http://web.expasy.org/protparam/).

2.1.8 Circular dichroism (CD) spectroscopy

Far UV circular dichroism was utilised to assess secondary structure content in solution for samples between 0.1 and 0.4 mg/ml in 10 mM Na_2HPO_4/NaH_2PO_4, pH 7.5, 150 mM NaF using a 0.2 mm path length quartz cuvette (Hellma) at 4 ˚C. Data were collected using a Jasco J-180 spectropolarimeter (Institute for Cell and Molecular Biosciences, Newcastle University) between 260 and 185 nm at 0.2 nm intervals with a response time of 4 seconds and a bandwidth of 2 nm. 9 accumulations were averaged and converted to mean residue ellipticity ([Θ]) (x1,000 $deg.cm^2.dmol^{-1}.residue^{-1}$) using equation 1

$$Mean\ residue\ ellipticity\ ([\theta]) = \frac{\theta.MRW}{10.P.CONC} \qquad (1)$$

where Θ is Theta Machine Units, measured in millidegrees, MRW is mean residue weight (calculated as protein atomic mass (Da) / residue number), P is pathlength, in centimetres, and CONC is protein concentration, in mg/ml.

Helical content can be estimated directly utilising the $[\Theta]_{208}$ and $[\Theta]_{222}$ values, which represent the two minima of an α-helical trace, using equations 2 and 3, respectively, below (Greenfield and Fasman, 1969; Morrisett *et al.*, 1973). $[\Theta]_{222}$ should provide a more accurate value as it is less affected by the signal of random coil or β-sheet.

$$fH = ([\theta]_{208} - 4{,}000)/(-33{,}000 - 4{,}000) \qquad (2)$$

$$fH = ([\theta]_{222} - 3{,}000)/(-36{,}000 - 3{,}000) \qquad (3)$$

where $[\Theta]_{xxx}$ is mean residue ellipticity at the specified wavelength in nanometres. -33,000 and -36,000 are the theoretical [Θ] values at 208 and 222 nm, respectively, for 100 % α-helical proteins. These equations account for the contribution of random coil to the signal at these wavelengths by subtraction.

The DiChroweb server (http://dichroweb.cryst.bbk.ac.uk) was used to estimate secondary structure composition using the CDSSTR algorithm (Sreerama and Woody, 2000).

Thermal denaturation of samples in 20 mM Tris, pH 8.0, 150 mM KCl (unless stated otherwise in the figure legend) was measured by CD, tracking the helical signal at 222 nm whilst increasing the temperature from 4 to 95 ˚C at 0.5 ˚C intervals every 15 seconds. Data were converted to mean residue ellipticity ($[\Theta]_{222}$) and plotted as percent folded ($[\Theta]_{222.x}$ - $[\Theta]_{222.5}$)/ ($[\Theta]_{222.95}$ - $[\Theta]_{222.5}$) which assumes a fully folded molecule at 5 ˚C and complete denaturation at 95 ˚C.

2.1.9 Size-exclusion chromatography multi-angle light scattering (SEC-MALS)

SEC-MALS was utilised to determine absolute molecular weights of protein species in solution. For small molecules, the scatting of laser light is both perfectly symmetrical and elastic and is referred to as Rayleigh scattering. The intensity of Rayleigh scattering is identical in all directions it can thus be accurately measured under ideal circumstances. The scattering intensity is directly proportional to molecular weight which can therefore be calculated.

Ideal circumstances assume that the size of the molecule remains beneath a limit of approximately one twentieth of the wavelength (wavelength of laser light is generally ~600 nm, so the dimension limit is approximately 30 nm, or ~30 kDa) and that there are no inter-particle effects. Both of these assumptions rarely hold true. Proteins are generally not small and therefore scatter light asymmetrically (Figure 2.1.1a). The only angle at which scattering is not affected by the size or shape of the molecule is at a scattering angle of zero which cannot be directly measured (as this is from where the incident beam originates). Further, it is impossible to analyse proteins in solution at a concentration of zero and therefore there are always inter-particle effects which introduce a non-ideality factor into the calculation of molecular weight. To eliminate the complications that the non-ideality factor introduces, estimations of scattering at an angle of zero and protein concentration of zero must be made.

These estimations are arrived at by extrapolation. By measuring light scattering at multiple angles across multiple concentrations, a Zimm plot can be produced (Figure 2.1.1b,c). This allows for the determination of the scattering value at an angle of zero degrees and a concentration of zero. Molecular weight can then be calculated using the Zimm equation (below, equation 4) (Harding and Jumel, 1998).

$$Kc/\Delta R(\theta, c) = 1/Mw \quad (4)$$

Samples were applied to a Superdex 200 Increase 10/300 GL size exclusion chromatography column (GE Healthcare) at 0.5 ml/min using an ÄKTA Pure (GE Healthcare). SYCP1 constructs were analysed in 20 mM Tris, pH 8.0, 150 mM KCl, 2 mM DTT whilst MAJIN-TERB2 constructs were analysed in 20 mM Tris, pH 8.0, 250 mM KCl, 2 mM DTT. The flow path continued through a DAWN HELEOS II MALS detector (Wyatt Technology) followed by an Optilab T-rEX differential refractometer (Wyatt Technology). The collected light scattering and differential refractive index data were analysed using ASTRA 6 software (Wyatt Technology) to calculate molecular weights by Zimm plot extrapolation using the d*n*/d*c* value 0.1850 ml/g, originally calculated for the gigantic haemoglobin of the earthworm (Zhu *et al.*, 1996).

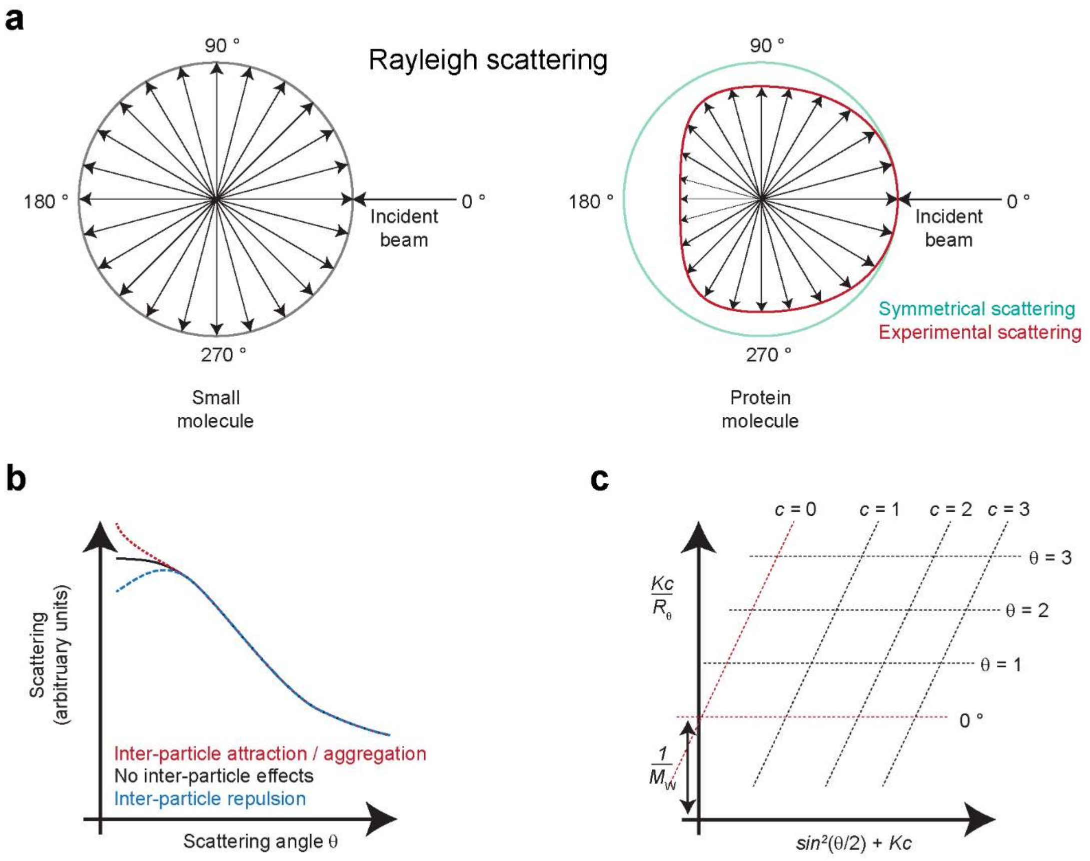
a
Rayleigh scattering
90 °
180 °
0 °
270 °
Incident beam
Small molecule
90 °
180 °
0 °
270 °
Incident beam
Symmetrical scattering
Experimental scattering
Protein molecule
b
Scattering (arbitruary units)
Inter-particle attraction / aggregation
No inter-particle effects
Inter-particle repulsion
Scattering angle θ
c
c = 0
c = 1
c = 2
c = 3
θ = 3
θ = 2
θ = 1
0 °
Kc/R_θ
1/M_W
sin²(θ/2) + Kc

Figure 2.1.1| Multi-angle light scattering. a) Small molecules exhibit Rayleigh scattering whilst larger protein molecules demonstrate asymmetric scattering in which only the scattering at an angle of zero degrees is independent of the molecules size and shape. **b)** Inter-particle effects effect the observed scattering, affecting most the observed scattering at small angles close to zero. Inter-particle attraction or aggregation results in increased scattering at low angles whilst inter-particle repulsion results in decreased scattering at low angles. **c)** A Zimm plot in which observed scattering values are plotted at multiple angles across a range of concentrations. The plot allows for the estimation of scattering values at a concentration of zero at an angle of zero degrees. The derived y-axis intercept allows for calculation of the molecular weight (M_w).

2.1.10 Size-exclusion chromatography small-angle x-ray scattering (SEC-SAXS)

SEC-SAXS is a technique used to characterise the solution state of molecules using the scattering of X-rays. After separation of different molecular species by size-exclusion chromatography, molecules within the solution scatter an incident beam of X-rays of which images are collected (Figure 2.1.2a) and radially integrated to produce a scattering curve which plots the intensity of scattered X-rays against the scattering angle (Figure 2.1.2b). Scattering is most intense at small angles and decays with an increase in scattering angle. The region closest to a scattering angle of zero is referred to as the Guinier region and through the Guinier approximation is treated as a region in which scattering intensity varies linearly with angle (Guinier, 1956). This region predominantly contains information about the overall shape of the molecule (its radius of gyration (Rg)) and its maximum dimension (D_{max}). High scattering angles contain proportionally more information regarding small inter-atomic distances, therefore higher resolution information, though data in this region is the weakest. The scattering curve can be converted to a real-space representation (a pairwise distance distribution plot) through a Fourier transform (Figure 2.1.2c). Figure 2.1.2c shows the distance distribution plot (or $P(r)$ curve) for differently shaped molecules of identical maximum inter-atomic distance (D_{max}) (Svergun and Koch, 2003). The D_{max} is taken from this plot as the x-axis intercept (indicated). Of particular relevance to the studies within this thesis, elongated rod-shaped molecules demonstrate a positively skewed $P(r)$ curve. These data can subsequently be utilised in modelling a three-dimensional envelope which describes the overall shape of individual molecules in the solution.

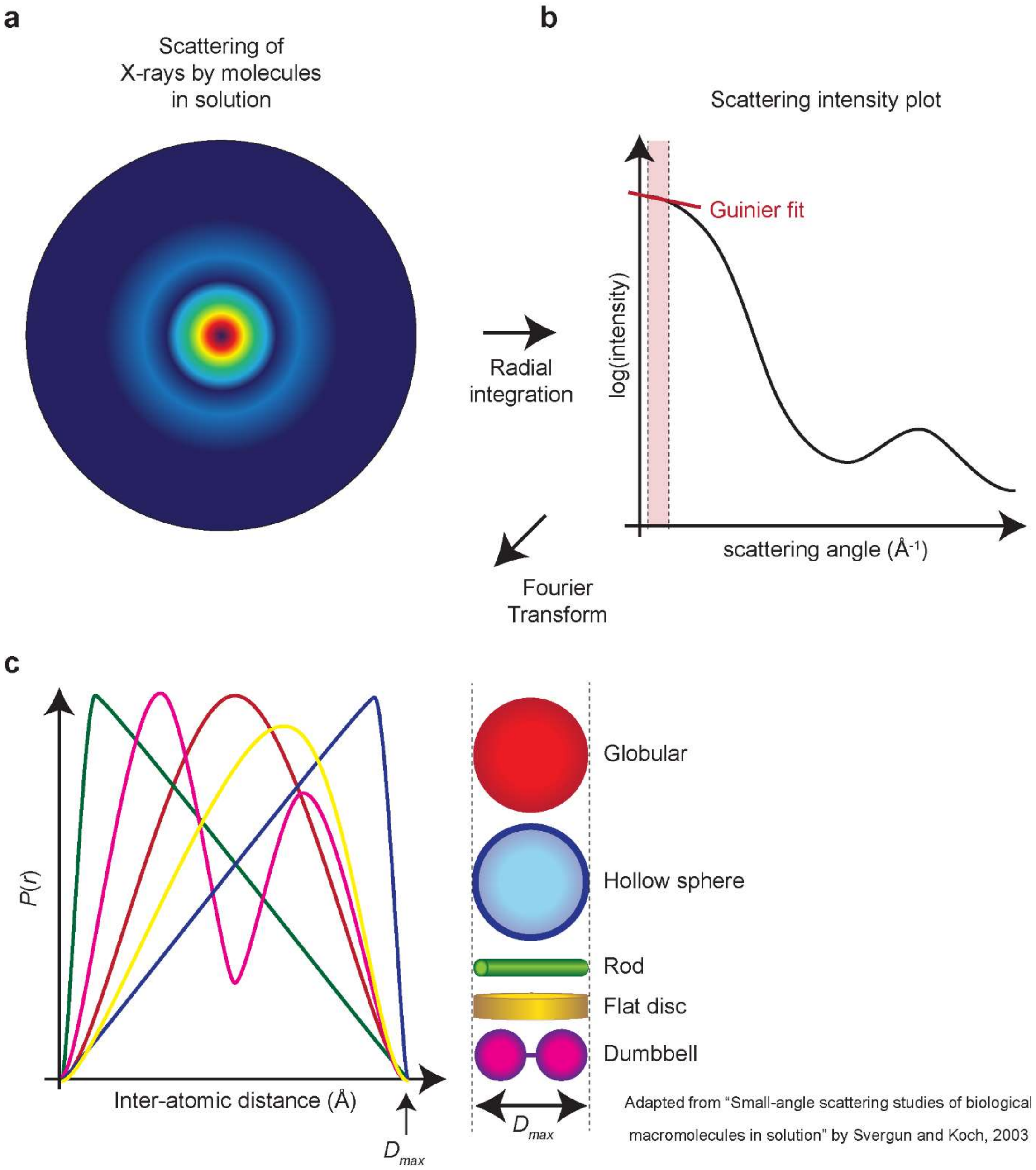
a
Scattering of X-rays by molecules in solution
Radial integration
b
Scattering intensity plot
Guinier fit
log(intensity)
scattering angle (Å^{-1})
Fourier Transform
c
P(r)
Inter-atomic distance (Å)
D_{max}
Globular
Hollow sphere
Rod
Flat disc
Dumbbell
D_{max}

Adapted from "Small-angle scattering studies of biological macromolecules in solution" by Svergun and Koch, 2003

Figure 2.1.2| The study of biomolecules using small angle X-ray scattering. a) A cartoon-representation of a small angle X-ray scattering image and **b)** represented as a two-dimensional plot after radial integration highlighting the highest intensity of scattering at the smallest angles. The Guinier region, in which scattering intensity is approximated to vary linearly with angle, is shaded in red with the Guinier fit represented by a red line. **c)** Fourier transform of the scattering intensity plot yields a pairwise distance-distribution plot in which the relative frequency of each inter-atomic distance is plotted. A characteristic curve for differently shaped molecules is depicted.

Data collected were collected at the Diamond Light Source (Oxfordshire, UK) on beamline B21. Samples were separated by size exclusion chromatography using a Superdex 200 increase 10/300 GL SEC column (GE healthcare) attached to an Agilent 1200 HPLC system equilibrated in 20 mM Tris pH 8.0, 150 mM KCl. System running at 0.5 ml/min. SYCP1 C-terminal constructs were also analysed in 50 mM sodium acetate, pH 5.5 or 4.6, 150 mM KCl. Data were recorded at 12.4 keV, in 3.0 s frames, with the detector at a distance of 4.014 m. Initial analysis of SAXS data was performed in ScÅtter 3.0 (http://www.bioisis.net). Buffer subtraction was achieved through the subtraction of frames either side of the protein elution peak. Frames of the protein peak were subsequently averaged. Guinier analysis was performed in ScÅtter to determine both the radius of gyration (R_g) and radius of gyration of the cross-section (R_c). Approximate values for the maximum inter-atomic distance of a sample were generated by http://www.bayesapp.org/ with distance distribution profiles (*P(r)*) subsequently generated in PRIMUS (Konarev *et al.*, 2003). Ab initio molecular envelopes were generated by DAMMIF run in interactive mode with random chain selected as expected shape. Ten to 20 independent runs were performed and averaged by DAMAVER (Petoukhov *et al.*, 2012). Structures and molecular models were docked within *ab initio* SAXS envelopes using SUPCOMB (Kozin and Svergun, 2001). Multiphase *ab initio* modelling using the scattering data of multiple components of the whole to model the overall architecture of a complex was performed using MONSA (Svergun, 1999). Rigid body docking and the modelling of linker sequences not present in docked crystal structures / molecular models was performed using CORAL, part of the ATSAS package (Petoukhov *et al.*, 2012). To assess how well a crystal structure or molecular model explains experimental SAXS data, theoretical scattering curves were generated and fitted against experimental data using CRYSOL (Svergun *et al.*, 1995).

2.1.11 Modelling coiled-coil structures using ROSETTA

Ab initio modelling of SYCP1 constructs was performed by Dr Owen Davies using ROSETTA and a library of decoys generated by QUARK (Xu and Zhang, 2012). A restraints file was utilised to guide structure modelling, such as imposing a maximum interatomic distance (i.e. length), inter-terminal residue distance maximum value (to select for chain orientation), and inter-chain maximum distance value to inhibit bulges.

2.1.12 Transmission Electron microscopy (TEM)

Electron microscopy was performed using a FEI Philips CM100 transmission electron microscope at the Electron Microscopy Research Services, Newcastle University. MBP fusion SYCP1 samples at 10 μM in 20 mM Tris pH 8.0, 250 mM KCl were incubated with 100 μM (per base pair) plasmid double-stranded DNA for 10 min. MAJIN-TERB2 samples at 5–10 μM, in 20 mM Tris pH 8.0, 250 mM KCl, were incubated with 10 μM (per base pair) plasmid double-stranded DNA for 10 min. Samples were then applied to carbon-coated electron microscopy grids prepared prior to use by glow discharge. Negative staining was performed using 2 % (w/v) uranyl acetate.

2.1.13 Electrophoretic mobility shift assay (EMSA)

DNA binding was assessed by EMSA and the exact protocol used in analysis the DNA binding capability of SYCP1 and MAJIN-TERB2 by EMSA differed. SYCP1 samples SYCP1$_{1\text{-}976}$, SYCP1$_{1\text{-}783}$, and MBP-fusions between 0 – 2.5 μM were incubated with 25 μ M (per base pair) 75 bp linear dsDNA substrate at the indicated concentrations in 20 mM Tris pH 8.0, 150 mM KCl. SYCP1$_{676\text{-}770}$ was analysed by EMSA at concentrations between 0 – 3.2 μM with 32 μM (per base pair) 470 bp linear dsDNA substrate in either 20 mM Tris pH 8.0, 150 mM KCl or 50 mM sodium acetate, pH 5.5, 150 mM KCl. Mixed samples were incubated on ice for 5 minutes. Glycerol to 3 % was added to samples prior to analysis by electrophoresis on a 0.5 % (w/v) agarose gel with running buffer 0.5x TBE (Tris-Borate-EDTA) pH 8.0 or 25 mM GABA (gamma-Aminobutyric acid) pH 5.5, at 25 V for 4 hours at 4 ˚C. DNA was visualised using SYBRsafe™ (ThermoFisher).

The DNA binding capability of MAJIN-TERB2 complexes was also assessed by EMSA. MAJIN-TERB2 complexes at the concentrations were incubated with 0.3 μM (per molecule) 75 bp linear random sequence dsDNA, in 20 mM Tris pH 8.0, 250 mM KCl for 1 h at 4 °C.

The sequence of the 75 bp sequence utilised in both studies is below:

GCGAACACCCTGCATCGTCCGACCGGCTCTACAGGTTCCACCGGTTCTACGGGCTCCGGC
CTGTATTTCTCTTCC

Glycerol was added at a final concentration of 3 %, and samples were analysed by electrophoresis on a 0.5 % (w/v) agarose gel in 0.5x TBE pH 8.0 at 20 V for 4 hours at 4 °C. DNA was detected by SYBR™ Gold (ThermoFisher).

2.1.14 Determination of apparent K_D by EMSA

Similar EMSA experiments with altered experimental parameters were utilised to quantify the strength of DNA-binding of the different MAJIN-TERB2 complexes. A fluorescent substrate, 25 nM 6-FAM (fluorescein amidite)-labelled 144 bp random sequence dsDNA, was utilised to allow for detection at low nucleotide concentrations. Protein concentrations were as indicated in the figures and refer to the concentration of the molecular oligomeric species. Fluorescent signal was enhanced by SYBR™ Gold (ThermoFisher) staining. Imaging was performed using a Typhoon™ FLA 9500 (GE Healthcare), with 473 nm laser at excitation wavelength 90 nm and emission wavelength 520 nm, using the LPB filter and a PMT voltage of 400 V. Gels were analysed using ImageJ software (https://imagej.nih.gov/ij/). The DNA-bound proportion was plotted against molecular protein concentration and fitted to the Hill equation (below, equation 5), with apparent K_D determined, using Prism8 (GraphPad).

$$\%\ \text{DNA bound} = C^n/(K_D^n + C^n) \tag{5}$$

The sequence of the 5' 6-FAM labelled dsDNA sequence is below:

TCCAGGGTTCCATGGAGATAAAGGTCAATAAATTAGAGTTAGAACTAGAAAGTGCCAAA
CAGAAATTTGGAGAAATCACAGACACCTATCAGAAAGAAATTGAGGACAAAAAGATATC
AGAATAATAACCATGGATATCGAATT

2.1.15 Assay for the determination of zinc content

10 µl protein samples between 0 – 100 µM were digested by adding 0.3 µl proteinase K at 20 mg/ml and incubating for 1 hour at 60 ˚C. A series of standards containing 0 – 100 µM zinc acetate were prepared. Subsequently, 10 µl of each standard or sample is mixed with 80 µl PAR (4-(2-pyridylazo)resorcinol) at 50 µM dissolved in 20 mM Tris pH 8.0, 150 mM KCl (no DTT). After 5 minutes at room temperature each sample in analysed by UV spectroscopy between 200 – 600 n. Zinc in solution is chelated by PAR resulting in an observable spectrophotometric shift from 414 to 494 nm.

2.1.16 Oxidation assay using Ellman's reagent (DTNB)

A series of standards containing 0 – 1.0 mM reduced glutathione (GSH) were prepared. 25 µl of each standard or sample at 0.5 mM were mixed with 250 µl 20 mM Tris pH 8.0, 150 mM KCl (no DTT) and 5 ul Ellman's reagent (5,5′-Dithiobis(2-nitrobenzoic acid) or DTNB) at 4 mg/ml and incubated at room temperature for 15 minutes. Samples were then analysed by UV spectroscopy between 200 – 600 nm. The extinction coefficient at 412 nm for TNB (2-nitro-5-thiobenzoate) is 14150 with a molecular weight of 396.34 allowing for calculation of TNB molarity, directly relating to the number of free thiol groups within the protein.

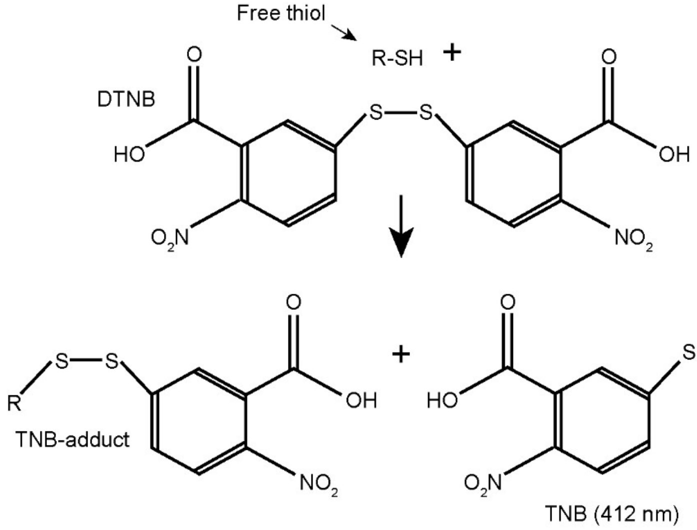

Figure 2.1.3| Ellman's reagent reacts with free thiols to release stoichiometric quantities of detectable TNB. Ellman's reagent (DTNB) readily reacts with free thiols to produce a single TNB-protein adduct and release a stoichiometric amount of TNB which absorbs maximally at 412 nm.

2.1.17 Protein crystallisation, X-ray data collection, and structure solution.

Proteins were crystallised as summarised in Table 2.2. The initial condition in which crystals grew is indicated, citing the name of the commercial screen utilised, in addition to the optimised crystallisation condition if applicable. The collection of X-ray diffraction data is detailed in Tables 2.3 and 2.4. Table 2.3 details the collection of diffraction datasets which did not lead to structure solution (but are integral to the following study) whilst Table 2.4 details the collection of datasets which resulted in the solution of protein structures. Tables 2.5 and 2.6 detail the processing of datasets, citing the software utilised and pertinent information such as resolution limit, spacegroup, unit cell dimensions and the number of molecules within the asymmetric unit (ASU) as predicted through calculation of the Matthew's coefficient (Matthews, 1968; Kantardjieff and Rupp, 2003). Crystal structures were solved using the methods summarised in Table 2.7. Interesting features of the structure solutions are detailed in Methods section 2.1.18. All data processing and crystal structure solution was performed by Dr Owen Davies.

Crystallisation conditions		
Protein	**Initial condition**	**Optimised condition**
SYCP1$_{640-783}$*	**PACT D7** 0.1 M Tris pH 8.0, 0.2 M sodium chloride, 20 % (v/v) PEG6000	0.2 M sodium chloride, 0.1 M Tris pH 8.0, 16.25 % (v/v) PEG6000, 0.1 M sodium citrate tribasic tetrahydrate
SYCP1$_{676-770}$ (native)*	**JCSG+ A5** 0.2 M magnesium formate, 20 % (v/v) PEG3350	0.2 M magnesium formate, 20 % (v/v) PEG3350
SYCP1$_{676-770}$ (Iodide)*	**JCSG+ A5** 0.2 M magnesium formate, 20 % (v/v) PEG3350	0.09 M magnesium formate, 14.4 % (v/v) PEG3350
SYCP1$_{676-770}$ (SeMet)*	**JCSG+ A5** 0.2 M magnesium formate, 20 % (v/v) PEG3350	0.15 M magnesium formate, 12.75 % (v/v) PEG3350, 0.1 M sodium iodide
SYCP1$_{101-175}$ I222	**JCSG+ D3** 0.2 M sodium chloride 0.1 M Na/K phosphate pH 6.2 50 % (v/v) PEG200	0.14 M sodium chloride, 0.07 M Na/K phosphate pH 6.2, 35 % (v/v) PEG200
SYCP1$_{101-206}$ I2	**MPD A3 and F3** **4 °C** 0.2 M ammonium fluoride or 0.1 M MES pH 6.0, 40 % (v/v) MPD	N/A
SYCP1$_{676-770}$ I4$_1$22	**Structure A12** 0.1 M sodium cacodylate pH 6.5 1.4 M sodium acetate	N/A
SYCP$_{676-770}$ C2	**Index C1** 3.5 M sodium formate pH 7.0	N/A
MAJIN$_{1-112}$ TERB2$_{168-220}$ SeMet	**Morpheus D4** 0.12 M alcohols, 0.1 M Buffer system 1 pH 6.5, 37.5 % MPD_P1K_P3350	N/A
MAJIN$_{1-106}$ TERB2$_{168-207}$	**Morpheus D12** 0.12 M alcohols, 0.1 M Buffer system 3 pH 8.5, 37.5 % MPD_P1K_P3350	0.12 M alcohols, 9.1 mM bicine pH 5.03 + 60.9 mM Trizma pH 10.83, 37.5 % MPD_P1K_P3350

Table 2.2| Summary of initial and optimised crystallisation conditions for SYCP1 and MAJIN-TERB2. Asterisks indicate crystals which did not lead to structure solution.

Data Collection for unsolved crystals					
Protein	**Experiment type**	**Beamline**	**Wavelength (Å)**	**No. images**	**Relevant datasets**
SYCP1$_{640-783}$	Native	I03	0.9795	2000	SYCP1-05_6, SYCP1-05_7
SYCP$_{676-770}$	Native	I03	0.9795	2000	S1C-20, S1C-11
SYCP1$_{676-770}$	SAD* - iodide	I04	1.9074	2000	S1C-01
SYCP$_{676-770}$	SAD - seleno-methionine	I03	0.9795 Å	7200	S1C-16, S1C-26

Table 2.3| Summary of data collections for SYCP1 constructs which are described in text but did not result in structure solution. All data collected at 100 K Pilatus 6 M detector. *SAD = single-wavelength anomalous diffraction

2.1.19 X-ray diffraction data collection for solved crystal structures

Data Collection for solved crystal structures					
Protein	**Experiment type**	**Beamline**	**Wavelength (Å)**	**No. images, osc. and exp.**	**Relevant datasets**
SYCP1$_{101-175}$ I222	SAD - Iodide	I02	1.7712 Å	7200 0.1 ˚, 0.05 s	S1N-5 dls230515
SYCP1$_{101-206}$ I2	Native	I04-1	0.9282 Å	3x 2000 0.1 ˚, 0.05 s	S1N-7, 12, 19 dls080517
SYCP1$_{676-770}$ I4122	Native	I02	0.9795 Å	2000 0.1 ˚, 0.08 s	S1C-13; dls160416
SYCP$_{676-770}$ C2	Native	I02	0.9795 Å	2000 0.1 ˚, 0.08 s	S1C-14; dls220216
MAJIN$_{1-112}$ TERB2$_{168-220}$ SeMet	SAD - seleno-methionine	I04-1	0.9159 Å	3x 3600 (10˚ kappa increments) 0.1 ˚, 0.05 s	MEIOB-12 dls150418
MAJIN$_{1-106}$ TERB2$_{168-207}$	Native	I03	0.9763 Å	2000 0.1 ˚, 0.05 s	MEIOB-35 dls030518

Table 2.4| Summary of data collections for SYCP1 constructs and MAJIN-TERB2 complexes which for which the structures were solved. All data collected at 100 K using Pilatus 6 M detector. *SAD = single-wavelength anomalous diffraction.

Data processing							
Construct	Indexing	Scaling	Merging	Resolution limit (Å)	Space-group	Unit cell dimensions (Å/°)	Molecules per ASU
SYCP1$_{640-783}$	XDS	XSCALE	Aimless	3.7	P1	$a = 44.23$, $b = 86.86$, $c = 101.75$ $\alpha = 101.54$, $\beta = 101.77$, $\gamma = 97.62$	6-10
SYCP1$_{676-770}$ (Native; S1C-20)	XDS	XSCALE	Aimless	2.52 (anisotropic limits: 3.20, 3.00, 2.30)	P2$_1$	$a = 87.80$, $b = 47.04$, $c = 138.12$, $\alpha = 90$, $\beta = 94.78$, $\gamma = 90$	4-6
SYCP1$_{676-770}$ (Native; S1C-11)	XDS	XSCALE	Aimless	2.55	P2$_1$	Similar to above	4-6
SYCP1$_{676-770}$ (Iodide; S1C-01)	XDS	XSCALE	Aimless	2.90	P2$_1$	$a = 87.58$, $b = 46.91$, $c = 138.71$, $\alpha = 90°$, $\beta = 94.90°$, $\gamma = 90°$	4
SYCP1$_{676-770}$ (SeMet; S1C-26)	XDS	XSCALE	Aimless	2.80	P2$_1$	$a = 89.28$, $b = 47.65$, $c = 139.15$, $\alpha = 90$, $\beta = 96.00$, $\gamma = 90$	2:2

Table 2.5| Summary of data processing for the unsolved crystals presented within this thesis. All data were processed by Dr Owen Davies. SAD = single-wavelength anomalous diffraction. XDS (Kabsch, 2010b). AutoPROC (Vonrhein *et al.*, 2011). XSCALE (Diederichs *et al.*, 2003). Aimless (Evans, 2011). UCLA diffraction anisotropy server (https://services.mbi.ucla.edu/anisoscale/) (Strong *et al.*, 2006). Number of molecules per asymmetric unit predicted through calculation of the Matthew's coefficient (Matthews, 1968; Kantardjieff and Rupp, 2003).

Data processing							
Construct	Indexing	Scaling	Merging	Anisotropic resolution limits (Å) / principal components (Å$_2$)	Space-group	Unit cell dimensions (Å/°)	Molecules per ASU
SYCP1$_{101-175}$	XDS	XSCALE	Aimless	1.9, 2.0, 2.1 / 13.25, -0.78, -14.08	I222	$a = 28.64$, $b = 39.38$, $c = 165.77$ $\alpha = 90$, $\beta = 90$, $\gamma = 90$	1
SYCP1$_{101-206}$	XDS in AutoPROC	3 datasets in XSCALE	Aimless	2.1, 2.1, 2.6 / 24.09, 6.01, -20.19	I2	$a = 65.67$, $b = 37.31$, $c = 108.52$, $\alpha = 90$, $\beta = 106.66$, $\gamma = 90$	2
SYCP1$_{676-770}$ (I4$_1$22)	XDS in AutoPROC	XSCALE	Aimless	2.9, 2.9, 2.5 / 16.05, 16.05, -32.09	I4$_1$22	$a = 43.38$, $b = 43.38$, $c = 292.18$, $\alpha = 90$, $\beta = 90$, $\gamma = 90$	1
SYCP1$_{676-770}$ (C2)	XDS in AutoPROC	XSCALE	Aimless	2.2, 2.3, 2.2 / 18.46, 3.44, -21.90	C2	$a = 233.42$, $b = 42.85$, $c = 43.69$, $\alpha = 90°$, $\beta = 93.61°$, $\gamma = 90°$	4
MAJIN$_{1-112}$ TERB2$_{168-220}$	XDS	XSCALE	Aimless	2.9 (no anisotropic limits)	P322$_1$	$a = 59.88$, $b = 59.88$, $c = 159.93$, $\alpha = 90$, $\beta = 90$, $\gamma = 120$	2:2
MAJIN$_{1-106}$ TERB2$_{168-207}$	XDS	XSCALE	Aimless	1.85 (no anisotropic limits)	C222$_1$	$a = 59.97$, $b = 88.39$, $c = 111.67$, $\alpha = 90$, $\beta = 90$, $\gamma = 90$	2:2

Table 2.6| Summary of data processing for the solved crystal structures presented within this thesis. All data were processed by Dr Owen Davies. SAD = single-wavelength anomalous diffraction. XDS (Kabsch, 2010b). AutoPROC (Vonrhein *et al.*, 2011). XSCALE (Diederichs *et al.*, 2003). Aimless (Evans, 2011). UCLA diffraction anisotropy server (https://services.mbi.ucla.edu/anisoscale/) (Strong *et al.*, 2006). Number of molecules per asymmetric unit predicted through calculation of the Matthew's coefficient (Matthews, 1968; Kantardjieff and Rupp, 2003).

Structure solution									
Construct	Solution strategy	Solved using	Initial building	Manual building and refinement	TLS groups	R /R_{free}	% in favoured region of Ramachandran	Clash-score	Molprob. score
SYCP1$_{101-175}$	SAD (iodide)	SHELX C/D/E in HKL2MAP	PHENIX Autobuild and refine	Coot and PHENIX refine	5	0.2272/ 0.2392	100	6.77	1.37
SYCP1$_{101-206}$	*Ab initio* MR	AMPLE w/ QUARK decoys	SHELX E and ARP/wARP PHENIX Autobuild	Coot and PHENIX refine	N/A	0.2264/ 0.2441	100	3.05	1.10
SYCP1$_{676-770}$	*Ab initio* MR	ARCIMBOLD_LITE	PHASER and SHELX E	Coot and PHENIX refine	N/A	0.2251/ 0.2517	100	1.24	0.84
SYCP1$_{676-770}$	*Ab initio MR*	ARCIMBOLDO_ SHREDDER	PHENIX Autobuild	Coot and PHENIX refine	N/A	0.2186/ 0.2526	100	6.86	1.38
MAJIN$_{1-112}$ TERB2$_{168-220}$	SAD (SeMet)	PHENIX Autosol	PHENIX Autobuild	Coot and PHENIX refine	18	0.2542/ 0.3039	98.4 (zero outliers)	0.46	0.66
MAJIN$_{1-106}$ TERB2$_{168-207}$	MR	PHASER	N/A	PHENIX Autobuild, Coot, PHENIX refine	3 per chain	0.1883/ 0.2072	98.49 (zero outlier)	0.22	0.58

Table 2.7| Summary of structure solution strategies and statistics for the crystal structures presented within this thesis. All structures were solved by Dr Owen Davies, bar SYCP1$_{676-770}$ structures which were solved by Dr Isabel Usón. SAD = single-wavelength anomalous diffraction. MR = Molecular replacement. HKL2MAP (Pape and Schneider, 2004). PHENIX (Adams *et al.*, 2010). AMPLE through CCP4 online (https://www.ccp4.ac.uk/ccp4online/) (Xu and Zhang, 2012). Coot (Emsley *et al.*, 2010). ARCIMBOLDO_LITE (Rodriguez *et al.*, 2009). ARCIMBOLDO_SHREDDER (Millán, 2017). PHASER (McCoy *et al.*, 2007). Molprobability (Chen *et al.*, 2010).

2.1.18 Notes of interest in the solution of crystal structures

SYCP1$_{101\text{-}175}$: To estimate phases, a five iodide sub-structure was solved for the asymmetric unit. Based upon anomalous difference maps, the five putative iodide sites were reduced to two sites and the structure completed through the placement of a triethylene glycol (PGE) molecule.

SYCP1$_{101\text{-}206}$: The data from three collections were scaled together in XSCALE prior to merging in Aimless (Diederichs *et al.*, 2003; Evans, 2011). The structure was completed by the placement of two MPD molecules and two chloride ions.

SYCP1$_{676\text{-}770}$ (I4$_1$22): Upon solution by ARCIMBOLDO_LITE, PHASER succeeded in placing two idealised 30-residue polyalanine helices, which were extended by auto-tracing by SHELXE using the Arcimboldo mode for coiled-coil structures (Caballero, 2017). A SHELXE Correlation Coefficient of 40.5 % signified a correct solution. The structure was complete through the addition of one acetate ligand.

SYCP1$_{676\text{-}770}$ (C2): ARCIMBOLDO_SHREDDER utilised the I4$_1$22 structure to generate a set of non-redundant, overlapping, 99-residue models from which partial solutions were obtained, combined, and used to solve the phase problem.

MAJIN$_{1\text{-}112}$-TERB2$_{168\text{-}220}$: Solved by SAD-phasing of MAJIN$_{1\text{-}112}$–TERB2$_{168\text{-}220}$ seleno-methionine derivative protein crystals. Eight selenium sites were identified, and PHENIX Autosol used to generate a density-modified experimental map utilising the combined unmerged intensity data.

MAJIN$_{1\text{-}106}$-TERB2$_{168\text{-}207}$: PHASER was used for the molecular replacement of a single MAJIN chain of the seleno-methionine derivative SAD structure to solve the structure.

2.1.19 Mammalian cell transfection and imaging

For studies of SYCP1 expression in mammalian cells, COS-7 cells were utilised. COS-7 cells are immortalised CV-1 cells (which in origin are kidney fibroblasts of the African green monkey) through transformation with a version of the SV40 virus which is replication deficient but produces the large T antigen. SYCP1 constructs were cloned into the pEGFP-C3 vector with contains an SV40 promoter allowing for their replication by the large T antigen (Ali and DeCaprio, 2001; Aruffo, 2001). I firstly replicated the experiments of Ollinger *et al.* using the human sequence for SYCP1, transfecting eGFP-SYCP1$_{1\text{-}976}$ into COS-7 cells using lipofectamine, as follows (Ollinger *et al.*, 2005). COS-7 cells were cultured in Dulbecco's Modified Eagle's Medium (DMEM) supplemented with 10 % foetal calf serum and 2 mM L-Glutamine. Cells were lifted by trypsinisation and cell density determined using a Cellometer Auto T4 (Nexcelom) and respective software. For each transfection experiment, 40,000 cells were plated (35 mm Cellview culture dish, Greiner) and incubated at 37 °C for 1.5 hours to allow adherence to the plate surface and subsequently flooded by the addition of 2 ml DMEM and incubated for 24 hours. Post-incubation, the media was discarded and replaced with 1.5 ml reduced serum media, Opti-MEM (Gibco, Thermo Fisher Scientific). Cells were incubated for 2 hours. Each transfection involved the addition of 500 µl of a lipid-DNA complex suspension in which cationic lipids facilitate the delivery of DNA by endocytosis (Chesnoy and Huang, 2000; Hirko *et al.*, 2003). This suspension was created by a two-step approach. In the first step, two stocks were created. Quantities indicated are per transfection. 1) – DNA+Opti-MEM: 4µg vector at approximately 400 ng/µl was added to Opti-MEM to a total volume of 250 µl. 2) – Lipofectamine+Opti-MEM: 7 µl lipofectamine (Life Technologies) was added to 243 µl Opti-MEM. These were incubated at room temperature for 10 minutes. In the second step, 250 µl DNA+Opti-MEM was added to 250 µl Lipofectamine+Opti-MEM dropwise before gently mixing by pipetting up and down. This mixture was incubated at room temperature for 20 minutes. Subsequently the full 500 µl DNA+Lipofectamine+Opti-MEM mixture was added to the cell culture and incubated at 37 °C.

After 24 hours, Fluorescence microscopy was utilised to visualise eGFP-SYCP1 polycomplexes (excitation 488 nm, emission = 509 nm) using An Inverted System Microscope IX71 (Olympus) between a magnification of 60 and 90 times. DNA was visualised by Hoechst 33342 (Sigma Aldrich) staining (excitation = 346 nm, emission = 460 nm). Images were acquired using a cooled CCD camera

(Micromax-1300Y, Sony) and analysed and pseudo-coloured using Metamorph software (Molecular Devices). Digital images were processed using Adobe Photoshop 5 (Adobe, Sane Jose). For analysis, 100 cells were counted per transfection and the percentage of cells in which SYCP1 polycomplexes were formed was calculated. Each experiment was performed in triplicate.

For experiments in which electron microscopy was subsequently utilised to analyse the ultrastructure of resultant SYCP1 polycomplexes, transfection was performed concurrent with the plating of cells, forgoing both the 24-hour period in which cells were allowed to adhere to the plate and the starvation period.

2.1.20 Thin slice preparation for Transmission EM (TEM)

The preparation of thin slices for analysis by transmission electron microscopy was performed by the Electron Microscopy Research Services at Newcastle University. Prior to each step, samples in Eppendorfs were centrifuged for 5 minutes at 3,000 g and the supernatant discarded without disturbing the pelleted sample. In each step, samples were resuspended fully and incubated for the indicated time. All H_2O used was deionised. All acetone used was from a desiccator. Samples were: 1) fixed in 2 % glutaraldehyde in 0.1 M sodium cacodylate, pH 7.4 (at least 1 hour). 2) Washed with 0.1 M cacodylate, pH 7.4 (2x 10 minutes). 3) Fixed in 1 % osmium tetroxide solution in H_2O (30 minutes). 4) Rinsed in H_2O (2x 10 minutes). 5) Dehydrated through serial washes in acetone (25, 50, 75 % in H_2O; 15 minutes each, 100 %; 2x 20 minutes). Then, 6) using the TAAB epoxy resin kit, samples were impregnated with increasing concentrations of epoxy resin (25, 50, 75 % in acetone; 30 minutes each, 100 %; 3x 1 hour). 7) Sample-containing Eppendorfs were filled with resin and re-spun (repeated once). 8) The resin was polymerised at 60 ˚C for 24 hours with the Eppendorf lids open. Sectioning was then performed by the Electron Microscopy Research Service team.

Chapter 3

The molecular basis of meiotic chromosome synapsis through SYCP1 self-assembly

INTRODUCTION

3.1.1 The transverse filament proteins and human SYCP1

The synaptonemal complex represents the morphological signature of the pachytene stage of meiotic prophase I. Holding homologous chromosomes in synapsis along their entire length, this enigmatic tripartite structure can be as long as 24 μm and consists of chromosomally-bound lateral elements connected to an electron-dense central element by perpendicularly orientated transverse filaments (TFs) (Figure 1.1.8) (Page and Hawley, 2004; Vranis *et al.*, 2010). The structure is extraordinarily conserved across evolution, with strikingly similar structures observed almost universally across sexually reproducing organisms including *Saccharomyces cerevisiae*, *Drosophila melanogaster*, and *Caenorhabditis elegans* with only a few notable exceptions such as *Saccharomyces pombe* and *Aspergillus nidulans* (overviewed in Section 1.1.15) (Zickler and Kleckner, 1999). Astoundingly, however, the structural protein components of the respective synaptonemal complex assemblies demonstrate little to no sequence homology between organisms of different phyla. This, therefore, likely demonstrates a case of convergent evolution in which functionally and morphologically similar structures have evolved to enact the same function whilst utilising proteins of distinct origin (Fraune *et al.*, 2012). This phenomenon is well demonstrated by the similar domain structure of the TF proteins of different organisms (such as those of mammals and *Drosophila*) despite sequence divergence. The presence of a transversal element in the synaptonemal complex is particularly evident in electron microscopy images of the SC, with rod-like structures visibly connecting the lateral elements to the midline central element (Figure 3.1.1) (Comings and Okada, 1971; Solari and Moses, 1973). The TFs of the hamster, in Figure 3.1.1a, were measured as having a width of 16 Å. This chapter proceeds with an introduction to the structure and function of TF proteins and their role within the SC.

3.1.2 Mammalian SYCP1

SYCP1 of mammals (SYN1 in hamster) form the TF protein of the SC within these organisms. They exhibit a high degree of sequence identity - 64 % sequence identity across the SYCP1 molecules of 343 vertebrate species, including fish, of which a subset is aligned in Appendix 1. The molecule was first identified as a 111 kDa protein localised to the synaptonemal complex of rat in 1992 by Meuwissen *et al.* through the screening of a testis cDNA expression library using antibodies

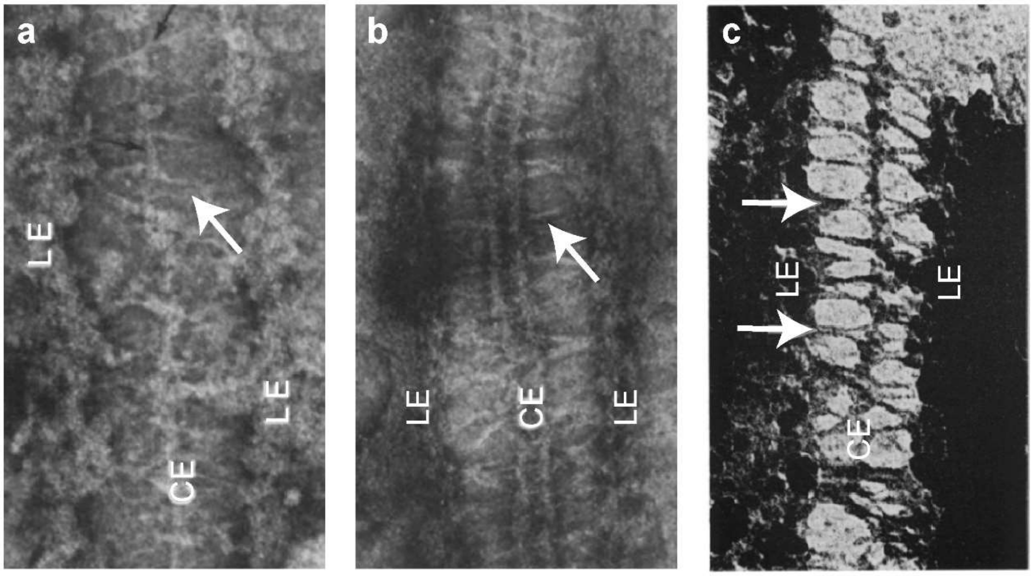

Mesocricetus auratus
Solari and Moses, 1973
J Cell Biol

Acheta domesticus
Solari and Moses, 1973
J Cell Biol

Coternix coturnix japonica
Comings and Okada, 1971
Exp Cell Res

Figure 3.1.1| The transverse filaments of the SC. a-c) Spread preparation synaptonemal complexes of **a)** Golden hamster (*Mesocricetus auratus*) (magnification x150000), **b)** House cricket (*Acheta domesticus*) (magnification x150000) and **c)** Japanese quail (*Coternix coturnix japonica*) (magnification x113000) which the central element (CE) and lateral elements (LE) are indicated. Transverse filaments (indicated by white arrows) are clearly visible and measured to have a diameter of 16 Å in hamster

which specifically recognise a purported SC protein of a corresponding molecular weight (Meuwissen *et al.*, 1992). The protein was later shown to be expressed specifically in the spermatocytes of male and oocytes of female (Pousette *et al.*, 1997; de Vries *et al.*, 2005). Soon after, in 1995, a homologous cDNA sequence was identified in mouse, predicting a translated protein of 993 residues (Sage *et al.*, 1995). It is now recognised that the coding sequence for rat SYCP1 described by Meuwissen *et al.* incorrectly missed coding sequence corresponding to 51 additional N-terminal residues correctly identified in the murine sequence, such that rat SYCP1 is 997 residues in length. cDNA encoding SYCP1 of *Homo sapiens* was identified later in 1997 and demonstrated an identical domain structure to that of rat and murine SYCP1 (Figure 3.1.2) (Meuwissen *et al.*, 1997). Human SYCP1 shall form the research focus of the following chapter. The TF proteins of budding yeast and *Drosophila* shall also be discussed as the similarities and differences between these proteins provide insights into their molecular functions and mechanisms.

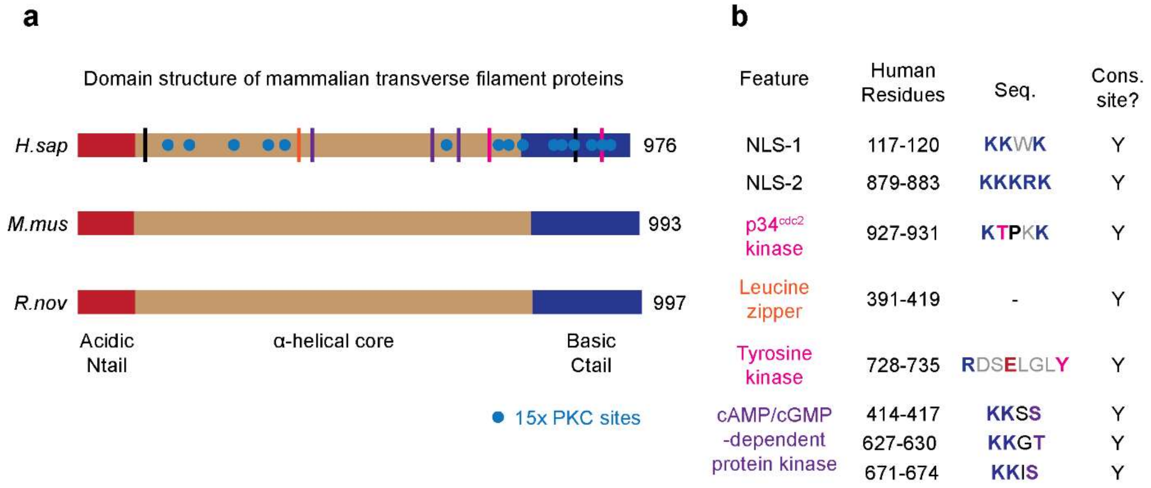

Feature	Human Residues	Seq.	Cons. site?
NLS-1	117-120	KKWK	Y
NLS-2	879-883	KKKRK	Y
$p34^{cdc2}$ kinase	927-931	KTPKK	Y
Leucine zipper	391-419	-	Y
Tyrosine kinase	728-735	RDSELGLY	Y
cAMP/cGMP -dependent protein kinase	414-417	KKSS	Y
	627-630	KKGT	Y
	671-674	KKIS	Y

Figure 3.1.2| Domain structure of the mammalian transverse filaments. a) Schematic representation of *Homo sapiens* SYCP1, *Mus musculus* SYCP1 and *Rattus norvegicus* SYCP1 with the unstructured, acidic tail in red, α-helical core in beige, and unstructured, basic tail in blue. Residue length is indicated. Sequence features detailed in (b) are marked against human SYCP1 – nuclear localisation signals (NLS) in black, $p34^{cdc2}$ and tyrosine kinase target sites in magenta, cAMP/cGMP-dependent protein kinase sites in purple, leucine zipper in orange and protein kinase C (PKC) sites as blue dots. **b)** Table of sequence features of SYCP1. Residue boundaries are indicated, and the human sequence is shown with consensus residues in bold. Basic residues are in blue, acidic in red and phosphorylated residues in magenta or purple. Whether the sequence is conserved between humans and rat/mouse is indicated (Y is conserved).

3.1.3 Bioinformatic analysis of SYCP1

Human SYCP1 contains a predicted central helical core encompassing amino acids 101-783 as determined by JPred4 (Figure 3.1.3) (Drozdetskiy *et al.*, 2015). Secondary structure prediction further suggests short stretches of α-helix and β-sheet within an otherwise largely unstructured C-terminus (residues 784-976). COILS suggests the likely folding of the SYCP1 helical core as a coiled-coil (Figure 3.1.3) (Parry, 1982; Lupas *et al.*, 1991; Lupas, 1997). This region of SYCP1 within human, rat and mouse shows similarity to myosin, but not beyond the level expected between non-related coiled-coil proteins, thus only reflecting the propensity to form coiled-coils. In comparison with rat and mouse, human SYCP1 lacks 21 amino acids within the central amphipathic α-helix, corresponding to an in-frame deletion of three heptad-repeats.

Using the EMBOSS application, charge, the gross charge distribution across SYCP1 is revealed (Rice *et al.*, 2000). The central helical core and unstructured N-terminus, rich in acidic residues, are net negatively charged (N-terminal residues 1-100 have a pI of 4.61) whereas the N-terminal tip of the helical core and the unstructured C-terminus (residues 784-976; pI 9.80) are net positively charged hinting at potential roles in DNA binding (Figure 3.1.3). A summary of additional sequence features within SYCP1 are detailed in Figure 3.1.2, including potential phosphorylation sites, nuclear localisation signals, and structural motifs. A full sequence alignment for SYCP1 can be found in Appendix 1.

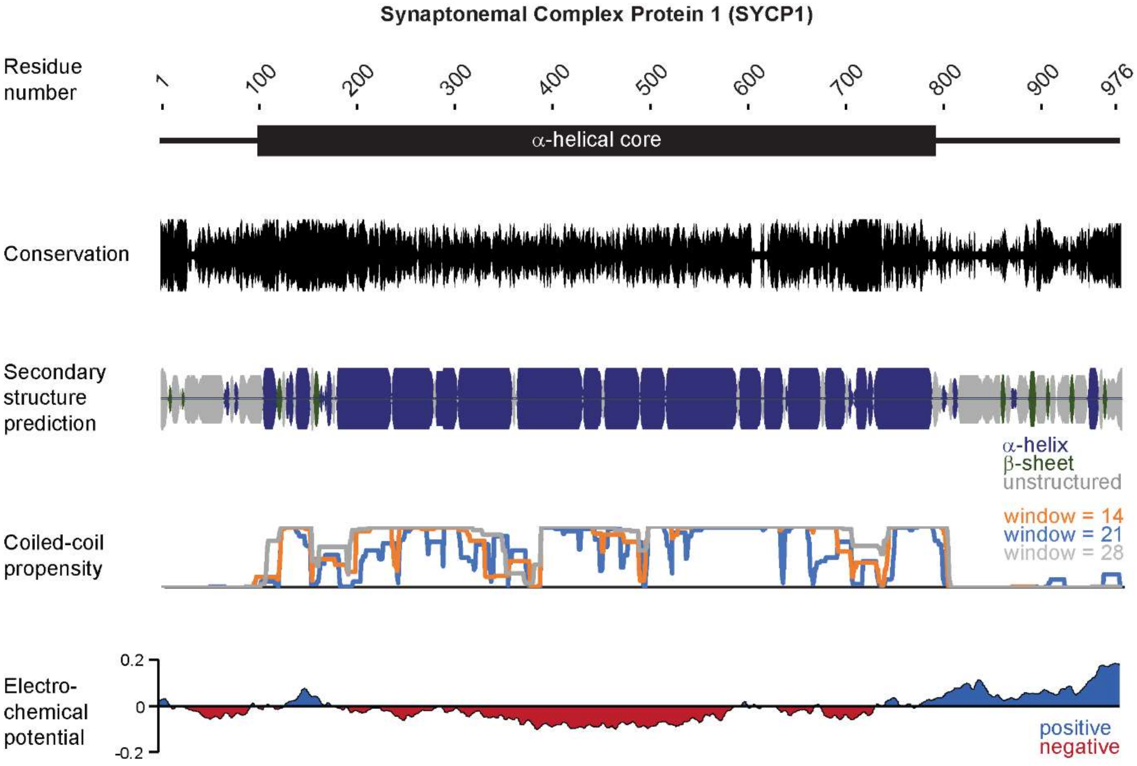

Figure 3.1.3| Bioinformatic analysis of SYCP1. Conservation scores per residue calculated by ConSurf using a manually edited alignment of 343 SYCP1 sequences to remove low quality and non-SYCP1 sequences (Berezin *et al.*, 2004; Ashkenazy *et al.*, 2016). Secondary structure prediction calculated by JPred4 using an alignment of 62 sequences compiled by ensembl and verified to contain only vertebrate species. α-helix in blue, β-sheet in green and unstructured in grey. A full alignment of SYCP1 is presented in Appendix 1 (Waterhouse *et al.*, 2009; Drozdetskiy *et al.*, 2015; Zerbino *et al.*, 2018). Coiled-coil propensity calculated by COILS demonstrates a predicted central coiled-coil domain (Parry, 1982; Lupas *et al.*, 1991; Lupas, 1997). The electrochemical potential distribution of SYCP1 was calculated by charge of the EMBOSS suite using a window size of 5 residues and subsequently averaged across 100 residues to demonstrate overall charge distribution. The central coiled-coil is largely acidic with a basic N-terminal tip whilst the unstructured C-terminus is highly basic.

3.1.4 SYCP1 bi-orients within the mammalian SC

Preliminary immuno-gold electron microscopy studies demonstrated that SYCP1 specifically localises to synapsed regions of meiotic chromosomes and hinted that SYCP1 was bi-orientated within the SC, with the C-terminus staining proximal to the chromosome axis (Meuwissen *et al.*, 1992). This supposition that SCP1 was bi-orientated within the SC, with the C-terminus anchored within the lateral elements was confirmed as being correct in two subsequent studies (performed concurrently and published back-to-back) (Liu *et al.*, 1996; Schmekel *et al.*, 1996). Both studies utilised antibodies raised towards rat SYCP1 though one study analysed the rat SC whilst the other focused on murine SC (I assume that the murine cDNA sequence only became available during their studies). The work of Schmekel *et al*. raised antibodies towards large regions of SYCP1, whilst Liu *et al*. created antibodies towards shorter, more specifically terminal regions of SYCP1. These are detailed in Figure 3.1.4a, converted to the corresponding sequences in human, and presented against the human SYCP1 sequence. As Schmekel *et al*. utilised the cDNA sequence of rat SYCP1 (which lacked 51 N-terminal residues), residue numbers have been corrected for this. Both studies effectively demonstrate that antibodies towards the N-terminus stain the central element of the SC whilst antibodies raised against the SYCP1 C-terminus recognise the lateral element (Figure 3.1.4b) (Liu *et al.*, 1996; Schmekel *et al.*, 1996). In fact, even antibodies raised against the entire unstructured C-terminus only stain the lateral elements suggesting that these sequences are buried within the lateral elements, making close, perhaps direct, contact with the chromosome axis and DNA (Schmekel *et al.*, 1996). As opposed to Liu *et al.*, which focused only on spread chromosomes, Schmekel *et al.* presented data regarding the concomitant localisation of the N and C-termini within both spread chromosomes and chromosomes within ultrathin sections of testicular tissue, nullifying arguments regarding the effects of chromosome spreading. Bi-orientation of the SYCP1 homologue in hamster, SYN1, was also demonstrated using a combination of immunofluorescence and immuno-gold electron microscopy (Dobson *et al.*, 1994).

This model was validated in 2014, by Schücker *et al.*, using super-resolution fluorescence microscopy (Schucker *et al.*, 2015). Interestingly, whilst the C-termini localise as two single threads at the lateral element, the N-termini of SYCP1 demonstrate a bi-layered configuration giving the SC a depth of approximately 100 nm (Schucker *et al.*, 2015). This bi-layered organisation has further been proffered by Hernandez-Hernandez *et al*. in 2016, basing this suggestion upon the bimodal co-localisation of the

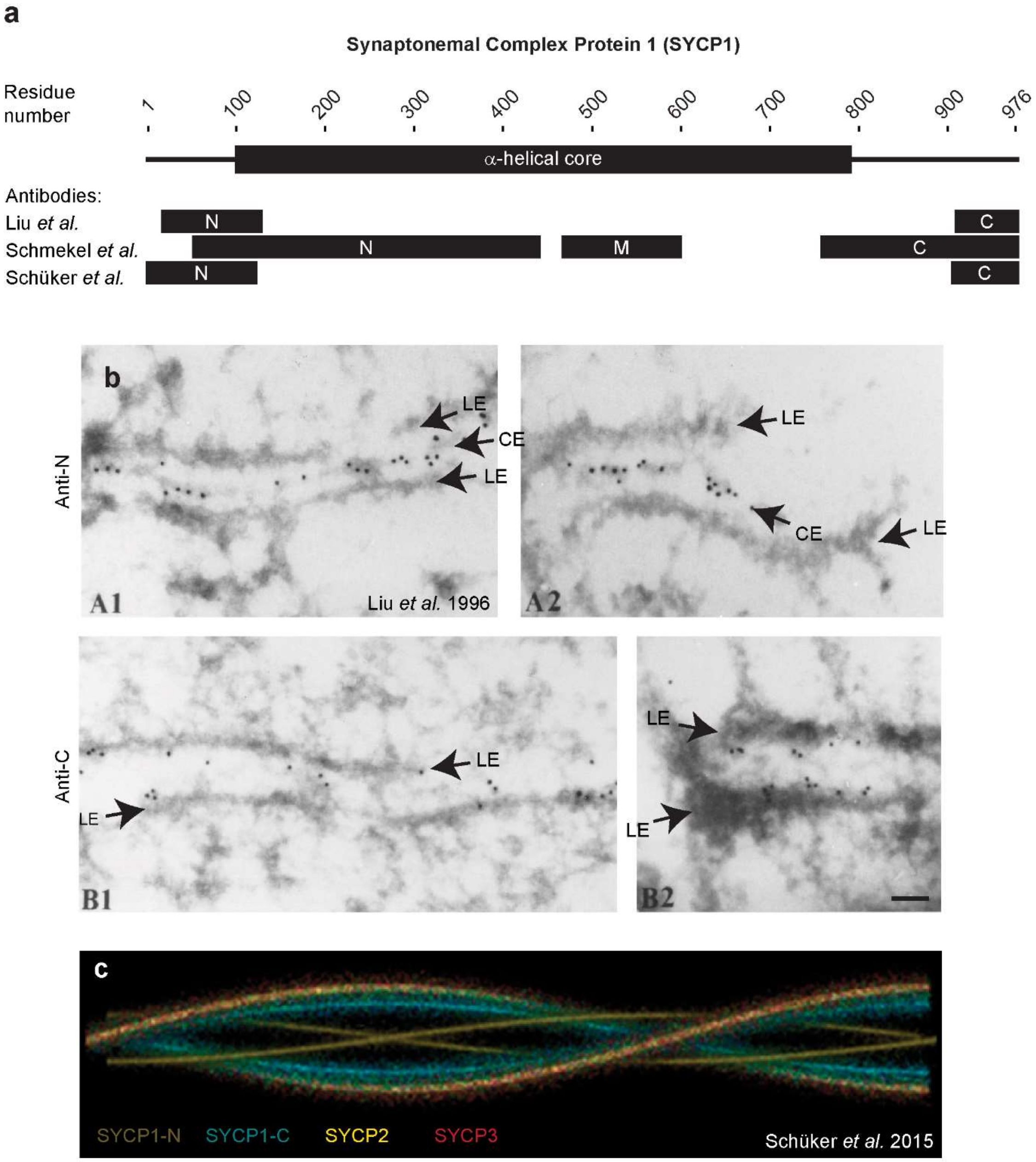
a
Synaptonemal Complex Protein 1 (SYCP1)
Residue number
1
100
200
300
400
500
600
700
800
900
976
α-helical core
Antibodies:
Liu et al.
N
C
Schmekel et al.
N
M
C
Schüker et al.
N
C
b
Anti-N
LE
CE
LE
A1
Liu et al. 1996
LE
CE
LE
A2
Anti-C
LE
LE
B1
LE
LE
B2
c
SYCP1-N
SYCP1-C
SYCP2
SYCP3
Schüker et al. 2015

Figure 3.1.4| SYCP1 within the SC. a) Schematic representation of SYCP1 aligned with the regions to which antibodies were raised in the indicated studies. Liu *et al*. raised antibodies against rat SYCP1 (murine residues 15-127 (N; corresponding to human residues 15-127); and murine residues 922-993 (C; corresponding to human residues 904-976)). Schmekel *et al*. raised antibodies against rat SCP1 (residues 52-442 (N; corresponding to human residues 52-441); residues 466-600 (M; corresponding to human residues 465-599); and residues 776-997 (C; corresponding to human residues 754-976)). Schücker *et al*. raised antibodies against rat SYCP1 (residues 1-124 (N; corresponding to human residues 1-124); and residues 922-997 (C; corresponding to human residues 900-976)). **b)** Immuno-gold electron microscopy analysis of spread meiotic chromosomes by Liu *et al*. 1996. A1 and A2 demonstrate central element localisation of the SYCP1 N-terminus whilst B1 and B2 show that the SYCP1 C-terminus is embedded within the lateral elements. The lateral elements (LE) and central element (CE) are indicated. Scale bar = 100 nm **c)** Three-dimensional reconstruction of the SC by Schücker *et al.* demonstrated the colocalization of the SYCP1 C-terminus with lateral element components SYCP2 and SYCP3 and the bi-layered organisation of the SYCP1 N-termini at the SC midline.

SYCP1 N-termini and SYCE3 protein in comparison with the monomodal and central distributions of SYCE1 and SYCE2 (Hernandez-Hernandez *et al.*, 2016). Schücker *et al*. disagree as to the localisation of SYCE1 and SYCE2, alternatively describing a bimodal distribution of these proteins. It remains to be confirmed which hypothesis is true, but given the breadth of studies, it is clear that the SC itself has a depth of approximately 100 nm, and as such, a multi-layered organisation is not unlikely. In Figure 3.1.5, I present the current model for the organisation of SYCP1 molecules within the SC, considering, for simplicity, a single layer of molecules. The N-termini of SYCP1 interdigitate at the midline of the SC, whilst the C-termini are embedded within the lateral elements, in association with the chromosome axis. SYCP1 molecules, given no evidence to the contrary, are represented as dimeric coiled-coils.

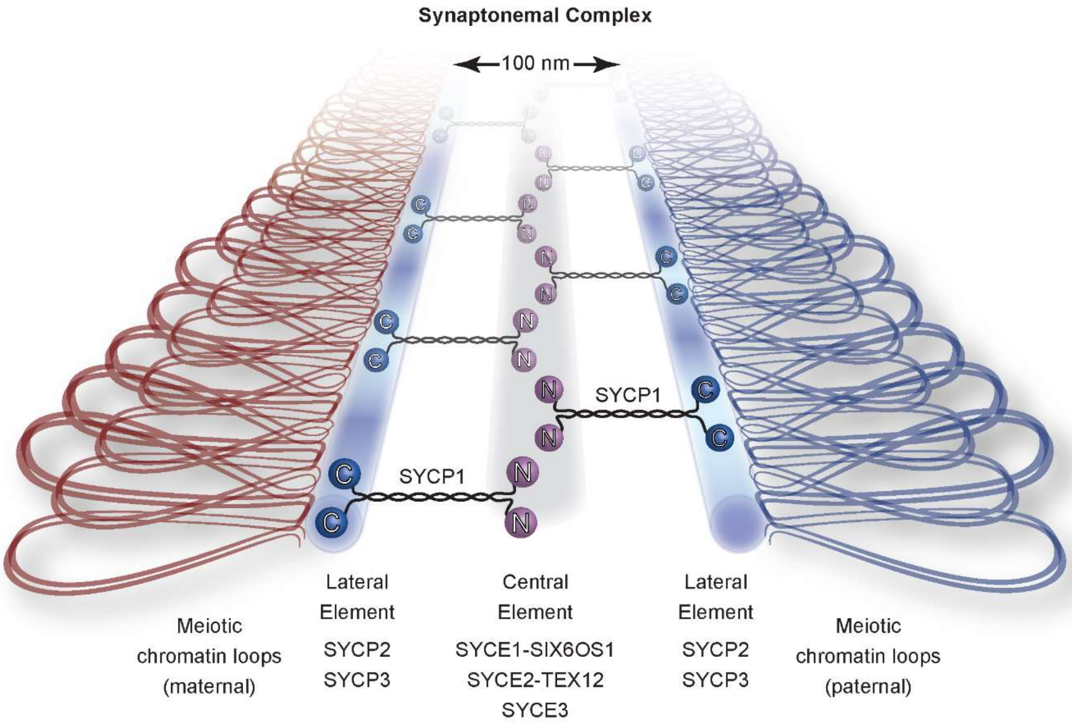
Synaptonemal Complex
100 nm
SYCP1
SYCP1
C
N
Meiotic chromatin loops (maternal)
Lateral Element
SYCP2
SYCP3
Central Element
SYCE1-SIX6OS1
SYCE2-TEX12
SYCE3
Lateral Element
SYCP2
SYCP3
Meiotic chromatin loops (paternal)

Figure 3.1.5| SYCP1 within the SC. SYCP1 is a 976 amino acid protein component of the synaptonemal complex with a central helical domain thought to fold as a dimeric coiled-coil. Its C-terminus is anchored within the lateral elements whilst its N-termini interdigitate at the central element. For simplicity, a single layer of SYCP1 molecules is depicted.

3.1.5 Unrelated proteins Zip1 and C(3)G localise to the SC, form TFs and share domain structure with SYCP1

Zip1: The corresponding TF protein in budding yeast (*Saccharomyces cerevisiae*) was identified through its ability to complement of a mutant defective in spore viability (Sym *et al.*, 1993). Termed Zip1, this protein of 875 residues is overtly similar to SYCP1 in domain structure, with a central α-helical core with coiled-coil propensity, an acidic, unstructured N-terminus and an unstructured basic C-terminus (Figure 3.1.6). As SYCP1, Zip1 is meiosis-specific and localises to the central region of the SC, firstly described by Sym *et al.* 1993 using immunofluorescence localisation experiments (Sym *et al.*, 1993).

C(3)G: Ultrastructural studies of *Drosophila* asynaptic mutant c(3)G^{17}, found the formation of short regions of central element but no further extension or formation of lateral elements (Rasmussen, 1975). In 2001, Page and Hawley published findings in which they localised the respective gene product, protein C(3)G, to the synaptonemal complex, and, given its contiguous staining along the entire SC, classified it as a structural component of the SC (Page and Hawley, 2001). In agreement with this classification, the SC does not form upon deletion of C(3)G (Smith and King, 1968). Page and Hawley utilised antibodies raised towards a bacterially expressed construct of C(3)G (residues 565-743). The antibody was confirmed to recognise a protein of a size matching the expected full-length size of C(3)G (744 residues in length) by Western blot of ovaries at 85 kDa. In agreement, no band was recognised for a C(3)G null strain, *c(3)G*^{68}, a background in which a stop codon is introduced, terminating translation after residue 77. The antibody was used to localise C(3)G between paired chromosomes, further corroborated by identical localisation of a C-terminal eGFP fusion to C(3)G (Page and Hawley, 2001). Similar to TF proteins in other organisms, C(3)G contains a central predicted helical domain flanked by unstructured termini (Figure 3.1.7).

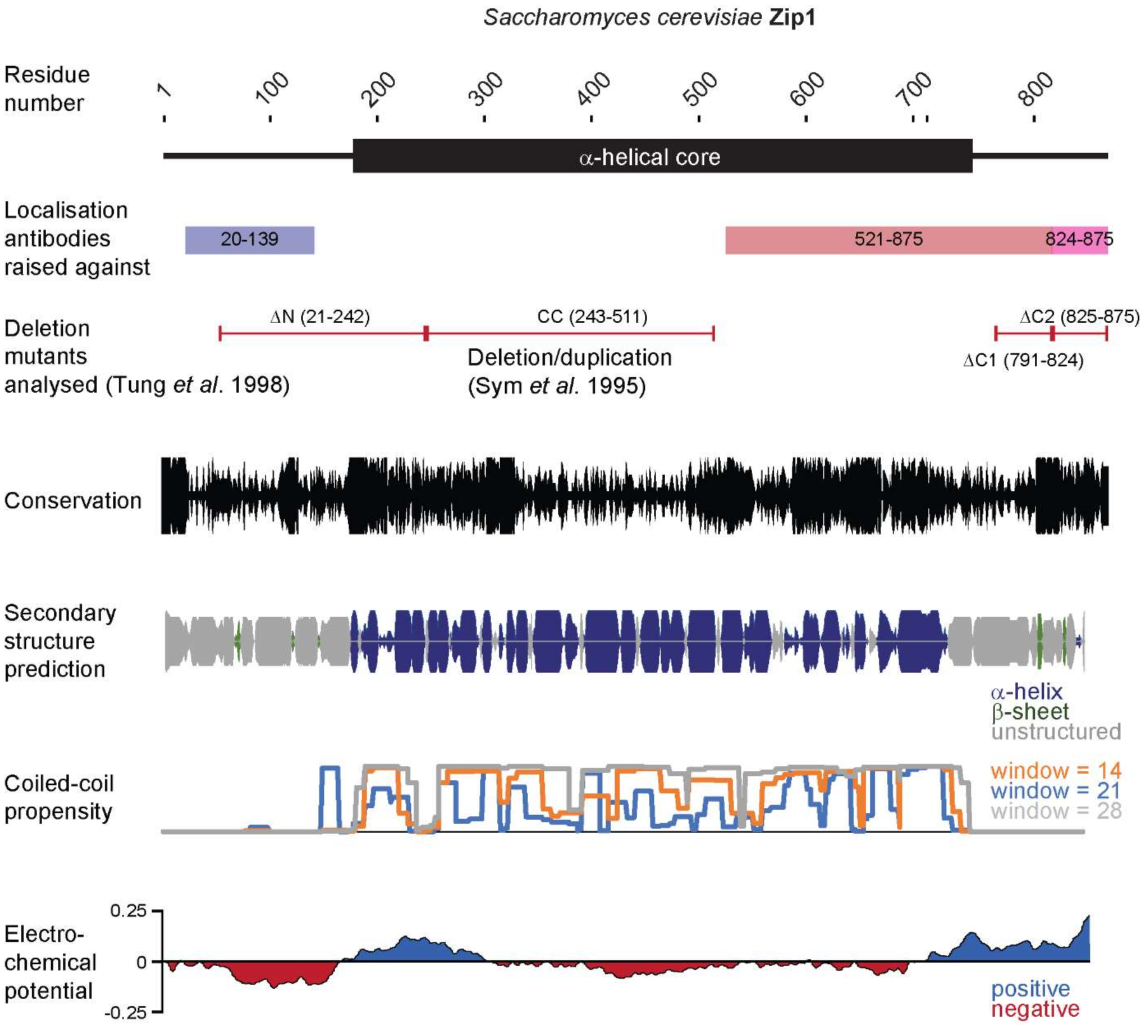

Figure 3.1.6| Bioinformatic analysis of Zip1. a) Zip1 is the 875 amino acid transverse filament protein of budding yeast (*Saccharomyces cerevisiae*). A schematic representation of its domain structure with unstructured N and C-termini flanking a central α-helical domain (residues 175-748). Antibodies utilised in orientation studies by Dong *et al*. 2000. Deletion/duplication mutants used to decipher Zip1 function and structure within the SC are aligned with the Zip1 sequence and the studies which they were utilised indicated. Conservation scores per residue calculated by ConSurf. Secondary structure prediction calculated by JPred4. α-helix in blue, β-sheet in green and unstructured in grey. Coiled-coil propensity calculated by COILS demonstrates a predicted central coiled-coil domain. The electrochemical potential distribution of Zip1 was calculated by charge of the EMBOSS suite using a window size of 5 residues and subsequently averaged across 88 residues to demonstrate overall charge distribution. The central coiled-coil is largely acidic with a basic N-terminal tip whilst the unstructured C-terminus is highly basic.

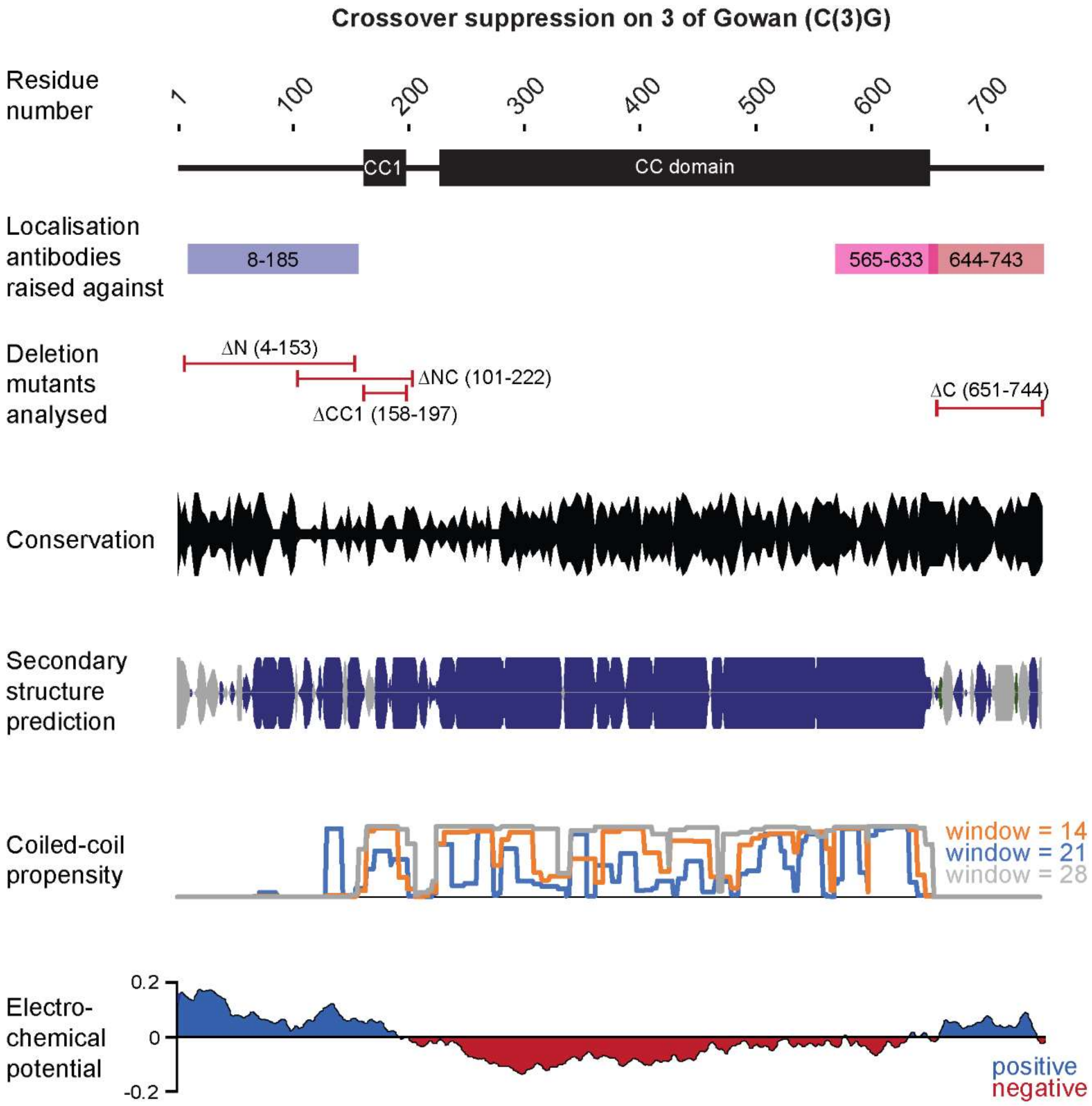

Figure 3.1.7| Bioinformatic analysis of *Drosophila melanogaster* C(3)G. a) C(3)G is a 744 amino acid protein containing a central helical domain predicted to adopt a coiled-coil (CC domain), preceded by a short coiled-coil region (CC1). Antibodies utilised to orientate C(3)G within the SC are aligned with the C(3)G sequence and deletion mutants utilised within the described experiments are indicated. Conservation scores per residue calculated by ConSurf. Secondary structure prediction calculated by JPred4. α-helix in blue, β-sheet in green and unstructured in grey. Coiled-coil propensity calculated by COILS demonstrates a predicted central coiled-coil domain. The electrochemical potential distribution of C(3)G was calculated by charge of the EMBOSS suite using a window size of 5 residues and subsequently averaged across 74 residues to demonstrate overall charge distribution. The central coiled-coil is largely acidic with a basic N-terminal tip whilst the unstructured C-terminus is highly basic.

3.1.6 Zip1 and C(3)G orientate as SYCP1 within the SC

Within the budding yeast SC, Zip1 molecules are organised such that the N-termini are within the central element and the C-termini are within the lateral elements, akin to the mammalian situation. This was ascertained by immuno-gold electron microscopy experiments, similar to those utilised to investigate SYCP1 within the mammalian SC, using antibodies raised towards the regions indicated in Figure 3.1.6 (Dong and Roeder, 2000).

C(3)G of *Drosophila* adopts an identical orientation within the SC as determined by Anderson et al. in 2004, once again by electron microscopic analysis of immuno-gold stained SCs (Anderson *et al.*, 2005). In this, antibodies towards the N-terminus (residues 8-185) localised at the SC central element whilst antibodies raised towards both the extreme C-terminus of C(3)G (residues 644-743) and the C-terminal end of the central coiled-coil region (residues 565-633) co-localised at the lateral elements. The regions to which antibodies were raised are highlighted in Figure 3.1.7.

3.1.7 The central coiled-coil domain of the TFs defines the inter-chromosomal distance

Through duplication and triplication of a coiled-coil sequence within Zip1 (residues 243-511; CC in Figure 3.1.6) it was shown that Zip1 is the primary determinant of spatial separation between chromosomes, corroborated by a further, similar, experiment in a separate study (Sym and Roeder, 1995; Tung and Roeder, 1998). In yeast expressing mutant Zip1 in which this coiled-coil segment is duplicated, the inter-chromosomal distance increases from 114 to 153 nm and upon triplication a further increase to 189 nm. As an increase of ~40 nm corresponds to approximately 270 residues folding as an α-helical coiled-coil, matching the length of the duplicated sequence, the observed differences in inter-chromosomal distance suggest that a single Zip1 molecule (rather than two Zip1 molecules) spans the entire inter-chromosomal distance, contrary to their localisation findings. This discrepancy may be explained by the effect of dehydration during sample preparation for visualisation, which may result in shrinkage and therefore decreasing the observed effect, as has been discussed by Schmekel et al. (Schmekel *et al.*, 1996).

3.1.8 The role of the C-terminus of TFs in chromosomal recruitment

In both budding yeast and *Drosophila*, deletion of regions corresponding to the unstructured C-terminus of the TF proteins results in defective chromosomal recruitment. In budding yeast, deletion of C-terminal residues 791-824 or 825-875 completely blocks chromosomal recruitment, with a phenotype cytologically similar to the Zip1-null mutant (Tung and Roeder, 1998). Residues 791-824 are not basic suggesting that they either contribute to chromosomal recruitment through protein-protein interaction rather than electrostatic association with DNA or must be modified, such as by phosphorylation, which may confer DNA binding capacity.

In *Drosophila*, deletion of the C(3)G C-terminus (residues 651-744; ΔC in Figure 3.1.7) also results in an inability to be recruited to the chromosome axis (Jeffress *et al.*, 2007). As with the other TFs, the C-terminus of C(3)G demonstrates an overall net positive charge (Figure 3.1.7). Given the failure to localise to the chromosome upon C-terminal deletion, it could be hypothesised that DNA-binding of the C-terminus drives chromosomal recruitment.

The effect of the corresponding C-terminal deletion in mammals is currently unknown. However, given its basic charge, initial recruitment to the chromosome axis may also be mediated by electrostatic interactions with the DNA backbone. The possibility of being recruited through protein-protein interactions should also not be ignored. A yeast-two hybrid interaction between the C-terminus of rat SYCP1 (residues 822-997) and the C-terminus of SYCP2 (residues 1376-1505, also found to interact with SYCP3) was reported, potentially providing a physical link to the lateral element, but due to the lack of negative controls should be considered cautiously (Winkel *et al.*, 2009; West *et al.*, 2019).

3.1.9 The unknown role of the N-termini of TFs and CE association

An extensive study of deletion and truncation mutations of the Zip1 protein was performed by Tung and Roeder in 1998, characterising the effect of each on chromosome morphology (Tung and Roeder, 1998). Here they claim that the N-terminus of Zip1 (residues 21-242) is dispensable for synapsis, as judged by pairing chromosomes, localisation of Zip1 to the chromosome axis, and negligible impact upon spore viability upon deletion of this region. However, the localisation of Zip1 lacking N-terminal residues, as observed by immunofluorescence utilising antibodies raised towards the Zip1 C-terminus (residues 611-875), is more punctate and is not continuous along the chromosomal axes and, morphologically, homologous chromosomes do not appear to be bound in tight synapsis, as in the wild-type situation (Tung and Roeder, 1998). This represents an inability to stabilise N-terminal contacts with the central element or in homotypic interactions. Higher-resolution imaging should be utilised to determine whether synapsis is truly achieved. As extensive pairing of chromosomes is achieved prior to SC formation and is retained in the mutant situation, it can more accurately be argued that the N-terminus of Zip1 is dispensable for meiotic progression with minor effects on sporulation and crossover formation. SC-independent pairing and other mechanisms, potentially only dependent upon the Zip1 C-terminus, likely act to ensure meiotic fidelity in budding yeast.

In contrast, truncation of the unstructured N-terminus of *Drosophila* C(3)G (ΔN; Figure 3.1.7), deletion of a short coiled-coil sequence preceding the central coiled-coil (ΔCC1) results in a complete failure to synapse chromosomes whilst the protein still localises to the chromosome axes, with a similar deletion (ΔNC) behaving identically (Jeffress *et al.*, 2007).

Currently, in mammals, the importance of the SYCP1 N-terminus is unknown. A yeast-two hybrid interaction suggesting the homotypic association of SYCP1 N-termini had been reported by Liu *et al.* but a lack of negative controls raises the question of whether the finding should be trusted (Liu *et al.*, 1996). Upon investigation, the constructs used in their study autoactivate, rendering their finding inconclusive (Davies, unpublished data).

3.1.10 A link to the central element

Ex vivo studies involving the heterologous expression of SYCP1, SYCE3 and SYCE1 have thus far provided the highest level of understanding regarding how SYCP1 connects to the central element (Hernandez-Hernandez *et al.*, 2016). Upon heterologous expression in mammalian cells, SYCP1 forms cytoplasmic filamentous basket-like structures, referred to as polycomplexes (Ollinger *et al.*, 2005) (Figure 3.1.9a,b). These structures shall be fully addressed in the following section. However, it was found that upon co-expression, SYCE3 is recruited to the SYCP1 polycomplexes and SYCE1 is only recruited to polycomplexes in the presence of SYCE3. SYCE3 therefore appears to form the sole link between the SYCP1 TFs and the central element. The regions/sequences that mediate these interactions remain to be addressed.

3.1.11 The TF proteins of the *Caenorhabditis elegans* SC

The distance between the central element and the lateral elements in the SC of *C. elegans* is not bridged by a single TF protein but a series of proteins: SYP-1, 2, 3, and 4 (Hawley, 2011; Schild-Prufert *et al.*, 2011). It would be interesting to find out if this usage of multiple proteins to form the TFs is common across other organisms which have a lattice-like central element such as those of the insects.

3.1.12 Polycomplex formation provides a clue for the assembly mechanism of TFs

Polycomplexes (PCs) represent large accumulations of TF proteins which, in budding yeast and *Drosophila*, can occur physiologically. They can be identified as heavily staining bodies and at an ultrastructural level display a striated appearance reminiscent of SYCP3 self-assemblies *in vivo* and reconstituted *in vitro* (Figure 3.1.8 and Figure 1.1.4). They more frequently occur in mutant strains of budding yeast in which chromosomal recruitment of Zip1 is impaired and are observed to form networks or dot-like structures (Sym and Roeder, 1995). The "dot"-like PCs of budding yeast can be visualised to constitute a series of electron-dense bands with fainter intermediate bands corresponding to associations C-terminus and N-terminus of Zip1, respectively (Dong and Roeder, 2000). Therefore, PCs represent SC-like assemblies in which C-termini self-associate, rather than associating with the chromosome axis. The coupling of N- and C-terminal associations results in a recursive assembly. An interesting polycomplex structure is formed upon deletion of the unstructured C-terminus of C(3)G which precludes chromosome association (Jeffress *et al.*, 2007). Here, a single hollow barrel-shaped PC is formed within the nucleus, displaying a similar banded appearance (Figure 3.1.8b).

Similar structures have been observed upon heterologous expression of SYCP1 in mammalian cells (Yuan *et al.*, 1996; Ollinger *et al.*, 2005). Upon overexpression of murine SYCP1 in Swiss-3T3 cells, large cytoplasmic aggregates can be visualised using antibodies raised towards the N-terminus, though these were not analysed by electron microscopy to ascertain ultrastructural features (Figure 3.1.9a) (Yuan *et al.*, 1996). Contrastingly, when overexpressed in COS-7 cells, murine SYCP1 forms cytoplasmic filamentous networks which when visualised by electron microscopy reveal the characteristic striated ultrastructure with a series of alternating dark and light bands corresponding, as in budding yeast, to the C and N-termini of SYCP1, respectively (Figure 3.1.9b) (Ollinger *et al.*, 2005). The differing appearance of polycomplexes in these two cell lines could be due to differences in cell origin. As described in Methods section 2.1.19, COS-7 cells originate from a transformed line of Green African monkey fibroblasts. Swiss-3T3 cells, however, originate from Swiss albino mouse embryonic tissue and were spontaneously immortalised using the "3T3 protocol" in which primary cells are split every 3 days (Todaro and Green, 1963). Differences in protein expression, regulatory factors, and basic cellular architecture may play a role in what form polycomplexes present.

As observed for Zip1 in relation to inter-chromosomal distances, upon duplication or deletion of a region of coiled-coil sequence within SYCP1 (residues 457-699), distances between sites of C-terminal self-association increased or decreased correspondingly (Figure 3.1.9A,B,C) (Ollinger *et al.*, 2005). This suggests that the coiled-coil region of SYCP1 is similarly the determinant of the inter-chromosomal distance (Ollinger *et al.*, 2005). It further raises the likelihood that the TF proteins possess mechanisms of self-assembly supported by sites within the N and C-termini which likely contribute to their assembly within the SC.

A model for how I currently believe SYCP1 self-assembles to create polycomplex structures is provided in Figure 3.1.9c. SYCP1 N and C-termini recursively self-associate to create a structure resembling "mini-SC" structures stacked back-to-back.

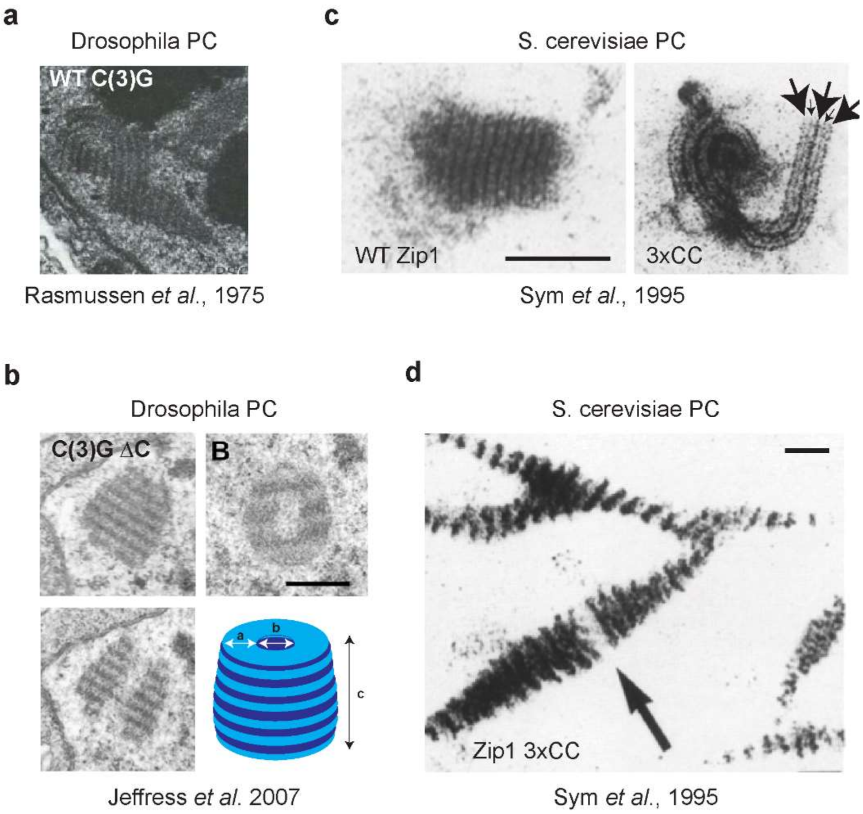
a
Drosophila PC
WT C(3)G
Rasmussen et al., 1975
c
S. cerevisiae PC
WT Zip1
3xCC
Sym et al., 1995
b
Drosophila PC
C(3)G ΔC
B
a
b
c
Jeffress et al. 2007
d
S. cerevisiae PC
Zip1 3xCC
Sym et al., 1995

Figure 3.1.8| Polycomplex formation in *Saccharomyces cerevisiae* Zip1 and *Drosophila melanogaster* C(3)G. a) *Drosophila* ovary section analysed by electron microscopy displaying a rare example of wild-type C(3)G forming a PC. **b)** Deletion of the C(3)G C-terminus consistently results in the formation of a single, nuclear, hollow barrel-shaped PC. A schematic representation of the structure is labelled with dimensions: a= ~200 nm, b= ~200 nm (diameter= 2a+b=600-900 nm), c= ~750 (350-770) nm. Scale bar = 500 nm. **c)** Spread Zip1 "dot" PCs of wild-type and a mutant in which a coiled-coil region (residues 243-511) is triplicated. Large arrows indicate lateral element-like structures whilst small arrows indicate central element-like structures. Scale bar = 1 µm. **d)** Zip1 polycomplexes can form in a network-like fashion. Scale bar = 200 nm.

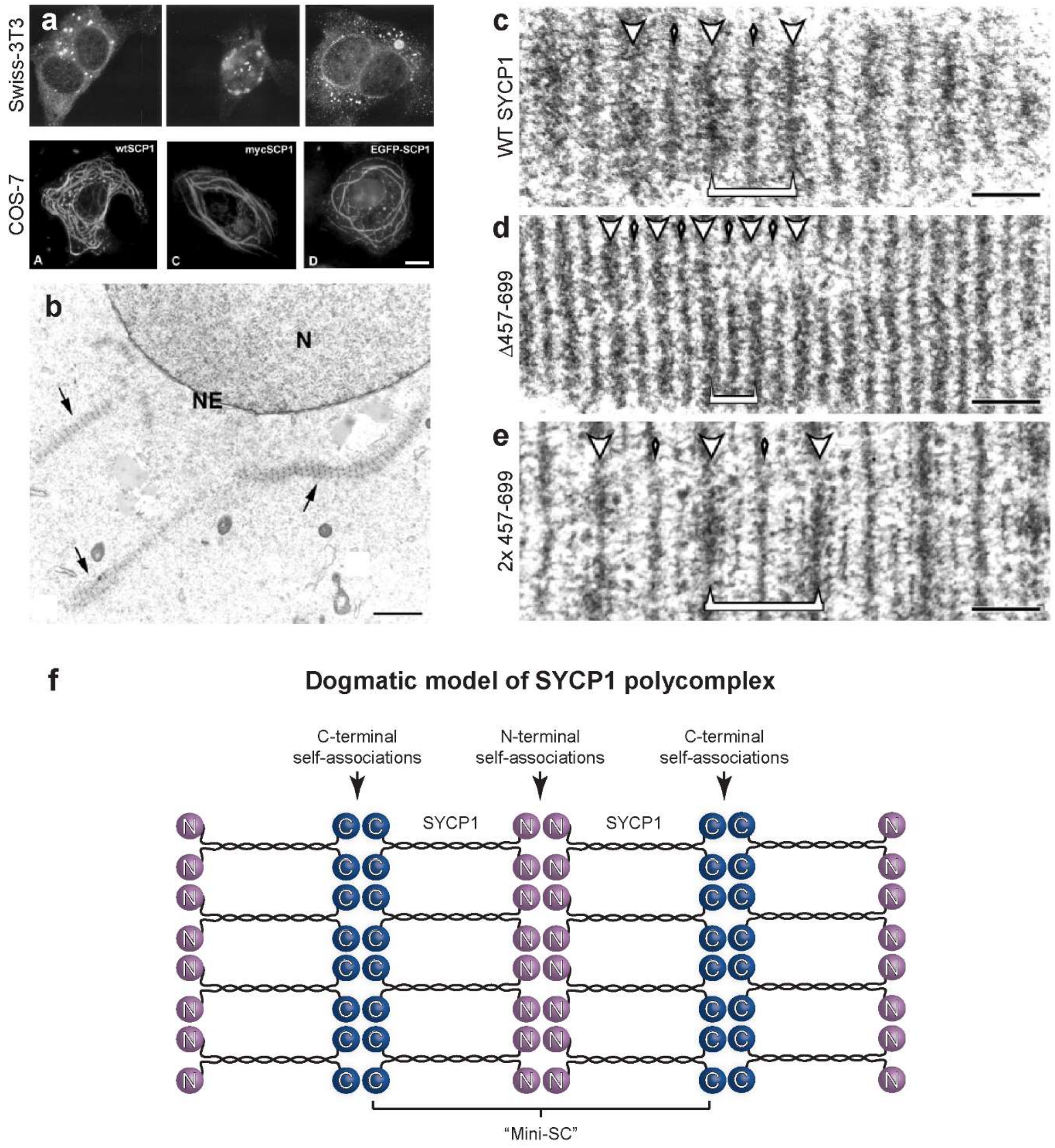
a
Swiss-3T3
COS-7
wtSCP1
mycSCP1
EGFP-SCP1
A
C
D
b
N
NE
c
WT SYCP1
d
Δ457-699
e
2x 457-699
f
Dogmatic model of SYCP1 polycomplex
C-terminal self-associations
N-terminal self-associations
C-terminal self-associations
SYCP1
SYCP1
N
C
"Mini-SC"

Figure 3.1.9| Polycomplex formation upon heterologous mammalian expression. a) Immunofluorescence imaging of Swiss-3T3 and COS-7 cells overexpressing SYCP1 showing the formation of large cytoplasmic aggregates and filamentous networks. Scale bar = 10 µm. **b)** Electron microscopic analysis of transfected cells COS-7 reveals ultrastructural details of SYCP1 polycomplexes, indicated by arrows. Scale, 1 µm. **c-e)** Polycomplexes formed within COS-7 cells expressing SYCP1 **c)** wild-type, **d)** Δ457-699, **e)** 2x 457-699. The N- and C-terminal associations of SYCP1 have been indicated with small and large arrowheads, respectively. **f)** A schematic model of SYCP1 assembly within a polycomplex. The polycomplex represents a series of back-to-back associated "mini-SC"-like assemblies in which N- and C-terminal associations permit recursive assembly. Am updated model based on the results presented within Chapter 3 is included on page 202.

3.1.13 TF-mediated synapsis is required for proper DNA repair

In mouse, it was found that, through its ablation, SYCP1 is required for fertility and that a reduced complement of SYCP1 results in apoptosis of spermatocytes as they enter the pachytene phase of meiosis (de Vries *et al.*, 2005). In the absence of SYCP1, homologous chromosomes still align and form axial associations, short-range associations of paired chromosomes at a separation of ~200 nm, a distance greater than that in synapsis (Figure 3.1.10) (de Vries *et al.*, 2005). This demonstrates that the initiation of double-strand breaks, the formation of homologous pairing, and the formation of axial associations, likely through single-end invasion and the formation of early DNA-repair intermediates (as shown by wild-type levels of γH2AX staining and RAD51 foci during leptotene) is independent of SYCP1-mediated synapsis (de Vries *et al.*, 2005).

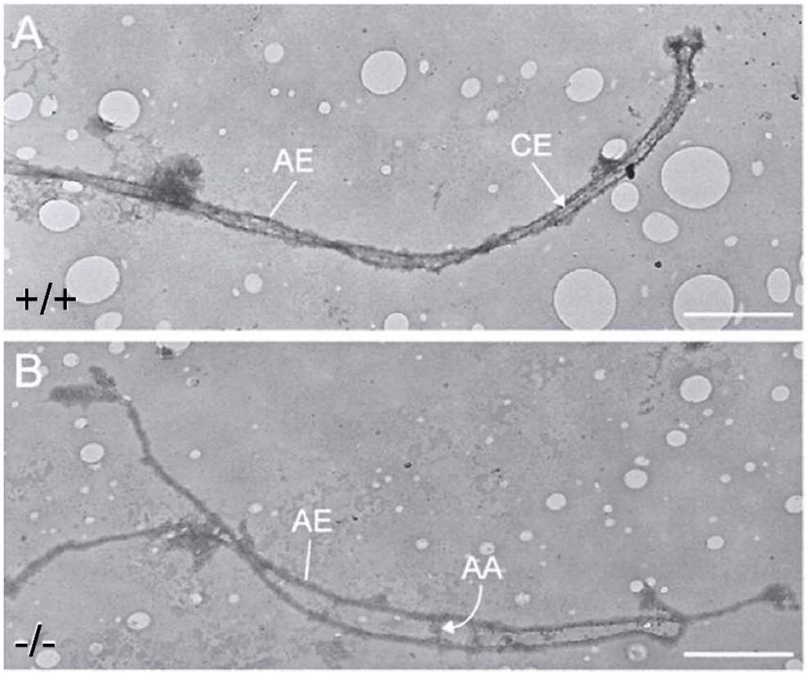

Purified and DNase-treated meiotic chromosomes of *Mus musculus*
de Vries et al., 2005
Genes Dev

Figure 3.1.10| SYCP1 is required for synapsis but not homologue pairing. A) Electron microscopic analysis of spread and DNase-treated meiotic chromosomes of wild-type mouse demonstrating proper synapsis. AE, axial element. CE, central element. **B)** SYCP1-null mice exhibit homologously-paired meiotic chromosomes, bound at axial associations (indicated; AA). Scale bars = 1 µm.

However, SYCP1-mediated synapsis appears to be involved in facilitating the maturation of early recombination nodules to late recombination nodules, i.e. the removal of RAD51/RPA/MSH4 foci, and the formation of MLH1/3 foci. In SYCP1-null mice, RAD51/RPA/MSH4 levels, despite accumulating to wild-type levels, persist through late pachytene (de Vries *et al.*, 2005). It is suggested that the SC introduces an architecture within which to process DNA repair intermediates, and, given the structural role of the TFs within the SC, that SYCP1-null mice cannot provide this architecture.

In budding yeast, Zip1 contributes to meiotic passage, likely through its involvement in the SC. However, it is not essential, with Zip1-null strains undergoing meiotic progression to form viable spores, albeit at reduced efficiency (Sym and Roeder, 1995). In this strain, homologous chromosomes still align, but do not synapse (Sym *et al.*, 1993). DSB intermediates are still processed, and, perhaps counter-intuitively, crossovers are formed at much higher levels (Tung and Roeder, 1998). This is likely through the ablation of crossover interference whereby the number of repair events by crossover is spatially limited such that crossovers are evenly distributed across the genome (Sym and Roeder, 1994).

The TFs potentially provide a link with the recombination machinery. In *Saccharomyces cerevisiae*, Zip1 was shown to interact with Zip3 and therefore indirectly with Zip2 by immunoprecipitation and yeast-two hybrid (though the vector encoding Zip1 appears to autoactivate) (Agarwal and Roeder, 2000). Zip3 and Zip2 do not localise along synapsed chromosomes in a contiguous manner as Zip1, colocalising as multiple discrete foci, colocalising with components of the early recombination nodule such as MSH4 (Agarwal and Roeder, 2000). The proposed link may not be direct between Zip1 and Zip3, but this finding does suggest a physical connection between synaptonemal complex components and the recombination machinery.

3.1.14 Functions of the TF proteins in centromeric pairing

In mice, SC components are retained at the centromeres after SC disassembly (Bisig *et al.*, 2012; Qiao *et al.*, 2012). Prior to the formation of the SC, centromeric localisation of SC components is not observed. This is in contrast with *Saccharomyces cerevisiae* in which the centromeric regions are paired in a Zip1-dependent manner (Tsubouchi and Roeder, 2005). A similar observation was made for C(3)G of *Drosophila* (Christophorou *et al.*, 2013). These roles appear to be fulfilled by cohesin complex proteins in mouse and plants (Zhang *et al.*, 2013; Ishiguro *et al.*, 2014). The role of Zip1 at the centromere appears to be to confer structural rigidity, reducing rotational freedom of the paired kinetochores with respect to one another, thus facilitating their bi-orientation and faithful segregation at metaphase (Gladstone *et al.*, 2009). This was proposed by Gladstone *et al.* in response to findings garnered through studying the disjunction of non-exchange chromosomes (i.e. chromosomes which do not form crossovers and therefore lack genetic linkage after the disassembly of the SC). As non-exchange chromosomes are rare in budding yeast, Gladstone *et al.* artificially ensured the presence of at least one non-exchange chromosome pair by replacing one copy of *chromosome V* with the homeologous copy from *Saccharomyces carlsbergensis* (Gladstone *et al.*, 2009). The homeologous *chromosome V* pair are able to pair in a homology-independent manner whilst rarely forming inter-homeologue chiasmata (Maxfield Boumil *et al.*, 2003). It was previously shown that successful disjunction is due to centromere pairing (Kemp *et al.*, 2004). Loss of Zip1 results in baseline levels of centromere pairing and asymmetric segregation of non-disjunction chromosomes (Gladstone *et al.*, 2009).

Whether a similar phenomenon exists in mammals is currently unknown. However, unpublished findings (Davies and Hunter) currently suggest that upon complete synapsis, with centromeres regions synapsis last of all, SYCP1 displaces centromere component Mis18α. Mis18α is a component of the Mis18 complex which localises to the centromere directly after mitotic division to facilitate recruitment of CENP-A, a histone-fold variant which may incorporate within nucleosomes, which is required for centromere specification (Stellfox *et al.*, 2013). The functional relevance of this is currently unknown though it could be postulated to be involved in terminating the recruitment of CENP-A prior to anaphase. Alternatively, perhaps remaining SC proteins play a role enforces structure between bound kinetochores to facilitate correct orientation of the homologous pairs on the metaphase plate, positioning the kinetochores for spindle attachment after the SC is disassembled.

3.1.15 SYCP1 in cancer

It is now well established that meiosis-specific proteins are commonly expressed in cancer (Rousseaux *et al.*, 2013). SYCP1 was first identified as a cancer/testis antigen in 1998, as, whilst supposedly being expressed specifically in sexual organs, many cancerous tissues demonstrate aberrant expression of SYCP1 (Tureci *et al.*, 1998). Genes associated with the DNA repair pathway are frequently misregulated in cancer, contributing to genome instability (Bishop and Schiestl, 2002). The mechanisms by which SYCP1 is repurposed in cancer have not been uncovered. Recombination proteins formed an attractive target for cancer therapy (Peng and Lin, 2011). Given their meiosis-specific nature SC proteins make attractive targets for therapy.

3.1.16 Uncovering the molecular structure and mechanism of assembly of SYCP1 within the SC

In summary, we thus far have a decent level of understanding regarding the localisation and orientation of SYCP1 molecules within the SC and its role in SC structure and facilitating meiotic progression. However, the molecular means by which SYCP1 is recruited to and assembles within SC and its atomic structure remain unknown. The work presented in the following chapter focuses on addressing these chasms in our knowledge base by elucidating the structure and function of the transverse filament protein SYCP1 of the human synaptonemal complex (SC). Despite the assertion that SYCP1 formed dimeric coiled-coils, on the basis of sequence prediction, this has never been formally addressed (Meuwissen *et al.*, 1992). During rudimentary biochemical attempts to purify *Saccharomyces cerevisiae* Zip1, it was suggested that Zip1 has the capacity to form dimers, tetramers and higher order assemblies (Dong and Roeder, 2000). However, this was based upon the size-exclusion profile of refolded material, stabilised by lysine cross-linking.

Although immuno-gold localisation and super-resolution fluorescence microscopy have effectively determined the placement of SYCP1 molecules within the SC, the geometry of individual SYCP1 molecules and their mechanisms of chromosomal recruitment and assembly within the SC remain unknown. (Liu *et al.*, 1996; Schmekel *et al.*, 1996; Schucker *et al.*, 2015). Investigation into the structure and function of SYCP1 *in vitro* has previously been hampered due to the inherent instability and aggregation properties of the molecule. For example, upon refolding from solubilised inclusion bodies, SYCP1 demonstrates significant degradation and forms a hydrogel-like substance (Owen Davies, unpublished findings).

The work presented within this chapter details the steps taken towards elucidating a molecular understanding of SYCP1 geometry by identifying and analysing a non-assembling truncation product of SYCP1 and its component domains through biophysical and crystallographic methods. I found that that the core structure of SYCP1 is formed of four helical chains which are held together in four-helical association at its N-terminus, forking at both termini into dimeric coiled-coils. The N-terminal coiled-coils are short and mediate homotypic associations, recapitulating SC midline self-association, whilst the C-termini are extended and rod-like, providing sufficient length to span the distance between the SC central element and lateral elements.

3.1.17 Coiled-coil proteins: structure and function relationships

To achieve this new-found knowledge, it was critical to understand the key features of our target structures – the coiled-coil fold. Coiled-coils are a common fold utilised across nature and serve largely structural roles, importantly introducing function-critical separations between domains located at the N and C-termini. They are formed by the inter-twining of two α-helices. α-helices are stabilised through hydrogen bonds which form between the backbone amine group hydrogen of one residue and the backbone carboxyl group oxygen of a residue positioned 3/4 residues later (Pauling *et al.*, 1951). More precisely, an α-helix has a 3.6 residues per turn with a pitch of 5.4 Å. The pitch of a coiled-coil, stabilised through "knobs-into-holes" hydrophobic interactions, is slightly reduced, at 3.5 residues per turn due to the left-handedness of the coiled-coil in comparison to the right-handedness of the α-helix (Crick, 1952). These knobs-into-holes associations are formed through hydrophobic docking of sidechains which occur within the amino acid sequence in a repetitive pattern. The residues of the "heptad repeat" are denoted *abcdefg* where *a* and *d* are generally hydrophobic.

Coiled-coils are the most prevalent fold across biology and vary as much in length as they do in function (Truebestein and Leonard, 2016). For example, bZIP transcription factors, such as GCN4 (the first crystallographically characterised coiled-coil), form short dimerization domains, whilst extremely long coiled-coils, such as NuMA or Giantin which mediate nuclear dynamics and Golgi-associated vesicle transport respectively, also exist (Rose and Meier, 2004). Coiled-coils may serve to provide architectural rigidity, such as the intermediate filaments, which assemble to form intracellular networks, enforcing shape upon the cellular membrane and positioning intracellular organelles. These proteins often form rod-like structures visible by electron microscopy (EM) and commonly self-assemble utilising sequences flanking the core fold. Such assemblies often display a paracrystalline appearance by EM with characteristic striations indicating parallel arrays of extended coiled-coils stacked end to end (Stewart *et al.*, 1989).

Pertinent to our research, all thus far identified structural components of the synaptonemal complex (SC) contain coiled-coil domains. The SC "zips" meiotic chromosomes along their entire length and its "zipper"-like structure displays many features of coiled-coil assembly by EM (Zickler and Kleckner, 2015). As previously described, many of the components of the SC have demonstrated *in vitro* their capability to self-assembly. This propensity for self-assembly, alongside the inherent flexibility of coiled-coil proteins provides a challenge when attempting to characterise these proteins through biochemical, biophysical and crystallographic techniques. However, their simplicity and repetitive nature also provides opportunity for their study both in solution and for their structural characterisation by X-ray crystallography.

3.1.18 Techniques suited for the study of coiled-coil molecules

Size and shape determination by small-angle X-ray scattering (SAXS)

Small-angle X-ray scattering is a powerful technique in the study of coiled-coil proteins as it can be used to determine the principal dimensions of a rod-like molecule such as thickness and length. The thickness of a coiled-coil relates to the number of chains within the cross-section (for example, a radius of 8 Å suggests 2 chains within the cross-section whilst a radius of 10 Å suggests 4 chains within the cross-section). The experimentally determined length of a coiled-coil can be compared with the theoretical length of the sequence as a canonical dimeric coiled-coil (1.5 Å per residue). Any discrepancies may be explained by additional folding events. Throughout this thesis, SAXS has proved a key technique in the characterisation of SYCP1.

X-ray crystallography: *Ab initio* molecular replacement strategies

The folding of a coiled-coil is highly predictable and as such the structure of an amino acid sequence may be modelled. In a bid to bypass the requirement for experimental phasing information during crystal structure solution, these models may be used in molecular replacement. Models must, however, be very accurate and as such a serial approach must be adopted. AMPLE is a pipeline which clusters and subsequently truncates fragments generated by programs such as QUARK and ROSETTA and submits these for serial molecular replacement trial through MrBUMP (Keegan and Winn, 2008; Rigden *et al.*, 2008; Bibby *et al.*, 2012; Xu and Zhang, 2012). Alternatively, rather than generating models, small fragments which may more accurately match a structure on a very local scale might be used to provide phases. ARCIMBOLDO is a program while relies upon the accurate placement of small secondary structural elements, derived from distant homologs, to acquire initial phase estimations (Millan *et al.*, 2015). This approach to structure solution is particularly powerful for alpha-helical proteins, though it does rely on high-resolution diffraction data.

RESULTS

Part I

3.2.1 The purification and refolding of full-length SYCP1 from inclusion bodies

I expressed full-length SYCP1 (976 residues) with an N-terminal His_6-tag (His_6-$SYCP1_{1-976}$) in *E. coli* and found SYCP1 to be largely insoluble upon induction at both 25 ˚C and 37 ˚C, as determined by its presence within the bacterial pellet and absence from the supernatant and 200 mM imidazole elution steps (Figure 3.2.1a,b). I therefore proceeded to purify SYCP1 from inclusion bodies.

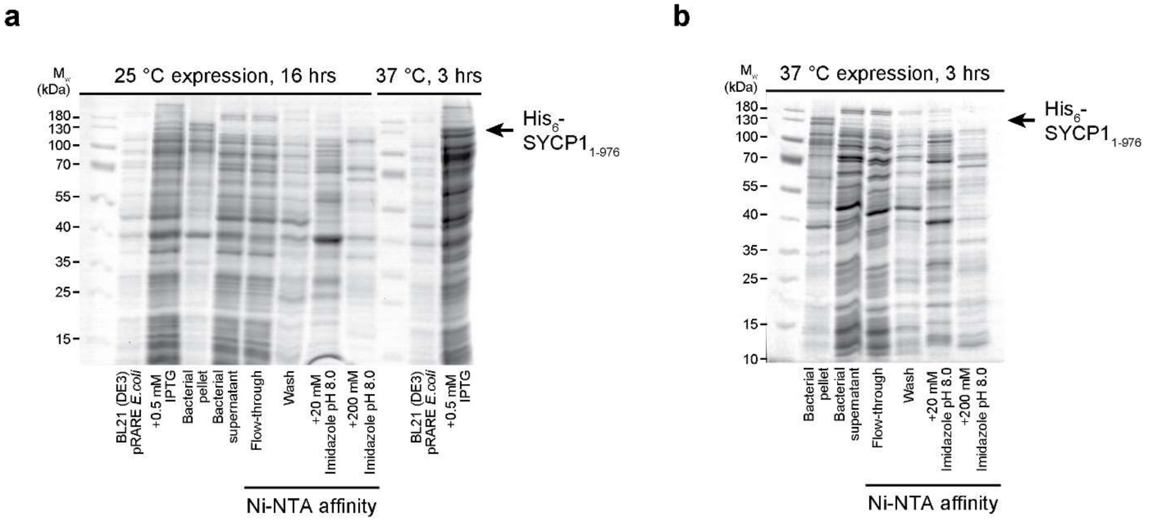
a
Mw (kDa)
25 °C expression, 16 hrs
37 °C, 3 hrs
180
130
100
70
55
40
35
25
15
His6-SYCP1 1-976
BL21 (DE3) pRARE E.coli
+0.5 mM IPTG
Bacterial pellet
Bacterial supernatant
Flow-through
Wash
+20 mM Imidazole pH 8.0
+200 mM Imidazole pH 8.0
BL21 (DE3) pRARE E.coli
+0.5 mM IPTG
Ni-NTA affinity
b
Mw (kDa)
37 °C expression, 3 hrs
180
130
100
70
55
40
35
25
15
10
His6-SYCP1 1-976
Bacterial pellet
Bacterial supernatant
Flow-through
Wash
+20 mM Imidazole pH 8.0
+200 mM Imidazole pH 8.0
Ni-NTA affinity

Figure 3.2.1| Full-length SYCP1 is insoluble in *E. coli.* **a)** SDS-PAGE analysis of the expression and attempted purification of full-length SYCP1 from BL21 (DE3) pRARE *E. coli* by Ni-NTA affinity chromatography followed by an induction test at 37 ˚C. **b)** SDS-PAGE analysis of the attempted purification of full-length SYCP1 from the soluble fraction of lysed cells induced at 37 ˚C by Ni-NTA affinity chromatography.

Inclusion bodies were prepared through washing and denaturation in 8 M Urea, as schematised in Figure 3.2.2a using the indicated buffers. Insoluble SYCP1 is solubilised in 8 M urea and exhibits heavy degradation (Figure 3.2.2b). UV spectroscopy suggested the presence of DNA, with a ratio of absorbance at 260 nm to absorbance at 280 nm (A260/280) of 1.07 corresponding to ~5 % DNA content by weight (green trace; Figure 3.2.2d) (Mach *et al.*, 2001). Refolding was initiated by sequential dialysis to Buffer 3, in which it remained soluble (i; Figure 3.2.2e). The presence of L-arginine, pH 8.0, in Buffer 3 likely limited protein aggregation by forming clusters around exposed hydrophobic residues during the refolding process (Das *et al.*, 2007; Lange and Rudolph, 2009). An A260/280 of 1.09 confirmed the persisting presence of ~5 % DNA (cyan trace; Figure 3.2.2d). Subsequent dialysis to Buffer 1 resulted in precipitation which formed a hydrogel upon centrifugation (ii; Figure 3.2.2e). It was noted that hydrogel formation could be prevented through prior anion-exchange chromatography in 8 M Urea (Figure 3.2.2c,e). A large peak in the elution profile during ion exchange (marked with an asterisk), confirmed to contain largely DNA by UV spectroscopy, suggested that protein-DNA electrostatic associations had been disrupted in a salt-dependent manner allowing for the differential elution of SYCP1 (black trace; Figure 3.2.2d). I therefore hypothesised that a combination of electrostatic association with bacterial DNA and hydrophobic association of protein molecules drove the formation of the observed hydrogels. Deviation from the baseline in the UV spectrum of refolded SYCP1 between wavelengths 320-400 nm is caused by Rayleigh scattering of light, indicative of the presence of aggregates in the solution (red trace; Figure 3.2.2d). Although SYCP1 demonstrated overall instability, with numerous degradation products, it was interesting to note its distinct double-banded appearance during early purification stages (orange box; Figure 3.2.2b). The distinct brown-yellow colour of the DNA-SYCP1 hydrogel (Figure 3.2.2e) suggested the presence of metals which have bound non-specifically, perhaps interacting with exposed cysteines and/or sample oxidation.

I performed electron microscopy (EM) on SYCP1 in a bid to observe ultrastructural features of SYCP1 self-assembly (Figure 3.2.3). Initially, samples not subjected to ion exchange chromatography were analysed. Soluble sample in 20 mM Tris, pH 8.0, 500 mM NaCl contained predominantly amorphous aggregates though I found a few examples of filamentous assemblies (Figure 3.2.3a-c). Ultra-thin sections of SYCP1 hydrogel (fixed in glutaraldehyde and embedded in resin as per Methods section 2.1.20) were imaged but no discernible structural features were readily distinguishable (Figure 3.2.3d-f). In L-arginine, SYCP1 remained soluble. However, by electron microscopy, large networks were observed, in which individual fibres of ~10 nm thickness were frequently separated by approximately 100 nm (Figure 3.2.3g-h). Secondly, purified SYCP1 (having been subjected to ion exchange chromatography) was analysed though only aggregation was observed (Figure 3.2.3i).

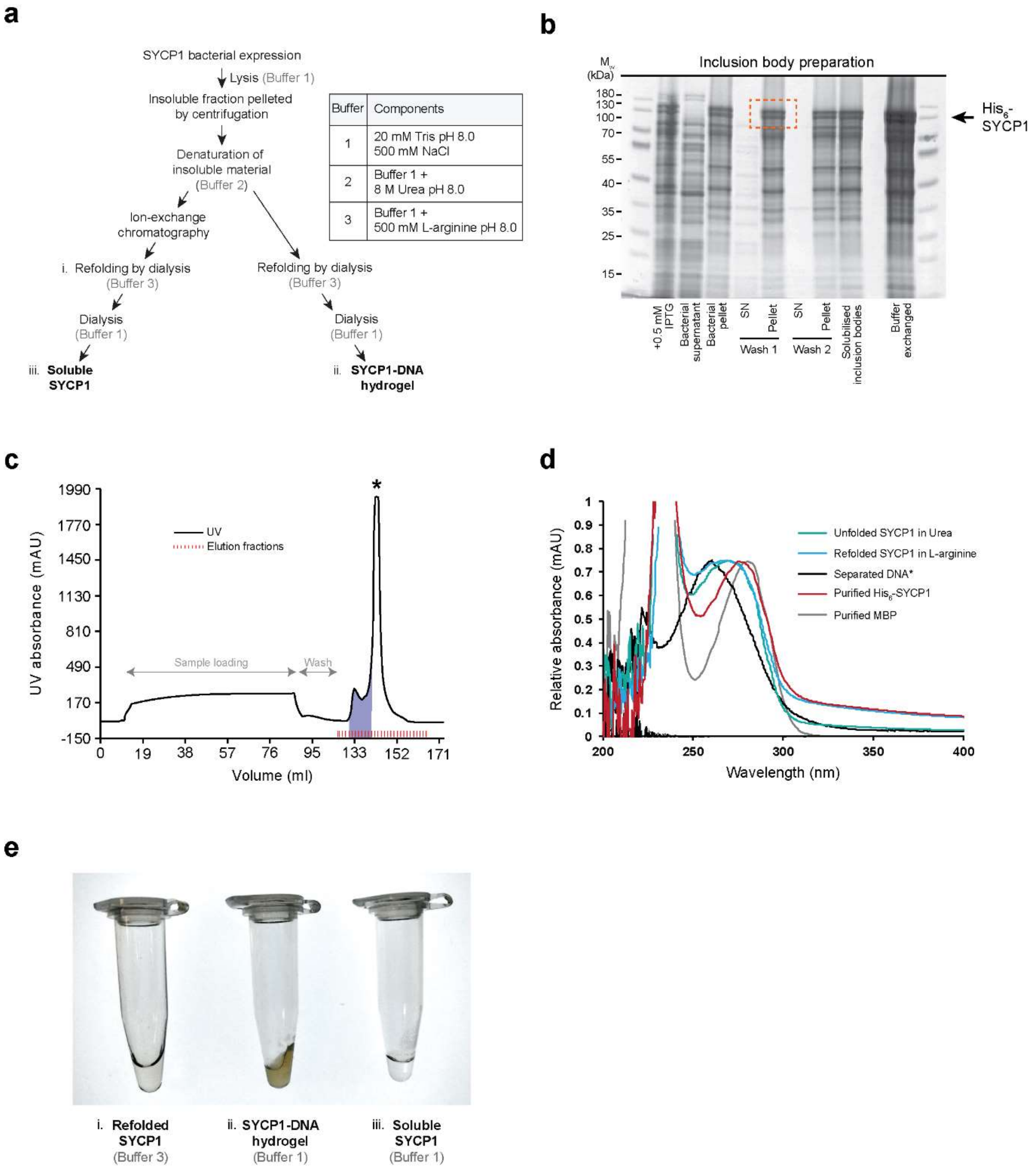

Figure 3.2.2| Refolding SYCP1 from solubilised inclusion bodies. a) A schematic representation of the purification and refolding process for SYCP1 from the insoluble fraction, as detailed in Methods section 2.1.7. **b)** SDS-PAGE analysis summarising the steps taken to prepare inclusion bodies prior to solubilisation. **c)** Chromatogram including the loading, washing and elution phases (as indicated) of ion-exchange chromatography for His$_6$-SYCP1 in 8 M Urea pH 8.0. SYCP1 containing fractions are highlighted and a DNA containing peak is marked with an asterisk. **d)** Normalised UV spectroscopy between 200 and 400 nm for His$_6$-SYCP1 at various stages of purification. Green, unfolded SYCP1 in Urea; cyan, refolded SYCP1 in L-arginine; black, DNA separated from SYCP1 by ion exchange; red, purified His$_6$-SYCP1; grey, purified MBP for comparison. **e)** Samples of **i** refolded SYCP1 in L-arginine; **ii**, SYCP1-DNA hydrogel; **iii**, soluble SYCP1 in the indicated buffers.

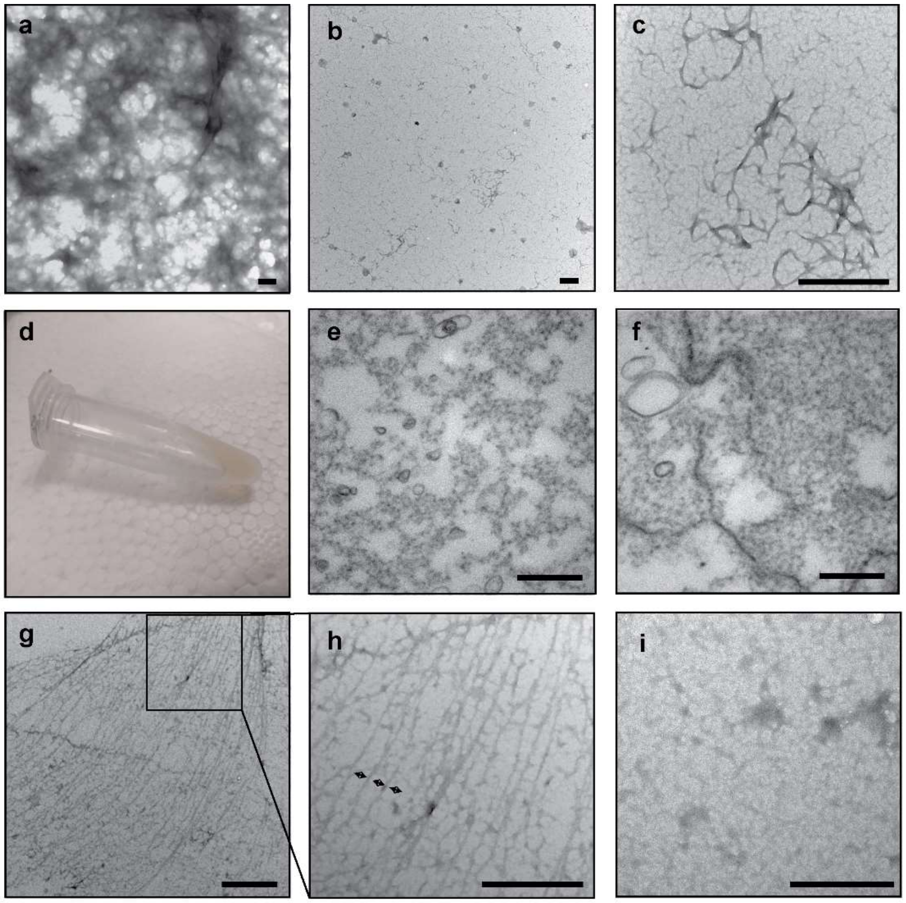

Figure 3.2.3| Electron microscopy analysis of SYCP1 samples. a-h) Samples not subjected to ion-exchange chromatography. **a-c)** EM analysis of the supernatant created by centrifugation of hydrogel-forming samples revealing the presence of **a,b)** amorphous aggregates and **c)** filamentous assemblies. **d)** Photograph of the SYCP1 hydrogel analysed in **e-f)** Thin slices of fixed hydrogel demonstrating no discernible ultrastructural features. **g)** SYCP1 forms network-like filamentous assemblies in L-arginine. **h)** A zoomed-in section of the indicated region of part **g** with arrows showing a regular 100 nm spacing between filaments. **i)** Refolded SYCP1 purified by ion exchange prior to dialysis to remove DNA. **a-i)** All scale bars represent 500 nm.

3.2.2 Optimised purification of His$_6$-SYCP1$_{1\text{-}976}$

In order to characterise SYCP1 *in vitro* its purification was optimised (described in detail in Methods section 2.1.7). Of note, DNase I was incorporated into the lysis buffer and an additional 1 M NaCl wash step utilised during inclusion body preparation (Figure 3.2.4a). As previous, ion exchange chromatography using HiTrap Q column was used to remove remaining DNA (of which there was little remaining) and an additional subsequent cation exchange step using HiTrap SP incorporated to enrich for full-length material (Figure 3.2.4b-e). Interestingly, the double-banded appearance became less prominent after cation exchange using a HiTrap SP column, suggesting a minor truncation of the N or C-terminus was sufficient to block/reduce binding to a negatively charged substrate, such as the DNA backbone (Figure 3.2.4e). Selected fractions were sequentially dialysed overnight to Buffer 3 and 1 for refolding. Refolded material was subjected to cation exchange chromatography using HiTrap SP and eluted fractions were pooled and concentrated. The purity of the final product was assessed by SDS-PAGE (Figure 3.2.4f).

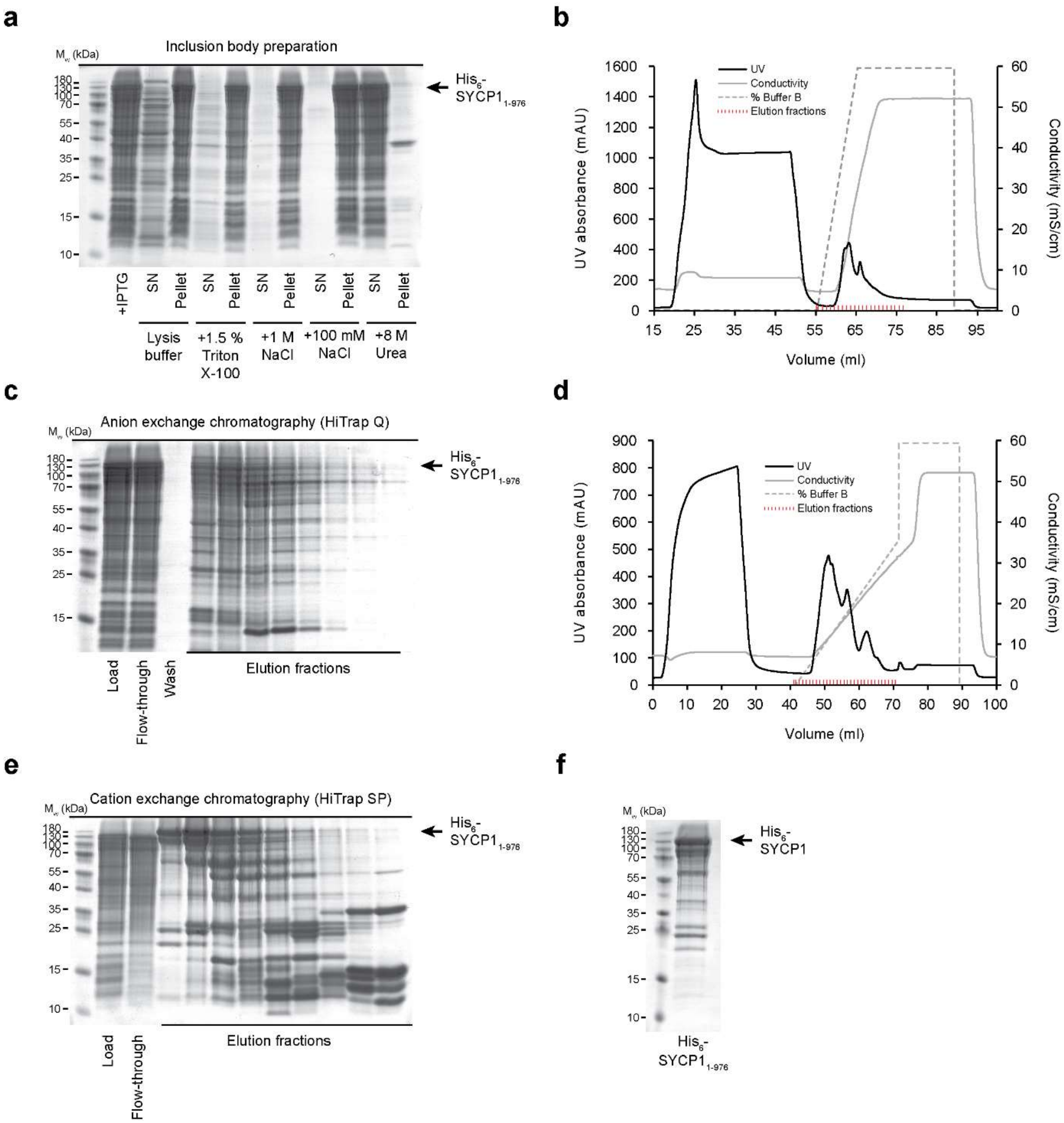

Figure 3.2.4| Optimised purification of SYCP1. a) SDS-PAGE analysis of **s**amples summarising the preparation of inclusion bodies indicating the sequential wash steps. All wash steps incorporated 50 mM DTT, 50 mM EDTA pH 8.0, and DNase. **b)** Ion exchange chromatogram showing the loading, wash, and elution phases for SYCP1 purified using HiTrap Q. **c)** SDS-PAGE analysis of load, flow-through, and elution fractions from **b**. **d)** Ion exchange chromatogram using HiTrap SP of SYCP1. **e)** SDS-PAGE analysis of load, flow-through, and elution fractions from **d**. **f)** SDS-PAGE analysis of purified His$_6$-SYCP1.

3.2.3 SYCP1 is helical and forms large assemblies in solution

To assess the success of the refolding process, a biophysical analysis of SYCP1 was performed. Far-UV circular dichroism spectroscopy was used to quantify secondary structure. A characteristic α-helical spectrum with minima at 208 and 222 nm allows for the estimation of helical content at 73 % using equations 2 and 3 (Methods section 2.1.8) (Figure 3.2.5a) (Greenfield and Fasman, 1969; Morrisett *et al.*, 1973). This closely matches the estimation by deconvolution by DichroWeb using the CDSSTR algorithm with reference data set 6 at 75 % (Sreerama and Woody, 2000; Whitmore and Wallace, 2004; Whitmore and Wallace, 2008). With the 976 amino acids of SYCP1 plus 37 residues of the His_6-tag and linker sequence, this corresponds to 758 ordered residues in helical arrangement, closely corresponding with the 683 residues of the predicted helical core. Further, cooperative unfolding at 38 ˚C was observed during thermal denaturation, by tracking the helical signal at 222 nm by CD spectroscopy, suggesting proper folding of the SYCP1 molecule (Figure 3.2.5b). The fraying of helical ends, occurring at a reduced temperature in comparison with the folded core of SYCP1, is highlighted by the early deviation from the sigmoidal curve between 5 and 35 ˚C (Figure 3.2.5b).

The polydispersity of purified SYCP1 and its oligomeric status was determined using multi-angle light scattering coupled with size-exclusion chromatography. I found that SYCP1 elutes soon after the void volume of the column, at 8.3 ml compared with 7.5 ml for the void (as determined by the elution volume of blue dextran which has a molecular weight of ~2 MDa), and ranges in molecular weight from 1.5 – 23 MDa, suggesting aggregation or, as we might predict from its role within the synaptonemal complex, some form of specific higher-order assembly (Figure 3.2.5c). A polydispersity of 1.27 highlights the presence of a heterogenous mixture of multimeric states.

3.2.4 Purification and characterisation of $SYCP1_{1\text{-}783}$

The double-banded appearance of SYCP1 during the early stages of its preparation could possibly be explained by a short C-terminal truncation. I reasoned that His_6-$SYCP1_{1\text{-}954}$ might be purifiable from *E. coli* in a soluble manner (Figure 3.2.7a). However, despite its presence within the Ni-NTA eluate, low expression levels and the double-banded appearance were both retained suggesting that residues 954-976 are not solely responsible the visible degradation which is likely to be more significant than just 22 residues (dashed box; Figure 3.2.7a). I therefore opted to remove the entire unstructured C-terminus and tested the expression and purification of SYCP1$_{1\text{-}783}$. Expression levels were much improved for both His$_6$- and His$_6$-MBP- fusions, with soluble SYCP1 clearly visible in the bacterial supernatant (Figure 3.2.6b-e). However, the majority of material did not bind the respective affinity resin suggesting occlusion of the N-terminal affinity tag (Figures 3.2.6b-e). I postulated that this may be due to N-terminal associations of the SYCP1 molecules, resulting in the formation of soluble aggregates which might represent *in vitro* assemblies which recapitulate self-assembly mechanisms utilised *in vivo*. I therefore attempted to chemically disrupt these associations by lysing cells in buffers containing either 10 % glycerol, 500 mM L-arginine pH 8.0, or 1.5 % Triton X-100 (Figure 3.2.6e). The addition of Triton X-100 resulted in a better yield of His$_6$-SYCP1$_{1\text{-}783}$, with protein visible in the Ni-NTA elution (gel 3, lane 7, Figure 3.2.6e). However, a larger quantity of protein, better enriched for non-degraded material, was achieved by utilising the previously described refolding procedure (Figure 3.2.6f). Circular dichroism analysis determined His$_6$-SYCP1$_{1\text{-}783}$ contained a proportionally greater percentage of α-helix when compared with SYCP1$_{1\text{-}976}$, at 83 %, corresponding to 679 helical residues of 820 total, perfectly matching the predicted 683 residues of the helical core, confirming the largely disordered nature of the SYCP1 N and C-termini (Figure 3.2.5a). Unfolding at 41 ˚C indicated it contained the same core fold as the full molecule (Figure 3.2.5b). SEC-MALS revealed megadalton assemblies, though noticeably smaller than observed for SYCP1$_{1\text{-}976}$, ranging from 0.6 – 8 MDa, the molecule retained propensity to aggregate, or assemble, in solution (Figure 3.2.5d).

Given this partial success, I postulated that the removal of the unstructured N-terminus (residues 1-100) might further improve expression in *E. coli* and subsequent purification. I therefore decided to purify residues 101-783 which encompass the predicted central helical domain (Figure 3.2.10a).

3.2.5 The unstructured C-terminus of SYCP1 binds DNA

The unstructured C-terminus of SYCP1 (residues 784-976) is highly basic and has previously been cited as having a DNA-binding function without providing experimental evidence (Schmekel *et al.*, 1996). I found, using electrophoretic mobility shift assays (EMSA), that SYCP1 binds double-stranded DNA, with 2.5 μM protein saturating 25 μM per base pair dsDNA (equating to 53.2 nM 470 bp linear dsDNA molecules) (Figure 3.2.5f). I therefore approximate a 10 bp footprint per SYCP1 monomer. I tested whether, as suggested, DNA binding was mediated by the unstructured C-terminus of SYCP1 which contains basic patches which may form obligate DNA binding modules. SYCP1$_{1\text{-}783}$, lacking residues 784-976, possessed negligible DNA binding capacity, highlighting the importance of the C-terminal tail for DNA association (Figure 3.2.5g). The intensity of free DNA observably decreases with an increase in SYCP1 concentration to 2.5 μM. This residual DNA binding may be mediated by the basic patch at the N-terminus of the SYCP1 helical core. Overall, these findings suggest that the SYCP1 C-terminus contains the key elements by which SYCP1 associates with DNA and may drive in its chromosomal assembly *in vivo*.

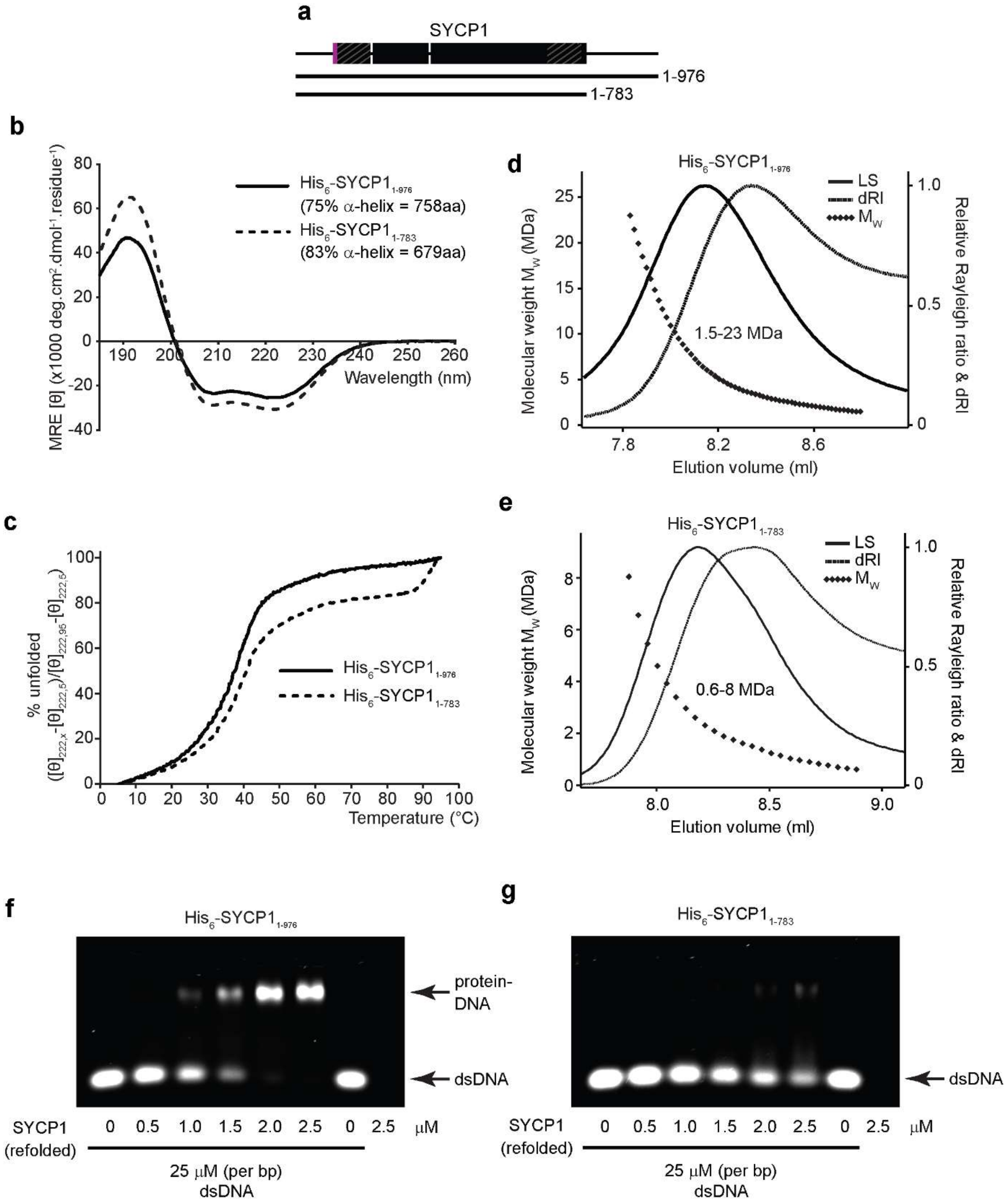

Figure 3.2.5| His$_6$-SYCP1 forms helical assemblies and binds DNA via its C-terminus. a) Schematic representation of SYCP1. The helical core is displayed as a segmented rectangle (demarcated on the basis of findings described throughout Chapter 3). Constructs analysed within this figure are aligned. A similar schematic shall be utilised throughout the figures of this chapter. **b)** Circular dichroism far-UV spectra were deconvoluted to estimate helical content (as indicated) of His$_6$-SYCP1 and SYCP1$_{1\text{-}783}$, with data fitted at normalised rmsd values of 0.005 and 0.006, respectively. **c)** Thermal denaturation of His$_6$-SYCP1 and SYCP1$_{1\text{-}783}$ displayed as % unfolded, calculated using the helical signal at 222 nm, revealed melting temperatures of 38 and 41 ˚C, respectively. **d,e)** SEC-MALS analysis of His$_6$-SYCP1 and SYCP1$_{1\text{-}783}$, demonstrating the formation of megadalton assemblies. Light scattering (LS) and differential refractive index (dRI) are plotted as solid and dashed lines, respectively, with molecular weights (Mw) shown as diamonds across elution peaks. **f,g)** EMSA analysis of SYCP1 and SYCP1$_{1\text{-}783}$.

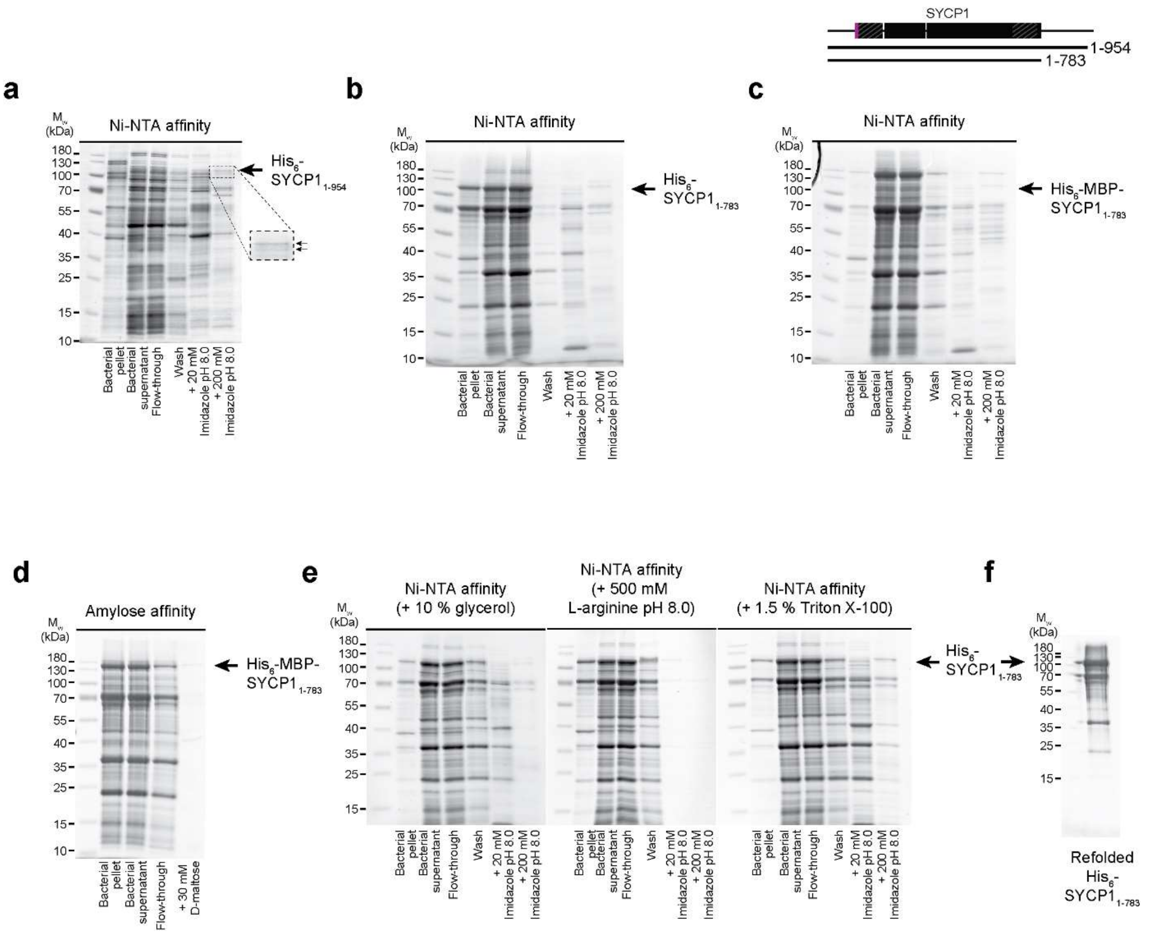
SYCP1
1-954
1-783
a
b
c
d
e
f
Mw (kDa)
Ni-NTA affinity
Amylose affinity
Ni-NTA affinity (+ 10 % glycerol)
Ni-NTA affinity (+ 500 mM L-arginine pH 8.0)
Ni-NTA affinity (+ 1.5 % Triton X-100)
His6-SYCP1 1-954
His6-SYCP1 1-783
His6-MBP-SYCP1 1-783
180
130
100
70
55
40
35
25
15
10
Bacterial pellet
Bacterial supernatant
Flow-through
Wash
+ 20 mM Imidazole pH 8.0
+ 200 mM Imidazole pH 8.0
+ 30 mM D-maltose
Refolded His6-SYCP1 1-783

Figure 3.2.6| Purification of SYCP1$_{1\text{-}783}$. a) SDS-PAGE analysis of Ni-NTA purification of His$_6$-SYCP1$_{1\text{-}954}$. The double-banded appearance is retained (dashed box). **b)** SDS-PAGE analysis of the attempted purification of His$_6$-SYCP1$_{1\text{-}783}$ by Ni-NTA affinity chromatography **c)** SDS-PAGE analysis of the attempted purification of His$_6$-MBP-SYCP1$_{1\text{-}783}$ by Ni-NTA affinity chromatography. **d)** SDS-PAGE analysis of the attempted purification of His$_6$-MBP-SYCP1$_{1\text{-}783}$ by amylose affinity chromatography. **e)** Ni-NTA affinity chromatography of His$_6$- SYCP1$_{1\text{-}783}$ lysed in the presence of + 10 % glycerol, 500 mM L-arginine pH 8.0, or 1.5 % Triton X-100. **f)** SDS-PAGE analysis of refolded His$_6$-SYCP1$_{1\text{-}783}$

3.2.6 Human SYCP1 also forms polycomplexes upon heterologous expression

It has been previously reported that upon heterologous expression of SYCP1 in COS-7 cells, large filamentous networks of SYCP1 assemble, named polycomplexes (PCs). The formation of PCs by rat SYCP1 is ablated upon deletion of the entire C-terminus (corresponding to a truncation of the human protein to residue 798) whilst a shorter truncation (corresponding to residue 891 in the human sequence) does not (Ollinger *et al.*, 2005). I found that human SYCP1 similarly forms PCs upon expression in COS-7 cells, visible by fluorescence as filamentous cytoplasmic networks (Figure 3.2.7a,). Many nest-like networks were observed without nuclei suggesting that filamentous assemblies remained stable after cellular apoptosis, confirmed by visualisation on brightfield; no intact cell membrane could be discerned, and cellular debris was visible (Figure 3.2.7b). Filamentous-network formation was graded from 1-5 (1; filamentous networks, 2-3; networks of a less extended appearance, 4; amorphous aggregation, 5; diffuse eGFP signal). The example images in Figure 3.2.7a have scores for each cell indicated in white. The efficiency of filamentous-network assembly was calculated for full-length SYCP1 at 44 ± 7 % (1-3 constitute assembly and 4-5 are classed as "no assembly") (Figure 3.2.8a). EM analysis reveals the familiar ultrastructure, with PCs resembling a back-to-back arrangement of SCs (Figure 3.2.7c,d). PCs were mostly frequently observed in close proximity to the nuclear membrane (indicated N).

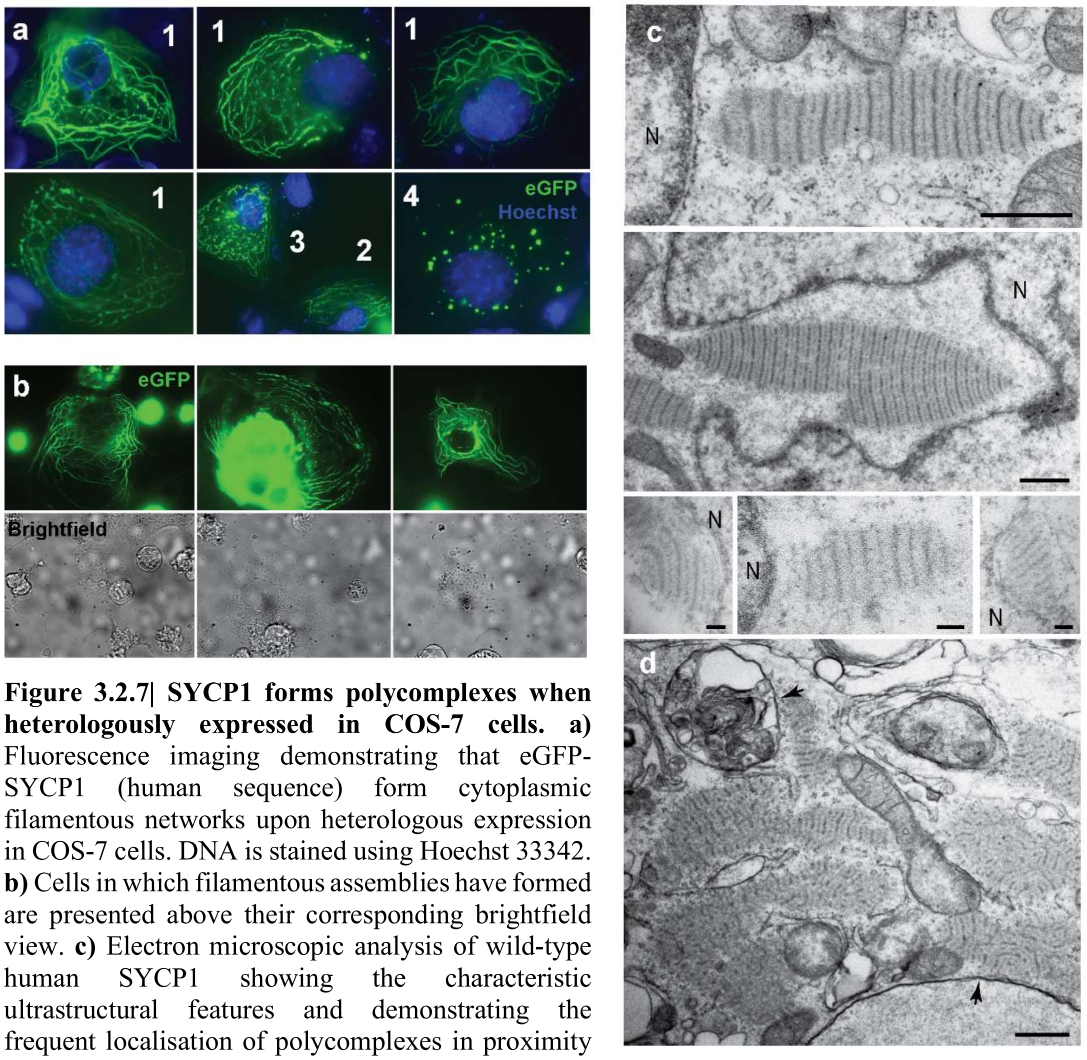

Figure 3.2.7| SYCP1 forms polycomplexes when heterologously expressed in COS-7 cells. a) Fluorescence imaging demonstrating that eGFP-SYCP1 (human sequence) form cytoplasmic filamentous networks upon heterologous expression in COS-7 cells. DNA is stained using Hoechst 33342. **b)** Cells in which filamentous assemblies have formed are presented above their corresponding brightfield view. **c)** Electron microscopic analysis of wild-type human SYCP1 showing the characteristic ultrastructural features and demonstrating the frequent localisation of polycomplexes in proximity to the nuclear envelope (N). Scale bars – 500 nm. **d)** Polycomplex ultrastructural order is not always completely regimented with many polycomplexes merging and sliced at many orientations. Scale bars – 500 nm. The nuclear envelope is indicated by an arrow.

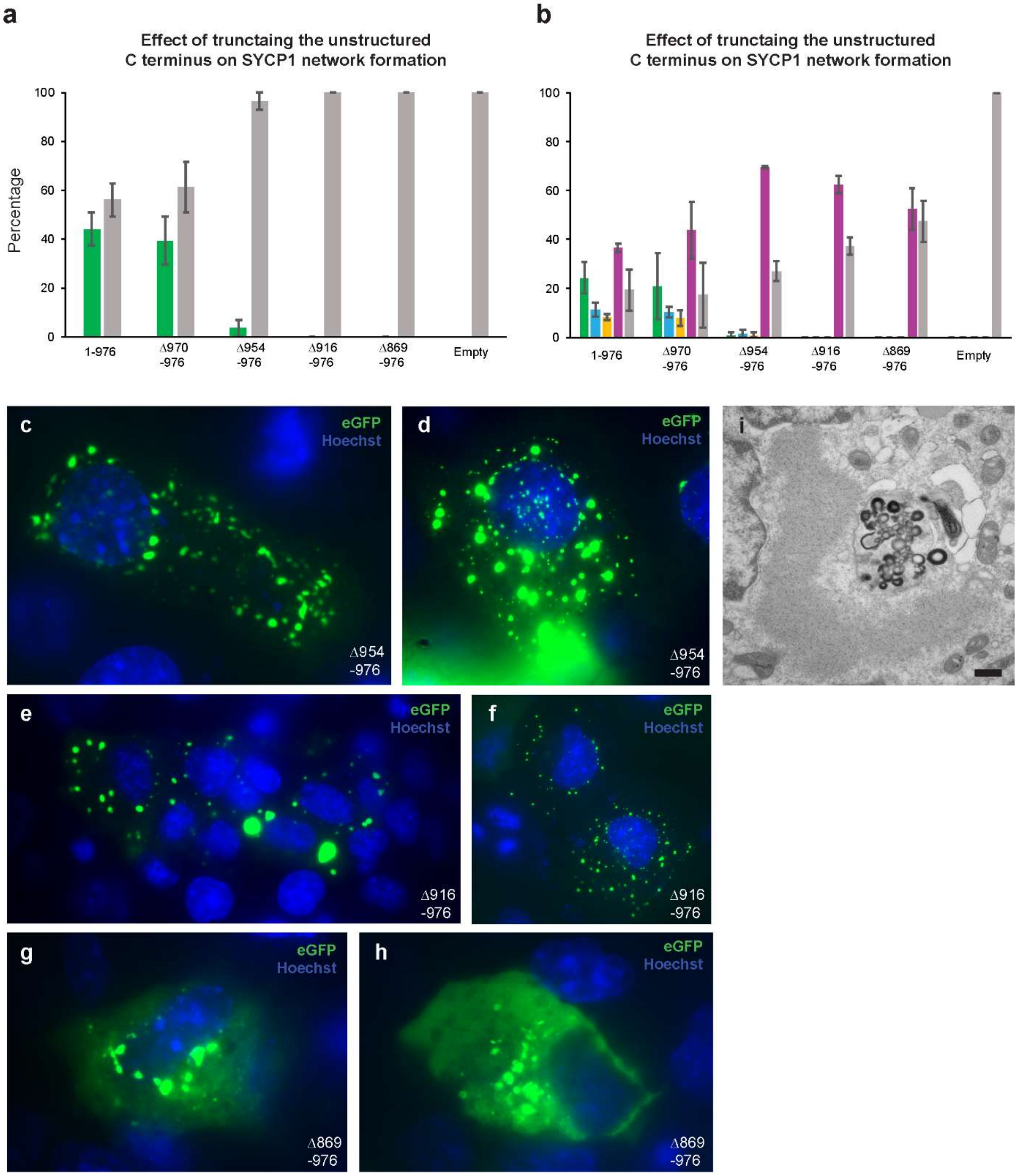

Figure 3.2.8| Blocking filamentous assembly of SYCP1 by C-terminal truncation. a) The efficiency of filamentous assembly is plotted as the percentage of transfected cells demonstrating filamentous assembly (green) and those displaying amorphous aggregates or diffuse GFP signals (grey). Each experiment was performed in triplicate with each experiment involving the counting and assignment of at least 100 cells. **b)** The same data presented in **a** but splitting assembly into its three component scores of 1-green, 2-blue, 3-yellow and splitting non-assembly into 4-purple and 5-grey. **c-h)** COS-7 cells expressing truncated constructs of SYCP1. The deletion is indicated in white text. **i)** Electron micrograph of sliced COS-7 cell expressing SYCP1$_{1\text{-}954}$ showing the formation of polycomplex structure.

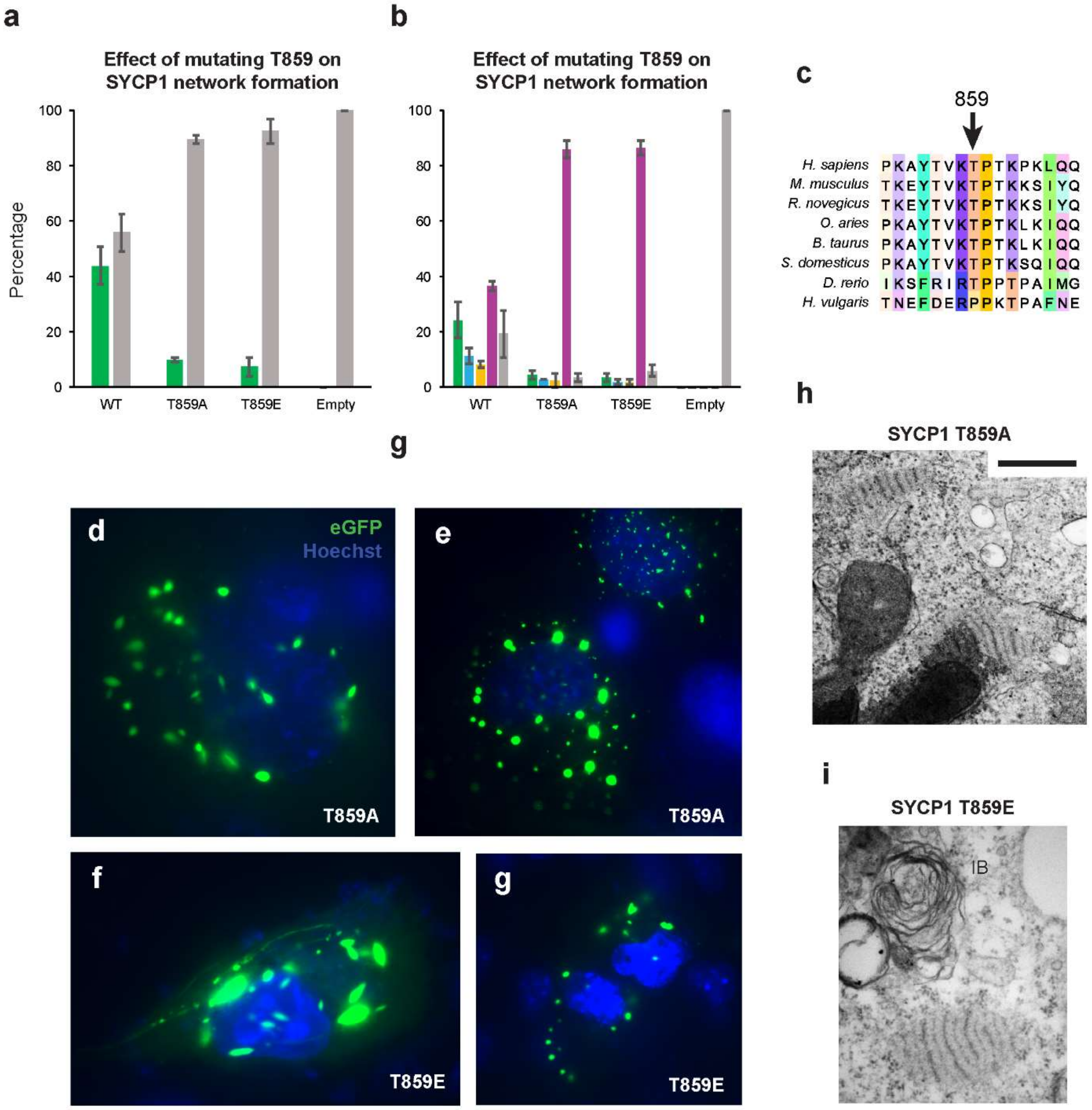

Figure 3.2.9| Blocking filamentous assembly of SYCP1 by mutation of T859. a) The efficiency of filamentous assembly in point mutations T859A and T859E within the context of GFP-SYCP1$_{1\text{-}976}$. Efficiency is plotted as the percentage of transfected cells demonstrating filamentous assembly (green) and those displaying amorphous aggregates or diffuse GFP signals (grey). Each experiment was performed in triplicate with each experiment involving the counting and assignment of at least 100 cells. **b)** The same data presented in **a** but splitting assembly into its three component scores of 1-green, 2-blue, 3-yellow and splitting non-assembly into 4-purple and 5-grey. **c)** Alignment of human SYCP1 sequence, residues 852-867. T859 is indicated. **d-g)** COS-7 cells expressing mutated constructs of SYCP1. The mutation is indicated in white text. **h,i)** Electron microscopic analysis of polycomplexes formed by COS-7 cells expressing GFP-SYCP1 T859E and T859A, respectively. An inclusion body (IB) is indicated

3.2.7 Truncation or mutation of the SYCP1 C-terminus blocks filamentous network formation

I then assessed a series of SYCP1 C-terminal truncations on their effect on filamentous-network formation. Network formation was unaffected by a 7-residue truncation (Δ970-976) which resulted in a non-significant decrease to 39 ± 10 % in network formation, whereas further truncation to SYCP1$_{1-954}$ (Δ954-976) almost fully ablated network formation with 3.5 ± 3.5 % assembly efficiency (Figure 3.2.8a). I was still able to identify polycomplex structure, however, in these cells (Figure 3.2.8i) Any further truncation (Δ916-976, Δ869-976) resulted in no assembly (Figure 3.2.8a). This indicates a key role for the unstructured C-terminal tail of SYCP1 in network formation though no EM analysis was performed.

Similarly, network formation was almost fully abolished through the mutation of residue T859 to either alanine or glutamate (10 ± 1 % and 6 ± 3 % respectively, Figure 3.2.9a). This residue is part of a TP motif, a potential CDK phosphorylation site, possibly implicating the phosphorylation of this residue in PC formation. Though network formation was ablated, analysis by electron microscopy readily identified polycomplex structures within the cytoplasm (Figure 3.2.9h,i). It is worth noting that in simply comparing network assembly efficiency, an interesting phenomenon is missed. In transfecting empty eGFP vector, a diffuse cytoplasmic fluorescence is observed. However, in the cases of the non-assembling truncations of SYCP1, 53 – 70 % of cells rather display punctate SYCP1 aggregates within the cytoplasm (Figure 3.2.8b; score 4). These aggregates are similar to those ovular-shaped cytoplasmic aggregates observed by Yuan *et al.* upon expression of SYCP1 in Swiss-3T3 cells (Figure 3.1.9a) and somewhat resemble the polycomplexes I have observed by electron microscopy in both size and shape (Figure 3.2.7c, Figure 3.2.8c-h, Figure 3.2.9c-f). This is particularly evident in Figures 3.2.8e and 3.2.9f.

An ultrastructural analysis of the cytoplasmic aggregates formed by truncated SYCP1 has never been performed. I tentatively suggest that SYCP1 assembly into polycomplex structures, observable by electron microscopy, is not disrupted by C-terminal truncation of SYCP1 or the mutation of T859. I suggest that filamentous network formation represents some other phenomenon, potentially recruitment of SYCP1 to an intermediate filament network, such as keratin.

3.2.8 The SYCP1 helical core possesses intrinsic self-assembly capacity

I expressed SYCP1$_{101\text{-}783}$ as an MBP-fusion encoded by a pMAT11 vector in BL21 (DE3) to promote solubility (Peranen *et al.*, 1996). Amylose affinity was utilised to perform the initial purification step (Figure 3.2.10a). To provide a sufficient yield, the lysate of at least 10 litres of bacterial culture were processed and the flow rate was reduced to 0.5 ml/min to allow binding. I imagine that the long length of the molecule acts somewhat like a parachute, creating a large surface area to catch the flow, resulting in stronger drag reducing binding efficiency. Attempted purification by Ni-NTA affinity resulted in the preferential purification of predominantly heavily degraded species and a faster flow rate resulted in significantly reduced yields (data not shown). Further purification through anion exchange chromatography using HiTrap Q was performed which successfully resolved non-degraded His$_6$-MBP-SYCP1$_{101\text{-}783}$ from free His$_6$-MBP (Figure 3.2.10b). Removal of the affinity tag was performed using enzymatic cleavage using TEV protease, which recognises the linker sequence between the His$_6$-MBP-tag and the initiating methionine (GSMSENLYFQGSM) resulting in a three-amino-acid extension to the N-terminus of the cleaved protein (GSM). Cleavage was enhanced through overnight incubation, gently rocking at 25 ˚C. A second anion exchange chromatography step was used to separate SYCP1$_{101\text{-}783}$ from the His$_6$-MBP-tag and TEV protease followed by size-exclusion chromatography (Figure 3.2.10c,d). An overview of the purification is given in Figure 3.2.10e.

SEC-MALS analysis of SYCP1$_{101\text{-}783}$ revealed the formation of heterogenous, megadalton assemblies, ranging from 1.2 – 20 MDa, demonstrating that, in solution, deletion of the unstructured N and C-termini does not ablate higher-order assembly (Figure 3.2.10f).

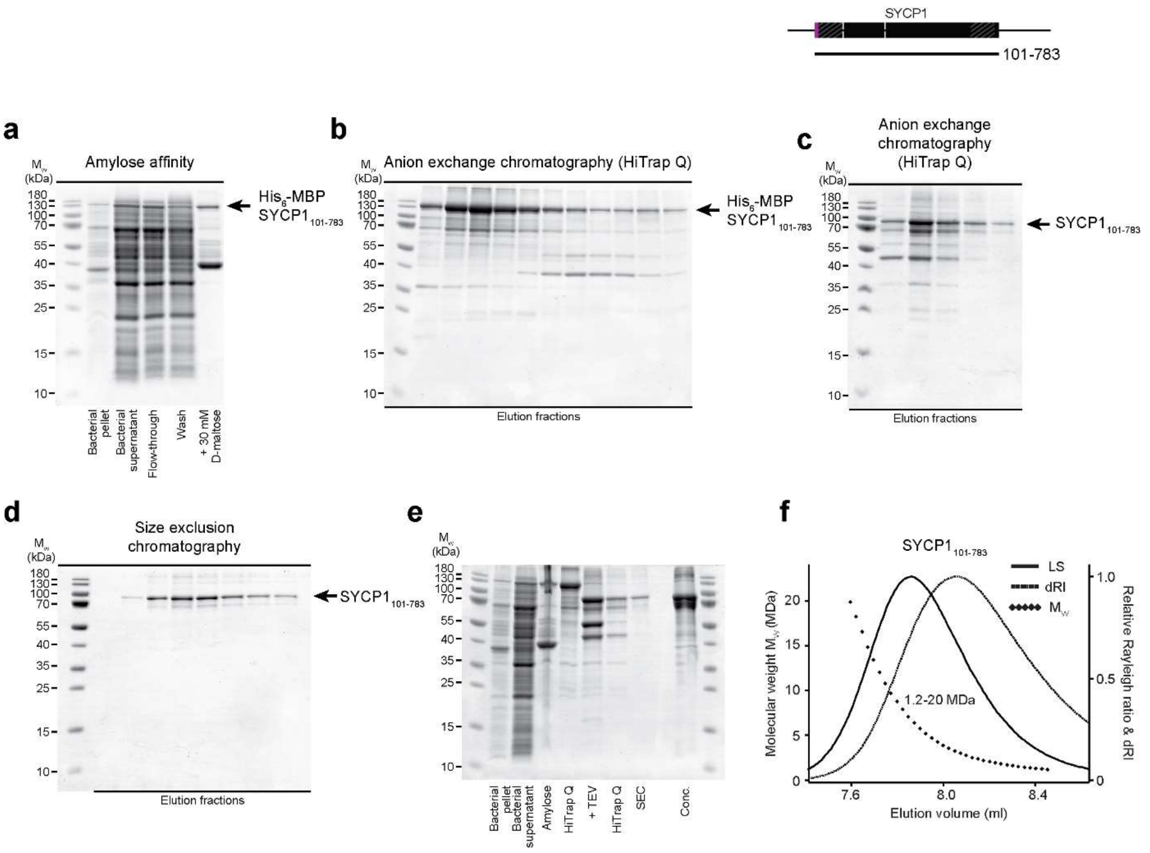

Figure 3.2.10| Purification and biophysical characterisation of SYCP$_{101\text{-}783}$. a) SDS-PAGE analysis of His$_6$-MBP-SYCP1$_{101\text{-}783}$ amylose affinity purification. **b)** SDS-PAGE analysis of ion exchange chromatography of His$_6$-MBP- SYCP1$_{101\text{-}783}$ elution fractions. **c)** SDS-PAGE analysis of ion exchange chromatography of cleaved SYCP1$_{101\text{-}783}$ elution fractions. **d)** SDS-PAGE analysis of size exclusion chromatography of SYCP1$_{101\text{-}783}$ elution fractions. **e)** SDS-PAGE analysis of samples summarising the purification of SYCP$_{101\text{-}783}$. **f)** SEC-MALS analysis of SYCP1$_{101\text{-}783}$ demonstrating the formation of megadalton assemblies. Light scattering (LS) and differential refractive index (dRI) are plotted as solid and dashed lines, respectively, with molecular weights (Mw) shown as diamonds across elution peaks.

3.2.9 Deletion of the SYCP1 αN-tip permits biophysical characterisation of obligate SYCP1

Deletion of 11 N-terminal residues (residues 101-111), termed the αN-tip, fully disrupts the assembly observed for SYCP1$_{101\text{-}783}$, with SYCP1$_{112\text{-}783}$ forming a stable, monodispersed, tetrameric species (Figure 3.2.11e). The purification for SYCP1$_{112\text{-}783}$ was performed as for SYCP1$_{101\text{-}783}$ (Figure 3.2.11a,b). Analysis by circular dichroism far-UV spectroscopy and deconvolution using DichroWeb reveals that of SYCP1$_{112\text{-}783}$ is almost fully α-helical (92 %, corresponding to 621 residues) with a melting temperature of 52 ˚C, determined through thermal denaturation tracking the helical signal at 222 nm by circular dichroism (Figure 3.2.11c,d) (Whitmore and Wallace, 2004). I suggest that this represents an obligate form of the SYCP1 molecule which lacks the ability to undergo higher-order self-assembly, dependent upon the presence of the SYCP1 αN-tip.

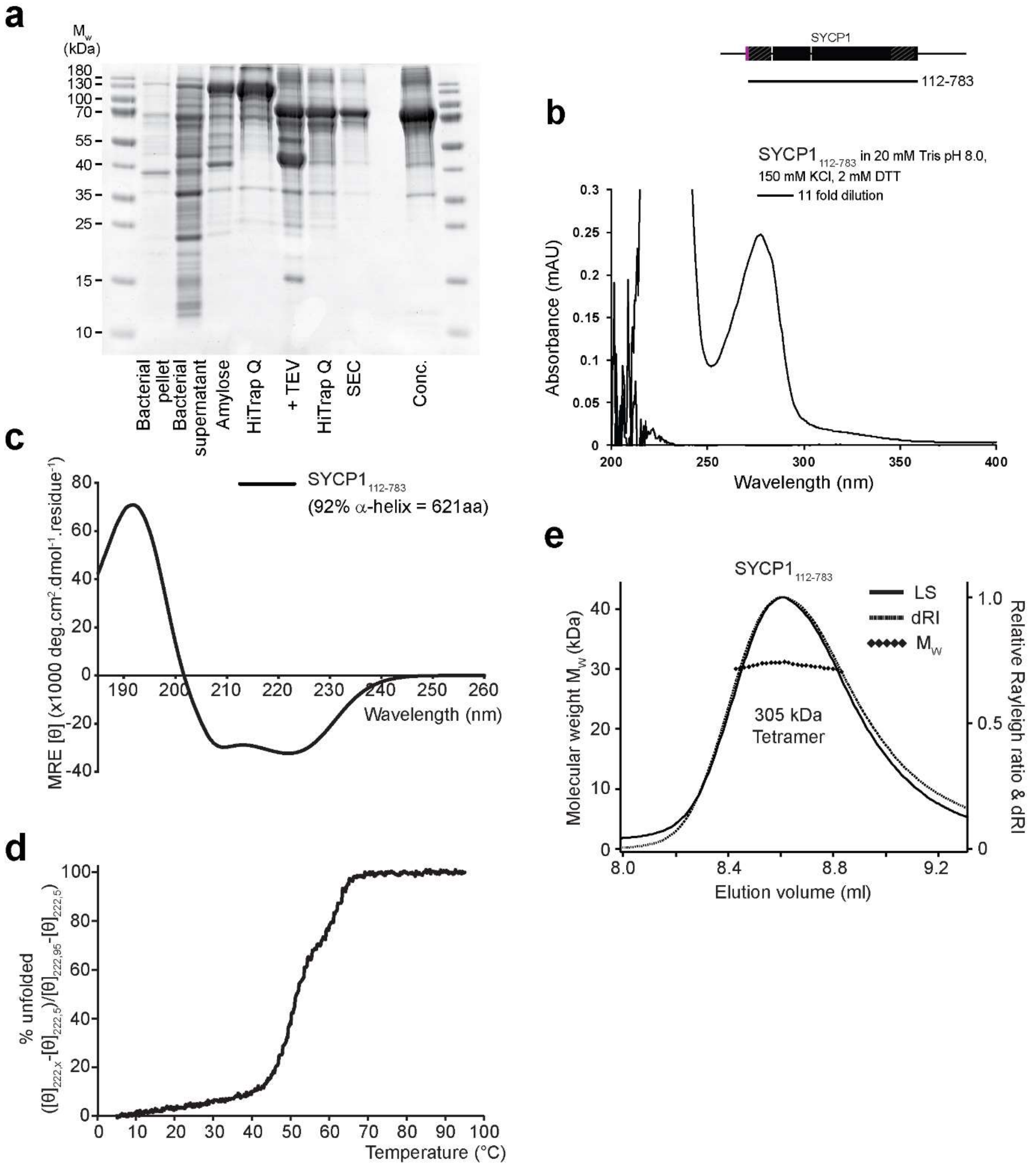

Figure 3.2.11| Purification and biophysical characterisation of SYCP1$_{112\text{-}783}$. a) SDS-PAGE analysis of samples summarising the purification of SYCP1$_{112\text{-}783}$. **b)** UV spectra for purified SYCP1$_{112\text{-}783}$. **c)** Circular dichroism far-UV spectra were deconvoluted to estimate helical content (as indicated) of SYCP1$_{112\text{-}783}$, with data fitted at a normalised rmsd value of 0.005. **d)** Thermal denaturation of SYCP1$_{112\text{-}783}$ displayed as % unfolded, calculated using the helical signal at 222 nm, revealed a melting temperature of 52 ˚C. **e)** SEC-MALS analysis of SYCP1$_{112\text{-}783}$ revealing the formation of a 305 kDa tetramer (theoretical tetramer – 320 kDa). Light scattering (LS) and differential refractive index (dRI) are plotted as solid and dashed lines, respectively, with molecular weights (Mw) shown as diamonds across elution peaks.

3.2.10 Size and shape determination of the SYCP1 structured core by X-ray scattering

We performed size-exclusion chromatography small angle X-ray scattering (SEC-SAXS) analysis to determine size and shape parameters (length and width) for obligate SYCP1. SEC-SAXS is particularly robust in the topological characterisation of asymmetric, elongated (rod-like) molecules, such as coiled-coils, and provided invaluable insights into the geometry of SYCP1 over the course of this study (Dunne and Davies, 2019b).

The steep gradient within the low *q* region (low scattering angle; low resolution) of the X-ray scattering profile hinted at a highly elongated shape (Figure 3.2.12a). Transformation of the data to real-space reveals the relative distribution of interatomic distances within a pairwise distance distribution profile, or *P(r)* curve (Sedlak *et al.*, 2017). The observed positive skew is typical for rod-like molecules, whilst the x-axis intercept indicates the maximum interatomic distance, or D_{max}, which equates to the molecule's length. The *P(r)* profile reveals a length of 900 Å, closely matching its theoretical length as an extended α-helical coiled-coil (1008 Å) (Figure 3.2.12b). This length would be sufficient to span over half the inter-chromosomal distance, in agreement with previous studies demonstrating the bi-orientation of SYCP1 with the SC (Liu *et al.*, 1996; Schmekel *et al.*, 1996; Schucker *et al.*, 2015).

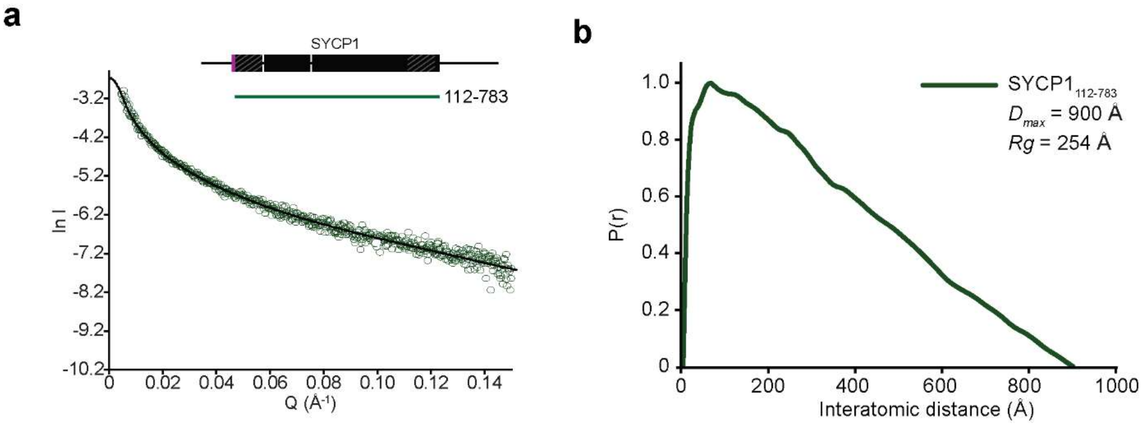

Figure 3.2.12| SYCP1$_{112\text{-}783}$ is elongated. a) Averaged small-angle X-ray scattering profile of SYCP1$_{112\text{-}783}$ with the fit used for *P(r)* distribution shown as a black line. **b)** SEC-SAXS *P(r)* distribution of SYCP1$_{112\text{-}783}$, maximum dimension (D_{max}) and radius of gyration (*Rg*) are indicated. *Rg* was calculated from real-space *P(r)* distribution rather than from Guinier analysis as the Guinier region was too narrow. SEC-SAXS analysis by Dr Orla Dunne.

3.2.11 A stable parallel coiled-coil caps the C-terminus of the SYCP1 helical core

Having defined the obligate form of SYCP1 as an elongated tetramer we sought to dissect its structure to learn the details of its molecular architecture. Previous work by Lucy J. Salmon identified a construct encompassing residues 640-783 which caps the C-terminus of the SYCP1 helical core and proved to express highly and solubly in *E. coli.*

$SYCP1_{640\text{-}783}$ was purified as summarised in Figure 3.2.13a. Circular dichroism far-UV spectroscopic analysis of $SYCP1_{640\text{-}783}$ demonstrated a typical helical spectrum, with negative peaks at 208 and 222 nm. Deconvolution of CD data using the CDSSTR algorithm and reference dataset 6 by DichroWeb provided an estimation of helical content at 85 %, corresponding to 125 out of 147 residues (Whitmore and Wallace, 2004).

The presence of three histidine residues and one cysteine within the sequence of $SYCP1_{640\text{-}783}$ prompted assaying for metal binding. I tested for the presence of bound zinc, as the presence of other metals would have been suggested by spectrophotometric features by UV spectroscopy which were not observed. I utilised a PAR assay in which divalent metal ions released from protein through proteolytic digestion are chelated by 4-(2-Pyridylazo)resorcinol (PAR) changing its spectrophotometric properties, from absorbing maximally at 414 nm to 494 nm. No metal binding was observed (Figure 3.2.13f).

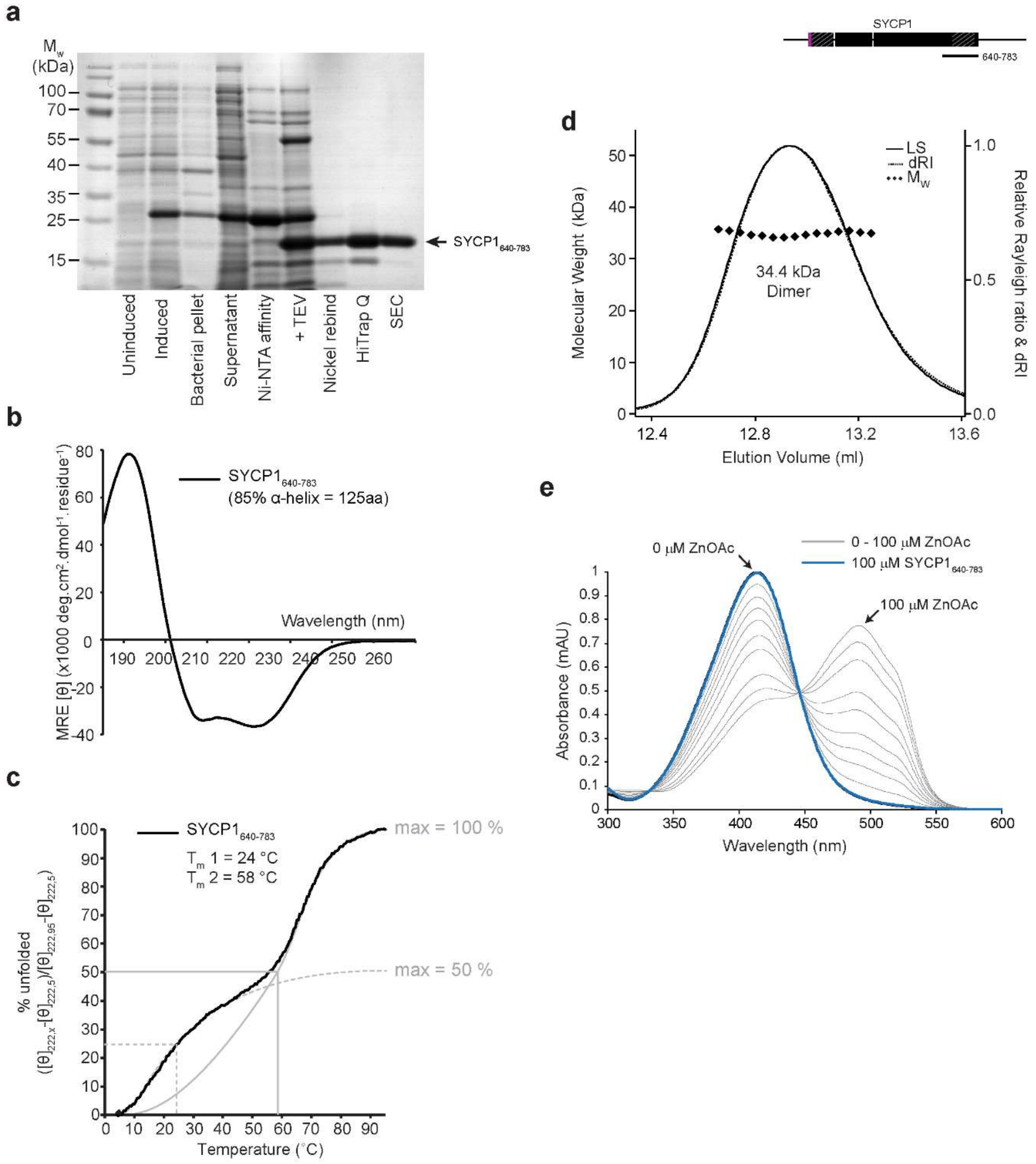

Figure 3.2.13| SYCP1$_{640-783}$ forms stable, helical domain capping the SYCP1 helical core. a) SDS-PAGE analysis of sample summarising the purification of SYCP1$_{640-783}$. **b)** Circular dichroism far-UV spectra, indicating percentage helix estimated by deconvolution, with data fitted at a normalised rmsd value of 0.003. **c)** Thermal denaturation demonstrating a biphasic unfolding pattern. The melting temperature of each unfolding event was estimated by manual extrapolation of the component curves at 24 and 58 °C. Data are plotted as % unfolded based on the helical signal at 222 nm. **d)** SEC-MALS analysis of SYCP1$_{640-783}$ revealing it forms a 34.4 kDa dimer (theoretical dimer – 34.6 kDa). Light scattering (LS) and differential refractive index (dRI) are plotted as solid and dashed lines, respectively, with molecular weights (Mw) shown as diamonds across elution peaks. **e)** PAR assay used to demonstrate the absence of zinc bound by SYCP1$_{640-783}$ (blue). Zn standards (0-100 μM) are shown in grey.

SEC-MALS determined the molecular weight to be 34.4 kDa, corresponding to a dimeric species (the theoretical dimeric molecular weight is 34 kDa) (Figure 3.2.13d). To unambiguously define the principal dimensions of SYCP1$_{640-783}$, we performed SEC-SAXS analysis (Figure 3.2.14). Given a pitch of 1 nm per heptad repeat (140 Å per residue), SYCP1$_{640-783}$ should demonstrate a length of 202 Å if it were to fold as a simple elongated coiled-coil (Truebestein and Leonard, 2016). A more elaborate fold, such as folding back on itself to create a four-helical bundle would demonstrate a reduced observed length and a larger cross-sectional radius (schematic; Figure 3.2.14d). As observed for SYCP1$_{112-783}$, the *P(r)* curve was positively skewed, indicating that it adopts an elongated conformation (Figure 3.2.14d). Determination of the cross-sectional radius of gyration (*Rc*) reveals the thickness of elongated molecules and thereby indicates the number of helices within a coiled-coil. SAXS data for SYCP1$_{640-783}$ revealed a *Rc* value of 9.3 Å suggesting the presence of between 2 and 4 helical chains within the cross-sectional radius (Figure 3.2.14c). The *P(r)* distribution indicates the maximum dimension of the molecule, which may be directly interpreted as its length for coiled-coils (Figure 3.2.14d). The *P(r)* maximum dimension of 196 Å closely matches its theoretical length of 202 Å as an extended coiled-coil. Thus, I conclude that SYCP1$_{640-783}$ folds as a simple, extended coiled-coil.

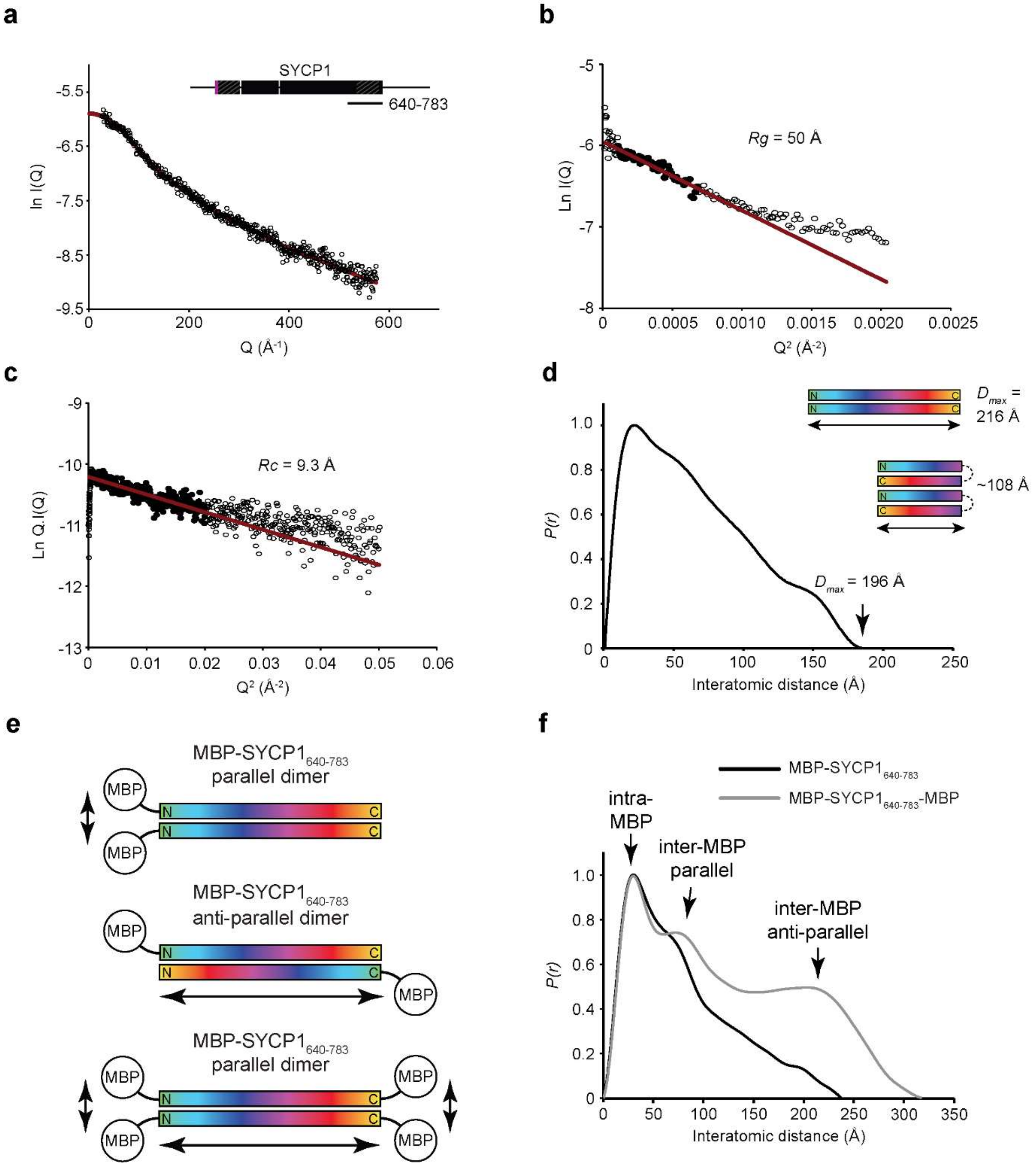

Figure 3.2.14| SEC-SAXS analysis of SYCP1$_{640-783}$. a) Averaged small-angle X-ray scattering profile of SYCP1$_{640-783}$ with the fit used for *P(r)* distribution shown as a red line. **b)** SEC-SAXS Guinier analysis to determine the radius of gyration (*Rg*) of SYCP1$_{640-783}$. The linear fit is in red and data points utilised highlighted in solid black. The *Q.Rc* value was < 1.3 with the *Rg* calculated at 50 Å. **c)** SEC-SAXS Guinier analysis to determine the radius of gyration of the cross-section (*Rc*) of SYCP1$_{640-783}$. The linear fit is in red and data points utilised highlighted in solid black. The *Q.Rc* value was < 1.3 with the *Rc* calculated as 9.3 Å. **d)** Inter-atomic distance distribution profile (*P(r)*) for SYCP1$_{640-783}$ demonstrating positive skew with the *D$_{max}$* indicated. Inset **s**chematic of possible helical folds for SYCP1$_{640-783}$ indicating theoretical lengths (*D$_{max}$*). **e)** Schematic representing different configurations an extended, MBP-tagged, coiled-coil could adopt with arrows indicating the inter-MBP distance. **f)** Inter-atomic distance distribution profiles (*P(r)*) for MBP-SYCP1$_{640-783}$ (black) and double-MBP fusion, MBP-SYCP1$_{640-783}$-MBP (grey). The locations of intra-, and parallel/anti-parallel inter-MBP peaks are indicated. SEC-SAXS analysis by Dr Orla Dunne.

3.2.12 Determining the orientation of helices within SYCP1$_{640\text{-}783}$

To determine the orientation of helices within the SYCP1$_{640\text{-}783}$ dimer, a SAXS method, previously utilised to determine the relative orientation of helices within SYCE1 (Dunne and Davies, 2019b), was employed in which a series of maltose-binding protein (MBP)-fused constructs were analysed, utilising the dominant features of the globular MBP-tags within inter-atomic distance distribution profiles to determine their relative positioning. Short ~70-Å inter-MBP distances would indicate a parallel orientation of helices, whilst additional long inter-MBP distances approximating the D_{max} would indicate an anti-parallel orientation (Figure 3.2.14e). Solely short inter-MBP distances observed for the N-terminal MBP-fusion of SYCP1$_{640\text{-}783}$ indicate a parallel orientation of helices (Figure 3.2.14f). Accordingly, a long inter-MBP distance was observed for MBP- SYCP1$_{640\text{-}783}$ -MBP (Figure 3.2.14e,f).

3.2.13 Modelling the SYCP1$_{640\text{-}783}$ coiled-coil structure *in silico*

Modelling the SYCP1$_{640\text{-}783}$ as a parallel, extended, coiled-coil using ROSETTA in combination with SAXS-derived distance restraints, predicted heptad repeat residues adopt classic coiled-coil interactions (modelling performed by Dr Owen Davies; Figure 3.2.15a-c). The residues of the heptad repeat are denoted *abcdefg* where *a* and *d* are generally hydrophobic. The model confines the chains in close association, forming canonical N- and C-terminal coiled-coils. Residues 640 to residue 664 for the N-terminal coiled-coil, with positions *a* being occupied by V643, L650, F657 and Y664 and *d* positions occupied by L646, A653 and I660 (Figure 3.2.15b). Residues 749-781 form the C-terminal coiled-coil, with L753, L760, L767, and A781 occupying the *a* positions and L749, L756, V763 and L777 occupying the *d* positions (non-canonical E770 and K774 are in heptad positions *d* and *a*, respectively) (Figure 3.2.15c).

The structure could not be modelled as a single continuous coiled-coil, with the intermediate sequence forming interspersed hydrophobic associations. The modelled structure does not fit the SAXS data; the fit of the calculated scattering curve of the modelled structure to the experimental scattering data is poor with a χ^2 value of 24.525 (Figure 3.2.15d). Docking of the modelled structure into *ab initio* generated molecular envelope demonstrates that the intermediate sequence likely splays apart (Figure 3.2.15e). This matches sequences prediction which suggests that coiled-coil sequence is only adopted by the N- and C-terminal sequences (Figure 3.2.15f).

Correspondingly, the thermal denaturation profile of SYCP1$_{640-783}$ suggests a two-step unfolding process, with melting temperatures estimated at 24 and 58 ˚C, indicative of the unfolding of two stabilising sequences within the construct (Figure 3.2.13c). The independent unfolding of the individual coiled-coil sequences likely explains the bimodal thermal denaturation profile with the unfolding of the C-terminal coiled-coil likely represented by the second transition as it contributes a greater number of interacting residues.

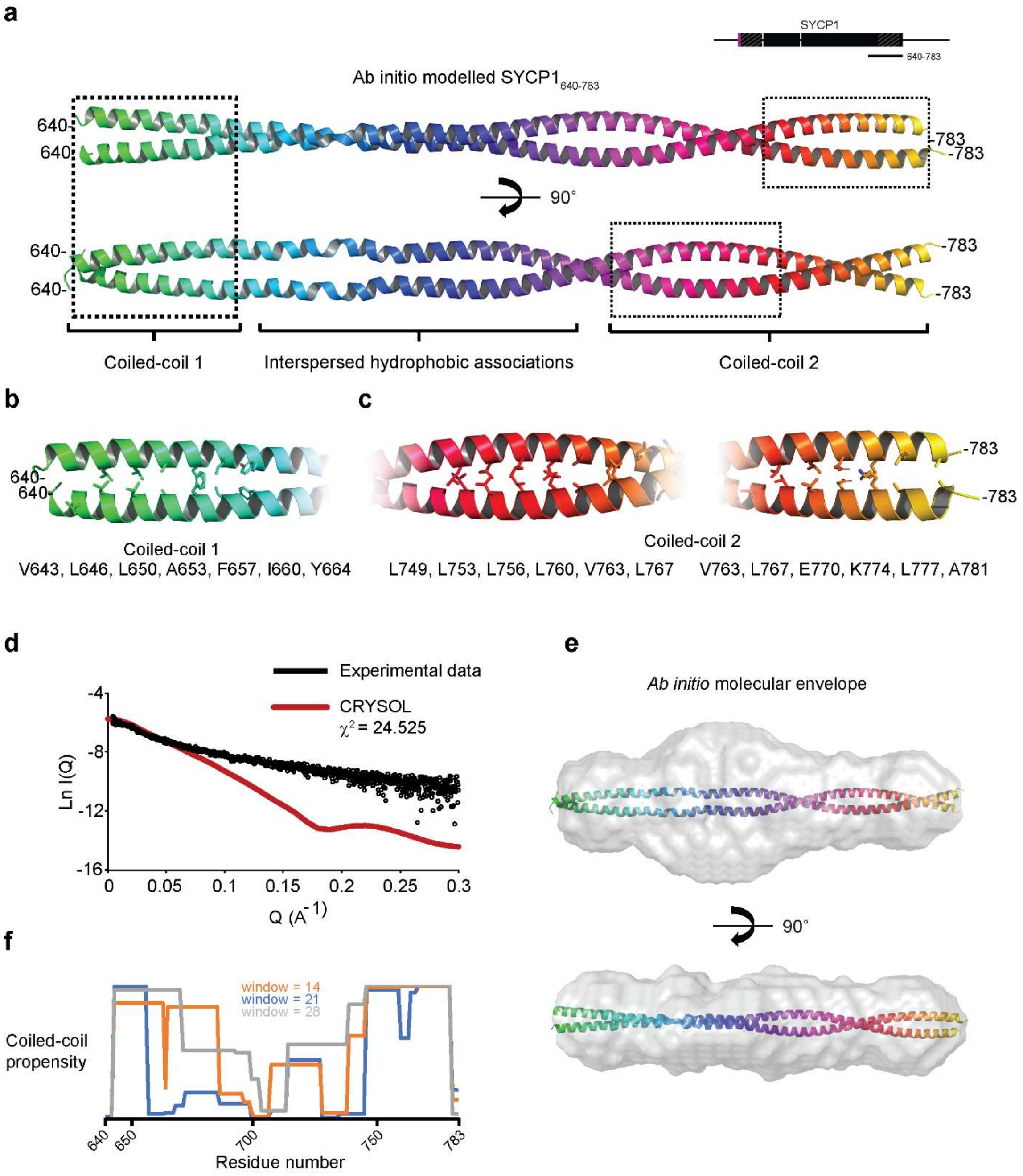
a
SYCP1
640-783
Ab initio modelled SYCP1$_{640\text{-}783}$
640-
640
-783
-783
90°
640-
640-
-783
-783
Coiled-coil 1
Interspersed hydrophobic associations
Coiled-coil 2
b
c
640-
640
-783
-783
Coiled-coil 1
V643, L646, L650, A653, F657, I660, Y664
Coiled-coil 2
L749, L753, L756, L760, V763, L767
V763, L767, E770, K774, L777, A781
d
Experimental data
CRYSOL
χ^2 = 24.525
Ln I(Q)
-4
-8
-12
-16
0
0.05
0.1
0.15
0.2
0.25
0.3
Q (Å^{-1})
e
Ab initio molecular envelope
90°
f
window = 14
window = 21
window = 28
Coiled-coil propensity
640
650
700
750
783
Residue number

Figure 3.2.15| Modelling the SYCP1$_{640\text{-}783}$ extended, parallel, coiled-coil. a) ROSETTA modelling of SYCP1$_{640\text{-}783}$ using SAXS-derived distance restraints. Coiled-coil sequences are bounded by dashed boxes. **b)** Heptad residues within coiled-coil 1 are shown. **c)** Heptad residues within coiled-coil 2 are shown. **d)** Experimental scattering data for SYCP1$_{640\text{-}783}$ (black) and calculated scattering data of the ROSETTA model (red). The calculated data fits the experimental with a χ^2 value of 24.525. **e)** SUPCOMB docking of modelled SYCP1$_{640\text{-}783}$ into an *ab initio* molecular envelope. 23 envelopes were calculated by DAMMIF and averaged by DAMAVER. **f)** COILS analysis of the SYCP1$_{640\text{-}783}$ demonstrating strong coiled-coil prediction at both the N- and C-terminal ends and weak prediction within the intermediate sequence. Modelling by Dr Owen Davies.

3.2.14 Dissecting the core structure of SYCP1

The finding that the C-terminus of the SYCP1 helical core forms a stable dimeric coiled-coil is immediately striking given the tetrameric state of SYCP1$_{112\text{-}783}$. I sought to determine the minimum sequence required to stabilise the tetrameric form of SYCP1.

A series of SYCP1 constructs were designed, cloned and purified and are summarised in Figure 3.2.16a. Extension of the C-terminal boundary further than amino acid 783 resulted in instability but had no effect on the dimeric oligomeric status (Figure 3.2.16a and Appendix 2). Extension of the N-terminal boundary to residue 206 resulted in the formation of a stable tetramer whilst extension to 358, 589 and 632 did not alter the dimeric status indicating that the sequence mediating tetramerization was within boundaries 206-358 (Figure 3.2.16a and 3.2.17b). SYCP1$_{358\text{-}783}$ proved particularly stable, as purified in Figure 3.2.17a. SEC-MALS data for SYCP1$_{358\text{-}783}$ are presented in Figure 3.2.18b, demonstrating the dimeric oligomeric status with a molecular weight of 96 kDa (theoretical molecular weight is 101 kDa).

Upon analysis by Matthew Ratcliff, we found that the N-terminus of the SYCP1 core (residues 112-362) retained a tetrameric oligomeric state (Figure 3.2.18c). SYCP1$_{112\text{-}362}$ demonstrated a single degradation product (marked with an asterisk) suggesting the presence of a stable core within (Figure 3.2.17b). Truncation of the N-terminal boundary to 206 resulted in a protein which migrated by SDS-PAGE the same as the degradation product of SYCP1$_{112\text{-}362}$ (Figure 3.2.17c,d). SYCP1$_{206\text{-}362}$ retained the tetrameric oligomeric status, with a molecular weight of 67 kDa (theoretical molecular weight is 76 kDa) (Figure 3.2.18d). Together, SYCP1$_{206\text{-}362}$ and SYCP1$_{358\text{-}783}$ fulfil the key oligomeric units within the SYCP1 core and were furthered for biophysical characterisation.

3.2.15 Biophysical characterisation of the SYCP1$_{206\text{-}362}$ and SYCP1$_{358\text{-}783}$

Circular dichroism far-UV spectroscopy reveals that, as expected, both constructs are almost entirely α-helical, with deconvolutions suggesting 93 and 90 % helicity for SYCP1$_{206\text{-}362}$ and SYCP1$_{358\text{-}783}$, respectively (Figure 3.2.18e). Their individual thermostabilities are less than that of SYCP1$_{112\text{-}783}$, with melting temperatures for SYCP1$_{206\text{-}362}$ at 38 ˚C and for SYCP1$_{358\text{-}783}$ at 37 ˚C in comparison to 52 ˚C for SYCP1$_{112\text{-}783}$ (Figure 3.2.18f). SEC-SAXS analysis revealed that both constructs exist as elongated, rod-like, molecules in solution, with lengths and cross-sectional radii of gyration (*Rc*) matching their theoretical parameters as coiled-coils (Figure 3.2.18g-j). SYCP1$_{206\text{-}362}$ has a D_{max} of 260 Å (theoretical length as a coiled-coil is 236 Å) and R_c of 10.3 Å, suggesting its folding as a four-helical bundle. In contrast, SYCP1$_{358\text{-}783}$ has a D_{max} of 645 Å (theoretical length as a coiled-coil is 639 Å) and R_c of 8.9 Å, indicating its folding as a dimeric coiled-coil. Interestingly, the R_c of SYCP1$_{358\text{-}783}$ (8.9 Å) indicates a diameter of 17.8 Å, closely matching the 16 Å measured thickness of the individual transverse filaments observed within the hamster SC by electron microscopy (Solari and Moses, 1973).

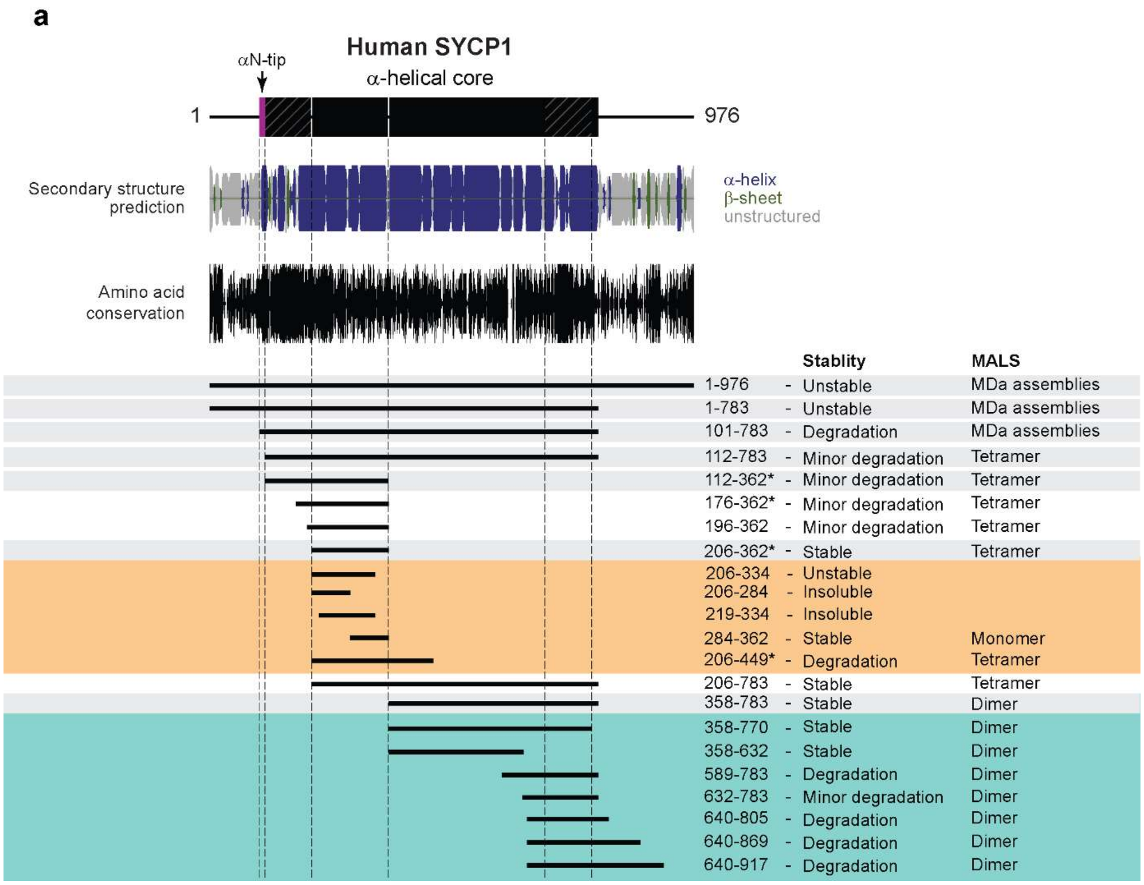
a
Human SYCP1
α-helical core
αN-tip
1
976
Secondary structure prediction
α-helix
β-sheet
unstructured
Amino acid conservation
Stablity
MALS
1-976 - Unstable MDa assemblies
1-783 - Unstable MDa assemblies
101-783 - Degradation MDa assemblies
112-783 - Minor degradation Tetramer
112-362* - Minor degradation Tetramer
176-362* - Minor degradation Tetramer
196-362 - Minor degradation Tetramer
206-362* - Stable Tetramer
206-334 - Unstable
206-284 - Insoluble
219-334 - Insoluble
284-362 - Stable Monomer
206-449* - Degradation Tetramer
206-783 - Stable Tetramer
358-783 - Stable Dimer
358-770 - Stable Dimer
358-632 - Stable Dimer
589-783 - Degradation Dimer
632-783 - Minor degradation Dimer
640-805 - Degradation Dimer
640-869 - Degradation Dimer
640-917 - Degradation Dimer

Figure 3.2.16| Dissecting the SYCP1 core. a) SYCP1 constructs analysed in the identification of SYCP1$_{206\text{-}362}$ and SYCP1$_{358\text{-}783}$. Amino acid boundaries, stability and oligomeric status as determined by SEC-MALS are indicated. Constructs originally purified and analysed by Matthew Ratcliff are indicated by an asterisk. Constructs in green are summarised in Appendix 2.

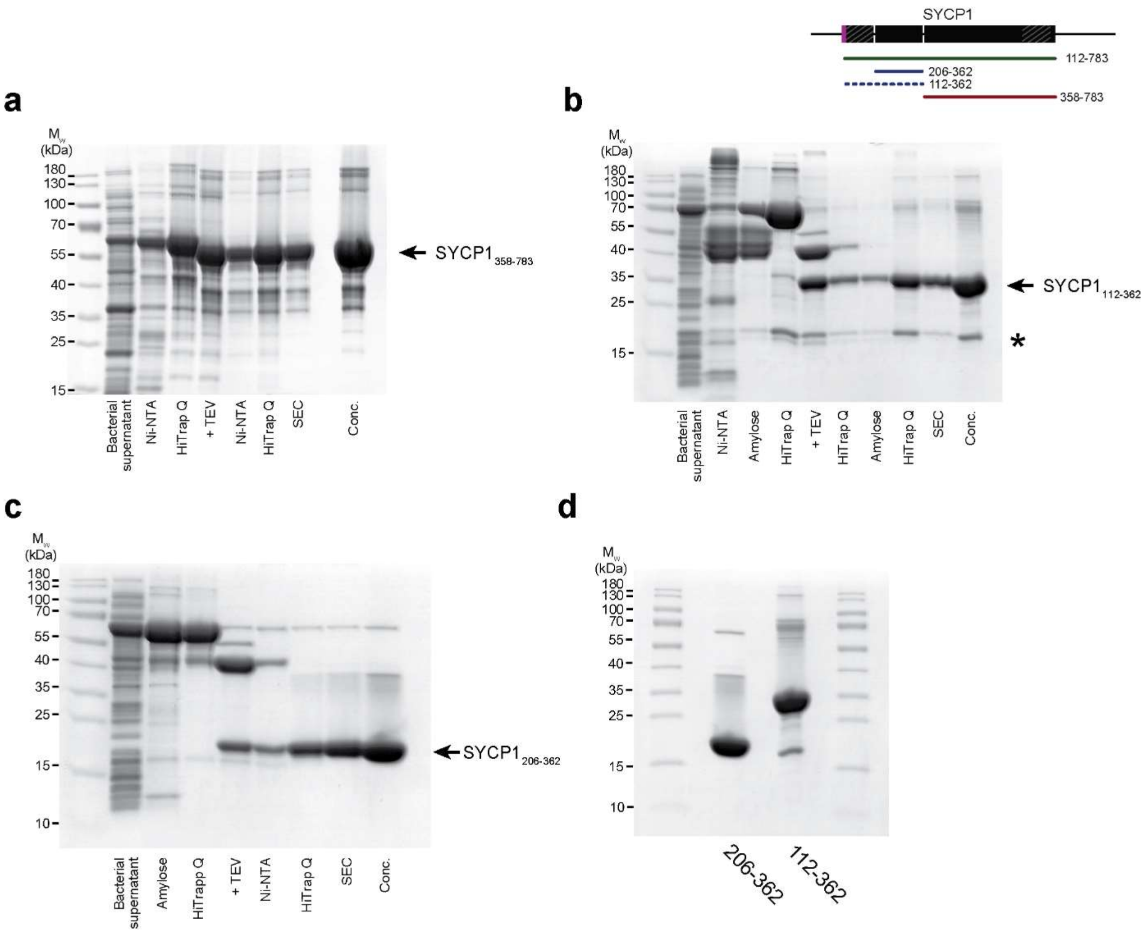
SYCP1
112-783
206-362
112-362
358-783
a
b
c
d
M$_w$ (kDa)
180
130
100
70
55
40
35
25
15
10
SYCP1$_{358\text{-}783}$
SYCP1$_{112\text{-}362}$
SYCP1$_{206\text{-}362}$
*
Bacterial supernatant
Ni-NTA
HiTrap Q
+ TEV
Ni-NTA
HiTrap Q
SEC
Conc.
Bacterial supernatant
Ni-NTA
Amylose
HiTrap Q
+ TEV
HiTrap Q
Amylose
HiTrap Q
SEC
Conc.
Bacterial supernatant
Amylose
HiTrapp Q
+ TEV
Ni-NTA
HiTrap Q
SEC
Conc.
206-362
112-362

Figure 3.2.17 (above)| Purification of SYCP1$_{358\text{-}783}$, SYCP1$_{112\text{-}362}$, and SYCP1$_{206\text{-}362}$. a-d) SDS-PAGE analysis of samples summarising the purification of **a)** SYCP1$_{358\text{-}783}$, **b)** SYCP1$_{112\text{-}362}$, **c)** SYCP1$_{206\text{-}362}$. The degradation product of SYCP$_{1112\text{-}362}$ is marked with an asterisk. **d)** Final purified samples of SYCP1$_{112\text{-}362}$ and SYCP1$_{206\text{-}362}$ showing the alignment of SYCP1$_{206\text{-}362}$ with the degradation product of SYCP1$_{112\text{-}362}$.

Figure 3.2.18 (right)| Biophysical characterisation of SYCP1$_{358\text{-}783}$, SYCP1$_{112\text{-}362}$, and SYCP1$_{206\text{-}362}$. a) Schematic of SYCP1 displaying analysed constructs. **b-d)** SEC-MALS analysis of **a)** SYCP1$_{358\text{-}783}$ (theoretical dimer – 101 kDa), **b)** SYCP1$_{112\text{-}362}$ (theoretical tetramer – 121 kDa), **c)** SYCP1$_{206\text{-}362}$ (theoretical tetramer – 76 kDa). **e)** Circular dichroism far-UV spectra for SYCP1$_{358\text{-}783}$ (red), SYCP1$_{112\text{-}362}$ (dashed blue), SYCP1$_{206\text{-}362}$ (blue). Data were deconvoluted to estimate percentage helix and fitted with a normalised rmsd values of 0.003, 0.003 and 0.009, respectively. **f)** Thermal denaturation of SYCP1$_{358\text{-}783}$ (red), SYCP1$_{112\text{-}362}$ (dashed blue), SYCP1$_{206\text{-}362}$ (blue) based on the helical signal at 222 nm was plotted as % unfolded revealing melting temperatures of 37, 38, and 38 ˚C. **g)** Averaged small-angle X-ray scattering profile of SYCP1$_{112\text{-}783}$ (green), SYCP1$_{358\text{-}783}$ (red) and SYCP1$_{206\text{-}362}$ (blue) with the fits used for P(r) distribution shown as black lines. **h)** Guinier analysis to determine the radius of gyration (*Rg*) of SYCP1$_{206\text{-}362}$ with data points within the linear region used for analysis shown in black. *Q.Rg* value was < 1.3. The Guinier region for SYCP1$_{358\text{-}783}$ was too narrow for analysis so was calculated using the real-space *P(r)* distance distribution. **i)** Guinier analysis to determine the radius of the cross-section (*Rc*) for SYCP1$_{358\text{-}783}$ (red) and SYCP1$_{206\text{-}362}$ (blue). Data points within the linear region used for calculation are highlighted in black. **j)** Inter-atomic distance distribution profiles (*P(r)*) for SYCP1$_{112\text{-}783}$ (green), SYCP1$_{358\text{-}783}$ (red) and SYCP1$_{206\text{-}362}$ (blue) indicating the maximum dimension (D_{max}). SEC-SAXS analysis by Dr Orla Dunne.

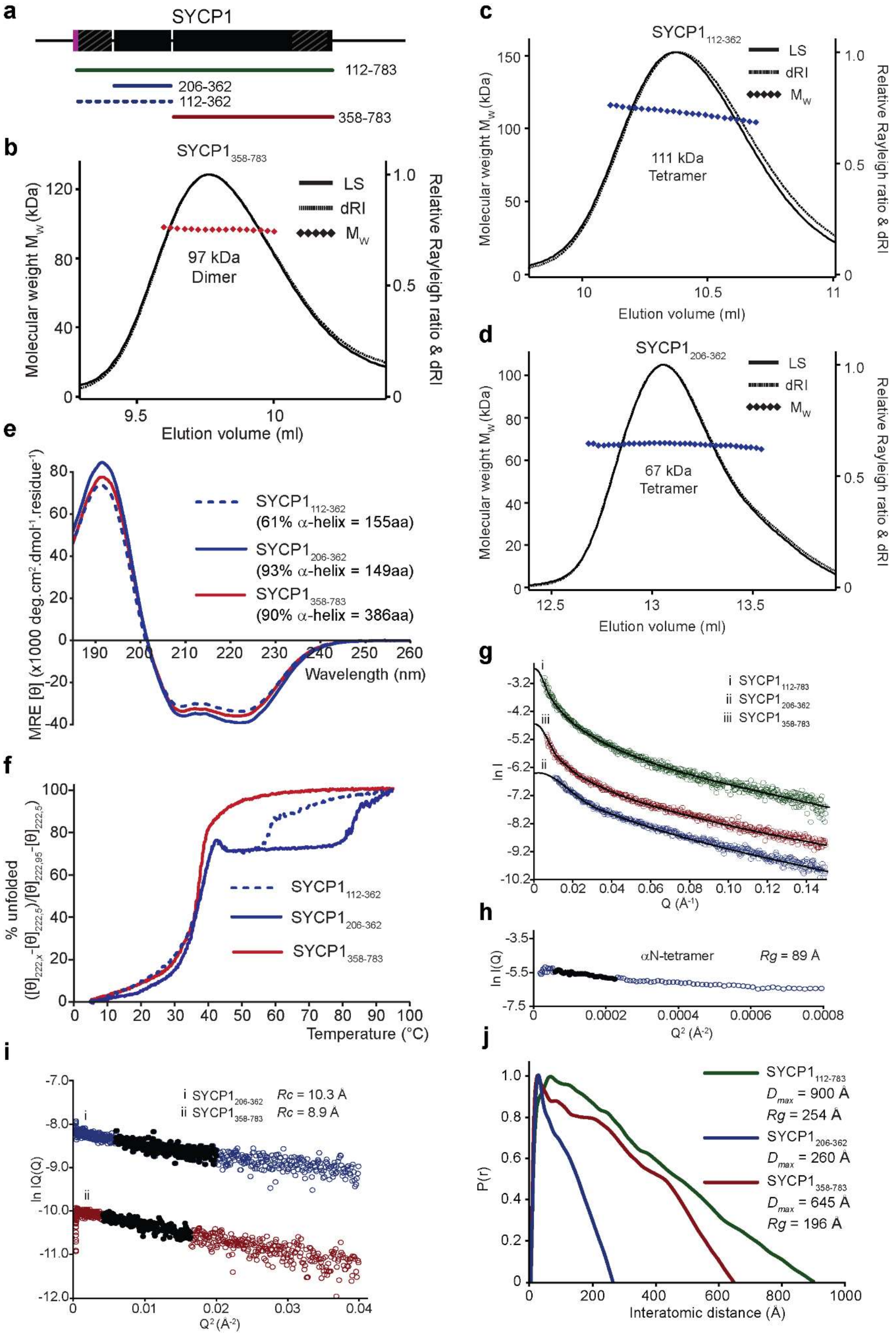
a
SYCP1
112-783
206-362
112-362
358-783
b
SYCP1358-783
LS
dRI
MW
97 kDa
Dimer
Molecular weight MW (kDa)
Relative Rayleigh ratio & dRI
Elution volume (ml)
c
SYCP1112-362
111 kDa
Tetramer
d
SYCP1206-362
67 kDa
Tetramer
e
MRE [θ] (x1000 deg.cm2.dmol-1.residue-1)
Wavelength (nm)
SYCP1112-362 (61% α-helix = 155aa)
SYCP1206-362 (93% α-helix = 149aa)
SYCP1358-783 (90% α-helix = 386aa)
f
% unfolded ([θ]222,x-[θ]222,5)/[θ]222,95-[θ]222,5)
Temperature (°C)
SYCP1112-362
SYCP1206-362
SYCP1358-783
g
i SYCP1112-783
ii SYCP1206-362
iii SYCP1358-783
ln I
Q (Å-1)
h
αN-tetramer
Rg = 89 Å
ln I(Q)
Q2 (Å-2)
i
i SYCP1206-362 Rc = 10.3 Å
ii SYCP1358-783 Rc = 8.9 Å
ln IQ(Q)
Q2 (Å-2)
j
SYCP1112-783 Dmax = 900 Å Rg = 254 Å
SYCP1206-362 Dmax = 260 Å
SYCP1358-783 Dmax = 645 Å Rg = 196 Å
P(r)
Interatomic distance (Å)

3.2.16 Determining the orientation of helices within SYCP1 reveals its overall geometry

To understand the orientation of helices within SYCP1 is critical to learning the overall geometry of the SYCP1 fold. To this end, I employed numerous techniques as the conclusions drawn from such experiments would dictate how we envisaged SC structure and absolute certainty was required. Firstly, the previously described SEC-SAXS method was utilised, in which the dominant features of globular MBP-tags within the distance-distribution profiles of MBP-fusion proteins are utilised to determine the inter-MBP distance within an oligomer. For coiled-coil proteins, this can be used to infer the orientation of helices within the structural unit as short inter-MBP distances would indicate a parallel arrangement whereas long inter-MBP distances would indicate an anti-parallel arrangement.

I purified a series of N-terminal MBP-fusions of SYCP1$_{112\text{-}783}$, SYCP1$_{358\text{-}783}$ and SYCP1$_{206\text{-}362}$ by sequential amylose affinity chromatography, anion exchange chromatography and size-exclusion chromatography (Figure 3.2.19b). SEC-MALS was used to confirm that the MBP-tag did not disrupt the expected oligomer formation (Figure 3.2.19c,d). SEC-SAXS analysis revealed that they all demonstrate a parallel arrangement, with strong inter-MBP peaks present at short inter-atomic distances (~70 Å) (Figure 3.2.19e-h). These findings are corroborated by the similar analysis of GST-fusions of SYCP1$_{206\text{-}362}$ and SYCP1$_{358\text{-}783}$, demonstrating inter-GST peaks at short inter-atomic distances for SYCP1$_{206\text{-}362}$ and no inter-GST peaks for SYCP1$_{358\text{-}783}$ as inter- and intra-GST distances conflate due to the constitutively dimeric state of GST (Figure 3.2.20d).

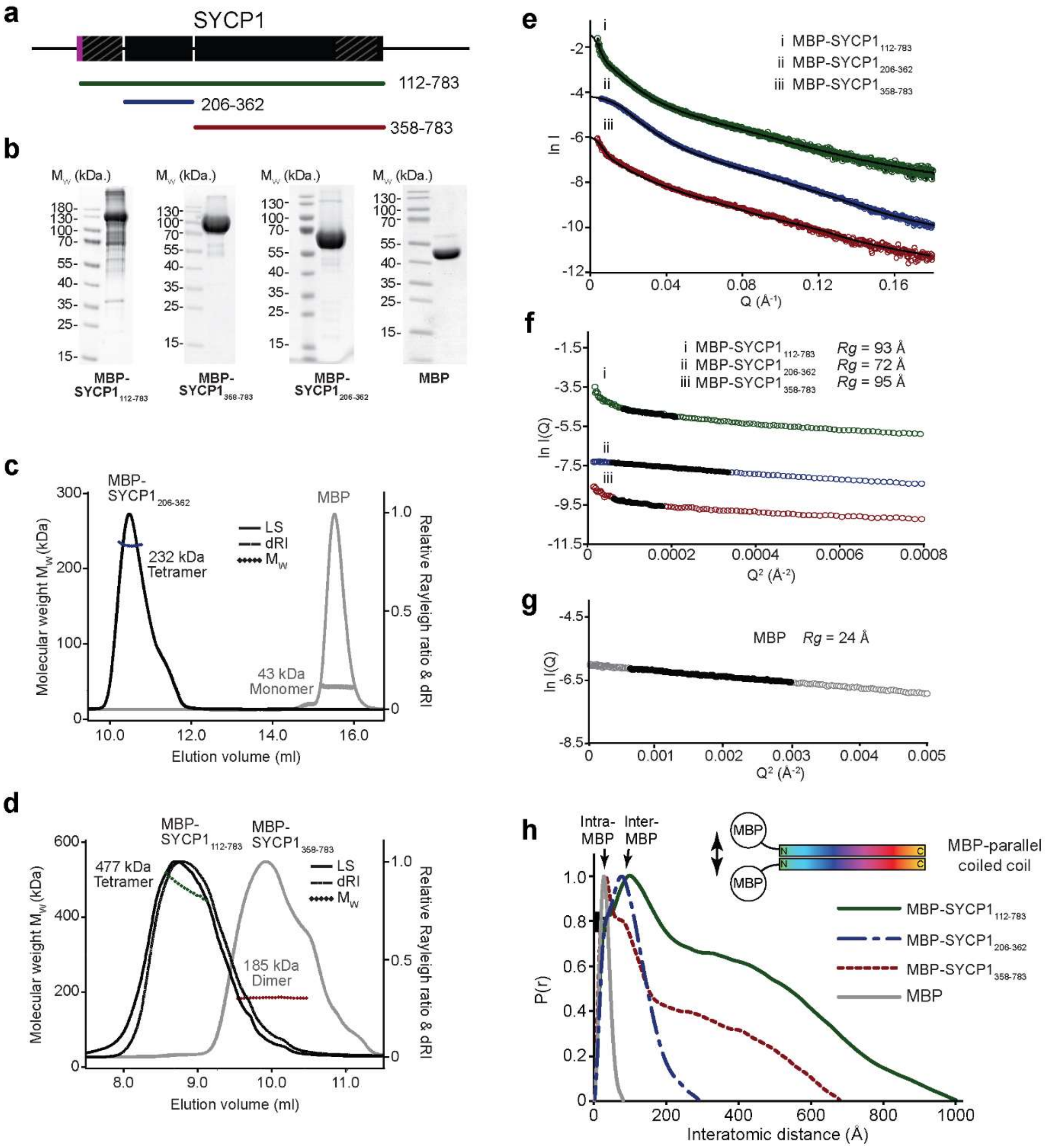

Figure 3.2.19| Determining helical orientation through SEC-SAXS analysis of MBP-fusions. a) Schematic of SYCP1 displaying analysed constructs. **b)** SDS-PAGE analysis of MBP-SYCP1$_{112-783}$, MBP-SYCP1$_{358-783}$, MBP-SYCP1$_{206-362}$, and MBP samples. **c-d)** SEC-MALS analysis of **c)** MBP-SYCP1$_{112-783}$ (theoretical tetramer – 499 kDa), MBP-SYCP1$_{358-783}$ (theoretical dimer – 191 kDa), **d)** MBP-SYCP1$_{206-362}$ (theoretical tetramer – 255 kDa), MBP (theoretical monomer – 45 kDa). Light scattering (LS) and differential refractive index (dRI) are plotted as solid and dashed lines, respectively, with molecular weights (Mw) shown as diamonds across elution peaks. **e)** Averaged small-angle X-ray scattering profile of MBP-SYCP1$_{112-783}$ (green), MBP-SYCP1$_{358-783}$ (red) and MBP-SYCP1$_{206-362}$ (blue) with the fits used for *P(r)* distribution shown as black lines. **f-g)** Guinier analysis to determine the radius of gyration (*Rg*) of **f)** MBP-SYCP1$_{112-783}$ (green), MBP-SYCP1$_{358-783}$ (red), MBP-SYCP1$_{206-362}$ (blue), and **g)** MBP (grey) with data points within the linear region used for analysis shown in black. *Q.Rg* value was < 1.3. **h)** Inter-atomic distance distribution profiles (*P(r)*) for MBP-SYCP1$_{112-783}$ (green), MBP-SYCP1$_{358-783}$ (red) and MBP-SYCP1$_{206-362}$ (blue) with intra- and inter-MBP distances indicated. Inset; schematised MBP-coiled-coil with arrow indicating short inter-MBP distance. SEC-SAXS analysis by Dr Orla Dunne.

The successful purification of coiled-coils fused at one terminus to constitutive oligomers is indicative of a parallel arrangement. The N-terminal fusion of the constitutive dimer GST to SYCP1$_{358\text{-}783}$ suggests parallel orientation of helices, in agreement with our previous findings that residues 640-783 adopt a parallel configuration (Figure 3.2.20a,e,f). To test the parallel orientation of all four chains within SYCP1$_{206\text{-}362}$, it was important to select a tetrameric unit which would be compatible with its sequence continuation as a parallel four-helical bundle. Therefore, the C-termini of the selected protein should emanate from the structure in close proximity to one another as to not disrupt oligomer formation. Through searching the Protein Data Bank, *E. coli* RecE (amino acid boundaries 606-866) was selected as its four C-termini are in close spatial proximity, separated by 18.1 – 25.6 Å (PDB 3H4R; Figure 3.2.20h). I cloned RecE$_{606\text{-}866}$ and RecE$_{606\text{-}866}$-SYCP1$_{206\text{-}362}$ connected by a 3 amino acid TGS-linker sequence into a pHAT4 vector for expression as N-terminal His$_6$-tagged proteins. Its successful purification, and tetrameric oligomeric status as confirmed by SEC-MALS is indicative of the parallel orientation of its four helical chains (Figure 3.2.20a,e,g).

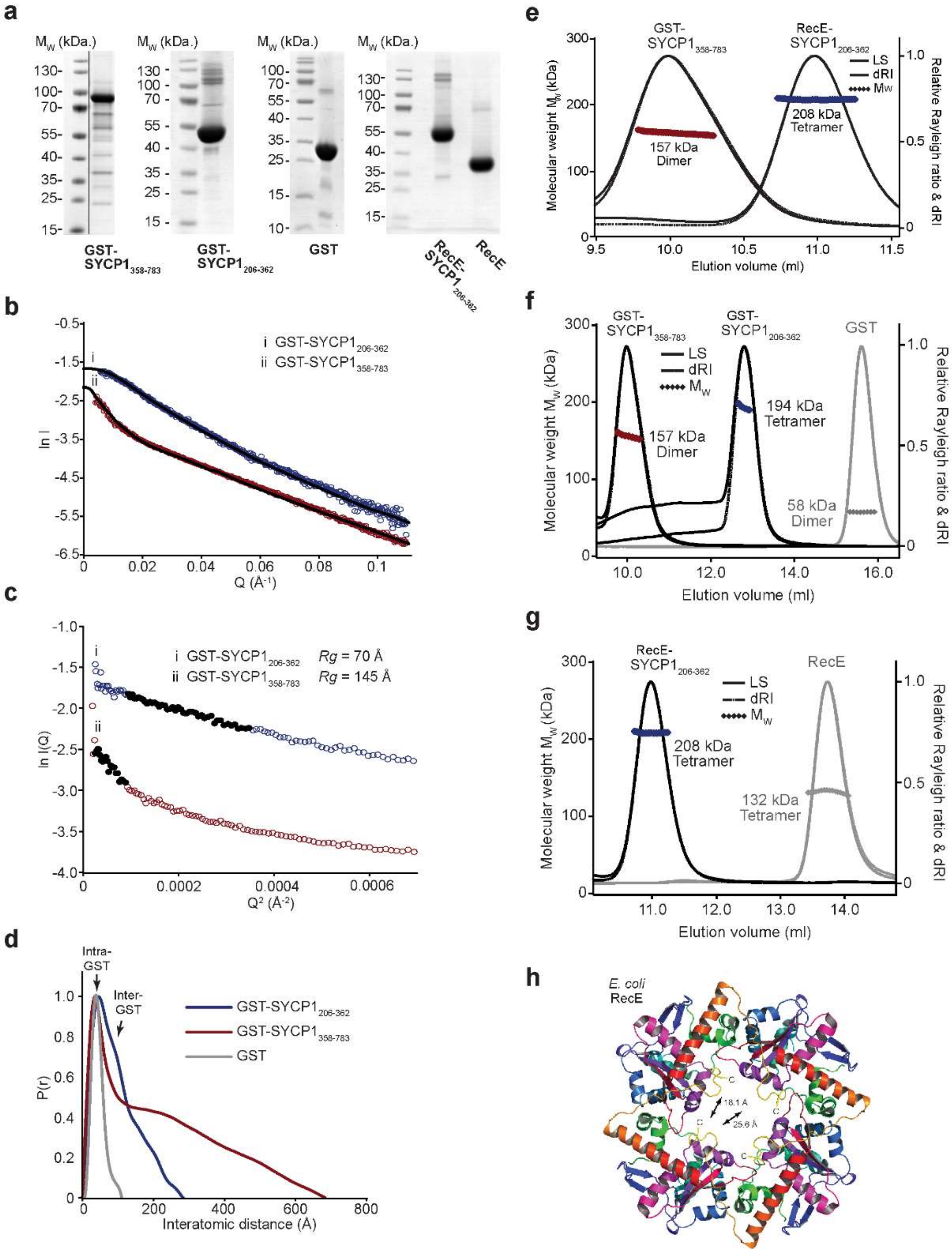

Figure 3.2.20| Orienting helices within SYCP1. a) SDS-PAGE analysis of analysed samples; GST-SYCP1$_{358-783}$, GST-SYCP1$_{206-362}$, GST, RecE-SYCP1$_{206-362}$ and RecE. **b)** Averaged small-angle X-ray scattering profile of GST-SYCP1$_{358-783}$ (red) and GST-SYCP1$_{206-362}$ (blue) with the fits used for *P(r)* distribution shown as black lines. **c)** Guinier analysis to determine the radius of gyration (*Rg*) of GST-SYCP1$_{358-783}$ (red) and GST-SYCP1$_{206-362}$ (blue) with data points within the linear region used for analysis shown in black. *Q.Rg* value was < 1.3. **d)** Inter-atomic distance distribution profiles (*P(r)*) for GST-SYCP1$_{358-783}$ (red) and GST-SYCP1$_{206-362}$ (blue) with intra- and inter-GST distances indicated. **e)** SEC-MALS analysis of GST-SYCP1$_{358-783}$ (theoretical dimer – 160 kDa) and RecE-SYCP1$_{206-362}$ (theoretical tetramer - 214 kDa). **f)** SEC-MALS analysis of GST-SYCP1$_{206-362}$ (theoretical tetramer – 195 kDa) alongside previously displayed GST-SYCP1$_{358-783}$ and GST (theoretical dimer – 59 kDa). **g)** SEC-MALS analysis of previously displayed RecE-SYCP1$_{206-362}$ alongside RecE (theoretical tetramer – 136 kDa). Light scattering (LS) and differential refractive index (dRI) are plotted as solid and dashed lines, respectively, with molecular weights (Mw) shown as diamonds across elution peaks. SEC-SAXS analysis by Dr Orla Dunne. **h)** The structure of the RecE tetramer (PDB 3H4R) indicating the distance between C-termini.

Thus, we may conclude that SYCP1 contains a tetrameric core, comprising four parallel α-helical chains. These stabilise SYCP1 in four-helical association at its N-terminus, forking into two long coiled-coil dimers which are capped at their C-terminus by a stable coiled-coil sequence from which unstructured C-termini emanate which possess DNA-binding capability (Figure 3.2.21a). I suggest that this comprises the obligate structure of SYCP1 and represents a building block from which SYCP1 assemblies might be built.

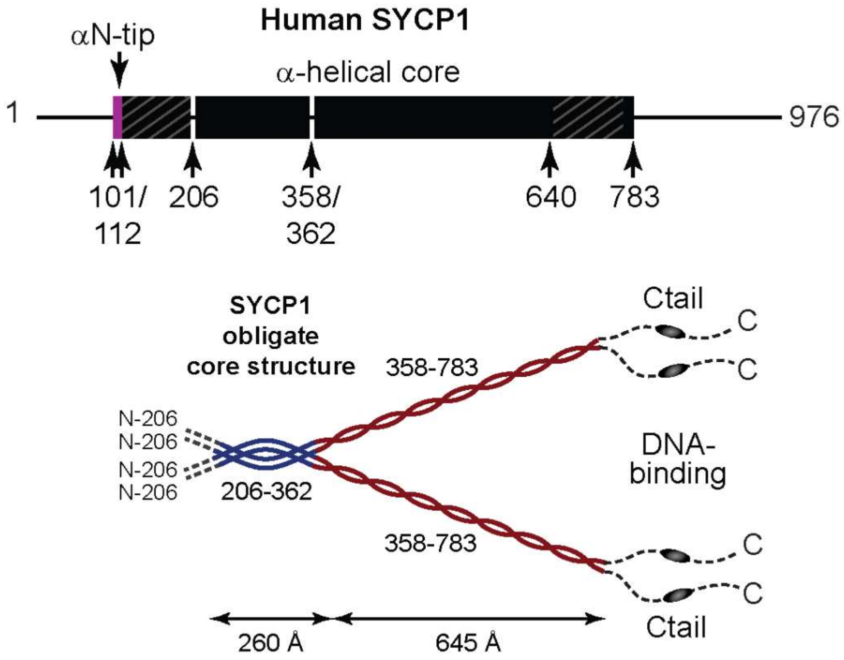
Human SYCP1
αN-tip
α-helical core
1
976
101/
112
206
358/
362
640
783
SYCP1
obligate
core structure
358-783
Ctail
C
C
N-206
N-206
N-206
N-206
206-362
DNA-
binding
358-783
C
C
Ctail
260 Å
645 Å

Figure 3.2.21| The molecular structure of obligate SYCP1. Schematic of the SYCP1 with key regions demarcated and residue boundaries indicated aligned with a molecular model for obligate SYCP1 which is stabilised as a parallel tetramer at its N-terminus which bifurcates as two long dimeric coiled-coils terminating with unstructured sequence capable of binding DNA. Schematic by Dr Owen Davies.

3.2.17 Initial recruitment of SYCP1 to the chromosome axis

I cloned, expressed and purified a series of N-terminal truncations of SYCP1 to assess the contribution of the SYCP1 oligomeric state to DNA binding. I initiated investigations through the attempted purification of residues 640-976 with an N-terminal His_6-tag. However, the construct exhibited major degradation with two distinct degradation products representing the removal of the majority of the unstructured C-terminus (Figure 3.2.22). I therefore opted for a rapid purification process to enrich for non-degraded material, utilising MBP-fusions and foregoing removal of the affinity tag, reasoning that it should not interfere with DNA binding.

SYCP1 residues 640-976 and 784-976 were cloned into pMAT11 vector for expression in *E. coli*. Purification was performed through subsequent amylose affinity chromatography and cation exchange chromatography using a HiTrap SP HP column (Figure 3.2.23a-c). Fractions were selected to enrich for non-degraded MBP-SYCP1. A summary of the purification for $\text{SYCP1}_{640\text{-}976}$ and $\text{MBP-SYCP1}_{784\text{-}976}$ and the purified samples for residues 101-976 and 358-976 are presented in Figure 3.2.23b-d. In keeping with our analysis of SYCP1 constructs lacking the unstructured C-terminus, SEC-MALS confirmed that $\text{MBP-SYCP1}_{101\text{-}976}$ forms megadalton assemblies, $\text{MBP-SYCP1}_{358\text{-}976}$ is dimeric (with an experimental molecular weight 206 kDa and theoretical dimeric molecular weight 234 kDa), and $\text{MBP-SYCP1}_{640\text{-}976}$ is dimeric (measured molecular weight = 144 kDa, theoretical dimeric molecular weight = 168 kDa) (Figure 3.2.23e-g). $\text{MBP-SYCP1}_{784\text{-}976}$ is monomeric in solution with a measured molecular weight matching its theoretical monomer (78 kDa and 67 kDa, respectively) (Figure 3.2.23h). The discrepancy in molecular weight is likely due to poor sample quality, i.e. a low analyte concentration resulting in a low signal to noise ratio, further compounded by aggregation levels. Cumulatively, these data demonstrate that the unstructured C-terminus does not contribute to the oligomeric state of SYCP1 and does not mediate higher-order assembly in solution.

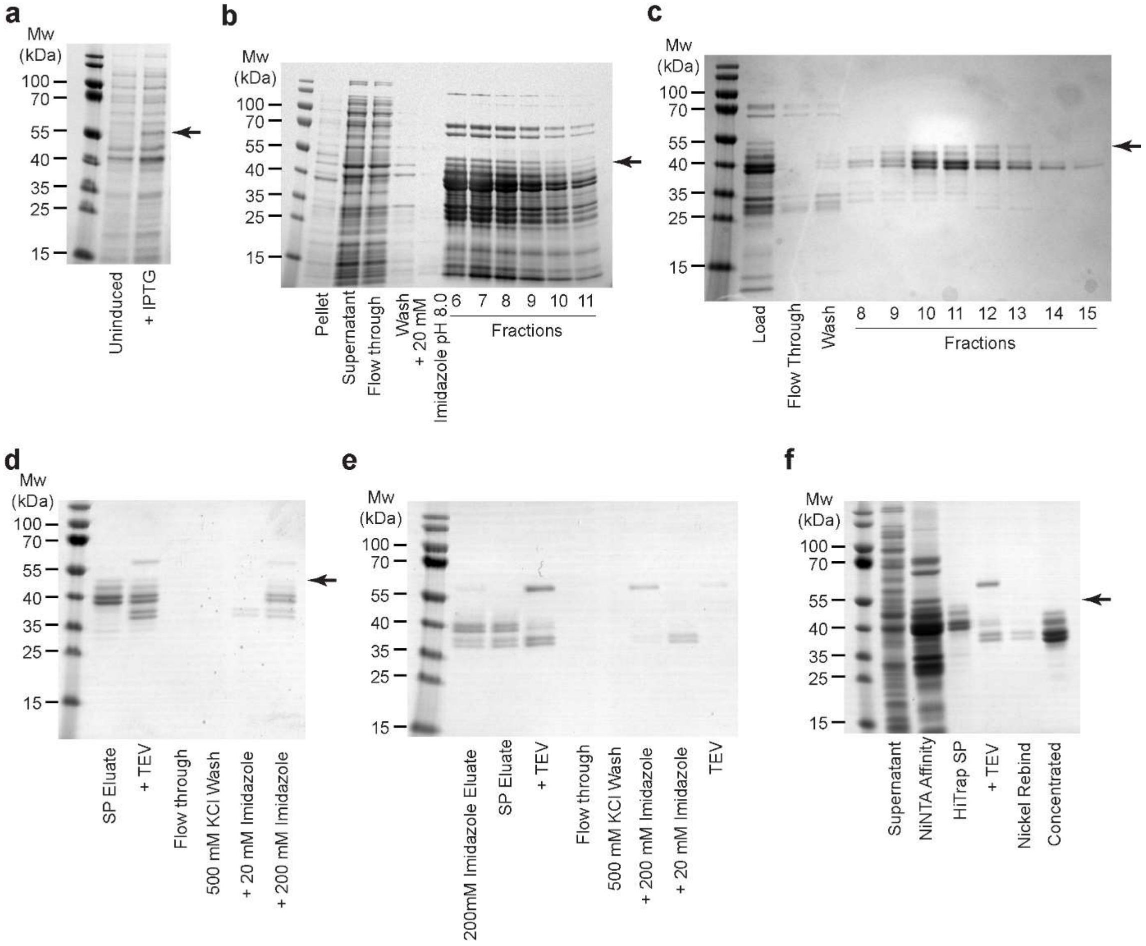
a
Mw (kDa)
100
70
55
40
35
25
15
Uninduced
+ IPTG
b
Mw (kDa)
100
70
55
40
35
25
15
Pellet
Supernatant
Flow through
Wash
+ 20 mM Imidazole pH 8.0
6
7
8
9
10
11
Fractions
c
Mw (kDa)
100
70
55
40
35
25
15
Load
Flow Through
Wash
8
9
10
11
12
13
14
15
Fractions
d
Mw (kDa)
100
70
55
40
35
25
15
SP Eluate
+ TEV
Flow through
500 mM KCl Wash
+ 20 mM Imidazole
+ 200 mM Imidazole
e
Mw (kDa)
100
70
55
40
35
25
15
200mM Imidazole Eluate
SP Eluate
+ TEV
Flow through
500 mM KCl Wash
+ 200 mM Imidazole
+ 20 mM Imidazole
TEV
f
Mw (kDa)
100
70
55
40
35
25
15
Supernatant
NiNTA Affinity
HiTrap SP
+ TEV
Nickel Rebind
Concentrated

Figure 3.2.22| The unstructured C-terminus of SYCP1 is highly unstable. a-f) SDS-PAGE analysis of samples as follows. Arrows are used to indicate the expected migration distance of His$_6$-SYCP1$_{640-976}$. a**)** Uninduced and IPTG induced *E. coli* cultures, the latter expressing His$_6$-SYCP1$_{640-976}$. **b)** Ni-NTA affinity chromatography. **c)** Ion exchange chromatography using HiTrap SP column. **d)** Attempted TEV cleavage and attempted purification by repeated Ni-NTA affinity demonstrating the inefficient cleavage of the affinity tag. **e)** The 200 mM imidazole elution from the previous step was re-purified through cation exchange chromatography using a HiTrap SP column and cleaved once again with an increased amount of TEV, resulting in an increased cleavage efficiency. TEV was removed from solution through repeated Ni-NTA affinity. The cleaved material eluted with 20 mM imidazole and was subsequently concentrated. **f)** SDS-PAGE analysis of samples summarising the purification of SYCP1$_{640-976}$.

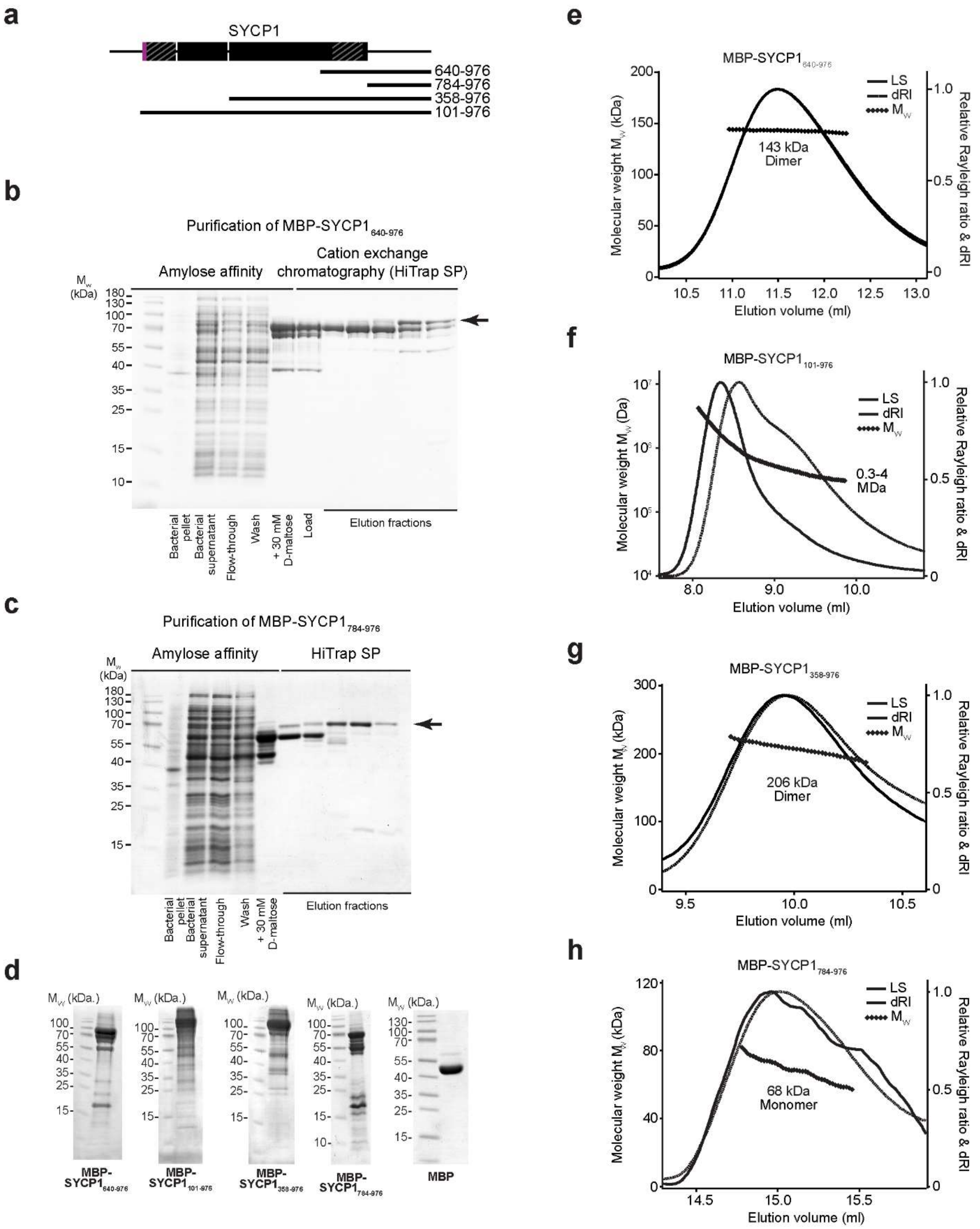

Figure 3.2.23| Purification and oligomeric state determination of MBP-SYCP1 constructs containing the unstructured C-terminus. a) Schematic of SYCP1 displaying analysed constructs. **b,c)** SDS-PAGE analysis of samples showing the purification of MBP-SYCP1$_{640-976}$ and MBP-SYCP1$_{784-976}$ by sequential amylose affinity and cation exchange chromatography. Arrows are used to indicate the expected migration distance of His$_6$-MBP-SYCP1 constructs. **d)** SDS-PAGE analysis of purified samples of MBP-SYCP1 constructs: 640-976, 101-976, 358-976, 784-976 and free MBP. **e-h)** SEC-MALS analysis with Light scattering (LS) and differential refractive index (dRI) are plotted as solid and dashed lines, respectively, with molecular weights (Mw) shown as diamonds across elution peaks. **e)** MBP-SYCP1$_{640-976}$ (theoretical dimer – 168 kDa). **f)** MBP-SYCP1$_{101-976}$. **g)** MBP-SYCP1$_{358-976}$ (theoretical dimer – 235 kDa). **h)** MBP-SYCP1$_{784-976}$ (theoretical monomer – 67 kDa).

I performed EMSA analysis of the purified samples to determine the contribution of the SYCP1 oligomeric state to DNA binding mode and affinity. I found that removal of the unstructured SYCP1 N-terminus did not overtly affect DNA binding, with MBP-SYCP$_{101-976}$, MBP-SYCP$_{358-976}$, and MBP-SYCP$_{640-976}$ all forming stable protein-DNA complexes at 2 – 2.5 µM protein with 25 µM dsDNA per base pair, implying a footprint of ~10 base pairs (Figure 3.2.25a), similar to that of full-length SYCP1. However, deletion of oligomer stabilising sequence of the wider molecule diminishes DNA binding, with MBP-SYCP1$_{784-976}$ demonstrating less stable DNA association (Figure 3.2.25a). Slightly enhanced DNA binding of MBP-SYCP1$_{101-976}$ and MBP-SYCP1$_{358-976}$ is observed over MBP-SYCP1$_{640-976}$ suggesting that the wider molecule may play some role in stabilising C-terminally mediated associations (Figure 3.2.25a). In agreement with previous findings, deletion of the SYCP1 unstructured C-terminus ablates DNA binding, with SYCP$_{101-783}$, SYCP1$_{358-783}$, and SYCP1$_{640-783}$ not interacting with DNA (Figure 3.2.25b,c) These results demonstrate that the SYCP1 unstructured C-terminus contains obligate DNA binding sequences, the binding of which is enhanced by the wider SYCP1 structure, likely reinforcing associations in a cooperative manner. This could provide the means by which the SYCP1 C-terminus is initially recruited to the chromosome axis (Figure 3.2.25f). Interestingly, electron microscopy reveals that MBP-SYCP1$_{640-976}$ forms smooth fibres with a thickness of approximately 10 nm when in complex with plasmid DNA. However, MBP-SYCP1$_{358-976}$ exhibits a more branched appearance possibly rod-like SYCP1 molecules protruding from a protein-DNA, lateral element-like, core structure (Figure 3.2.25d).

During the formation of the mammalian SC, the chromosome axis is initially organised and compacted by the recruitment of lateral element proteins SYCP2 and SYCP3 (Schalk *et al.*, 1998; West *et al.*, 2019). SYCP3 forms recursive striated structures *in vivo* and *in vitro* (Yuan *et al.*, 1998; Syrjanen *et al.*, 2014). These structures appear compatible with DNA binding and their intrinsic assembly required for the compaction of DNA (Syrjanen *et al.*, 2017). I wondered whether, by EM, I might be able to observe direct binding of SYCP1 molecules to SYCP3-DNA complexes. Interestingly, the SYCP3-DNA structures observed in the presence of SYCP1 do develop a wider appearance with what appear to be proteinaceous surface plaques (Figure 3.2.25e). However, I could not discern individual transverse filaments and antibody staining against SYCP1 would be required to confirm its recruitment. SYCP3 was purified as demonstrated in Figure 3.2.24.

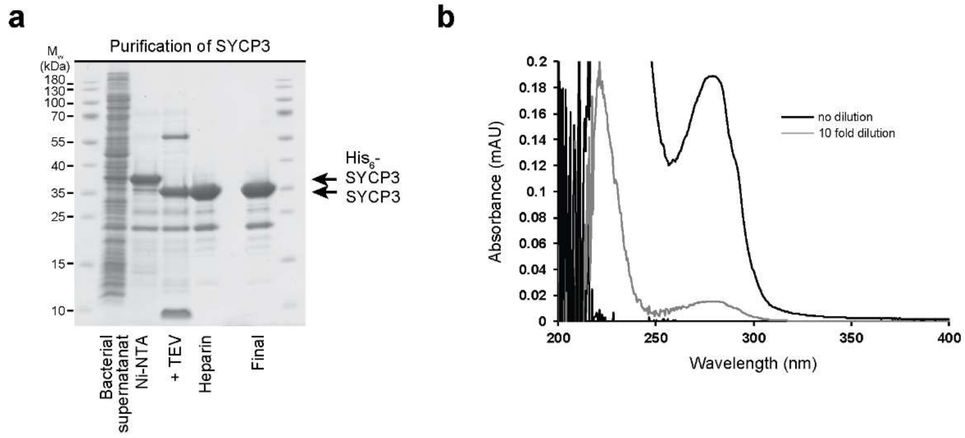

Figure 3.2.24| Purification of SYCP3. a) SDS-PAGE analysis of samples summarising the purification of SYCP3. **b)** UV spectrum for SYCP3.

From these findings, I suggest a model for the initial recruitment of SYCP1 to the chromosome through direct DNA binding interactions (Figure 3.2.25f). I next sought to characterise how SYCP1 molecules might assemble within the SC. Our first course of action was to investigate further the role of the SYCP1 αN-tip (the 11 amino acids which proved essential in the formation of large assemblies *in vitro*). Given the high conservation of this region, and its central localisation within the SC, it is possible that this region might mediate either homo- or heterotypic interactions to either connect bi-orientated SYCP1 molecules or to connect them, via their N-termini, to the central element, respectively.

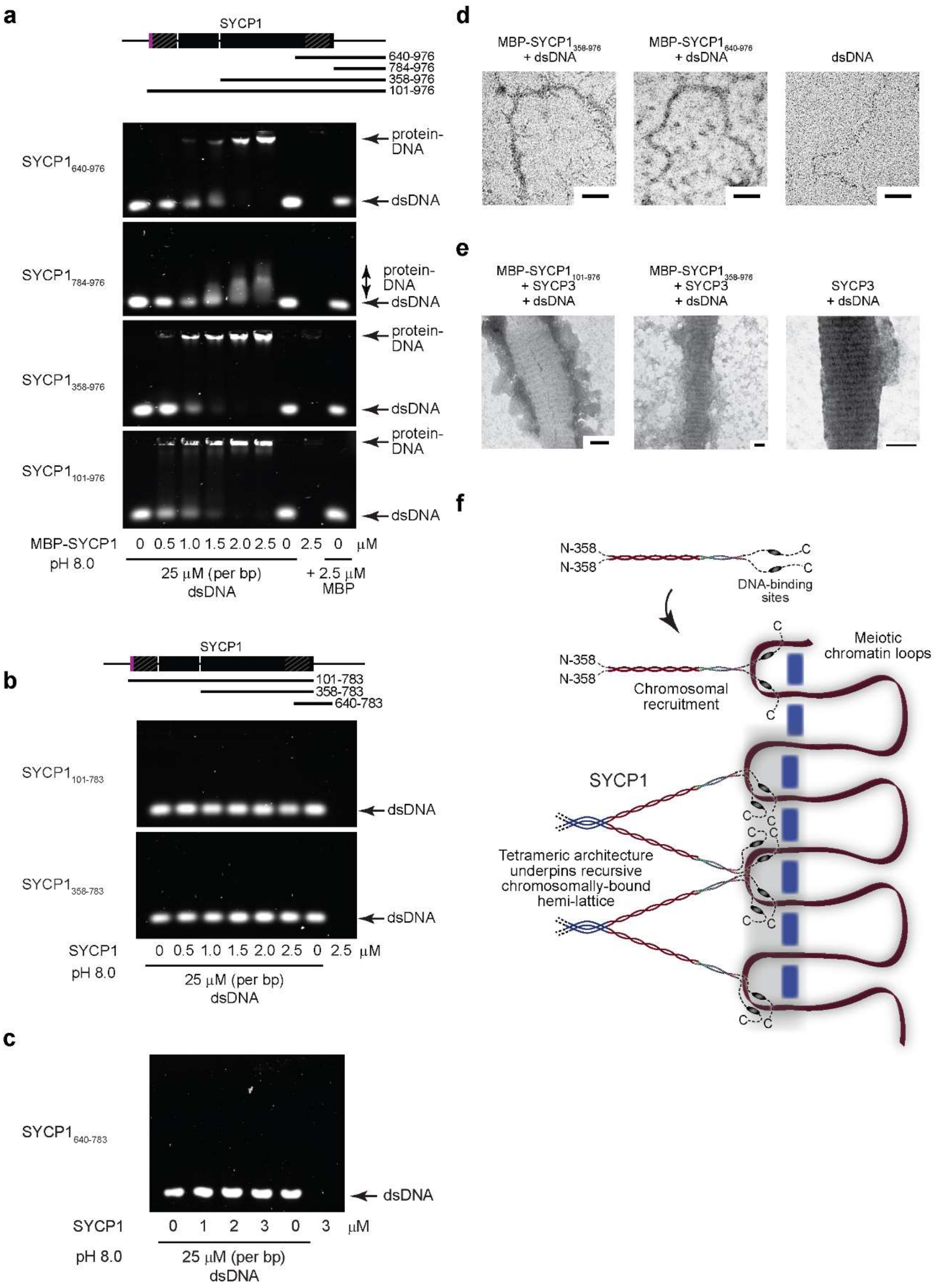

Figure 3.2.25| A model for the chromosomal recruitment and assembly of SYCP1. a) Schematic of SYCP1 displaying analysed constructs and EMSA analysis of indicated MBP-SYCP1 constructs. **b,c)** EMSA analysis of the corresponding SYCP1 constructs without the unstructured basic constructs. **d,e)** Electron microscopy analysis of **d)** linear dsDNA incubated with MBP-SYCP1$_{640\text{-}976}$, MBP-SYCP1$_{358\text{-}976}$ or alone, and **e)** SYCP3 incubated with linear dsDNA in the presence and absence of MBP-SYCP1$_{101\text{-}976}$ and MBP-SYCP1$_{358\text{-}976}$. Scale bars = 50 nm **f)** A model for the chromosomal recruitment of SYCP1 via obligate DNA binding sequences within the unstructured basic C-terminus.

Part II

SYCP1 architecture and N-terminal self-association provide the basis for SC midline assembly

3.3.1 SYCP1 N-terminal self-assembly is mediated by the αN-tip

The self-assembly of the SYCP1 to form megadalton species *in vitro* was dependent upon the αN-tip (residues 101-111) which caps of the N-terminus of the SYCP1 helical core (Figures 3.2.10, 3.2.11). The sequence is part of a highly conserved N-terminal region (residues 101-206) which directly precedes the unit which stabilised tetramerization (residues 206-362). I sought to understand the way in which these residues mediate higher order assembly of SYCP1 molecules *in vitro,* with a particular focus on the role of the αN-tip. A significant portion of the work in this chapter stems from investigations performed by Matthew Ratcliff and any of the data he generated presented herein will be acknowledged in the respective figure legends.

I expressed and purified three sequences corresponding to the highly conserved N-terminal region: residues 101-206, 101-175 and 1-175 (Figure 3.3.1a-d). The high pI of these sequences meant that they could be purified effectively through cation exchange chromatography using the HiTrap SP column. By SDS-PAGE, a faint gel dimer is visible for SYCP1$_{101\text{-}175}$ and SYCP1$_{101\text{-}206}$ and a more intense gel dimer for SYCP1$_{1\text{-}175}$. SYCP1$_{101\text{-}206}$ and SYCP1$_{1\text{-}175}$ each have 2 cysteines within their sequences raising the possibility that these may represent minor oxidation products. However, SYCP1$_{101\text{-}175}$ has no cysteines, suggesting that these constructs may have capacity to form a dimer. By SEC-MALS, however, the constructs are found to be monomeric (Figure 3.3.1g). Further, analysis by circular dichroism reveals that these sequences are relatively unstructured and fold in a non-cooperative manner (Figure 3.2.1e,f). SYCP1$_{101\text{-}175}$ and SYCP1$_{101\text{-}206}$ are approximately 50 % unfolded, whilst SYCP1$_{1\text{-}175}$, which contains the full N-terminal tail sequence, which is predicted to be unstructured, is 75 % unstructured (Figure 3.2.1e). Despite this, I opted to attempt crystallisation.

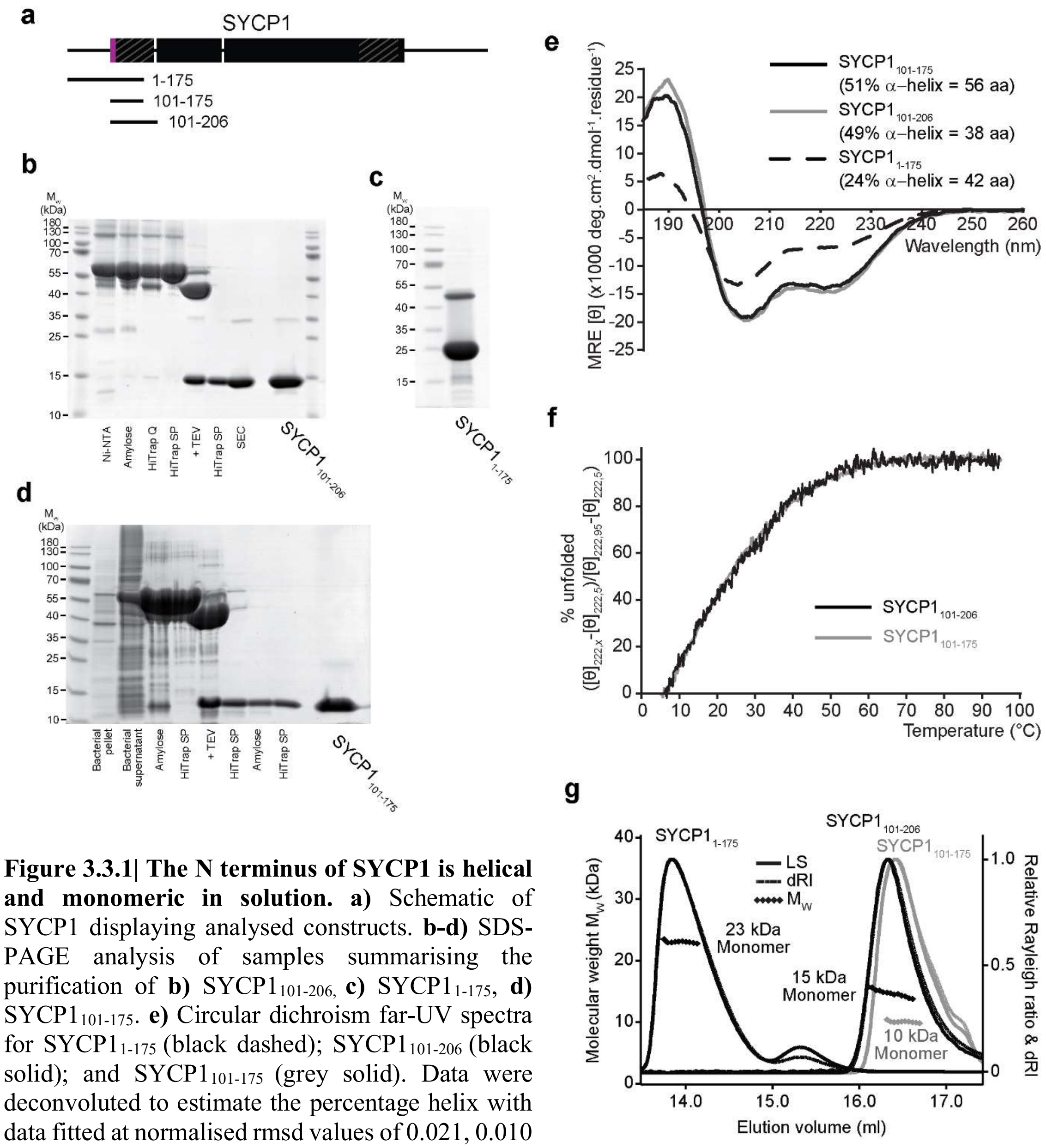

Figure 3.3.1| The N terminus of SYCP1 is helical and monomeric in solution. a) Schematic of SYCP1 displaying analysed constructs. **b-d)** SDS-PAGE analysis of samples summarising the purification of **b)** SYCP1$_{101-206}$, **c)** SYCP1$_{1-175}$, **d)** SYCP1$_{101-175}$. **e)** Circular dichroism far-UV spectra for SYCP1$_{1-175}$ (black dashed); SYCP1$_{101-206}$ (black solid); and SYCP1$_{101-175}$ (grey solid). Data were deconvoluted to estimate the percentage helix with data fitted at normalised rmsd values of 0.021, 0.010 and 0.005, respectively. **f)** Thermal denaturation of SYCP1$_{101-206}$ and SYCP1$_{101-175}$ were recorded as percentage unfolded based on the helical signal at 222 nm. Non-cooperative unfolding was observed with melting temperatures estimated at 24 and 23 ˚C, respectively. **g)** SEC-MALS analysis of SYCP$_{1-175}$, SYCP1$_{101-206}$ and SYCP1$_{101-175}$ reveals monomeric states in solution (theoretical monomers – 20, 13, 9 kDa, respectively). Light scattering (LS) and differential refractive index (dRI) are plotted as solid and dashed lines, respectively, with molecular weights (Mw) shown as diamonds across elution peaks. SYCP1$_{101-175}$ and SYCP1$_{1-175}$ purification and analysis by Matthew Ratcliff.

3.3.2 Crystallisation and data collection of SYCP1$_{101\text{-}206}$ and SYCP1$_{101\text{-}175}$

No crystals were obtained for SYCP1$_{101\text{-}206}$ at room temperature, though it crystallised in multiple MPD-containing conditions at 4 ˚C including **1)** 200 mM ammonium fluoride, 40 % (v/v) MPD and **2)** 100 mM MES pH 6.0, 40 % (v/v) MPD (Figure 3.3.2a, Table 2.2.). 40 % (v/v) MPD proved sufficient to act as a cryo-protectant during cryo-cooling in liquid nitrogen. X-ray diffraction data were collected to 2 Å (Figure 3.2.2b). The determined unit cell had dimensions of a = 65.67 Å, b = 37.31 Å, c = 108.52 Å, α = 90°, β = 106.66°, γ = 90° and possessed I2 symmetry. Calculation of the Matthew's coefficient predicted the presence of two chains of SYCP1$_{101\text{-}206}$ in the asymmetric unit.

Matthew Ratcliff performed crystallisation screening for SYCP1$_{101\text{-}175}$ and obtained crystals in 140 mM NaCl, 70 mM Na/K phosphate pH 6.2, 35 % (v/v) PEG200 at 20 ˚C (Figure 3.2.2c). Dr Owen Davies had found that, in his experience with SYCP3 crystals, that crystals soaked in a solution containing sodium iodide actually diffracted better than native crystals for some unbeknownst reason (possibly relating to reduced B-factors of sidechains interacting with iodide ions, or minor dehydration effects during the handling process) so we tried that. SYCP1$_{101\text{-}175}$ crystals were soaked in crystallisation solution containing 40 % PEG200 and 100 mM NaI prior to cryo-cooling. X-ray diffraction data were collected at the longer wavelength of 1.9074 Å in order to observe anomalous scattering by iodide. The utilised wavelength is not at the absorption edge for iodine, but high energy remote, with a significant difference between f' and f'' and so should still yield observable anomalous scattering. A dataset at 1.91 Å was collected and processed by Dr Owen Davies as described in the Methods section 2.1.17. The crystals possessed I222 symmetry with unit cell dimensions a = 28.64 Å, b = 39.38 Å, c = 165.77 Å, α = 90°, β = 90°, γ = 90°. For these crystals, the asymmetric unit contained a single SYCP1$_{101\text{-}175}$ chain.

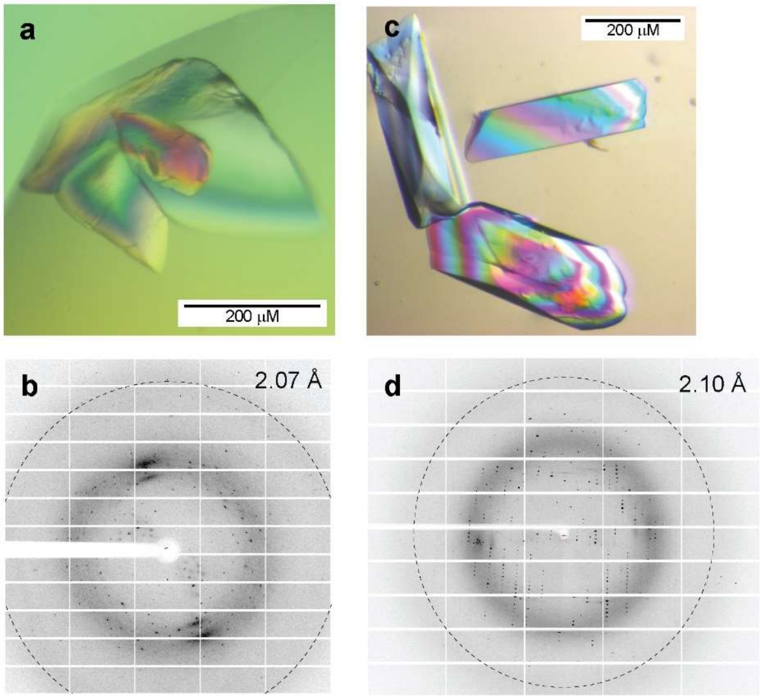

Figure 3.3.2| Crystallisation and X-ray diffraction data collection for SYCP1$_{101-206}$ and SYCP1$_{101-175}$. a) SYCP1$_{101-206}$ protein crystals grown in 200 mM ammonium fluoride, 40 % (v/v) MPD. **b)** X-ray diffraction image for SYCP1$_{101-206}$. The circle indicates the 2.1 Å resolution cut-off. **c)** SYCP1$_{101-175}$ protein crystal grown in 140 mM NaCl, 70 mM Na/K phosphate pH 6.2, 35 % (v/v) PEG200 by Matthew Ratcliff. **d)** X-ray diffraction image for SYCP1$_{101-175}$. The circle indicates the 2.1 Å resolution cut-off. SYCP1$_{101-175}$ crystallised by Matthew Ratcliff.

3.3.3 Solution of SYCP1$_{101-175}$ crystal structure

SYCP1$_{101-175}$ was the first of the two constructs to be crystallised. The structure was solved by Dr Owen Davies; the method he used to solve the structure is described in full in the Methods section 2.1.17-18. Briefly, anomalous signal from bound iodide was used in single wavelength anomalous diffraction (SAD) experiments to solve a five “supposed”-iodide sub-structure within the asymmetric unit. The resulting phase estimates were used and improved through cycling rounds of model building and refinement to produce a complete model of the structure. The crystal structure, refined against a dataset at 1.91 Å, revealed that SYCP1$_{101-175}$ formed a single, continuous helix with residues 101-173 visible within the electron density map (Figure 3.3.3a; crystallographic statistics can be found in Table 3.1). Based upon anomalous difference maps, iodide was found to be bound at two sites, one at the N-terminal tip of the construct and another buried next to R145. Additionally, bound proximal to the N-terminus is a single PEG (triethylene glycol, in this case) molecule. Imposition of symmetry finds that two

SYCP1$_{101-175}$ chains wrap around each other in coiled-coil association, with an identifiable heptad repeat from L102 to N169 (Figure 3.3.3b). A stammer disrupts the heptad repeat continuity between residues 119-130. Whilst the central region provides close association of 7 heptad repeats, the N- and C-terminal ends of the coiled-coil do not remain in coiled-coil association, splaying apart with an increase in inter-α-carbon (inter-Cα) distance between heptad residues from 6.3 Å at residue I148 (approximating the average inter-Cα distance for GCN4 (6.0 Å), a classic leucine-zipper coiled-coil, to over 10 Å at each termini (Figure 3.3.3b,c). A major increase in inter-Cα is introduced by a wedge-like structure formed by I116 and W119 which act to force apart the coiled-coils (Figure 3.3.3d). The presence of glutamine at position 144 is stabilised through homotypic inter-chain salt bridges, formed as these residues occupy this place in two rotamer positions with 50 % occupancy each (Figure 3.3.4a). K130 is also stabilised by an inter-chain salt bridge, electrostatically interacting with the hydroxyl group of E131 (Figure 3.3.4b).

Data collection for SYCP1$_{101-175}$ (merged datasets: S1N-5)		
Space group	I 2 2 2	
Cell dimensions		
a, *b*, *c* (Å)	28.64, 39.38, 165.77	
α, *β*, *γ* (°)	90.00, 90.00, 90.00	
	Overall	Outer Shell
Low resolution limit (Å)	41.44	1.91
High resolution limit (Å)	1.95	1.91
R_{merge} (all I+ & I-)	0.028	0.678
R_{pim} (all I+ & I-)	0.017	0.541
$I / \sigma I$	27.9	1.8
$CC_{1/2}$	1.000	0.839
Completeness (%)	99.3	92.1
Multiplicity	5.9	3.7
Refinement		
Resolution (Å)	41.44 – 1.91	
UCLA anisotropy (Å)	1.9, 2.0, 2.1	
Number of reflections	6754	
R_{work} / R_{free}	0.2272 / 0.2392	
Number of atoms	677	
Protein	633	
Ligand/ion	12	
Water	32	
B-factors	58.37	
Protein	57.72	
Ligand/ion	83.91	
Water	61.74	
R.m.s deviations		
Bond lengths (Å)	0.009	
Bond angles (°)	1.020	

Table 3.1| X-ray crystallographic statistics for SYCP1$_{101-175}$. Data processed by Dr Owen Davies

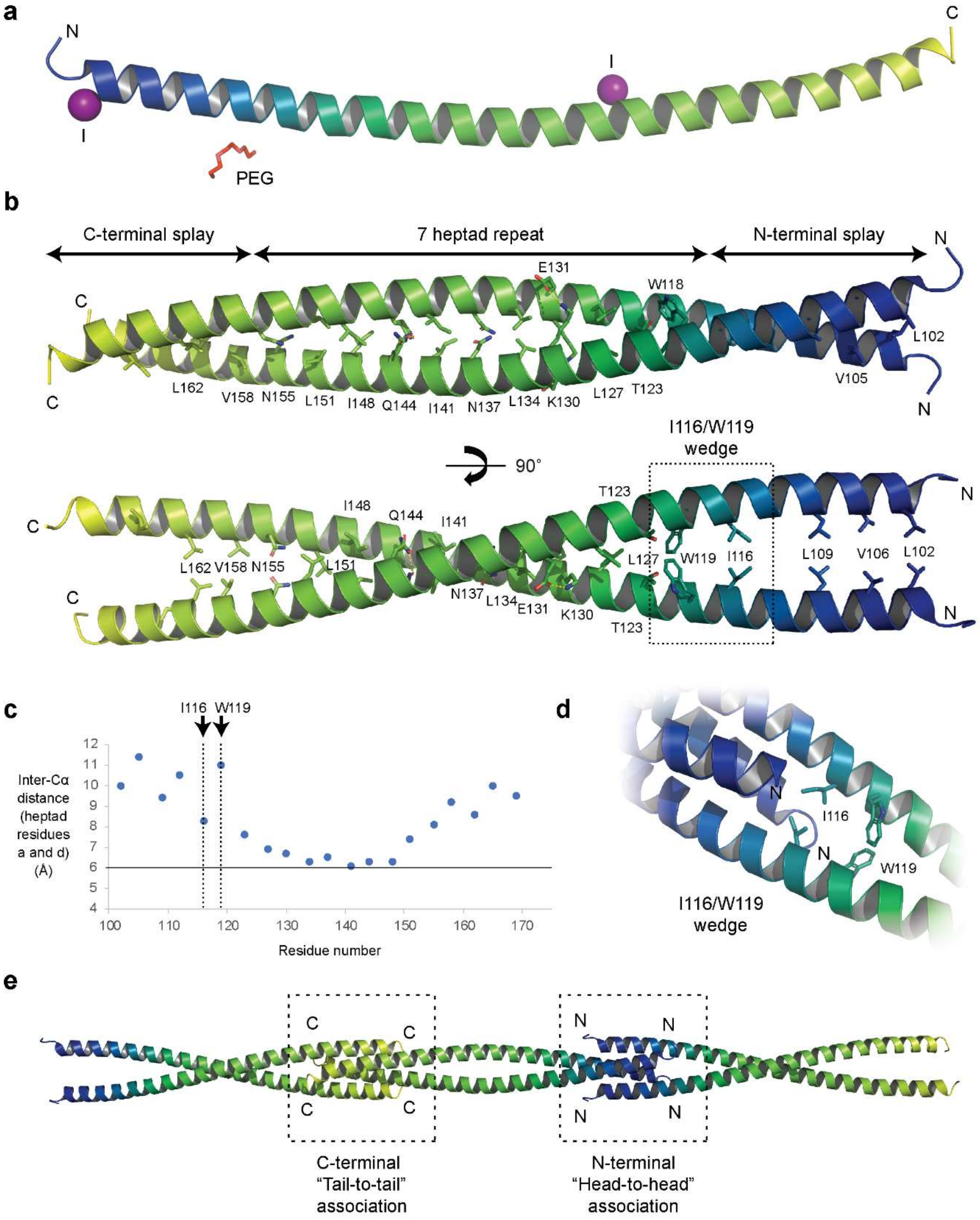
a
N
C
I
I
PEG
b
C-terminal splay
7 heptad repeat
N-terminal splay
E131
W118
C
C
N
N
L102
V105
L162
V158
N155
L151
I148
Q144
I141
N137
L134
K130
L127
T123
I116/W119
wedge
90°
T123
I148
Q144
I141
C
C
L162
V158
N155
L151
N137
L134
E131
K130
T123
L127
W119
I116
L109
V106
L102
N
N
c
I116
W119
Inter-Cα distance (heptad residues a and d) (Å)
12
11
10
9
8
7
6
5
4
100
110
120
130
140
150
160
170
Residue number
d
N
N
I116
W119
I116/W119
wedge
e
C
C
C
C
N
N
N
N
C-terminal "Tail-to-tail" association
N-terminal "Head-to-head" association

Figure 3.3.3| The crystal structure of SYCP1$_{101\text{-}175}$. a) The asymmetric unit contains a single chain of SYCP1$_{101\text{-}175}$. It is entirely helical. Two iodides and a PEG molecule are indicated. **b)** A two-fold symmetry operator creates a parallel coiled-coil in which 7 heptad repeats stabilise the fold through holes in knobs hydrophobic associations. The N- and C-terminal ends splay apart such that terminal residues are not in direct contact. **c)** Graph plotting inter-Cα distances between heptad residues across the crystal structure. Positions of I116 and W119 are indicated. Horizontal line at 6.0 Å represents average inter-Cα distance for GCN4 (6 Å; PDB 2ZTA). **d)** I116/W116 form a wedge, forcing the coiled-coil chains apart. **e)** The crystal lattice is formed of recursive head-to-head and tail-to-tail associations of parallel coiled-coils, indicated by dashed boxes. These associations explain and stabilise the splaying at the termini of the coiled-coils.

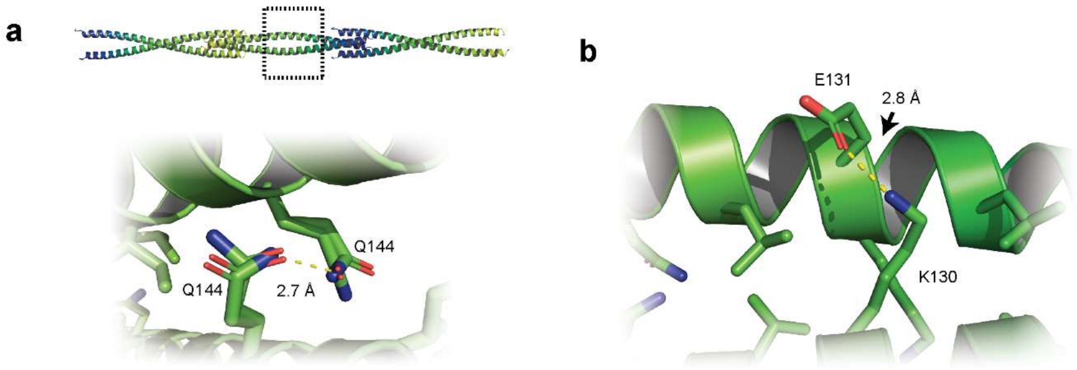

Figure 3.3.4| Coiled-coil stabilising associations between SYCP1$_{101-175}$ chains. a,b) Salt bridges between residues within heptad repeat positions allow their position within the coiled-coil interaction: **a)** Two conformations of Q144 at heptad position d (50 % occupancy) allows it to hydrogen bond with itself (distance, 2.7 Å) and **b)** K130 fulfils position d within heptad repeat and rather than forming hydrophobic associations it electrostatically interacts with E131 (distance, 2.8 Å).

3.3.4 Differentiating physiologically relevant interactions and crystallographic artefacts within the crystal lattice

The N- and C-terminal splaying of the coiled-coil is enforced by symmetry-related copies of the coiled-coil by forming head-to-head and tail-to-tail self-associations, creating a continuous rope-like structure (Figure 3.3.3e). The N-terminal head-to-head association was immediately striking as it is mediated by the association of bi-orientated parallel coiled-coils via the 11 residues of the αN-tip, implicated in the assembly of SYCP1 molecules. This interface forms a four-helical bundle stabilised with a hydrophobic core of V105 and L109, assisted by midline and lateral interfaces (Figure 3.3.5a-c). Heptad residues V105 and E112 contribute to the midline interface whilst L102 and L109 stabilise the lateral interface. Flanking aromatic stacking associations of tyrosine residues Y106 and Y110 contribute to the lateral interface (Figure 3.3.5b,c).

Within the crystal lattice, each dimeric coiled-coil creates both N- and C-terminal, interlocking, head-to-head/tail-to-tail contacts (Figure 3.3.3e). The N-terminal contacts are mediated by the 11 amino acids of the αN-tip and provided a potential way in which SYCP1 molecules might self-associate within the SC midline.

The N-terminal head-to-head association is mediated by the residues of the αN-tip (residues 101-111) which were shown to be critical in mediating megadalton assembly of SYCP1$_{101-783}$. Within the interface heptad residues L102, V105, L109, and E112 contribute alternately to lateral and midline interfaces between anti-parallel chains with the lateral interface further stabilised by the aromatic stacking of Y106 and Y110 (Figure 3.3.5a-c). Residues V105 and L109 further contribute by forming a hydrophobic core (Figure 3.3.5a). Given their importance in the assembly of SYCP1$_{101-783}$, we sought to test whether this crystallographic interface is responsible for *in vitro* assembly.

Purification of SYCP1$_{101-362}$ (which includes both SYCP1$_{206-362}$ (tetrameric) and the crystallised construct, SYCP1$_{101-175}$ (shown to undergo head-to-head associations)) and its analysis by SEC-MALS reveals the reconstitution of higher-order self-assembly as previously observed for the SYCP1$_{101-783}$ (Figure 3.3.6a-c). This propensity for assembly is retained, though slightly diminished, in the presence of the unstructured N-terminus (SYCP1$_{1-362}$; Figure 3.3.6d). As previously shown, the assembly of SYCP1$_{112-362}$ is blocked by removal of the αN-tip. Similarly, mutation of hydrophobic core residues V105 and L109 to glutamate blocks assembly suggesting that the association formed within the crystal structure also mediates assembly of SYCP1$_{101-362}$ in solution (Figure 3.3.6c).

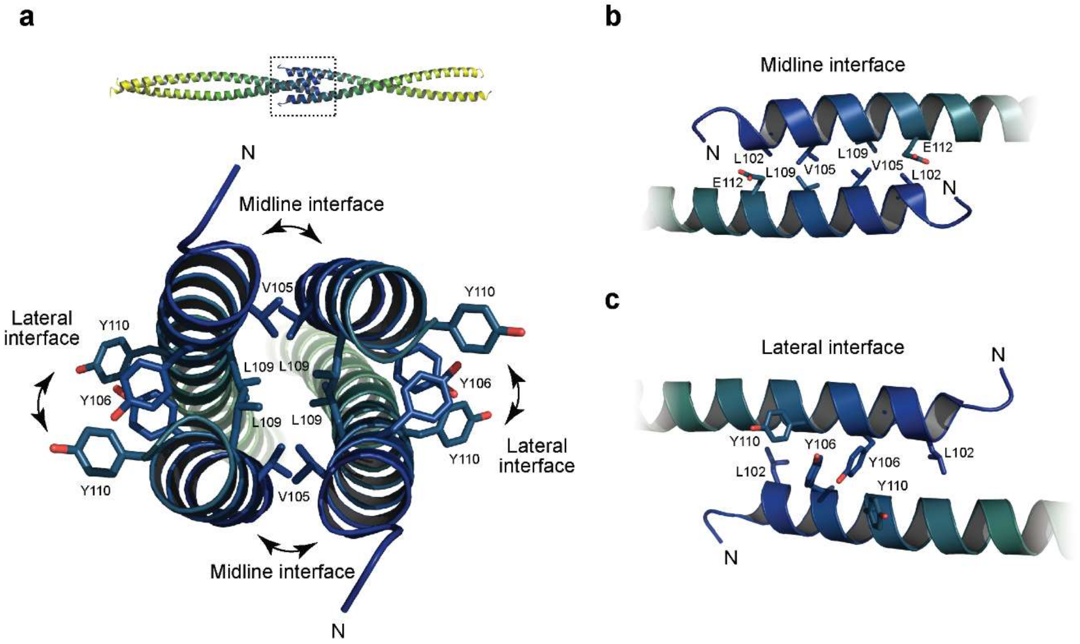
a
N
Midline interface
V105
Y110
Lateral interface
Y110
L109 L109
Y106
Y106
L109 L109
Y110
Lateral interface
Y110
V105
Midline interface
N
b
Midline interface
N
L102
L109
E112
E112
L109
V105
V105
L102
N
c
Lateral interface
N
Y110
Y106
L102
Y106
L102
Y110
N

Figure 3.3.5| N-terminal contacts within the SYCP1$_{101-175}$ crystal lattice. a) N-terminal head-to-head interface constitutes a four-helical bundle stabilised with a hydrophobic core of V105 and L109 and midline and lateral interfaces. **b)** The midline interface is stabilised through V105 and E112. **c)** Residues L102 and L109 contribute to the lateral interface whilst aromatic stacking of flanking Y106 and Y110 stabilises the interface.

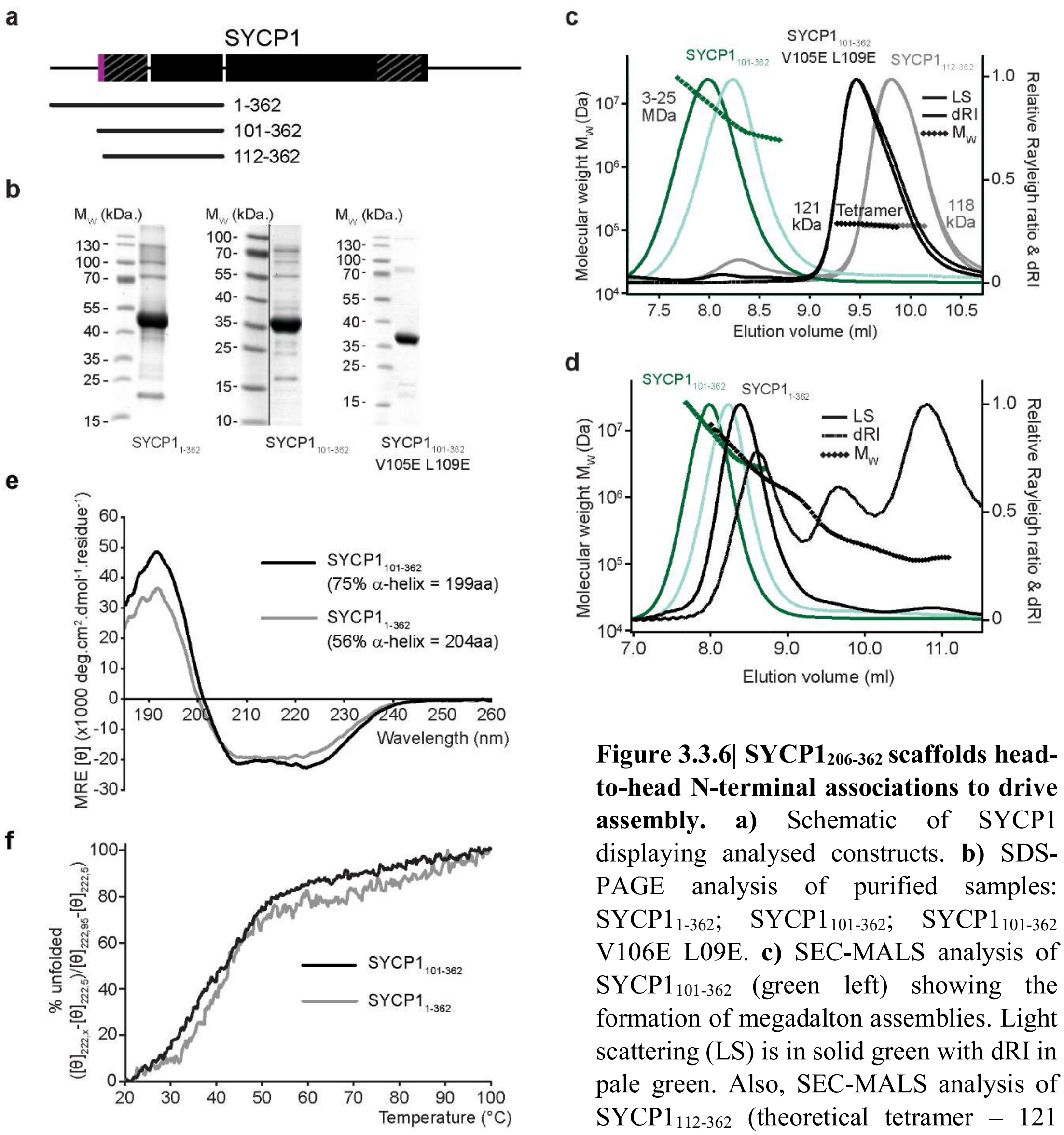

Figure 3.3.6| SYCP1$_{206\text{-}362}$ scaffolds head-to-head N-terminal associations to drive assembly. **a)** Schematic of SYCP1 displaying analysed constructs. **b)** SDS-PAGE analysis of purified samples: SYCP1$_{1\text{-}362}$; SYCP1$_{101\text{-}362}$; SYCP1$_{101\text{-}362}$ V106E L09E. **c)** SEC-MALS analysis of SYCP1$_{101\text{-}362}$ (green left) showing the formation of megadalton assemblies. Light scattering (LS) is in solid green with dRI in pale green. Also, SEC-MALS analysis of SYCP1$_{112\text{-}362}$ (theoretical tetramer – 121 kDa) and SYCP1$_{101\text{-}362}$ V106E L09E (grey; theoretical tetramer – 126 kDa). **d)** SEC-MALS analysis of SYCP1$_{1\text{-}362}$ (black) showing the formation of megadalton assemblies, similar to SYCP1$_{101\text{-}362}$ (green). Light scattering (LS) and differential refractive index (dRI) are plotted as solid and dashed lines, respectively, with molecular weights (Mw) shown as diamonds across elution peaks. **e)** Circular dichroism far-UV spectra for SYCP1$_{101\text{-}362}$ and SYCP1$_{1\text{-}362}$. Data were deconvoluted to estimate the percentage helix with data fitted at normalised rmsd values of 0.007 and 0.012, respectively. **f)** Thermal denaturation of SYCP1$_{101\text{-}362}$ and SYCP1$_{1\text{-}362}$ were recorded as percentage unfolded based on the helical signal at 222 nm. Melting temperatures were estimated at 41 °C.

3.3.5 The C-terminal tail-to-tail contact appears to be induced by the crystal lattice

Unlike the N-terminal association, the C-terminal "tail-to-tail" association was difficult to incorporate into a model for midline assembly of SYCP1. The association is stabilised through the formation of a hydrophobic core containing residues V158 and L162, lateral associations of I166, L162 and I173, and midline associations of K157 and K161 with E168 and E164, respectively, by forming salt bridges (Figure 3.3.7a-c). We considered the possibility that this association might be an artefact of crystallisation and thus employed a similar mutagenesis approach as had been applied for the N-terminal contact. Matthew Ratcliff performed mutagenesis experiments. He mutated residues K157 and K161 to glutamate and found no effect on the assembly of SYCP1$_{101-362}$ (data not shown). Further to this, I aimed to solve the crystal structure of SYCP1$_{101-206}$; if the additional residues of this construct adopt a similar tail-to-tail association, their relevance should be further considered. If they do not, the association is more likely to be an artefact of crystallisation.

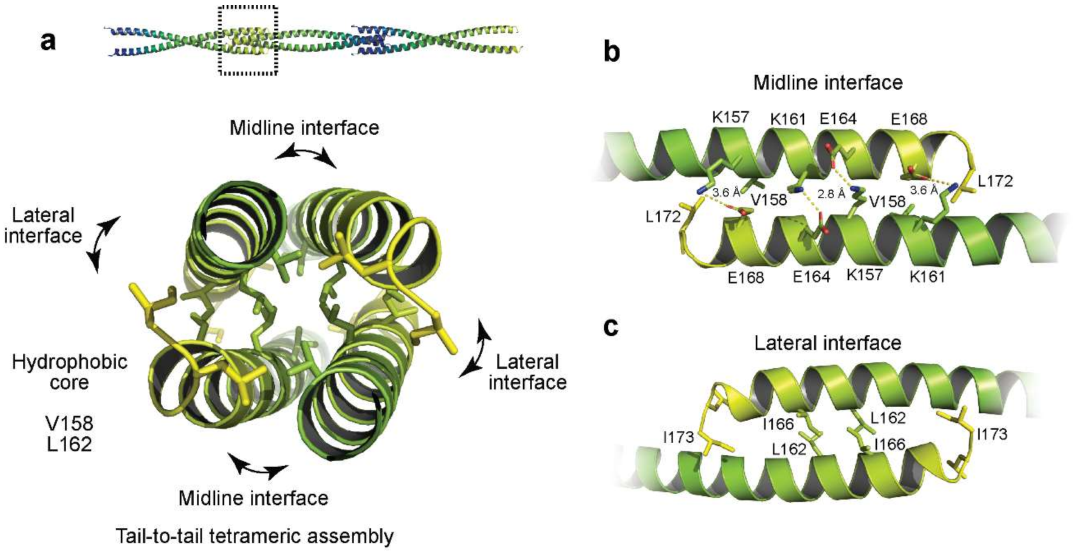
a
Midline interface
Lateral interface
Hydrophobic core
V158
L162
Lateral interface
Midline interface
Tail-to-tail tetrameric assembly
b
Midline interface
K157
K161
E164
E168
3.6 Å
V158
2.8 Å
V158
3.6 Å
L172
L172
E168
E164
K157
K161
c
Lateral interface
I173
I166
L162
L162
I166
I173

Figure 3.3.7| C-terminal contacts within the SYCP1$_{101-175}$ crystal lattice. a) C-terminal contacts of SYCP1$_{101-175}$ coiled-coils are mediated through the formation of a "tail-to-tail" tetrameric assembly in which V158 and L162 form a hydrophobic core, stabilised by further midline and lateral associations between anti-parallel chains. **b)** The midline interface is stabilised by salt bridges between K157 and E168 (distance, 3.6 Å) and K161 and E164 (distance, 2.8 Å). **c)** The lateral interface is stabilised by anti-parallel coiled-coil association of hydrophobic residues L162, I166 and I173.

3.3.6 Solution of the SYCP1$_{101-206}$ crystal structure

The crystal structure of SYCP1$_{101-206}$ was solved by Dr Owen Davies. A full description of the methods he utilised in the structure solution are described in Methods section 2.1.17. Briefly, the data from three crystals were merged. AMPLE pipeline on CCP4 online was utilised to generate a series of model fragments utilising ab initio QUARK decoys and, through serial molecular replacement attempts using Mr Bump, solved the structure which was subsequently built to completion and refined (Table 3.2). The structure revealed a parallel dimeric coiled-coil in which heptad residues I116 to I148 forming similar coiled-coil associations. In contrast, however, residues C-terminal to I148 continue in close coiled-coil association, not reciprocating the tail-to-tail association within the crystal structure of SYCP1$_{101-175}$ (Figure 3.3.8a,b). We therefore dismissed the tail-to-tail association as being an artefact of crystallisation.

The N-termini of SYCP1$_{101-206}$ are, in similarity with the structure of SYCP1$_{101-175}$, splayed apart, forced open by the I116/W119 wedge-like structure (Figure 3.3.8c). This allows for the formation of a similar head-to-head association mediated by the residues of the αN-tip (Figure 3.3.8d).

Data collection for SYCP1$_{101-206}$ (merged datasets: S1N-7, 12, 19)		
Space group	I 2	
Cell dimensions		
a, *b*, *c* (Å)	65.67, 37.31, 108.52	
α, *β*, *γ* (°)	90.00, 106.66, 90.00	
	Overall	Outer Shell
Low resolution limit (Å)	34.87	2.12
High resolution limit (Å)	2.06	2.06
R_{merge} (all I+ & I-)	0.071	0.919
R_{pim} (all I+ & I-)	0.023	0.286
$I / \sigma I$	15.0	1.8
$CC_{1/2}$	0.999	0.969
Completeness (%)	99.9	100.0
Multiplicity	11.0	11.4
Refinement		
Resolution (Å)	27.23 – 2.07	
UCLA anisotropy (Å)	2.1, 2.1, 2.6	
Number of reflections	12467	
R_{work} / R_{free}	0.2264 / 0.2441	
Number of atoms	1866	
Protein	1744	
Ligand/ion	18	
Water	104	
B-factors	42.79	
Protein	42.51	
Ligand/ion	62.91	
Water	44.02	
R.m.s deviations		
Bond lengths (Å)	0.002	
Bond angles (°)	0.334	

Table 3.2| X-ray crystallographic statistics for SYCP1$_{101-206}$. Data processed by Dr Owen Davies

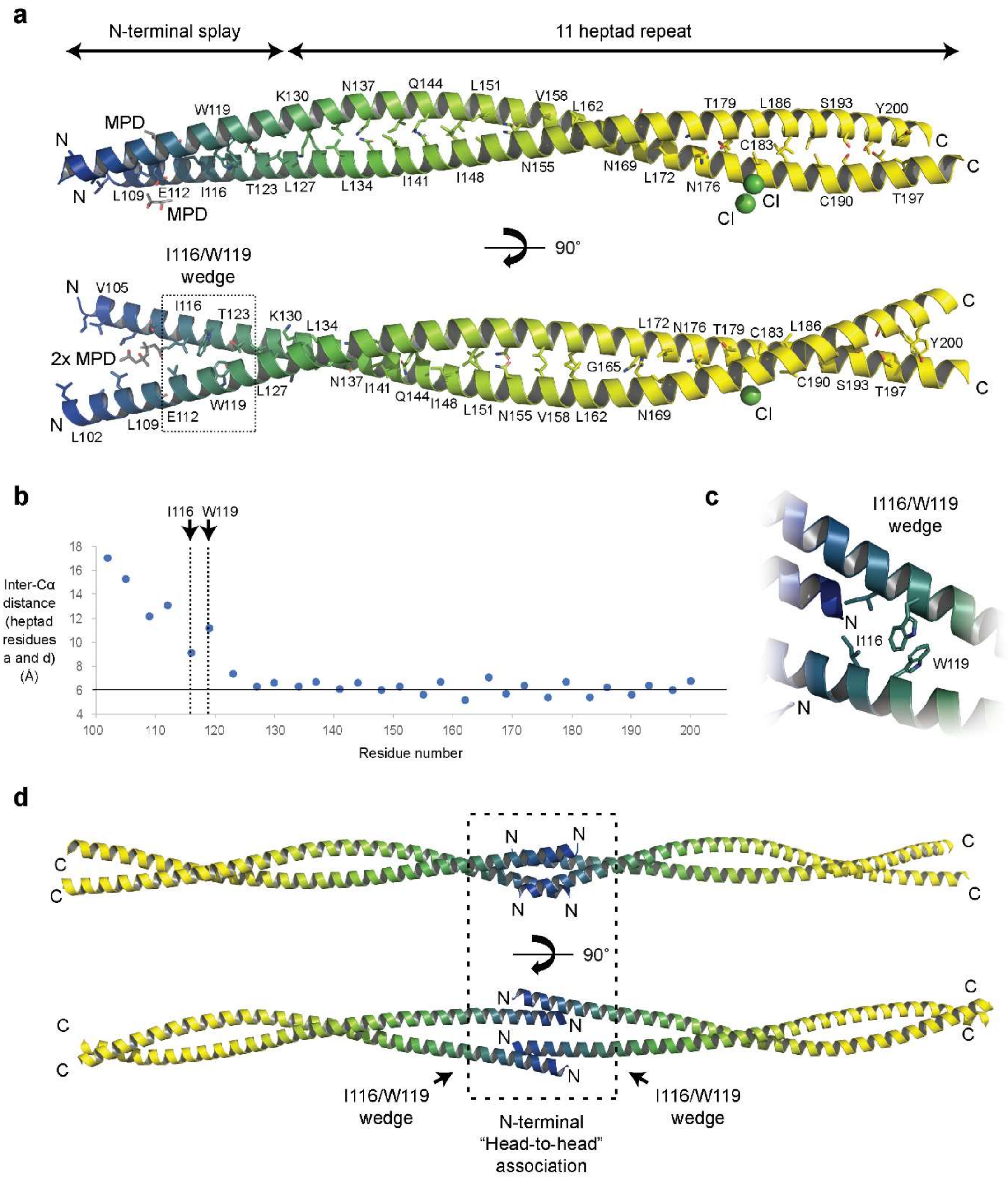
a
N-terminal splay
11 heptad repeat
N
N
MPD
MPD
W119
K130
N137
Q144
L151
V158
L162
T179
L186
S193
Y200
C
C
L109
E112
I116
T123
L127
L134
I141
I148
N155
N169
L172
N176
C183
C190
T197
Cl
Cl
90°
I116/W119
wedge
V105
2x MPD
L102
G165
b
I116
W119
Inter-Cα distance (heptad residues a and d) (Å)
18
16
14
12
10
8
6
4
100
110
120
130
140
150
160
170
180
190
200
Residue number
c
I116/W119
wedge
d
I116/W119
wedge
N-terminal
"Head-to-head"
association

Figure 3.3.8| The crystal structure of SYCP1$_{101\text{-}206}$. a) The asymmetric unit contains two chains of SYCP1$_{101\text{-}206}$. It is entirely helical and formed a parallel dimeric coiled-coil. 2 bound MPD molecules and heptad repeat residues are indicated. **b)** Graph plotting inter-Cα distances between heptad residues across the crystal structure. Positions of I116 and W119 are indicated. Horizontal line at 6.0 Å represents average inter-Cα distance for GCN4 (6 Å; PDB 2ZTA). **c)** I116/W116 form a wedge, forcing the coiled-coil chains apart. **d)** The crystal lattice contains a head-to-head association of SYCP1$_{101\text{-}206}$ coiled-coils, mediated by the αN-tip yet lacks the C-terminal association observed in the crystal structure of SYCP1$_{101\text{-}175}$.

The head-to-head association of SYCP1$_{101-206}$ displays an asymmetric, open conformation, contrasting with the symmetric, closed, conformation of SYCP1$_{101-175}$ (Figure 3.3.9a). The association maintains one of the midline contacts of the closed conformation, mediated by V105 and E112 and both lateral contacts mediated by L102 and L109, with flanking aromatic stacking of Y106 and Y110 (Figure 3.3.9a-c). The switch from a closed to an open conformation appears to be mediated by a rotamer flip of Y106 which switches from a flanking location in the closed conformation to being within the cleft of the open conformation. The open cleft is stabilised by the presence of two MPD molecules which sit within. Perhaps these molecules mimic the manner in which an interacting protein might association with this highly conserved region of the protein? If not, the possibility for dynamic switching between the closed and open conformations might allow greater torsional flexibility at the head-to-head interface within the SC midline *in vivo*.

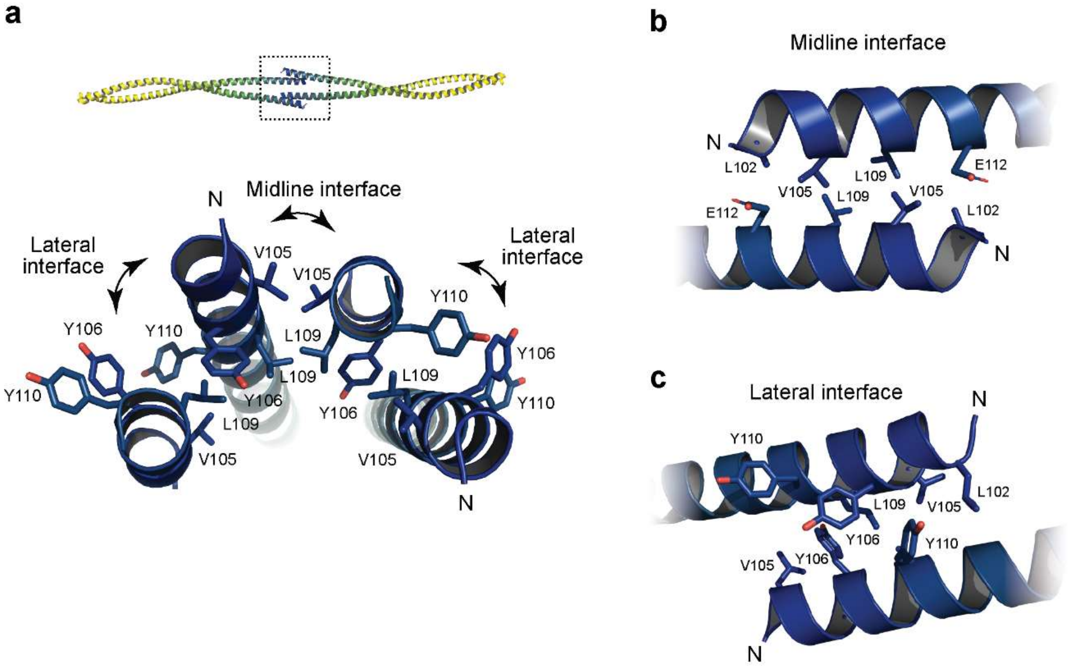
a
N
Midline interface
Lateral interface
Lateral interface
V105
V105
Y110
Y106
Y110
L109
L109
Y106
Y110
Y106
Y106
L109
Y106
Y110
L109
V105
V105
N
b
Midline interface
N
L102
L109
E112
V105
L109
V105
E112
L102
N
c
Lateral interface
N
Y110
L109
V105
L102
Y106
Y110
V105
Y106
N

Figure 3.3.9| N-terminal contacts within the SYCP1$_{101-206}$ crystal lattice. a) N-terminal contacts of SYCP1$_{101-206}$ coiled-coils are mediated through the formation of a "head-to-head" association of αN-tip residues in which V105, Y106 and L109 form a hydrophobic core, stabilised by further midline and lateral associations between anti-parallel chains. **b)** The midline interface is stabilised by V105 and E112 **c)** The lateral interface is stabilised by L102, L109 and aromatic stacking of Y106 and Y110. **c)** Lateral interfaces are mediated through aromatic stacking of tyrosine residues 106 and 110.

3.3.7 Midline assembly of SYCP1 through homotypic association of the αN-tip

The structures presented here contradict the in solution studies of both SYCP1$_{101\text{-}175}$ and SYCP1$_{101\text{-}206}$ which demonstrate high levels of disorder, with approximately 50 % of residues calculated as being disordered (Figure 3.3.1e,f). However, as demonstrated by our mutagenesis studies, the associations appear to be mediating the assembly of SYCP1$_{101\text{-}362}$ (Figure 3.3.6c). Therefore, I propose that the tetrameric core of SYCP1 can scaffold the 101-206 sequence such that it is poised to engage in head-to-head contact, and this might occur in a dynamic fashion, with head-to-head contacts cycling between associated and disassociated states (Figure 3.3.10a). Upon association, the coiled-coil sequence is stabilised with this this process occurring in a recursive manner to allow for potentially limitless assembly (Figure 3.3.10b).

The dynamic nature of this association provides a model for the remodelling of initial SYCP1-mediated contacts between meiotic homologues. Initial contacts are likely to be often erroneous or non-productive. By breaking erroneous contacts and allowing the cooperative extension of correct associations, the self-assembly of a continuous lattice which tracks the entire length of a homologous chromosome pair would be facilitated (Figure 3.3.11a).

It might be advantageous at certain stages of the meiotic cycle, such as during pachytene during which the SC is fully assembled, to be able to induce stability into the structure. I noted the presence of two cysteine residues occupying heptad positions 183 and 190 (Figure 3.3.11b). In solution, oxidation results in the formation of a ladder-like spread of oligomers visualised by SDS-PAGE (Figure 3.3.11c). It would be interesting to speculate whether cysteine oxidation can play an *in vivo* role in the stabilisation of proteinaceous assemblies.

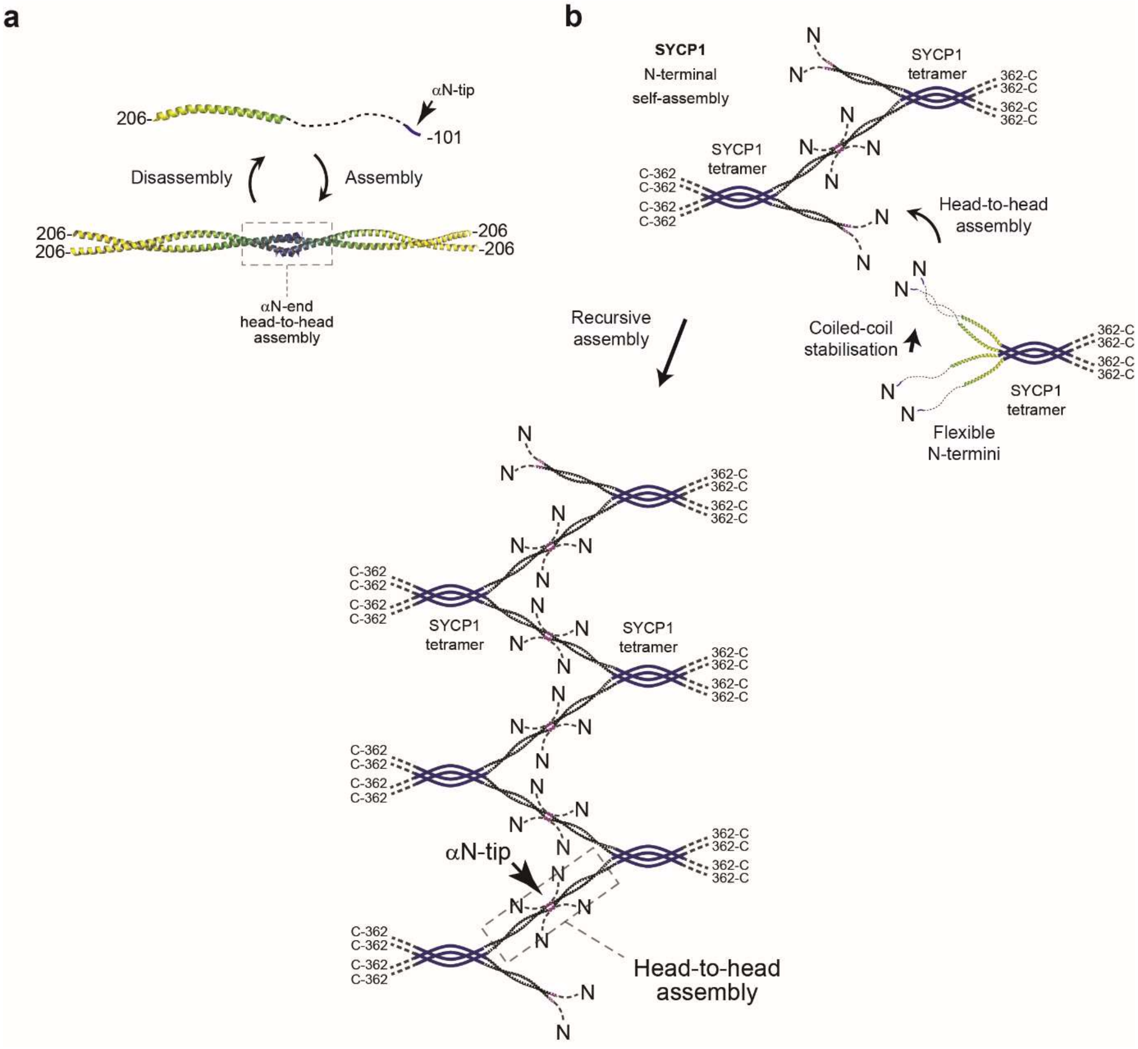
a
αN-tip
206-
-101
Disassembly
Assembly
206-
206-
-206
-206
αN-end
head-to-head
assembly
b
SYCP1
N-terminal
self-assembly
SYCP1
tetramer
362-C
362-C
362-C
362-C
C-362
C-362
C-362
C-362
N
Head-to-head
assembly
Coiled-coil
stabilisation
Flexible
N-termini
Recursive
assembly
αN-tip
Head-to-head
assembly

Figure 3.3.10| N-terminal head-to-head contacts drive lattice-like assembly of SYCP1 molecules. a) $SYCP1_{101\text{-}206}$ is approximately 50 % disordered in solution but adopts an entirely α-helical structure within a crystal lattice. In solution, this likely occurs at high concentrations and might be stabilised in a cooperative manner upon recruitment to the SC *in vivo*. I therefore propose a dynamic switching between a disordered monomeric state and ordered, interacting, state. **b)** A model for the incorporation of SYCP1 molecules within a growing SYCP1 lattice. The tetrameric architecture of SYCP1 stabilises the helical state of the 101-206 sequence, promoting head-to-head association. Head-to-head association can then occur in a recursive manner to allow for the continuous growth of the SYCP1 lattice.

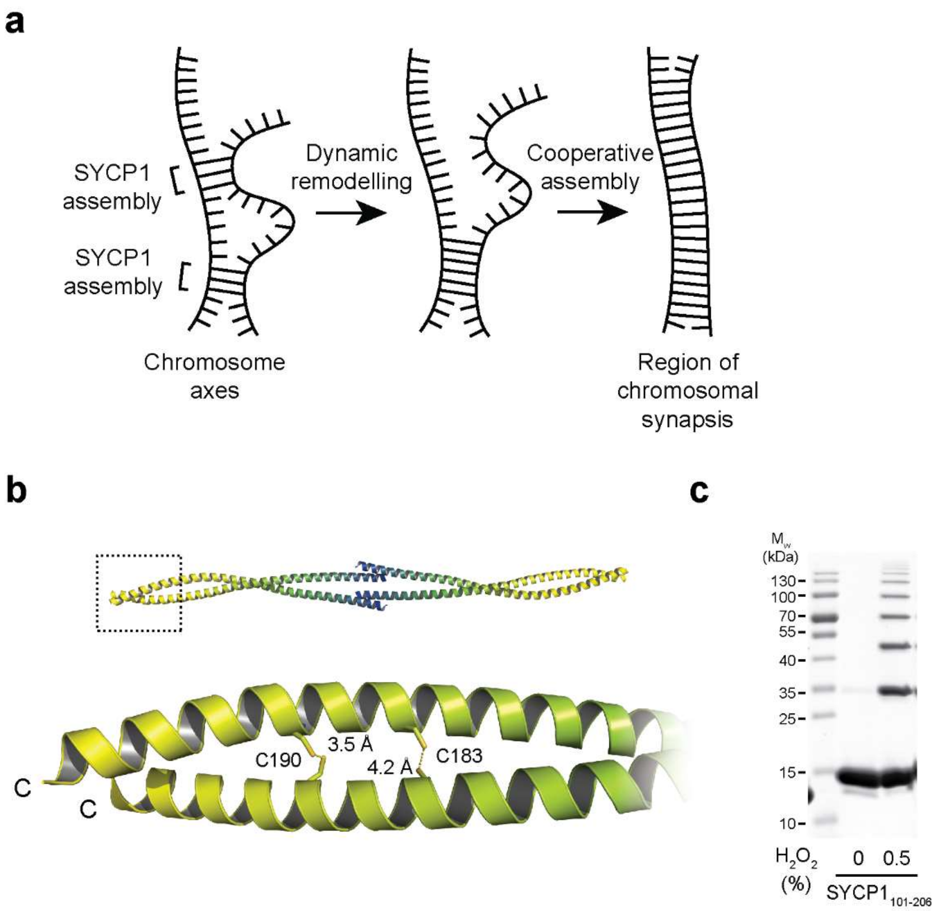
a
SYCP1 assembly
SYCP1 assembly
Dynamic remodelling
Cooperative assembly
Chromosome axes
Region of chromosomal synapsis
b
C190
3.5 Å
4.2 Å
C183
C
C
c
Mw (kDa)
130
100
70
55
40
35
25
15
10
H2O2 (%)
0
0.5
SYCP1 101-206

Figure 3.3.11| Remodelling of the SC midline through dynamic and cooperative self-association. **a)** Individually weak SYCP1 associations likely rely upon cooperativity to allow uninterrupted synapsis allowing for initial erroneous associations to be broken and remodelled. **b)** The location and distance between two cysteine residue pairs which occupy heptad positions within the C-terminus of the SYCP1$_{101\text{-}206}$ structure. **c)** Oxidation of two cysteine residues within the SYCP1$_{101\text{-}206}$ structure may contribute to stabilisation of associations once formed. *In vitro,* oxidation by hydrogen peroxide results in the formation of discrete multimeric species. Chromosome schematic in panel **a** by Dr Owen Davies.

3.3.8 The SYCP1 N-termini stabilise long range extension of synapsis

I sought to assess the role of the SYCP1 N-terminus within the formation of polycomplex structures as a model system for chromosome synapsis *in vivo*. I found that filamentous networks still formed even when only expressing the C-terminal end of the SYCP1 central coiled-coil and the extended C-terminus (residues 640-976). As this construct does not demonstrate any ability to self-assemble in solution I again considered the probability that cytoplasmic networks are not representative of SYCP1 assembly and in fact represent some form of recruitment to an intermediate filament network such as keratin (Figure 3.3.12a). Analysis by electron microscopy is therefore a better determinant of the effect of mutations and/or truncations in these types of experiments. Upon deletion of the SYCP1 N-terminus (Δ1-198; residues 199-976), I found that polycomplex-like structures still form, with a predominant localisation around the nucleus (Figure 3.3.12b). However, the polycomplex structures I observed appeared to be more disorganised and central element-like bands within these were either short or discontinuous (Figure 3.3.12b). It therefore appears that N-terminal associations of SYCP1 are not absolutely essential for polycomplex formation but play a role in the long-range extension of assembly.

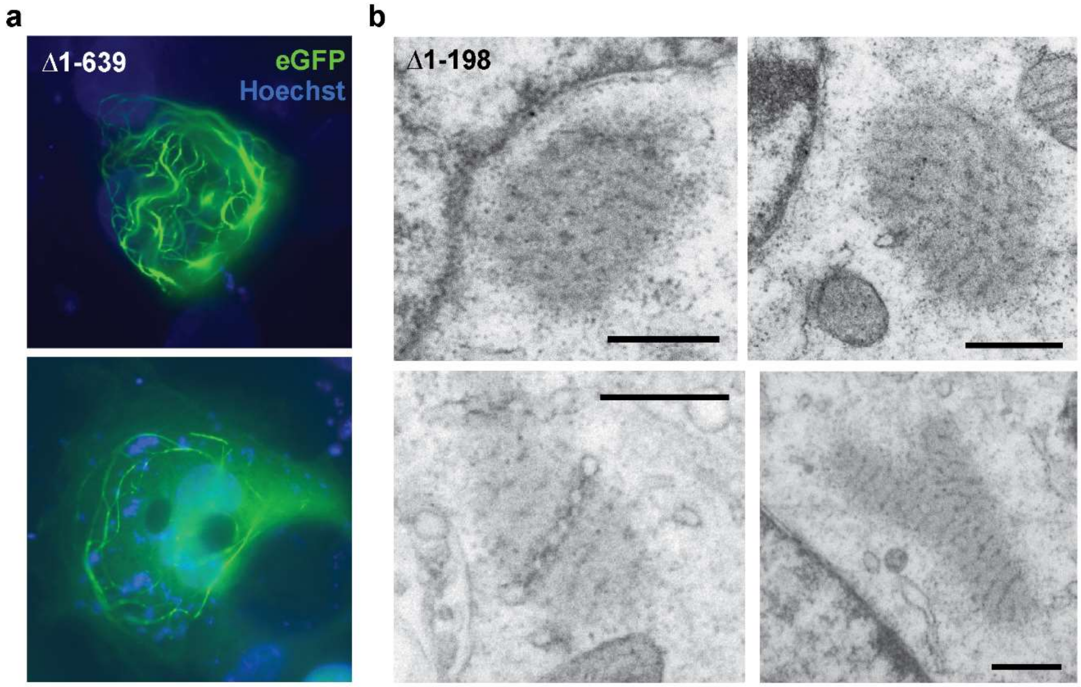

Figure 3.3.12| The N-terminus of SYCP1 stabilises long range assembly. a) Filamentous networks formed upon the overexpression of eGFP-SYCP1$_{640-976}$ in COS-7 cells. **b)** Electron micrographs showing polycomplex structures formed upon the overexpression of eGFP-SYCP1$_{199-976}$ in COS-7 cells. Scale bars = 500nm.

Part III

Chromosomal self-assembly of SYCP1

3.4.1 Role of the stable, extended, dimeric coiled-coil SYCP1$_{640\text{-}783}$

Given the domain's high conservation and localisation proximal to the chromosome axis, I wondered whether the previously characterised sequence capping the C-terminus of the SYCP1 helical core (residues 640-783) could mediate a similar, yet distinct, mechanism of self-association to the SYCP1 N-terminus. I predicted that given its localisation proximal to the meiotic chromosome axis, it might play some role in chromosomal association. I therefore sought to solve the crystal structure of this domain.

3.4.2 Attempts to solve the SYCP1$_{640\text{-}783}$ crystal structure

Upon initial sparse matrix screening for chemical conditions in which SYCP1$_{640\text{-}783}$ crystallises, many crystals were obtained (Figure 3.4.1a). However, these crystals suffered from anisotropic crystal growth, resulting in one-dimension being significantly thinner than the other two, with crystals appearing somewhat two-dimensional. Further, crystals frequently appeared to contain multiple lattices, a defect not significantly improved upon optimisation of the crystallisation conditions. Additive screening yielded larger crystals displaying a single lattice (Figure 3.4.1b). The best diffracting crystals grew in 0.1 M Tris pH 8.0, 0.2 M NaCl, 16.25 % PEG6000 with 0.1 M sodium citrate tribasic tetrahydrate (Figure 3.4.1c).

Two X-ray diffraction datasets (SYCP1-05_6, and SYCP1-05_7; dls100515) were collected at beamline I03, Diamond Light Source, Oxfordshire, UK. Initial processing involved indexing and integration in XDS (Kabsch, 2010b; Kabsch, 2010a) and scaling in xscale (Diederichs *et al.*, 2003). The two datasets were merged in Aimless and truncated to a maximum resolution of 3.7 Å with an $I/\sigma I$ of 1.2 and $CC½$ of 0.529 in the outer shell (Table 3.3) (Evans and Murshudov, 2013). The crystal belonged to a P1 space-group with unit cell dimensions a= 44.23, b= 86.86, c= 101.75, α= 101.54, β= 101.77, γ= 97.62. The data were highly anisotropic, as assessed by Staraniso (Strong *et al.*, 2006) with suggested anisotropic resolution limits at 5.98 Å, 5.45 Å, and 3.34 Å at an *I/σI* of 1.5. Anisotropy is likely a consequence of both the crystal morphology and the internal organisation of the crystal lattice in which it is likely that coiled-coil molecules form lateral contacts along their lengths, and end-on contacts in a rope-like manner (Figure 3.4.1d). Calculation of the Matthew's coefficient by MATTPROB was used to estimate the number of molecules in the asymmetric unit at between 6 to 10 with a solvent content of 42-54 % (i.e. 3 to 5 dimers) (Matthews, 1968; Kantardjieff and Rupp, 2003). Low resolution, high anisotropy and a large asymmetric unit lead us to attempt the optimisation of the construct's amino acid boundaries. However, it must be stated that these crystals were isomorphic and grew to a such a size that multiple data sets could have been collected using the same crystal and subsequently merged to improve the data quality.

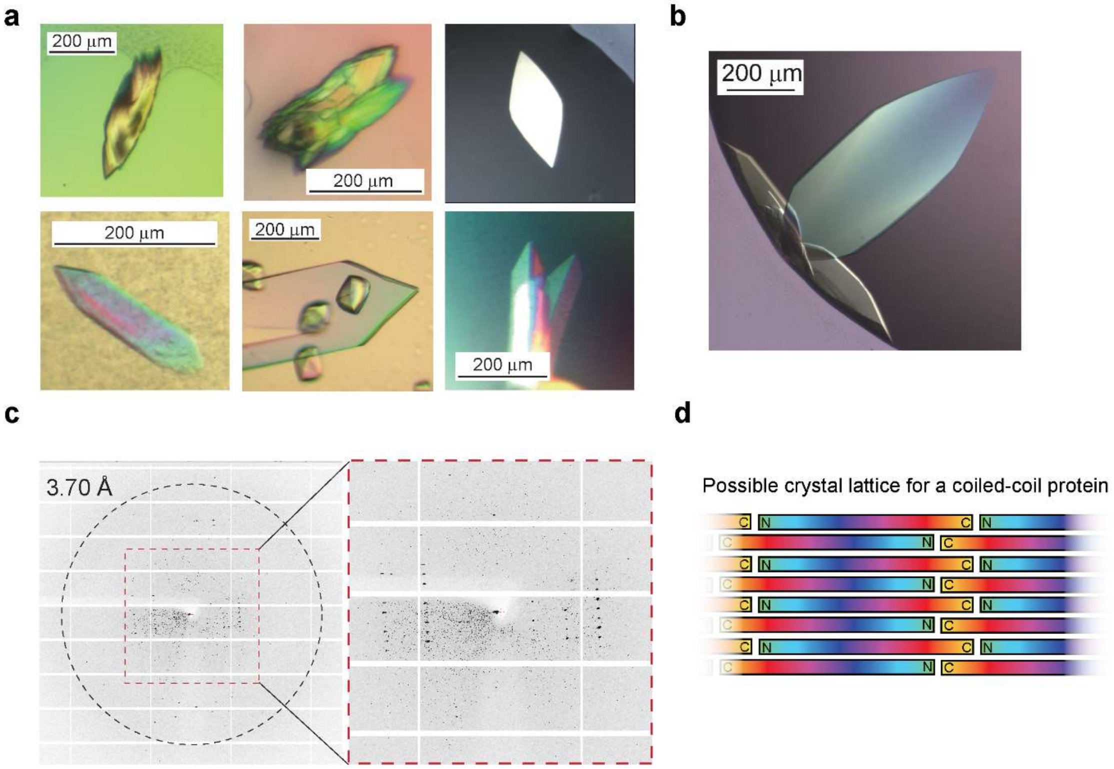

Figure 3.4.1| Crystallographic trials of SYCP1$_{640-783}$. a) Example SYCP1$_{640-783}$ crystals demonstrating two-dimensionality and the regular formation of multiple lattices. **b)** Large SYCP1$_{640-783}$ crystal with a single lattice. **c)** X-ray diffraction image for the crystal in **b** with resolution at 3.7 Å circled. A close-up is displayed bounded by a red dashed box. **d)** A possible crystal lattice for a coiled-coil protein, shown as coloured rectangles with N and C-termini indicated. The lattice is mediated by end-on and lateral contacts.

Native data collection for SYCP1$_{640-783}$ (dataset SYCP1C-05)			
Space group	P1		
Cell dimensions			
a, *b*, *c* (Å)	44.23, 86.86, 101.75		
α, *β*, *γ* (°)	101.54, 101.54, 97.62		
	Overall	Inner Shell	Outer Shell
Low resolution limit (Å)	46.95	46.95	4.05
High resolution limit (Å)	3.70	9.06	3.70
R$_{meas}$ (all I+ & I-)	0.316	0.054	1.438
R$_{pim}$ (all I+ & I-)	0.163	0.028	0.757
Total number of observations	55387	3769	12587
Total number unique	15041	1017	3606
Mean (I/σI)	3.5	16.7	1.2
CC (1/2)	0.993	0.998	0.529
Completeness (%)	98.7	97.8	98.9
Multiplicity	3.7	3.7	3.5

Table 3.3| X-ray crystallographic statistics for SYCP1$_{640-783}$. Data processed by Dr Owen Davies

3.4.3 Construct optimisation identifies SYCP1$_{676-770}$ as a new crystal target

To identify a construct which produces better diffracting crystals, a series of N- and C-terminal truncations (and a single N- terminal extension) of SYCP1$_{640-783}$ were constructed (Figure 3.4.2a). These were then expressed and purified for the purposes of comparing protein yield and purity by SDS-PAGE, stability by circular dichroism thermal denaturation and oligomeric state by SEC-MALS (Figure 3.4.2b-e). Purified samples visualised in Figure 3.4.2b were not subject to prior size-exclusion chromatography, hence the major degradation product of SYCP1$_{640-783}$ not present in the final sample presented in Figure 3.2.13 is visible. The presence of this degradation product did however suggest that truncation of one or both terminus/termini of this domain may improve the quality of the preparation and, hopefully, improve chances of structure solution.

N-terminal truncation to residue 676 improved final yield resulting in a 1.3-fold increase (Figure 3.4.2e). Degradation for construct 676-783 was visualised as a smear beneath the band representing the majority species by SDS-PAGE (Figure 3.4.3b). The simultaneous truncation of both the N and C-terminus, to 676-770, drastically improved the expression of the construct, resulting in a yield of 22 mg/l which was further purified by size-exclusion chromatography to homogeneity (Figure 3.4.2e and Figure 3.4.3a). A slight N-terminal extension to residue 632 had deleterious effects, with a reduced final yield for construct 632-770 of 2.8 mg/l, with SDS-PAGE analysis highlighting the presence of multiple, potentially bacterial, contaminants and degradation products (Figure 3.4.2b). SEC-MALS analysis of these constructs revealed that dimeric oligo status is retained (Figure 3.4.2e). However, C-terminally truncated constructs 640-752 and 676-752 formed monomers in solution and demonstrated decreased yields, with 4.5 and 6 mg/l, respectively (Figure 3.4.2e). Far-UV circular dichroism spectroscopy revealed that construct 676-770 contained 89 % α-helix and thermal denaturation demonstrated a single unfolding event at 35 ˚C, likely representing the unfolding of the coiled-coil sequence between residues 749-770 (Figure 3.4.2c,d). These analyses indicate that the sequence of residues 752-770 are necessary for dimer formation, likely through coiled-coil type interactions, whilst the predicted coiled-coil sequence between residues 640-664 on its own is not sufficient to stabilise dimer formation.

Taking these findings into consideration, construct 676-770 was selected for crystallisation trials. A summary of its purification is presented in Figure 3.4.3a. In keeping with our previous findings on SYCP1$_{640\text{-}783}$, SYCP1$_{676\text{-}770}$ demonstrates helical content of 89 %, corresponding to 87 residues (Figure 3.4.2c). Size and shape determination using SEC-SAXS methods reveal an elongated conformation, with a length of 143 Å and R_c of 7.8 Å, suggesting it's folding as a dimeric coiled-coil (Figure 3.4.3c-f). Similarly to SYCP$_{640\text{-}783}$, MBP-fusions of SYCP1$_{676\text{-}770}$ demonstrated only short inter-MBP distances by SEC-SAXS, suggesting their parallel orientation (Figure 3.4.4a-e). The theoretical X-ray scattering of a ROSETTA generated model of SYCP1$_{676\text{-}770}$ (generated by Dr Owen Davies) as an extended dimeric coiled-coil matches well the experimental scattering data with a χ^2 value of 1.455 (Figure 3.4.4d,e) Parallel orientation of the two α-helical chains was confirmed through the purification of an N-terminal GST fusion. SEC-MALS analysis confirmed the formation of a stable dimer and SEC-SAXS demonstrated an inter-GST peak at ~30 Å, consistent with GST alone (Figure 3.4.5a-f). Unlike with MBP-fusions, intra- and inter-GST peaks conflate due to the constitutively dimeric state of GST (Figure 3.4.5f).

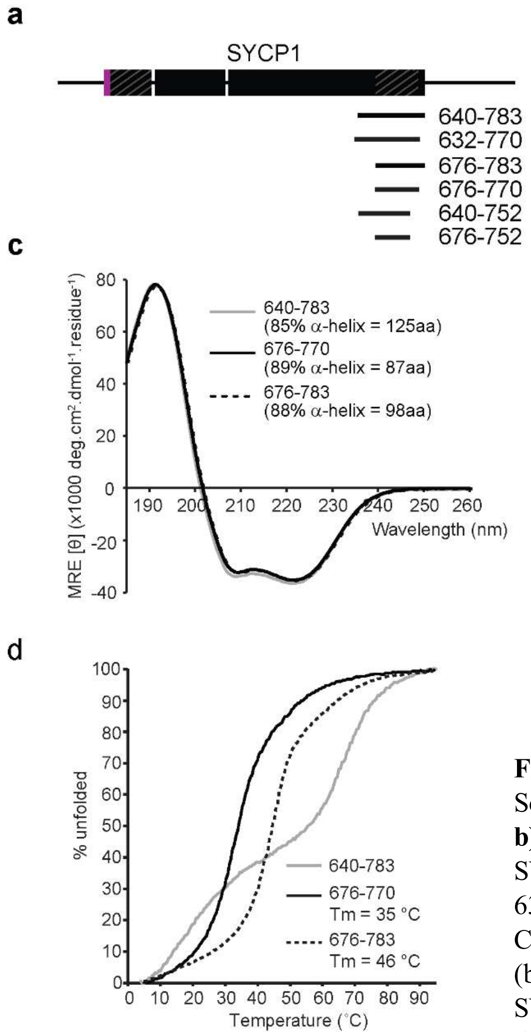

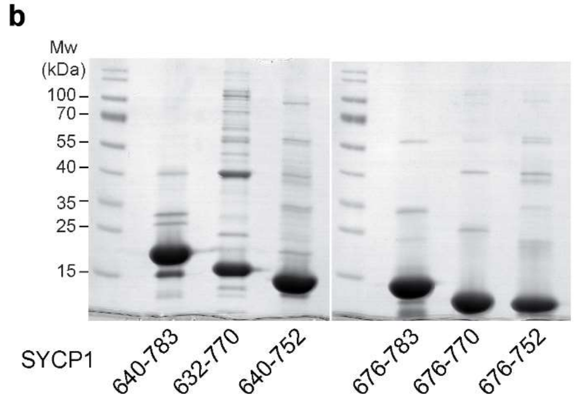

e

Construct boundaries	Yield (mg/l)	Monomer M_w	MALS M_w	Oligomer
640-783	6.5	17.3	34.4	Dimer
632-770	2.8	16.6	27.2	Dimer
676-783	8.7	13.0	26.3	Dimer
676-770	22.2	11.4	22.1	Dimer
640-752	4.5	13.6	14.3	Monomer
676-752	6.0	9.3	10.4	Monomer

Figure 3.4.2| Identification of SYCP$_{676\text{-}770}$. a) Schematic of SYCP1 displaying analysed constructs. **b)** SDS-PAGE analysis of the final purified sample of SYCP1 constructs with residue boundaries: 640-783; 632-770; 640-752; 676-783; 676-770; 676-752. **c)** Circular dichroism far-UV spectra for SYCP1$_{676\text{-}770}$ (black solid) and SYCP1$_{676\text{-}783}$ (black dashed) alongside SYCP$_{640\text{-}783}$ for comparison (grey). Data were deconvoluted to estimate the percentage helix with data fitted at normalised rmsd values of 0.004. **d)** Thermal denaturation of SYCP1$_{676\text{-}770}$ and SYCP1$_{676\text{-}783}$ were recorded as percentage unfolded based on the helical signal at 222 nm. Melting temperatures were estimated at 35 and 46 ˚C, respectively. The biphasic denaturation profile for SYCP1$_{640\text{-}783}$ is shown alongside for comparison (grey). **e)** Table summarising the yield (mg/L), monomeric molecular weight (Mw), experimental molecular weight as determined by SEC-MALS (data in Appendix 3), and the determined oligomer.

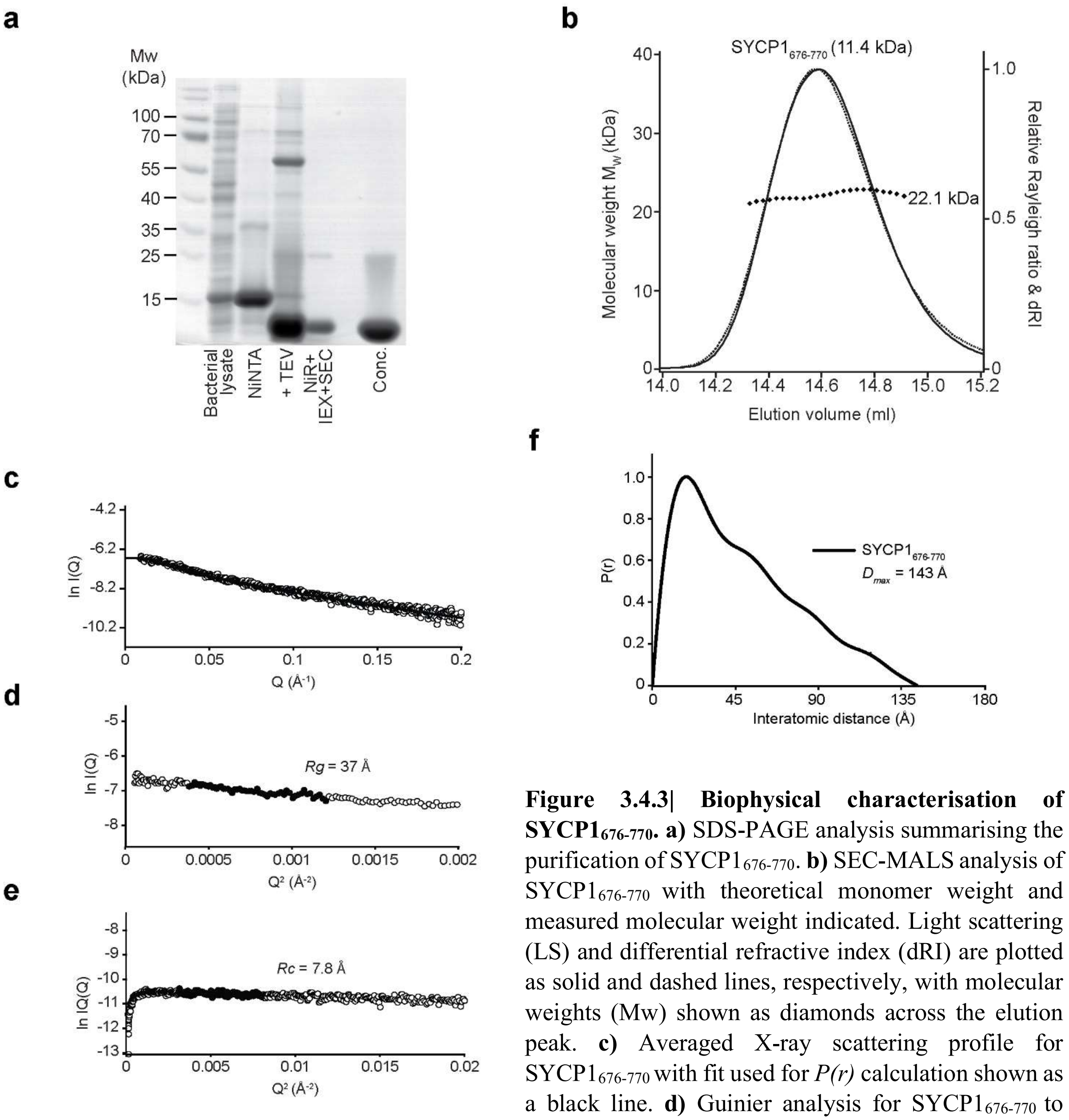

Figure 3.4.3| Biophysical characterisation of SYCP1$_{676-770}$. a) SDS-PAGE analysis summarising the purification of SYCP1$_{676-770}$. **b)** SEC-MALS analysis of SYCP1$_{676-770}$ with theoretical monomer weight and measured molecular weight indicated. Light scattering (LS) and differential refractive index (dRI) are plotted as solid and dashed lines, respectively, with molecular weights (Mw) shown as diamonds across the elution peak. **c)** Averaged X-ray scattering profile for SYCP1$_{676-770}$ with fit used for *P(r)* calculation shown as a black line. **d)** Guinier analysis for SYCP1$_{676-770}$ to calculate the radius of gyration (*Rg*) (indicated) with points within the linear region used for calculation highlighted in black. **e)** Guinier analysis to calculate the radius of gyration of the cross-section (*Rc*) (indicated) with points within the linear region used for calculation highlighted in black. **f)** Inter-atomic distance distribution profile for SYCP1$_{676-770}$ with the maximum interatomic distance (D_{max}) indicated.

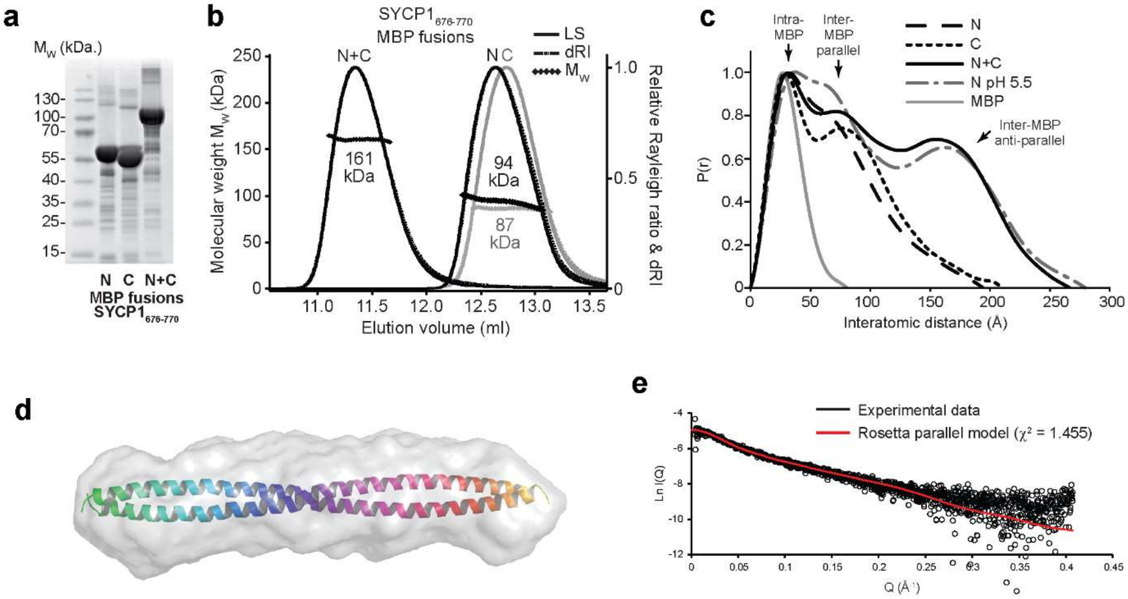

Figure 3.4.4| The SYCP1$_{676-770}$ dimeric coiled-coil is parallel. a) SDS-PAGE analysis of purified MBP-fusions of SYCP1$_{676-770}$. **b)** SEC-MALS analysis of SYCP1$_{676-770}$ MBP-fusions confirming dimeric state. Theoretical dimeric molecular weights: MBP-676-770-MBP, 194 kDa; MBP-676-770, 112 kDa; 676-770-MBP, 104 kDa. **c)** Inter-atomic distance distribution profile for MBP-fusions of SYCP1$_{676-770}$ with intra-MBP and inter-MBP (parallel and anti-parallel) peaks indicated. **d)** SUPCOMB docked ROSETTA model of SYCP1$_{676-770}$ into an *ab initio* generated molecular envelope by DAMMIF and DAMAVER. **e)** The theoretical X-ray scattering profile of the SYCP1$_{676-770}$ ROSETTA model (red) closely matches the experimental data (black) with a χ^2 value of 1.455. SEC-SAXS analysis by Dr Orla Dunne.

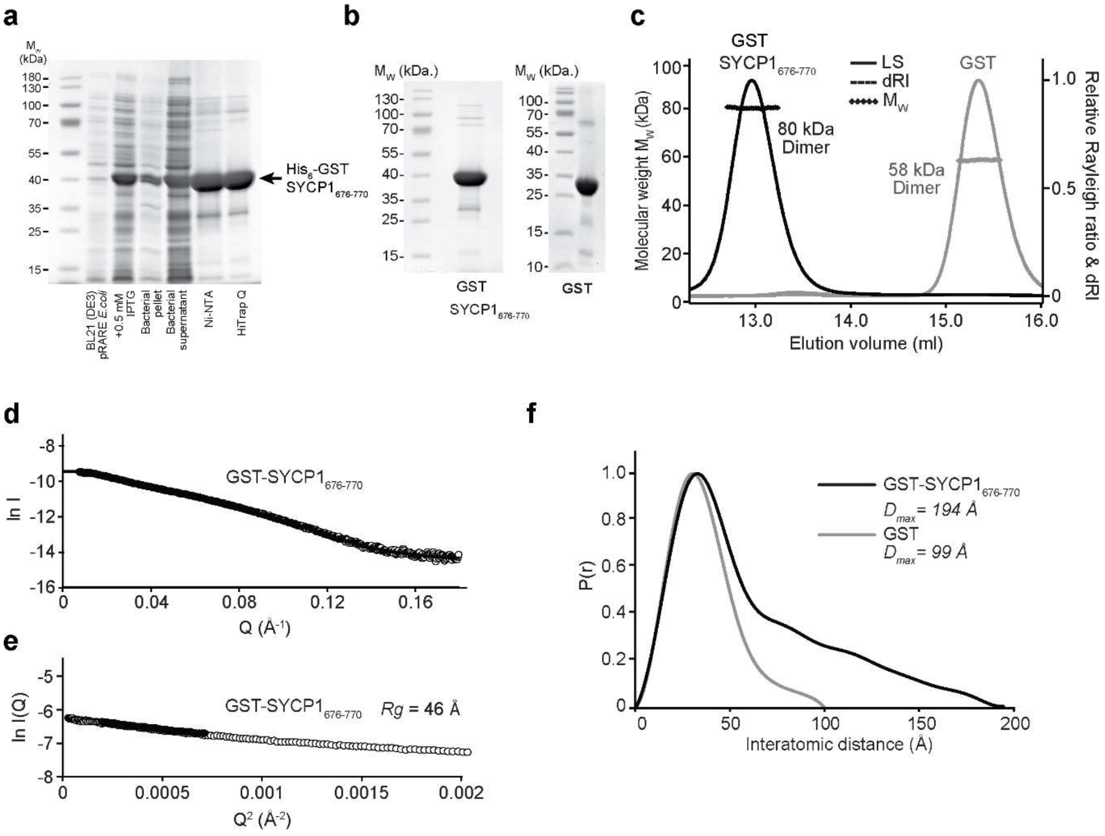

Figure 3.4.5| Purification and characterisation of GST-fused SYCP1$_{676-770}$. a) SDS-PAGE analysis of samples summarising the purification of GST-SYCP$_{676-770}$. **b)** Purified sample of GST-SYCP1$_{676-770}$ and GST. **c)** SEC-MALS analysis of GST-SYCP1$_{676-770}$ and GST (theoretical dimer weights – 82 and 59 kDa, respectively). Light scattering (LS) and differential refractive index (dRI) are plotted as solid and dashed lines, respectively, with molecular weights (Mw) shown as diamonds across elution peaks. **d)** Averaged small-angle X-ray scattering profile of GST-SYCP1$_{676-770}$ with the fit used for *P(r)* distribution shown as a black line. **e)** Guinier analysis to determine the radius of gyration (*Rg*) of GST-SYCP1$_{676-770}$ (indicated). **f)** Inter-atomic distance distribution profiles (*P(r)*) for GST-SYCP1$_{676-770}$ and GST indicating the maximum dimension (D_{max}). SEC-SAXS analysis by Dr Orla Dunne

3.4.4 SYCP1$_{676\text{-}770}$ crystals have pathologies which inhibit structure solution

Initial crystals were grown in 200 nl drops in sitting drop format in 0.2 M magnesium formate 20 % PEG3350 (Table 2.2). Optimised SYCP1$_{676\text{-}770}$ protein crystals were grown in 20 % PEG3350, 200 mM magnesium formate by vapour diffusion in hanging drops (Figure 3.4.6a). Native data (dataset S1C-20; dls070316) were collected at Diamond Light Source, Oxfordshire, UK, as described in the Methods section 2.1.17, and subsequently indexed, using XDS, revealing unit cell dimensions a= 87.80, b= 47.04, c= 138.12, α= 90, β= 94.78, γ= 90 and processed to 2.52 Å with an $I/\sigma I$ of 1.0 and a $CC_{1/2}$ of 0.501 in the outer resolution shell (Table 3.4). Scaling was executed in xscale and data were merged using Aimless. The crystal belonged to a $P2_1$ spacegroup. The data were highly anisotropic with anisotropic resolution limits of 3.20 Å, 3.00 Å and 2.30 Å at an $I/\sigma I$ of 1.5. It was noted that many reflections are not accounted for by the assigned unit cell dimensions and spacegroup (Figure 3.4.6c). This may suggest the presence of multiple lattices; however, the reflections may also belong to the same lattice and appear on multiple images due to anisotropic mosaicity. Calculation of the Matthew's coefficient suggests that there were between 4 and 6 dimers in the asymmetric unit with a solvent content between 40-60 %.

Native data collection for SYCP1$_{676\text{-}770}$ (dataset S1C-20)			
Space group	$P2_1$		
Cell dimensions			
a, b, c (Å)	87.80, 47.04, 138.12		
α, β, γ (°)	90, 94.78, 90		
	Overall	Inner Shell	Outer Shell
Low resolution limit (Å)	47.02	47.02	2.62
High resolution limit (Å)	2.52	9.09	2.52
R_{meas} (all I+ & I-)	0.109	0.023	2.078
R_{pim} (all I+ & I-)	0.056	0.013	1.070
Total number of observations	142582	2847	15716
Total number unique	38472	887	4326
Mean (I/σI)	8.8	32.8	1.0
CC (1/2)	0.999	0.999	0.501
Completeness (%)	99.6	98.3	99.7
Multiplicity	3.7	3.2	3.6

Table 3.4| X-ray crystallographic statistics for SYCP1$_{676\text{-}770}$. Data processed by Dr Owen Davies

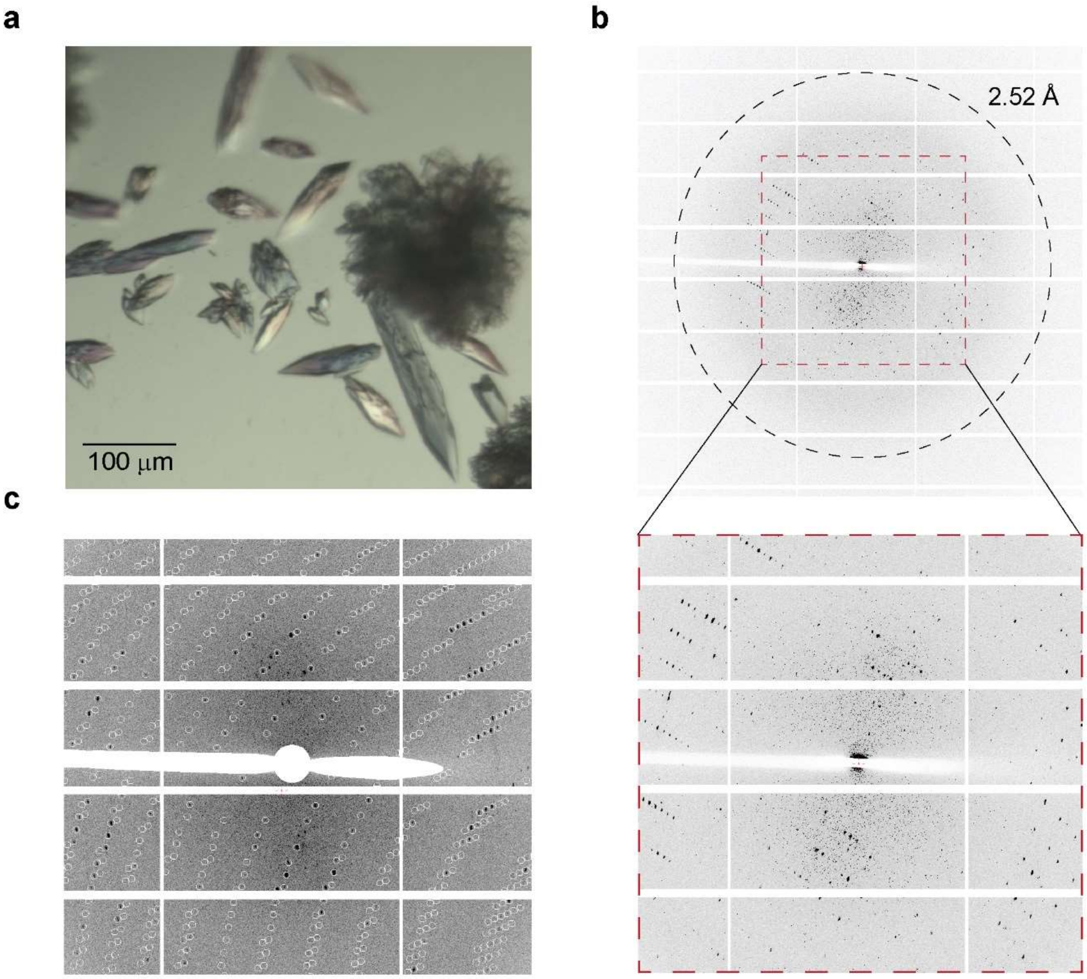

Figure 3.4.6| Initial crystallisation of SYCP$_{676\text{-}770}$. a) SYCP1$_{676\text{-}770}$ crystals grown in 200 mM magnesium formate, 20 % PEG3350. **b)** X-ray diffraction data for SYCP1$_{676\text{-}770}$ processed to 2.52 Å. The crystals belonged to a P2$_1$ space group with unit cell dimensions a= 87.75, b= 47.02, c=138.05, α= 90, β= 94.75, γ= 90. Below a close up of the low-resolution reflection demonstrating large voids indicating translational non-crystallographic symmetry. **c)** White circles highlight the predicted coordinates of predicted. Additional reflections to those predicted are visible. The white area corresponds with an untrusted region in which data were not used in indexing and downstream processing. This zone aligns with the beam stop.

3.4.5 Patterson Function reveals translational symmetry

The Patterson map for native SYCP1$_{676-770}$ (dataset S1C-20) was calculated by Peakmax (Figure 3.4.7a-e). The map reveals a large Patterson peak at each lattice point of the unit cell as expected. However, emanating from these peaks in a linear spread are Patterson peaks of decreasing intensity separated by approximately 5 Å relating to the pitch of an alpha helix, indicating the helices within the unit cell are organised in a parallel arrangement (Figure 3.4.7e). A pseudo-centring vector is present such that the Patterson map closely resembles that of C2 spacegroup. A higher symmetry spacegroup would greatly reduce the volume of the asymmetric unit (ASU) and aid in structure solution; however, this peak is only 17 % of the intensity of the peaks located at lattice points. This peak is likely the result of translational or pseudo- non-crystallographic symmetry which impacts heavily upon intensity statistics during molecular replacement and anomalous difference maps in experimental phasing, hindering structure solution.

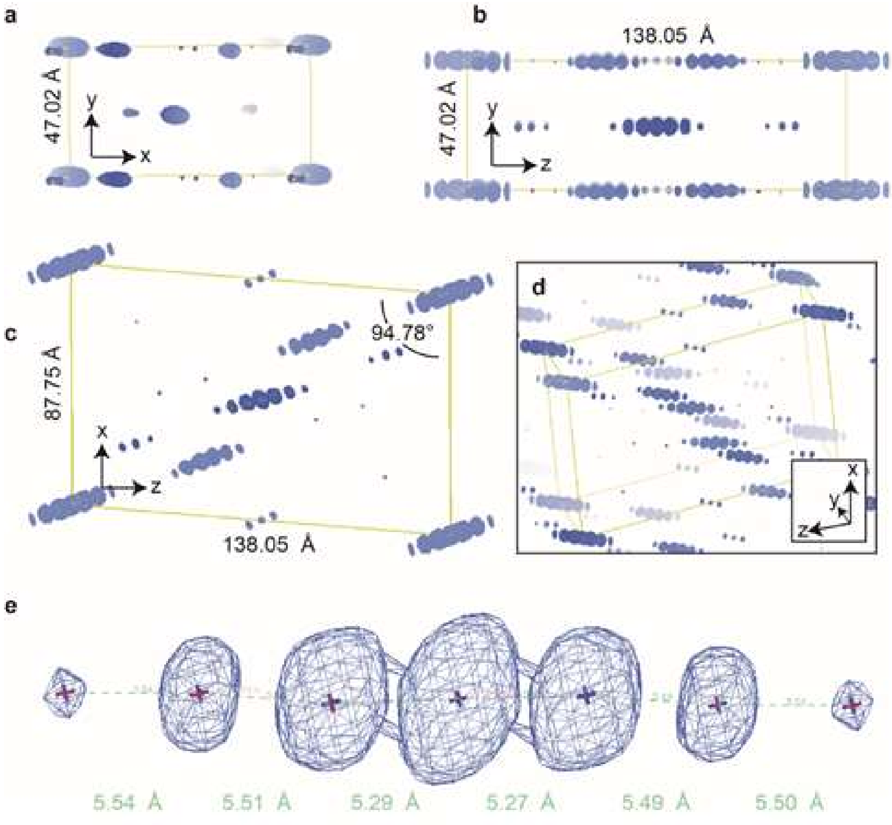

Figure 3.4.7| Native Patterson map generated for SYCP1$_{676-770}$. a-c) 2-dimensional perspectives of the Patterson map. **d)** 3-dimensional view of the Patterson map. **e)** Patterson peaks in a linear spread, separated by an inter-peak distance of approximately 5 Å.

3.4.6 Experimental phasing strategies

I experienced no success in solving the structure using *ab initio* approaches. Therefore, in order to overcome the phase problem, single-wavelength anomalous diffraction (SAD) experiments were performed. Sections 3.4.6-8 describe these attempts. For success through alternative means, see section 3.4.9. In these SAD experiments, heavy elements are introduced into the protein crystal, which scatter X-rays anomalously, the result being that the centro-symmetry of the diffraction pattern is broken. This is identified as measurable differences in the amplitudes of Friedel mates (reflections related by 180˚) and Bijvoet pairs (symmetry-related reflections). These differences are maximised by using X-rays at a specific wavelength, dependent upon the heavy atom type, termed the absorption edge. By measuring these differences in intensity, the locations of the heavy atoms can be determined, providing initial phase estimations. Subsequent building into the electron density map calculated using these phase estimations allows for further improvements in phase estimation. Iterative building and refinement cycles thereafter improve the phase estimations until the atomic model explains the diffraction data as closely as possible such that the phase estimations can be considered correct, though they will never be perfect.

3.4.7 Iodide soaking

To incorporate heavy atoms into our crystals, I adopted two approaches concurrently. The first involved soaking native crystals in mother liquor containing a heavy atom. The success of this method depends upon the heavy atom diffusing through the crystal and associating with the protein at the same location/s in every asymmetric unit of each unit cell of the crystal lattice. I soaked crystals with 100 mM sodium iodide and collected diffraction data using X-rays at the high energy remote wavelength of 1.9074 Å (S1C-01 dataset; dls160416) (Figure 3.4.8a-c and Figure 3.4.9a,b). This wavelength, although not at the absorption edge for iodine, the difference between f' and f'' should mean that any iodide atoms bound at the same location in the asymmetric unit would result in detectable anomalous scattering (Figure 3.4.9a). The data were processed using AutoPROC, scaled in Xscale and merged in aimless (Table 3.5). S1C-01 had unit cell dimensions a= 87.58, b= 46.91, c= 138.71, α= 90, β= 94.90, γ= 90 and belonged to spacegroup $P2_1$. The $I/\sigma I$ value was 1.2 in the outer shell, with data to 2.90 Å. Phenix Xtriage detects measurable anomalous signal to approximately 4.0 Å. Deviation from a linear plot and a non-spherical dispersion of points in the two graphs indicates the presence of detectable anomalous scattering (Figure 3.4.9b). Dr Owen Davies attempted to locate iodide sites using Phenix Autosol, SHELX, hkl2map, and

CRANK2 (Pape and Schneider, 2004; Terwilliger *et al.*, 2009; Sheldrick, 2010; Pannu *et al.*, 2011). However, identified sites correlated with the 5 Å repeat of the Patterson peaks and boasted unrealistic occupancies (in excess of 1) and the phases these provided did not yield sensible electron density maps in which to build.

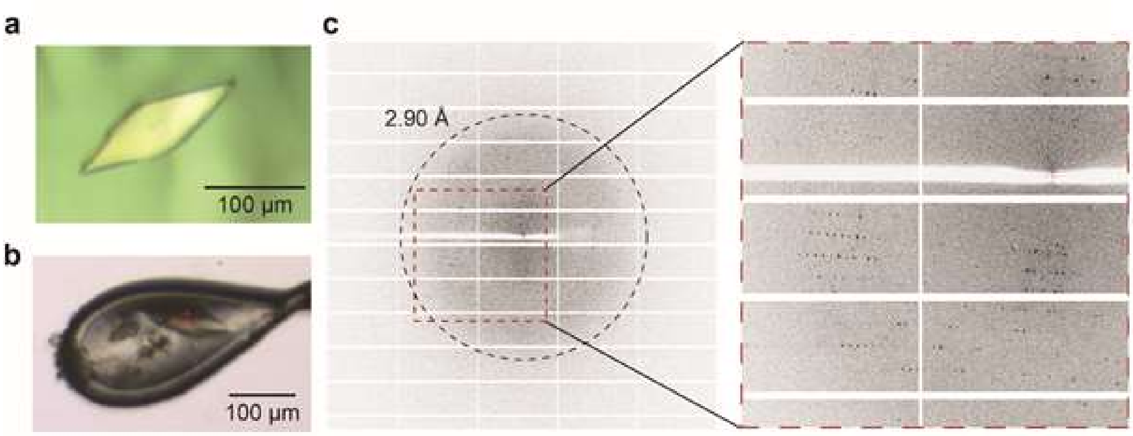

Figure 3.4.8| Soaking SYCP1$_{676\text{-}770}$ crystals in sodium iodide solution to gain phasing information. **a)** Native SYCP1$_{676\text{-}770}$ crystal grown in 14.4 % PEG3350, 90 mM magnesium formate and subsequently soaked in the same solution plus 100 mM sodium iodide and **b)** Crystal positioning within the X-ray beam. **c)** X-ray diffraction image with data to 2.90 Å circled and a close up of low-resolution reflections within a bounding box.

Native data collection for iodide-SYCP1$_{676-770}$ (dataset S1C-01)			
Space group	P2$_1$		
Cell dimensions			
a, *b*, *c* (Å)	87.58, 46.91, 138.71		
α, *β*, *γ* (°)	90, 94.90, 90		
	Overall	Inner Shell	Outer Shell
Low resolution limit (Å)	46.07	46.07	3.08
High resolution limit (Å)	2.90	8.70	2.90
R$_{meas}$ (within I+/I-)	0.173	0.034	1.932
R$_{pim}$ (within I+/I-)	0.107	0.021	1.174
Total number of observations	110674	4122	18005
Total number unique	24564	992	3838
Mean (I/σI)	8.1	32.9	1.2
CC (1/2)	0.996	0.998	0.421
Completeness (%)	96.9	97.5	95.2
Multiplicity	4.5	4.2	4.7
Anomalous completeness	92.0	96.3	91.1
Anomalous multiplicity	2.2	2.5	2.4
DelAnom correlation between half-sets	0.401	0.553	0.222
Mid-slope of Anom Normal Probability	1.303	-	-

Table 3.5| X-ray crystallographic statistics for iodide derivative SYCP1$_{676-770}$. Data processed by Dr Owen Davies

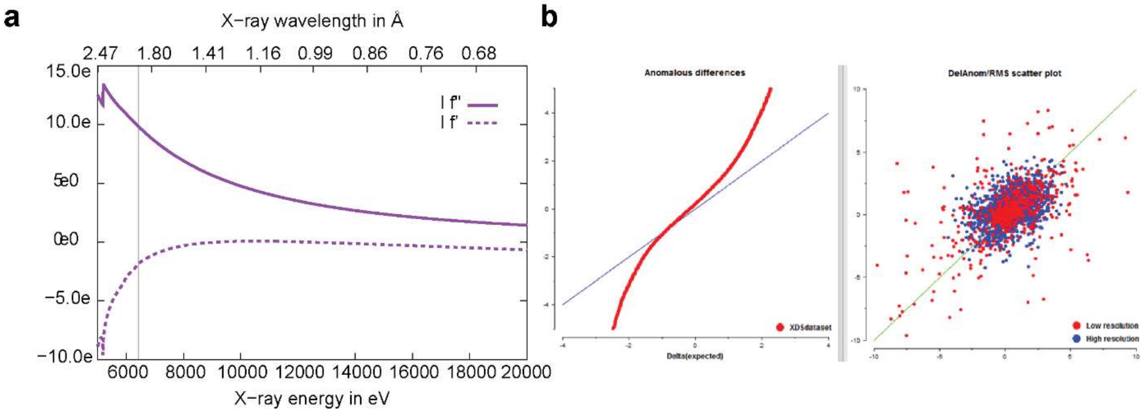

Figure 3.4.9| Anomalous data collection for SYCP1$_{676-770}$ iodide derivative. a) Absorption spectra for iodine. The wavelength at which anomalous data were collected is indicated by a vertical line. **b)** Left plot **-** ΔI/σΔI plot displaying deviance from the normal probability indicating the presence of anomalous scattering. Right plot - A scatter plot correlating two half datasets. A spherical clustering is expected for native data. A lateral spread is indicative of anomalous signal. These graphs were generated by Aimless using S1C-01 data. Data processing performed by Dr Owen Davies.

3.4.8 Seleno-methionine incorporation

Secondly, we incorporated the heavy atom selenium by expressing and purifying a seleno-methionine (SeMet) derivative of SYCP1$_{676\text{-}770}$ as described in Methods section 2.1.17. The SeMet derivative crystallised in 12.75 % PEG3350, 150 mM magnesium formate, 100 mM sodium iodide (Figure 3.4.10). SAD data were collected at the selenium absorption edge (0.9795 Å; dataset S1C-26, dls031015). S1C-26 had unit cell dimensions $a = 89.28$, $b = 47.65$, $c = 139.15$, $\alpha = 90$, $\beta = 96.00$, $\gamma = 90$ and also belonged to the spacegroup P2$_1$. An example diffraction image is displayed in Figure 3.4.10c. Statistics for S1C-26 data collection and scaling statistics using an upper resolution limit of 2.80 Å are detailed in Table 3.6. Phenix Xtriage optimistically detects anomalous signal to 3.8 Å (Figure 3.4.10d,e). MAD data were also collected but were unusable as the individual datasets were collected at non-isomorphous points of the same crystal and resultant data sets could also not be processed.

Native data collection for SeMet-SYCP1$_{676\text{-}770}$ (dataset S1C-26)			
Space group	P2$_1$		
Cell dimensions			
a, *b*, *c* (Å)	89.28, 47.65, 139.15		
α, β, γ (°)	90, 96.00, 90		
	Overall	Inner Shell	Outer Shell
Low resolution limit (Å)	46.13	46.13	2.95
High resolution limit (Å)	2.80	8.85	2.80
R_{meas} (within I+/I-)	0.184	0.039	1.963
R_{pim} (within I+/I-)	0.099	0.021	1.066
Total number of observations	187542	5613	26437
Total number unique	29178	990	4189
Mean (I/σI)	8.1	36.1	1.4
CC (1/2)	0.998	0.999	0.717
Completeness (%)	99.6	98.1	99.6
Multiplicity	6.4	5.7	6.3
Anomalous completeness	98.7	96.3	98.8
Anomalous multiplicity	3.3	3.2	3.2
DelAnom correlation between half-sets	0.404	0.552	0.038
Mid-slope of Anom Normal Probability	1.175	-	-

Table 3.6| X-ray crystallographic statistics for seleno-methionine SYCP1$_{676\text{-}770}$. Data processed by Dr Owen Davies

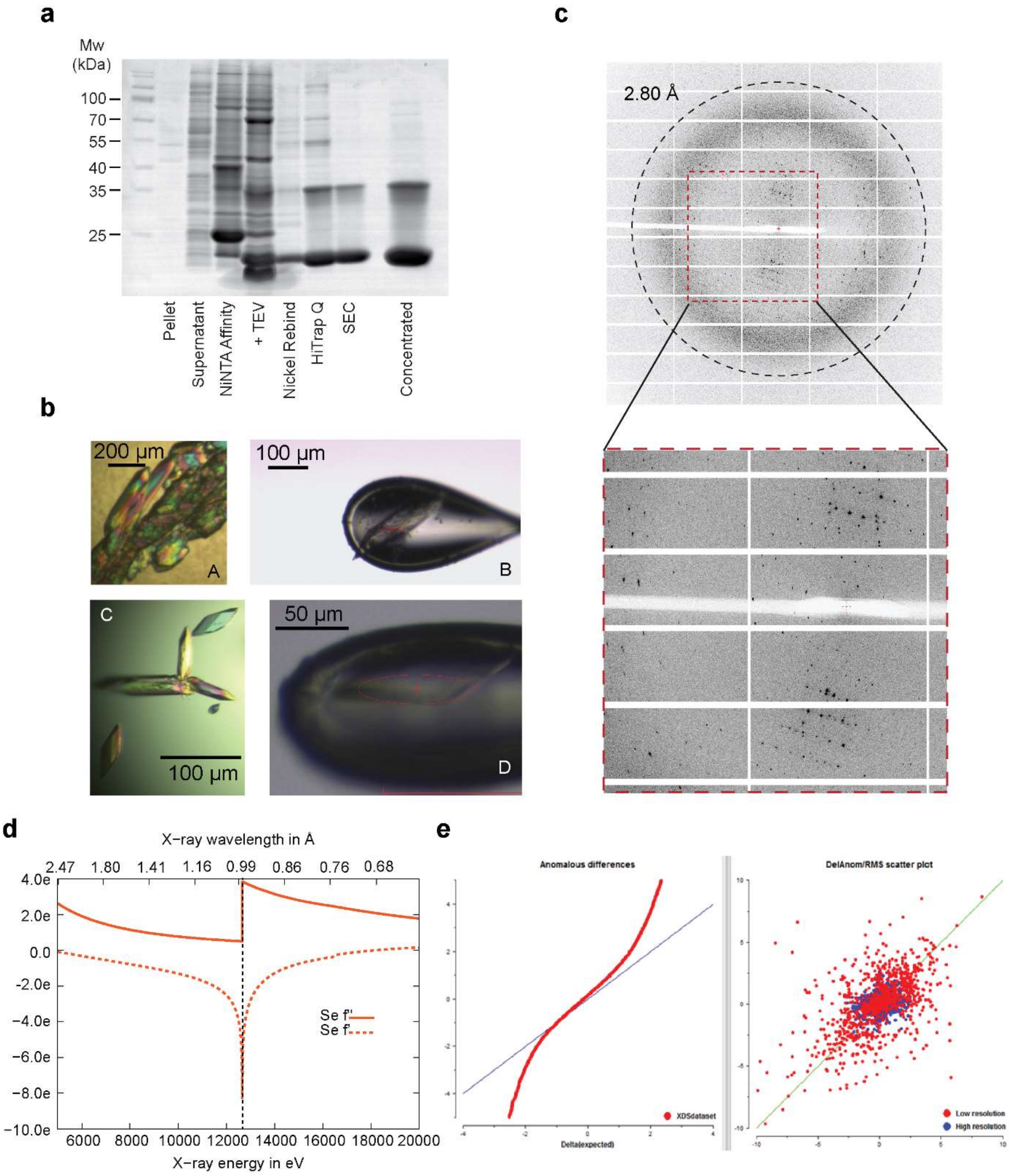

Figure 3.4.10| Seleno-methionine derivate SYCP1$_{676\text{-}770}$ crystals. a) SDS-PAGE analysis of samples summarising the purification of seleno-methionine SYCP1$_{676\text{-}770}$. **b)** SeMet-SYCP1$_{676\text{-}770}$ crystals grown in 12.75 % PEG3350, 150 mM magnesium formate, 0.1 M sodium iodide and 12.5 % PEG3350, 150 mM magnesium formate with their respective mountings at the beamline. **c)** X-ray diffraction image for SeMet-SYCP1$_{676\text{-}770}$ with data to 2.80 Å circled and a close up of low-resolution reflections in bounding box. **d)** Absorption spectra for selenium. X-ray diffraction data were collected at 0.9795 Å, indicated by a vertical dashed black line. **e)** Left plot **-** ΔI/σΔI plot displaying deviance from the normal probability indicating the presence of anomalous scattering. Right plot - A scatter plot correlating two half datasets. A spherical clustering is expected for native data. A lateral spread is indicative of anomalous signal. These graphs were generated by Aimless using S1C-26 data input.

3.4.9 SYCP1$_{676\text{-}770}$ crystallisation

Reinspection of the initial crystallisation screens for SYCP1$_{676\text{-}770}$ after 2 months revealed previously absent crystal hits in Structure A12 (0.1 M sodium cacodylate pH 6.5, 1.4 M sodium acetate) and Index C1 (3.5 M sodium formate pH 7.0) (Figure 3.4.11a,b). Crystals from INDEX C1 and Structure A12 conditions were transferred to 6 M sodium formate pH 7.0 and 0.1 M sodium cacodylate pH 6.5, 1.4 M sodium acetate, 20 % PEG400, respectively, and cryo-cooled in liquid nitrogen. X-ray diffraction data were collected at Diamond Light Source, Oxfordshire, UK.

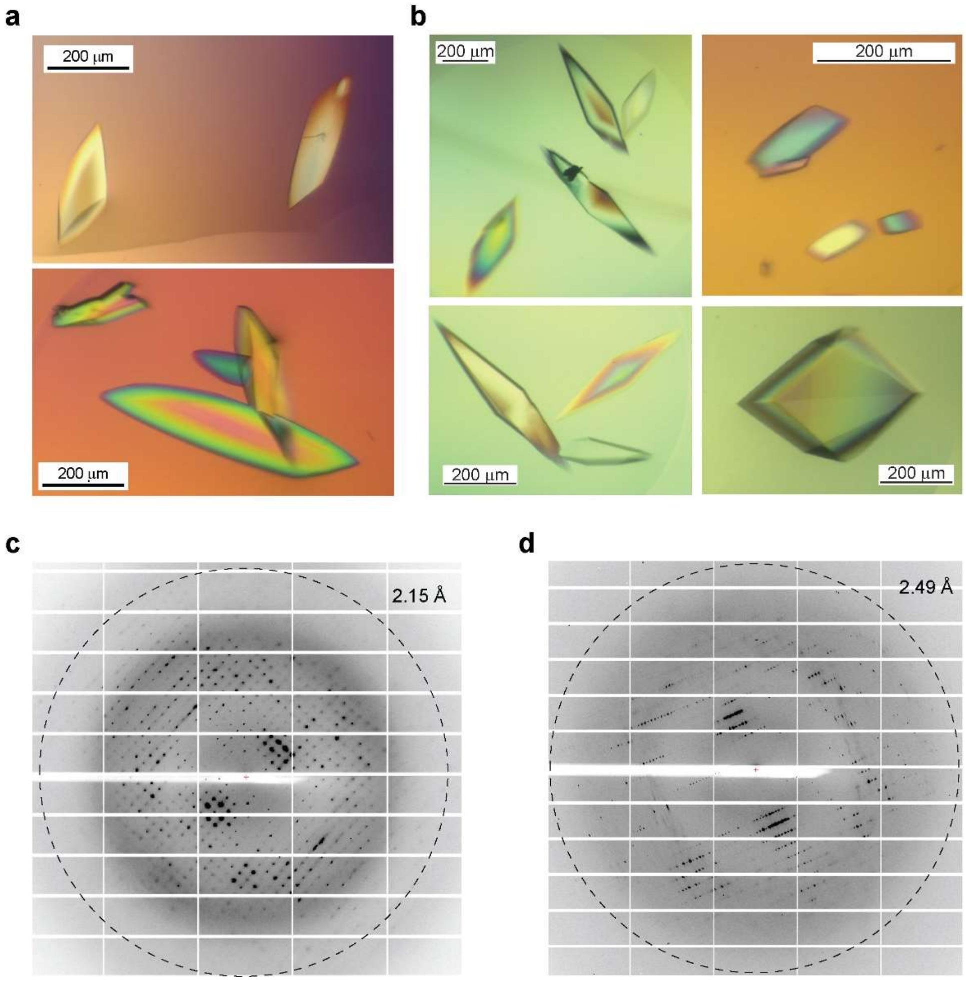

Figure 3.4.11| Crystallisation and X-ray diffraction collection for SYCP1$_{676\text{-}770}$. a) SYCP1$_{676\text{-}770}$ crystals grown in Index C1 - 3.5 M sodium formate pH 7.0. **b)** SYCP1$_{676\text{-}770}$ crystals grown in Structure A12 - 0.1 M sodium cacodylate pH 6.5, 1.4M sodium acetate. **c)** X-ray diffraction image for SYCP1$_{676\text{-}770}$ crystal from Index C1. **d)** X-ray diffraction image for SYCP1$_{676\text{-}770}$ crystal from Structure A12.

3.4.10 Structure solution of SYCP1$_{676\text{-}770}$ in spacegroup I4$_1$22

SYCP1$_{676\text{-}770}$ crystals of condition Structure A12 (0.1 M sodium cacodylate pH 6.5, 1.4 M sodium acetate) diffracted to 2.49 Å and were found to contain a lattice of unit cells with dimensions a = 43.38 Å, b = 43.38 Å, c = 292.18 Å, α = 90°, β = 90°, γ = 90° and belonged to the tetragonal spacegroup I4$_1$22 (data were processed by Dr Owen Davies as described in the Methods section 2.1.17. Calculation of the Matthew's coefficient revealed that the asymmetric unit contained a single SYCP1 chain per asymmetric unit. The structure was solved by Dr Isabel Usón using ARCIMBOLDO_LITE and subsequently built and refined by Dr Owen Davies. (S1C-13; dls160416; Table 3.7) (Rodriguez *et al.*, 2009).

In contrast to our biophysical analysis of SYCP1$_{676\text{-}770}$ in solution, which demonstrated an elongated coiled-coil conformation, within the X-ray crystal structure of SYCP$_{676\text{-}770}$, two parallel coiled-coil dimers assemble back-to-back to form an anti-parallel four α-helical bundle (Figure 3.4.12a). I propose that this distinct conformation represents an assembled form of SYCP1$_{676\text{-}770}$ which underpins a mechanism by which the C-terminus of SYCP1 may assemble at the chromosome axis.

Data collection for SYCP1$_{676\text{-}770}$ (dataset S1C-13)		
Space group	I4$_1$22	
Cell dimensions		
a, b, c (Å)	43.38, 43.38, 292.18	
α, β, γ (°)	90.00, 90.00, 90.00	
	Overall	Outer Shell
Low resolution limit (Å)	42.91	2.48
High resolution limit (Å)	2.58	2.48
R_{merge} (all I+ & I-)	0.080	2.567
R_{pim} (all I+ & I-)	0.023	0.727
$I / \sigma I$	14.8	1.5
$CC_{1/2}$	1.000	0.935
Completeness (%)	99.8	99.7
Multiplicity	13.2	13.2
Refinement		
Resolution (Å)	39.62 – 2.49	
UCLA anisotropy (Å)	2.9, 2.9, 2.5	
Number of reflections	4138	
R_{work} / R_{free}	0.2251 / 0.2517	
Number of atoms	806	
Protein	786	
Ligand/ion	4	
Water	16	
B-factors	60.86	
Protein	60.80	
Ligand/ion	81.59	
Water	58.92	
R.m.s deviations		
Bond lengths (Å)	0.004	
Bond angles (°)	0.575	

Table 3.7| X-ray crystallographic statistics for SYCP1$_{676\text{-}770}$ (I4$_1$22). Data processed by Dr Owen Davies

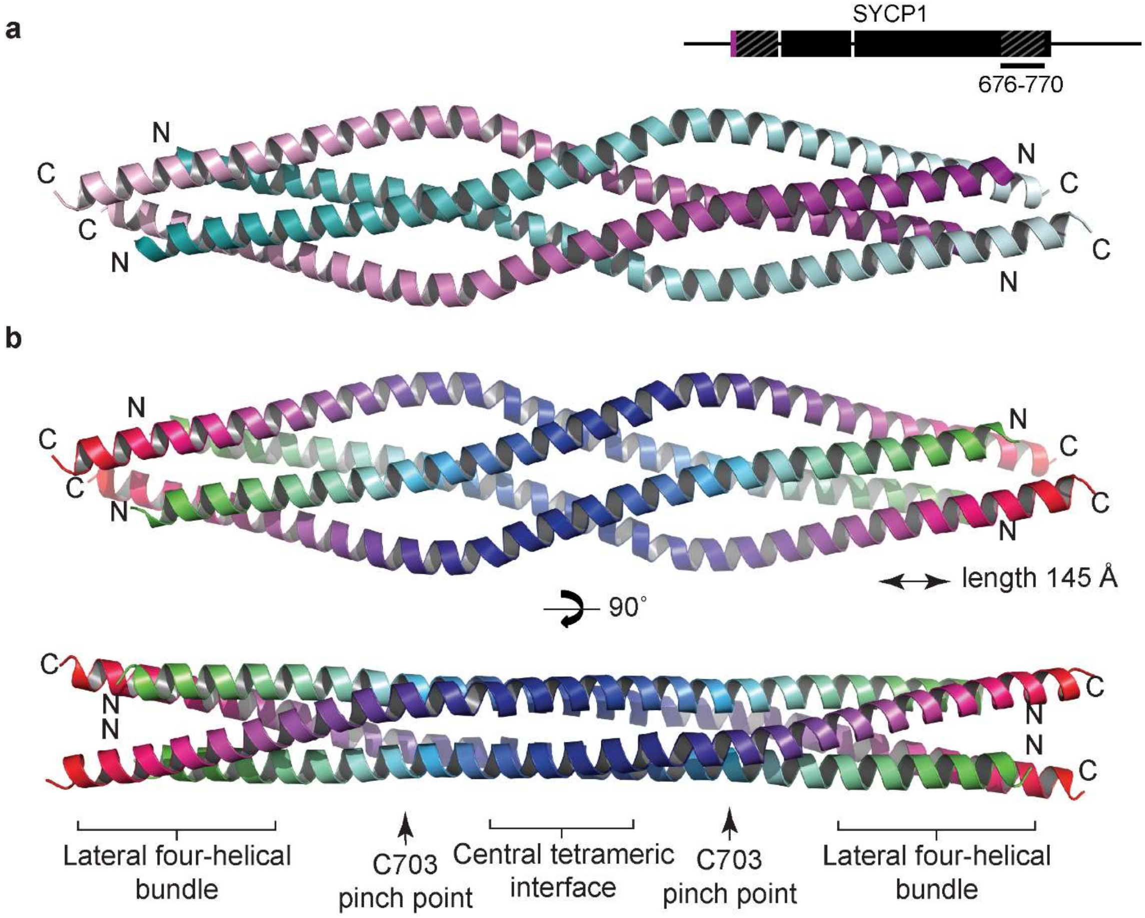
a
SYCP1
676-770
N
C
C
N
N
C
C
N
b
N
C
C
N
N
C
C
N
length 145 Å
90˚
C
N
N
C
N
N
C
Lateral four-helical bundle
C703 pinch point
Central tetrameric interface
C703 pinch point
Lateral four-helical bundle

Figure 3.4.12| The SYCP1$_{676-770}$ crystal structure (I4$_1$22) reveals an anti-parallel association of parallel chains. a) Crystal structure of SYCP1$_{676-770}$, revealing an anti-parallel association of two parallel dimers coloured in blue (N-termini in deep teal to the C-termini in pale cyan) and purple (N-termini in deep purple and the C-termini in light pink). **b)** Alternative colouring scheme, with N-termini in green and C-termini in red, to highlight the anti-parallel tetrameric organisation of the chains within the structure, emphasising the presence of a central tetrameric interface (in blue). The structure measures 142 Å in length. The central tetrameric interface with flanking C703 pinch points (partially oxidised) and two lateral interfaces.

3.4.11 The SYCP1$_{676-770}$ I4$_1$22 crystal lattice

The I4$_1$22 crystal lattice is formed through the symmetric, lateral, anti-parallel association of α-helical chains of biological tetramers angled at 90˚ to one another (Figure 3.4.13a). The interface is mediated by two symmetry related sets of interactions comprising two salt bridges (formed between Q740 and S748 (2.4 Å) and E752 and K736 (3.4 Å)) and the coordination of an acetate molecule by residues E759 and D729, each (Figure 3.4.13b,c).

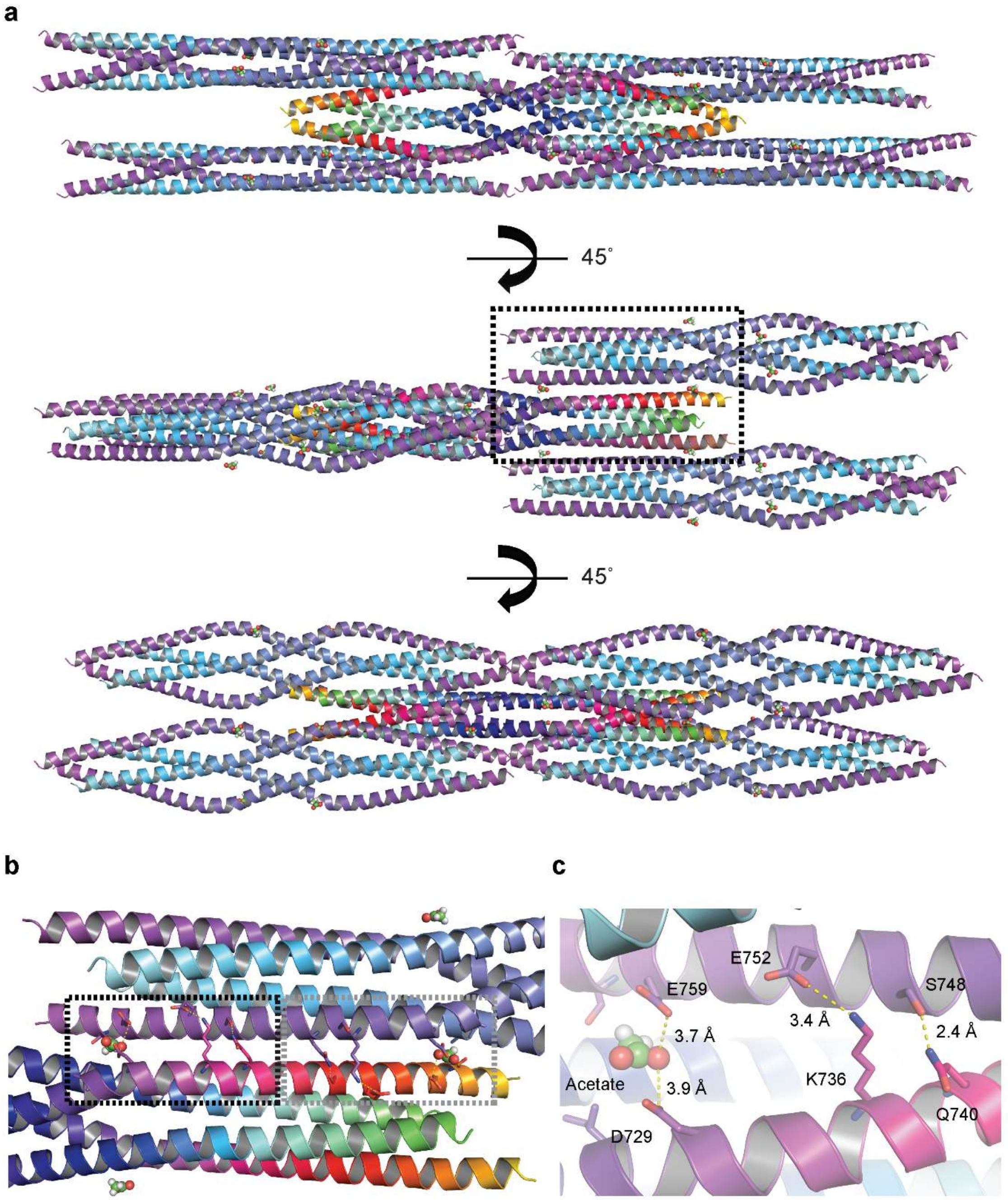

Figure 3.4.13| The details of the SYCP1$_{676\text{-}770}$ I4$_1$22 crystal lattice. a) A single four-chain biological assembly of SYCP1$_{676\text{-}770}$ coloured yellow to green, with four symmetry related tetramers making identical anti-parallel associations between laterally orientated chains, displayed in a series of 45˚ rotations. **b)** The region bounded in **a** is shown with two symmetry related sets of side chains forming salt bridge crystal contacts and acetate mediated crystal contact. A single set is bounded by a dashed box. **c)** Crystal contacts are mediated by a salt bridge between residues Q740 to S748, K736 to E752 whilst an acetate ion is coordinated by D729 and E759.

3.4.12 Structure solution of SYCP1$_{676\text{-}770}$ in spacegroup C2

SYCP1$_{676\text{-}770}$ crystals of condition Index C1 (3.5 M sodium formate pH 7.0) diffracted to 2.15 Å and were found to contain a lattice of unit cells with dimensions a = 233.42 Å, b = 42.85 Å, c = 43.69 Å, α = 90°, β = 93.61°, γ = 90° and belonged to the monoclinic spacegroup C2 (S1C-14; dls220216; Table 3.8). Calculation of the Matthew's coefficient estimated the presence of four SYCP1 chains per asymmetric unit (Matthews, 1968; Kantardjieff and Rupp, 2003). Dr Isabel Usón utilised ARCIMBOLDO_SHREDDER and the I4$_1$22 structure to generate fragments, and subsequently models, which were used to solve the structure by molecular replacement (solution strategy described in full in Methods section 2.1.17-18 (Figure 3.4.14a) (Millán, 2017).

Data collection for SYCP1$_{676\text{-}770}$ (dataset S1C-14)		
Space group	C2	
Cell dimensions		
a, b, c (Å)	233.42, 42.85, 43.69	
α, β, γ (°)	90.00, 93.61, 90.00	
	Overall	Outer Shell
Low resolution limit (Å)	116.48	2.15
High resolution limit (Å)	2.27	2.15
R_{merge} (all I+ & I-)	0.052	0.695
R_{pim} (all I+ & I-)	0.032	0.429
$I / \sigma I$	12.4	1.9
$CC_{1/2}$	0.998	0.872
Completeness (%)	97.4	88.0
Multiplicity	3.6	3.5
Refinement		
Resolution (Å)	58.26 – 2.15	
UCLA anisotropy (Å)	2.2, 2.3, 2.2	
Number of reflections	21416	
R_{work} / R_{free}	0.2186 / 0.2526	
Number of atoms	3318	
Protein	3143	
Ligand/ion	0	
Water	175	
B-factors	46.97	
Protein	47.30	
Ligand/ion	N/A	
Water	41.20	
R.m.s deviations		
Bond lengths (Å)	0.004	
Bond angles (°)	0.511	

Table 3.8| X-ray crystallographic statistics for SYCP1$_{676\text{-}770}$ (C2). Data processed by Dr Owen Davies

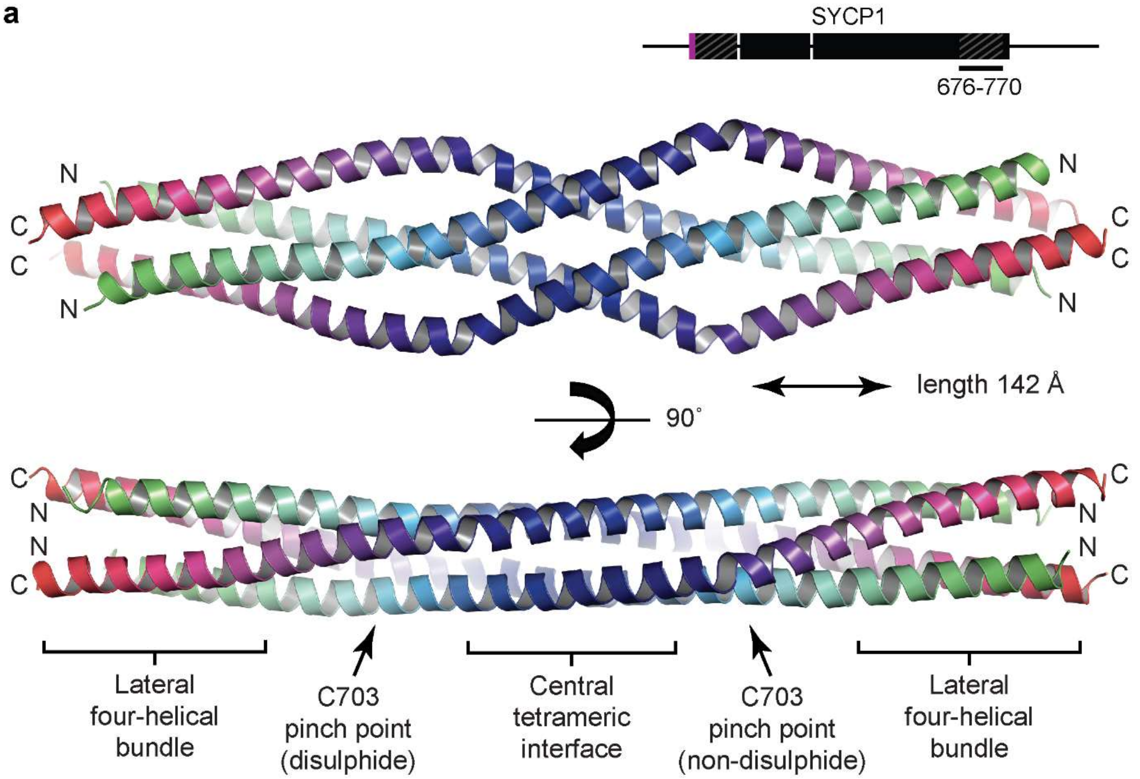
a
SYCP1
676-770
N
C
C
N
N
C
C
N
length 142 Å
90˚
C
N
N
C
C
N
N
C
Lateral four-helical bundle
C703 pinch point (disulphide)
Central tetrameric interface
C703 pinch point (non-disulphide)
Lateral four-helical bundle

Figure 3.4.14| The almost identical structure of SYCP1$_{676\text{-}770}$ in spacegroup C2. a) Crystal structure of SYCP1$_{676\text{-}770}$ in spacegroup C2, revealing an anti-parallel association of parallel dimers with a length 142 Å, with N-termini in green and C-termini in red. Similar to the I4$_1$22 structure, the structure can be divided into a central tetrameric interface with flanking C703 pinch points and two lateral interfaces. However, in contrast to the I4$_1$22 structure, one C703 pinch point is oxidised, and the other is reduced.

3.4.13 An analysis of the SYCP1$_{676\text{-}770}$ crystal structures

The C2 crystal lattice, having four chains per asymmetric unit, is stabilised by many more discrete associations than the I4$_1$22 structure, but is largely mediated through salt bridges between laterally orientated chains. The following structural analysis is based up the higher resolution, lower symmetry, C2 structure, though specific elements will be compared between the structures throughout. The structure is stabilised at two key regions: a central tetrameric interface and flanking lateral interfaces, adjoined through intermediate sequence (Figure 3.4.14a). Following the sequence from N to C-terminus, two parallelly orientated chains stabilised as part of an anti-parallel four-helical association at the lateral interface, described shortly, converge at a pinch point centred at C703. In the C2 spacegroup, these form disulphide and non-disulphide bonds at rigid and loose ends of the structure, respectively, whereas in the I4$_1$22 structure, symmetry related pinch points display partial disulphide bonds (compared in Figure 3.4.16). Parallel chains emanating from the central interface diverge, splaying to a maximal spatial separation of ~30 Å to flank the C703 pinch points, which exist in either oxidised or reduced states. Within the I4122, pinch sites are partially oxidised and whilst in the C2 structure one pinch site is oxidised and exhibits a smooth chain angulation and decreased-factors, whilst the other is reduced and exhibits a sharp angulation about E731 with comparatively increased B-factors (Figure 3.4.15a,b and Figure 3.4.16a-e). This difference in angulation is particularly pronounced in Figure 3.4.16b and is indicated with an arrow.

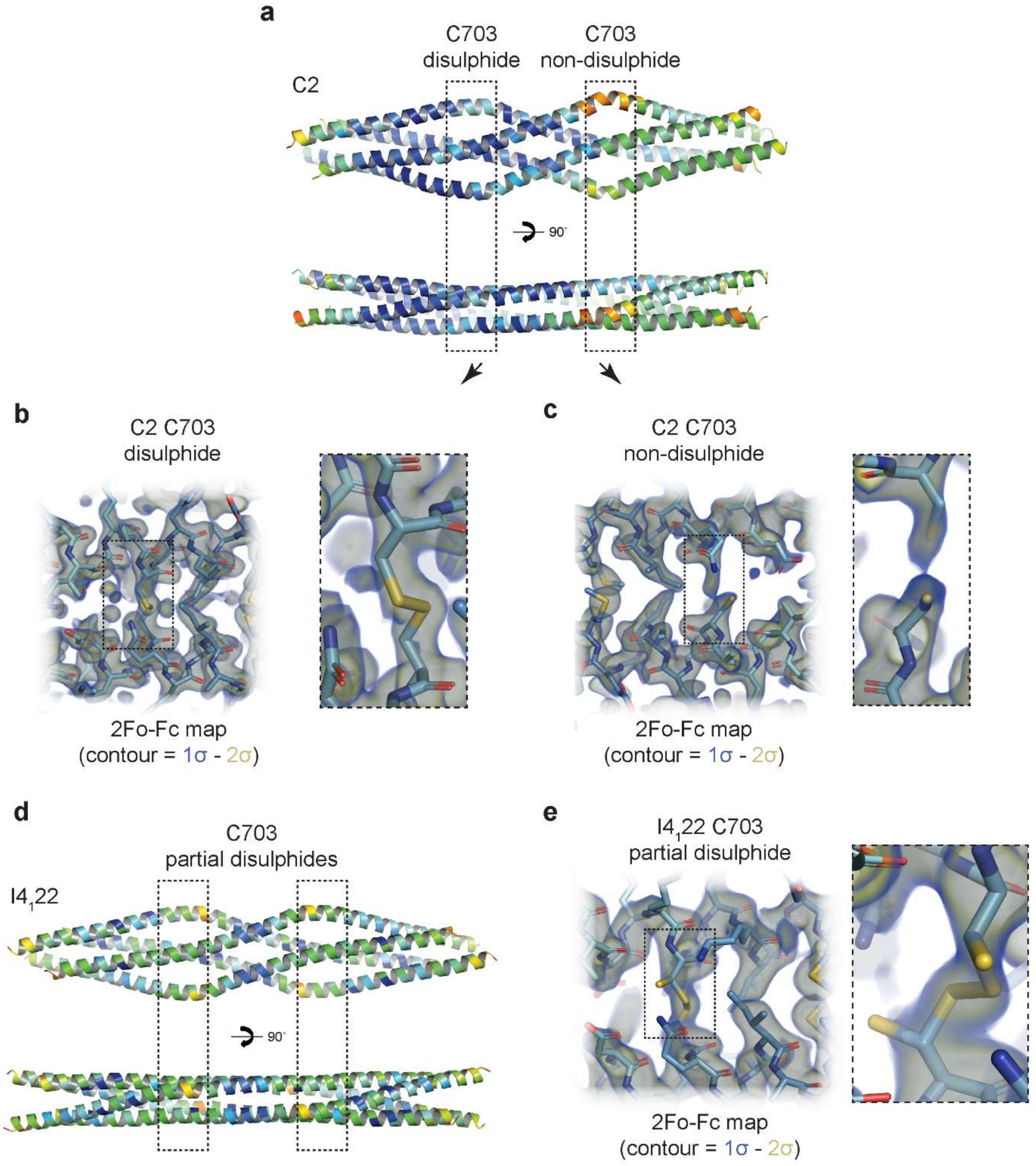
a
C703
disulphide
C703
non-disulphide
C2
90°
b
C2 C703
disulphide
2Fo-Fc map
(contour = 1σ - 2σ)
c
C2 C703
non-disulphide
2Fo-Fc map
(contour = 1σ - 2σ)
d
C703
partial disulphides
I4$_1$22
90°
e
I4$_1$22 C703
partial disulphide
2Fo-Fc map
(contour = 1σ - 2σ)

Figure 3.4.15| Oxidation of C703 decreases chain flexibility. a) The C2 structure of SYCP1$_{676-770}$ coloured by B-factor (Blue= low B-factor, Red/orange= high B-factor). The C2 structure demonstrates the lowest B-factors at the tetrameric interface and on the smoothly angulated, oxidised end of the structure (left side). **b)** Electron density map with the docked model of the C2 structure. Residues C703 forming a disulphide linkage are presented. **c)** Electron density map with the docked model of the C2 structure. Reduced residues C703 not forming a disulphide linkage are presented. **d)** The I4$_1$22 structure (coloured by B-factor) demonstrates the lowest B-factors at the tetrameric interface with relative flexibility at partially oxidised C703 pinch points, when compared to the oxidised end of the C2 structure. **e)** Electron density map with the docked model of the I4$_1$22 structure. Residues C703 forming a partial disulphide linkage are shown.

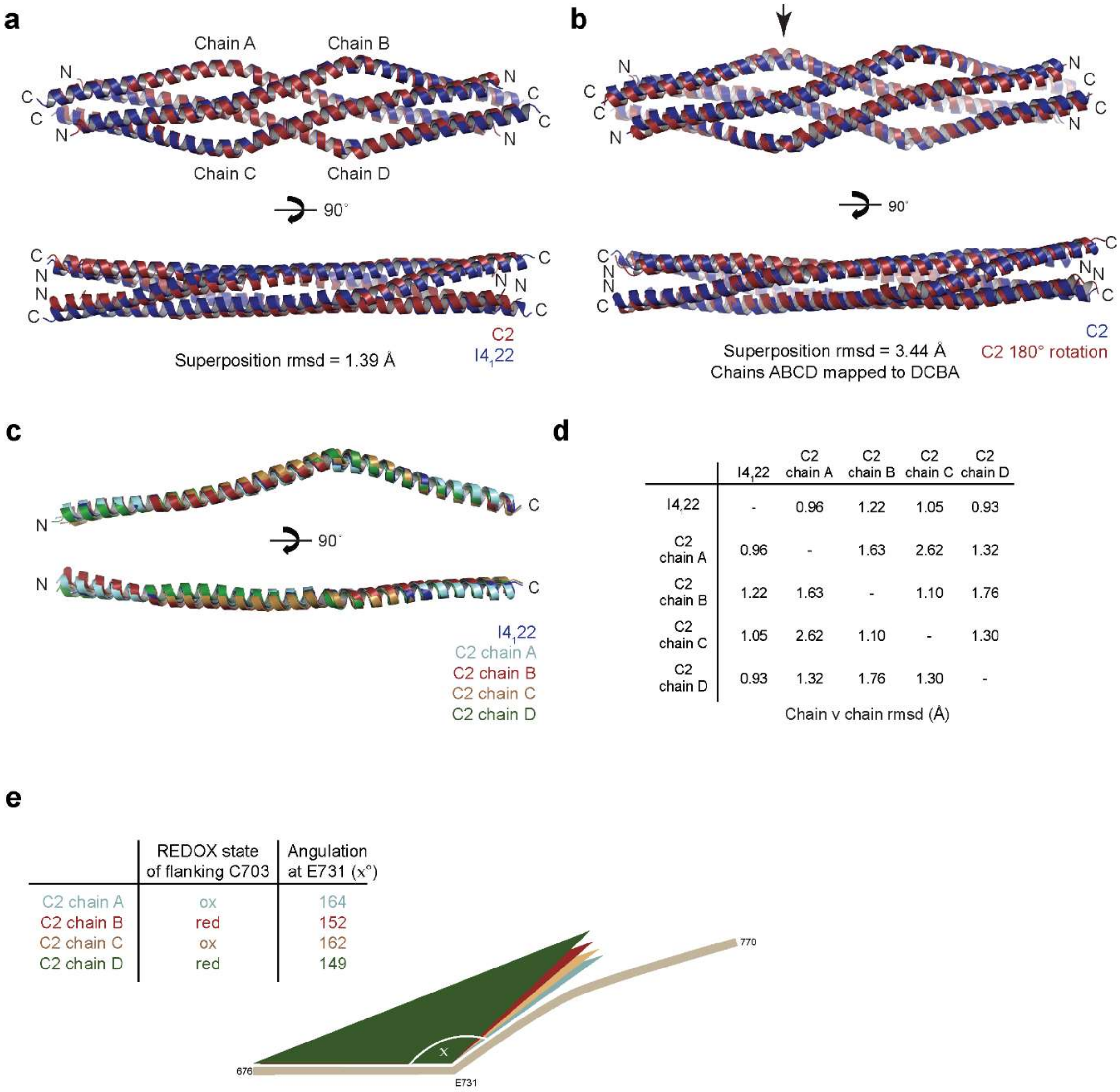
a
Chain A
Chain B
Chain C
Chain D
N
C
90°
C2
I4$_1$22
Superposition rmsd = 1.39 Å
b
90°
C2
C2 180° rotation
Superposition rmsd = 3.44 Å
Chains ABCD mapped to DCBA
c
N
C
90°
I4$_1$22
C2 chain A
C2 chain B
C2 chain C
C2 chain D
d
e
676
E731
770
x

	I4$_1$22	C2 chain A	C2 chain B	C2 chain C	C2 chain D
I4$_1$22	-	0.96	1.22	1.05	0.93
C2 chain A	0.96	-	1.63	2.62	1.32
C2 chain B	1.22	1.63	-	1.10	1.76
C2 chain C	1.05	2.62	1.10	-	1.30
C2 chain D	0.93	1.32	1.76	1.30	-

Chain v chain rmsd (Å)

	REDOX state of flanking C703	Angulation at E731 (x°)
C2 chain A	ox	164
C2 chain B	red	152
C2 chain C	ox	162
C2 chain D	red	149

Figure 3.4.16| Comparison of SYCP1$_{676\text{-}770}$ in spacegroups I4$_1$22 and C2. a) Superimposition of forms 1 (red) and 2 (blue) highlighting overall similarity with rmsd 1.39 Å. **b)** Superimposition of chains A, B, C, D to chains D, C, B, A of the C2 (form 1) structure, representing a 180˚ rotation with an rmsd of 3.44 Å, demonstrating internal asymmetry largely due to backbone differences between the smooth oxidised end and angulated reduced end of the structure. **c)** Superimposition of chains A, B, C, D of form 1 (C2) structure with the sole chain of the I4$_1$22 form 2 structure with rmsd values indicated. **d)** Chain vs chain rmsd values for superimposition of unique SYCP1$_{676\text{-}770}$ chains of the I4122 and C2 structures **e)** The angulation of chains A, B, C and D about E731 are detailed, stating the oxidation state of the flanking C703 residues. The chain is more angulated when flanked by reduced C703 residues (chains A and C).

3.4.14 The SYCP1$_{676-770}$ tetrameric interface

After the C703 pinch points, the sequence continues into a tetrameric interface mediated by a highly conserved hydrophobic core of H717 and Y721 (Figure 3.4.17a). In this, aromatic stacking between H717 imidazole groups (Figure 3.4.17b; 3.3 - 3.4 Å) and a hydrogen bonding network (detailed in Figure 3.4.17c-e) collaborate to stabilise the fold. Briefly, the hydroxyl group of Y721 hydrogen bonds with the amine group (Nδ1) of H717 which in turn, through its second amine group (Nε2) hydrogen bonds with the hydroxyl group of Q720. The hydroxyl groups of Y721 further coordinate a centrally located water molecule (Figure 3.4.17a,c,d). Within the C2 structure, this water molecule is coordinated by four tyrosine hydroxyl groups through two short and two long hydrogen bonds (Figure 3.4.17c). The short hydrogen bonds are likely formed between the hydrogen of the two tyrosine hydroxyl groups and a lone pair of electrons of the water molecule's oxygen whilst the longer hydrogen bonds are likely formed between the two hydrogens of the water and a lone pair of electrons of the other two tyrosine hydroxyl oxygens. Within the $I4_122$ structure, however, the water molecule would be placed at a special position and so, crystallographically, should not exist. Re-processing in a low symmetry spacegroup might reveal whether it is present or not. Assuming its presence, the four tyrosine side chains are positioned equidistant from the water's oxygen. Regardless, the hydrogen bonding network should be satisfied in the presence or absence of this water molecule.

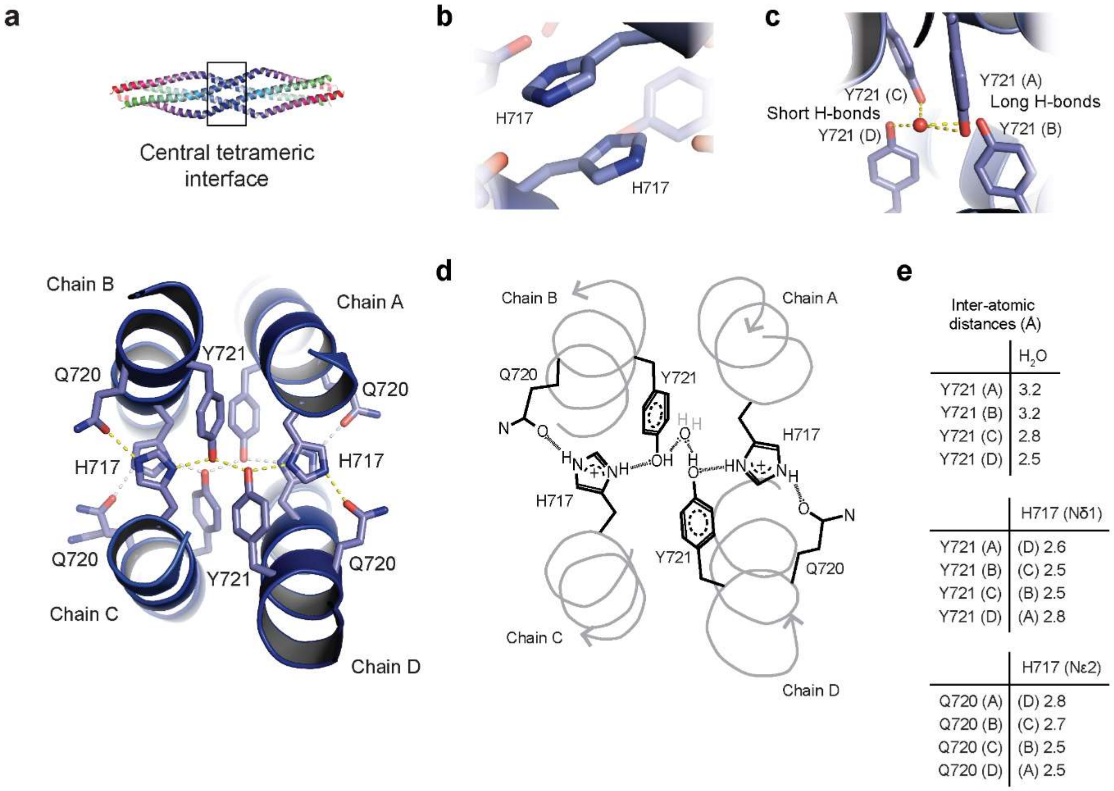
a
Central tetrameric interface
b
H717
H717
c
Y721 (C)
Short H-bonds
Y721 (D)
Y721 (A)
Long H-bonds
Y721 (B)
Chain B
Chain A
Y721
Q720
Q720
H717
H717
Q720
Q720
Y721
Chain C
Chain D
d
Chain B
Chain A
Q720
Y721
N
O
HN
+
NH
OH
O
H H
H
O
HN
+
NH
H717
H717
O
N
Y721
Q720
Chain C
Chain D
e

Inter-atomic distances (Å)

	H_2O
Y721 (A)	3.2
Y721 (B)	3.2
Y721 (C)	2.8
Y721 (D)	2.5

	H717 (Nδ1)
Y721 (A)	(D) 2.6
Y721 (B)	(C) 2.5
Y721 (C)	(B) 2.5
Y721 (D)	(A) 2.8

	H717 (Nε2)
Q720 (A)	(D) 2.8
Q720 (B)	(C) 2.7
Q720 (C)	(B) 2.5
Q720 (D)	(A) 2.5

Figure 3.4.17| A hydrogen bonding network and aromatic stacking stabilised the tetrameric interface. a) The central tetrameric interface is formed of two stacked layers containing residues H717 and Y721 which in coordination with distal Q720 form two discrete hydrogen bonding networks. The layers are related through aromatic stacking of H717 and potential coordination of a single water molecule shared between four tyrosine residues. **b)** H717 residues stack through π-π stacking. **c-e)** Details of the hydrogen bond network within the tetrameric interface. Hydrogen bonds are assigned donor and acceptor atoms within 2.6 – 3.3 Å. **c)** Four tyrosine residues coordinate a single water molecule. Y721 from chains C and D associate through short hydrogen bonds whilst Y721 of chains A and B associate through long hydrogen bonds. **d)** Cartoon diagram of a single hydrogen-bond network forming layer of Q720, H717 and Y721 with atomistic details. Hydrogen bonds are represented by dashed lines. **e)** The distances between donor and acceptor atoms involved in each hydrogen bond are detailed.

3.4.15 The SYCP1$_{676\text{-}770}$ lateral interfaces

The two chains subsequently re-converge at four-helical lateral interfaces stabilised by hydrophobic cores coupled with anti-parallel coiled-coil interactions (Figure 3.4.18a-c). The heptad repeat residues predicted to stabilise the C-terminal end of the coiled-coil dimer through formation of a leucine zipper (L760, V763, L767) form similar interactions in this structure, with further contribution from residues L749, L753, L756 and N-terminal residues L678, V682, A685, A689, A692 which do not fall into a traditional heptad repeat sequence. Notably, residues L679 and I688, which do not appear to be involved in dimer stabilisation, appear to mediate associations between anti-parallel chains so may be specific to tetramer stabilisation.

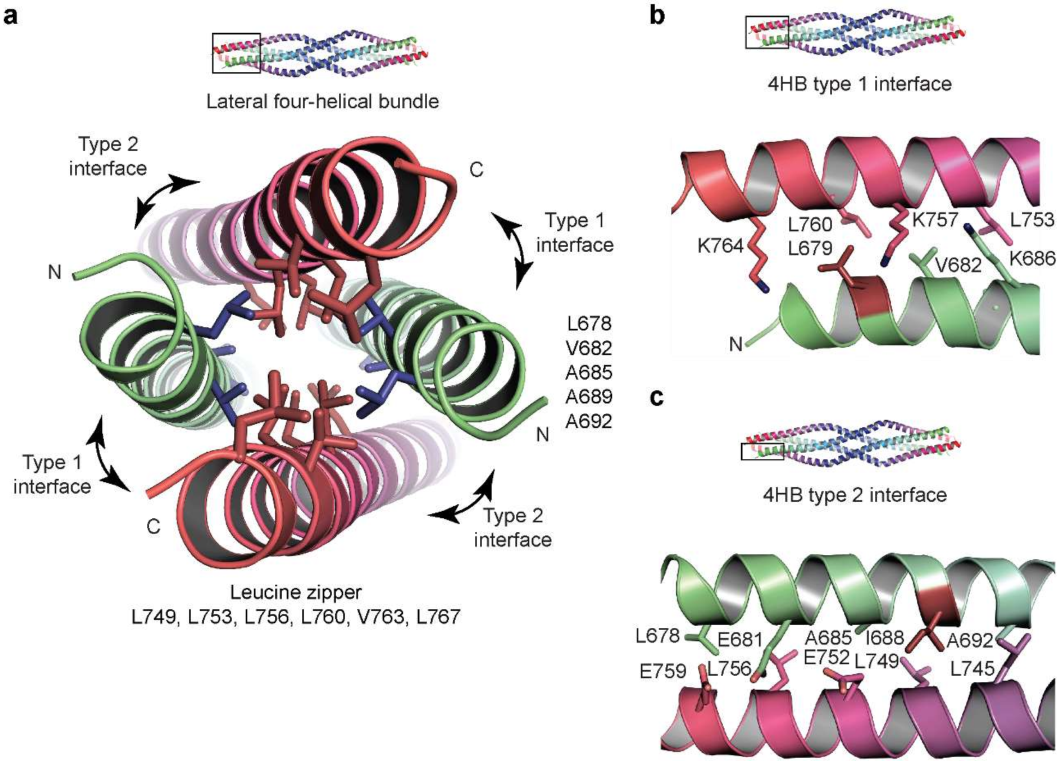
a
Lateral four-helical bundle
Type 2 interface
C
Type 1 interface
N
L678
V682
A685
A689
A692
N
Type 1 interface
C
Type 2 interface
Leucine zipper
L749, L753, L756, L760, V763, L767
b
4HB type 1 interface
K764
L760
L679
K757
L753
V682
K686
N
c
4HB type 2 interface
L678
E681
A685
I688
A692
E759
L756
E752
L749
L745

Figure 3.4.18| The lateral interface of the SYCP1$_{676\text{-}770}$ tetramer is stabilised by coiled-coil type interactions. a) The lateral interface forms a hydrophobic core of residues which further contribute to the anti-parallel association of helical chains. L679 and I688 are highlighted in blue as being the sole residues which mediate only contacts between anti-parallel chains. **b)** The type 1 interface is formed through the anti-parallel coiled-coil association of L679, V682 and K686, L753, K757, L760 and K764. **c)** The type 2 interface is mediated by the anti-parallel association of heptad residues L678, E681, A685, I688 and A692, L745, L749, E752, L756 and E759.

3.4.16 Identification of the solution conditions required for assembly

The structure of SYCP1$_{676\text{-}770}$ immediately suggested that it may represent an assembled form of the elongated, dimeric form previously observed in solution and might provide the structural basis of a mechanism by which SYCP1 can assemble via its C-terminus at the chromosome axis. I sought to determine the conditions in solution which can trigger this assembly.

3.4.17 The SYCP1$_{676\text{-}770}$ undergoes dynamic remodelling in response to pH changes

Due to the integral role of histidine residue H717 within the tetrameric core of the SYCP1$_{676\text{-}770}$ structure, I predicted its protonation might be required to trigger assembly in solution. Therefore, I reduced the pH of samples by their dilution in 100 mM sodium acetate pH 4.6 or 5.5, 150 mM or 1 M KCl. SYCP1$_{676\text{-}770}$ precipitated at pH 4.6 and therefore a screen was performed, diluting SYCP1$_{676\text{-}770}$ in buffers with a series of pH values (from 4.6 to 5.5) and found it remained in solution at pH 5.5 (Figure 3.4.20a). SYCP1$_{676\text{-}783}$ and SYCP1$_{640\text{-}783}$ remained soluble at pH 4.6. SEC-MALS revealed a dimer to tetramer oligomeric shift for SYCP1$_{676\text{-}770}$ at pH 5.5 also observed for SYCP1$_{676\text{-}783}$ and SYCP1$_{640\text{-}783}$ (to a lesser extent) at pH 4.6 (Figures 3.4.20c-e). SYCP1$_{676\text{-}783}$ was ~50 % tetrameric at pH 5.2 (Figure 3.4.20d). SYCP1$_{676\text{-}783}$ and SYCP1$_{640\text{-}783}$ contain additional coiled-coil sequence which is glutamate-rich which may both act as a buffer and stabilise the dimeric form through additional coiled-coil interactions, accounting for the requirement of a lower pH. Interestingly, tetramerization was inhibited by the oxidation of the sample prior to dilution (Figure 3.4.27e). We performed further SEC-SAXS on SYCP1$_{676\text{-}770}$ at pH 5.5, revealing a length of 161 Å (compared to 143 Å at pH 8.0) and cross-sectional radii of 10.1 Å (compared to 7.8 Å at pH 8.0) in keeping with a dimer to tetramer transition (Figure 3.4.21a-d). Whilst the dimensions of the solution dimer closely match those of a dimeric coiled-coil, those of the solution tetramer closely match those of the crystal structure. The crystal structure was docked into an *ab initio* molecular envelope using SUPCOMB (Figure 3.4.21e,f). SEC-SAXS analysis of SYCP1$_{676\text{-}783}$ at pH 8.0 and 4.6 confirmed that assembly of the extended molecule occurs in the same manner (Figure 3.4.22a-f).

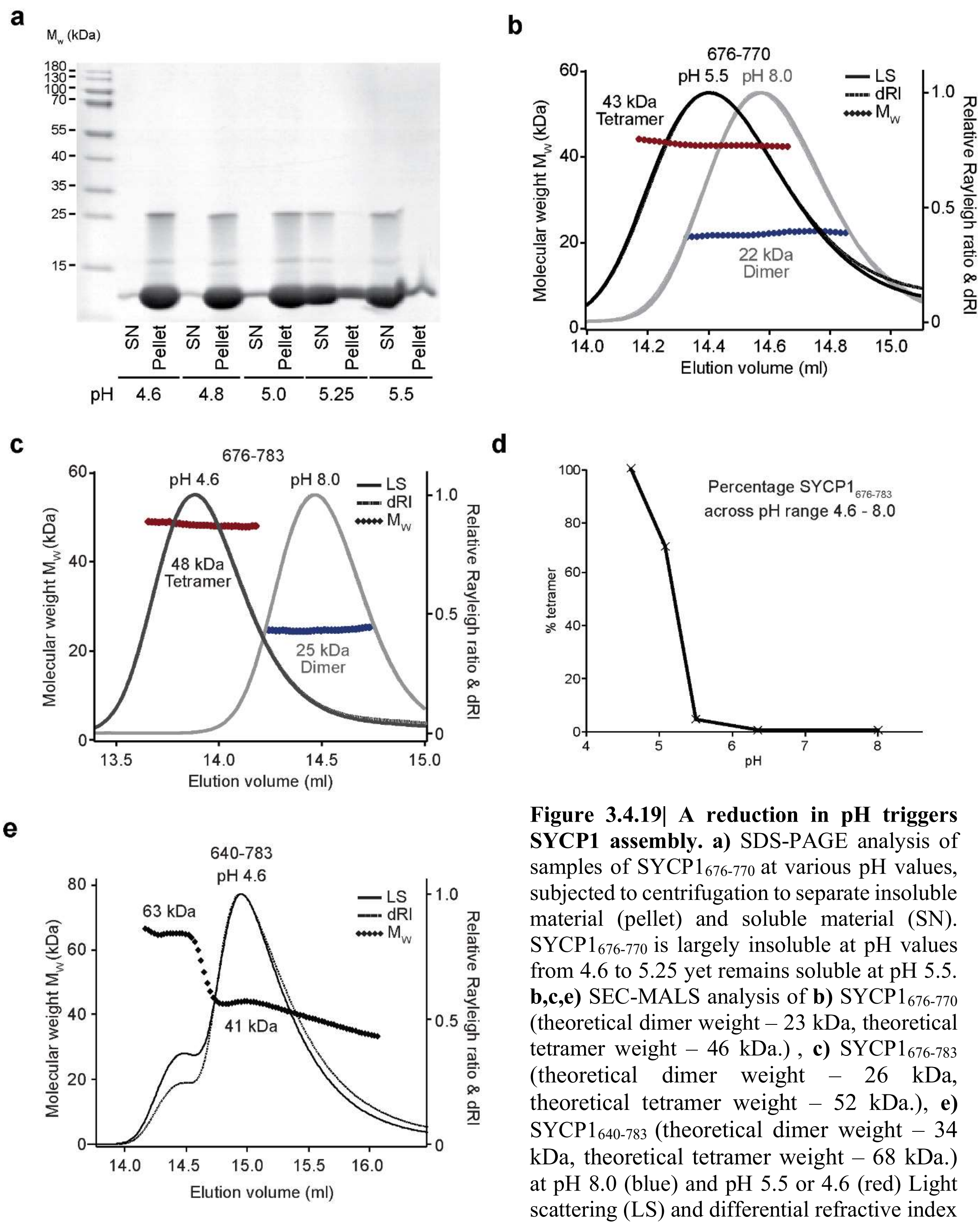

Figure 3.4.19| A reduction in pH triggers SYCP1 assembly. a) SDS-PAGE analysis of samples of SYCP1$_{676-770}$ at various pH values, subjected to centrifugation to separate insoluble material (pellet) and soluble material (SN). SYCP1$_{676-770}$ is largely insoluble at pH values from 4.6 to 5.25 yet remains soluble at pH 5.5. **b,c,e)** SEC-MALS analysis of **b)** SYCP1$_{676-770}$ (theoretical dimer weight – 23 kDa, theoretical tetramer weight – 46 kDa.) , **c)** SYCP1$_{676-783}$ (theoretical dimer weight – 26 kDa, theoretical tetramer weight – 52 kDa.), **e)** SYCP1$_{640-783}$ (theoretical dimer weight – 34 kDa, theoretical tetramer weight – 68 kDa.) at pH 8.0 (blue) and pH 5.5 or 4.6 (red) Light scattering (LS) and differential refractive index (dRI) are plotted as solid and dashed lines, respectively, with molecular weights (Mw) shown as diamonds across elution peaks. **d)** The percentage by mass of SYCP1$_{676-783}$ molecules in a tetrameric oligomeric state as determined by SEC-MALS analysis across a range of pH values.

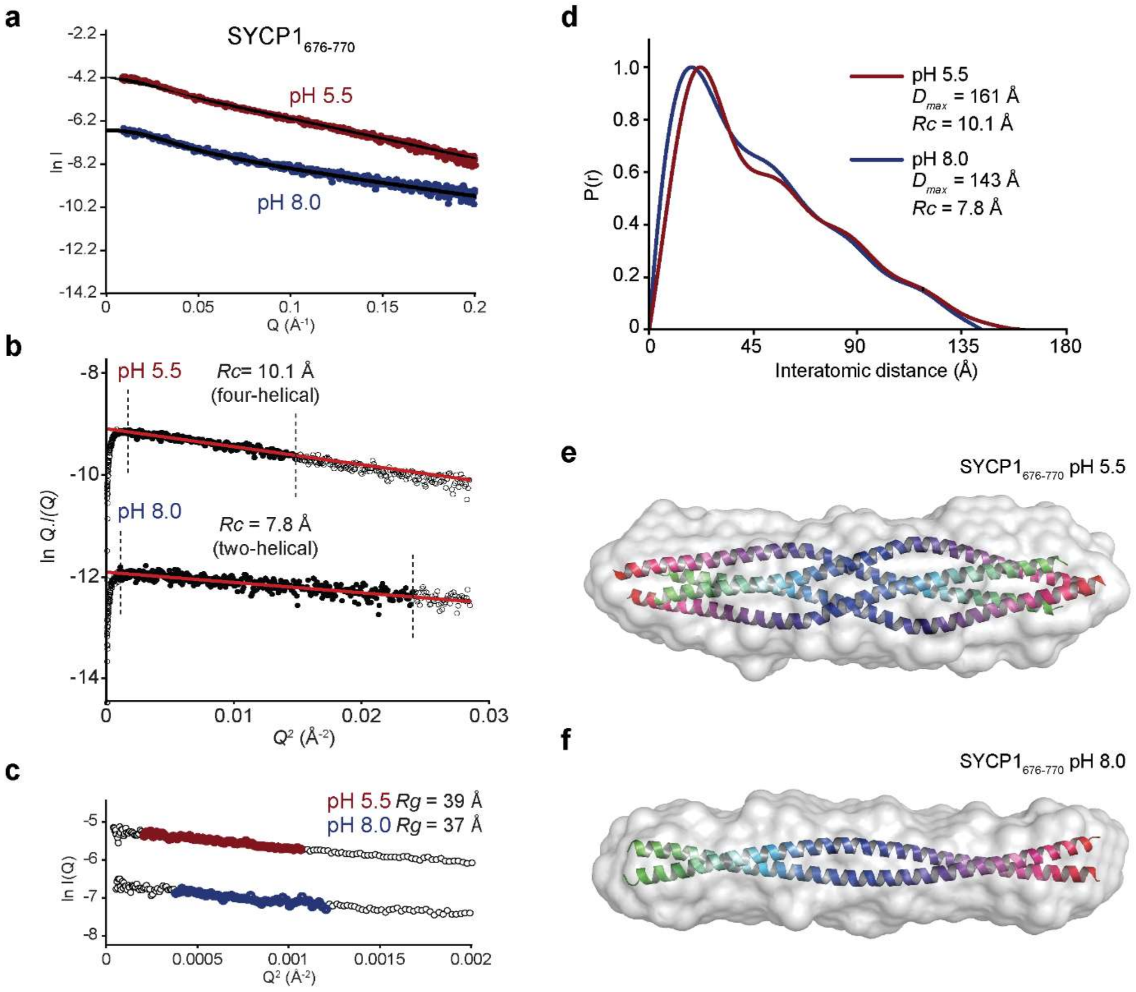

Figure 3.4.20| A reduction in pH triggers SYCP1$_{676\text{-}770}$ assembly. a) Averaged small-angle X-ray scattering profiles of SYCP1$_{676\text{-}770}$ at pH 8.0 (blue) and pH 5.5 (red) with the fits used for *P(r)* distributions shown as black lines. **b)** Guinier analysis to determine the radius of the cross-section (*Rc*) of SYCP1$_{676\text{-}770}$ at pH 8.0 and 5.5. The data within the linear region utilised for calculation are highlighted in black and bounded by dashed lines. **c)** Guinier analysis to determine the radius of gyration (Rg) of SYCP1$_{676\text{-}770}$ at pH 8.0 and 5.5. The data within the linear region utilised for calculation are highlighted in red (pH 5.5) and blue (pH 8.0). **d)** Inter-atomic distance distribution profile for SYCP1$_{676\text{-}770}$ at pH 8.0 (blue) and pH 5.5 (red) with maximum dimensions (D_{max}) and radius of the cross-section (*Rc*) indicated. **e,f)** SUPCOMB docking of the SYCP1$_{676\text{-}770}$ crystal structure and a model coiled-coil docked into the calculated *ab initio* molecular envelopes at pH 5.5 and 8.0, respectively. SEC-SAXS data analysis by Dr Orla Dunne.

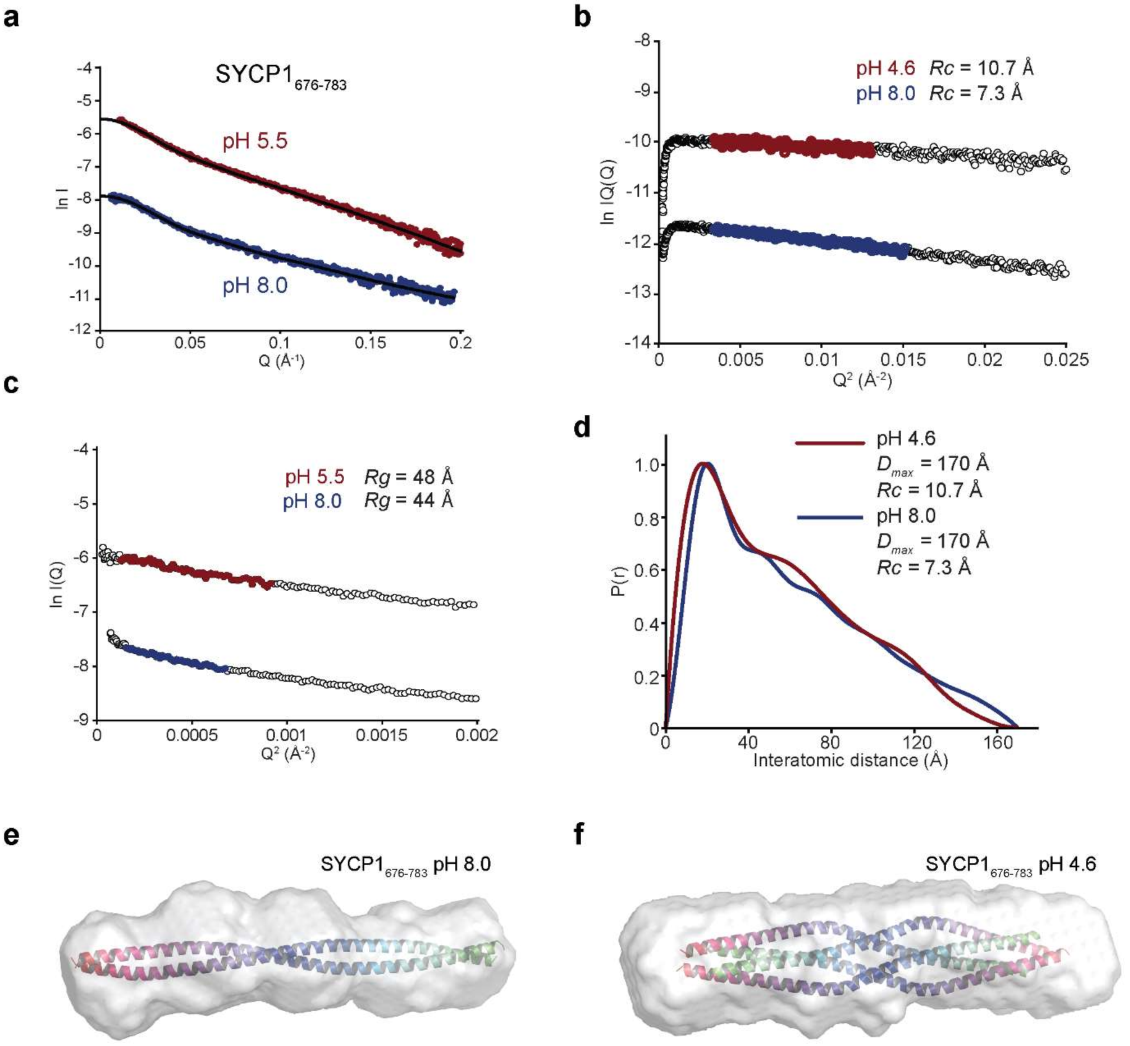

Figure 3.4.21| A reduction in pH triggers SYCP1$_{676-783}$ assembly. a) Averaged small-angle X-ray scattering profiles of SYCP1$_{676-783}$ at pH 8.0 (blue) and pH 4.6 (red) with the fits used for *P(r)* distributions shown as black lines. **b)** Guinier analysis to determine the radius of the cross-section (*Rc*) of SYCP1$_{676-783}$ at pH 8.0 and 4.6. The data within the linear region utilised for calculation are highlighted in black and bounded by dashed lines. **c)** Guinier analysis to determine the radius of gyration (*Rg*) of SYCP1$_{676-783}$ at pH 8.0 and 4.6. The data within the linear region utilised for calculation are highlighted in red (pH 4.6) and blue (pH 8.0). **d)** Inter-atomic distance distribution profile for SYCP1$_{676-783}$ at pH 8.0 (blue) and pH 5.5 (red) with maximum dimensions (D_{max}) and radius of the cross-section (*Rc*) indicated. **e,f)** SUPCOMB docking of the SYCP1$_{676-770}$ crystal structure and a model coiled-coil docked into the calculated *ab initio* molecular envelopes at pH 4.6 and 8.0, respectively. SEC-SAXS data analysis by Dr Orla Dunne.

Tetramerization driven by the reduced pH resulted in stabilisation as assessed by thermal denaturation, with SYCP1$_{676-770}$ melting at 35 and 38 ˚C and SYCP1$_{676-783}$ melting at 46 and 60 ˚C, at pH 8.0 and 5.5/4.6, respectively (Figure 3.4.23c,d). Interestingly, the presence of 1M KCl increased stability of SYCP1$_{676-770}$ (the melting temperature is increased from 38 to 62 ˚C) and further elicited the formation of an octameric species showing propensity for further assembly (Figure 3.4.23c and Figure 3.4.24a). It is possible that SYCP1$_{676-770}$ undergoes further domain-swap self-associations to drive the dimerization of tetrameric units (modelled in Figure 3.4.24b,c). This may occur in a recursive manner to drive a lattice-like assembly of SYCP1$_{676-770}$ molecules.

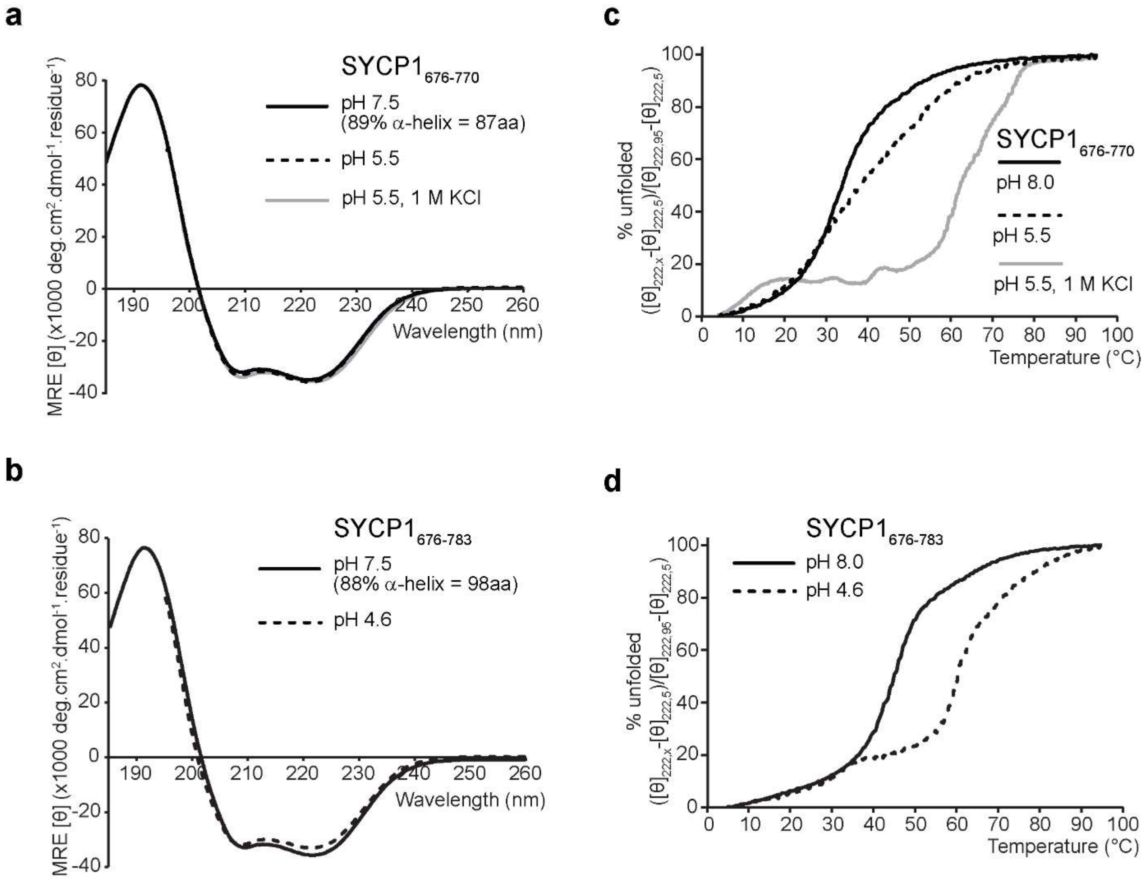

Figure 3.4.22| The dimer-tetramer shifts results in increased stability. a) Circular dichroism far-UV spectra for SYCP1$_{676-770}$ at pH 7.5 (black solid), 5.5 (black dashed) or 5.5 at 1 M KCl (grey solid) demonstrating equivalent helicity. **b)** Circular dichroism far-UV spectra for SYCP1$_{676-783}$ at pH 7.5 (black solid) and 4.6 (black dashed) demonstrating equivalent helicity. **c)** Thermal denaturation of SYCP1676-770 at pH 8.0, 5.5 and pH 5.5 in the presence of 1 M KCl demonstrating increased stability at pH 5.5 (with melting temperatures of 35 and 38 ˚C) and a further increase in stability in 1 M KCl with a melting temperature of 62 ˚C. **d)** Thermal denaturation of SYCP1$_{676-783}$ at pH 8.0 and 4.6, demonstrating an increase in melting temperature from 46 to 60 ˚C with a reduction in pH.

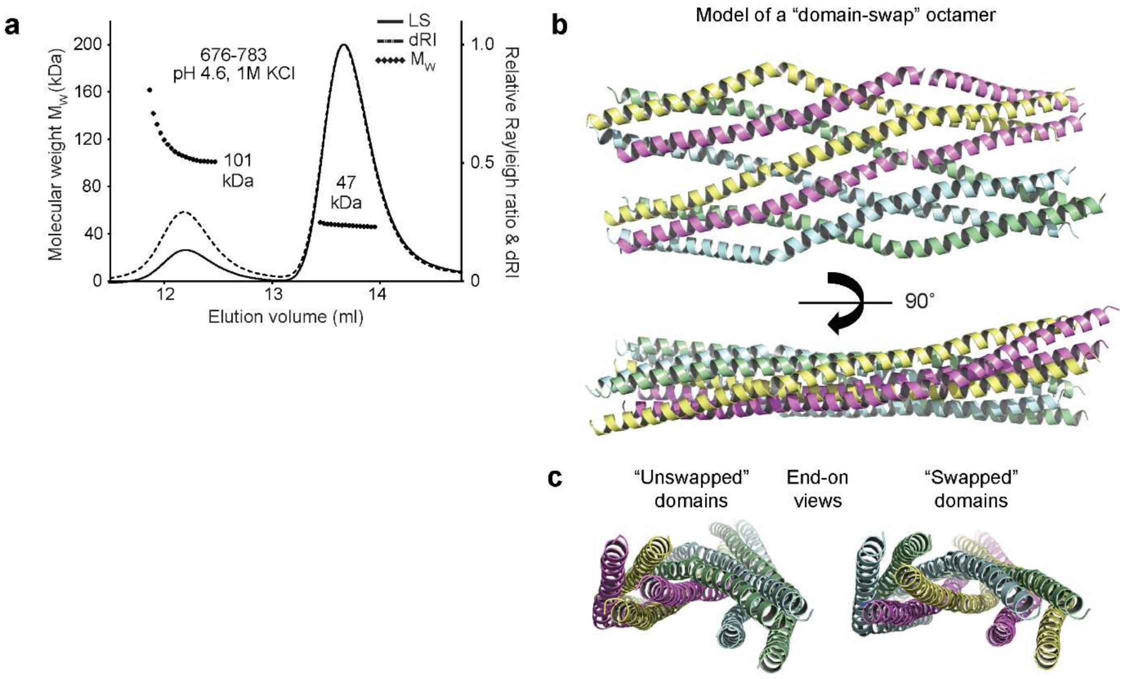

Figure 3.4.23| A high salt concentration elicits higher oligomer formation. a) SEC-MALS analysis of SYCP1$_{676\text{-}783}$ at pH 4.6 in the presence of 1 M KCl, demonstrating tetrameric assembly with the further formation of an octameric-higher order assembling species. **b)** Molecular model of an octamer through the domain swap of helical chains to create an interlaced assembly. **c)** End-on views display ends of the structure in which chains are non-swapped and swapped. The assembly can occur in a recursive manner to generate a lattice of SYCP1$_{676\text{-}770}$ molecules.

I wanted to confirm that the tetramer represents an assembled form of two parallel dimers in anti-parallel association. I purified a tethered dimer of two consecutive SYCP1$_{676\text{-}770}$ sequences connected by a flexible GQTNPGTNPTG linker. The formation of a monomer of a length approximating that of the SYCP1$_{676\text{-}770}$ dimer at pH 8.0 would suggest the capability to adopt an anti-parallel conformation whilst the formation of dimer of tethered dimers, as observed by SEC-MALS, indicates a parallel orientation of helical chains (Figure 3.2.24a-c). The massively shifted elution volume of the dimer of tethered dimers (12.5 ml compared to 14.5 ml of the SYCP1$_{676\text{-}770}$ dimer) suggests a highly elongated, end-to-end, arrangement of two parallel dimers, as confirmed by SEC-SAXS which reveals a D_{max} of 241 Å and cross-sectional radius of 8.8 Å (Figure 3.4.24d-f). At pH 5.5, the construct retains its dimer of dimers oligomeric status, yet, as illustrated by its elution volume of 14.5 ml (matching that of SYCP1$_{676\text{-}770}$ at pH 5.5), length of 156 Å, and cross-sectional radius of 10.7 Å, it adopts a compact conformation with dimensions matching those of the anti-parallel tetramer, representing the folding of the dimer of tethered dimers on itself (Figure 3.4.24c-f).

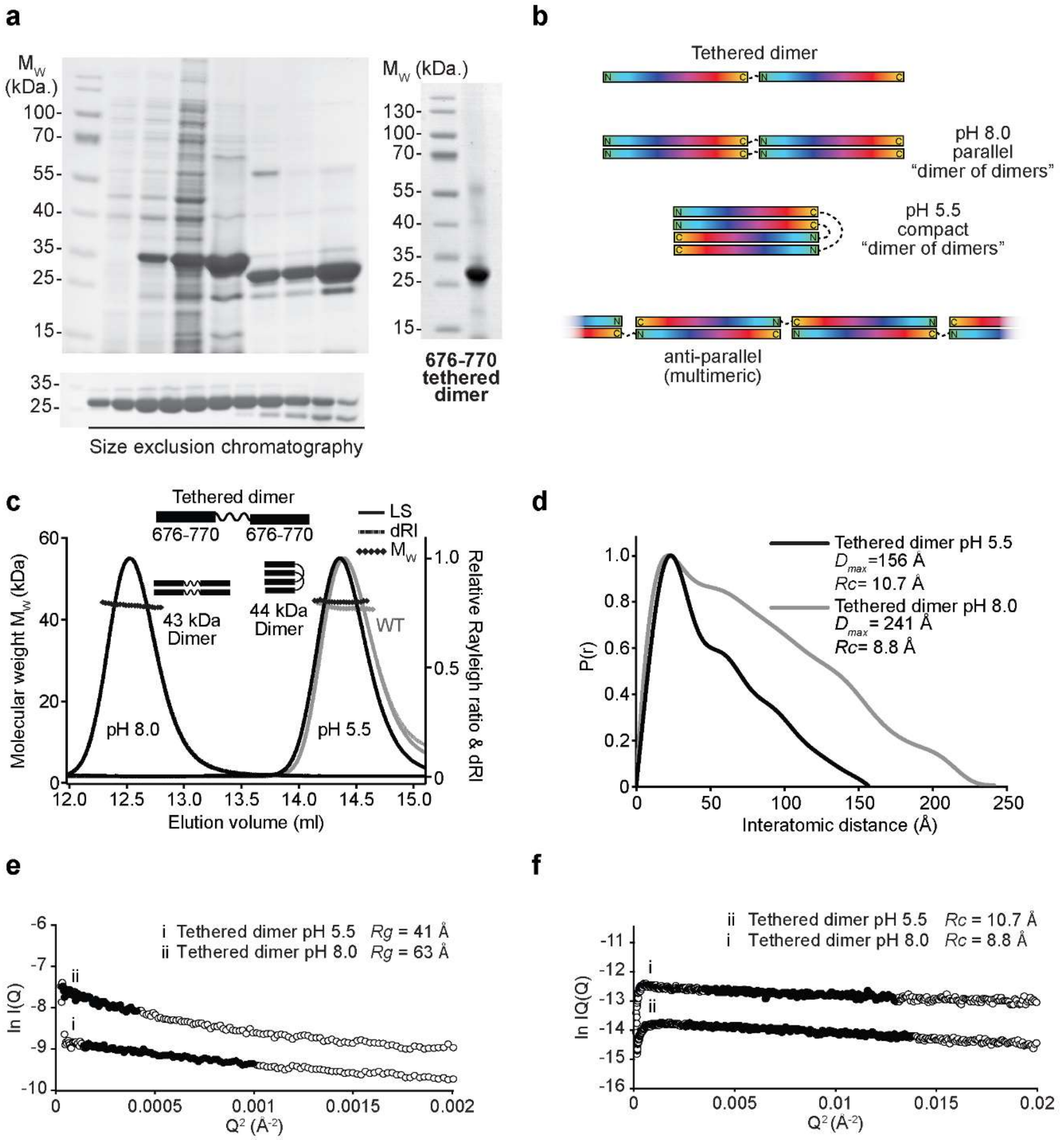

Figure 3.4.24| Analysis of a tethered SYCP1$_{676\text{-}770}$ construct confirms tetrameric assembly. a) SDS-PAGE analysis of the purification of SYCP1$_{676\text{-}770}$ tethered dimer, size-exclusion chromatography elution fractions and the final purified sample. **b)** Schematic representation of the tethered dimer with linker sequence as a dashed line followed by a model of the predicted structures for a parallel orientation at pH 8.0 and 5.5 and a model for an anti-parallel coiled-coil at pH 8.0. **c)** SEC-MALS analysis of an SYCP1$_{676\text{-}770}$ tethered dimer at pH 8.0 (black left; theoretical dimer of dimers – 47 kDa), demonstrating a shifted elution volume, and at pH 5.5 (black right) which shows an elution volume similar to SYCP1$_{676\text{-}770}$ at pH 5.5 (grey). **d)** Inter-atomic distance distribution profile for SYCP1$_{676\text{-}770}$ tethered dimer at pH 8.0 (grey) and pH 5.5 (black) with maximum dimensions (*D$_{max}$*) and radius of the cross-section (*Rc*) indicated. **e)** Guinier analysis to determine the radius of gyration (*Rg*) of SYCP1$_{676\text{-}770}$ tethered dimer at pH 8.0 and 5.5. The data within the linear region utilised for calculation are highlighted in black. **f)** Guinier analysis to determine the radius of the cross-section (*Rc*) of SYCP1$_{676\text{-}770}$ tethered dimer at pH 8.0 and 5.5. The data within the linear region utilised for calculation are highlighted in black. SEC-SAXS data analysis by Dr Orla Dunne.

Finally, MBP-tagged SYCP1$_{676-770}$ tetramerised at pH 5.5 and upon analysis by SEC-SAXS demonstrated maxima within the interatomic distance-distribution profile representing interatomic distances between MBP molecules at either end of the molecule (Figure 3.4.25a-e). I therefore conclude that the pH-dependent assembly observed in solution constitutes the anti-parallel association of parallel SYCP1$_{676-770}$ coiled-coil dimers.

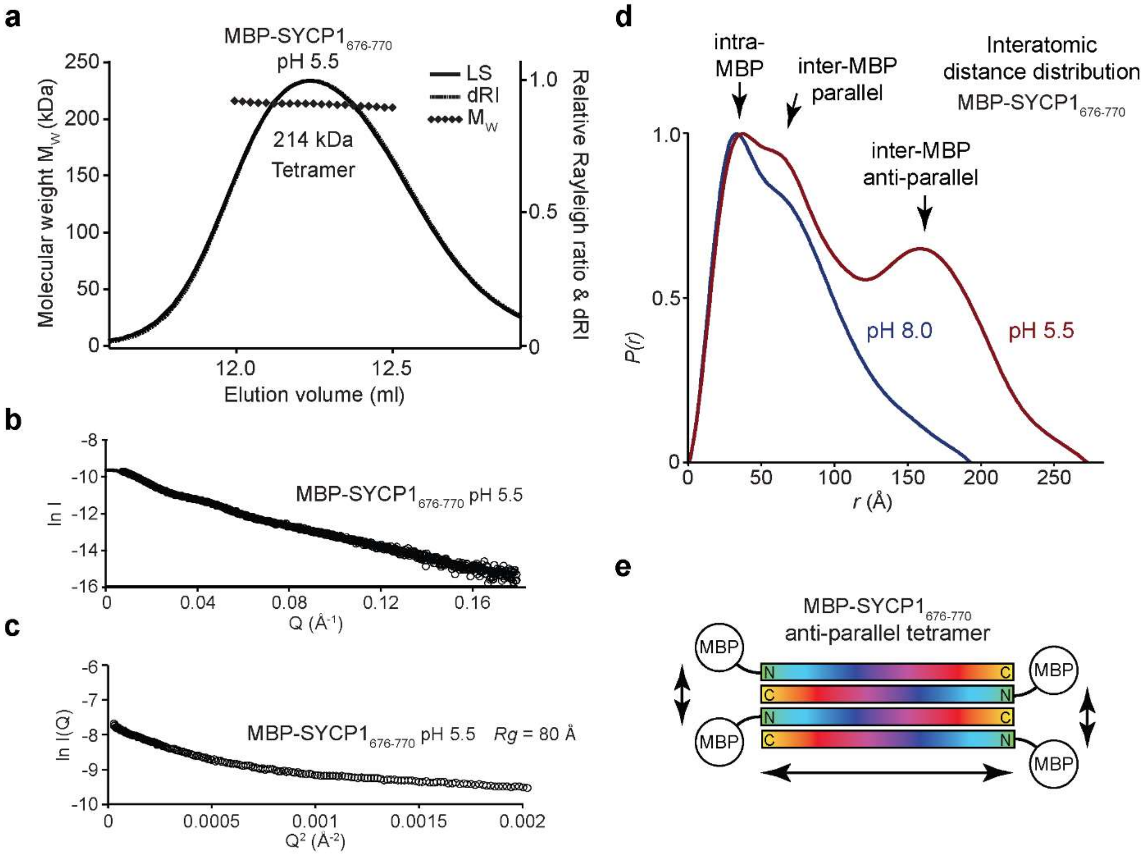

Figure 3.4.25| SEC-SAXS analysis of MBP-SYCP1$_{676-770}$ confirms anti-parallel helical assembly. a) SEC-MALS analysis of MBP-SYCP1$_{676-770}$ at pH 5.5 demonstrating tetramer formation (theoretical tetramer – 224 kDa). **b)** Averaged small-angle X-ray scattering profiles of MBP-SYCP1$_{676-770}$ at pH 5.5 with the fit used for *P(r)* distribution shown as a black line. **c)** Guinier analysis to determine the radius of gyration (*Rg*) of MBP-SYCP1$_{676-770}$ at pH 5.5. The data within the linear region utilised for calculation are highlighted in black. **d)** Inter-atomic distance distribution profile for MBP-SYCP1$_{676-770}$ at pH 8.0 (blue) and pH 5.5 (red) with intra-, and inter-MBP peaks indicated. **e)** Schematic model of MBP-SYCP1$_{676-770}$ at pH 5.5 with short and long inter-MBP distances indicated. SEC-SAXS data analysis by Dr Orla Dunne.

3.4.18 Mutagenesis of SYCP1$_{676\text{-}770}$ central tetrameric interface

The residues stabilising the tetramer hydrophobic core display absolute conservation across mammalian species (Figure 3.4.26a,b). I performed mutagenesis experiments with SYCP1$_{676\text{-}783}$, as the additional sequence accentuated the difference in the elution volumes of the dimeric and tetrameric forms. A summary of tested mutants can be found in Table 3.9. Most remarkably, I was able to stabilise the tetrameric form of SYCP1$_{676\text{-}783}$ through the double mutation H717W Y721F (Figure 3.4.26c,d). The success of this mutation is due to the tryptophan replicating the hydrogen bond to glutamine 720 through its Nε1 whilst undergoing similar aromatic stacking interactions of H717 and contributing to a hydrophobic core (Figure 3.4.26d). Tetramer formation could be disrupted by mutation of H717 to glutamate whilst substitutions to phenylalanine or tryptophan were tolerated. Surprisingly, mutation of Y721 to either alanine or glutamate had no effect on tetramer formation at pH 4.6.

Tetramer formation could also be disrupted though mutation of L679 and I688 to alanine (Figure 3.4.26c,e). As these residues are specific to interactions between anti-parallel chains of the tetramer in the lateral interface, dimer formation remains unaffected. At pH 4.6, it still formed a tetramer but at a dramatically reduced efficiency, demonstrating 22 % tetramer formation, 78 % dimer formation (Figure 3.4.26c).

I reasoned that the three histidine residues of the structure might act as pH sensors. As histidine has a side chain pKa of 6.0, it can oscillate between a protonated/deprotonated state at pH values below and above this value, respectively. Having established that H717 protonation is not essential for tetramerization (as tetramer formation is unaffected by the mutation H717F) I tested for the effect of mutating H705 and H719 which are both solvent exposed within the tetrameric crystal structure and dimeric *ab initio* model, not apparently stabilising interactions in either structure. H719, which is situated proximal to the tetrameric interface, does not appear to contribute to tetramerization as when mutated to alanine, lysine, leucine or phenylalanine, it still forms a tetramer at pH 4.6. Further, the mutation of H719 to D or E within the context of H717W Y721F does not stabilise or destabilise tetramer formation at pH 8.0.

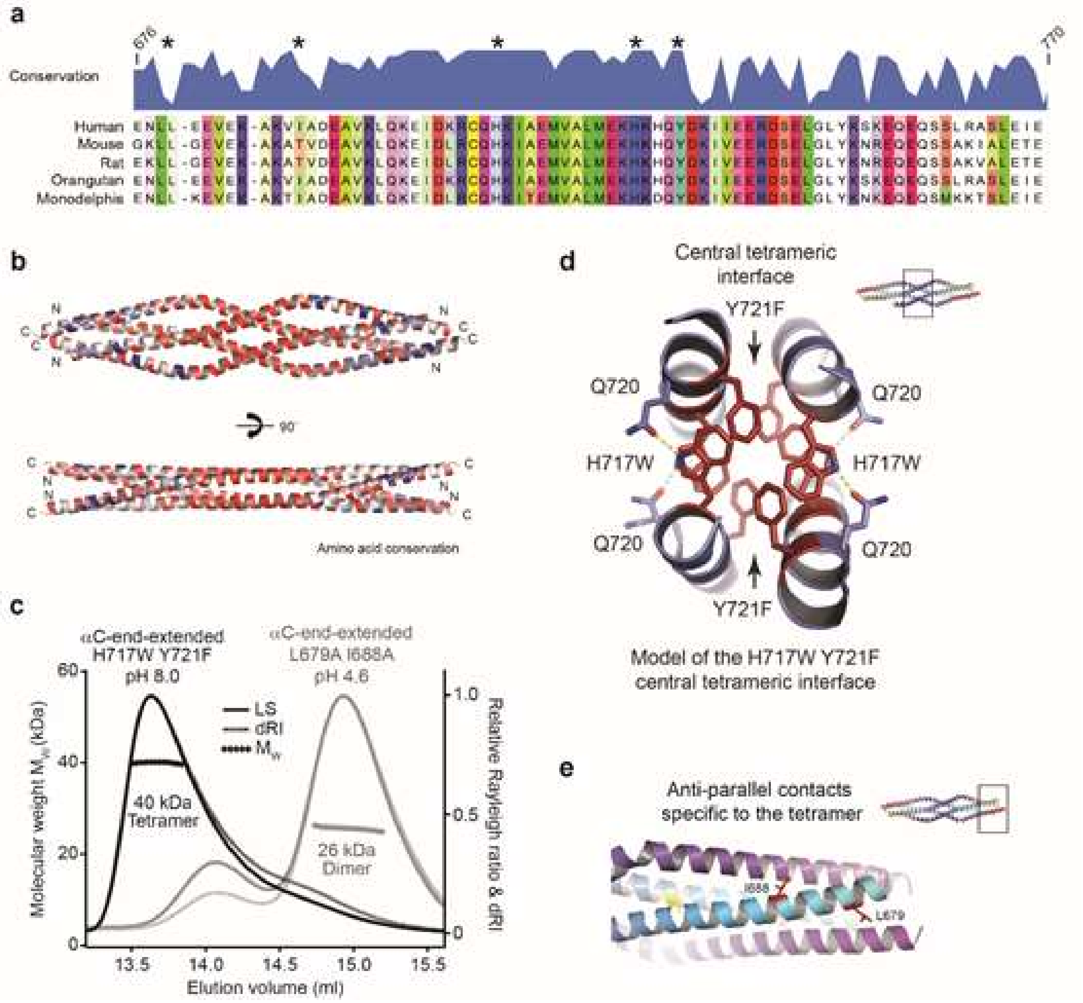

Figure 3.4.26| Mutational analysis of SYCP$_{676\text{-}783}$. a) An alignment of the human SYCP1 between residues 676 and 770 aligned with a conservation plot. Key residues are indicated by asterisks. **b)** The crystal structure of SYCP1$_{676\text{-}770}$ coloured by conservation with conserved residues in red and those non-conserved in blue. **c)** SEC-MALS analysis of SYCP1$_{676\text{-}783}$ mutants H717W/Y721F and L679A/I688A. Theoretical tetramer molecular weight – 52 kDa. Light scattering (LS) and differential refractive index (dRI) are plotted as solid and dashed lines, respectively, with molecular weights (Mw) shown as diamonds across elution peaks. **d)** Model of the tetrameric interface incorporating mutated residues H717W and Y721F. The hydrophobic core is conserved whilst maintaining hydrogen bonding to Q720 through the nitrile group of tryptophan. **e)** The residues I688 and L679 are highlighted in red as being the sole residues which mediate specific contact between anti-parallel chains.

Given its location, it is perplexing that mutation of H705 to A or E almost completely ablates tetramer formation at pH 4.6. Triple mutation H705A H717A H719A did not enhance this effect whilst their mutation to glutamate blocked tetramer formation totally, though this is likely due to the dominant effect of H717E. Given the localisation of H705 at the pinch points within the tetramer, it could be that H705 protonation triggers a conformational remodelling of the dimer, which is transmitted along the coiled-coil, opening up the structure and allowing parallel chains to associate in an anti-parallel manner.

However, the mechanism is not completely protonation dependent given the partial refolding of a mutant devoid of histidine residues.

3.4.19 What is the role of the C703 pinch points?

As disulphide bonds are present in the crystal structure, I wondered whether they play a role in tetramer formation or stabilisation. I initially assayed for the presence of disulphide bonds within the purified material using Ellman's reagent assay and UV spectrophotometry. Ellman's reagent (DTNB) reacts with free thiol groups, releasing a stoichiometric amount of TNB which can be detected by its absorption of UV light at 412 nm (see Methods section 2.1.16). Purified SYCP1$_{676\text{-}770}$ reacted readily with DTNB, observed as a maxima at 412 nm, whilst the oxidised form, subjected to 0.5 % hydrogen peroxide at room temperature overnight, did not, confirming the non-oxidised state of purified SYCP1$_{676\text{-}770}$ and the reactivity of C703 as the role cysteine residue (Figure 3.4.27a).

I assayed for the effect of oxidation on oligomeric state by incubating samples with increasing concentrations of hydrogen peroxide, incubating for 2 hours at room temperature and analysing by SDS-PAGE (Figure 3.4.27b). 0.5 % hydrogen peroxide results in maximal oxidation of SYCP1$_{676\text{-}770}$ with the majority of protein migrating as a disulphide-stabilised gel dimer (Figure 3.4.27b). Circular dichroism reveals that whilst SYCP1$_{676\text{-}770}$ in both reduced and oxidised states demonstrates equal helicity, thermal denaturation revealed that oxidation stabilised the dimer, resulting in an increase in melting temperature from 35 to 51 ˚C (Figure 3.4.27c,d).

I finally tested the effect of mutating C703 to alanine or serine to check whether the structural contribution of the cysteine was important for tetramer formation upon a reduction in pH. SEC-MALS revealed that this was not the case with both mutants forming stable tetramers at pH 4.6 (Figure 3.4.27f and Table 3.9).

Mutations of SYCP1$_{676-783}$		
Mutation	**Oligomer at pH 8.0**	**Oligomer at pH 4.6**
H717L	Dimer	Untested
H717F	Dimer	Untested
H717W	Dimer	Partial disruption
H719A	Dimer	Precipitates
H719K	Dimer	Partial disruption
H719L	Dimer	Tetramer
H719F	Dimer	Tetramer
Y721A	Dimer	Tetramer
Y721E	Dimer	Tetramer
Y721L	Dimer	Untested
Y721F	Dimer	Untested
H717A H719K	Dimer	Precipitates
H717A Y721A	Dimer	Tetramer
H717W Y721F	Tetramer	Tetramer
L679A I688A	Dimer	Dimer/tetramer
L679E E681K D690K L761K	Dimer	Untested
H705A	Dimer	Partial disruption
H705 A H717A H719A	Dimer	Dimer/tetramer
H705E H717E H719E	Dimer	Dimer
H717W H719D Y721F	Tetramer	Untested
H717W H719E Y721F	Tetramer	Untested
C703A	Untested	Tetramer
C703s	Untested	Tetramer

Table 3.9| Summary of SEC-MALS analysis for SYCP1$_{676-783}$ mutants

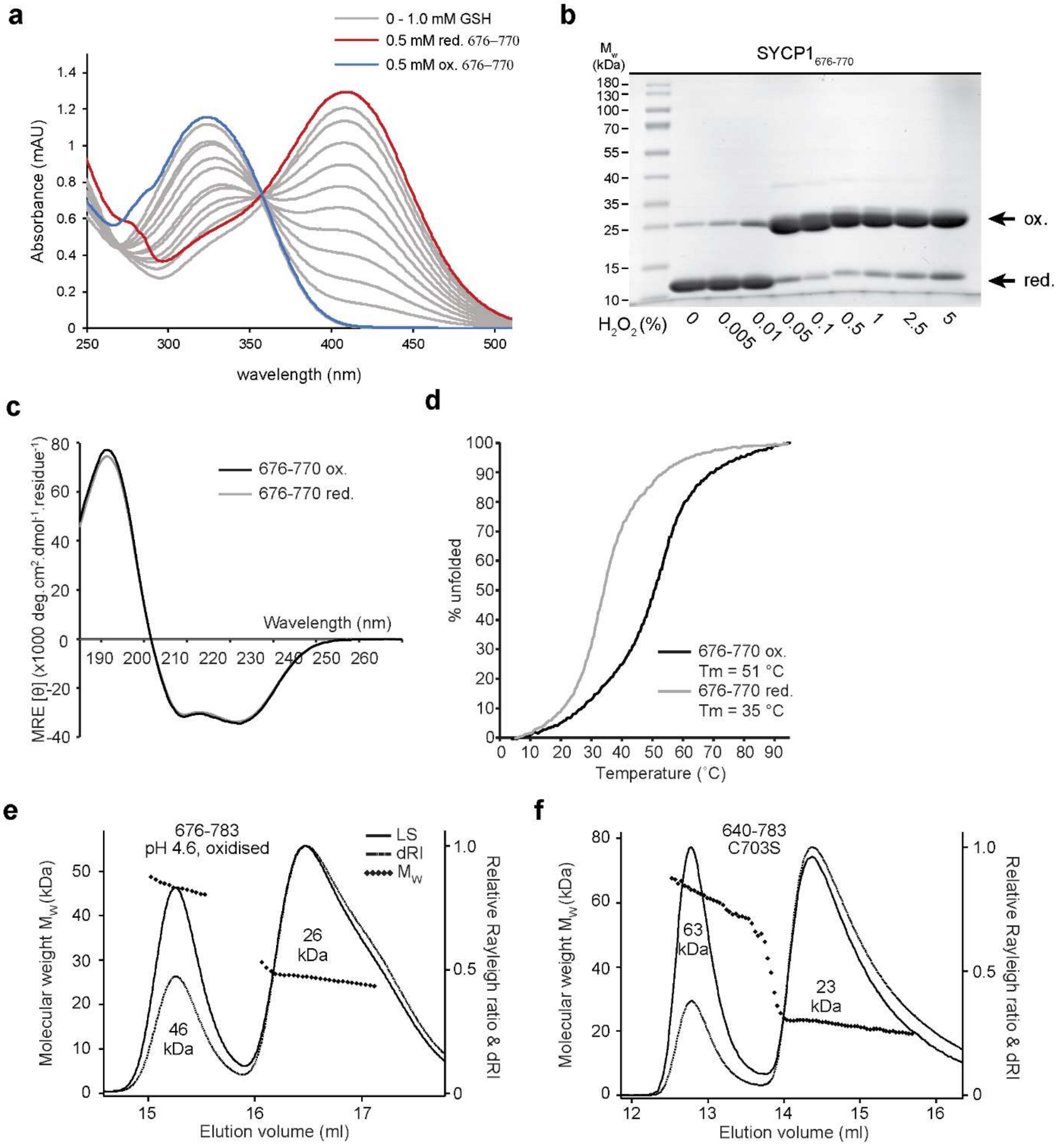

Figure 3.4.27| Oxidation within SYCP$_{676-770}$. a) Assay for oxidation as described in Methods section 2.1.16. Glutathione **(**GSH) standards from 0 – 1.0 mM in the presence of DTNB, shown in grey, show an increasing absorbance at 412 nm. In the presence of oxidised SYCP1$_{676-770}$ (blue), no TNB is released into solution whilst maximal signal at 412 nm is achieved with 0.5 mM reduced SYCP1$_{676-770}$ (red). **b)** SDS-PAGE analysis demonstrating the formation of a gel dimer in the presence of increasing concentrations of hydrogen peroxide for SYCP1$_{676-770}$ **c)** Circular dichroism far-UV spectra of SYCP1$_{676-770}$ in the reduced and oxidised states. **d)** Thermal denaturation of SYCP1$_{676-770}$ in the reduced and oxidised states were recorded as percentage unfolded based on the helical signal at 222 nm. Melting temperatures were estimated at 35 and 51 ˚C, respectively. **e)** SEC-MALS of oxidised SYCP1$_{676-783}$ at pH 4.6 demonstrating partial inhibition of tetramerization. **f)** SEC-MALS of SYCP1$_{640-783}$ C703S at pH 4.6 showing that mutation of the pinch point C703 has no effect upon tetramerization.

3.4.20 DNA binding of SYCP1$_{676\text{-}770}$ and chromosomal assembly

I noted the presence of a series of basic surfaces on the surface of the SYCP1$_{676\text{-}770}$ structure, separated by approximately ~30 Å, suggesting the possibility that the assembled form of SYCP1$_{676\text{-}770}$ may mediate further interactions with the DNA backbone. I observed by EMSA that SYCP1$_{676\text{-}770}$ interacts with DNA at pH 5.5, but not at pH 8.0 (Figure 3.4.28a,b). As both surfaces of the tetramer display basic patches, it is possible that the structure mediates recursive DNA interactions, resulting in large protein-DNA assemblies and likely accounting for the range of species observed by EMSA.

I predicted that SYCP1$_{676\text{-}770}$ assembly might contribute to SYCP1 assembly at the chromosomal axis. Histidine protonation could occur within close proximity to the chromosomal axis where the local proton concentration results in an acidic microenvironment, with a pH value two orders of magnitude below that of the bulk solvent (Hanlon *et al.*, 1997). Being a dynamic remodelling event, this would provide an elegant mechanism to prevent the erroneous assembly of SYCP1 molecules outside of the SC. However, a mechanism for chromosomal recruitment would be required to correctly localise the SYCP1$_{676\text{-}770}$.

I propose a model in which SYCP1 is initially recruited to the chromosome axis through putative DNA-binding sites within the unstructured and basic C-terminus. In proximity to the chromosome axis, the domain corresponding to SYCP1$_{676\text{-}770}$ undergoes back-to-back assembly in a protonation dependent manner, allowing for its association with chromosomal DNA (Figure 3.4.28c). This would strengthen SYCP1 association with the axis and provide a level of regulation, preventing the erroneous assembly of SYCP1 molecules via the C-termini in the absence of the chromosome.

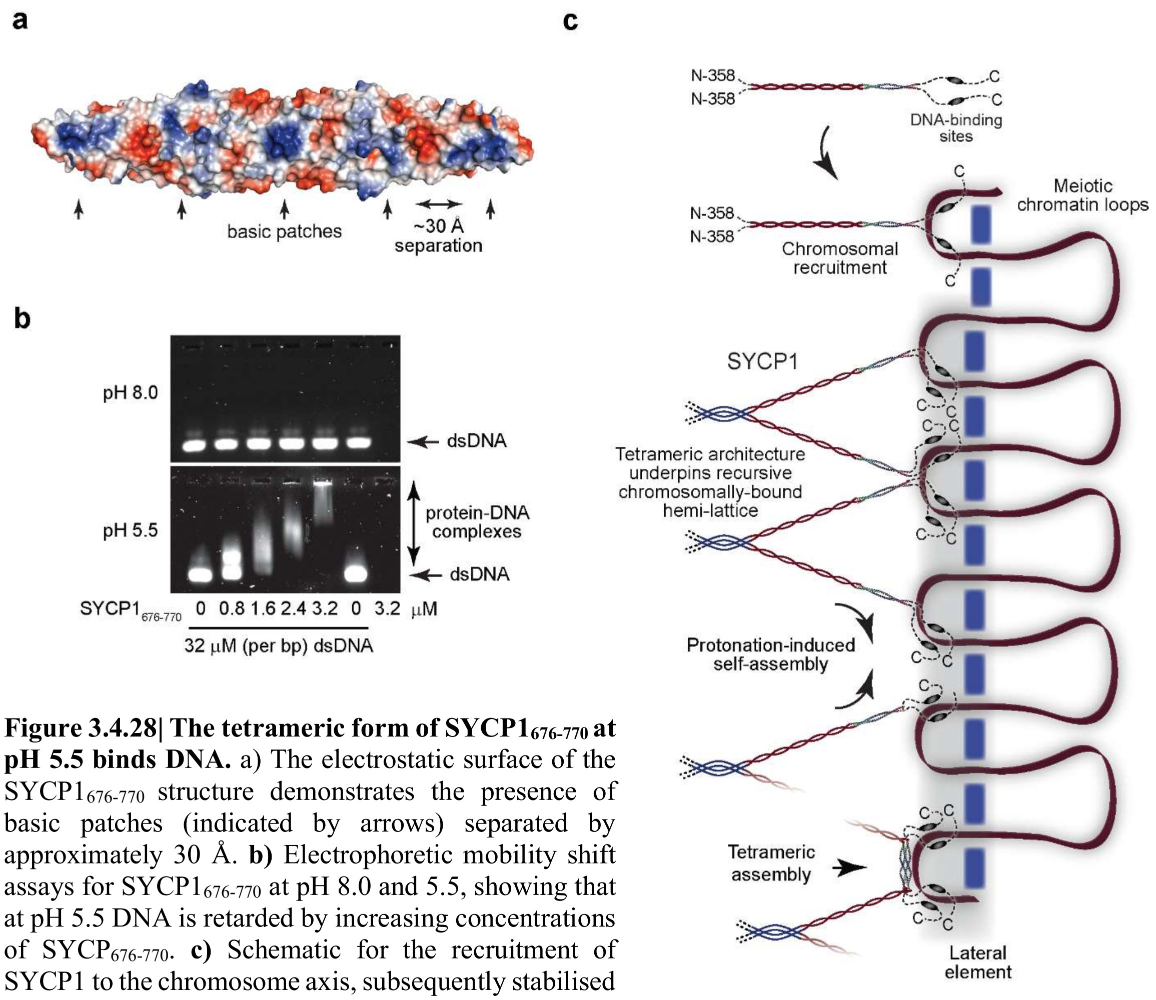
a
basic patches
~30 Å
separation
b
pH 8.0
dsDNA
pH 5.5
protein-DNA
complexes
dsDNA
SYCP1$_{676-770}$ 0 0.8 1.6 2.4 3.2 0 3.2 μM
32 μM (per bp) dsDNA
c
N-358
N-358
C
C
DNA-binding
sites
N-358
N-358
Chromosomal
recruitment
C
C
Meiotic
chromatin loops
SYCP1
Tetrameric architecture
underpins recursive
chromosomally-bound
hemi-lattice
C
C
C
C
C
C
Protonation-induced
self-assembly
C
C
C
Tetrameric
assembly
C
C
C
C
Lateral
element

Figure 3.4.28| The tetrameric form of SYCP1$_{676\text{-}770}$ at pH 5.5 binds DNA. a) The electrostatic surface of the SYCP1$_{676\text{-}770}$ structure demonstrates the presence of basic patches (indicated by arrows) separated by approximately 30 Å. **b)** Electrophoretic mobility shift assays for SYCP1$_{676\text{-}770}$ at pH 8.0 and 5.5, showing that at pH 5.5 DNA is retarded by increasing concentrations of SYCP$_{676\text{-}770}$. **c)** Schematic for the recruitment of SYCP1 to the chromosome axis, subsequently stabilised through the protonation-dependent, back-to-back assembly of SYCP1 molecules.

3.4.21 Back-to-back assembly might play a role in polycomplex formation

DNA-binding of back-to-back assemblies of the SYCP1 central core provided an attractive mechanism by which initial chromosome association through putative DNA-binding sites within the unstructured C-terminus could be stabilised. I wondered whether this mechanism could provide the basis for C-terminal associations within polycomplex structures (which form within the cytoplasm upon heterologous overexpression) in the absence of a chromosome axis. To test these I analysed two SYCP1 mutants: 1) an internal deletion in which residues 635-784 are removed and 2) a mutant which destabilises the second coiled-coil region of SYCP1$_{640\text{-}783}$. This mutant was L756P in which a leucine residue within a heptad position was converted to a proline. The purified protein retained a dimeric state but was significantly reduced in helicity (Figure 3.4.29a-c). In agreement with our suggestion that the second transition within the biphasic melting curve for SYCP1$_{640\text{-}783}$ represents the unfolding of the second, longer, coiled-coil sequence, the second melting transition for SYCP1$_{640\text{-}783}$ L756P is reduced, from 58 to 41 ˚C (Figure 3.4.29b).

I found that upon overexpression in COS-7 cells, SYCP1 Δ634-784 readily formed cytoplasmic networks at an efficiency double that of wild-type (Figure 3.4.30a-c). Upon destabilisation of the coiled-coil sequence by L756P, the formation of networks was almost completely blocked, though they could still form (Figure 3.4.30a-c). These observations fit with our current thinking that filamentous networks might represent the C-terminal recruitment of SYCP1 to an intermediate filament network. Upon deletion of residues 635-784, back-to-back assembly, which might drive polycomplex formation, would be completely blocked and therefore favour the formation of cytoplasmic networks. Mutation L756P likely disrupts the second stabilising coiled-coil sequence within SYCP1$_{640\text{-}783}$. This region is stabilised by a salt bridge between E770 and K774 and is otherwise glutamate rich. *In vivo*, this region may need to be neutralised in order to disrupt the salt bridge and weaken the dimeric state to allow for the opening of the chains and back-to-back tetramerization. If this were to be true, it would be expected that SYCP1$_{640\text{-}783}$ L756P form a tetramer at a less acidic pH than wild-type, though this has not been tested. Destabilization may have removed this requirement and thus facilitate polycomplex formation, hence the increased propensity of cytoplasmic aggregates which I hypothesise may be polycomplex structures, though this has not been formally addressed.

Contradicting a requirement for this region for polycomplex formation, however, is the observation that upon expression of SYCP1 Δ635-784 in COS-7 cells, polycomplex structures are still visible by electron microscopy (Figure 3.4.30). It therefore remains unclear as to how polycomplexes form within the cytoplasm. These findings do suggest a role for SYCP1$_{640-783}$ back-to-back assembly within polycomplexes but it remains unclear as to exactly what that role entails.

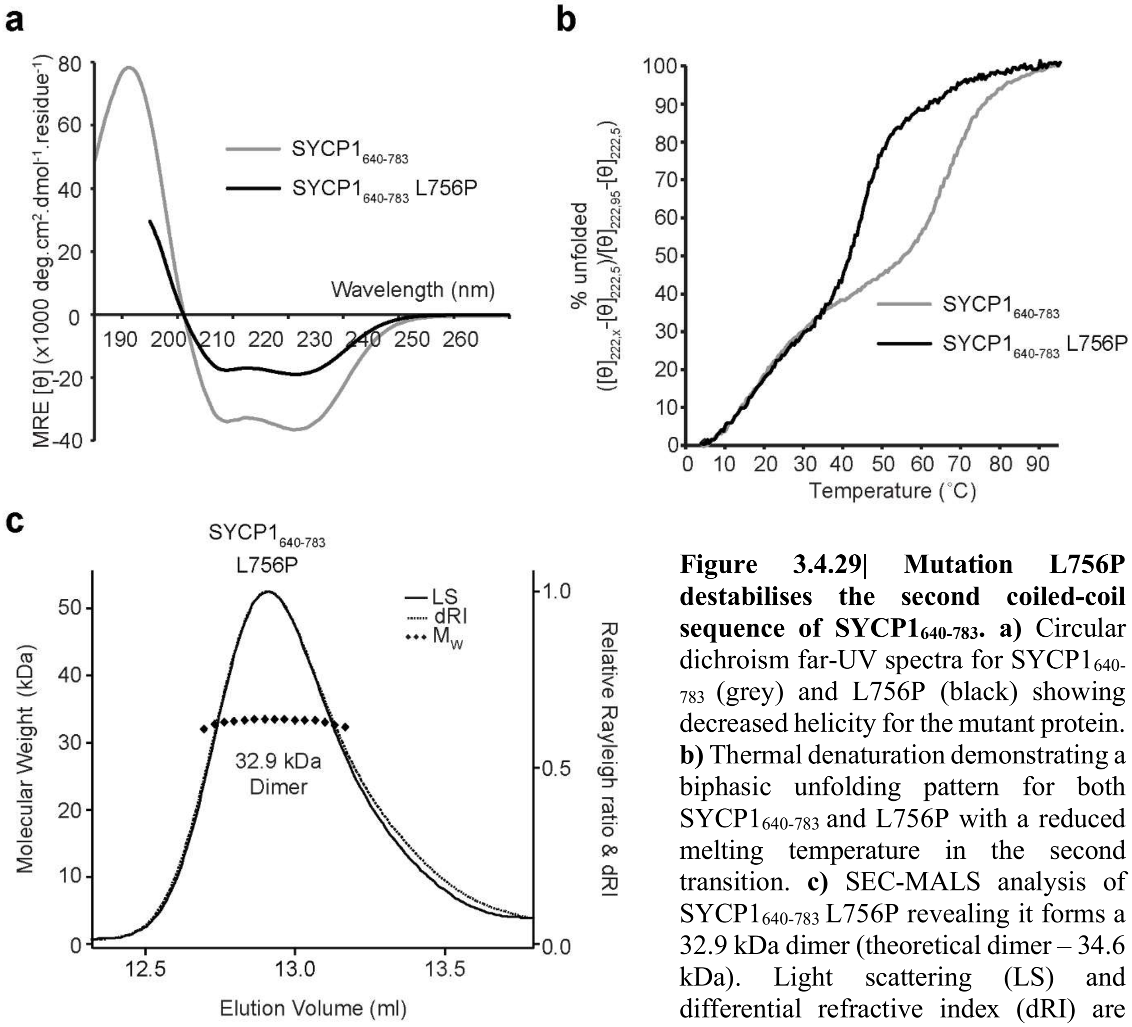

Figure 3.4.29| Mutation L756P destabilises the second coiled-coil sequence of SYCP1$_{640-783}$. a) Circular dichroism far-UV spectra for SYCP1$_{640-783}$ (grey) and L756P (black) showing decreased helicity for the mutant protein. **b)** Thermal denaturation demonstrating a biphasic unfolding pattern for both SYCP1$_{640-783}$ and L756P with a reduced melting temperature in the second transition. **c)** SEC-MALS analysis of SYCP1$_{640-783}$ L756P revealing it forms a 32.9 kDa dimer (theoretical dimer – 34.6 kDa). Light scattering (LS) and differential refractive index (dRI) are plotted as solid and dashed lines, respectively, with molecular weights (Mw) shown as diamonds across elution peaks.

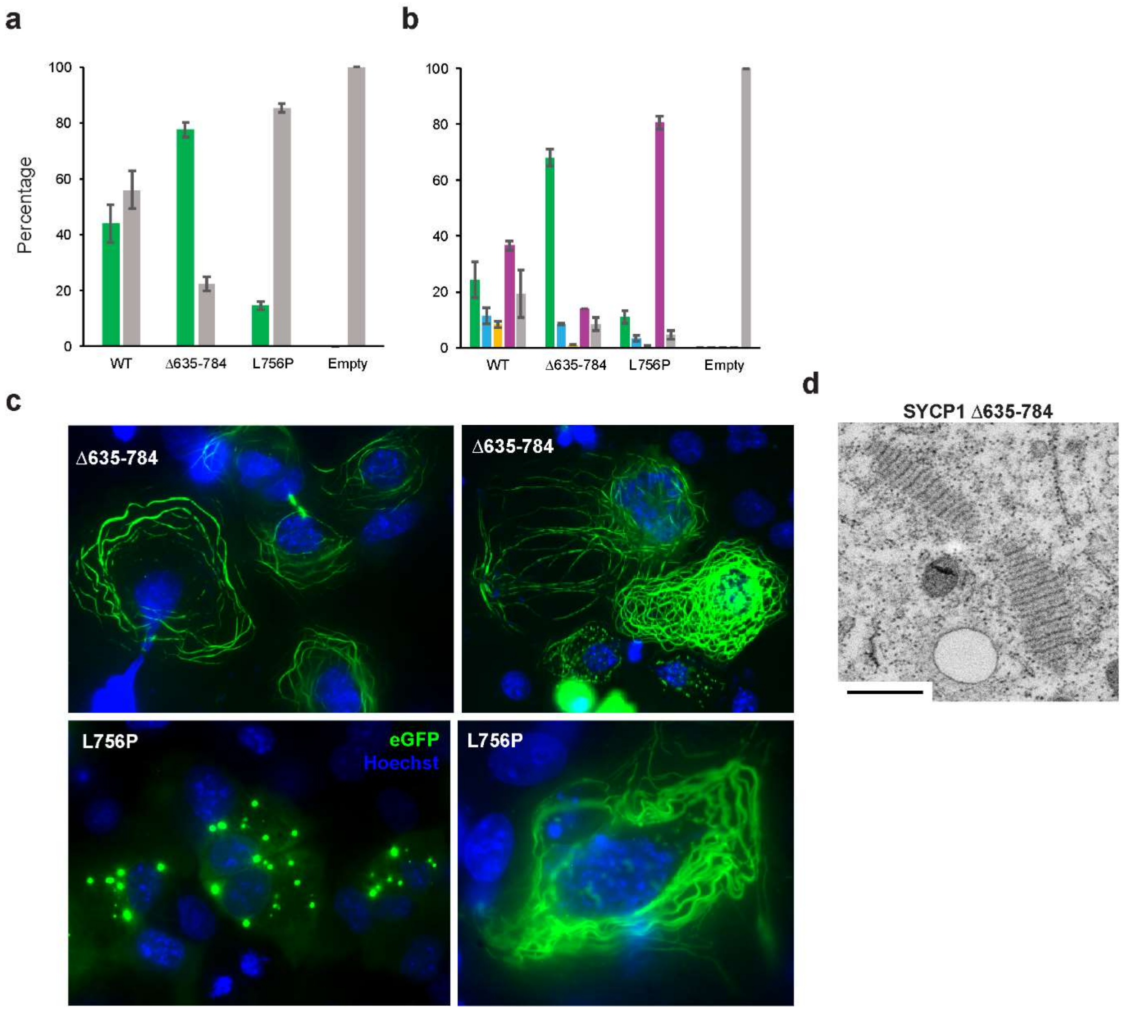

Figure 3.4.30| Polycomplex formation upon C-terminal disruption. a) The efficiency of filamentous assembly is plotted as the percentage of transfected cells demonstrating filamentous assembly (green) and those displaying amorphous aggregates or diffuse GFP signals (grey). Each experiment was performed in triplicate with each experiment involving the counting and assignment of at least 100 cells. **b)** The same data presented in **a** but splitting assembly into its three component scores of 1-green, 2-blue, 3-yellow and splitting non- assembly into 4-purple and 5-grey. **c)** COS-7 cells expressing deletion mutant Δ635-784 and point mutant L756P GFP-SYCP1. The deletion is indicated in white text. **d)** Electron microscopic analysis of polycomplexes formed by GFP-SYCP1 Δ635-784.

DISCUSSION

3.5.1 The structure of SYCP1 and its role in SC formation

Through a combination of biophysical characterisation and crystal structure solution of two key domains within SYCP1, I have developed a molecular understanding of its obligate structure and the mechanisms by which it may assemble within the synaptonemal complex. SYCP1 adopts a tetrameric conformation, stabilised at its N-terminus as a four-helical bundle which forks at its C-terminus into two, long, coiled-coils. These are flanked by unstructured sequences: An N-terminal unstructured sequence of no known function and a C-terminal unstructured sequence that contains obligate DNA binding sites (Figure 3.5.1). Our model matches the currently known parameters of the SC. For example, the experimentally determined diameter of $\text{SYCP1}_{358\text{-}783}$ is 17.8 Å, closely matching the measured width of transverse filaments of the hamster SC (16 Å) (Solari and Moses, 1973). The length of the SYCP1 structured core (900 Å) is sufficient to span more than half of the central region which measures approximately 1000 Å by electron microscopy. This commonly cited width may in fact be an underestimation due to dehydration steps utilised within sample preparations (Schmekel *et al.*, 1996).

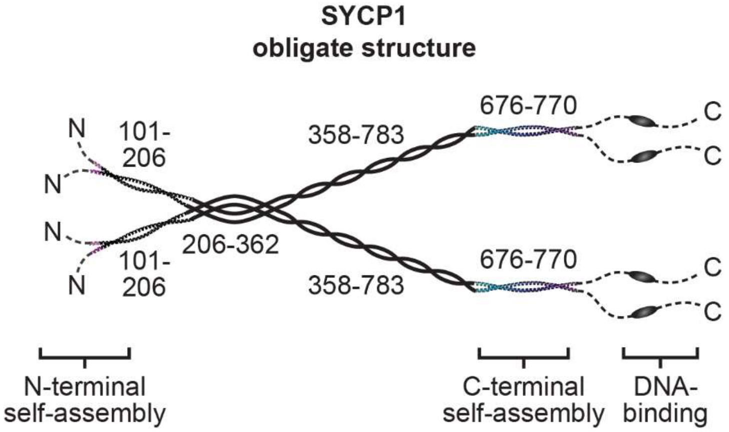

Figure 3.5.1| A model for the obligate structure of SYCP1. a) A schematic of SYCP1 with key domains annotated and demarcated aligned with a molecular model for non-assembled SYCP1. SYCP1 is stabilised as a tetramer by an elongated four-helical bundle structure which splays apart at its N and C-terminus into parallel coiled-coils flanked by sequences capable of mediating self-associations. The N and C-termini are unstructured with the latter containing obligate DNA binding sequences. Schematic by Dr Owen Davies.

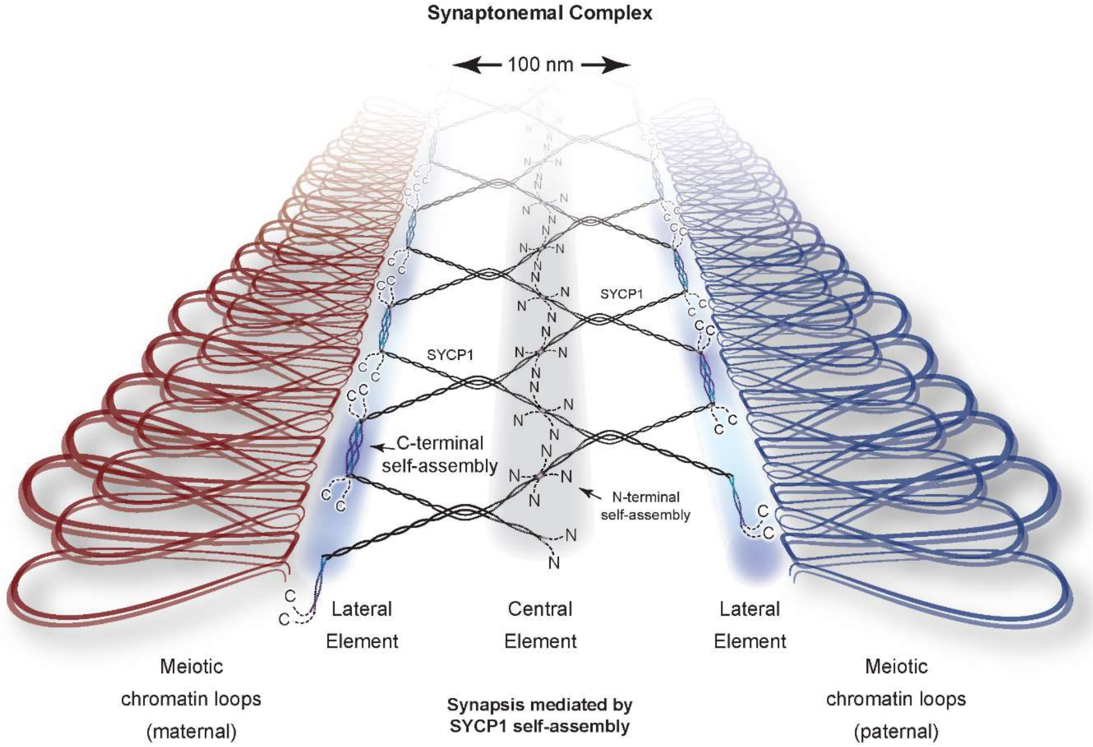
Synaptonemal Complex
100 nm
SYCP1
SYCP1
C-terminal self-assembly
N-terminal self-assembly
N
C
Lateral Element
Central Element
Lateral Element
Meiotic chromatin loops (maternal)
Synapsis mediated by SYCP1 self-assembly
Meiotic chromatin loops (paternal)

Figure 3.5.2| A model for SYCP1-mediated synapsis of meiotic chromosomes. a) The sequences flanking the helical core of SYCP1 can undergo similar, yet distinct, mechanisms of self-assembly. The N-termini recursively associate through staggered head-to-head interactions of bioriented SYCP1 molecules in a dynamic and cooperative manner allowing for structural plasticity and remodelling. The C-termini are recruited to the chromosome axis through obligate DNA binding sequences within the unstructured C-terminus with chromosomal association being strengthened through the protonation-dependent, back-to-back assembly. In combination, these self-assembly mechanisms allow for the formation of a continuous lattice-like array of SYCP1 molecules along the entire chromosome length.

Through solution of their crystal structures, I identified two similar, yet distinct, mechanisms of SYCP1 self-assembly which may mediate higher-order assembly of SYCP1. The so-called αN-tip of SYCP1 (residues 101-111) is absolutely critical for the self-assembly of SYCP1 molecules *in vitro*, mediating head-to-head associations between bi-orientated SYCP1 molecules whilst C-terminal sequences (residues 676-770) undergo protonation-dependent back-to-back assembly to mediate chromosomal axis association. Scaffolded by the SYCP1 architecture, these mechanisms of self-assembly allow for the recursive assembly of SYCP1 molecules within the SC (Figure 3.5.2).

3.5.2 Self-assembly is a recurrent feature of SC proteins

These findings were published, joining a nascent list of articles which mark the foundations for the structural investigations into the structural of mammalian SC proteins and the molecular basis for their incorporation within the SC (Dunce *et al.*, 2018a). It is becoming increasingly clear that self-assembly plays an intrinsic role within SC formation with this self-assembly being mediated by short amino acid sequences which flank structural cores of the constituent proteins. For example, SYCP3 assembly, which presents striking striated ultrastructural features by electron microscopy, can be totally blocked by a truncation of 6 C-terminal amino acids (Syrjanen *et al.*, 2014). Similarly, the assembly of fibrous SYCE2-TEX12 assemblies, also visible by electron microscopy, can also be eradicated by a 10 amino acid truncation at the C-terminus of TEX12 (unpublished findings, Davies lab: Dr Lucy Salmon) (Davies *et al.*, 2012). Recent studies have revealed many mechanisms by which SYCE3 undergoes stepwise oligomerisation in solution, involving domain-swapping in which an SYCE3 dimer unfolds and mediate reconstitutive coiled-coil associations with two further SYCE3 chains to create an elongated SYCE3 tetramer. This, coupled with lateral associations mediated by surface aromatics, allows for limitless assembly of SYCE3 molecules. This observation, coupled with its association with SYCP1 (which initially disrupts SYCP1 lattice structure (unpublished findings, Davies group)) provides a model by which SYCE3 is incorporated within the SC, dependent upon its ability to self-assemble (Figure 3.5.3b).

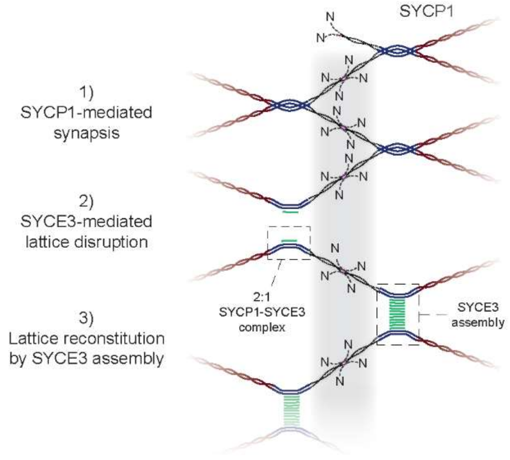
SYCP1
1) SYCP1-mediated synapsis
2) SYCE3-mediated lattice disruption
3) Lattice reconstitution by SYCE3 assembly
2:1 SYCP1-SYCE3 complex
SYCE3 assembly
N

Figure 3.5.3| SYCE3 dynamically remodels the SYCP1 lattice. SYCE3 interacts with the SYCP1 N-terminal tetramer, remodelling it to form a 2:1 SYCP1-SYCE3 complex. SYCE3 within these complexes can subsequently recruit further SYCE3 molecules to reform a continuous synapsis between bound chromosomes.

3.5.3 The sexually dimorphic structure of the SC – length and width.

Many aspects of the meiotic cycle demonstrate sexual dimorphism. The structure of the SC is no exception; female chromosomes in synapsis are approximately 60 % longer than those of male (Jones and Croft, 1989; Wallace and Wallace, 2003; Tease and Hulten, 2004) with similar observations for width (Agostinho *et al.*, 2018). This difference could be accounted for by geometric alterations within the structure of SYCP1; a greater angulation of the N-terminal contacts and SYCP1$_{358-783}$ coiled-coils would reduce SC width (Figure 3.5.4). SYCP1 therefore may act as a concertina to dynamically allow variation in inter-chromosomal distance. If this model is correct, we would expect the same chromosome to be coated by the same number of SYCP1 molecules in male and female, but for the recruitment density to be lower in the longer chromosomes of female. How could this difference arise? The difference appears to be due to a difference in the compaction of DNA at the lateral elements as the meiotic loops of females are twice as short as those of males. This could be due to expression levels of axis proteins or their stability at the axis. A greater axis density, resulting in shorter loops and longer synapsed chromosomes, might be important in females promote stability over years, as more cohesin molecules will associate to bind sister chromatids.

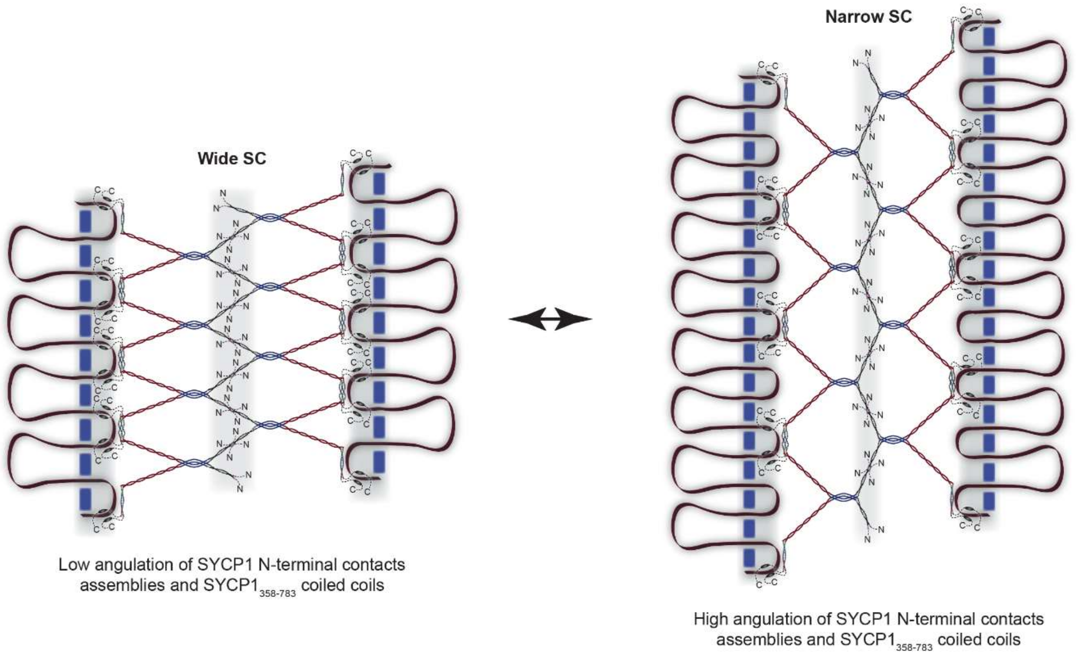

Low angulation of SYCP1 N-terminal contacts assemblies and SYCP1$_{358-783}$ coiled coils

High angulation of SYCP1 N-terminal contacts assemblies and SYCP1$_{358-783}$ coiled coils

Figure 3.5.4| SYCP1 geometry facilitates changes in SC width. The angulation of the N-terminal contacts and SYCP1$_{358-783}$ coiled-coils of SYCP1 may change to allow for changes in inter-chromosomal distance. Schematic by Dr Owen Davies.

3.5.3 Long-range synapsis is dependent upon other SC proteins

Although SYCP1 can be recruited to chromosomes through DNA binding of its C-terminus, it was shown that SYCP1 alone is not sufficient to complete chromosome synapsis with SC central element component knockout mice demonstrating only short stretches of synapsis and SYCP1 null mice showing a complete lack of synapsis (de Vries *et al.*, 2005; Hamer *et al.*, 2006; Bolcun-Filas *et al.*, 2007; Hamer *et al.*, 2008; Bolcun-Filas *et al.*, 2009). As I have shown, SYCP1 assembly in solution is mediated through the homotypic association of the αN-tip which undergoes head-to-head association, bi-orientating opposed molecules. This, I believe, is what mediates initial synapsis events during the installation of the SC. However, *in vivo,* it appears that SYCP1 assembly requires stabilisation through association of SYCE1 and SYCE3 and elongation factors SYCE2 and TEX12 for long range synapsis. How these factors associate has yet to be formalised though it has become biochemically evidenced that SYCE3 is the sole central element interactor of SYCP1, in agreement with a previous suggestion based up the observation that SYCE3 is required for SYCE1 recruitment to SYCP1 “polycomplexes”, i.e. cytoplasmic filamentous networks (Hernandez-Hernandez *et al.*, 2016). This highlights the variable nature of the SC suggesting both temporal and spatial differences in SC structure and composition exist throughout meiosis and along its length.

3.5.2 Are the structure of SYCP1 and its mechanisms of self-assembly conserved across phyla?

The oligomeric state of other transverse filaments from other organisms has not been definitely shown. Tentative data regarding Zip1 proposed that the molecules oligomerise as homo-tetramers which may consist of a dimeric coiled-coil building block (Dong and Roeder, 2000). However these studies utilised bacterially expressed constructs expressed in the insoluble fraction, denatured in 8 M urea and subsequently renatured and stabilised by lysine crosslinking (Dong and Roeder, 2000). Electron microscopic analysis of Zip1$_{1\text{-}700}$, which lacks the unstructured C-terminus, revealed a length of 51 nm (matching the theoretical length of the coiled-coil region). Therefore, it appears that the overall architecture of Zip1 might be something similar to SYCP1. Whether this structure is reciprocated by C(3)G of *Drosophila* currently remains unknown.

How about the mechanisms of self-assembly which allow SYCP1 to create a lattice-like array between synapsed chromosomes – are they conserved across phyla? Within metazoans, the domain structure and sequence of SC proteins are quite conserved. In species as evolutionarily distant as the Medaka fish and *Hydra* species, significant sequence similarity exists. SYCP1 (and SYCP3) of these species contain highly similar domain organisation, with a central helical domain flanked by unstructured N and C-termini (Iwai et al., 2006). Overall, 20 % sequence identity and 45 % sequence similarity exists between the rat sequence of SCP1 and that of medaka fish (Fraune et al., 2012). With rat SCP1 again, the corresponding sequence of *Hydra vulgaris*, shares 18 % identity and 46 % similarity within the central helical domain, 10 % identity and 26 % similarity within the unstructured N-terminus, and the unstructured C-terminus shares 13 % identity and 34 % similarity. These levels of conservation are not particularly interesting, however, what is most interesting, is that the sequences I identified as having self-assembly capabilities are the most conserved regions across the entire sequence. *Hydra* residues corresponding to rat sequence 106-188 (residues 105-187 in humans) encompass the region I attributed to N-terminal self-assembly and show 41 % identity and 67 % similarity. *Hydra* residues corresponding to rat sequence 724-754 (residues 702-732) are embedded within the region I attributed to chromosomal assembly and show 32 % identity and 65 % similarity (Fraune et al., 2012). These values indicate that these regions of the protein are not only important across vertebrates, but also across phyla within metazoans including those as distant as *Cnidaria*. Similar results are presented for SYCP3, showing highly conserved regions flanking the coiled-coil domain which were shown to be involved in its polymerisation and formation of recursive structures *in vivo* and *in vitro*.

It remains to be shown whether functionally similar, yet sequence divergent, sequences within divergent transverse filaments, such as ZIP1 and C(3)G exist. In ZIP1, an interesting mutant of exists in which 4 leucine residues (643, 650, 657, 664) are mutated to alanine. These residues are within the C-terminal end of the Zip1 coiled-coil domain and their mutation results in meiotic blockage during pachytene, with a fully assembled SC (Mitra and Roeder, 2007). It remains unclear as to how these mutations might have such an effect.

3.5.2 The unknown function of the SYCP1 N-terminal unstructured region

A direct role for the unstructured N-terminus of SYCP1 has not been identified. Higher-order assembly of SYCP1 molecules via the αN-tip is independent of unstructured residues 1-100. However, given the range and smaller size of molecular species revealed upon analysis of SYCP1$_{1\text{-}362}$ (in comparison with SYCP1$_{101\text{-}362}$) by SEC-MALS, it is possible that these residues partially inhibit assembly. By their modification, they might enact a regulatory mechanism which stabilises or destabilises midline assembly. It has been shown that the N-terminus of ZIP1 is similarly not required for synapsis (Tung and Roeder, 1998).

I noted the presence of a 4 amino acid sequence, FVPP, at the extreme N-terminus of SYCP1 (residues 10-13). This sequence, also present within BRCA2, and other regulators of recombinases, has been shown to mediate interactions with DMC1 (Thorslund *et al.*, 2007; Dunlop *et al.*, 2011). Although I did not detect an interaction between the N-terminus of SYCP1 and DMC1 biochemically, I have found that similar interactions are generally quite unstable and therefore the possibility may not be excluded.

Could the N-terminus of SYCP1 be involved in the recombination process? Bioinformatic analysis of SYCP1 revealed that the N-terminal tip of the central helical domain is highly basic. The basic residues which confer this charge are within the αN-tip sequence and create a highly basic solvent exposed patch (Figure 3.5.5). Could this sequence, localised within the midline of the assembled SC, play a role in the stabilisation of DNA repair intermediates during the process of recombination. Perhaps the SYCP1 N-terminus specifically recognises and stabilises the double Holliday Junction to facilitate its processing? A similar basic patch exists within the sequence of ZIP1, suggesting a potentially evolutionary conserved mechanism.

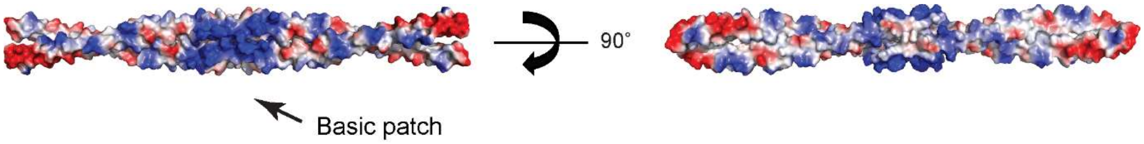

Figure 3.5.5| Electrostatic surface of SYCP1$_{101\text{-}175}$. The αN-tip sequence stabilises head-to-head contacts between bi-orientated SYCP1 coiled-coils. Surface exposed basic residues cluster at the head-to-head interface to create a highly charged basic patch. Blue represented basic residues, red is acidic.

3.5.2 DNA-binding constitutes the only known link to the chromosome axis

I have shown that the C-terminus of SYCP1 is required for association with DNA. The supposition that SYCP1 is a DNA binding protein was first raised upon its discovery by Meuwissen et al. in 1992 in which they describe a basic unstructured C-terminus with SP/TP-XX sites characteristic of DNA-binding proteins (Meuwissen *et al.*, 1992). Using EMSA, I provided the first biochemical evidence that SYCP1 associates with DNA, and tentatively suggest a footprint of around 10 bases of DNA per SYCP1 molecule. The interaction is mediated by the C-terminal unstructured amino acids a feature consistent across transverse filaments of diverse evolutionary history. For example, C(3)G of *Drosophila melanogaster* also contains a basic C-terminus. Upon its deletion, C(3)G is no longer recruited to the lateral elements of chromosomes, and otherwise forms interesting, barrel-shaped polycomplexes demonstrating a striated ultrastructure by electron microscopy (Anderson *et al.*, 2005). This suggests that self-assembly of the transverse filament protein is not precluded by removal of the unstructured C-terminus but is essential for chromosomal recruitment. Similarly, the C-terminus of ZIP1 is essential for its chromosomal recruitment in *Saccharomyces cerevisiae* (Tung and Roeder, 1998). Similar experiments have not been performed in mammals. To test the importance of the SYCP1 C-terminus, I analysed the effect of its removal on polycomplex formation, on the (now realised to be flawed) understanding that cytoplasmic networks, referred to as polycomplexes, represented self-assembled structures consisting of SYCP1 molecules. I found that its removal blocked the formation of these networks, resulting alternatively in the formation of large cytoplasmic aggregates, observed in a previous study by Yuan *et al.* (Yuan *et al.*, 1996). I question, as discussed below, the true identity of cytoplasmic networks and therefore published findings concerning the effect of mutations and truncations upon the ability of SYCP1 to self-assemble.

3.4.5 SYCP1 polycomplexes represent misunderstood entities

The finding that cytoplasmic networks still formed upon the overexpression of SYCP1$_{640\text{-}976}$ in COS-7 cells was the critical finding in realising that these networks cannot be the self-assembled recursive structures observed by electron microscopy, as previously described (Ollinger *et al.*, 2005). The cytoplasmic aggregates which I have observed by fluorescence often have an ovular appearance, much like the polycomplexes which I observed by electron microscopy for wild-type SYCP1. The suggestion that these aggregates constitute the structures observed by electron microscopy is supported by the finding that despite not regularly observing filamentous assemblies for SYCP1$_{1\text{-}954}$, SYCP1 T859A and SYCP1 T859E, striated polycomplex structures were still identified.

I therefore propose that the cytoplasmic networks are in fact a network of an intermediate filament protein, such as keratin, to which SYCP1 has been recruited in a manner dependent upon its basic C-terminus (Figure 3.5.6a) (Portet *et al.*, 2015). This is feasible given the net acidic charge of the coiled-coil domain of keratin (Figure 3.5.6b). The effect of all mutations and truncations upon polycomplex formation by SYCP1 would therefore need to be reassessed to draw reasonable conclusions from their formation. This would have to be done by electron microscopy as analysis by fluorescence runs the risk of conflating other cytoplasmic aggregate-like structures which may be formed by SYCP1 such as collagenous fibres, inclusion bodies (Figure 3.5.6e for comparison (Sakuragawa, 1976)), and granules (Figure 3.5.6d-f). Whether SYCP1 constitutes these features would need to be confirmed by immune-gold antibody staining.

The idea that an intermediate filament could form a basis for synaptonemal complex assembly is a truly exciting possibility. Intermediate filament proteins might constitute a component of the axial elements and provide a mechanism (possibly in addition to DNA binding) for recruitment of SYCP1 to axial elements.

Further, if true polycomplexes were formed by SYCP1$_{1\text{-}783}$, for example, this might be used as a model for studying SYCP1 assembly in COS-7 cells, negating the issue of SYCP1 recruitment to filamentous networks. This would allow for further studies, such as answering the question of what else constitutes a polycomplex? Polycomplexes have been purported to contain other components such as DNA and RNA (Goldstein, 1987). It is unknown whether they contain other SC proteins which might be minimally expressed in COS-7 cells, despite dividing mitotically. In *Drosophila* it was found that polycomplex formation is upregulated upon mutation of an E3 ligase, Sina (Hughes *et al.*, 2019). To these polycomplexes, another SC component, Corolla, is recruited. Perhaps other SC proteins of humans are essential for the formation of SYCP1 polycomplexes? This can be addressed through antibody staining of polycomplexes with antibodies raised towards further components.

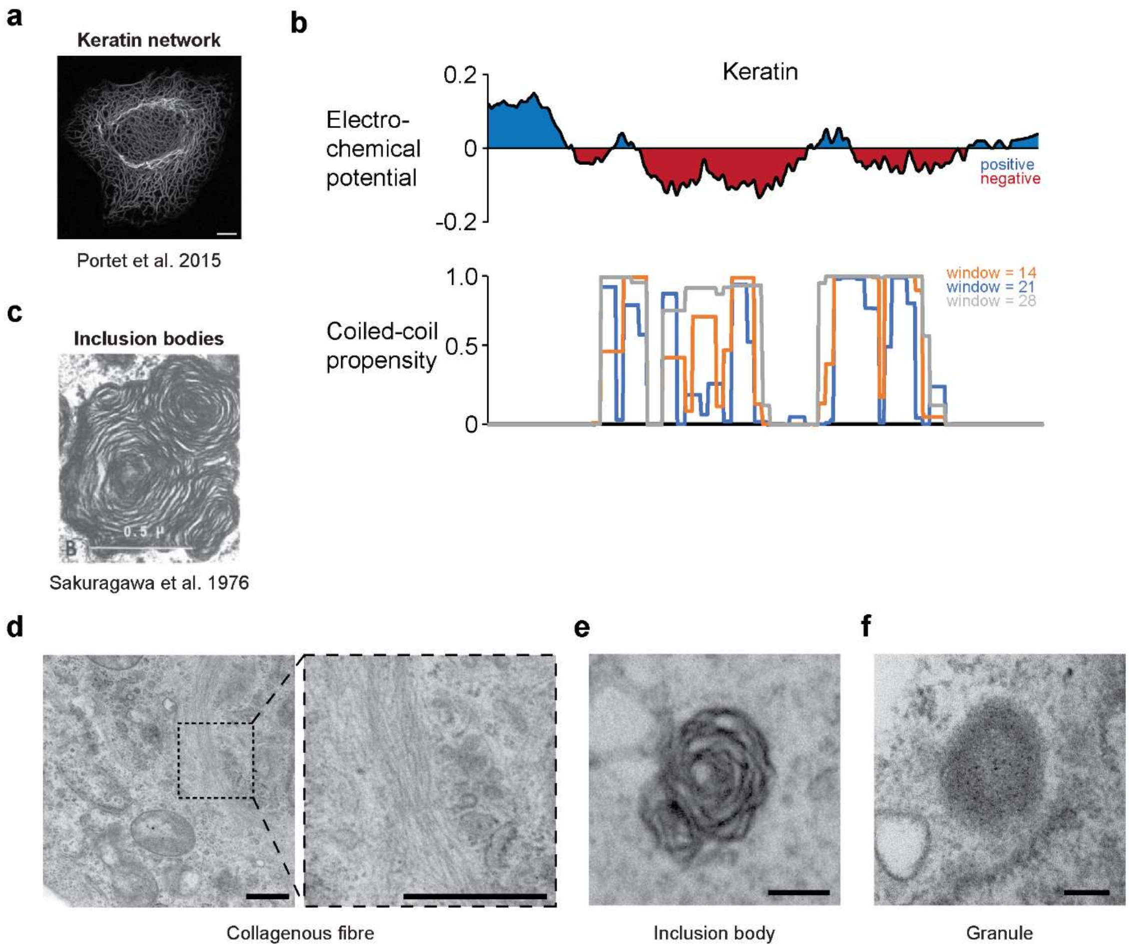
a
Keratin network
Portet et al. 2015
b
Keratin
0.2
Electro-
chemical
potential
0
-0.2
positive
negative
1.0
Coiled-coil
propensity
0.5
0
window = 14
window = 21
window = 28
c
Inclusion bodies
B
0.5 μ
Sakuragawa et al. 1976
d
e
f
Collagenous fibre
Inclusion body
Granule

Figure 3.5.6| Uncertainty surrounding the nature of SYCP1 polycomplexes. a) An example keratin network in hepatocellular carcinoma-derived PLC cell from Portet et al. 2015. Scale bar – 10 µm. **b)** Charge distribution and coiled-coil propensity of the keratin sequence as determined by charge of the EMBOSS suite and COILS. **c)** An inclusion body within a glial cell of an albino rat after injection of the hypocholesteremic agent, trans-1,4-bis(2-chlorobenzylaminomethyl) cyclohexane dihydrochloride. **d)** Electron microscopy of a collagenous structure within COS-7 cells and a close-up. Scale bars – 500 nm. **e)** An inclusion body of COS-7 cells upon over-expression of GFP-SYCP1$_{1\text{-}976}$. Scale bar – 500 nm. **f)** A granule of COS-7 cells upon over-expression of GFP-SYCP1$_{1\text{-}976}$. Scale bar – 100 nm.

3.4.5 What is the structure of an SYCP1 polycomplex?

Images of polycomplexes presented thus far have shown a frontal view in which polycomplexes appear as a series of alternating light and dark bands, identified as constituting sites of N- and C-terminal self-assembly (Ollinger *et al.*, 2005). These could be mediated by the sequences identified as possessing self-assembly properties (Figure 3.5.7b). These light and dark bands are visible in multiple species, such as in *Ascaris suum* (Figure 3.5.7a) (Goldstein, 1987). However, the N-termini have not definitively been shown to be localised to the lighter bands – only antibody localisation of the C-termini was performed. In fact, in top-down views of the polycomplex, such as that presented in Figure 3.5.7c, these lighter bands are not visible. The array of dense dots likely represents vertical pillars (LE-like structures) through which a slice has been made to visualise the consistent adoption of a trigonal arrangement. Could it be that the lighter bands visible in the frontal view are in fact also LE-like assemblies but in a different plane and in fact do not represent central element-like assemblies?

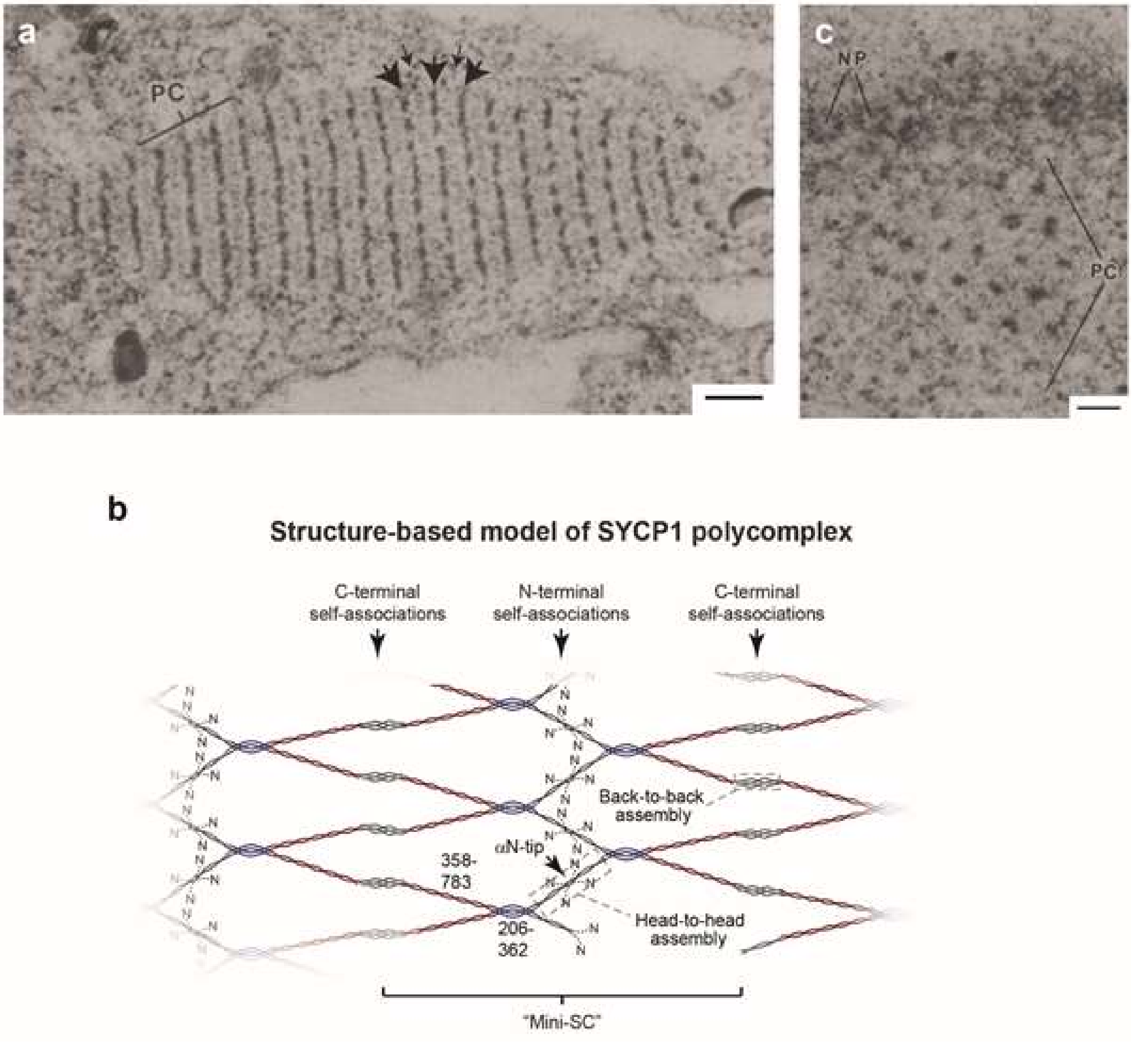
a
PC
c
NP
PC
b
Structure-based model of SYCP1 polycomplex
C-terminal self-associations
N-terminal self-associations
C-terminal self-associations
N
Back-to-back assembly
αN-tip
358-783
206-362
Head-to-head assembly
"Mini-SC"

Figure 3.5.7| Polycomplex formation in *Ascaris suum* and a 2-dimensional model for polycomplex structure. a) An ovular-shaped polycomplex within the cytoplasm of *Ascaris suum*. Lateral and central element-like structures can be seen in this "frontal" view indicated by large and small arrows, respectively. Scale bar = 0.2 µm **b)** A 2-dimensional model for the structure of a polycomplex in which N-terminal self-associations form midline like assemblies whilst C-terminal self-assembly sites. **c)** A polycomplex of *Ascaris suum* presumed to represent a slice through the polycomplex structure such that dense lateral element-like bands appear as dots. Nuclear pore complexes embedded within the nuclear envelope are indicated NP. Scale bar = 0.1 µm.

To answer this question, I performed a rudimentary geometric analysis of a polycomplex using a top-down view (Figure 3.5.8). By drawing lines across the planes of LE-like pillars, an array of tessellating triangles is identified (Figure 3.5.8a,b). The constituent triangles can then be separated and sequentially aligned then averaged to create the "average triangle" which can be re-tessellated to create an idealised polycomplex devoid of deviations due to changes in structure across the complex (Figure 3.5.8c). This ideal polycomplex lattice closely matches the original (Figure 3.5.8d). Assuming N-terminal self-assembly of the transverse filament protein does contribute to polycomplex formation, there are two possible locations for N-terminal self-associations – on the axes between LE-like dots or central to the "triangles" (Figure 3.5.8e). The inter-LE-like dot is not affected by either possibility, but a longer LE-like to central element-like dot is increased from 50 nm to 58 nm.

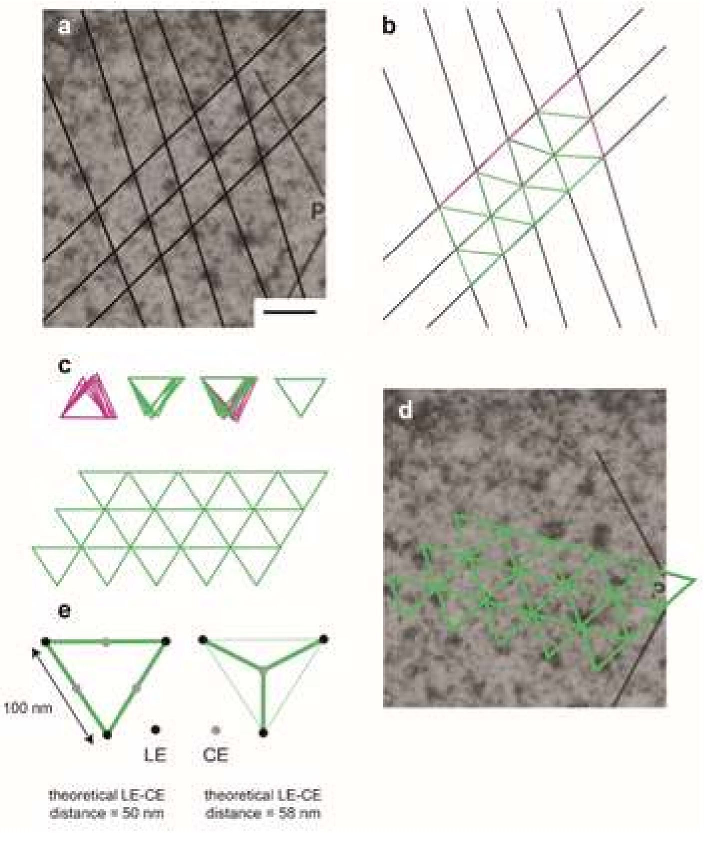
a
P
b
c
d
e
100 nm
LE
CE
theoretical LE-CE distance = 50 nm
theoretical LE-CE distance = 58 nm

Figure 3.5.8| Geometric analysis of the polycomplex structure. a) Electron micrograph showing a top-down view of an *Ascaris suum* polycomplex. Planes connecting the LE-like pillars are indicated, dissecting the structure into rhomboid units. **b)** Each rhomboid may be halved to create triangles. **c)** Averaging of these triangles creates an equilateral triangle which may be tessellated. **d)** The resulting tessellation closely approximates the lattice observed by EM. **e)** The location of N-terminal contacts with respect to C-terminal contacts is unknown. These might be situated along the inter-LE planes or central to the constituent triangles. The location affects the distance between LE-like pillars and sites of N-terminal association.

3.5.6 Controlling chromosomal recruitment and stability of SYCP1

Initial recruitment to the chromosome axis is mediated through direct DNA association of sites within the unstructured C-terminus of SYCP1. C-terminal self-assembly in which two dimeric coiled-coils undergo protonation-dependent back-to-back assembly results in the formation of a tetrameric assembly which possesses DNA binding capability. The formation of this structure specifically in the proximity of the chromosome axis provides an elegant mechanism to prevent precocious self-assembly in the absence of the chromosome. Its binding might support initial contacts to create a robust chromosomal attachment. Further, on the basis of the observation that SYCP1$_{676\text{-}783}$ forms of an octamer and higher-order assemblies at pH 4.6 in 1 M KCl, I tentatively propose a mechanism by which these tetrameric assemblies might undergo domain-swap associations to create planar lattices of molecules in which all basic patches are aligned creating an extensive DNA interacting surface (Figure 3.5.9a). This requirement for a high salt concentration might be a reasonable requirement within the context of the micro-environment proximal to the chromosome in which high anion concentrations exist in an "ion atmosphere" around DNA molecules (Jacobson and Saleh, 2017).

The chromatin status of DNA at the chromosomal axis is unknown. However, supposing DNA is packaged within nucleosomes, there is a potential that the separation between the basic patches of the SYCP1 tetrameric self-assembly (~30 Å) is such that association of both DNA duplexes, which wrap the nucleosome core, is facilitated (Figure 3.5.9b).

In addition to protein-DNA associations, chromosomal association may be stabilised through protein-protein associations, though no interactions of the SYCP1 C-terminus have conclusively been demonstrated. Weak yeast 2-hybrid data suggests that SYCP2 interacts with the C-terminus of SYCP1 but the published data are lacking negative controls (Feng et al., 2017). However, this finding was not reproduced in further yeast 2-hybrid experiments (Owen Davies, unpublished).

How could chromosomal disassembly be achieved? Phosphorylation of SYCP1 (potentially by PLK1 and CDK1) appears to be important for the disassembly of the synaptonemal complex (Parra *et al.*, 2003; Jordan *et al.*, 2012). The unstructured C-terminus of SYCP1 contains many potential phosphorylation sites. Of note, T859 is highly conserved and could be part of a consensus S/TPXX motif, commonly associated with DNA binding property of gene regulatory proteins (Suzuki, 1989) or a site for phosphorylation by cyclin-dependent kinases (Nash *et al.*, 2001). I found that mutation of T859 results in the ablation of filamentous network assembly in COS-7 cells, which might, according to our theories regarding the identity of such networks, represent a blocked ability to associate with electro-positive molecules. In *Saccharomyces cerevisiae*, deletion of residues 791-824 in Zip1 results in a complete block of chromosomal assembly. This region encodes the following sequence: **VDHISKSRINSSKETSKFNDEFDLSSSSNDDLEL**. This serine rich series of amino acids is not particularly basic so likely doesn't contribute directly to DNA binding in an unmodified state but is a probable target for phosphorylation. Perhaps the negative charge conferred upon phosphorylation of these regions are required to facilitate DNA association? If true, could this mechanism of control also exist in humans? If so, which sites within the SYCP1 are phosphorylated?

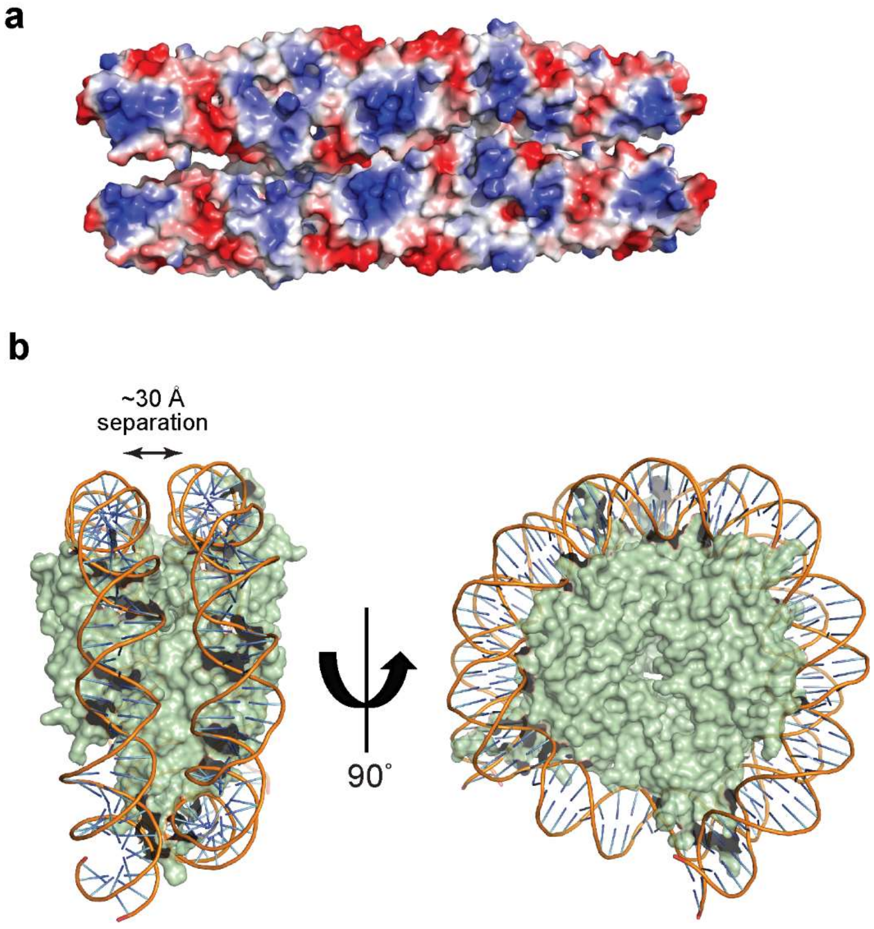

Figure 3.5.9| Chromosomal association through SYCP1$_{676-770}$ assembly. a) The electrostatic surface of the modelled SYCP1$_{676-770}$ octamer presented in Figure 3.4.23 shows the alignment of basic patches. **b)** The structure of the nucleosome (PDB 3AFA (Tachiwana *et al.*, 2010)) showing the winding of the DNA double-helix around the octameric histone core, with a separation of approximately 30 Å between the two strands.

3.5.7 Another structure of the SYCP1$_{676-770}$ region

Interestingly, during the period within which we were writing an article based upon the discussed findings, another group published a similar structure (PDB 4YTO) (Seo *et al.*, 2016). However, the group failed to recognise the true biological unit, opting to report an anti-parallel dimer in the absence of sufficient supporting biochemical or biophysical data whilst ignoring the published literature concerning the orientation of SYCP1 molecules within the SC. However, the structure they solved is largely similar to both the $I4_122$ and C2 structures. The main difference is found upon superimposition of their structure with our C2 structure (Figure 3.5.10a). The C-termini of 4YTO parallel chains splay apart, maintaining only associations between anti-parallel chains. Further, the sequences between the lateral and central interfaces exhibit reduced B-factors in the 4YTO structure in comparison with the $I4_122$ structure and the non-disulphide end of the C2 structure (Figure 3.5.10b). This is likely a consequence of crystal packing as, in contrast the $I4_122$ and C2 crystal lattices which were stabilised by lateral helical associations, the crystal lattice of the 4YTO structure is formed through angled perpendicular associations mediated through solvent exposed residues within the intermediate sequence, bounded by dashed boxes (Figure 3.5.10c,d).

3.5.8 SYCP1 as the basis for the synapsis of meiotic chromosomes

SYCP1 is the primary component of the mammalian synaptonemal complex, capable of being recruited to meiotic chromosomes in the absence of any other SC component and being absolutely essential in initiating the process of synapsis (de Vries *et al.*, 2005). Here we have determined the underlying geometry of the SYCP1 molecule and elucidated two distinct mechanisms of its self-assembly which utilise sequences flanking its structural core. Its tetrameric forking structure scaffolds these sites, positioning N-termini for recursive head-to-head associations to drive midline assembly whilst C-terminal sites assemble back-to-back to reinforce chromosomal associations. Short stretches of SYCP1 mediated synapsis must then be reinforced and remodelled by other SC components and it will be interesting to learn how this is achieved within the highly dynamic structure of the SC. Within the next chapter, I discuss and present findings regarding the structure and function of the meiotic telomere complex, an assembly required for the transmission of cytoskeletal forces to the chromosomes ends such that rapid prophase movements may facilitate the synapsis of meiotic chromosomes.

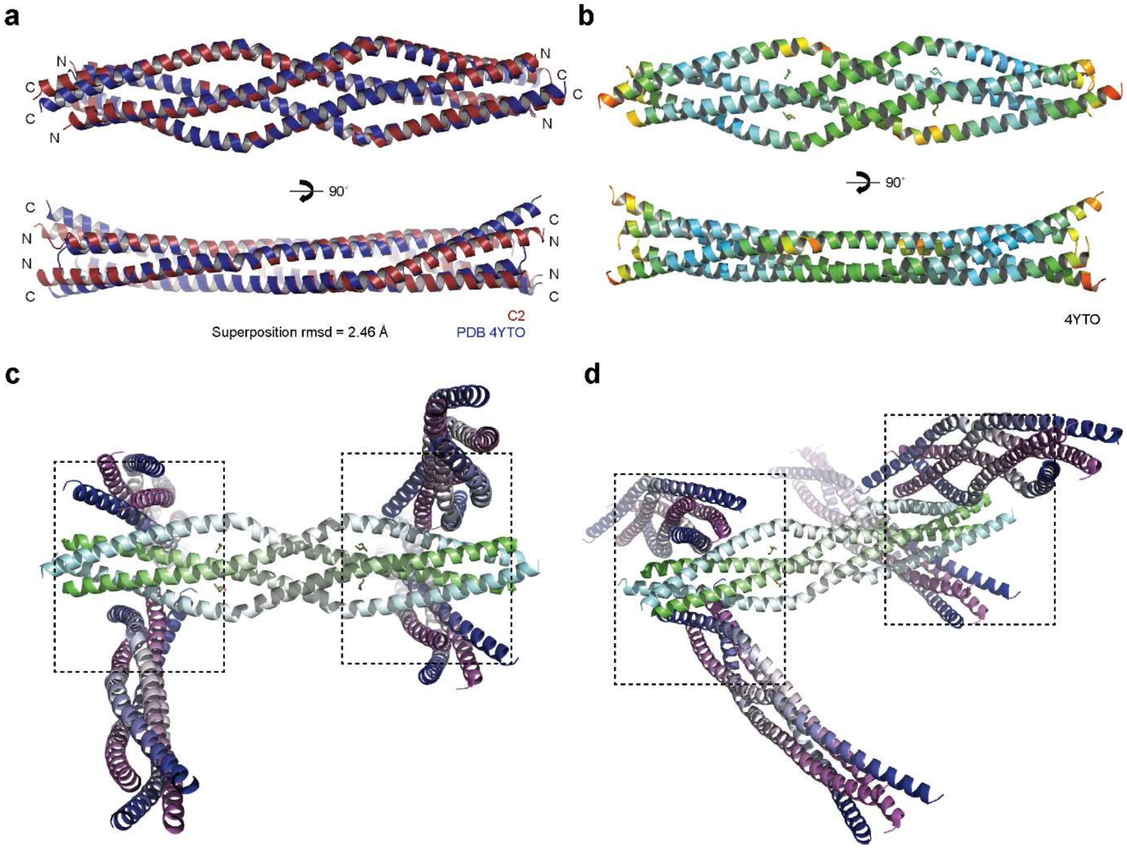
a
N
C
C
N
N
C
C
N
90°
C
N
N
C
C
N
N
C
Superposition rmsd = 2.46 Å
C2
PDB 4YTO
b
90°
4YTO
c
d

Figure 3.5.10| Comparison of the SYCP1$_{676-770}$ to the concurrently solved 4YTO structure. a) Superimposition of crystal form 1 (brick red) with PDB 4YTO (blue) showing overall backbone similarity with deviation at the C- terminus. **b)** The 4YTO structure demonstrates B-factors at the sequences between the central and lateral interfaces. **c-d)** Crystal packing of the 4YTO structure demonstrates perpendicular contacts with angulated tetramers mediated by sequences within the intermediate sequence between the central and lateral interfaces. **c)** Frontal view. **d)** Angled perspective.

Chapter 4

The MAJIN-TERB2 structure scaffolds the meiotic telomere complex and telomeric DNA

INTRODUCTION

4.1.1 Homologue pairing is facilitated by rapid prophase movements of chromosomes

The process of forming complete chromosome synapsis is facilitated by a process of rapid chromosomal movements in which cytoskeletal forces are transmitted to chromosomes via their telomeric ends anchored within the nuclear envelope. These so-called rapid prophase movements are conserved across evolution and appear to function in disentangling interlocked chromosomes and facilitating homology searching. This chapter focuses on the molecular movers in this scheme, with particular attention paid to the recently discovered meiotic telomere complex which plays a role in recruiting, and maintaining attachment of, the telomeric ends of chromosomes to the nuclear envelope.

Rapid prophase movement (RPM) of meiotic chromosomes occurs during zygotene (Zickler and Kleckner, 1998). Cytologically, RPMs are visible as dramatic chromatin movements in which chromosomes undergo dynamic special organisation, culminating in the formation of the "meiotic bouquet", a polarised chromosome organisation in which chromosome telomeres are clustered at one nuclear envelope location with chromatin looping into the nucleoplasm (Figure 4.1.1a). Although the product of RPMs is evolutionarily conserved, the mode and direction of RPMs, differs across species. In mammals, in which the nuclear envelope eventually breaks down during metaphase to allow microtubular attachment to the kinetochore during division, the nucleus remains spherical and rotates whilst chromosomes move within the nuclear envelope, led by nuclear envelope associated telomeres (Lee *et al.*, 2015). In contrast, in yeast, in which the nuclear envelope remains intact throughout division, telomere-led movements drag chromosomes back and forth between the poles of an elongated nucleus (Chikashige *et al.*, 1994).

How do rapid prophase movements facilitate chromosome synapsis? It was originally suggested that RPMs help to align chromosomes for the formation of synapsis. However, as global alignment has already been achieved during leptotene and RPMs occur in zygotene this suggestion has been abandoned. Although not formally confirmed, it is now proposed that rapid prophase movements are required in order to resolve issues which arise during chromosome pairing. Firstly, during the initial stages of homologous recombination, strand invasion may occur between homologous regions on non-homologous chromosomes and these erroneous connections must be broken. Secondly, chromosome interlocks, the result of chromosome axes encircling another chromosome and forming short stretches of synapsis either side of a trapped chromosome, must be resolved (Koszul and Kleckner, 2009). It had been suggested that DNA topoisomerase II might be used to release interlocks by allowing for passage of one chromosome through another (von Wettstein *et al.*, 1984). However, the presence of highly proteinaceous chromosome axes makes this unlikely. It is now proposed that the physical action of rapid chromosome movements might be enough to disentangle interlocks and erroneous contacts between non-homologous chromosomes (Zickler and Kleckner, 2015).

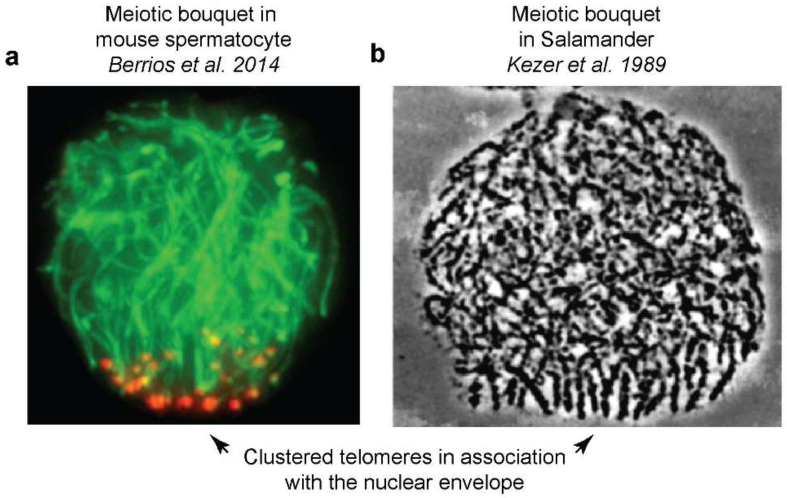

Figure 4.1.1| The meiotic bouquet. a,b) The meiotic bouquet structure in **a)** mouse spermatocytes and **b)** salamander during late zygotene in which telomeric chromosome ends are localised to one nuclear pole with synapsed chromosomes looping into the nucleoplasm.

4.1.2 The generation of rapid prophase movements

Despite differences in the movement of chromosomes within the nucleus, the major commonality between RPMs of different species is the role of cytoplasmic microtubules, destabilisation of which results in disruption of RPMs (Paluh *et al.*, 2004; Lee *et al.*, 2015). This raises the question of how are RPMs powered? As cytoskeletal forces appear to drive the movement of meiotic chromosomes, cytoplasmic motor proteins are implicated. Through inhibition studies, it was found that in mammalian cells, dynein in complex with dynactin, the sole positive-negative motor protein in the cytoplasm (in comparison to the numerous and diverse negative-positive kinesin molecules) generates the required force (Lee *et al.*, 2015; Reck-Peterson *et al.*, 2018). Dynein-dynactin bind to microtubules and move from the plus end to the minus end of the polymer. Therefore, there must be a physical linkage between dynein-dynactin and the telomeres of meiotic chromosomes. In fact, such a structure is visible by electron microscopy with lateral elements thickening as the SC abuts the nuclear envelope (Figure 4.1.2a,b). This chapter shall focus on the structural basis for the transmission of this dynein movement along microtubules to the telomeric ends. This is achieved through a concert of inter-connected protein assemblies including: 1) The Linker of Nucleoskeleton and of Cytoskeleton (LINC) complex, 2) The meiotic telomere complex and 3) the Shelterin complex. The following discussion shall aim to cover the molecular mechanisms and structures employed by these three complexes to facilitate RPM.

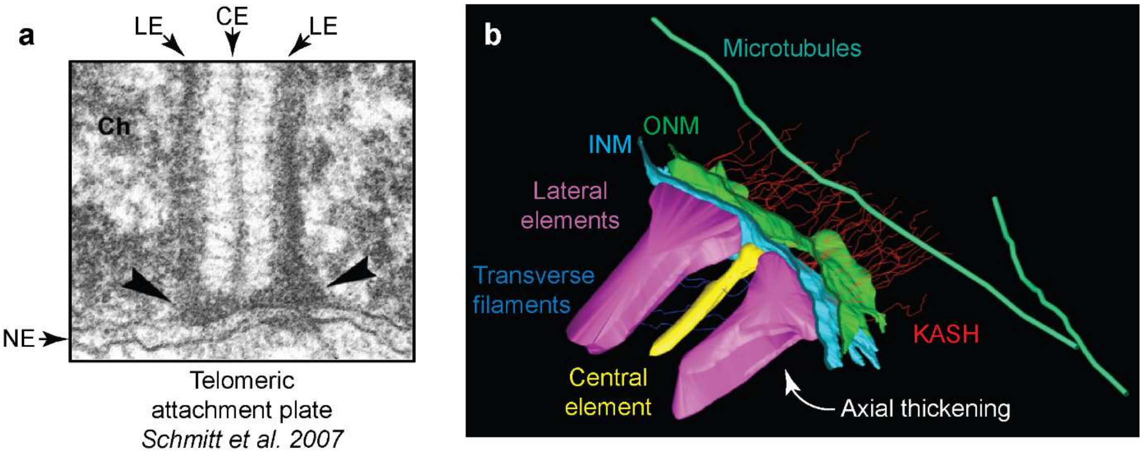

Figure 4.1.2| The telomeric attachment plate. a) Electron micrograph of the synaptonemal complex of mouse fused with the nuclear envelope. The lateral and central elements and the nuclear envelope are indicated (LE, CE and NE, respectively). At the attachment plate, the lateral elements thicken. **b)** Imaging of multiple planes through a membrane bound synaptonemal complex by electron microscopy allows for 3-dimensional rendering of the structure. This reveals electron dense tubular structures running tangentially to the nuclear envelope towards which fibrillar structures emanate from the nuclear envelope. These are postulated to be microtubules and KASH proteins, respectively.

4.1.3 Transmission of cytoskeletal forces through the nuclear envelope by the LINC complex

RPMs are dependent upon the SUN and KASH proteins (Lee *et al.*, 2015). LINC complexes represent a distinct group of complexes consisting of a Sad1/UNC-84 (SUN) -domain containing protein and a Klarsicht/ANC-1/Syne/homology (KASH) -domain containing nesprin. LINC complexes localise specifically to the nuclear envelope and are ubiquitously expressed, functioning to mediate nuclear positioning (Zhang *et al.*, 2009).

The N-terminus of SUN1 is nucleoplasmic, forming direct interactions via its extended N-terminus with the nuclear lamina, a 400 – 600 Å thick proteinaceous meshwork associated with the inner nuclear membrane (Haque *et al.*, 2006; Lu *et al.*, 2008). This tight association with the nuclear lamina allows for cytoskeletal forces to drive nuclear rotations and movement (Wu and Kengaku, 2018). However, this association would be recalcitrant for chromosome end motility. It has been suggested that to this end, that phosphorylation of SUN1 at 3 sites in its nucleoplasmic domain weakens lamin association, allowing for fluid movement within the plane of the nuclear envelope (Patel *et al.*, 2014).

The same study in which the lamin interaction was identified also found through selective permeabilization of the nuclear membranes that the SUN1 C-terminal domain is located within the perinuclear space (Figure 4.1.4). This domain, termed the SUN domain, is conserved across SUN proteins 1-5 in mammals, and across phyla with a similar domain located within Mps1 of *Saccharomyces cerevisiae* and SUN-1 of *Caenorhabditis elegans* (Conrad *et al.*, 2007; Woglar and Jantsch, 2014). Within the perinuclear space, KASH molecules, via their C-terminus interact with the SUN domain (Kim *et al.*, 2015). The structures of SUN2-KASH1 and SUN2-KASH2 have been solved (Figure 4.1.3a,b). Each subunit consists of a globular SUN1 β-sandwich fold at the end of an α-helical stalk. On the basis of these structures and the gel filtration elution profile of SUN1 (from which authors suggest stability as both trimers and monomers), the authors declared that the complex is trimeric, with a trimeric SUN2 interacting with 3 KASH peptides (Sosa *et al.*, 2012; Zhou *et al.*, 2012). However, lack of biophysical characterisation meant that a head-to-head association of SUN-KASH trimeric complexes present within the crystal lattice was dismissed (Figure 4.1.3c). A similar crystal lattice contact exists between SUN1-KASH1/4/5 complexes with biophysical evidence, including SEC-MALS and SAXS, demonstrating that this interaction is present in solution and is tight (Manickam and Davies, unpublished findings). This has implications upon how we perceive SUN-KASH architecture within the nuclear envelope. KASH proteins also contain a transmembrane helix, N-terminal to their SUN-interacting KASH domain, which spans the outer nuclear membrane (Starr, 2011). The role of the LINC complex in connecting the inner and outer nuclear membranes is concomitant with the finding that disruption of the LINC complex results in increases in perinuclear space in some cell types (Cain and Starr, 2015). In fact, LINC complexes are the only other known connections between the inner and outer nuclear membranes in addition to the nuclear pore complex (Crisp *et al.*, 2006). The extended N-terminal sequence of the KASH molecule, which is highly divergent between molecules KASH1-5 of mammals, is therefore localised within the cytoplasm and found to associate with an array of cytoskeleton-associated motor proteins (Starr, 2011).

KASH5 was identified as being a meiosis-specific KASH protein (Morimoto *et al.*, 2012). It was found to interact with SUN1 and localises to the telomeric ends of chromosomes anchored at the nuclear envelope and interestingly, in many cells, it was noted that KASH5 preferentially localises to the nuclear pole proximal to the spindle pole body (Horn *et al.*, 2013). An interaction between dynein and dynactin was identified through immunoprecipitation from mouse testis extract, similarly to how KASH1 and KASH2 interact with kinesin (Zhang *et al.*, 2009; Morimoto *et al.*, 2012).

However, there is a final missing link. As LINC complexes are constitutively expressed, and the fact that chromosome ends are not by nature fused with the nuclear envelope indicates that the telomeres of meiotic chromosomes must be modified, with additional components required to associate telomeres with NE-confined LINC complexes (Shibuya and Watanabe, 2014). This is where the meiotic telomere complex plays a role. Figure 4.1.4 summarises the knowledge thus far described for how cytoskeletal forces are transmitted across the nuclear membrane to the telomeres of meiotic chromosomes.

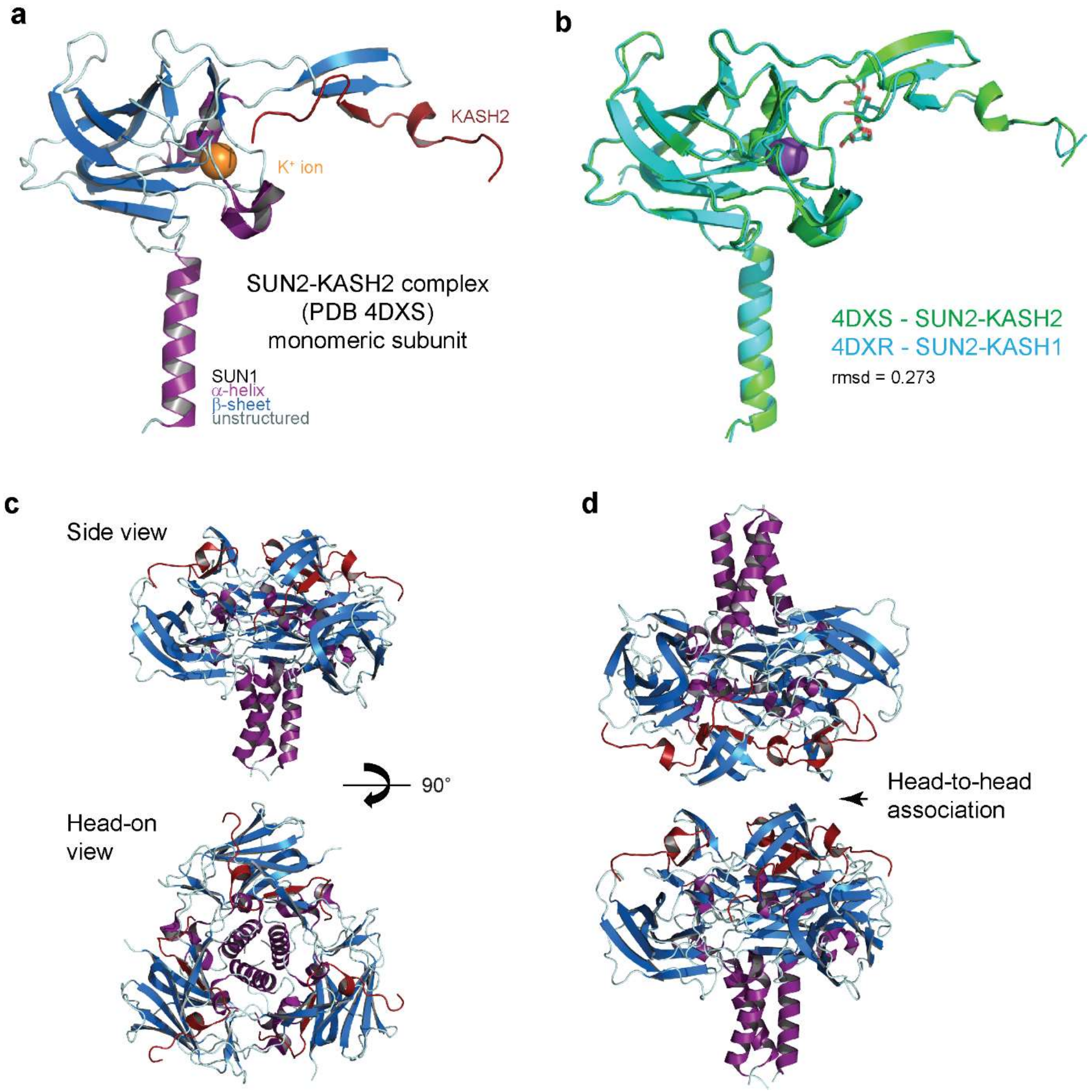
a
KASH2
K^+ ion
SUN2-KASH2 complex
(PDB 4DXS)
monomeric subunit
SUN1
α-helix
β-sheet
unstructured
b
4DXS - SUN2-KASH2
4DXR - SUN2-KASH1
rmsd = 0.273
c
Side view
90°
Head-on
view
d
Head-to-head
association

Figure 4.1.3| The structure of the SUN-KASH complex. a) The monomer structure of SUN2-KASH2 (PDB 4DXS), coloured by secondary structural elements with the KASH2 peptide in red. SUN2 forms a β-sandwich fold at the end of an α-helical stalk. **b)** Alignment of SUN2-KASH2 with SUN2-KASH1 (PDB 4DXR) showing the adoption of an identical structure (all-atom rmsd = 0.273). **c)** Trimeric SUN2-KASH2 structure from both side and head-on views. **d)** Symmetry-related trimeric complexes form a head-to-head contact.

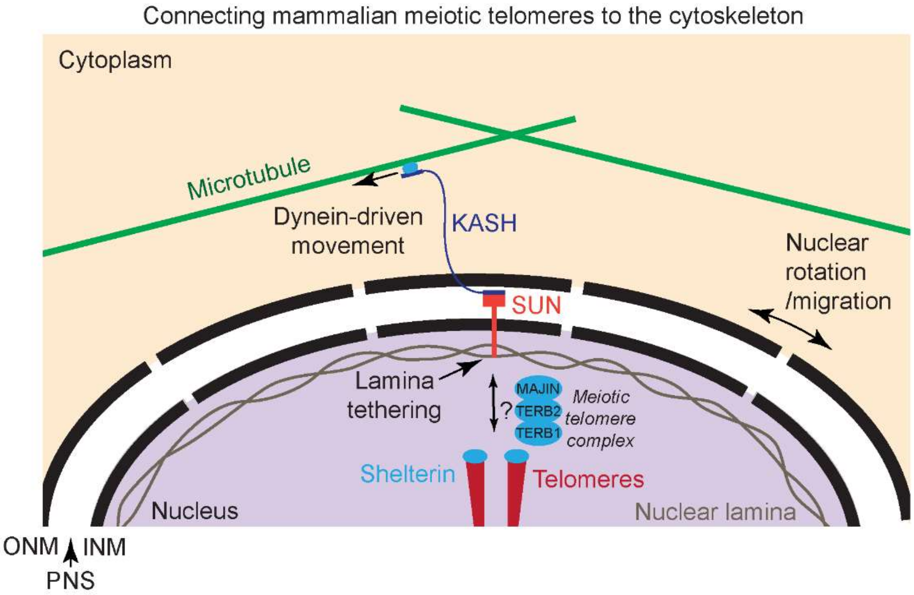
Connecting mammalian meiotic telomeres to the cytoskeleton
Cytoplasm
Microtubule
Dynein-driven movement
KASH
Nuclear rotation /migration
SUN
Lamina tethering
?
MAJIN
TERB2
TERB1
Meiotic telomere complex
Shelterin
Telomeres
Nucleus
Nuclear lamina
ONM
INM
PNS

Figure 4.1.4| Cytoskeletal forces drive rapid prophase movements of meiotic chromosomes. A schematic showing the protein-protein interactions involved in connecting cytoskeletal forces, powered by a dynein-dynactin motor, to the telomeres of meiotic chromosomes through the LINC complex. To allow for the movement of telomeres, association of SUN proteins with the nuclear lamina must be disrupted. It is known that the meiotic telomere complex (composed of MAJIN, TERB1, and TERB2) is important in nuclear tethering of telomeres though its structure, assembly, and mechanism are unknown.

4.1.4 Connecting telomeres with the LINC complex

Such that forces transmitted through the nuclear envelope may be exerted upon the telomeres, telomeres must be physically associated with the LINC complex. The mechanism was first well characterised in fission yeast, *Saccharomyces pombe*, in which an interaction network was identified, indirectly linking the orthologous LINC complex (formed by Sad1-Kms1, which localise to the spindle pole body within the nuclear envelope) with the telomere-associated Shelterin complex (Chikashige *et al.*, 2007). Both Bqt1 and Bqt2 are required for the attachment of telomeres to Sad1 with telomeric attachment being mediated by an interaction (dependent upon both Bqt1 and Bqt2) with Shelterin component Rap1 (Chikashige *et al.*, 2006). Rap1 is associated with telomeres through an interaction with Taz1 which directly binds to telomeric repeat DNA (Kanoh and Ishikawa, 2001). This interaction network is summarised in Figure 4.1.5.

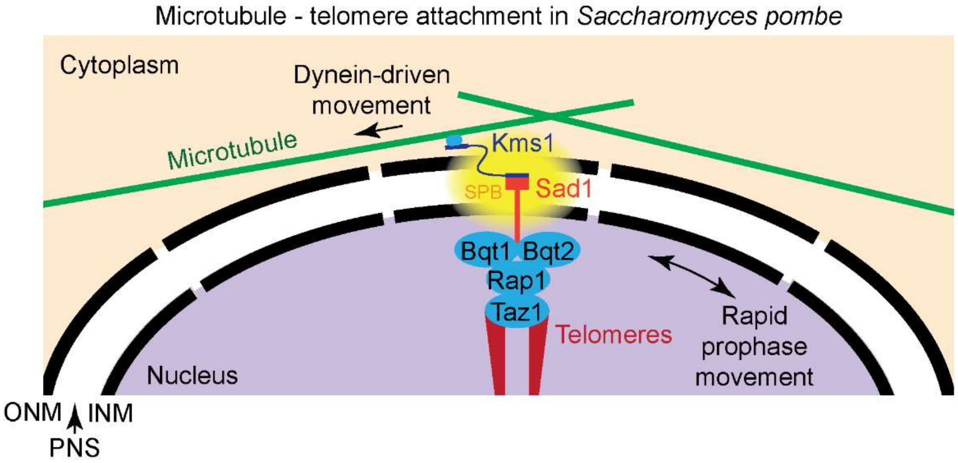

Figure 4.1.5| Cytoskeletal force transmission in fission yeast. Bqt1 and Bqt2 form a link between the LINC complex of *S. pombe* and the telomeric ends by binding Shelterin component Rap1. LINC components Sad1 and Kms1 are components of the spindle pole body which is embedded within the nuclear envelope. Dynein-driven microtubular movements then drive telomere movement back and forth between opposing pole of the nucleus in rapid prophase movements.

In mammals, TERB1 provides this link between the telomeres and the LINC complex (Daniel *et al.*, 2014; Shibuya *et al.*, 2014). Through screening for proteins upregulated in meiosis, two independent studies identified TERB1, demonstrated its colocalization with TRF1 (a mammalian orthologue of Taz1) and SUN1. Through yeast two-hybrid assays, it was identified that TERB1 interacts with the SUN1 N-terminus via its N-terminus whilst interacting with the TRF1 dimerization domain via its C-terminus (Figure 4.1.10). Interestingly, TERB1 did not demonstrate interaction with TRF2 which is structurally similar (Fairall *et al.*, 2001; Shibuya *et al.*, 2014). TRF1 (439 amino acids in humans) consists of a largely α-helical dimerization domain (TRFH; residues 62-265) of which the crystal structure was solved (Figure 4.1.6; PDB 1H6O) (Fairall *et al.*, 2001). Its C-terminus, which is largely non-conserved, is terminated by a conserved Myb-domain (residues 375-432). The crystal structure of the Myb-domain was solved demonstrating a direct recognition of the DNA major groove through the insertion of a single α-helix. Interestingly, the authors who solved the structure, as well as that of the highly similar TRF2 Myb-domain, classify the fold as that of a homeodomain, rather than a Myb motif, due to the presence of an N-terminal "arm" which specifically recognises the minor groove (Figure 4.1.6c,d). The three-helical structure, of which the two latter constitute a helix-turn-helix motif, is stabilised by a hydrophobic core whilst sequence specificity is conferred by residues K421, D422, and R425 which recognise the major groove and R378 which inserts into the minor groove (Figure 4.1.6d).

Unlike its interaction with SUN1, a molecular understanding of the interaction of TERB1 with TRF1 is more advanced having solved the structure of a short sequence of TERB1 binding TRF1 within the cleft formed between the two subunits of the dimer (Long *et al.*, 2017; Pendlebury *et al.*, 2017).

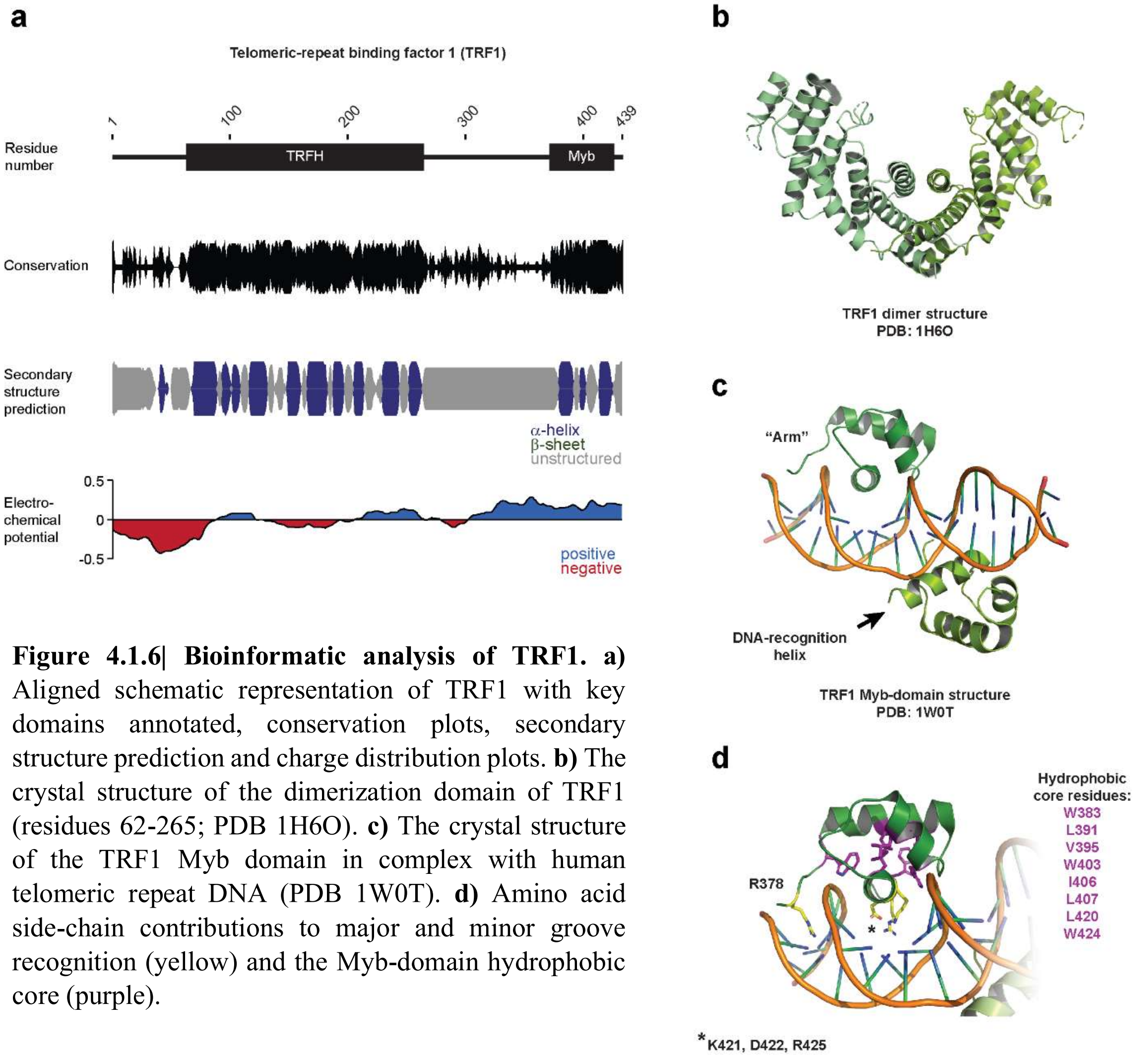
a
Telomeric-repeat binding factor 1 (TRF1)
Residue number
1
100
200
300
400
439
TRFH
Myb
Conservation
Secondary structure prediction
α-helix
β-sheet
unstructured
Electro-chemical potential
0.5
0
-0.5
positive
negative
b
TRF1 dimer structure
PDB: 1H6O
c
"Arm"
DNA-recognition helix
TRF1 Myb-domain structure
PDB: 1W0T
d
Hydrophobic core residues:
W383
L391
V395
W403
I406
L407
L420
W424
R378
*
*K421, D422, R425

Figure 4.1.6| Bioinformatic analysis of TRF1. a) Aligned schematic representation of TRF1 with key domains annotated, conservation plots, secondary structure prediction and charge distribution plots. **b)** The crystal structure of the dimerization domain of TRF1 (residues 62-265; PDB 1H6O). **c)** The crystal structure of the TRF1 Myb domain in complex with human telomeric repeat DNA (PDB 1W0T). **d)** Amino acid side-chain contributions to major and minor groove recognition (yellow) and the Myb-domain hydrophobic core (purple).

The crystal structure of TERB1-bound TRF1, solved through soaking TRF1 crystals with a TERB1 peptide sequence, revealed a binding mode reminiscent of TRF1 binding to TIN2, another Shelterin component (Figure 4.1.7a,b) (Chen *et al.*, 2008). Within the structure, the interaction is stabilised by a short anti-parallel β-sheet. Further, two leucine residues, L646 and L647, hydrophobically dock within the TRF1 cleft and two hydrogen bonds (one between TERB1 R652 and the backbone oxygen of TRF1 L138 and another between TERB1 R650 and TRF1 Q141) provide additional support. The interaction is complete by hydrophobic stacking association between TERB1 P649 and TRF1 F142. T648, which has been implicated in CDK2-mediated phosphorylation and resultant interaction disruption, is solvent exposed (Shibuya *et al.*, 2015; Viera *et al.*, 2015). The crystal structure suggests a possible 2:2 stoichiometry, counter to our observations and those made for TRF1-TIN2 within Shelterin in which a 2:1 stoichiometry is demonstrated, where a single TERB1 molecule binds to a TRF1 dimer (Lim *et al.*, 2017; Dunce *et al.*, 2018b). This is likely due to steric constraints not present when studying a short peptide sequence in the absence of other complex components. The association appears to be physiologically critical with disruptive mutants of TERB1 (L647A, T648E, P649A) diminishing TRF1 association and causing infertility, though curiously only in males (Long *et al.*, 2017). This is in contrast to knockout mice of which both sexes are infertile (Shibuya *et al.*, 2014).

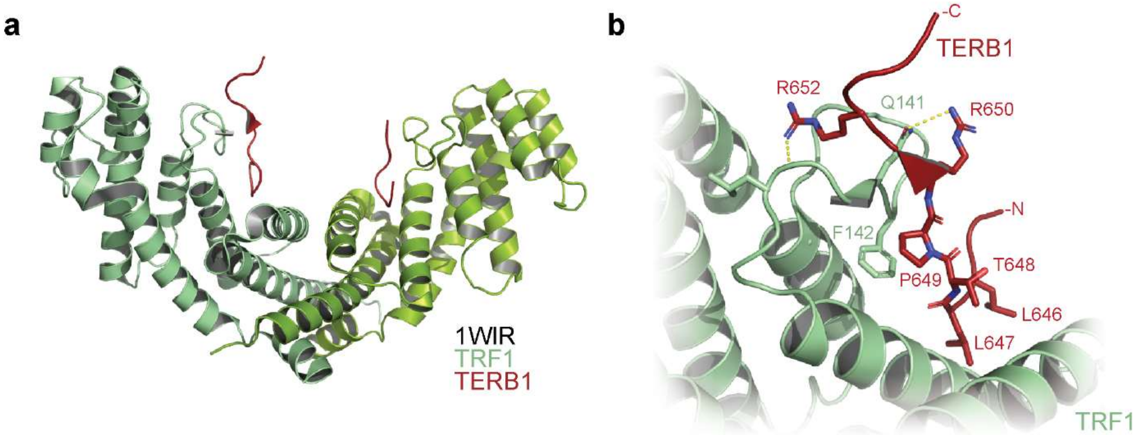

Figure 4.1.7| The TRF1-TERB1 association. a) The crystal structure of TRF1 bound to two TERB1 peptide sequences (PDB 1WIR). **b)** The interaction between TRF1 and TERB1 is stabilised through the formation of a short anti-parallel β-sheet, hydrophobic associations and hydrogen bonds.

4.1.5 The meiotic telomere complex: MAJIN and TERB2

Further to TERB1, two additional proteins have been identified, through immunoprecipitation from mouse testis extract by TERB1, which play key roles in telomere recruitment to the nuclear envelope: MAJIN and TERB2 (Shibuya *et al.*, 2015). As with TERB1, these proteins localise to nuclear membrane-bound telomeres and their homozygous knockout results in meiotic failure and infertility. More specifically, cells arrest during the zygotene stage as telomeres fail to associate with SUN-KASH complexes disallowing rapid prophase movements and synapsis. As both TERB1 and TERB2 localise to telomeres in the context of MAJIN null spermatocytes, MAJIN appears to fulfil a role in nuclear envelope attachment – likely mediated by its putative C-terminal transmembrane helix (Figure 4.1.9a). Further, without MAJIN, the telomeric attachment plate still forms but is distant from the nuclear envelope (Figure 4.1.6a). Contrastingly, TERB1 null mice display a diffuse localisation of MAJIN and TERB2 on the nuclear envelope implicating it in telomeric recruitment of MAJIN and TERB2 (Shibuya *et al.*, 2015). This is in keeping with its proposed interaction with the N-terminus of SUN1 (Shibuya *et al.*, 2014). The finding that TERB2 displays differential localisation in either MAJIN or TERB1 null backgrounds possibly suggests a physical association exists between TERB2 and both proteins. Electron microscopic analysis of telomeric ends of TERB1 and TERB2 null mice show no formation of the telomeric attachment plate, suggesting integral architectural roles for both proteins (Figure 4.1.8).

The homozygous knockout of SUN1, which has no impact upon telomeric attachment to the nuclear envelope, indicates that the meiotic telomere complex is sufficient for nuclear envelope recruitment but cannot mediate connection with the cytoskeletal motor proteins (Shibuya *et al.*, 2015). Therefore, we may conclude that meiotic telomere complex and LINC complex fulfil distinct yet complementary and essential roles in mammalian meiosis. However, SUN1 and SUN2 may be functionally redundant in telomeric recruitment to the nuclear envelope as SUN2 was found to localise to the telomeric attachment plate (Schmitt *et al.*, 2007).

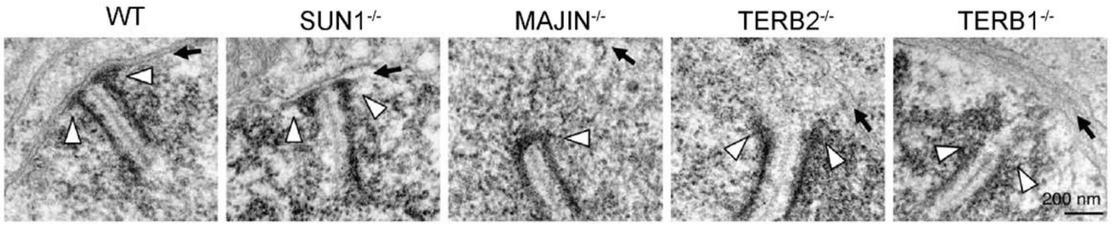

Figure 4.1.8| The telomeric attachment plate structure in mouse knockouts of the meiotic telomere complex components. In wild-type mice, synapsed chromosomes are visualised fused with the inner nuclear membrane. Structurally, the knockout of SUN1 has no effect, forming an intact telomeric attachment plate. The telomeric ends of meiotic chromosomes in MAJIN null mice appear to be capped by a proteinaceous sheath but do not attach to the nuclear envelope. Telomeres of TERB2 and TERB1 null mice show no distinct structure and do not attach to the nuclear envelope. Arrows point to the telomeres.

4.1.6 Bioinformatic and structural analysis of meiotic telomere complex components

MAJIN is a 254 amino acid protein with a conserved N-terminal structured core, predicted to consist of a mixture of α-helix and β-sheet (Core; residues 1-112) and a non-conserved unstructured C-terminus with a conserved transmembrane helix (TM; 230-248) at its extreme C-terminal end (Figure 4.1.9a). The sole interacting partner of MAJIN within the meiotic telomere complex, TERB2, contains 220 amino acids and is largely unstructured, with highly conserved N- and C-terminal domains which interact with TERB1 (N; residues 1-107) and MAJIN (C; residues 168-207), respectively (Figure 4.1.9b). TERB1 interacts with TERB2 through a C-terminal sequence (T2B; residues 585-642) flanked by TRF1-binding sequences (TRFB; residues 561-658) which precedes a telomeric DNA binding domain, the Myb domain (residues 666-719). TERB1 contains a large N-terminal domain, predicted to fold predominantly as armadillo-repeat domain, potentially capped at its C-terminus by a short coiled-coil (Figure 4.1.9c). The extreme C-terminus of TERB1 encodes a Myb domain, similar to that of TRF1, which is also essential for rapid prophase movements (Zhang *et al.*, 2017). Additionally, an unstructured region of high pI of MAJIN (indicated “Basic patches” in Figure 4.1.9a) was found to be essential for DNA binding by electrophoretic mobility shift assay (Shibuya *et al.*, 2015).

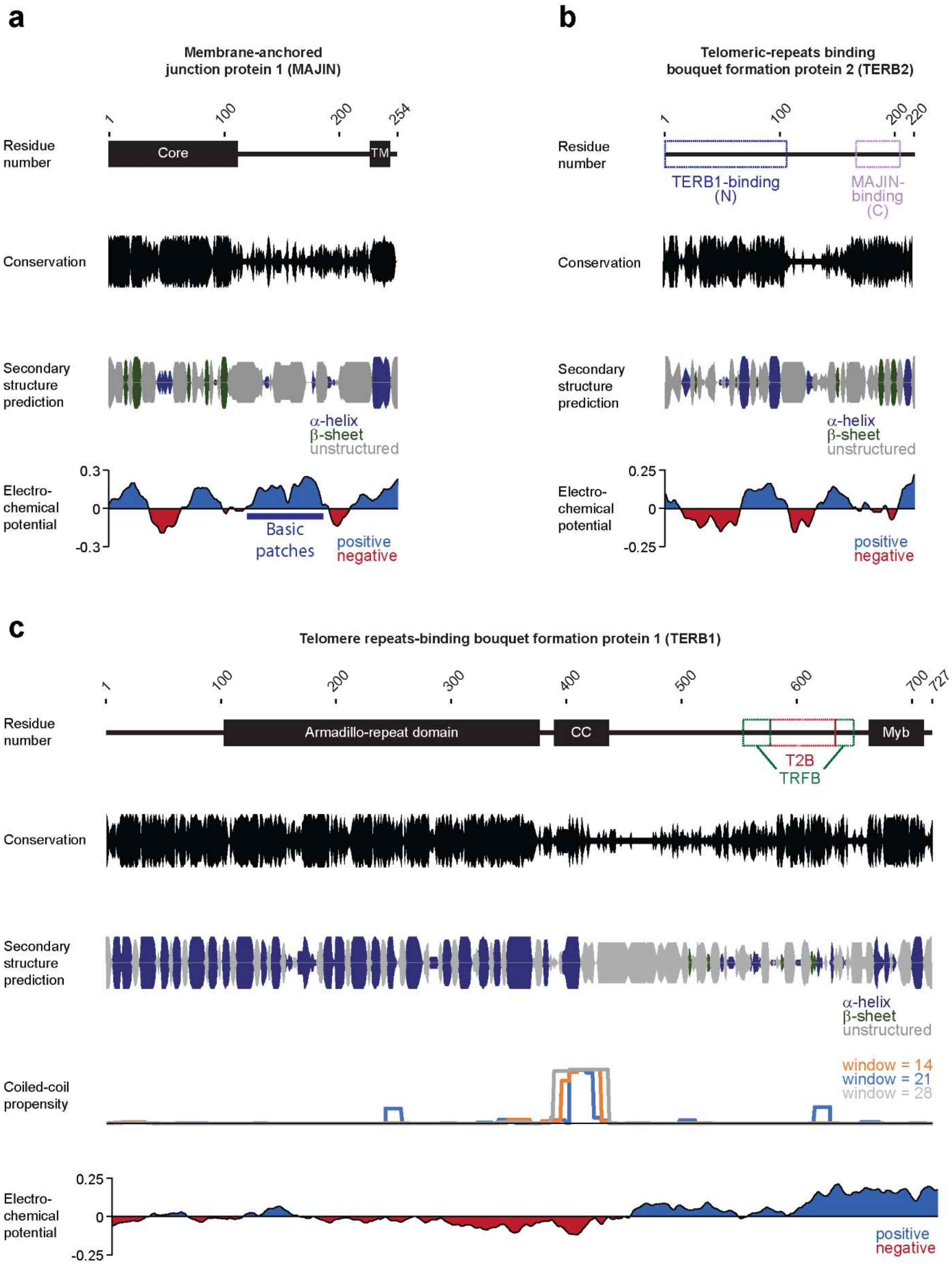

Figure 4.1.9| Bioinformatic analysis of meiotic telomere complex components. a-c) Aligned schematic representation with key domains annotated, conservation plots, secondary structure prediction and charge distribution plots for **a)** MAJIN, **b)** TERB2, and **c)** TERB1. T2B= TERB2-binding site. TRFB= TRF1-binding sites.

4.1.7 Connecting components: a meiotic collaboration

As discussed previously, TERB1 is recruited directly to the telomeres through its interaction with TRF1 through a short peptide sequence (residues 642-658) and is proposed to associate with SUN1 through its N-terminal armadillo-repeat domain (Shibuya *et al.*, 2014; Long *et al.*, 2017; Pendlebury *et al.*, 2017). Further interactions between the components of the meiotic telomere complex were mapped by yeast two-hybrid and are summarised in Figure 4.1.10 (Shibuya *et al.*, 2015). The presented interacting regions have been optimised through truncation analysis performed by both myself, Master's student Lee Thung Sen, and PhD student Amy Milburn. Briefly, MAJIN interacts with the TERB2 C-terminus (residues 168-207) through its conserved N-terminal domain (residues 1-112). TERB2 then mediates TERB1 (residues 585-642) association through its N-terminal domain (residues 1-107) for which the structure was solved demonstrating the formation of an α-helical globular domain (Figure 4.1.11a) (Wang *et al.*, 2019). We identified a second sequence which stabilises TRF1 association directly N-terminal to the TRF1 binding region (residues 561-585).

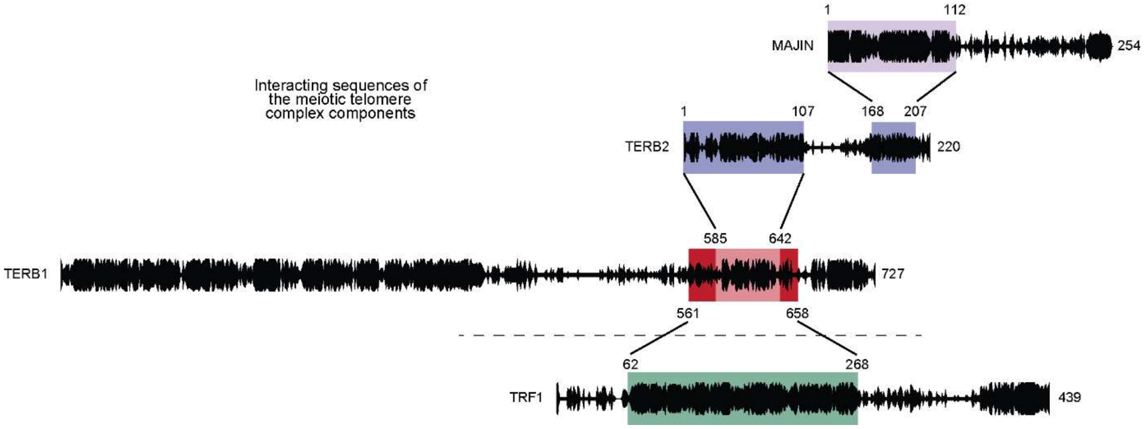
Interacting sequences of the meiotic telomere complex components
MAJIN
1
112
254
TERB2
1
107
168
207
220
TERB1
585
642
727
561
658
TRF1
62
268
439

Figure 4.1.10| Mapping the interactions between meiotic telomere complex components. The inter-molecular interactions between protein components of the meiotic telomere complex (MAJIN, TERB1, and TERB2) and the Shelterin complex component, TRF1, mapped in previous studies (Shibuya *et al.*, 2015; Long *et al.*, 2017; Pendlebury *et al.*, 2017; Zhang *et al.*, 2017) and refined by a previous masters student, Lee Thung Sen through biochemical screening. Amino acid conservation is plotted against linearly presented protein sequences. The height of the black plots is representative of conservation score. The amino acid boundaries and residue length of interacting regions and proteins have been annotated.

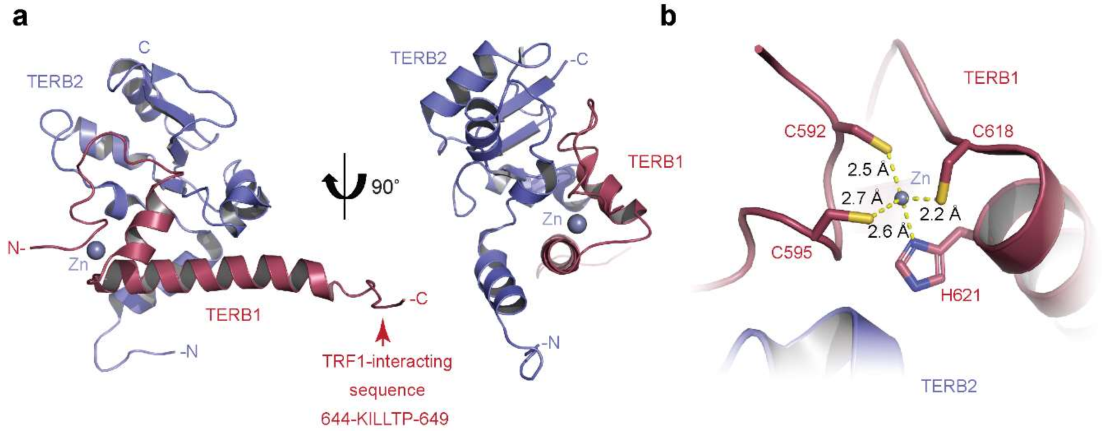

Figure 4.1.11| Structure of the human TERB1$_{590\text{-}649}$-TERB2$_{4\text{-}110}$ complex. a) Cartoon representation of TERB1 and TERB2 interacting to form a globular α-helical domain (PDB 6J07). TERB1 forms two α-helices separate by a short turn and flanked by short sequences without secondary structure. The N-terminal sequence coordinates a zinc ion, as depicted in b. **b)** TERB1 residues C592, C595, C618 and H621 coordinate a zinc ion.

4.1.8 Interplay between the meiotic telomere complex and the Shelterin complex

It was interestingly noted that TRF1 appears to not perfectly colocalise with TERB1 upon telomeric association with the nuclear envelope, with TRF1 appearing to be offset, forming a ring like structure around a TERB1 focus (Pendlebury *et al.*, 2017). This phenomenon was shown to hold true also for MAJIN and TERB2 and was coined as, controversially, "telomere cap exchange", suggesting that upon binding to the meiotic telomere complex, TRF1 (in association with other Shelterin components) is fully displaced from the telomeres (Figure 4.1.12) (Shibuya *et al.*, 2015). As Shelterin components remain in association with the telomere, it more appears as if TRF1 is displaced to the telomeric periphery rather than a true exchange of caps. If the Shelterin complex were to be no longer "capping" telomeric ends, would this not have important consequences for the suppression of the DNA damage response and for obscuring the true end of the DNA sequence (de Lange, 2009)? It remains to be shown whether TRF1 and the other Shelterin complex components remain in association with telomeric DNA.

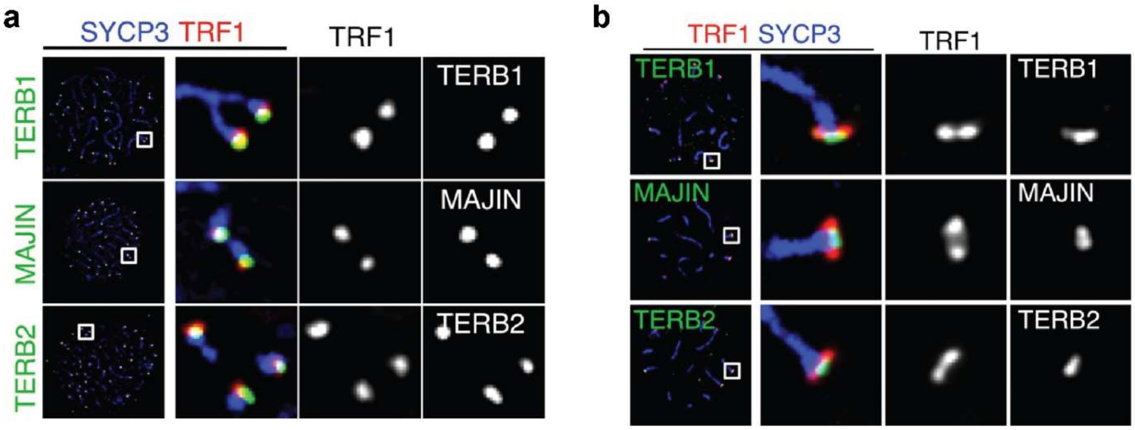

Figure 4.1.12| Displacement of TRF1 during the zygotene to pachytene transition. a) Fluorescence imaging during **a)** zygotene and **b)** pachytene demonstrating the initial colocalization of MAJIN, TERB1 and TERB2 with TRF1 and the subsequent displacement of TRF1 to the telomeric periphery.

4.1.9 Uncovering the structural basis for telomere tethering to the nuclear envelope by the meiotic telomere complex

In the present study, we focussed our efforts towards the structural characterisation of the meiotic telomere complex. Assembly of the meiotic telomere complex and the contribution to telomere tethering to the nuclear envelope is a critical step in meiosis with ablation of any components resulting in complete meiotic blockage. We thus far lack any structural understanding of how this complex assembles, achieves telomeric binding, or how it mediates recruitment to the nuclear envelope. Initial progress was made during a project initiated by former Masters student Lee Thung Sen who made significant progress in biochemically reconstituting the interactions reported by H. Shibuya and Y. Watanabe (Shibuya *et al.*, 2015). Fellow PhD student, Gurusaran Manickam, and I, furthered his work and solved the crystal structure of the MAJIN-TERB2 core and, in combination with another PhD student, Amy Milburn, we achieved a near-full biophysical characterisation of the meiotic telomere complex (Dunce *et al.*, 2018b). In this chapter, I shall briefly describe the work of Lee Thung Sen and our efforts which lead to the solution of the crystal structure of the MAJIN-TERB2 core complex and our subsequent work in characterising the wider MAJIN-TERB2 complex and its role in telomere association. Throughout I shall clearly cite collaborative work in which Gurusaran Manickam was involved by acknowledging data he collected within figure legend text.

RESULTS

4.2.1 Initial purification and crystallisation of the MAJIN-TERB2 complex

Lee found that bacterial expression of the individual meiotic telomere complex components yielded insoluble protein, indicating misfolding and the requirement for a constitutive binding partner. Through co-expression of interacting protein fragments identified by previous studies (Shibuya *et al.*, 2015; Long *et al.*, 2017; Pendlebury *et al.*, 2017; Zhang *et al.*, 2017), highly stable and soluble protein complexes could be purified. In Figure 4.2.1a, the purification of the MAJIN$_{1\text{-}147}$ TERB2$_{147\text{-}220}$ complex is summarised in which the MAJIN N-terminus was expressed as an N-terminal His$_6$-fusion with the TERB2 C-terminus as a His$_6$-MBP-fusion. Purification was achieved through sequential Ni-NTA and amylose affinity chromatography, further purified by anion exchange chromatography using a HiTrap Q column, prior to removal of the affinity tags through enzymatic cleavage by TEV protease. The purification was completed by cation exchange chromatography using a HiTrap SP column and size-exclusion chromatography. SEC-MALS analysis revealed a molecular weight of 42 kDa, closely corresponding to a stoichiometry of 2 MAJIN molecules to 1 TERB2 (Figure 4.2.1b). The asymmetrically shaped elution peak, the divergence of the light scattering and differential refractive index in the second half of the peak, and the sloping molecular weight fit, suggest a dissociation between the two components. Lee found that this effect was exaggerated by decreasing salt concentration below 250 mM KCl, yet not further improved by increasing beyond 250 mM KCl. All SEC-MALS data presented henceforth utilises a buffer containing 250 mM KCl. This calls into question of whether the 2:1 oligomeric state suggested on the basis of these data was accurate.

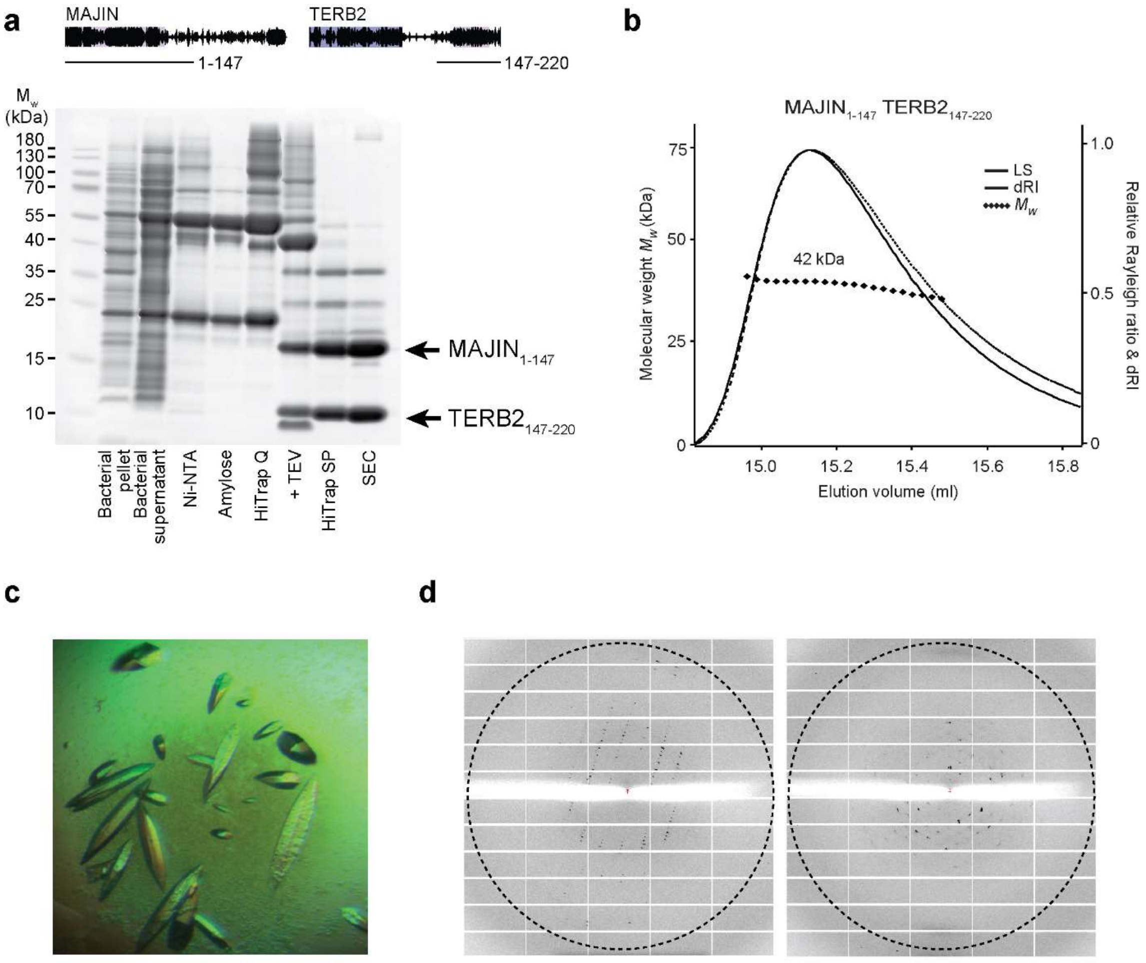

Optimised PACT E4
(150 mM KSCN, 18% PEG3350)

X-ray diffraction processed to
4.08 Å in SG $P3_121$

Figure 4.2.1| Initial purification and crystallisation of a MAJIN-TERB2 complex. a) Schematic representation of MAJIN and TERB2 indicating the amino acid boundaries of constructs analysed in the presented figure. SDS-PAGE analysis summarising the purification of $\text{MAJIN}_{1\text{-}147}$ $\text{TERB2}_{147\text{-}220}$. **b)** SEC-MALS analysis of $\text{MAJIN}_{1\text{-}147}$ $\text{TERB2}_{147\text{-}220}$ demonstrating the formation of a 42 kDa species (theoretical molecular weight of a 2:1 complex= 43 kDa, 2:2 complex= 52 kDa). **c)** $\text{MAJIN}_{1\text{-}147}$ $\text{TERB2}_{147\text{-}220}$ protein crystals which grew in 150 mM KSCN, 18 % PEG3350 over 3 months and **d)** diffraction images. The dotted line demarcates data to 4.08 Å. The data and crystals presented in this figure are a result of the work of Lee Thung Sen.

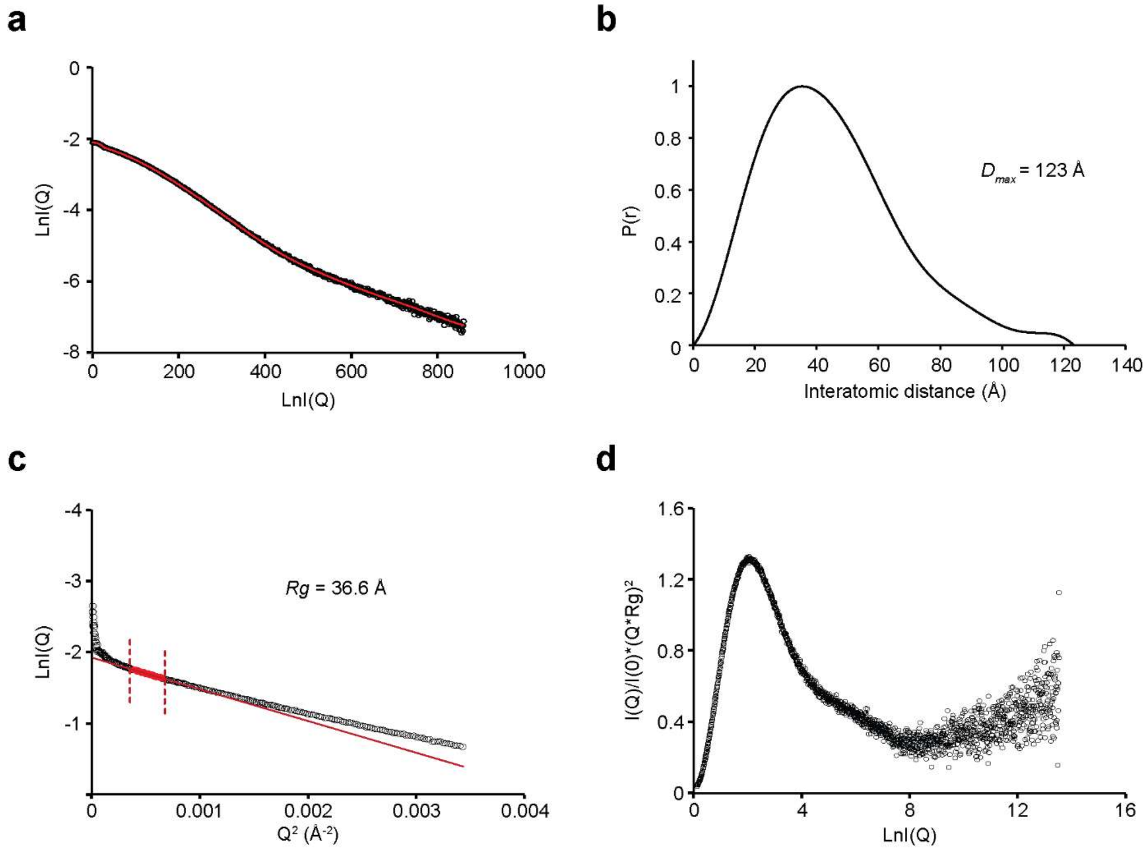

Figure 4.2.2| SEC-SAXS data analysis of MAJIN$_{1\text{-}147}$ TERB2$_{147\text{-}220}$. a) Averaged small-angle X-ray scattering profile of MAJIN$_{1\text{-}147}$ TERB2$_{147\text{-}220}$ with the fit used for *P(r)* distribution shown as a red line. **b)** SEC-SAXS *P(r)* distribution of MAJIN$_{1\text{-}147}$ TERB2$_{147\text{-}220}$; maximum dimension (D_{max}) is indicated. **c)** SEC-SAXS Guinier analysis to determine the radius of gyration (*Rg*) of MAJIN$_{1\text{-}147}$ TERB2$_{147\text{-}220}$. The linear fit is plotted in red and the linear region highlighted and demarcated by dotted lines. The *Q.Rc* value was < 1.3 with the *Rg* calculated at 36.6 Å. **d)** Normalised Kratky plot for MAJIN$_{1\text{-}147}$ TERB2$_{147\text{-}220}$. The near-Gaussian distribution demonstrated an overall globular shape whilst the tailing indicates the presence of unstructured residues. The data presented in this figure are a result of the work of Lee Thung Sen. SEC-SAXS analysis by Dr Owen Davies.

Lee was able to crystallise the complex, attaining multiple crystal hits in initial sparse-matrix screening and, through optimisation of a single condition containing sodium thiocyanate and PEG3350 produced crystals which diffracted to 4.08 Å (Figure 4.2.1c,d). However, these crystals took at least 3 months to grow and upon SDS-PAGE analysis of the protein crystals themselves found them to be formed of a MAJIN-TERB2 complex in which both components were heavily truncated (data not shown).

4.2.2 Unstructured termini of MAJIN and TERB2 inhibit crystal growth

Solution studies of the $\text{MAJIN}_{1\text{-}147}$ $\text{TERB2}_{147\text{-}220}$ complex by SEC-SAXS revealed an interatomic distance distribution profile with a predominantly Gaussian distribution-like shape, with an elongated tail to an x-axis intercept (indicative of the molecules maximum interatomic distance (D_{max})) of 123 Å (Figure 4.2.2b). Together with the Kratky profile, which tails to indicate the presence of flexible extensions, our data suggested that this construct on which Lee was working contained long-flexible termini (Figure 4.2.2d). We hypothesised that these unstructured termini would inhibit protein crystal growth, and that the thus-far produced crystals only grew after spontaneous proteolytic truncation of these termini over time.

4.2.3 Construct boundary optimisation

To improve crystal growth, we opted to truncate both MAJIN and TERB2 sequences. Gurusaran Manickam purified and attempted the crystallisation of $\text{MAJIN}_{1\text{-}147}$ $\text{TERB2}_{157\text{-}220}$ and I proceeded to clone and purify a range of MAJIN and TERB2 constructs. MAJIN-TERB2 complex formation and stability was retained upon the simultaneous truncation of MAJIN to residues 1-112, removing a sequence of predicted unstructured residues, and TERB2 to residues 147-207, removing the 13 C-terminal residues of which 5 of the final 7 residues are basic (Figure 4.2.3a, lane 1).

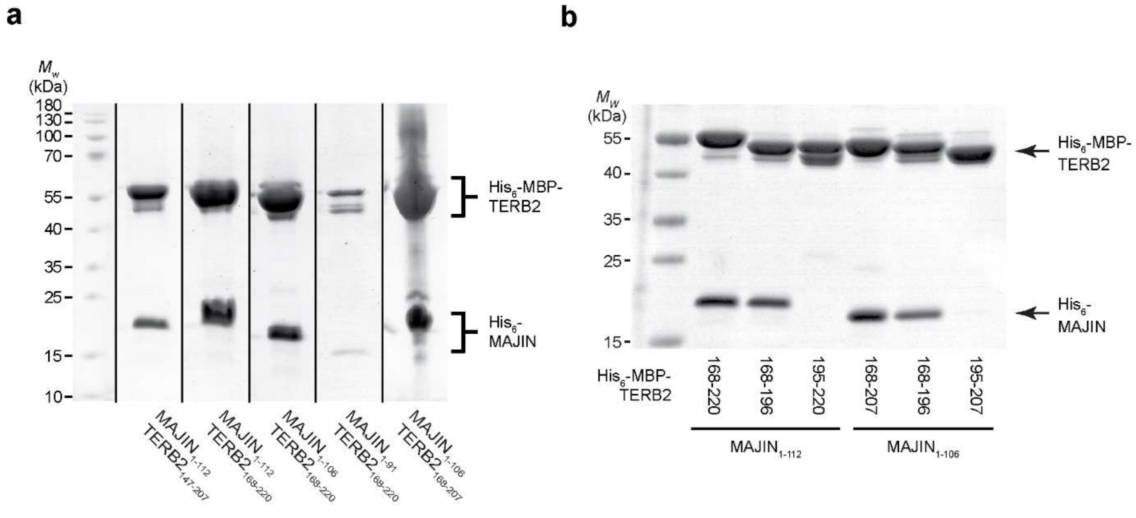
a
M_w (kDa)
180
130
100
70
55
40
35
25
15
10
His$_6$-MBP-TERB2
His$_6$-MAJIN
MAJIN$_{1\text{-}112}$ TERB2$_{147\text{-}207}$
MAJIN$_{1\text{-}112}$ TERB2$_{168\text{-}220}$
MAJIN$_{1\text{-}106}$ TERB2$_{168\text{-}220}$
MAJIN$_{1\text{-}91}$ TERB2$_{168\text{-}220}$
MAJIN$_{1\text{-}106}$ TERB2$_{168\text{-}207}$
b
M_w (kDa)
55
40
35
25
15
His$_6$-MBP-TERB2
His$_6$-MAJIN
His$_6$-MBP-TERB2
168-220
168-196
195-220
168-207
168-196
195-207
MAJIN$_{1\text{-}112}$
MAJIN$_{1\text{-}106}$

Figure 4.2.3| Optimised the MAJIN-TERB2 construct amino acid boundaries. a,b) SDS-PAGE analysis of Ni-NTA and amylose affinity purified MBP-fused TERB2 constructs co-expressed with His_6-tagged MAJIN constructs with residue boundaries indicated.

N-terminal truncation of the TERB2 sequence, to residue 168, results in a drastically improved protein yield (Figure 4.2.3a, lane 2). Further truncation of the MAJIN sequence to residue 106 is tolerated in complex with TERB2 residues 168-220 but results in fantastic protein yields when co-expressed with MAJIN residues 1-106 (lane 5). Truncation of the MAJIN sequence to residue 1-91 results in drastic protein instability, observed as a greatly reduced protein yield. Dissection of the TERB2 sequence into its two halves (residues 168-196 and 195-207/220) reveals that the N- terminal half is sufficient for interaction (Figure 4.2.3b).

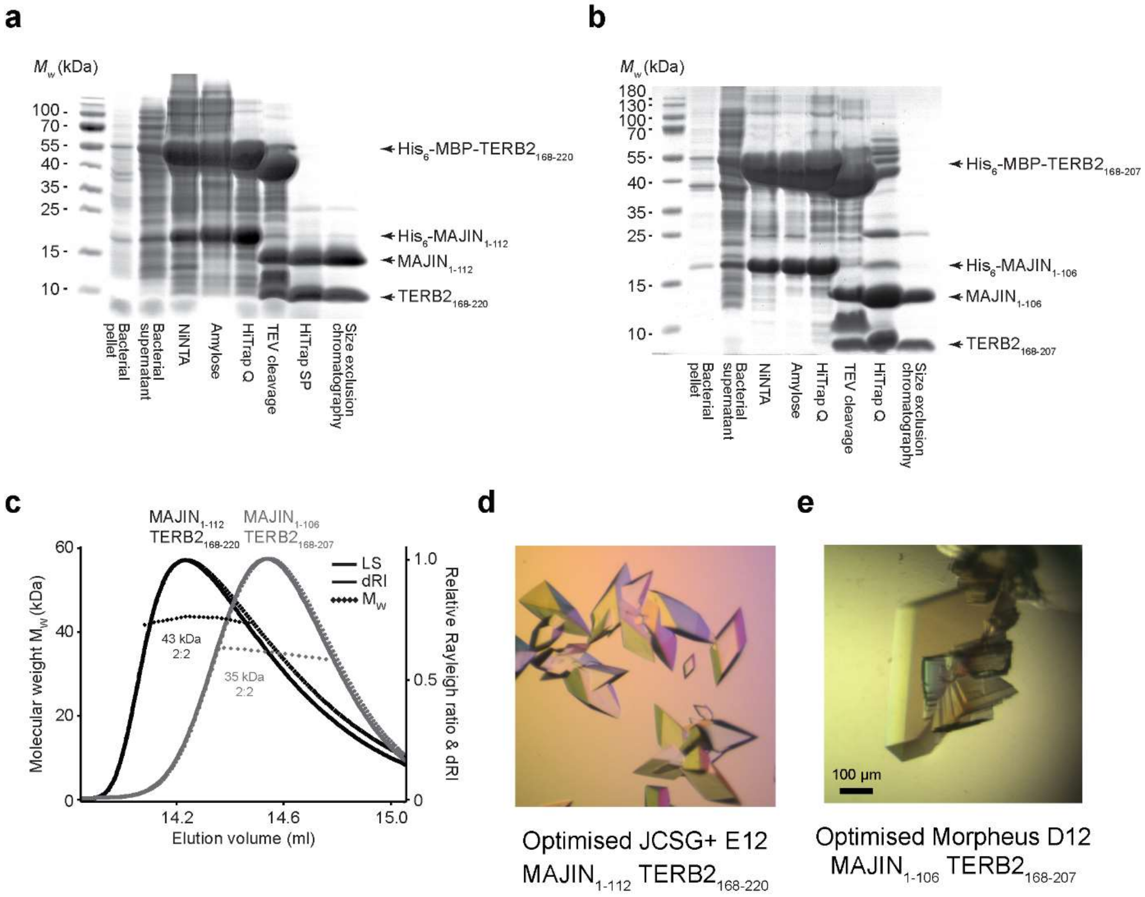

Figure 4.2.4| Purification and crystallisation of MAJIN-TERB2 complexes. a,b) SDS-PAGE analysis summarising the purification of **a)** MAJIN$_{1-112}$ TERB2$_{168-220}$ and **b)** MAJIN$_{1-106}$ TERB2$_{168-207}$. **c)** SEC-MALS analysis of MAJIN$_{1-112}$ TERB2$_{168-220}$ (black; theoretical 2:2 complex= 40 kDa) and MAJIN$_{1-106}$ TERB2$_{168-207}$ (grey; theoretical 2:2 complex= 35 kDa). **d-e)** Protein crystals for **d)** MAJIN$_{1-112}$ TERB2$_{168-220}$ and **e)** MAJIN$_{1-106}$ TERB2$_{168-207}$ optimised from the indicated initial sparse matrix screening conditions.

4.2.4 Crystallisation of the MAJIN-TERB2 complex

Complexes of $\text{MAJIN}_{1\text{-}112}$ $\text{TERB2}_{168\text{-}220}$ and $\text{MAJIN}_{1\text{-}106}$ $\text{TERB2}_{168\text{-}207}$ were selected for crystallisation trials. Both complexes were purified to homogeneity through the purification procedure described for $\text{MAJIN}_{1\text{-}147}$ $\text{TERB2}_{147\text{-}220}$ (Figure 4.2.4a,b). SEC-MALS analysis of $\text{MAJIN}_{1\text{-}112}$ $\text{TERB2}_{168\text{-}220}$ and $\text{MAJIN}_{1\text{-}106}$ $\text{TERB2}_{168\text{-}207}$ revealed molecular weights perfectly matching the theoretical values of a 2:2 stoichiometry (Figure 4.2.4c). The familiar elution profile characteristics of the MAJIN-TERB2 complex (i.e. asymmetry and deviation between light scattering and differential refractive index) are retained by $\text{MAJIN}_{1\text{-}112}$ $\text{TERB2}_{168\text{-}220}$ yet absent for the shorter $\text{MAJIN}_{1\text{-}106}$ $\text{TERB2}_{168\text{-}207}$ complex implicating unstructured sequences in the presence of this phenomenon (Figure 4.2.4c). Crystals were readily obtained for both constructs with the best crystals for $\text{MAJIN}_{1\text{-}112}$ $\text{TERB2}_{168\text{-}220}$ growing in 100 mM imidazole pH 8.0, 10 % PEG8000 and the best for $\text{MAJIN}_{1\text{-}106}$ $\text{TERB2}_{168\text{-}207}$ growing in 0.12 M 1,6 hexanediol; 0.12 M 1-butanol; 0.12 M 1,2-propanediol (racemic); 0.12 M 2-propanol; 0.12 M 1,4-butanediol; 0.12 M 1,3-propanediol, 39.1 mM bicine pH 5.03, 60.9 mM Trizma pH 10.83; 12.5 % w/v PEG 1000; 12.5 % w/v PEG3350; 12.5 % v/v MPD (Figure 4.2.4d,e). Both crystals contained a 2:2 heterotetramer in the asymmetric unit though crystals of $\text{MAJIN}_{1\text{-}112}$ $\text{TERB2}_{168\text{-}220}$ belonged to spacegroup $C3_221$ with unit cell dimensions a = 59.88 Å, b = 59.88 Å, c = 159.93 Å, α = 90°, β = 90°, γ = 120° whilst crystals of $\text{MAJIN}_{1\text{-}106}$ $\text{TERB2}_{168\text{-}207}$ belonged to spacegroup $C222_1$ with unit cell dimensions a = 59.97 Å, b = 88.39 Å, c = 111.67 Å, α = 90°, β = 90°, γ = 90°.

4.2.5 Crystal structure solution of the MAJIN-TERB2 complex

In order to solve the structure, Gurusaran Manickam purified and crystallised a seleno-methionine derivative of $\text{MAJIN}_{1\text{-}112}$ $\text{TERB2}_{168\text{-}220}$, allowing Dr Owen Davies to utilise the anomalous signal to solve an 8-selenium atom sub-structure, providing initial phase estimates to allow the placement of a single α-helix, which, through both automated and manual building was converted into a near-complete build at 2.90 Å. A 1.85 Å structure of the MAJIN-TERB2 complex in spacegroup $C222_1$ was subsequently solved through molecular replacement of the SAD-structure (Table 4.1). This process is described in full in the Methods section 2.1.17-18. The following analysis is based upon the high-resolution $C222_1$ structure.

4.2.6 Analysis of the MAJIN-TERB2 crystal structure

MAJIN-TERB2 constitutes a heterotetrameric complex in which a dimeric MAJIN core, is encapsulated by two TERB2 chains (Figure 4.2.5a,b). MAJIN adopts a β-grasp fold in which a central amphipathic α-helix is grasped by a 4-stranded β-sheet, in a β(2)-α(2)-β(3) configuration (Figure 4.2.5c,d). The TERB2 N-terminus is situated at the interface between the two MAJIN protomers, contributing to the hydrophobic interface through the sidechain of Y176. The TERB2 chain meanders around the MAJIN molecular surface, completing the closure of the central α-helix of MAJIN, forming anti-parallel β - sheet associations with β1 and β5 of MAJIN (Figure 4.2.5b-e).

The MAJIN β-grasp is formed through hydrophobic associations between one face of the central amphipathic α-helix and the inner face of the grasping β-sheet (Figure 4.2.6a,b). TERB2 contributes by hydrophobically packing against the bottom-end of the central α-helix through F185 and L189 whilst the solvent-exposed upper portion comprises largely charged or polar residues (Figure 4.2.6a). Interestingly, I identified a single water-mediated association in which a water molecule bridges the highly conserved MAJIN residues D60 and K76 (Figure 4.2.6c).

The TERB2 chain wraps around MAJIN and is stabilised through the insertion of hydrophobic residues into hydrophobic pockets on the MAJIN molecular surface (Figure 4.2.7a,b). Further, the MAJIN-TERB2 interface is stabilised through salt bridges between MAJIN R14 and TERB2 D191 and MAJIN D50 (on the surface of the central α-helix) and TERB2 K184 (Figure 4.2.7c). Finally, H17 Nδ1 hydrogen bonds with the hydroxyl oxygen of Y199 (Figure 4.2.7d).

Figure 4.2.5| The MAJIN-TERB2 structure. a,b) The crystal structure of the MAJIN$_{1\text{-}106}$ TERB2$_{168\text{-}207}$ 2:2 heterotetramer in **a)** cartoon and **b)** molecular surface representation of MAJIN with cartoon TERB2 chains. MAJIN forms a symmetrical bilobed, globular structure, around which TERB2 chains wrap. **c)** Cartoon representation of the MAJIN-TERB2 protomer. MAJIN folds as a β-grasp in which a central α-helical chain is enclosed by grasping MAJIN β-sheets and the TERB2 chain. **d)** Topology diagram of the MAJIN-TERB2 protomer demonstrating a β(2)-α(2)-β(3) configuration, with β5 and β6 forming a β-sheet appendage inserted between β4 and β7. TERB2 wraps around the MAJIN surface and contains a short 3_{10} helix. TEBR2 β1' strand forms a β-sheet with MAJIN β1 and TERB2 β2' forms a β-sheet with the MAJIN β5/6-appendage. The MAJIN-TERB2 crystal structure was solved by molecular replacement of 6GNX, which was solved through SAD-phasing of a seleno-methionine derivative, purified and crystallised by Gurusaran Manickam. Structure solved by Dr Owen Davies.

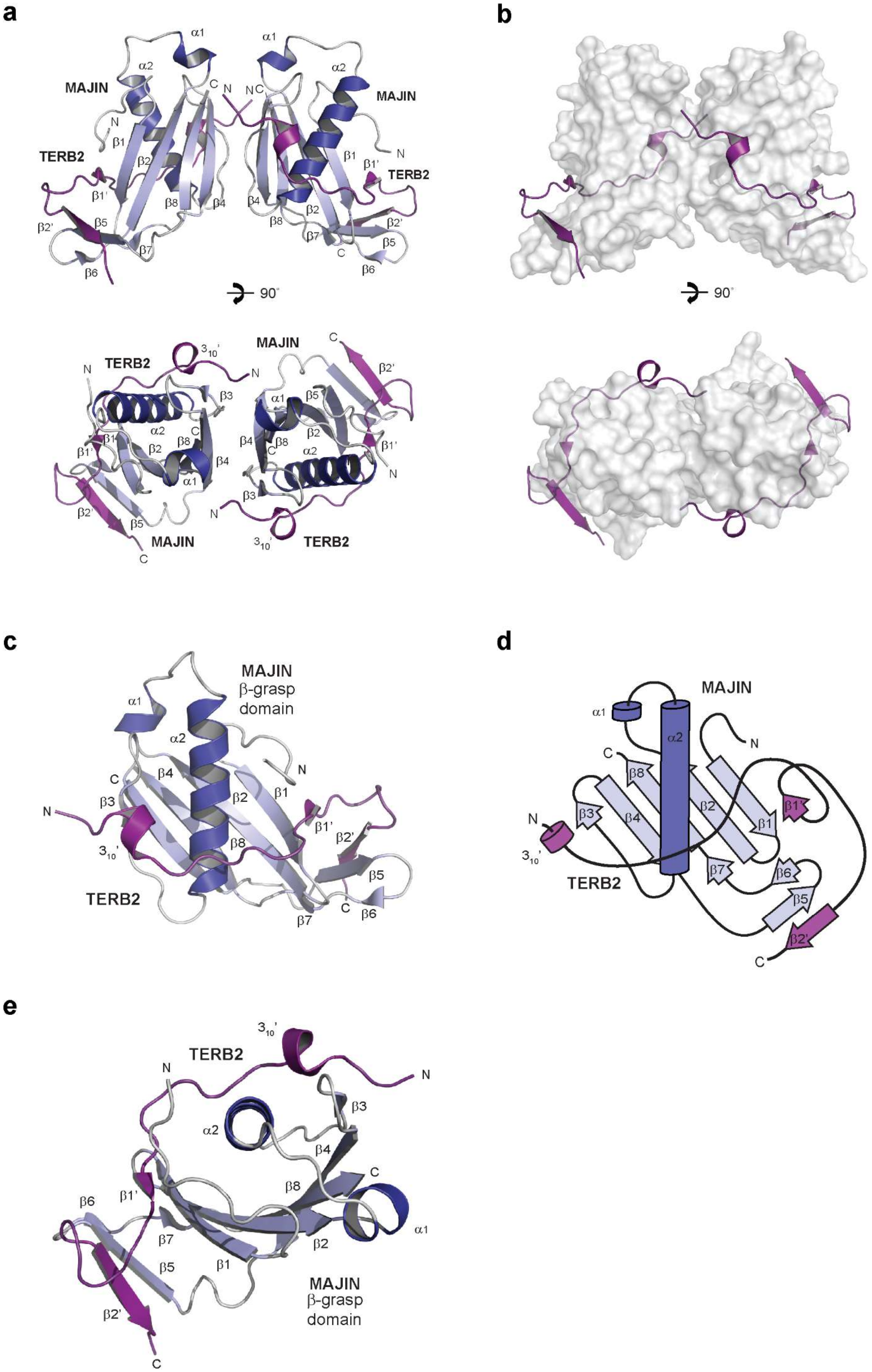
a
α1
α1
α2
α2
MAJIN
MAJIN
C
N
N
C
N
N
β1
β1
TERB2
TERB2
β2
β1'
β1'
β8
β4
β4
β2
β2'
β5
β8
β2'
β7
β7
C
β5
β6
β6
90°
TERB2
3_{10}'
MAJIN
C
β2'
N
N
β3
α1
β5
β1
α2
β8
C
β2
β1'
β2
β4
β4
β8
C
α2
β1'
α1
N
β3
β2'
β5
N
C
MAJIN
3_{10}'
TERB2
b
90°
c
MAJIN
β-grasp
domain
α1
α2
C
β4
β2
β1
N
N
β3
β1'
β2'
3_{10}'
β8
β5
TERB2
β7
C
β6
d
MAJIN
α1
α2
N
C
β8
β2
β3
β4
β1
β1'
N
3_{10}'
β7
β6
TERB2
β5
β2'
C
e
3_{10}'
TERB2
N
N
β3
α2
β4
C
β8
β6
β1'
α1
β7
β2
β5
β1
MAJIN
β-grasp
domain
β2'
C

	MAJIN$_{1\text{-}112}$ / TERB2$_{168\text{-}220}$ Seleno-methionine derivative (6GNX)	MAJIN$_{1\text{-}106}$ / TERB2$_{168\text{-}207}$ (PDB 6GNY)
Data collection		
Space group	$P3_221$	$C222_1$
Cell dimensions	59.88, 59.88, 159.93	59.97, 88.39, 111.67
	90.00, 90.00, 90.00	90.00, 90.00, 90.00
Wavelength (Å)	0.9159	0.9763
Resolution (Å)	49.23 – 2.90 (3.08 – 2.90)	45.35 – 1.85 (1.89 – 1.85)
R_{meas} (all I+ & I-)	0.136 (3.015)	0.039 (1.374)
R_{pim} (all I+ & I-)	0.024 (0.553)	0.014 (0.504)
$I / \sigma I$	28.2 (2.3)	23.1 (1.5)
$CC_{1/2}$	1.000 (0.885)	0.999 (0.744)
Completeness (%)	100.0 (100.0)	100.0 (100.0)
Multiplicity	56.6 (55.1)	7.3 (7.3)
Refinement		
Resolution (Å)	49.33 – 2.90	45.35 – 1.85
Number of reflections	7865	35690
R_{work} / R_{free}	0.2542 / 0.3039	0.1883 / 0.2072
Number of atoms	2197	2413
Protein	2197	2286
Ligand/ion	0	8
Water	0	119
B-factors	130.46	64.58
Protein	130.46	64.72
Ligand/ion	N/A	130.48
Water	N/A	57.49
R.m.s deviations		
Bond lengths (Å)	0.003	0.003
Bond angles (°)	0.539	0.627

Table 4.1| X-ray crystallographic statistics for MAJIN-TERB2 structures. X-ray diffraction data processed and crystal structures solved by Dr Owen Davies

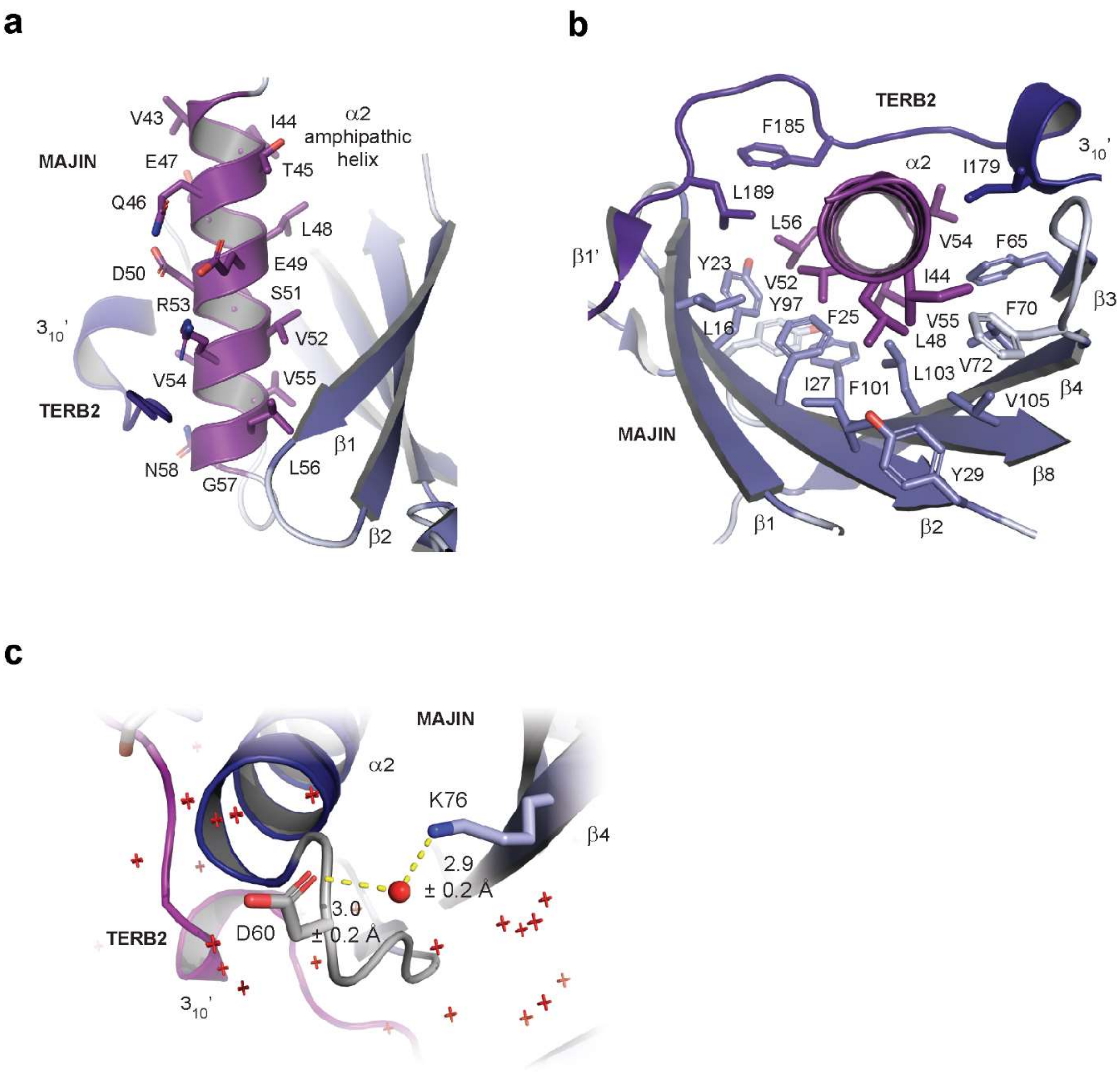
a
V43
I44
α2
amphipathic
helix
MAJIN
E47
T45
Q46
L48
D50
E49
S51
R53
V52
3_{10}'
V54
V55
TERB2
β1
N58
G57
L56
β2
b
TERB2
F185
3_{10}'
α2
I179
L189
L56
V54
F65
β1'
Y23
V52
I44
β3
Y97
F70
L16
F25
V55
L48
V72
I27
F101
L103
β4
V105
MAJIN
Y29
β8
β1
β2
c
MAJIN
α2
K76
β4
2.9
± 0.2 Å
3.0
± 0.2 Å
TERB2
D60
3_{10}'

Figure 4.2.6| Side-chain contribution to the MAJIN-TERB2 β-grasp structure. a) The central α2 forms an amphipathic helix with β-sheet facing residues (I44, L48, V52, V54, V55 and L56) being hydrophobic and solvent exposed residues (E47, Q46, E49, D50, R53, and N58) being charged or polar. **b)** Top-down view down the barrel of the α2-helix demonstrating the hydrophobic associations stabilising the β-grasp. L16 (β1); Y23, F25, I27, Y29 (β2); F65 (β3); F70, V72 (β4); F101, L103, V105 (β8) of the MAJIN β-sheet collaborate with TERB2 residues I179, F185 and L189 to hydrophobically associate the central α2-helix. **c)** A water-mediated association exists between D60 and K76 of MAJIN with hydrogen bonds lengths indicated, with an angle of 107˚. The interacting atoms of the sidechains are otherwise separated by 4.8 Å. The water molecule of interest is represented as a red sphere with others represented as small red crosses. The bond was identified using HCBS software (Gurusaran *et al.*, 2016)

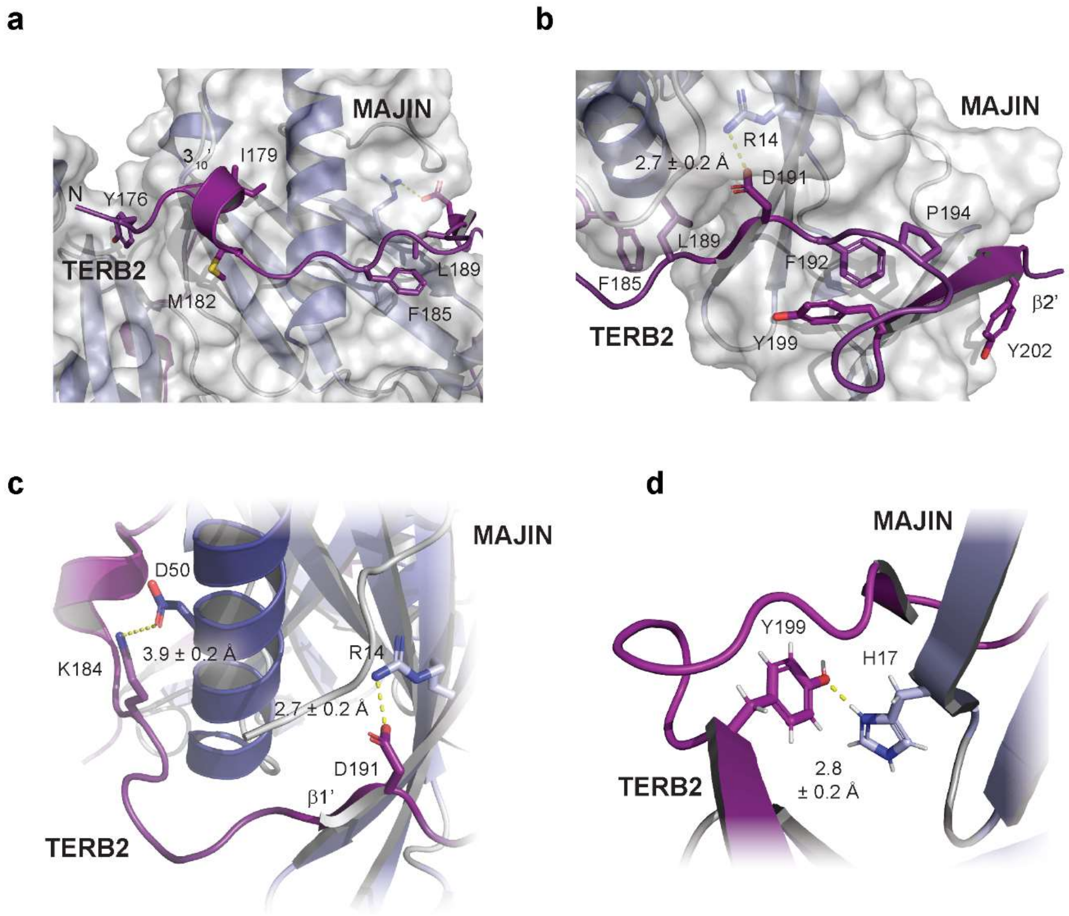
a
MAJIN
3₁₀'
I179
N
Y176
TERB2
M182
L189
F185
b
MAJIN
R14
2.7 ± 0.2 Å
D191
P194
L189
F192
F185
C
β2'
TERB2
Y199
Y202
c
MAJIN
D50
K184
3.9 ± 0.2 Å
R14
2.7 ± 0.2 Å
D191
β1'
TERB2
d
MAJIN
Y199
H17
TERB2
2.8
± 0.2 Å

Figure 4.2.7| TERB2 side-chain contributions to the MAJIN-TERB2 interface. a,b) TERB2 side-chains dock into hydrophobic pockets of the MAJIN molecular surface. **c)** Salt bridges exist between MAJIN R14 and D50 and TERB2 D191 and K184, respectively with distances, and errors, indicated. Errors were assigned using SBPS software (Gurusaran *et al.*, 2014). **d)** A hydrogen bond between MAJIN H17 and TERB2 Y199 contributes to the fold. Bond identified and error assigned using HBCS software (Gurusaran *et al.*, 2016). A hydrogen bond is defined as a donor-acceptor pair with a separation of 2.6-3.3 Å.

4.2.7 Comparison of the high-resolution native, seleno-methionine and a competitor's structure

Soon after publication of the MAJIN-TERB2 structure (Dunce *et al.*, 2018b), another group published a SeMet-derivative structure of the same complex at a resolution of 2.9 Å, similar to that of our SeMet-derivative (Wang *et al.*, 2019). The SeMet-derivative structures are almost identical with an all-atom rmsd value of 0.82, exhibiting greater similarity between each other than with the native, higher resolution structure (Figure 4.2.8a). This discrepancy is most likely due to the presence of an ordered loop region between β2 and α2, not resolved in either SeMet-structure. The overall fold is overtly similar and symmetrical with no real differences observed between MAJIN-TERB2 protomers (Figure 4.2.8b).

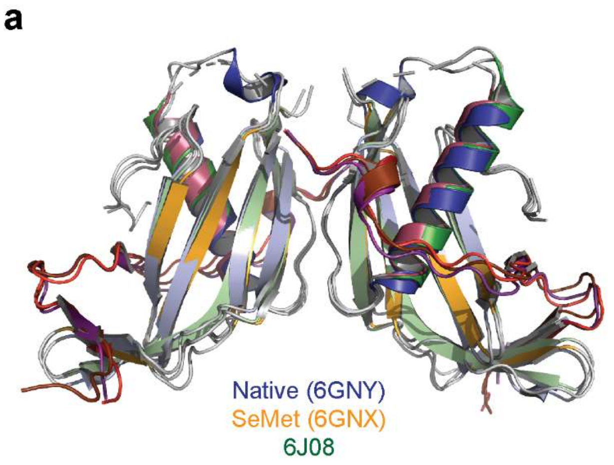

	Native (6GNY)	SeMet (6GNX)	6J08
Native (6GNY)	-	1.61	1.18
SeMet (6GNX)	1.61	-	0.82
6J08	1.18	0.82	-

Chain v chain rmsd (Å)

	Native (6GNY) A/B	Native (6GNY) C/D	SeMet (6GNX) A/B	SeMet (6GNX) C/D	6J08 B/E	6J08 C/F
Native (6GNY) A/B	-	0.49	0.46	0.64	0.75	0.47
Native (6GNY) C/D	0.49	-	0.56	0.63	0.74	0.50
SeMet (6GNX) A/B	0.46	0.56	-	0.41	0.55	0.39
SeMet (6GNX) C/D	0.64	0.63	0.41	-	0.49	0.41
6J08 B/E	0.75	0.74	0.55	0.49	-	0.50
6J08 C/F	0.47	0.50	0.39	0.41	0.50	-

Chain v chain rmsd (Å)

Figure 4.2.8| Structure comparison. a) Superimposition and respective all-atom rmsd values of the 1.85 Å MAJIN-TERB2 structure (6GNY), the seleno-methionine derivative structure (6GNX) and a structure which was solved concurrently and published 2 months after the release of our publication (6J08) (Dunce *et al.*, 2018b; Wang *et al.*, 2019). **b)** Superimposition of the two MAJIN-TERB2 protomers from the 6GNY, 6GNX and 6J08 structures and the respective all-atom rmsd values.

4.2.8 The solution structure of the MAJIN-TERB2 core complex

SEC-SAXS analysis revealed that the MAJIN$_{1\text{-}106}$ TERB2$_{168\text{-}207}$ solution structure closed matched the crystal structure, producing an average X-ray scattering profile closely matching the theoretical scattering curve of the crystal structure with a χ^2 value of 1.62 (Figure 4.2.9a). In contrast, the experimental scattering data for MAJIN$_{1\text{-}112}$ TERB2$_{168\text{-}220}$ did not match the theoretical scattering of the crystal structure, demonstrating a χ^2 value of 17.96, likely due to the presence of 6 additional MAJIN residues and 13 additional TERB2 residues (Figure 4.2.9a). This is represented within the interatomic distance-distribution profiles of both constructs in which the shorter MAJIN$_{1\text{-}106}$ TERB2$_{168\text{-}207}$ presents a more compact form with a D_{max} of 80 Å in comparison to 120 Å of MAJIN$_{1\text{-}112}$ TERB2$_{168\text{-}220}$ (Figure 4.2.9b). The MAJIN$_{1\text{-}112}$ TERB2$_{168\text{-}220}$ solution structure appears more elongated, indicated through asymmetry of the distance-distribution profile (near-Gaussian in the case of MAJIN$_{1\text{-}106}$ TERB2$_{168\text{-}207}$) and an increased radius of gyration (*Rg*) value (30 Å in comparison to 24 Å of MAJIN$_{1\text{-}106}$ TERB2$_{168\text{-}207}$; Figure 4.2.9c,d). Interestingly, analysis by circular dichroism far-UV spectroscopy and thermal denaturation suggests an increased secondary structure content and increased thermostability of the extended MAJIN$_{1\text{-}112}$ TERB2$_{168\text{-}220}$ complex, potentially due to stabilising or structural contributions of the extreme C-terminus of TERB2 (Figure 4.2.9e,f). *Ab initio* molecular envelopes match the crystal structure of the compact MAJIN$_{1\text{-}106}$ TERB2$_{168\text{-}207}$ complex and reveals additional electron density positioned laterally the MAJIN-TERB2 core structure, for which we do not currently have a substantiated explanation but is likely explained by the additional residues of the longer construct (Figure 4.2.10a,b).

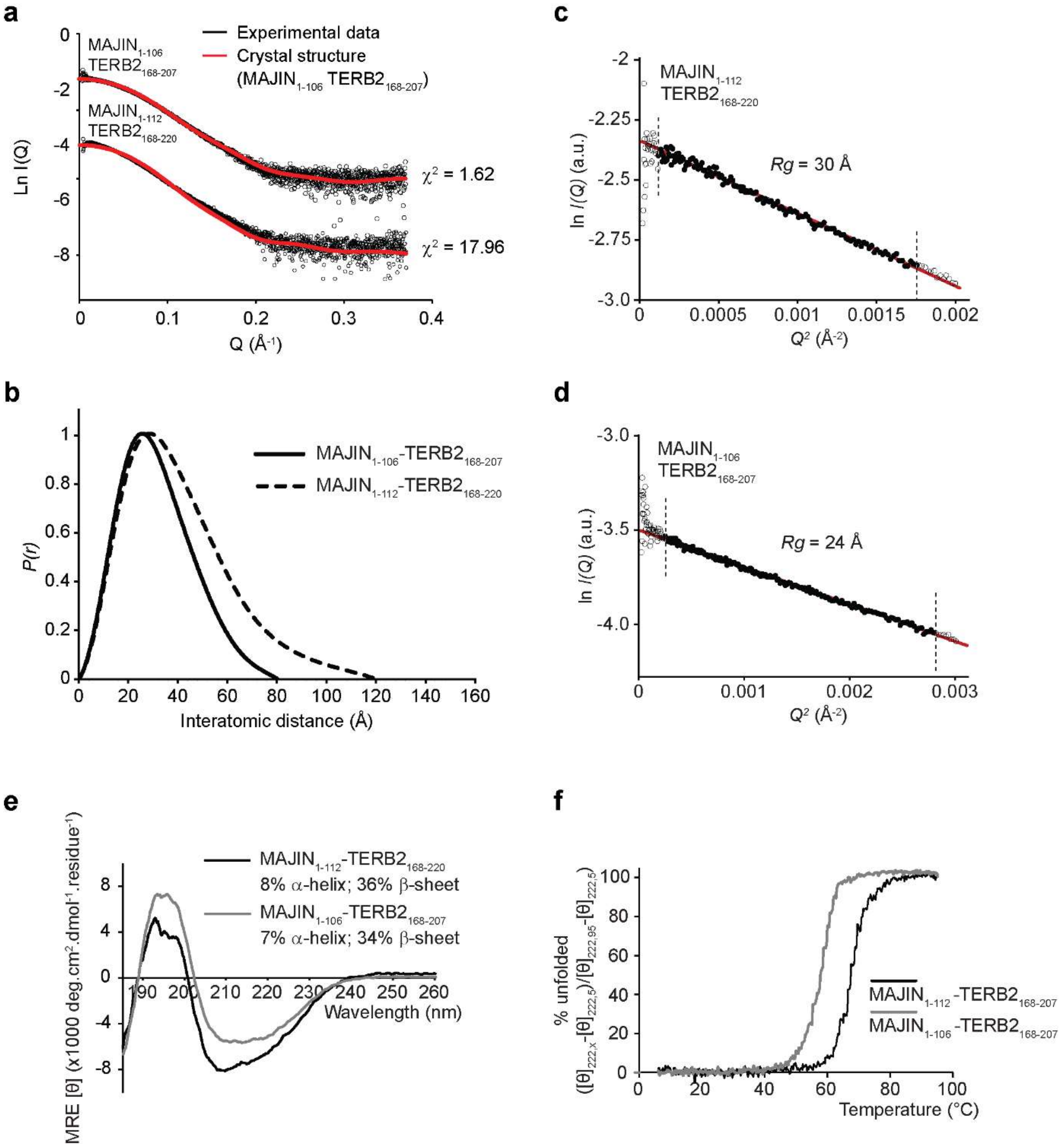

Figure 4.2.9| The solution structure of MAJIN-TERB2. a) Averaged small-angle X-ray scattering profile of MAJIN$_{1-106}$ TERB2$_{168-207}$ and MAJIN$_{1-112}$ TERB2$_{168-220}$ overlaid with the theoretical scattering profile of the MAJIN$_{1-106}$ TERB2$_{168-207}$ crystal structure with indicated χ^2 values. **b)** SEC-SAXS *P(r)* distribution of MAJIN$_{1-106}$ TERB2$_{168-207}$ (solid) and MAJIN$_{1-112}$ TERB2$_{168-220}$ (dashed) demonstrating D_{max} values of 80 and 120 Å, respectively. **c-d)** SEC-SAXS Guinier analysis to determine the radius of gyration (*Rg*) of **c)** MAJIN$_{1-112}$ TERB2$_{168-220}$ and **d)** MAJIN$_{1-106}$ TERB2$_{168-207}$. The linear fit is plotted in red and the linear region highlighted and demarcated by dotted lines. The Q.Rc value was < 1.3 with the *Rg* calculated at 30 and 24 Å, respectively. **e)** Circular dichroism far-UV spectra for MAJIN$_{1-112}$ TERB2$_{168-220}$ (black) and MAJIN$_{1-106}$ TERB2$_{168-207}$ (grey), indicating percentage α-helix and β-sheet estimated by deconvolution, with data fitted at a normalised rmsd values of 0.061 and 0.055, respectively. **f)** Thermal denaturation of MAJIN$_{1-112}$ TERB2$_{168-220}$ (black) and MAJIN$_{1-106}$ TERB2$_{168-207}$ (grey), demonstrating melting temperatures of 66 and 59 ˚C, respectively. SEC-SAXS analysis by Dr Owen Davies.

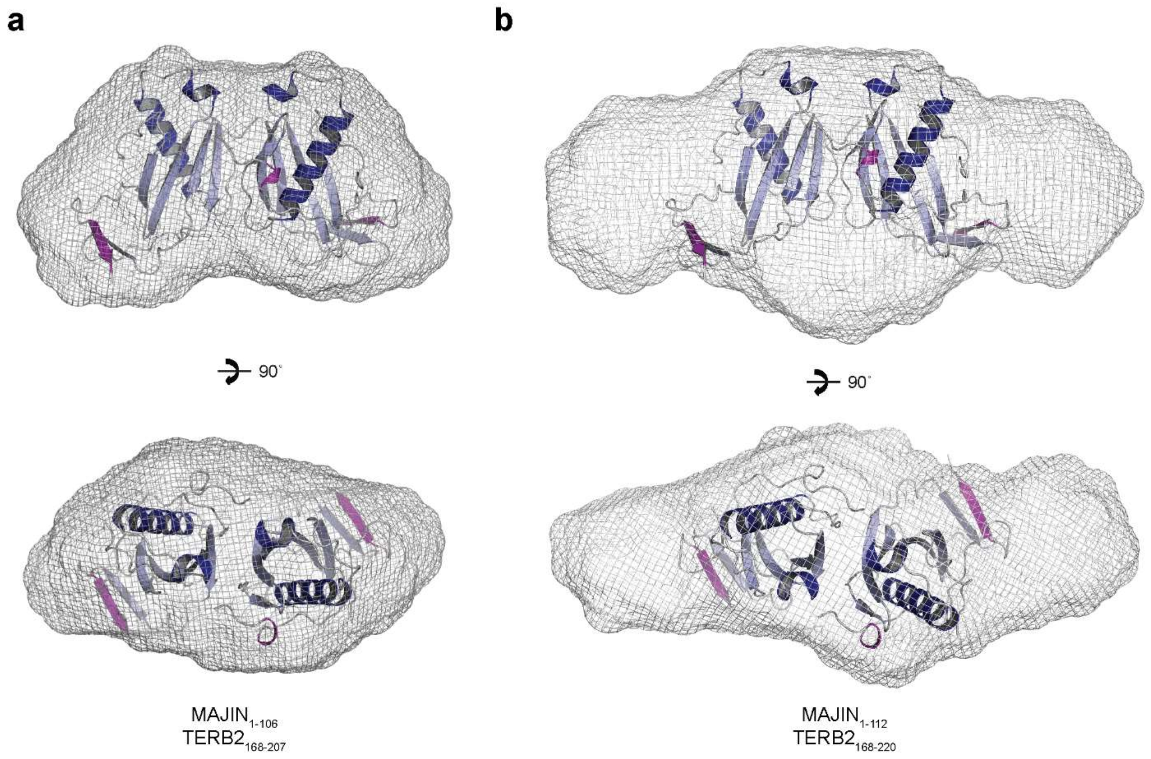

Figure 4.2.10| SAXS-derived molecular envelopes for MAJIN-TERB2. a,b) SUPCOMB docking of the MAJIN-TERB2 crystal structure into an *ab initio* molecular envelope for **a)** $\text{MAJIN}_{1\text{-}106}$ $\text{TERB2}_{168\text{-}207}$ and **b)** $\text{MAJIN}_{1\text{-}112}$ $\text{TERB2}_{168\text{-}220}$. SEC-SAXS analysis by Dr Owen Davies.

4.2.9 The MAJIN C-terminus is unstructured and extended

In order to characterise the structure of the MAJIN C-terminus and uncover how the MAJIN core is connected to the membrane-embedded C-terminal transmembrane helix, I cloned and purified MAJIN-TERB2 complexes including unstructured MAJIN residues 106-147 or 106-233 and lacking TERB2 residues 208-220 to negate their contribution to observed flexibility during SEC-SAXS experiments. Purification was achieved through sequential Ni-NTA and amylose affinity chromatography (both proteins were His_6-MBP-tagged) followed by cation exchange chromatography using HiTrap SP column to exploit the highly basic charge of the unstructured C-terminal tail of MAJIN. Affinity tags were removed by TEV-cleavage and the purification completed by further cation exchange and size-exclusion chromatography. SDS-PAGE analysis of samples to summarise the purification of $\text{MAJIN}_{1\text{-}147}$ $\text{TERB2}_{168\text{-}207}$ and the final purified sample of $\text{MAJIN}_{1\text{-}233}$ $\text{TERB2}_{168\text{-}207}$ are displayed in Figure 4.2.11a.

SEC-MALS analysis of both complexes yielded unexpected results with molecular weights far below their theoretical 2:2 heterotetrameric states (Figure 4.2.11b). MAJIN$_{1\text{-}233}$ TERB2$_{168\text{-}207}$ and MAJIN$_{1\text{-}147}$ TERB2$_{168\text{-}207}$ were fit to molecular weights of 44 and 37 kDa, respectively, only slightly above the molecular weight of 35 kDa for MAJIN$_{1\text{-}106}$ TERB2$_{168\text{-}207}$. We think that MALS does not accurately determine the molecular weight of proteins incorporating large regions of flexibility with dominant scattering centres accounting for the majority of light scattering and skewing the calculation of molecular weight.

Somewhat bizarrely, the additional 31 unstructured residues of MAJIN$_{1\text{-}147}$ do not contribute as greatly to an increase in maximum interatomic distance as do the 13 C-terminal residues of TERB2 (Figure 4.2.11c). As expected, a significant increase in D_{max} is observed for MAJIN$_{1\text{-}233}$ TERB2$_{168\text{-}207}$. The presence of additional scattering atoms is reflected by *Rg* values for both constructs and the suggestion that they are largely unstructured is supported by circular dichroism far-UV spectroscopy which demonstrates a spectrum characteristic of random coil (Figure 4.2.11d-f).

The averaged experimental X-ray scattering profiles of both constructs do not match the theoretical scattering profile of the MAJIN$_{1\text{-}106}$ TERB2$_{168\text{-}207}$ crystal structure, unsurprisingly. Modelling of the unstructured C-terminal tails of MAJIN (performed by Dr Owen Davies using CORAL which utilises scattering information to build missing loop sequences) predicts their extended conformation, spanning up to 90 Å in the case of MAJIN$_{1\text{-}233}$ TERB2$_{168\text{-}207}$ (Petoukhov *et al.*, 2012) (Figure 4.2.11g-i). The theoretical scattering of such modelled structures closely matches the experimental scattering of both MAJIN$_{1\text{-}233}$ TERB2$_{168\text{-}207}$ and MAJIN$_{1\text{-}147}$ TERB2$_{168\text{-}207}$, with χ^2 values of 1.95 and 1.34, respectively.

These findings combine to suggest that the MAJIN-TERB2 core structure is linked to the nuclear membrane through long, flexible linker sequences which led to transmembrane helices embedded in the inner nuclear membrane (Figure 4.2.11i).

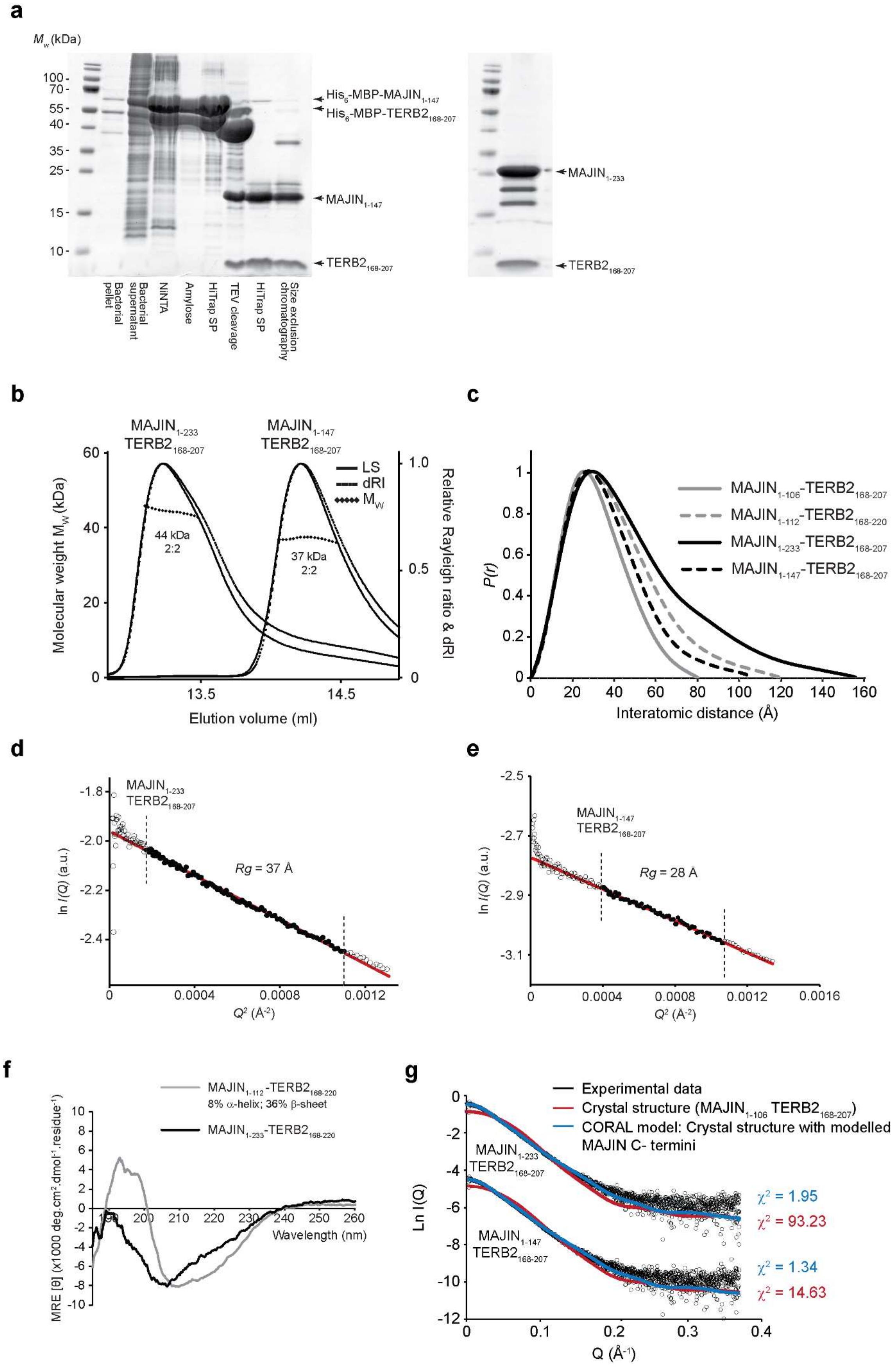
a
Mw (kDa)
100
70
55
40
35
25
15
10
His6-MBP-MAJIN1-147
His6-MBP-TERB2168-207
MAJIN1-147
TERB2168-207
MAJIN1-233
TERB2168-207
Bacterial pellet
Bacterial supernatant
NiNTA
Amylose
HiTrap SP
TEV cleavage
HiTrap SP
Size exclusion chromatography
b
MAJIN1-233
TERB2168-207
MAJIN1-147
TERB2168-207
LS
dRI
MW
44 kDa
2:2
37 kDa
2:2
Molecular weight MW (kDa)
Relative Rayleigh ratio & dRI
Elution volume (ml)
13.5
14.5
c
MAJIN1-106-TERB2168-207
MAJIN1-112-TERB2168-220
MAJIN1-233-TERB2168-207
MAJIN1-147-TERB2168-207
P(r)
Interatomic distance (Å)
d
MAJIN1-233
TERB2168-207
Rg = 37 Å
ln I(Q) (a.u.)
Q2 (Å-2)
e
MAJIN1-147
TERB2168-207
Rg = 28 Å
ln I(Q) (a.u.)
Q2 (Å-2)
f
MAJIN1-112-TERB2168-220
8% α-helix; 36% β-sheet
MAJIN1-233-TERB2168-220
MRE [θ] (x1000 deg.cm2.dmol-1.residue-1)
Wavelength (nm)
g
Experimental data
Crystal structure (MAJIN1-106 TERB2168-207)
CORAL model: Crystal structure with modelled MAJIN C- termini
MAJIN1-233
TERB2168-207
MAJIN1-147
TERB2168-207
χ2 = 1.95
χ2 = 93.23
χ2 = 1.34
χ2 = 14.63
Ln I(Q)
Q (Å-1)

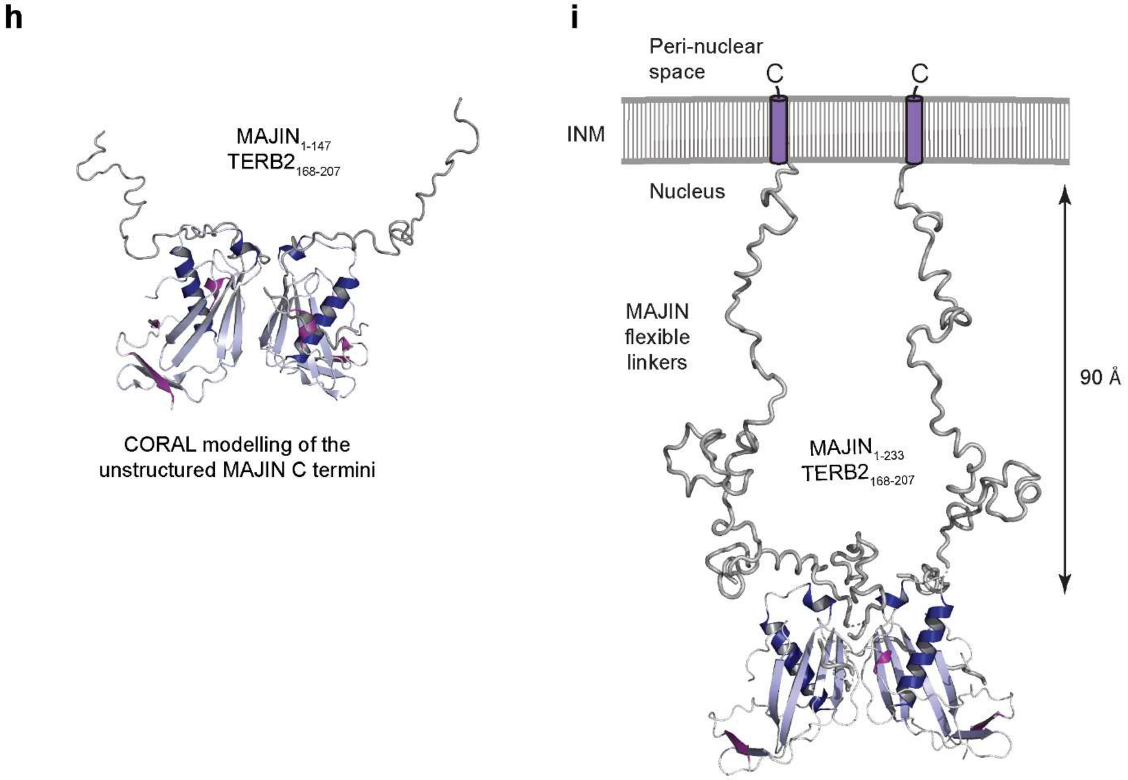

Figure 4.2.11| The MAJIN C-terminus is unstructured and extended. a) SDS-PAGE analysis summarising the purification of $MAJIN_{1\text{-}147}$ $TERB2_{168\text{-}207}$ and the final purified sample of $MAJIN_{1\text{-}233}$ $TERB2_{168\text{-}207}$ which was purified by the same method. **b)** SEC-MALS analysis of $MAJIN_{1\text{-}233}$ $TERB2_{168\text{-}207}$ (left; theoretical molecular weight of a 2:2 heterotetramer= 63 kDa) and $MAJIN_{1\text{-}147}$ $TERB2_{168\text{-}207}$ (right; theoretical molecular weight of a 2:2 heterotetramer= 49 kDa). **c)** SEC-SAXS *P(r)* distribution of $MAJIN_{1\text{-}233}$ $TERB2_{168\text{-}207}$ (grey, solid) and $MAJIN_{1\text{-}147}$ $TERB2_{168\text{-}207}$ (grey, dashed). The *P(r)* distributions for $MAJIN_{1\text{-}106}$ $TERB2_{168\text{-}207}$ and $MAJIN_{1\text{-}112}$ $TERB2_{168\text{-}220}$ are displayed in grey for comparison. **d-e)** SEC-SAXS Guinier analysis to determine the radius of gyration (*Rg*) of **d)** $MAJIN_{1\text{-}233}$ $TERB2_{168\text{-}207}$ and **e)** $MAJIN_{1\text{-}147}$ $TERB2_{168\text{-}207}$. The linear fit is plotted in red and the linear region highlighted and demarcated by dotted lines. The *Q.Rc* value was < 1.3 with the *Rg* calculated at 37 and 28 Å, respectively. **f)** Circular dichroism far-UV spectra for $MAJIN_{1\text{-}233}$ $TERB2_{168\text{-}220}$ (black) and $MAJIN_{1\text{-}112}$ $TERB2_{168\text{-}220}$ (grey) for comparison. **g)** Averaged small-angle X-ray scattering profile for $MAJIN_{1\text{-}233}$ $TERB2_{168\text{-}207}$ and $MAJIN_{1\text{-}147}$ $TERB2_{168\text{-}207}$ overlaid with the theoretical scattering profile of the MAJIN-TERB2 crystal structure with (blue) and without (red) CORAL modelled C-termini (residues 107-233 and 107-147) with indicated χ^2 values. **h-i)** Cartoon representation of the MAJIN-TERB2 crystal structure with CORAL modelled unstructured MAJIN C-termini, **h)** residues 107-147 and **i)** residues 107-233. The unstructured termini lead to transmembrane helices embedded within the inner nuclear membrane. SEC-SAXS analysis by Dr Owen Davies.

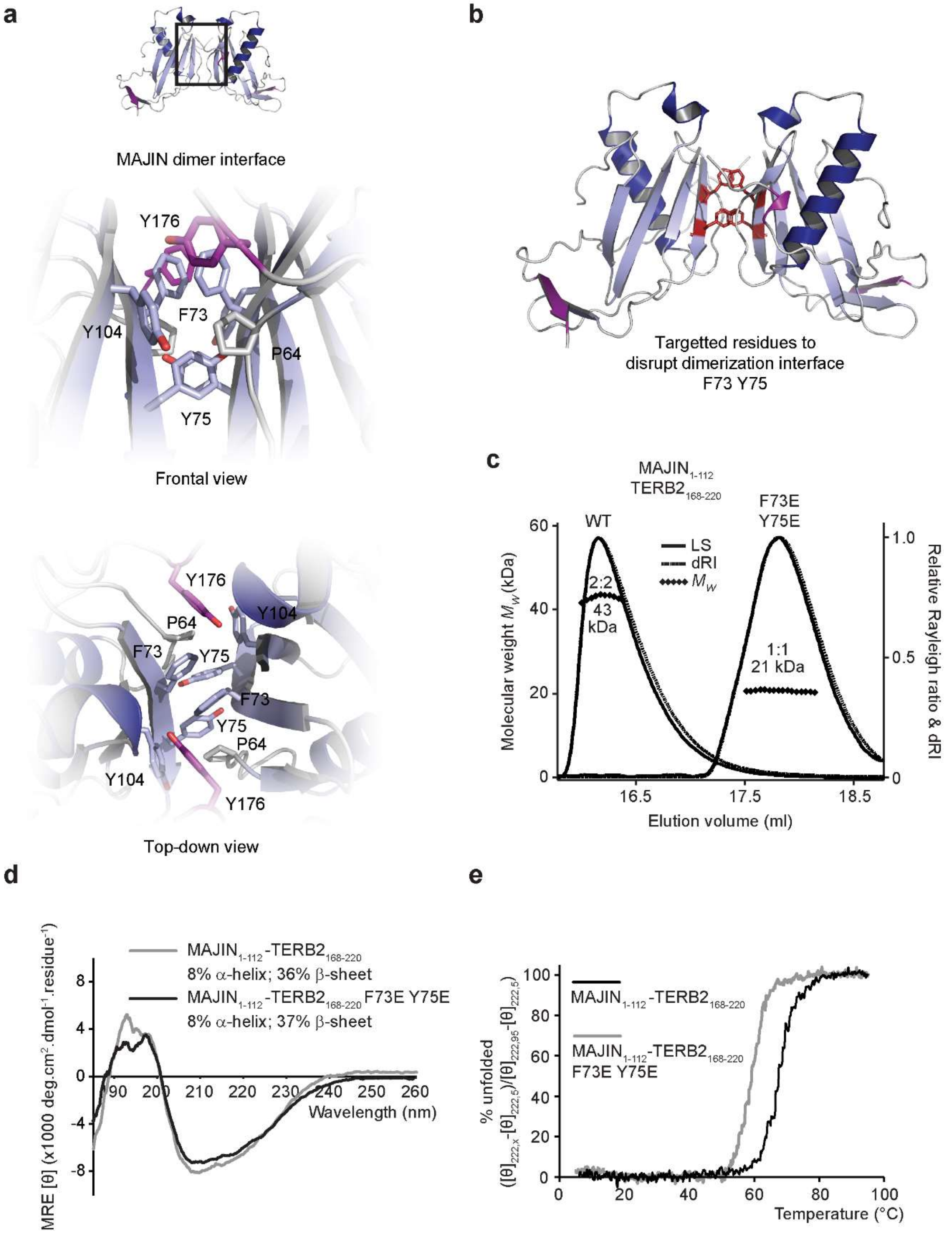

Figure 4.2.12| Mutational disruption of the MAJIN-TERB2 dimer interface. a) A frontal and top-down view of the MAJIN dimer interface. A hydrophobic core is formed of MAJIN residues P64, F73, Y75 and Y104 and TERB2 Y176. **b)** Cartoon representation of the MAJIN-TERB2 structure highlighting in red residues F73 and Y75, selected for mutation to glutamate to disrupt the dimer interface. **c)** SEC-MALS analysis of wild-type and mutant F73E Y75E MAJIN$_{1-112}$ TERB2$_{168-220}$ demonstrating a shifted elution volume and a halved molecular weight (theoretical molecular weight of a 1:1 heterodimer is 20 kDa). **d)** Circular dichroism far-UV spectra for MAJIN$_{1-112}$ TERB2$_{168-220}$ F73E Y75E (black) and MAJIN$_{1-112}$ TERB2$_{168-220}$ (grey) for comparison, indicating percentage α-helix and β-sheet estimated by deconvolution, with data fitted at a normalised rmsd values of 0.063 and 0.061, respectively. **e)** Thermal melts MAJIN$_{1-112}$ TERB2$_{168-220}$ F73E Y75E (grey) and MAJIN$_{1-112}$ TERB2$_{168-220}$ (black) demonstrating melting temperatures of 59 and 66 ˚C.

4.2.10 Disruption of the dimerization interface between MAJIN-TERB2 protomers

The MAJIN-TERB2 dimeric interface is mediated by a hydrophobic core comprising MAJIN residues P64, F73, Y75 and TERB2 Y176 (Figure 4.2.12a). We selected MAJIN residues F73 and Y75 for mutation to glutamate to disrupt the interface (Figure 4.2.12b). I cloned a MAJIN$_{1\text{-}112}$ construct containing mutations F73E Y75E which was subsequently purified in complex with TERB2$_{168\text{-}220}$ by Gurusaran Manickam using the method described previously for wild-type. SEC-MALS analysis revealed that the mutation successfully disrupted the dimerization interface, demonstrating the formation of a stable 1:1 complex with a molecular weight of 21 kDa (theoretical molecular weight= 20 kDa) in comparison to the 2:2 heterotetrameric molecular weight of 43 kDa (Figure 4.2.12c). Circular dichroism far-UV spectroscopy confirmed that the fold contained a near identical percentage of secondary structural elements whilst thermal denaturation, tracked by measuring the α-helical content at 222 nm, demonstrating slightly reduced stability of the 1:1 complex (Figure 4.2.12d,e).

4.2.11 The MAJIN-TERB2 complex binds dsDNA and does so in a cooperative manner

Each MAJIN-TERB2 protomer of the hetero-tetrameric structure displays a large basic surface which are orientated bi-directionally. The presence of such a surface and highly basic unstructured TERB2 C-termini suggested a potential role in DNA-binding, as might be expected for a telomere associated protein (Figure 4.2.13a). We analysed the ability of the MAJIN$_{1\text{-}112}$ TERB2$_{168\text{-}220}$ complex to bind dsDNA using electrophoretic mobility shift assays which clearly demonstrated strong affinity for DNA which was lost with deletion of the basic C-termini of TERB2 (Figure 4.2.13b). Disruption of the dimeric interface between MAJIN-TERB2 protomers through the mutation F73E Y75E resulted in an overt decrease in affinity of DNA, only resulted in the formation of unstable protein-DNA complexes as indicated by the formation of a smear between free DNA and protein-DNA complex (Figure 4.2.13b). By electron microscopy, MAJIN-TERB2 complexes with plasmid dsDNA to form amorphous plaques and ring-like protein-DNA structures connected by dsDNA strands (Figure 4.2.13c). These interesting inter-connected ring-like structures are present in the absence of DNA and suggest an underlying mechanism for the self-assembly of MAJIN-TERB2 complexes (Figure 4.2.13c). Although plaque-like assemblies are retained in the dimerization mutant, ring-like structures are not observed demonstrating a dependency on dimerization for higher-order oligomerisation (Figure 4.2.13c).

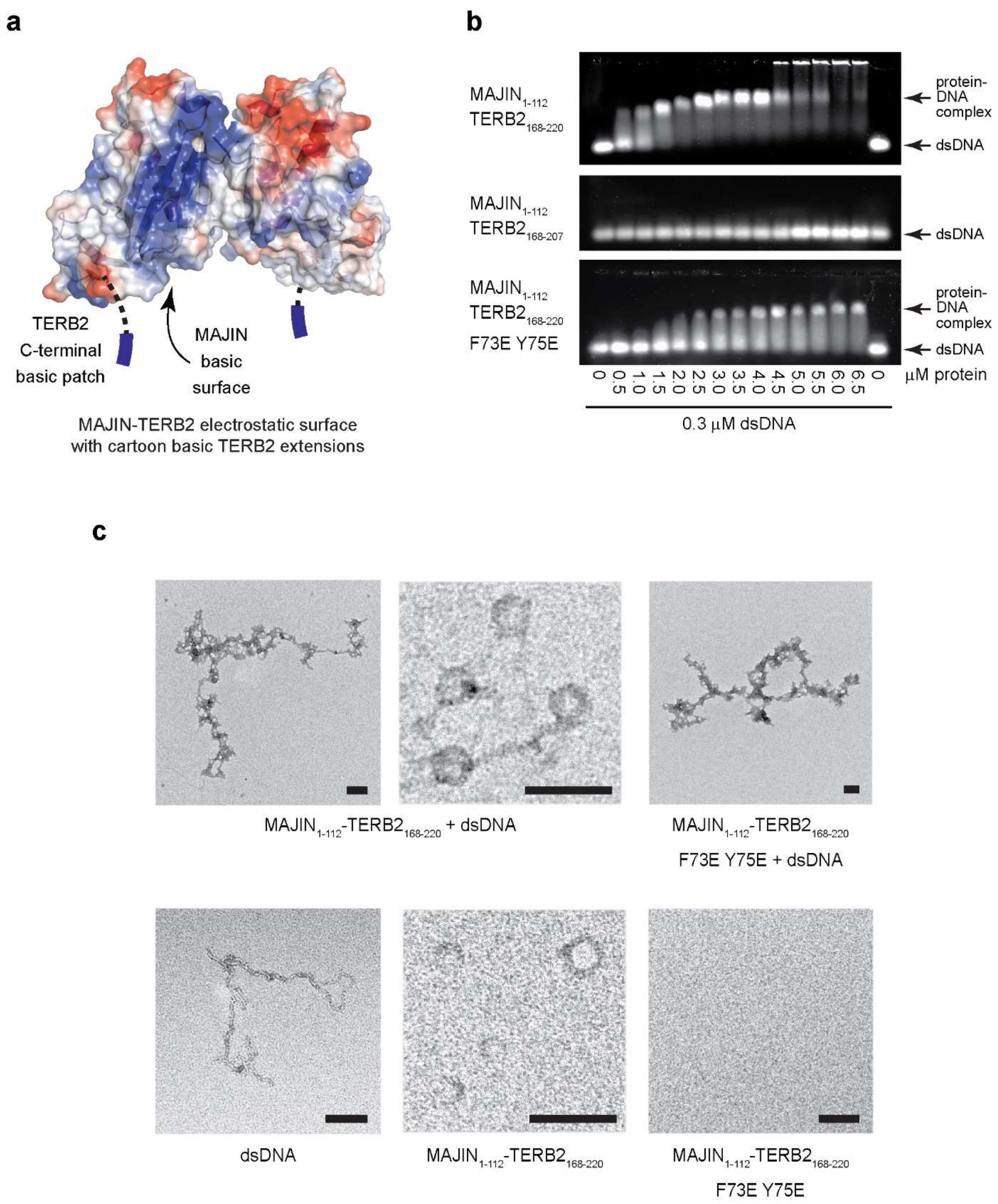
a
TERB2
C-terminal
basic patch
MAJIN
basic
surface
MAJIN-TERB2 electrostatic surface
with cartoon basic TERB2 extensions
b
MAJIN1-112
TERB2168-220
protein-DNA complex
dsDNA
MAJIN1-112
TERB2168-207
dsDNA
MAJIN1-112
TERB2168-220
F73E Y75E
protein-DNA complex
dsDNA
0 0.5 1.0 1.5 2.0 2.5 3.0 3.5 4.0 4.5 5.0 5.5 6.0 6.5 0
µM protein
0.3 µM dsDNA
c
MAJIN1-112-TERB2168-220 + dsDNA
MAJIN1-112-TERB2168-220
F73E Y75E + dsDNA
dsDNA
MAJIN1-112-TERB2168-220
MAJIN1-112-TERB2168-220
F73E Y75E

Figure 4.2.13| The MAJIN-TERB2 core binds DNA. a) Electrostatic surface representation of the MAJIN-TERB2 structure. Basic residues are coloured blue, whilst acidic residues are coloured in red. **b)** Electrophoretic mobility shift assays demonstrating the ability of MAJIN–TERB2 constructs (as indicated) to interact with 0.3 µM (per molecule) linear double-stranded DNA (dsDNA). **c)** Electron microscopy imaging of $\text{MAJIN}_{1\text{-}112}$ $\text{TERB2}_{168\text{-}220}$, $\text{MAJIN}_{1\text{-}112}$ $\text{TERB2}_{168\text{-}220}$ F73E Y75E, with and without dsDNA. Scale bars= 100 nm.

4.2.12 Method for measuring the affinity of MAJIN-TERB2 for dsDNA

We modified our protocol for electrophoretic mobility shift assays and developed a system by which we could measure the affinity for dsDNA by the various MAJIN-TERB2 complexes. In this, we performed EMSA in triplicate using 5'-FAM-labelled dsDNA at 25 nM, below the expected K_D value for the MAJIN-TERB2 complex with DNA. ImageJ software (Schneider *et al.*, 2012) was utilised to quantify the proportion of dsDNA remaining unbound and converted to percentage bound. The percentage bound was subsequently plotted against MAJIN-TERB2 concentration and fitted to the Hill Equation from which the K_D was calculated (Figure 4.2.14).

4.2.13 Quantification of DNA-binding affinities

Using the above method, the K_D for MAJIN$_{1\text{-}112}$ TERB2$_{168\text{-}220}$ was calculated at 0.55 µM, similar to the previously reported affinity of TRF1 Myb-domain for dsDNA at 0.2 µM (Figure 4.2.15a) (Hanaoka *et al.*, 2005). Accordingly, we measured the affinity of full-length, dimeric, TRF1 at 0.1 µM suggesting a cooperative enhancement to binding; data not shown). In a similar manner, cooperative enhancement for DNA binding is demonstrated by MAJIN-TERB2 as the dimerization mutant F73E Y75E displays a three-fold reduced apparent affinity of 1.81 µM (Figure 4.2.15a). Deletion of the basic C-terminus TERB2, however, completely ablates the ability to bind DNA, demonstrating its crucial role in the interaction (Figure 4.2.15a).

4.2.14 The basic surface of MAJIN is essential for DNA binding

The residues which form the basic surface of MAJIN are highly conserved and include K24, K26, R28, R34, K31 and R81 (Figure 19a). In order to remove this interaction surface, we designed mutations utilising the ROSIE Rosetta Sequence Tolerance Server (Smith and Kortemme, 2011) (Figure 4.2.17). The server employs an algorithm in which selected mutation sites are screening for tolerant mutations which are predicted to not negatively impact upon backbone geometry and folding. The more frequently a residue appears in its simulations, the more likely the mutation is to be tolerated by the structure. On this basis, we introduced the mutations K24M, K26E, R28E, R34D, K31E and R81D (Figure 4.2.16a,b). We found that introduction of the basic surface mutations results in the complete disruption of DNA-binding (Figure 4.2.16c,d).

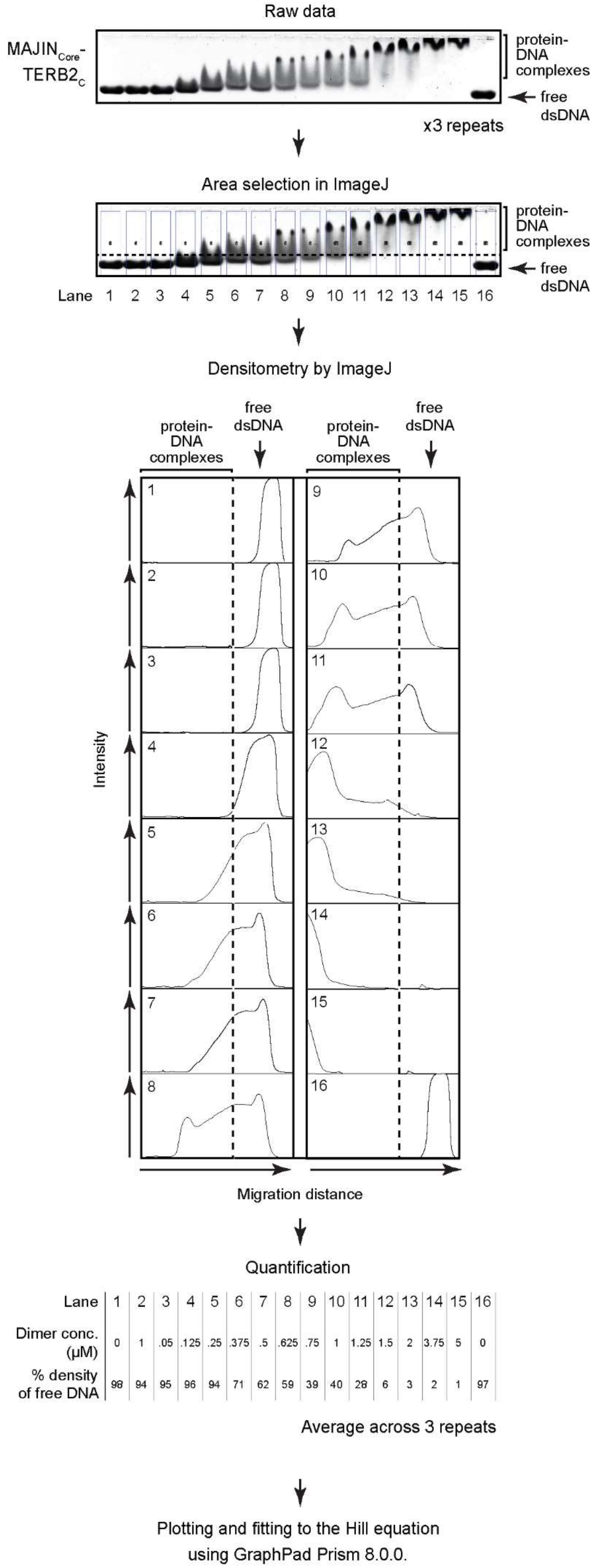
Raw data
MAJIN$_{Core}$-
TERB2$_C$
protein-
DNA
complexes
free
dsDNA
x3 repeats
Area selection in ImageJ
protein-
DNA
complexes
free
dsDNA
Lane 1 2 3 4 5 6 7 8 9 10 11 12 13 14 15 16
Densitometry by ImageJ
protein-
DNA
complexes
free
dsDNA
protein-
DNA
complexes
free
dsDNA
Intensity
1
2
3
4
5
6
7
8
9
10
11
12
13
14
15
16
Migration distance
Quantification
Average across 3 repeats
Plotting and fitting to the Hill equation
using GraphPad Prism 8.0.0.

Lane	1	2	3	4	5	6	7	8	9	10	11	12	13	14	15	16
Dimer conc. (μM)	0	1	.05	.125	.25	.375	.5	.625	.75	1	1.25	1.5	2	3.75	5	0
% density of free DNA	98	94	95	96	94	71	62	59	39	40	28	6	3	2	1	97

Figure 4.2.14| Method to quantify MAJIN-TERB2-dsDNA binding affinities. EMSA analysis of MAJIN-TERB2 construct was utilised to analyse binding of 5'-FAM labelled dsDNA (25 nM per molecule). Densitometry was performed to quantify the percentage of dsDNA unbound and subsequently plotted and fitted to the Hill equation to determine K_D values (Methods section 2.1.14).

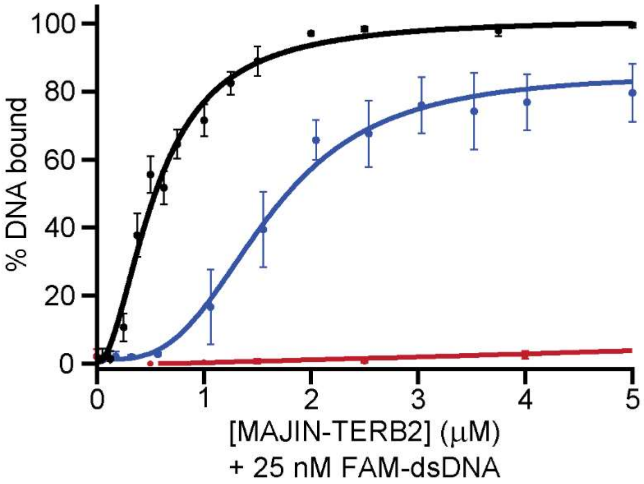

MAJIN-TERB2	K_D (μM)
1-112/168-220	0.55 ± 0.04
1-112/168-220 F73E Y75E	1.81 ± 0.21*
1-112/168-207	n.d.

Figure 4.2.15| Quantification of MAJIN-TERB2 core DNA-binding. Quantification of DNA-binding by MAJIN–TERB2 constructs (MAJIN$_{1-112}$ TERB2$_{168-220}$, black; MAJIN$_{1-12}$ TERB2$_{168-220}$ F73E Y75E, blue; MAJIN$_{1-112}$ TERB2$_{168-207}$, red) with K_D values indicated. Error bars indicate standard error, n = 3 EMSAs. *Apparent K_D was estimated graphically from the concentration at 50 % DNA-binding as binding saturation was not achieved

---

4.2.15 The unstructured MAJIN C-termini enhance DNA-binding

The unstructured and extended C-termini of MAJIN contain two distinct basic patches, just C-terminal to the structured core, creating a continuous DNA-associating interface spanning the TERB2 C-termini, the MAJIN basic surfaces and the unstructured C-termini (Figure 4.2.18a). Inclusion of these sequences in MAJIN$_{1-233}$ TERB2$_{168-220}$ enhances DNA-binding with an increased affinity of 0.12 μM in comparison to 0.55 μM of the structured core (Figure 4.2.18b,c). Further, their inclusion rescues DNA-binding in the absence of the TERB2 C-termini, exhibiting an apparent affinity of 0.2 μM (Figure 4.2.18b,c). Together, our DNA-binding studies suggest that DNA-binding my the MAJIN-TERB2 complex is facilitated through the cooperative DNA association of the TERB2 C-termini, the two MAJIN basic surfaces, and the unstructured MAJIN C-termini.

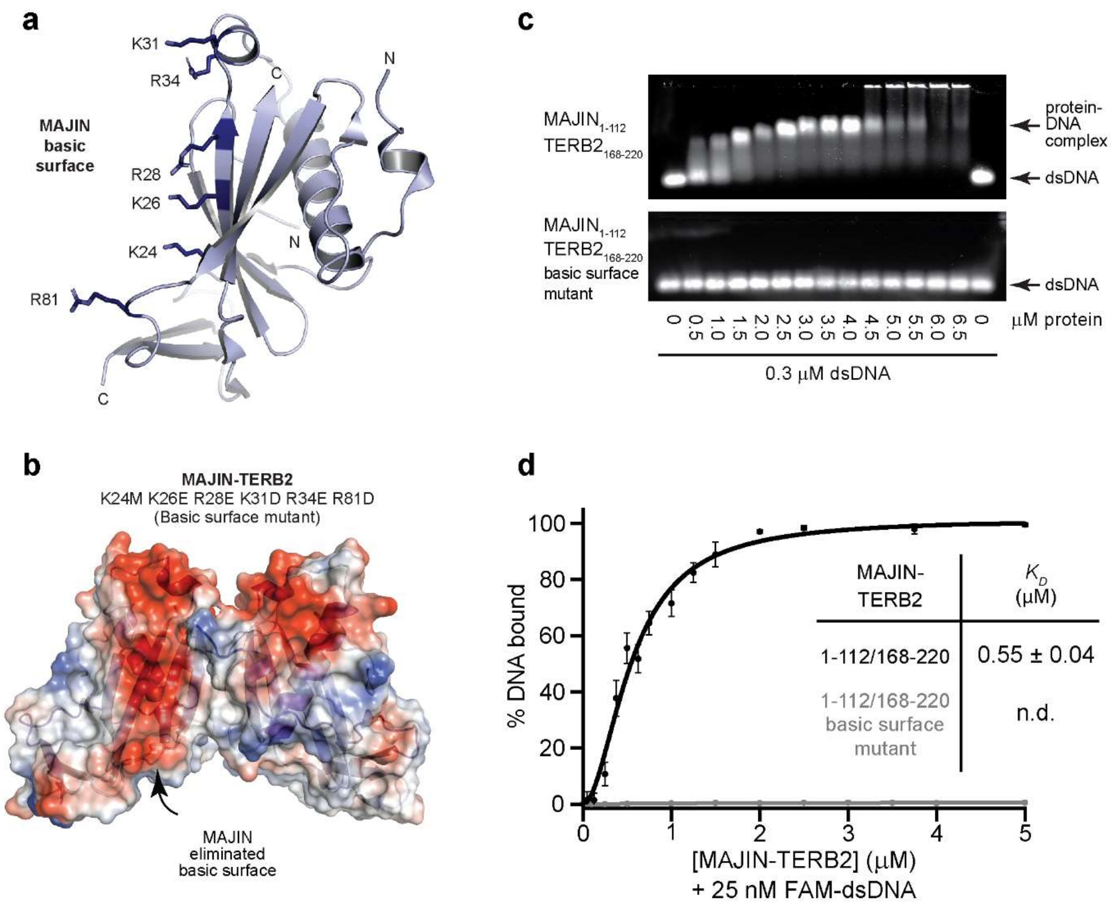

Figure 4.2.16| The basic surface of the MAJIN core is essential for DNA binding. a) The MAJIN-TERB2 protomer is displayed in cartoon format with basic residues which together form the basic surface of MAJIN are shown in blue. **b)** Electrostatic surface representation of MAJIN-TERB2 Basic surface mutant incorporating mutations K24M K26E R28E K31D R34E R81D which were predicted to be tolerated within the MAJIN-TERB2 fold by the ROSIE Rosetta Sequence Tolerance Server (Smith and Kortemme, 2011). **c)** EMSA analysis of $\text{MAJIN}_{1\text{-}112}$ $\text{TERB2}_{168\text{-}220}$ basic surface mutant and wild-type (for comparison) to visualise the effect of the basic surface mutations to interact with 0.3 µM (per molecule) linear double-stranded DNA (dsDNA). **d)** Quantification of DNA-binding by MAJIN–TERB2 constructs ($\text{MAJIN}_{1\text{-}112}$ $\text{TERB2}_{168\text{-}220}$, black; $\text{MAJIN}_{1\text{-}112}$ $\text{TERB2}_{168\text{-}220}$ basic surface mutant, grey) with K_D values indicated. Error bars indicate standard error, n = 3 EMSAs.

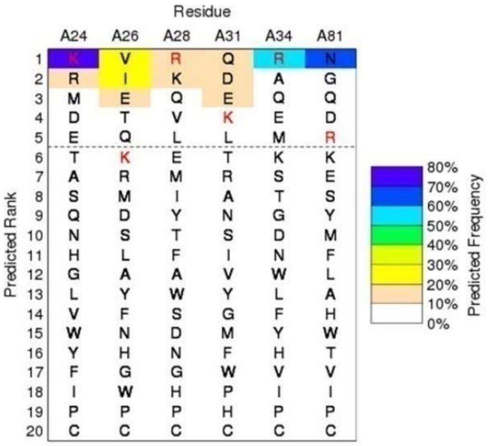
Residue
Predicted Rank
Predicted Frequency
80%
70%
60%
50%
40%
30%
20%
10%
0%

Predicted Rank	A24	A26	A28	A31	A34	A81
1	K	V	R	Q	R	N
2	R	I	K	D	A	G
3	M	E	Q	E	Q	Q
4	D	T	V	K	E	D
5	E	Q	L	L	M	R
6	T	K	E	T	K	K
7	A	R	M	R	S	E
8	S	M	I	A	T	S
9	Q	D	Y	N	G	Y
10	N	S	T	S	D	M
11	H	L	F	I	N	F
12	G	A	A	V	W	L
13	L	Y	W	Y	L	A
14	V	F	S	G	F	H
15	W	N	D	M	Y	W
16	Y	H	N	F	H	T
17	F	G	G	W	V	V
18	I	W	H	P	I	I
19	P	P	P	H	P	P
20	C	C	C	C	C	C

Selected: K24M K26E R28E
mutations K31D R34E R81D

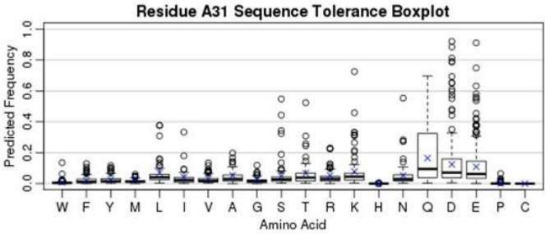

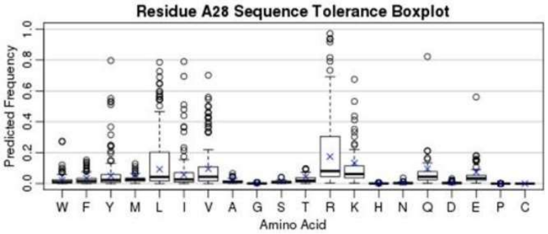

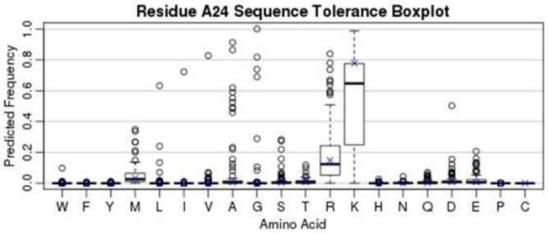

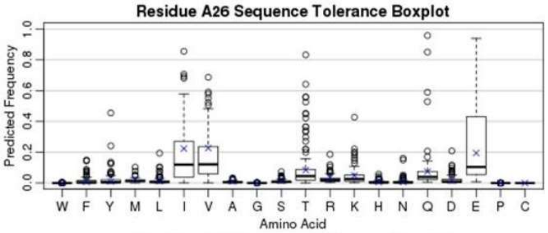

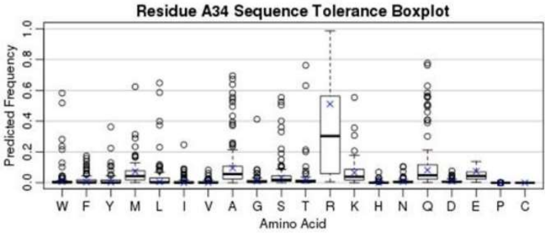

Figure 4.2.17| Design of the basic surface mutant. The ROSIE Rosetta Sequence Tolerance Server was utilised to determine mutations which would be tolerated within the MAJIN structure. Box plots representing the tolerance profile of each amino acid. Residue mutations with the highest frequency represent those which are likely most tolerated within the protein fold. The tolerated mutations of each residue are ranked with selected mutations detailed.

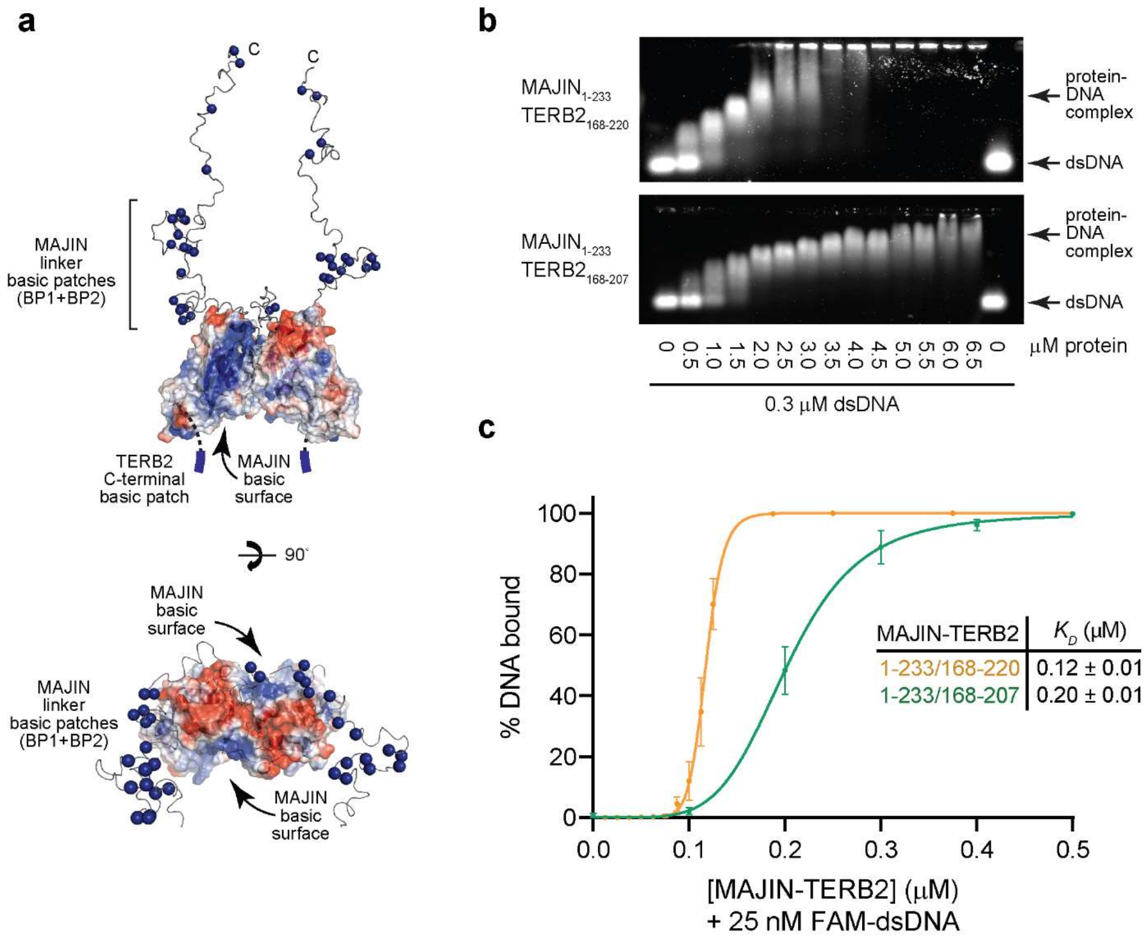

Figure 4.2.18| The unstructured C-terminus of MAJIN binds DNA. a) Electrostatic surface representation of the MAJIN-TERB2 core with CORAL-modelled unstructured MAJIN C-termini with basic residues highlighted as blue spheres. **b)** EMSA analysis of $\text{MAJIN}_{1\text{-}233}$ $\text{TERB2}_{168\text{-}220}$ and $\text{MAJIN}_{1\text{-}233}$ $\text{TERB2}_{168\text{-}207}$. **c)** Quantification of DNA-binding by MAJIN–TERB2 constructs ($\text{MAJIN}_{1\text{-}233}$ $\text{TERB2}_{168\text{-}220}$, yellow; $\text{MAJIN}_{1\text{-}233}$ $\text{TERB2}_{168\text{-}207}$, green) with K_D values indicated. Error bars indicate standard error, n = 3 EMSAs.

DISCUSSION

4.3.1 MAJIN-TERB2 structure confers 2-fold symmetry to the wider meiotic telomere complex

Here I have described the structure solution of the MAJIN-TERB2 hetero-tetrameric complex in which a globular MAJIN dimer is encircled by two TERB2 molecules. MAJIN adopts a β-grasp fold in which a 4-stranded β-sheet encloses around a central α-helix, stabilised through hydrophobic association, with closure completed on the opposite side by hydrophobically docked TERB2 sidechains. The structure represents a symmetrical dimer presenting flanking 3-stranded β-sheet appendages to each side. This symmetrical core likely acts as an organising centre for the wider meiotic telomere complex.

Our further studies, and those of another group, identified that the C-terminus of TERB1 forms a complex with the TERB2 N-terminus with a 1:1 stoichiometry with the crystal structure demonstrating a small globular fold in agreement with our characterisation by SAXS (Dunce *et al.*, 2018b; Wang *et al.*, 2019). In keeping with this finding, the MAJIN-TERB2 provides the architectural basis for a 2:2:2 complex between MAJIN-TERB2-TERB1 (Dunce *et al.*, 2018b). In keeping with the 1:1 stoichiometry of the TERB2-TERB1 complex and the 2:1 interaction between TRF1 and TERB1, TRF1-TERB1-TERB2 forms a 2:1:1 complex and MAJIN-TERB2-TERB1-TRF1 forms a 2:2:2:4 complex (Long *et al.*, 2017; Pendlebury *et al.*, 2017; Dunce *et al.*, 2018b). These combined findings allow for the generation for a molecular model of the complete meiotic telomere complex, schematised in Figure 4.3.1. These findings are reminiscent of the overall architecture provided by the Shelterin complex in which the components POT1, TPP1, TIN2, TRF1, and RAP1 form a 1:1:1:2:2 complex in which TRF1 interacts with a single TIN2 molecule (TIN2 associates with TRF1 in a manner similar to TERB1) (Lim *et al.*, 2017).

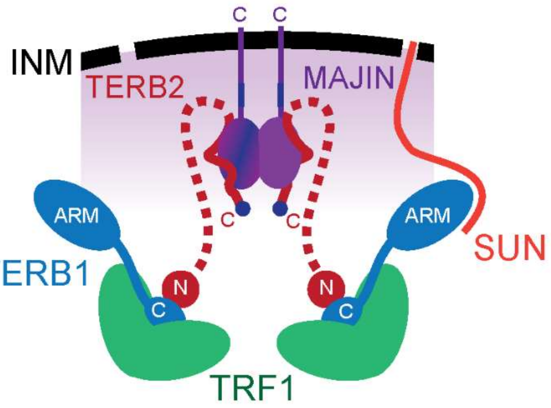

Figure 4.3.1| Model for molecular architecture of the Meiotic telomere complex. The nuclear-membrane embedded MAJIN dimer interacts with two TERB2 molecules which each interact with a further TERB1 molecule via their N-termini. Each TERB1 molecule recruits a TRF1 dimer resulting in the formation of a 2:2:2:4 MAJIN-TERB2-TERB1-TRF1 complex.

4.3.2 What is the functional significance of a long unstructured MAJIN C-terminus?

Our model for the MAJIN-TERB2 complex predicts an extensive distance between the MAJIN-TERB2 core and its nuclear envelope embedded C-terminal transmembrane helices, theoretically upwards of 400 Å. The length of the MAJIN unstructured sequences confers spatial freedom to the MAJIN-TERB2 core with respect to the transmembrane helices. This may facilitate the assembly of the complex during meiosis at the nuclear membrane which is coated on its nucleoplasmic surface by the nuclear lamina. Their length, which may be as long as 400 Å, might be long enough to span through the nuclear lamina which is between 400 – 600 Å in thickness in mitotic cells (Fawcett, 1966; Gerace and Huber, 2012). During mitotic division, SUN1 anchors telomeres within the nuclear membrane through interaction with type-A lamin such that they are immobile (Haque *et al.*, 2006). Rapid prophase movements may be facilitated in two ways. Firstly, the interaction is disrupted through the phosphorylation of the SUN1 C-terminus (Haque *et al.*, 2006). Secondly, the composition of the nuclear lamina is altered during meiosis. During meiosis, a specific type-A lamin isoform, lamin C2, is expressed (Link *et al.*, 2013). Despite not being required for telomeric attachment, the knockout of lamin C2 delays formation of the telomeric bouquet suggesting it plays a role in the allowing telomeric motility (Link *et al.*, 2013). Lamin C2 therefore appears to play a key role in allowing telomeric movements, possibly through altered dynamics within the nuclear membrane, such as altered fluidity and thickness.

4.3.3 DNA binding by MAJIN-TERB2 and its incorporation within the attachment plate?

The MAJIN dimer presents large basic surfaces on its front and back. Emanating from the C-termini of the MAJIN core, localised at the top of the MAJIN dimeric interface, are two long unstructured sequences (residues 106-233 of 254) containing highly basic sequences directly proximal to the MAJIN core whilst from the TERB2 C-termini, localised at the bottom of the flanking β-sheet appendages are short and highly basic (207-220). Solution of the crystal led to the realisation that these two basic interfaces may be connected through the surface basic patch to form a continuous DNA interacting surface with the symmetry of the structure allowing for a model in which DNA is looped over the MAJIN dimer (Figure 4.3.2a).

Fluorescence imaging reveals that telomeric DNA is looped up out of the SC, localising distal to the SYCP3-stained lateral elements and TERB2-stained meiotic telomere complex (Figure 4.3.2b). This localisation is concomitant with our model in which we expect DNA to track the unstructured MAJIN C-termini which extend towards the nuclear membrane. Telomeric DNA may therefore form an integral part of the telomeric attachment plate. We demonstrated *in vitro* that the DNA binding sequences with the MAJIN C-termini confer an enhancement to DNA binding with their importance *in vivo* demonstrated through the finding that MAJIN harbouring mutated basic patches does not fully rescue meiotic defects in MAJIN null mice (Shibuya *et al.*, 2015).

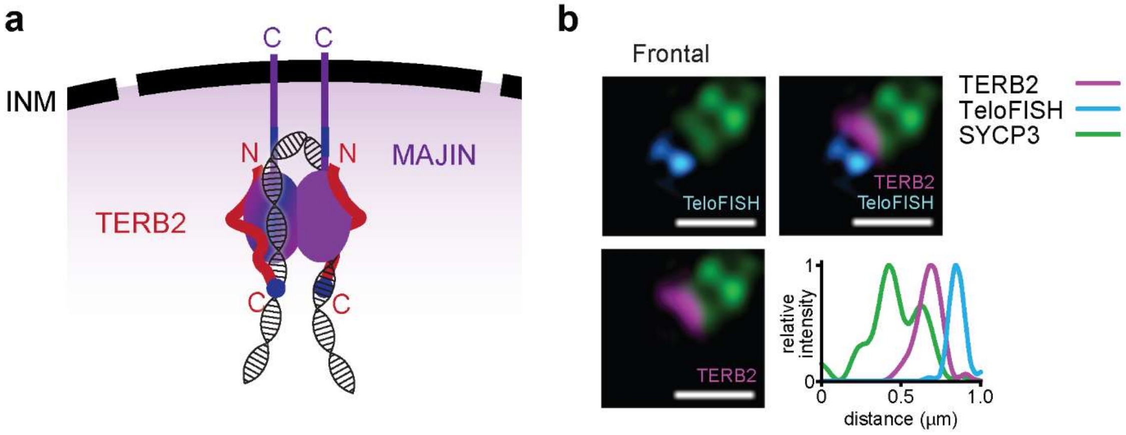

Figure 4.3.2| Model for the DNA binding mode of the MAJIN-TERB2 complex. C-terminal transmembrane helices embedded within the inner nuclear membrane anchor unstructured C-termini of MAJIN. Each protomer of the MAJIN dimer presents a basic surface (blue) which face in opposite directions. In addition, basic patches within the MAJIN unstructured C-termini and basic patches at the C-termini of the TERB2 (red) molecules (blue circles) create a continuous DNA interacting surface allowing DNA to loop over the top of the molecule. **b)** Late pachytene chromosomes of spread mouse spermatocytes stained with anti-TERB2 (magenta) in combination with telomere fluorescence in situ hybridisation (cyan; TeloFISH). Scale bars, 0.3 µm and 0.5 µm. A normalised intensity-distance plot is shown representing an average of multiple images (n = 25 telomeres). Work presented in this panel was performed by Irene da Cruz of the Ricardo Benavente group, University of Würzburg, Germany.

4.3.4 The dynamics of DNA binding at the meiotic telomere complex

Telomeric DNA is ordinarily protected from the DNA damage response by the Shelterin complex, of which TRF1 is a key component (de Lange, 2009). DNA binding is mediated through the Myb-domains of TRF1 which are specific for telomeric DNA (Hanaoka *et al.*, 2005). TERB1 further possesses Myb domain, thus combining with its affinity for TRF1 to mediate its telomeric recruitment (Long *et al.*, 2017; Pendlebury *et al.*, 2017; Zhang *et al.*, 2017). In further studies we found that TRF1 binds DNA with an apparent affinity of 0.1 µM (Dunce *et al.*, 2018b).

Through quantifying the relative affinities for DNA of MAJIN-TERB2 complexes harbouring various truncations and mutations, the essentiality and relative contribution of basic patches within its structure were determined. We found that both the C-terminus of TERB2 and the basic surface of MAJIN are essential for DNA binding in contrast to a contributory role of the MAJIN unstructured C-termini (these enhance the apparent affinity from 0.55 to 0.12 µM). Further studies found that the TERB2 interacting sequence of TERB1 does not contribute majorly to DNA binding with an apparent affinity of 0.46 µM

(Dunce *et al.*, 2018b). In contrast to our finding, another study found that the basic patches within the unstructured C-termini are essential for DNA binding (Shibuya *et al.*, 2015). However, their experiments were performed with MAJIN purified in the absence of TERB2 and demonstrated an elution volume by size exclusion chromatography indicative of aggregation. This suggests that the MAJIN protein they analysed by electrophoretic mobility shift assay was misfolded and likely did not harbour the basic surface present within our crystal structure. Therefore, the basic patches within the unstructured termini represented the sole sequences capable of binding DNA. This is in keeping with our finding that MAJIN is largely insoluble in the absence of TERB2, indicating that their complexation is likely constitutive.

We therefore have two complexes capable of mediating association with telomeric DNA. It appears that DNA binding by both complexes is not mutually exclusive with TRF1-association resulting in the super-shift of MAJIN-TERB2-TERB2:DNA complexes by electrophoretic mobility shift assay (Dunce *et al.*, 2018b). However, the mode of DNA binding which mediate telomeric association may alter upon nuclear envelope recruitment.

4.3.5 The spatial displacement of Shelterin – a consequence of structural rearrangement?

It was demonstrated that TRF1 in association with the other Shelterin complex components undergoes spatial displacement during the zygotene to pachytene transition (Shibuya *et al.*, 2015) (Figure 4.1.12). During zygotene, TRF1 colocalises with MAJIN, TERB2 and TERB1 whilst localising as a ring about MAJIN during pachytene. This was proposed to represent a mechanism of exchange in which TRF1 is dislodged from telomeric DNA and replaced by the meiotic telomere complex. It was found that the association between TRF1 and TERB1 is weakened by a phosphorylation event dependent upon CDK1 (Shibuya *et al.*, 2015; Dunce *et al.*, 2018b). This could suggest that upon nuclear envelope recruitment, cell-cycle controlled phosphorylation events drive the dissociation of TRF1 from the meiotic telomere complex resulting in its displacement. However, from microscopic observations, it appears more likely that TRF1 is merely spatially shifted and is in fact retained in association with telomeric DNA. The observation could therefore be explained by the combined effects of dissociating TRF1 upon phosphorylation and steric effects upon DNA binding of the meiotic telomere complex upon nuclear envelope recruitment of the telomeres. We therefore postulate a change in the mode of DNA binding during the zygotene to pachytene transition, as depicted in Figure 4.3.3,4. During zygotene, DNA binding is mediated by the Myb-domains of TRF1 and TERB1 (Figure 4.3.3). During late pachytene, upon CDK1-dependent phosphorylation which results in disruption of the interaction between the meiotic telomere complex and TRF1, DNA is looped over the meiotic telomere complex and TRF1 is displaced to peripheral telomeric with which it remains associated (Figure 4.3.4).

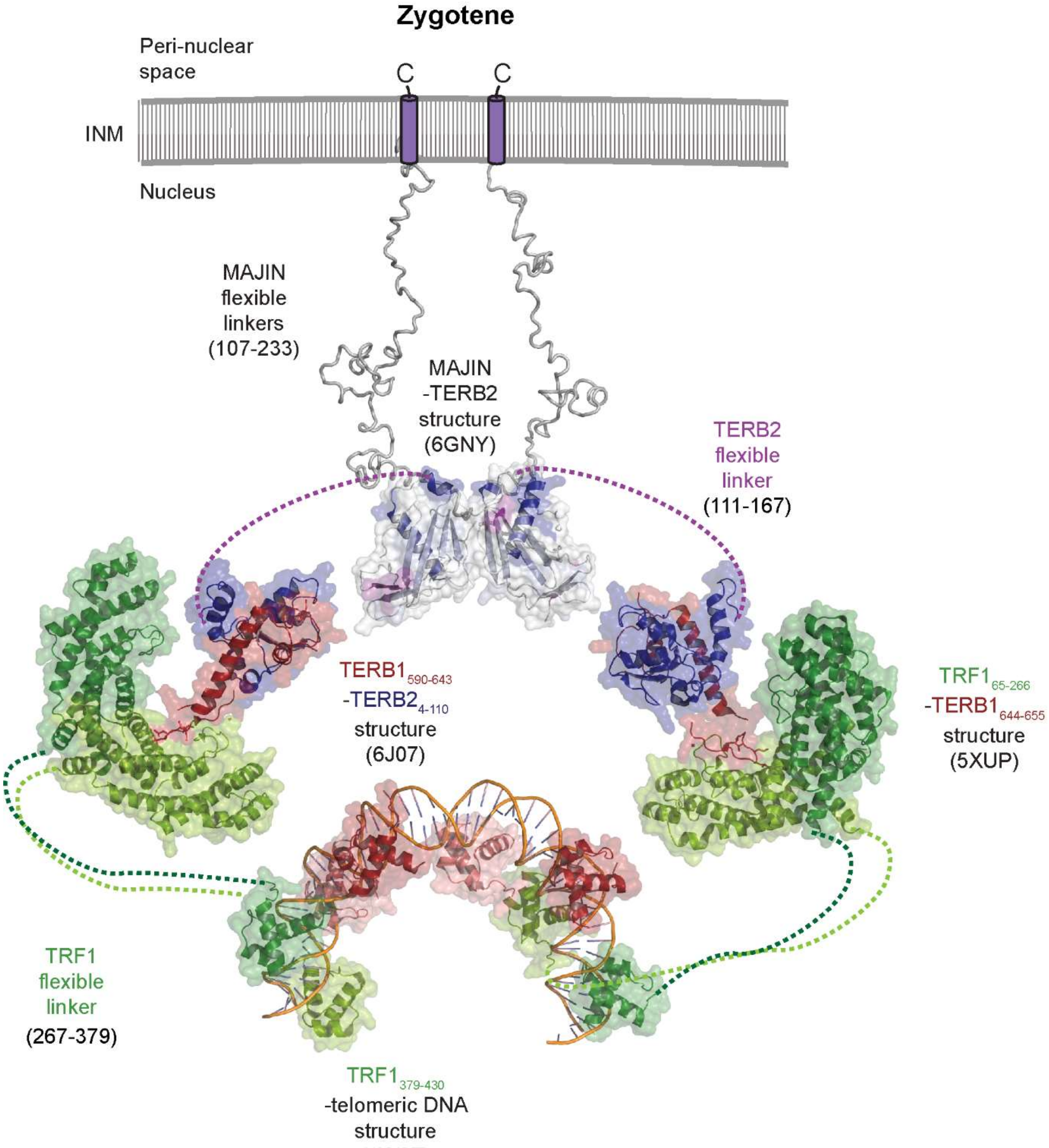
Zygotene
Peri-nuclear space
C
C
INM
Nucleus
MAJIN flexible linkers (107-233)
MAJIN -TERB2 structure (6GNY)
TERB2 flexible linker (111-167)
TERB1 590-643 -TERB2 4-110 structure (6J07)
TRF1 65-266 -TERB1 644-655 structure (5XUP)
TRF1 flexible linker (267-379)
TRF1 379-430 -telomeric DNA structure (1W0T)

Figure 4.3.3| The telomere bound structure of the meiotic telomere complex during zygotene. DNA association is mediated through the Myb-domains of TRF1 and TERB1 during zygotene. The telomeric ends are recruited to the meiotic telomere complex through interactions of TERB1 with TRF1.

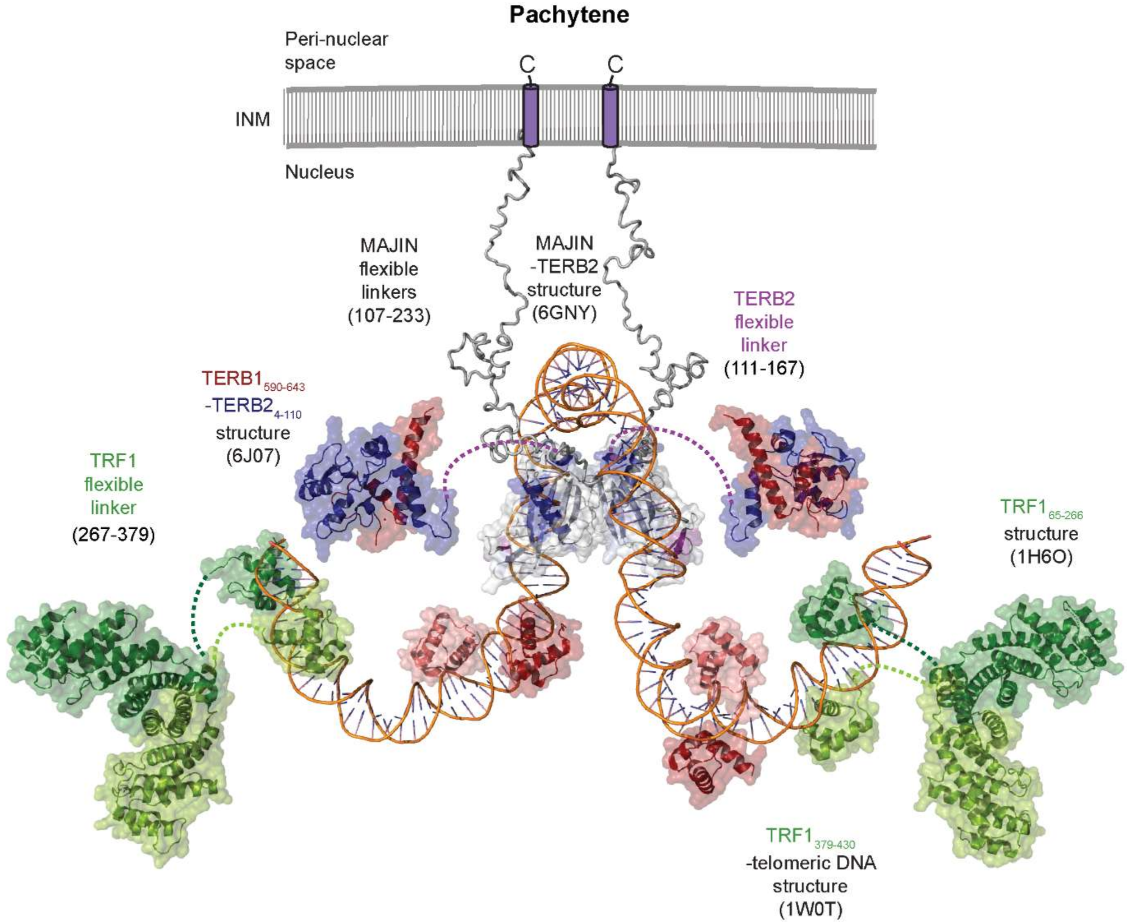
Pachytene
Peri-nuclear space
INM
Nucleus
C
C
MAJIN flexible linkers (107-233)
MAJIN -TERB2 structure (6GNY)
TERB2 flexible linker (111-167)
TERB1 590-643 -TERB2 4-110 structure (6J07)
TRF1 flexible linker (267-379)
TRF1 65-266 structure (1H6O)
TRF1 379-430 -telomeric DNA structure (1W0T)

Figure 4.3.4| The meiotic telomere complex during pachytene. The TRF1-TERB1 interact is disrupted during late-pachytene which allows for its displacement to the telomeric periphery. Telomeric DNA is further associated by the MAJIN-TERB2 complex in a looping fashion, facilitating its inclusion into the nuclear lamina.

Interestingly, the ring-like organisation of Shelterin is similar to the pachytene localisation of TERB2 which also encircles the telomeric MAJIN focus (Figure 4.3.5a,b) (Dunce *et al.*, 2018b). This could suggest a wide-scale rearrangement of telomere associated proteins. A major difference between zygotene and pachytene is the speed of chromosome movements with rapid prophase movements peaking during zygotene and being minimal during pachytene (Lee *et al.*, 2015). During such movements, tension is likely exerted upon the unstructured linker sequences, such as the C-terminal ends of MAJIN and the sequence connecting the N and C-termini of TERB2. As such, complexes would be linearly stretched in plane with the direction of telomere movement (Figure 4.3.5c). In pachytene, without such strain, complexes could compact and more closely associate with the inner nuclear membrane, potentially causing meiotic telomere components to spread out from the MAJIN central focus (Figure 4.3.5d). If this phenomenon were to exist, we might expect to see a linear distribution of meiotic telomere complex components at the telomere during zygotene. However, the effect would only be visible in live cells as tension would be lost during nuclei preparation. It would be interesting to know how the effects of tension by RPMs and the steric constraints of nuclear membrane adhesion effect the structure of the meiotic telomere complex and how the previous described mechanisms such as TRF1 dissociation and DNA binding contribute. A major challenge for microscopic studies of structural features by fluorescence is found in determining what are real structural changes, taking into account preparation artefacts and the contribution of antibody size and orientation.

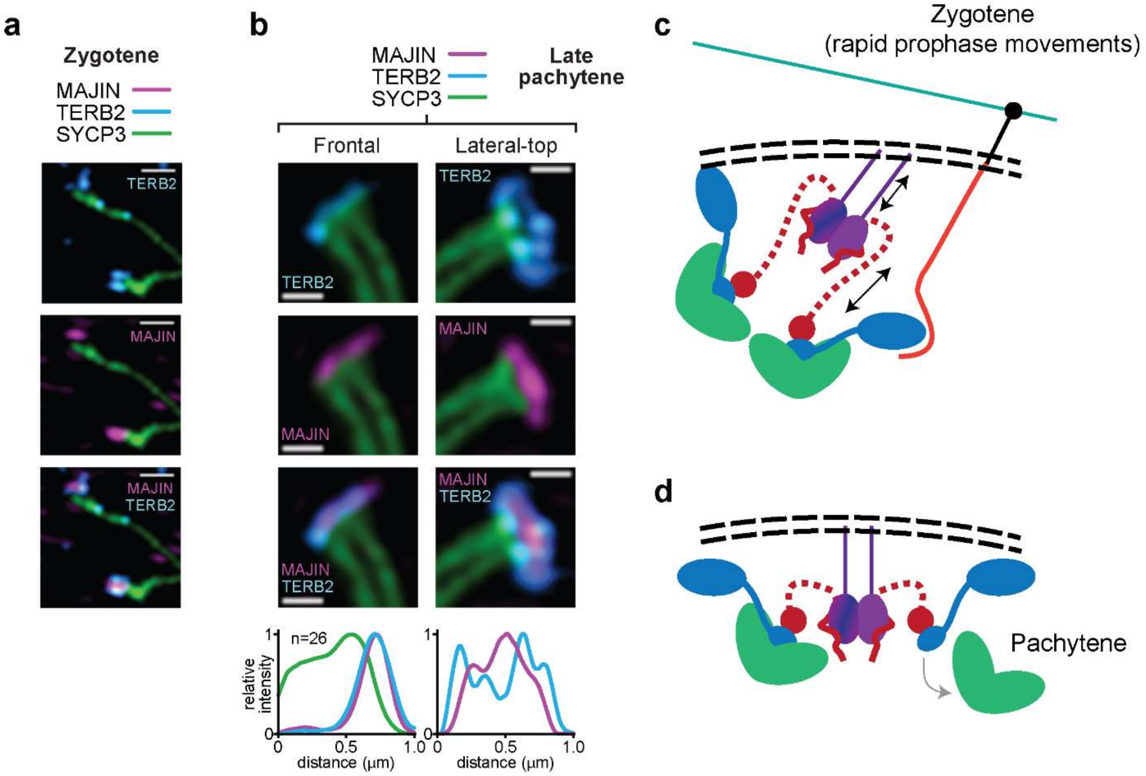
a
Zygotene
MAJIN
TERB2
SYCP3
TERB2
MAJIN
MAJIN
TERB2
b
MAJIN
TERB2
SYCP3
Late pachytene
Frontal
Lateral-top
TERB2
TERB2
MAJIN
MAJIN
MAJIN
TERB2
MAJIN
TERB2
n=26
relative intensity
1
0
0
0.5
1.0
distance (μm)
1
0
0
0.5
1.0
distance (μm)
c
Zygotene
(rapid prophase movements)
d
Pachytene

Figure 4.3.5| Super-resolution fluorescence imaging of telomeric ends to visualise MAJIN-TERB2 localisation. a-b) Antibodies towards SYCP3 (green), TERB2 (cyan) and MAJIN (magenta) were utilised to stain **a)** chromosomes of spread mouse zygotene spermatocytes and **b)** chromosomes of spread mouse pachytene spermatocytes. Scale bars, 0.3 µm. Normalised intensity-distance plots are shown. The frontal plot represents an average of multiple images (n = 26 telomeres). The lateral-top plot represents an individual image. Work presented in this figure was performed by Irene da Cruz of the Ricardo Benavente group, University of Würzburg, Germany. **c)** Schematic to show meiotic telomere complex during zygotene rapid prophase movements. Tensile forces, which cause stretching of unstructured linker sequences, are indicated by double-headed arrows. **d)** During pachytene, rapid prophase movements are minimal allowing linker sequences to adopt unstretched conformations. This may result in spatial displacement of telomeric components about a MAJIN focus which may occur in tandem with TRF1 dissociation (grey arrow).

4.3.6 Higher order assembly to create the telomere attachment plate

In pachytene, nuclear envelope attachment of the synaptonemal complex appears as an electron dense assembly in which the SC fuses with the inner nuclear membrane (Holm and Rasmussen, 1977). This structure is referred to as the telomeric attachment plate. We noted by electron microscopy that MAJIN-TERB2 forms ring-like structures, connected by fine threads, upon incubation with DNA (Figure 4.2.13c) with similar results for the wider MAJIN-TERB2-TERB1 core complex (Dunce *et al.*, 2018b). These may represent forms of higher order assembly which are abolished upon disruption of the MAJIN dimer through mutation of the hydrophobic interface (Figure 4.2.12-13). For recursive assembly, there must be two modes of lateral association between MAJIN-TERB2 complexes. A possible interaction is present within the $P3_221$ MAJIN-TERB2 crystal lattice in which Y202 and K86 contribute to a hydrophobic interface between anti-parallel β-appendages of TERB2 (Figure 4.3.6). This interaction and the MAJIN dimeric interface may provide the molecular basis for recursive assembly of MAJIN-TERB2 molecules on the inner nuclear membrane and provide a plane of DNA associative molecules about which telomeric DNA may be looped and embedded. The cumulative strength of these associations would make for a robust attachment of telomeric DNA to the nuclear envelope, possibly of great importance given the speed at which telomeres are moved about the nuclear envelope (100 nm/s) (Lee *et al.*, 2015). Given our finding that MAJIN-TERB2 is stable as a 1:1 complex (upon disruption of the dimeric interface), a dimeric architecture must be functionally important and the above provides a possible function.

4.3.7 MAJIN-TERB2: the structural basis for meiotic telomere attachment

We have found that the MAJIN-TERB2 core structure provides an architectural basis for the formation of the wider meiotic telomere complex, coordinating, through TERB1, the TRF1 component of the Shelterin complex to mediate telomere recruitment. Further studies to those presented here demonstrated that flexible linkers attach the MAJIN-TERB2 core structure to globular TERB1-TERB2 domains which are mobile with respect to the core. The precise arrangement of the components within the cell, and during different phases of the meiotic cycle, might be determinable through a combination of high-resolution mapping of the complex components, potentially by cryo-electron microscopy and correlative light and electron microscopy. How the proteinaceous complex interfaces with a matrix of looped telomeric DNA is further key to our understanding of how the telomere attachment plate forms a robust attachment to the nuclear envelope. The mechanisms behind the dynamics of this complex through the zygotene to pachytene transition are still poorly understood, as is how this complex integrates with the LINC complex to transmit cytoskeletal force to the telomeric ends. Understanding of the latter will come from further experiments into characterising the SUN1-TERB1 interaction. More key questions within the same vein of scientific interest remain unanswered, such as how does KASH5 associate with cytoskeleton-associated dynein-dynactin complex? The molecular mechanisms of each of these aspects, and many more, are key to developing a complete understanding of how the molecular movers of the meiotic cycle drive chromosome dynamics and facilitate meiotic progression.

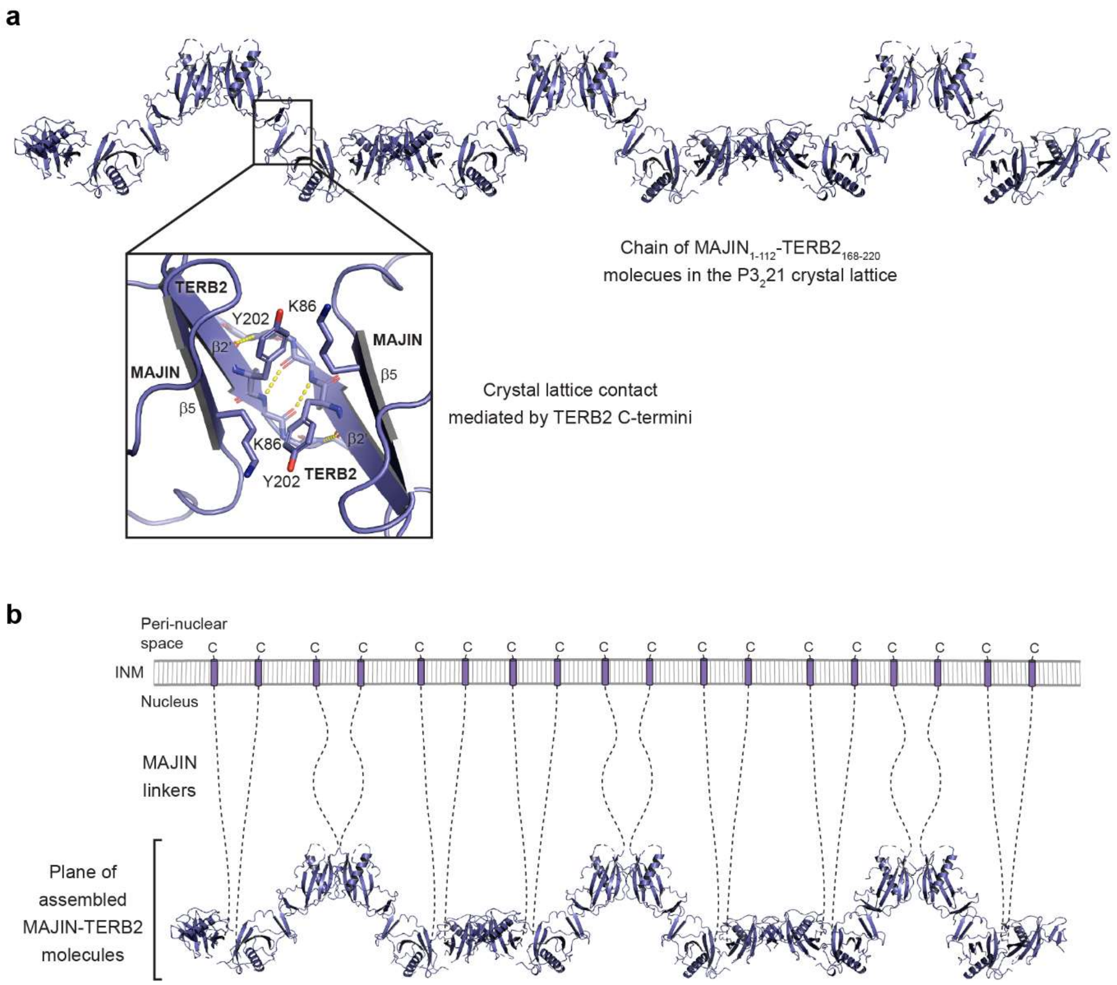
a
Chain of MAJIN1-112-TERB2168-220 molecues in the P3221 crystal lattice
TERB2
Y202
K86
β2
MAJIN
β5
MAJIN
β5
K86
β2
Y202
TERB2
Crystal lattice contact mediated by TERB2 C-termini
b
Peri-nuclear space
C
INM
Nucleus
MAJIN linkers
Plane of assembled MAJIN-TERB2 molecules

Figure 4.3.6| Recursive assembly of MAJIN-TERB2 at the nuclear envelope. a) The $P3_221$ lattice of $MAJIN_{1\text{-}112}$-$TERB2_{168\text{-}220}$ crystals is mediated laterally through anti-parallel associations of the β-appendage in which residues Y202 and K86 contribute to a hydrophobic interface. **b)** The dimeric architecture of the MAJIN-TERB2 complex in association with the anti-parallel associations of the β-appendages allows for a planar assembly on the inner nuclear membrane. Figure created by Dr Owen Davies.

Concluding remarks: Towards a molecular understanding of mammalian meiosis

Prior to the past five years, details regarding the mechanisms of synaptonemal complex structure and dynamics lacked atomistic details. Since, much progress has been made with newfound understanding regarding the initial steps in the synapsis of meiotic chromosomes by SYCP1 and the molecular basis for the recruitment of telomeres to the nuclear envelope by the meiotic telomere complex, ensuring robust attachments are in place prior to rapid prophase movements. The essentiality of both of these complexes underpins their importance within the meiotic division. The fact that evolution has moulded such an elaborate, highly orchestrated and finely tuned series of events to achieve reductional cell division, whilst introducing genetic diversity, in a manner which is largely conserved across almost all sexually reproducing organisms, truly suggests that the meiotic cycle, as we visualise it today, is close to, if not already, the most effective and efficient mechanism for doing so possible. This makes the pursuit of studying the machines and their components which drive this process, and the regulators which control them, of great interest. Although we do not understand all the hows and whys, and never will, it is humbling to know that we are studying something that is truly optimised and could not likely be improved through human intervention.

Publications resulting from this work

Dunce, J.M., Dunne, O.M., Ratcliff, M., Millan, C., Madgwick, S., Uson, I. and Davies, O.R. (2018a) 'Structural basis of meiotic chromosome synapsis through SYCP1 self-assembly', *Nat Struct Mol Biol*, 25(7), pp. 557-569.

Dunce, J.M.*, Milburn, A.E.*, Gurusaran, M.*, da Cruz, I.*, Sen, L.T., Benavente, R. and Davies, O.R. (2018b) 'Structural basis of meiotic telomere attachment to the nuclear envelope by MAJIN-TERB2-TERB1', *Nat Commun*, 9(1), p. 5355.

* These authors contributed equally to this work.

REFERENCES

Adams, P.D., Afonine, P.V., Bunkoczi, G., Chen, V.B., Davis, I.W., Echols, N., Headd, J.J., Hung, L.W., Kapral, G.J., Grosse-Kunstleve, R.W., McCoy, A.J., Moriarty, N.W., Oeffner, R., Read, R.J., Richardson, D.C., Richardson, J.S., Terwilliger, T.C. and Zwart, P.H. (2010) 'PHENIX: a comprehensive Python-based system for macromolecular structure solution', *Acta Crystallogr D Biol Crystallogr*, 66(Pt 2), pp. 213-21.

Agarwal, S. and Roeder, G.S. (2000) 'Zip3 provides a link between recombination enzymes and synaptonemal complex proteins', *Cell*, 102(2), pp. 245-55.

Agostinho, A. and Hoog, C. (2016) 'REC8 density along chromosomes prevents illegitimate synapsis', *Cell Cycle*, 15(19), pp. 2543-2544.

Agostinho, A., Kouznetsova, A., Hernandez-Hernandez, A., Bernhem, K., Blom, H., Brismar, H. and Hoog, C. (2018) 'Sexual dimorphism in the width of the mouse synaptonemal complex', *J Cell Sci*, 131(5).

Agostinho, A., Manneberg, O., van Schendel, R., Hernandez-Hernandez, A., Kouznetsova, A., Blom, H., Brismar, H. and Hoog, C. (2016) 'High density of REC8 constrains sister chromatid axes and prevents illegitimate synaptonemal complex formation', *EMBO Rep*, 17(6), pp. 901-13.

Ali, S.H. and DeCaprio, J.A. (2001) 'Cellular transformation by SV40 large T antigen: interaction with host proteins', *Semin Cancer Biol*, 11(1), pp. 15-23.

Allen, J.W., Dix, D.J., Collins, B.W., Merrick, B.A., He, C., Selkirk, J.K., Poorman-Allen, P., Dresser, M.E. and Eddy, E.M. (1996) 'HSP70-2 is part of the synaptonemal complex in mouse and hamster spermatocytes', *Chromosoma*, 104(6), pp. 414-21.

Anderson, L.K., Doyle, G.G., Brigham, B., Carter, J., Hooker, K.D., Lai, A., Rice, M. and Stack, S.M. (2003) 'High-resolution crossover maps for each bivalent of Zea mays using recombination nodules', *Genetics*, 165(2), pp. 849-65.

Anderson, L.K., Royer, S.M., Page, S.L., McKim, K.S., Lai, A., Lilly, M.A. and Hawley, R.S. (2005) 'Juxtaposition of C(2)M and the transverse filament protein C(3)G within the central region of Drosophila synaptonemal complex', *Proc Natl Acad Sci U S A*, 102(12), pp. 4482-7.

Armstrong, S.J., Franklin, F.C. and Jones, G.H. (2001) 'Nucleolus-associated telomere clustering and pairing precede meiotic chromosome synapsis in Arabidopsis thaliana', *J Cell Sci*, 114(Pt 23), pp. 4207-17.

Aruffo, A. (2001) 'Transient expression of proteins using COS cells', *Curr Protoc Neurosci*, Chapter 4, p. Unit 4.7.

Ashkenazy, H., Abadi, S., Martz, E., Chay, O., Mayrose, I., Pupko, T. and Ben-Tal, N. (2016) 'ConSurf 2016: an improved methodology to estimate and visualize evolutionary conservation in macromolecules', *Nucleic Acids Res*, 44(W1), pp. W344-50.

Bahler, J., Wyler, T., Loidl, J. and Kohli, J. (1993) 'Unusual nuclear structures in meiotic prophase of fission yeast: a cytological analysis', *J Cell Biol*, 121(2), pp. 241-56.

Barlow, A.L., Benson, F.E., West, S.C. and Hulten, M.A. (1997) 'Distribution of the Rad51 recombinase in human and mouse spermatocytes', *Embo j*, 16(17), pp. 5207-15.

Baudat, F., Buard, J., Grey, C., Fledel-Alon, A., Ober, C., Przeworski, M., Coop, G. and de Massy, B. (2010) 'PRDM9 is a major determinant of meiotic recombination hotspots in humans and mice', *Science*, 327(5967), pp. 836-40.

Baudat, F. and de Massy, B. (2007) 'Regulating double-stranded DNA break repair towards crossover or non-crossover during mammalian meiosis', *Chromosome Res*, 15(5), pp. 565-77.

Baudat, F., Manova, K., Yuen, J.P., Jasin, M. and Keeney, S. (2000) 'Chromosome synapsis defects and sexually dimorphic meiotic progression in mice lacking Spo11', *Mol Cell*, 6(5), pp. 989-98.

Baumann, P. and West, S.C. (1998) 'Role of the human RAD51 protein in homologous recombination and double-stranded-break repair', *Trends Biochem Sci*, 23(7), pp. 247-51.

Bellani, M.A., Boateng, K.A., McLeod, D. and Camerini-Otero, R.D. (2010) 'The expression profile of the major mouse SPO11 isoforms indicates that SPO11beta introduces double strand breaks and suggests that SPO11alpha has an additional role in prophase in both spermatocytes and oocytes', *Mol Cell Biol*, 30(18), pp. 4391-403.

Berezin, C., Glaser, F., Rosenberg, J., Paz, I., Pupko, T., Fariselli, P., Casadio, R. and Ben-Tal, N. (2004) 'ConSeq: the identification of functionally and structurally important residues in protein sequences', *Bioinformatics*, 20(8), pp. 1322-4.

Bhalla, N. and Dernburg, A.F. (2008) 'Prelude to a division', *Annu Rev Cell Dev Biol*, 24, pp. 397-424.

Bibby, J., Keegan, R.M., Mayans, O., Winn, M.D. and Rigden, D.J. (2012) 'AMPLE: a cluster-and-truncate approach to solve the crystal structures of small proteins using rapidly computed ab initio models', *Acta Crystallogr D Biol Crystallogr*, 68(Pt 12), pp. 1622-31.

Bishop, A.J. and Schiestl, R.H. (2002) 'Homologous Recombination and Its Role in Carcinogenesis', *J Biomed Biotechnol*, 2(2), pp. 75-85.

Bishop, D.K. (1994) 'RecA homologs Dmc1 and Rad51 interact to form multiple nuclear complexes prior to meiotic chromosome synapsis', *Cell*, 79(6), pp. 1081-92.

Bishop, D.K. and Zickler, D. (2004) 'Early decision; meiotic crossover interference prior to stable strand exchange and synapsis', *Cell*, 117(1), pp. 9-15.

Bisig, C.G., Guiraldelli, M.F., Kouznetsova, A., Scherthan, H., Hoog, C., Dawson, D.S. and Pezza, R.J. (2012) 'Synaptonemal complex components persist at centromeres and are required for homologous centromere pairing in mouse spermatocytes', *PLoS Genet*, 8(6), p. e1002701.

Biswas, U., Hempel, K., Llano, E., Pendas, A. and Jessberger, R. (2016) 'Distinct Roles of Meiosis-Specific Cohesin Complexes in Mammalian Spermatogenesis', *PLoS Genet*, 12(10), p. e1006389.

Blat, Y., Protacio, R.U., Hunter, N. and Kleckner, N. (2002) 'Physical and functional interactions among basic chromosome organizational features govern early steps of meiotic chiasma formation', *Cell*, 111(6), pp. 791-802.

Boateng, K.A., Bellani, M.A., Gregoretti, I.V., Pratto, F. and Camerini-Otero, R.D. (2013) 'Homologous pairing preceding SPO11-mediated double-strand breaks in mice', *Dev Cell*, 24(2), pp. 196-205.

Bolcun-Filas, E., Costa, Y., Speed, R., Taggart, M., Benavente, R., De Rooij, D.G. and Cooke, H.J. (2007) 'SYCE2 is required for synaptonemal complex assembly, double strand break repair, and homologous recombination', *J Cell Biol*, 176(6), pp. 741-7.

Bolcun-Filas, E., Hall, E., Speed, R., Taggart, M., Grey, C., de Massy, B., Benavente, R. and Cooke, H.J. (2009) 'Mutation of the mouse Syce1 gene disrupts synapsis and suggests a link between synaptonemal complex structural components and DNA repair', *PLoS Genet*, 5(2), p. e1000393.

Bolor, H., Mori, T., Nishiyama, S., Ito, Y., Hosoba, E., Inagaki, H., Kogo, H., Ohye, T., Tsutsumi, M., Kato, T., Tong, M., Nishizawa, H., Pryor-Koishi, K., Kitaoka, E., Sawada, T., Nishiyama, Y., Udagawa, Y. and Kurahashi, H. (2009) 'Mutations of the SYCP3 Gene in Women with Recurrent Pregnancy Loss', in *Am J Hum Genet*. pp. 14-20.

Branstetter, M.G., Childers, A.K., Cox-Foster, D., Hopper, K.R., Kapheim, K.M., Toth, A.L. and Worley, K.C. (2018) 'Genomes of the Hymenoptera', *Curr Opin Insect Sci*, 25, pp. 65-75.

Brouwer, I., Moschetti, T., Candelli, A., Garcin, E.B., Modesti, M., Pellegrini, L., Wuite, G.J. and Peterman, E.J. (2018) 'Two distinct conformational states define the interaction of human RAD51-ATP with single-stranded DNA', *Embo j*, 37(7).

Bugreev, D.V., Pezza, R.J., Mazina, O.M., Voloshin, O.N., Camerini-Otero, R.D. and Mazin, A.V. (2011) 'The resistance of DMC1 D-loops to dissociation may account for the DMC1 requirement in meiosis', *Nat Struct Mol Biol*, 18(1), pp. 56-60.

Caballero, I., Sammito, M., Millán, C., Lebedev, A., Soler, N., Usón, I. (2017) 'ARCIMBOLDO on Coiled Coils', *Acta Crystallogr D Biol Crystallogr*, In Press

Cahoon, C.K. and Hawley, R.S. (2016) 'Regulating the construction and demolition of the synaptonemal complex', *Nat Struct Mol Biol*, 23(5), pp. 369-77.

Cahoon, C.K., Yu, Z., Wang, Y., Guo, F., Unruh, J.R., Slaughter, B.D. and Hawley, R.S. (2017) 'Superresolution expansion microscopy reveals the three-dimensional organization of the Drosophila synaptonemal complex', *Proc Natl Acad Sci U S A*, 114(33), pp. E6857-e6866.

Cain, N.E. and Starr, D.A. (2015) 'SUN proteins and nuclear envelope spacing', in *Nucleus*. pp. 2-7.

Carofiglio, F., Sleddens-Linkels, E., Wassenaar, E., Inagaki, A., van Cappellen, W.A., Grootegoed, J.A., Toth, A. and Baarends, W.M. (2018) 'Repair of exogenous DNA double-strand breaks promotes chromosome synapsis in SPO11-mutant mouse meiocytes, and is altered in the absence of HORMAD1', *DNA Repair (Amst)*, 63, pp. 25-38.

Cha, R.S., Weiner, B.M., Keeney, S., Dekker, J. and Kleckner, N. (2000) 'Progression of meiotic DNA replication is modulated by interchromosomal interaction proteins, negatively by Spo11p and positively by Rec8p', *Genes Dev*, 14(4), pp. 493-503.

Chen, V.B., Arendall, W.B., Headd, J.J., Keedy, D.A., Immormino, R.M., Kapral, G.J., Murray, L.W., Richardson, J.S. and Richardson, D.C. (2010) 'MolProbity: all-atom structure validation for macromolecular crystallography', *Acta Crystallographica Section D-Biological Crystallography*, 66, pp. 12-21.

Chen, Y., Yang, Y., van Overbeek, M., Donigian, J.R., Baciu, P., de Lange, T. and Lei, M. (2008) 'A shared docking motif in TRF1 and TRF2 used for differential recruitment of telomeric proteins', *Science*, 319(5866), pp. 1092-6.

Chesnoy, S. and Huang, L. (2000) 'Structure and function of lipid-DNA complexes for gene delivery', *Annu Rev Biophys Biomol Struct*, 29, pp. 27-47.

Chikashige, Y., Ding, D.Q., Funabiki, H., Haraguchi, T., Mashiko, S., Yanagida, M. and Hiraoka, Y. (1994) 'Telomere-led premeiotic chromosome movement in fission yeast', *Science*, 264(5156), pp. 270-3.

Chikashige, Y., Haraguchi, T. and Hiraoka, Y. (2007) 'Another way to move chromosomes', *Chromosoma*, 116(6), pp. 497-505.

Chikashige, Y., Tsutsumi, C., Yamane, M., Okamasa, K., Haraguchi, T. and Hiraoka, Y. (2006) 'Meiotic proteins bqt1 and bqt2 tether telomeres to form the bouquet arrangement of chromosomes', *Cell*, 125(1), pp. 59-69.

Christophorou, N., Rubin, T. and Huynh, J.R. (2013) 'Synaptonemal complex components promote centromere pairing in pre-meiotic germ cells', *PLoS Genet*, 9(12), p. e1004012.

Colaiacovo, M.P., MacQueen, A.J., Martinez-Perez, E., McDonald, K., Adamo, A., La Volpe, A. and Villeneuve, A.M. (2003) 'Synaptonemal complex assembly in C. elegans is dispensable for loading strand-exchange proteins but critical for proper completion of recombination', *Dev Cell*, 5(3), pp. 463-74.

Comings, D.E. and Okada, T.A. (1971) 'Fine structure of the synaptonemal complex. Regular and stereo electron microscopy of deoxyribonuclease-treated whole mount preparations', *Exp Cell Res*, 65(1), pp. 104-16.

Conrad, M.N., Lee, C.Y., Wilkerson, J.L. and Dresser, M.E. (2007) 'MPS3 mediates meiotic bouquet formation in Saccharomyces cerevisiae', *Proc Natl Acad Sci U S A*, 104(21), pp. 8863-8.

Costa, Y., Speed, R., Ollinger, R., Alsheimer, M., Semple, C.A., Gautier, P., Maratou, K., Novak, I., Hoog, C., Benavente, R. and Cooke, H.J. (2005) 'Two novel proteins recruited by synaptonemal complex protein 1 (SYCP1) are at the centre of meiosis', *J Cell Sci*, 118(Pt 12), pp. 2755-62.

Crick, F.H.C. (1952) 'Is α-Keratin a Coiled Coil?', *Nature*, 170(4334), pp. 882-883.

Crisp, M., Liu, Q., Roux, K., Rattner, J.B., Shanahan, C., Burke, B., Stahl, P.D. and Hodzic, D. (2006) 'Coupling of the nucleus and cytoplasm: role of the LINC complex', *J Cell Biol*, 172(1), pp. 41-53.

Daniel, K., Trankner, D., Wojtasz, L., Shibuya, H., Watanabe, Y., Alsheimer, M. and Toth, A. (2014) 'Mouse CCDC79 (TERB1) is a meiosis-specific telomere associated protein', *BMC Cell Biol*, 15, p. 17.

Das, U., Hariprasad, G., Ethayathulla, A.S., Manral, P., Das, T.K., Pasha, S., Mann, A., Ganguli, M., Verma, A.K., Bhat, R., Chandrayan, S.K., Ahmed, S., Sharma, S., Kaur, P., Singh, T.P. and Srinivasan, A. (2007) 'Inhibition of protein aggregation: supramolecular assemblies of arginine hold the key', *PLoS One*, 2(11), p. e1176.

Davies, O.R., Forment, J.V., Sun, M., Belotserkovskaya, R., Coates, J., Galanty, Y., Demir, M., Morton, C.R., Rzechorzek, N.J., Jackson, S.P. and Pellegrini, L. (2015) 'CtIP tetramer assembly is required for DNA-end resection and repair', *Nat Struct Mol Biol*, 22(2), pp. 150-157.

Davies, O.R., Maman, J.D. and Pellegrini, L. (2012) 'Structural analysis of the human SYCE2-TEX12 complex provides molecular insights into synaptonemal complex assembly', *Open Biol*, 2(7), p. 120099.

Davies, O.R. and Pellegrini, L. (2007) 'Interaction with the BRCA2 C terminus protects RAD51-DNA filaments from disassembly by BRC repeats', *Nat Struct Mol Biol*, 14(6), pp. 475-83.

de Lange, T. (2009) 'How telomeres solve the end-protection problem', *Science*, 326(5955), pp. 948-52.

De Magistris, P. and Antonin, W. (2018) 'The Dynamic Nature of the Nuclear Envelope', *Curr Biol*, 28(8), pp. R487-r497.

De Muyt, A., Zhang, L., Piolot, T., Kleckner, N., Espagne, E. and Zickler, D. (2014) 'E3 ligase Hei10: a multifaceted structure-based signaling molecule with roles within and beyond meiosis', *Genes Dev*, 28(10), pp. 1111-23.

de Vries, F.A., de Boer, E., van den Bosch, M., Baarends, W.M., Ooms, M., Yuan, L., Liu, J.G., van Zeeland, A.A., Heyting, C. and Pastink, A. (2005) 'Mouse Sycp1 functions in synaptonemal complex assembly, meiotic recombination, and XY body formation', *Genes Dev*, 19(11), pp. 1376-89.

Diederichs, K., McSweeney, S. and Ravelli, R.B. (2003) 'Zero-dose extrapolation as part of macromolecular synchrotron data reduction', *Acta Crystallogr D Biol Crystallogr*, 59(Pt 5), pp. 903-9.

Ding, D.Q., Haraguchi, T. and Hiraoka, Y. (2013) 'The role of chromosomal retention of noncoding RNA in meiosis', *Chromosome Res*, 21(6-7), pp. 665-72.

Ding, R., West, R.R., Morphew, D.M., Oakley, B.R. and McIntosh, J.R. (1997) 'The spindle pole body of Schizosaccharomyces pombe enters and leaves the nuclear envelope as the cell cycle proceeds', *Mol Biol Cell*, 8(8), pp. 1461-79.

Dix, D.J., Allen, J.W., Collins, B.W., Poorman-Allen, P., Mori, C., Blizard, D.R., Brown, P.R., Goulding, E.H., Strong, B.D. and Eddy, E.M. (1997) 'HSP70-2 is required for desynapsis of synaptonemal complexes during meiotic prophase in juvenile and adult mouse spermatocytes', *Development*, 124(22), pp. 4595-603.

Dobson, M.J., Pearlman, R.E., Karaiskakis, A., Spyropoulos, B. and Moens, P.B. (1994) 'Synaptonemal complex proteins: occurrence, epitope mapping and chromosome disjunction', *J Cell Sci*, 107 (Pt 10), pp. 2749-60.

Dong, H. and Roeder, G.S. (2000) 'Organization of the yeast Zip1 protein within the central region of the synaptonemal complex', *J Cell Biol*, 148(3), pp. 417-26.

Drozdetskiy, A., Cole, C., Procter, J. and Barton, G.J. (2015) 'JPred4: a protein secondary structure prediction server', *Nucleic Acids Res*, 43(W1), pp. W389-94.

Du, L. and Luo, Y. (2013) 'Structure of a filament of stacked octamers of human DMC1 recombinase', *Acta Crystallogr Sect F Struct Biol Cryst Commun*, 69(Pt 4), pp. 382-6.

Dunce, J.M., Dunne, O.M., Ratcliff, M., Millan, C., Madgwick, S., Uson, I. and Davies, O.R. (2018a) 'Structural basis of meiotic chromosome synapsis through SYCP1 self-assembly', *Nat Struct Mol Biol*, 25(7), pp. 557-569.

Dunce, J.M., Milburn, A.E., Gurusaran, M., da Cruz, I., Sen, L.T., Benavente, R. and Davies, O.R. (2018b) 'Structural basis of meiotic telomere attachment to the nuclear envelope by MAJIN-TERB2-TERB1', *Nat Commun*, 9(1), p. 5355.

Dunlop, M.H., Dray, E., Zhao, W., Tsai, M.S., Wiese, C., Schild, D. and Sung, P. (2011) 'RAD51-associated protein 1 (RAD51AP1) interacts with the meiotic recombinase DMC1 through a conserved motif', *J Biol Chem*, 286(43), pp. 37328-34.

Dunne, O.M. and Davies, O.R. (2019a) 'A molecular model for self-assembly of the synaptonemal complex protein SYCE3', *J Biol Chem*.

Dunne, O.M. and Davies, O.R. (2019b) 'Molecular structure of human synaptonemal complex protein SYCE1', *Chromosoma*.

Egel-Mitani, M., OLSON, L.W. and EGEL, R. (1982) 'Meiosis in Aspergillus nidulans: Another example for lacking synaptonemal complexes in the absence of crossover interference', 97(2), pp. 179-187.

Eijpe, M., Heyting, C., Gross, B. and Jessberger, R. (2000) 'Association of mammalian SMC1 and SMC3 proteins with meiotic chromosomes and synaptonemal complexes', *J Cell Sci*, 113 (Pt 4), pp. 673-82.

Emsley, P., Lohkamp, B., Scott, W.G. and Cowtan, K. (2010) 'Features and development of Coot', *Acta Crystallogr D Biol Crystallogr*, 66(Pt 4), pp. 486-501.

Evans, P.R. (2011) 'An introduction to data reduction: space-group determination, scaling and intensity statistics', *Acta Crystallogr D Biol Crystallogr*, 67(Pt 4), pp. 282-92.

Evans, P.R. and Murshudov, G.N. (2013) 'How good are my data and what is the resolution?', *Acta Crystallogr D Biol Crystallogr*, 69(Pt 7), pp. 1204-14.

Fairall, L., Chapman, L., Moss, H., de Lange, T. and Rhodes, D. (2001) 'Structure of the TRFH dimerization domain of the human telomeric proteins TRF1 and TRF2', *Mol Cell*, 8(2), pp. 351-61.

Fang, M. and Huang, H.L. (2001) '[Advances in in vitro refolding of inclusion body proteins]', *Sheng Wu Gong Cheng Xue Bao*, 17(6), pp. 608-12.

Fawcett, D.W. (1966) 'On the occurrence of a fibrous lamina on the inner aspect of the nuclear envelope in certain cells of vertebrates', *Am J Anat*, 119(1), pp. 129-45.

Feng, J., Fu, S., Cao, X., Wu, H., Lu, J., Zeng, M., Liu, L., Yang, X. and Shen, Y. (2017) 'Synaptonemal complex protein 2 (SYCP2) mediates the association of the centromere with the synaptonemal complex', *Protein Cell*, 8(7), pp. 538-543.

Forsburg, S.L. (2002) 'Only connect: linking meiotic DNA replication to chromosome dynamics', *Mol Cell*, 9(4), pp. 703-11.

Fraune, J., Alsheimer, M., Volff, J.N., Busch, K., Fraune, S., Bosch, T.C. and Benavente, R. (2012) 'Hydra meiosis reveals unexpected conservation of structural synaptonemal complex proteins across metazoans', *Proc Natl Acad Sci U S A*, 109(41), pp. 16588-93.

Fraune, J., Wiesner, M. and Benavente, R. (2014) 'The synaptonemal complex of basal metazoan hydra: more similarities to vertebrate than invertebrate meiosis model organisms', *J Genet Genomics*, 41(3), pp. 107-15.

Fu, J., Hagan, I.M. and Glover, D.M. (2015) 'The centrosome and its duplication cycle', *Cold Spring Harb Perspect Biol*, 7(2), p. a015800.

Garcia-Saez, I., Menoni, H., Boopathi, R., Shukla, M.S., Soueidan, L., Noirclerc-Savoye, M., Le Roy, A., Skoufias, D.A., Bednar, J., Hamiche, A., Angelov, D., Petosa, C. and Dimitrov, S. (2018) 'Structure of an H1-Bound 6-Nucleosome Array Reveals an Untwisted Two-Start Chromatin Fiber Conformation', *Mol Cell*.

Gerace, L. and Huber, M.D. (2012) 'Nuclear lamina at the crossroads of the cytoplasm and nucleus', *J Struct Biol*, 177(1), pp. 24-31.

Gladstone, M.N., Obeso, D., Chuong, H. and Dawson, D.S. (2009) 'The synaptonemal complex protein Zip1 promotes bi-orientation of centromeres at meiosis I', *PLoS Genet*, 5(12), p. e1000771.

Gladyshev, E. and Kleckner, N. (2014) 'Direct recognition of homology between double helices of DNA in Neurospora crassa', *Nat Commun*, 5, p. 3509.

Goldberg, M.W. (2017) 'Nuclear pore complex tethers to the cytoskeleton', *Semin Cell Dev Biol*, 68, pp. 52-58.

Goldberg, M.W. and Allen, T.D. (1996) 'The nuclear pore complex and lamina: three-dimensional structures and interactions determined by field emission in-lens scanning electron microscopy', *J Mol Biol*, 257(4), pp. 848-65.

Goldstein, P. (1987) 'Multiple synaptonemal complexes (polycomplexes): origin, structure and function', *Cell Biol Int Rep*, 11(11), pp. 759-96.

Goloborodko, A., Imakaev, M.V., Marko, J.F. and Mirny, L. (2016) 'Compaction and segregation of sister chromatids via active loop extrusion', *Elife*, 5.

Gomez, H.L., Felipe-Medina, N., Sanchez-Martin, M., Davies, O.R., Ramos, I., Garcia-Tunon, I., de Rooij, D.G., Dereli, I., Toth, A., Barbero, J.L., Benavente, R., Llano, E. and Pendas, A.M. (2016) 'C14ORF39/SIX6OS1 is a constituent of the synaptonemal complex and is essential for mouse fertility', *Nat Commun*, 7, p. 13298.

Greenfield, N. and Fasman, G.D. (1969) 'Computed circular dichroism spectra for the evaluation of protein conformation', *Biochemistry*, 8(10), pp. 4108-16.

Guinier, A.a.F., G. (1956) 'Small angle scattering of X-rays. A. Guinier and G. Fournet. Translated by C. B. Wilson and with a bibliographical appendix by K. L. Yudowitch. Wiley, New York, 1955. 268 pp. $7.50', 19(93), pp. 594-594.

Gurusaran, M., Shankar, M., Nagarajan, R., Helliwell, J.R. and Sekar, K. (2014) 'Do we see what we should see? Describing non-covalent interactions in protein structures including precision', *IUCrJ*, 1(Pt 1), pp. 74-81.

Gurusaran, M., Sivaranjan, P., Dinesh Kumar, K.S., Radha, P., Thulaa Tharshan, K.P.S., Satheesh, S.N., Jayanthan, K., Ilaiyaraja, R., Mohanapriya, J., Michael, D. and Sekar, K. (2016) 'Hydrogen Bonds Computing Server (HBCS): an online web server to compute hydrogen-bond interactions and their precision', *Journal of Applied Crystallography*, 49(2), pp. 642-645.

Hamer, G., Gell, K., Kouznetsova, A., Novak, I., Benavente, R. and Hoog, C. (2006) 'Characterization of a novel meiosis-specific protein within the central element of the synaptonemal complex', *J Cell Sci*, 119(Pt 19), pp. 4025-32.

Hamer, G., Wang, H., Bolcun-Filas, E., Cooke, H.J., Benavente, R. and Hoog, C. (2008) 'Progression of meiotic recombination requires structural maturation of the central element of the synaptonemal complex', *J Cell Sci*, 121(Pt 15), pp. 2445-51.

Hanaoka, S., Nagadoi, A. and Nishimura, Y. (2005) 'Comparison between TRF2 and TRF1 of their telomeric DNA-bound structures and DNA-binding activities', *Protein Sci*, 14(1), pp. 119-30.

Hanlon, S., Wong, L. and Pack, G.R. (1997) 'Proton equilibria in the minor groove of DNA', *Biophys J*, 72(1), pp. 291-300.

Haque, F., Lloyd, D.J., Smallwood, D.T., Dent, C.L., Shanahan, C.M., Fry, A.M., Trembath, R.C. and Shackleton, S. (2006) 'SUN1 interacts with nuclear lamin A and cytoplasmic nesprins to provide a physical connection between the nuclear lamina and the cytoskeleton', *Mol Cell Biol*, 26(10), pp. 3738-51.

Harding, S.E. and Jumel, K. (1998) 'Light Scattering', *Current Protocols in Protein Science*.

Hassold, T. and Hunt, P. (2001) 'To err (meiotically) is human: the genesis of human aneuploidy', *Nat Rev Genet*, 2(4), pp. 280-91.

Hawley, R.S. (2011) 'Solving a meiotic LEGO puzzle: transverse filaments and the assembly of the synaptonemal complex in Caenorhabditis elegans', *Genetics*, 189(2), pp. 405-9.

Hernandez-Hernandez, A., Masich, S., Fukuda, T., Kouznetsova, A., Sandin, S., Daneholt, B. and Hoog, C. (2016) 'The central element of the synaptonemal complex in mice is organized as a bilayered junction structure', *J Cell Sci*, 129(11), pp. 2239-49.

Hillers, K.J. and Villeneuve, A.M. (2003) 'Chromosome-wide control of meiotic crossing over in C. elegans', *Curr Biol*, 13(18), pp. 1641-7.

Hirko, A., Tang, F. and Hughes, J.A. (2003) 'Cationic lipid vectors for plasmid DNA delivery', *Curr Med Chem*, 10(14), pp. 1185-93.

Hoelz, A., Debler, E.W. and Blobel, G. (2011) 'The structure of the nuclear pore complex', *Annu Rev Biochem*, 80, pp. 613-43.

Holloway, J.K., Sun, X., Yokoo, R., Villeneuve, A.M. and Cohen, P.E. (2014) 'Mammalian CNTD1 is critical for meiotic crossover maturation and deselection of excess precrossover sites', *J Cell Biol*, 205(5), pp. 633-41.

Holm, P.B. and Rasmussen, S.W.J.C.R.C. (1977) 'Human meiosis I. The human pachytene karyotype analyzed by three dimensional reconstruction of the synaptonemal complex', 42(4), p. 283.

Horn, H.F., Kim, D.I., Wright, G.D., Wong, E.S., Stewart, C.L., Burke, B. and Roux, K.J. (2013) 'A mammalian KASH domain protein coupling meiotic chromosomes to the cytoskeleton', *J Cell Biol*, 202(7), pp. 1023-39.

Hughes, S.E., Hemenway, E., Guo, F., Yi, K., Yu, Z. and Hawley, R.S. (2019) 'The E3 ubiquitin ligase Sina regulates the assembly and disassembly of the synaptonemal complex in Drosophila females', *PLoS Genet*, 15(5), p. e1008161.

Hunter, N. (2015) 'Meiotic Recombination: The Essence of Heredity', *Cold Spring Harb Perspect Biol*, 7(12).

Hunter, N. and Kleckner, N. (2001) 'The single-end invasion: an asymmetric intermediate at the double-strand break to double-holliday junction transition of meiotic recombination', *Cell*, 106(1), pp. 59-70.

Ishiguro, K., Kim, J., Shibuya, H., Hernandez-Hernandez, A., Suzuki, A., Fukagawa, T., Shioi, G., Kiyonari, H., Li, X.C., Schimenti, J., Hoog, C. and Watanabe, Y. (2014) 'Meiosis-specific cohesin mediates homolog recognition in mouse spermatocytes', *Genes Dev*, 28(6), pp. 594-607.

Ito, M., Kugou, K., Fawcett, J.A., Mura, S., Ikeda, S., Innan, H. and Ohta, K. (2014) 'Meiotic recombination cold spots in chromosomal cohesion sites', *Genes Cells*, 19(5), pp. 359-73.

Iwai, T., Yoshii, A., Yokota, T., Sakai, C., Hori, H., Kanamori, A. and Yamashita, M. (2006) 'Structural components of the synaptonemal complex, SYCP1 and SYCP3, in the medaka fish Oryzias latipes', *Exp Cell Res*, 312(13), pp. 2528-37.

Jacobson, D.R. and Saleh, O.A. (2017) 'Counting the ions surrounding nucleic acids', in *Nucleic Acids Res*. pp. 1596-605.

Jaspersen, S.L. and Winey, M. (2004) 'The budding yeast spindle pole body: structure, duplication, and function', *Annu Rev Cell Dev Biol*, 20, pp. 1-28.

Jeffress, J.K., Page, S.L., Royer, S.K., Belden, E.D., Blumenstiel, J.P., Anderson, L.K. and Hawley, R.S. (2007) 'The formation of the central element of the synaptonemal complex may occur by multiple mechanisms: the roles of the N- and C-terminal domains of the Drosophila C(3)G protein in mediating synapsis and recombination', *Genetics*, 177(4), pp. 2445-56.

Jensen, R.B., Wang, S.C. and Shapiro, L. (2002) 'Dynamic localization of proteins and DNA during a bacterial cell cycle', *Nat Rev Mol Cell Biol*, 3(3), pp. 167-76.

Jones, G.H. and Croft, J.A. (1989) 'Chromosome pairing and chiasma formation in spermatocytes and oocytes of Dendrocoelum lactem (Turbellaria, Tricladida); a cytogenetical and ultrastructural study', *Heredity*, 63(1), pp. 97-106.

Jordan, P.W., Karppinen, J. and Handel, M.A. (2012) 'Polo-like kinase is required for synaptonemal complex disassembly and phosphorylation in mouse spermatocytes', *J Cell Sci*, 125(Pt 21), pp. 5061-72.

Joyce, E.F., Apostolopoulos, N., Beliveau, B.J. and Wu, C.t. (2013) 'Germline Progenitors Escape the Widespread Phenomenon of Homolog Pairing during Drosophila Development', in *PLoS Genet*.

Judis, L., Chan, E.R., Schwartz, S., Seftel, A. and Hassold, T. (2004) 'Meiosis I arrest and azoospermia in an infertile male explained by failure of formation of a component of the synaptonemal complex', *Fertil Steril*, 81(1), pp. 205-9.

Kabsch, W. (2010a) 'Integration, scaling, space-group assignment and post-refinement', *Acta Crystallogr D Biol Crystallogr*, 66(Pt 2), pp. 133-44.

Kabsch, W. (2010b) 'XDS', *Acta Crystallogr D Biol Crystallogr*, 66(Pt 2), pp. 125-32.

Kanoh, J. and Ishikawa, F. (2001) 'spRap1 and spRif1, recruited to telomeres by Taz1, are essential for telomere function in fission yeast', *Curr Biol*, 11(20), pp. 1624-30.

Kantardjieff, K.A. and Rupp, B. (2003) 'Matthews coefficient probabilities: Improved estimates for unit cell contents of proteins, DNA, and protein-nucleic acid complex crystals', *Protein Sci*, 12(9), pp. 1865-71.

Keegan, R.M. and Winn, M.D. (2008) 'MrBUMP: an automated pipeline for molecular replacement', *Acta Crystallogr D Biol Crystallogr*, 64(Pt 1), pp. 119-24.

Keeney, S. (2008) 'Spo11 and the Formation of DNA Double-Strand Breaks in Meiosis', *Genome Dyn Stab*, 2, pp. 81-123.

Keeney, S., Giroux, C.N. and Kleckner, N. (1997) 'Meiosis-specific DNA double-strand breaks are catalyzed by Spo11, a member of a widely conserved protein family', *Cell*, 88(3), pp. 375-84.

Kemp, B., Boumil, R.M., Stewart, M.N. and Dawson, D.S. (2004) 'A role for centromere pairing in meiotic chromosome segregation', *Genes Dev*, 18(16), pp. 1946-51.

Kim, D.I., Birendra, K.C. and Roux, K.J. (2015) 'Making the LINC: SUN and KASH protein interactions', *Biol Chem*, 396(4), pp. 295-310.

Klapholz, S., Waddell, C.S. and Esposito, R.E. (1985) 'The role of the SPO11 gene in meiotic recombination in yeast', *Genetics*, 110(2), pp. 187-216.

Kleckner, N. (2006) 'Chiasma formation: chromatin/axis interplay and the role(s) of the synaptonemal complex', *Chromosoma*, 115(3), pp. 175-94.

Klein, F., Mahr, P., Galova, M., Buonomo, S.B., Michaelis, C., Nairz, K. and Nasmyth, K. (1999) 'A central role for cohesins in sister chromatid cohesion, formation of axial elements, and recombination during yeast meiosis', *Cell*, 98(1), pp. 91-103.

Kneitz, B., Cohen, P.E., Avdievich, E., Zhu, L., Kane, M.F., Hou, H., Jr., Kolodner, R.D., Kucherlapati, R., Pollard, J.W. and Edelmann, W. (2000) 'MutS homolog 4 localization to meiotic chromosomes is required for chromosome pairing during meiosis in male and female mice', *Genes Dev*, 14(9), pp. 1085-97.

Konarev, P.V., Volkov, V.V., Sokolova, A.V., Koch, M.H.J. and Svergun, D.I. (2003) 'PRIMUS: a Windows PC-based system for small-angle scattering data analysis', 36(5), pp. 1277-1282.

Koszul, R. and Kleckner, N. (2009) 'Dynamic chromosome movements during meiosis: a way to eliminate unwanted connections?', *Trends Cell Biol*, 19(12), pp. 716-24.

Kouznetsova, A., Benavente, R., Pastink, A. and Hoog, C. (2011) 'Meiosis in mice without a synaptonemal complex', *PLoS One*, 6(12), p. e28255.

Kouznetsova, A., Novak, I., Jessberger, R. and Hoog, C. (2005) 'SYCP2 and SYCP3 are required for cohesin core integrity at diplotene but not for centromere cohesion at the first meiotic division', *J Cell Sci*, 118(Pt 10), pp. 2271-8.

Kozin, M.B. and Svergun, D.I. (2001) 'Automated matching of high- and low-resolution structural models', 34(1), pp. 33-41.

Krogh, B.O. and Shuman, S. (2000) 'Catalytic mechanism of DNA topoisomerase IB', *Mol Cell*, 5(6), pp. 1035-41.

Krueger, C., King, M.R., Krueger, F., Branco, M.R., Osborne, C.S., Niakan, K.K., Higgins, M.J. and Reik, W. (2012) 'Pairing of homologous regions in the mouse genome is associated with transcription but not imprinting status', *PLoS One*, 7(7), p. e38983.

Kutay, U. and Hetzer, M.W. (2008) 'Reorganization of the nuclear envelope during open mitosis', *Curr Opin Cell Biol*, 20(6), pp. 669-77.

Lammers, J.H., Offenberg, H.H., van Aalderen, M., Vink, A.C., Dietrich, A.J. and Heyting, C. (1994) 'The gene encoding a major component of the lateral elements of synaptonemal complexes of the rat is related to X-linked lymphocyte-regulated genes', *Mol Cell Biol*, 14(2), pp. 1137-46.

Lange, C. and Rudolph, R. (2009) 'Suppression of protein aggregation by L-arginine', *Curr Pharm Biotechnol*, 10(4), pp. 408-14.

Lee, C.Y., Horn, H.F., Stewart, C.L., Burke, B., Bolcun-Filas, E., Schimenti, J.C., Dresser, M.E. and Pezza, R.J. (2015) 'Mechanism and regulation of rapid telomere prophase movements in mouse meiotic chromosomes', *Cell Rep*, 11(4), pp. 551-63.

Lenzi, M.L., Smith, J., Snowden, T., Kim, M., Fishel, R., Poulos, B.K. and Cohen, P.E. (2005) 'Extreme heterogeneity in the molecular events leading to the establishment of chiasmata during meiosis i in human oocytes', *Am J Hum Genet*, 76(1), pp. 112-27.

Li, M.Z. and Elledge, S.J. (2012) 'SLIC: a method for sequence- and ligation-independent cloning', *Methods Mol Biol*, 852, pp. 51-9.

Lim, C.J., Zaug, A.J., Kim, H.J. and Cech, T.R. (2017) 'Reconstitution of human shelterin complexes reveals unexpected stoichiometry and dual pathways to enhance telomerase processivity', *Nat Commun*, 8(1), p. 1075.

Link, J., Jahn, D., Schmitt, J., Gob, E., Baar, J., Ortega, S., Benavente, R. and Alsheimer, M. (2013) 'The meiotic nuclear lamina regulates chromosome dynamics and promotes efficient homologous recombination in the mouse', *PLoS Genet*, 9(1), p. e1003261.

Liu, J.G., Yuan, L., Brundell, E., Bjorkroth, B., Daneholt, B. and Hoog, C. (1996) 'Localization of the N-terminus of SCP1 to the central element of the synaptonemal complex and evidence for direct interactions between the N-termini of SCP1 molecules organized head-to-head', *Exp Cell Res*, 226(1), pp. 11-9.

Loidl, J., Scherthan, H., Den Dunnen, J.T. and Klein, F. (1995) 'Morphology of a human-derived YAC in yeast meiosis', *Chromosoma*, 104(3), pp. 183-8.

Long, J., Huang, C., Chen, Y., Zhang, Y., Shi, S., Wu, L., Liu, Y., Liu, C., Wu, J. and Lei, M. (2017) 'Telomeric TERB1-TRF1 interaction is crucial for male meiosis', *Nat Struct Mol Biol*, 24(12), pp. 1073-1080.

Lu, J., Gu, Y., Feng, J., Zhou, W., Yang, X. and Shen, Y. (2014) 'Structural insight into the central element assembly of the synaptonemal complex', *Sci Rep*, 4, p. 7059.

Lu, W., Gotzmann, J., Sironi, L., Jaeger, V.M., Schneider, M., Luke, Y., Uhlen, M., Szigyarto, C.A., Brachner, A., Ellenberg, J., Foisner, R., Noegel, A.A. and Karakesisoglou, I. (2008) 'Sun1 forms immobile macromolecular assemblies at the nuclear envelope', *Biochim Biophys Acta*, 1783(12), pp. 2415-26.

Luo, M., Yang, F., Leu, N.A., Landaiche, J., Handel, M.A., Benavente, R., La Salle, S. and Wang, P.J. (2013) 'MEIOB exhibits single-stranded DNA-binding and exonuclease activities and is essential for meiotic recombination', *Nature Communications*, 4, p. 2788.

Lupas, A. (1997) 'Predicting coiled-coil regions in proteins', *Curr Opin Struct Biol*, 7(3), pp. 388-93.

Lupas, A., Van Dyke, M. and Stock, J. (1991) 'Predicting coiled coils from protein sequences', *Science*, 252(5009), pp. 1162-4.

Mach, H., Middaugh, C.R. and Denslow, N. (2001) 'Determining the identity and purity of recombinant proteins by UV absorption spectroscopy', *Curr Protoc Protein Sci*, Chapter 7, p. Unit 7.2.

MacQueen, A.J., Phillips, C.M., Bhalla, N., Weiser, P., Villeneuve, A.M. and Dernburg, A.F. (2005) 'Chromosome sites play dual roles to establish homologous synapsis during meiosis in C. elegans', *Cell*, 123(6), pp. 1037-50.

Martinez, J.S., von Nicolai, C., Kim, T., Ehlen, A., Mazin, A.V., Kowalczykowski, S.C. and Carreira, A. (2016) 'BRCA2 regulates DMC1-mediated recombination through the BRC repeats', *Proc Natl Acad Sci U S A*, 113(13), pp. 3515-20.

Maruyama, D., Ohtsu, M. and Higashiyama, T. (2016) 'Cell fusion and nuclear fusion in plants', *Semin Cell Dev Biol*, 60, pp. 127-135.

Matthews, B.W. (1968) 'Solvent content of protein crystals', *J Mol Biol*, 33(2), pp. 491-7.

Matzuk, M.M. and Lamb, D.J. (2002) 'Genetic dissection of mammalian fertility pathways', *Nat Cell Biol*, 4 Suppl, pp. s41-9.

Maxfield Boumil, R., Kemp, B., Angelichio, M., Nilsson-Tillgren, T. and Dawson, D.S. (2003) 'Meiotic segregation of a homeologous chromosome pair', *Mol Genet Genomics*, 268(6), pp. 750-60.

McCoy, A.J., Grosse-Kunstleve, R.W., Adams, P.D., Winn, M.D., Storoni, L.C. and Read, R.J. (2007) 'Phaser crystallographic software', *J Appl Crystallogr*, 40(Pt 4), pp. 658-674.

McKim, K.S., Jang, J.K. and Manheim, E.A. (2002) 'Meiotic recombination and chromosome segregation in Drosophila females', *Annu Rev Genet*, 36, pp. 205-32.

Meuwissen, R.L., Meerts, I., Hoovers, J.M., Leschot, N.J. and Heyting, C. (1997) 'Human synaptonemal complex protein 1 (SCP1): isolation and characterization of the cDNA and chromosomal localization of the gene', *Genomics*, 39(3), pp. 377-84.

Meuwissen, R.L., Offenberg, H.H., Dietrich, A.J., Riesewijk, A., van Iersel, M. and Heyting, C. (1992) 'A coiled-coil related protein specific for synapsed regions of meiotic prophase chromosomes', *Embo j*, 11(13), pp. 5091-100.

Millan, C., Sammito, M. and Uson, I. (2015) 'Macromolecular ab initio phasing enforcing secondary and tertiary structure', *IUCrJ*, 2(Pt 1), pp. 95-105.

Millán, M., Sammito, M.D., McCoy, M.J., Ziem, A.F., Petrillo, N.G., Oeffner, R.D., Domínguez-Gil, T., Hermoso, J.A., Read, R.J. and Usón, I. (2017) 'Exploiting distant homologs for phasing through generation of compact fragments, local fold refinement and partial solution combination ', *Acta Crystallogr D Biol Crystallogr*, In Press

Mitra, N. and Roeder, G.S. (2007) 'A novel nonnull ZIP1 allele triggers meiotic arrest with synapsed chromosomes in Saccharomyces cerevisiae', *Genetics*, 176(2), pp. 773-87.

Miyamoto, T., Hasuike, S., Yogev, L., Maduro, M.R., Ishikawa, M., Westphal, H. and Lamb, D.J. (2003) 'Azoospermia in patients heterozygous for a mutation in SYCP3', *Lancet*, 362(9397), pp. 1714-9.

Morimoto, A., Shibuya, H., Zhu, X., Kim, J., Ishiguro, K., Han, M. and Watanabe, Y. (2012) 'A conserved KASH domain protein associates with telomeres, SUN1, and dynactin during mammalian meiosis', *J Cell Biol*, 198(2), pp. 165-72.

Morrisett, J.D., David, J.S., Pownall, H.J. and Gotto, A.M., Jr. (1973) 'Interaction of an apolipoprotein (apoLP-alanine) with phosphatidylcholine', *Biochemistry*, 12(7), pp. 1290-9.

Moses, M.J. (1956) 'Chromosomal structures in crayfish spermatocytes', *J Biophys Biochem Cytol*, 2(2), pp. 215-8.

Nash, P., Tang, X., Orlicky, S., Chen, Q., Gertler, F.B., Mendenhall, M.D., Sicheri, F., Pawson, T. and Tyers, M. (2001) 'Multisite phosphorylation of a CDK inhibitor sets a threshold for the onset of DNA replication', *Nature*, 414(6863), pp. 514-21.

Nasmyth, K. (2001) 'Disseminating the genome: joining, resolving, and separating sister chromatids during mitosis and meiosis', *Annu Rev Genet*, 35, pp. 673-745.

Nasmyth, K. and Haering, C.H. (2005) 'The structure and function of SMC and kleisin complexes', *Annu Rev Biochem*, 74, pp. 595-648.

Nasmyth, K. and Haering, C.H. (2009) 'Cohesin: its roles and mechanisms', *Annu Rev Genet*, 43, pp. 525-58.

Nimonkar, A.V., Genschel, J., Kinoshita, E., Polaczek, P., Campbell, J.L., Wyman, C., Modrich, P. and Kowalczykowski, S.C. (2011) 'BLM-DNA2-RPA-MRN and EXO1-BLM-RPA-MRN constitute two DNA end resection machineries for human DNA break repair', *Genes Dev*, 25(4), pp. 350-62.

Novak, I., Wang, H., Revenkova, E., Jessberger, R., Scherthan, H. and Hoog, C. (2008) 'Cohesin Smc1beta determines meiotic chromatin axis loop organization', *J Cell Biol*, 180(1), pp. 83-90.

Offenberg, H.H., Schalk, J.A., Meuwissen, R.L., van Aalderen, M., Kester, H.A., Dietrich, A.J. and Heyting, C. (1998) 'SCP2: a major protein component of the axial elements of synaptonemal complexes of the rat', *Nucleic Acids Res*, 26(11), pp. 2572-9.

Olins, D.E. and Olins, A.L. (2003) 'Chromatin history: our view from the bridge', *Nat Rev Mol Cell Biol*, 4(10), pp. 809-14.

Oliver-Bonet, M., Turek, P.J., Sun, F., Ko, E. and Martin, R.H. (2005) 'Temporal progression of recombination in human males', *Mol Hum Reprod*, 11(7), pp. 517-22.

Ollinger, R., Alsheimer, M. and Benavente, R. (2005) 'Mammalian protein SCP1 forms synaptonemal complex-like structures in the absence of meiotic chromosomes', *Mol Biol Cell*, 16(1), pp. 212-7.

Onn, I., Heidinger-Pauli, J.M., Guacci, V., Unal, E. and Koshland, D.E. (2008) 'Sister chromatid cohesion: a simple concept with a complex reality', *Annu Rev Cell Dev Biol*, 24, pp. 105-29.

Page, J.M. and Silver, R.M. (2016) 'Genetic Causes of Recurrent Pregnancy Loss', *Clin Obstet Gynecol*, 59(3), pp. 498-508.

Page, S.L. and Hawley, R.S. (2001) 'c(3)G encodes a Drosophila synaptonemal complex protein', *Genes Dev*, 15(23), pp. 3130-43.

Page, S.L. and Hawley, R.S. (2004) 'The genetics and molecular biology of the synaptonemal complex', *Annu Rev Cell Dev Biol*, 20, pp. 525-58.

Paluh, J.L., Killilea, A.N., Detrich, H.W., 3rd and Downing, K.H. (2004) 'Meiosis-specific failure of cell cycle progression in fission yeast by mutation of a conserved beta-tubulin residue', *Mol Biol Cell*, 15(3), pp. 1160-71.

Pannu, N.S., Waterreus, W.J., Skubak, P., Sikharulidze, I., Abrahams, J.P. and de Graaff, R.A. (2011) 'Recent advances in the CRANK software suite for experimental phasing', *Acta Crystallogr D Biol Crystallogr*, 67(Pt 4), pp. 331-7.

Pape, T. and Schneider, T.R. (2004) 'HKL2MAP: a graphical user interface for macromolecular phasing with SHELX programs', *Journal of Applied Crystallography*, 37(5), pp. 843-844.

Parra, M.T., Viera, A., Gomez, R., Page, J., Carmena, M., Earnshaw, W.C., Rufas, J.S. and Suja, J.A. (2003) 'Dynamic relocalization of the chromosomal passenger complex proteins inner centromere protein (INCENP) and aurora-B kinase during male mouse meiosis', *J Cell Sci*, 116(Pt 6), pp. 961-74.

Parry, D.A. (1982) 'Coiled-coils in alpha-helix-containing proteins: analysis of the residue types within the heptad repeat and the use of these data in the prediction of coiled-coils in other proteins', *Biosci Rep*, 2(12), pp. 1017-24.

Parvanov, E.D., Tian, H., Billings, T., Saxl, R.L., Spruce, C., Aithal, R., Krejci, L., Paigen, K. and Petkov, P.M. (2017) 'PRDM9 interactions with other proteins provide a link between recombination hotspots and the chromosomal axis in meiosis', *Mol Biol Cell*, 28(3), pp. 488-499.

Passy, S.I., Yu, X., Li, Z., Radding, C.M., Masson, J.Y., West, S.C. and Egelman, E.H. (1999) 'Human Dmc1 protein binds DNA as an octameric ring', *Proc Natl Acad Sci U S A*, 96(19), pp. 10684-8.

Patel, J.T., Bottrill, A., Prosser, S.L., Jayaraman, S., Straatman, K., Fry, A.M. and Shackleton, S. (2014) 'Mitotic phosphorylation of SUN1 loosens its connection with the nuclear lamina while the LINC complex remains intact', *Nucleus*, 5(5), pp. 462-73.

Pauling, L., Corey, R.B. and Branson, H.R. (1951) 'The structure of proteins: Two hydrogen-bonded helical configurations of the polypeptide chain', 37(4), pp. 205-211.

Pellegrini, L., Yu, D.S., Lo, T., Anand, S., Lee, M., Blundell, T.L. and Venkitaraman, A.R. (2002) 'Insights into DNA recombination from the structure of a RAD51-BRCA2 complex', *Nature*, 420(6913), pp. 287-93.

Pelttari, J., Hoja, M.R., Yuan, L., Liu, J.G., Brundell, E., Moens, P., Santucci-Darmanin, S., Jessberger, R., Barbero, J.L., Heyting, C. and Hoog, C. (2001) 'A meiotic chromosomal core consisting of cohesin complex proteins recruits DNA recombination proteins and promotes synapsis in the absence of an axial element in mammalian meiotic cells', *Mol Cell Biol*, 21(16), pp. 5667-77.

Pendlebury, D.F., Fujiwara, Y., Tesmer, V.M., Smith, E.M., Shibuya, H., Watanabe, Y. and Nandakumar, J. (2017) 'Dissecting the telomere-inner nuclear membrane interface formed in meiosis', *Nat Struct Mol Biol*, 24(12), pp. 1064-1072.

Peng, G. and Lin, S.Y. (2011) 'Exploiting the homologous recombination DNA repair network for targeted cancer therapy', *World J Clin Oncol*, 2(2), pp. 73-9.

Peranen, J., Rikkonen, M., Hyvonen, M. and Kaariainen, L. (1996) 'T7 vectors with modified T7lac promoter for expression of proteins in Escherichia coli', *Anal Biochem*, 236(2), pp. 371-3.

Petoukhov, M.V., Franke, D., Shkumatov, A.V., Tria, G., Kikhney, A.G., Gajda, M., Gorba, C., Mertens, H.D., Konarev, P.V. and Svergun, D.I. (2012) 'New developments in the ATSAS program package for small-angle scattering data analysis', *J Appl Crystallogr*, 45(Pt 2), pp. 342-350.

Petronczki, M., Siomos, M.F. and Nasmyth, K. (2003) 'Un menage a quatre: the molecular biology of chromosome segregation in meiosis', *Cell*, 112(4), pp. 423-40.

Phillips, C.M. and Dernburg, A.F. (2006) 'A family of zinc-finger proteins is required for chromosome-specific pairing and synapsis during meiosis in C. elegans', *Dev Cell*, 11(6), pp. 817-29.

Portet, S., Madzvamuse, A., Chung, A., Leube, R.E. and Windoffer, R. (2015) 'Keratin dynamics: modeling the interplay between turnover and transport', *PLoS One*, 10(3), p. e0121090.

Pousette, A., Leijonhufvud, P., Arver, S., Kvist, U., Pelttari, J. and Hoog, C. (1997) 'Presence of synaptonemal complex protein 1 transversal filament-like protein in human primary spermatocytes', *Hum Reprod*, 12(11), pp. 2414-7.

Prieto, I., Suja, J.A., Pezzi, N., Kremer, L., Martinez, A.C., Rufas, J.S. and Barbero, J.L. (2001) 'Mammalian STAG3 is a cohesin specific to sister chromatid arms in meiosis I', *Nat Cell Biol*, 3(8), pp. 761-6.

Qiao, H., Chen, J.K., Reynolds, A., Hoog, C., Paddy, M. and Hunter, N. (2012) 'Interplay between synaptonemal complex, homologous recombination, and centromeres during mammalian meiosis', *PLoS Genet*, 8(6), p. e1002790.

Rasmussen, S.W. (1975) 'Ultrastructural studies of meiosis in males and females of the c(3)G17 mutant of Drosphila melanogaster Meigen.', *Compt.Rend.Trav.Lab.Carlsberg*, 40(14), pp. 163–173.

Rasmussen, S.W. (1977) 'The transformation of the Synaptonemal Complex into the 'elimination chromatin' in Bombyx mori oocytes', *Chromosoma*, 60(3), pp. 205-21.

Rasmussen, S.W.H., P.B. (1979) 'Chromosome pairing in autotetraploid Bombyx females. Mechanism for exclusive bivalent formation', *Carlsberg Res. Commun.*, 44: 101.

Reck-Peterson, S.L., Redwine, W.B., Vale, R.D. and Carter, A.P. (2018) 'The cytoplasmic dynein transport machinery and its many cargoes', *Nat Rev Mol Cell Biol*, 19(6), pp. 382-398.

Rice, P., Longden, I. and Bleasby, A. (2000) 'EMBOSS: the European Molecular Biology Open Software Suite', *Trends Genet*, 16(6), pp. 276-7.

Rigden, D.J., Keegan, R.M. and Winn, M.D. (2008) 'Molecular replacement using ab initio polyalanine models generated with ROSETTA', *Acta Crystallogr D Biol Crystallogr*, 64(Pt 12), pp. 1288-91.

Rodriguez, D.D., Grosse, C., Himmel, S., Gonzalez, C., de Ilarduya, I.M., Becker, S., Sheldrick, G.M. and Uson, I. (2009) 'Crystallographic ab initio protein structure solution below atomic resolution', *Nature Methods*, 6(9), pp. 651-U39.

Roeder, G.S. (1997) 'Meiotic chromosomes: it takes two to tango', *Genes Dev*, 11(20), pp. 2600-21.

Romanienko, P.J. and Camerini-Otero, R.D. (2000) 'The mouse Spo11 gene is required for meiotic chromosome synapsis', *Mol Cell*, 6(5), pp. 975-87.

Rose, A. and Meier, I. (2004) 'Scaffolds, levers, rods and springs: diverse cellular functions of long coiled-coil proteins', *Cell Mol Life Sci*, 61(16), pp. 1996-2009.

Rousseaux, S., Wang, J. and Khochbin, S. (2013) 'Cancer hallmarks sustained by ectopic activations of placenta/male germline genes', in *Cell Cycle*. United States, pp. 2331-2.

Sage, J., Martin, L., Cuzin, F. and Rassoulzadegan, M. (1995) 'cDNA sequence of the murine synaptonemal complex protein 1 (SCP1)', *Biochim Biophys Acta*, 1263(3), pp. 258-60.

Sakuragawa, M. (1976) 'Niemann-Pick disease-like inclusions caused by a hypocholesteremic agent', *Invest Ophthalmol*, 15(12), pp. 1022-7.

Santucci-Darmanin, S., Neyton, S., Lespinasse, F., Saunieres, A., Gaudray, P. and Paquis-Flucklinger, V. (2002) 'The DNA mismatch-repair MLH3 protein interacts with MSH4 in meiotic cells, supporting a role for this MutL homolog in mammalian meiotic recombination', *Hum Mol Genet*, 11(15), pp. 1697-706.

Santucci-Darmanin, S., Walpita, D., Lespinasse, F., Desnuelle, C., Ashley, T. and Paquis-Flucklinger, V. (2000) 'MSH4 acts in conjunction with MLH1 during mammalian meiosis', *Faseb j*, 14(11), pp. 1539-47.

Schalk, J.A., Dietrich, A.J., Vink, A.C., Offenberg, H.H., van Aalderen, M. and Heyting, C. (1998) 'Localization of SCP2 and SCP3 protein molecules within synaptonemal complexes of the rat', *Chromosoma*, 107(8), pp. 540-8.

Schild-Prufert, K., Saito, T.T., Smolikov, S., Gu, Y., Hincapie, M., Hill, D.E., Vidal, M., McDonald, K. and Colaiacovo, M.P. (2011) 'Organization of the synaptonemal complex during meiosis in Caenorhabditis elegans', *Genetics*, 189(2), pp. 411-21.

Schmekel, K., Meuwissen, R.L., Dietrich, A.J., Vink, A.C., van Marle, J., van Veen, H. and Heyting, C. (1996) 'Organization of SCP1 protein molecules within synaptonemal complexes of the rat', *Exp Cell Res*, 226(1), pp. 20-30.

Schmitt, J., Benavente, R., Hodzic, D., Hoog, C., Stewart, C.L. and Alsheimer, M. (2007) 'Transmembrane protein Sun2 is involved in tethering mammalian meiotic telomeres to the nuclear envelope', *Proc Natl Acad Sci U S A*, 104(18), pp. 7426-31.

Schneider, C.A., Rasband, W.S. and Eliceiri, K.W. (2012) 'NIH Image to ImageJ: 25 years of image analysis', *Nat Methods*, 9(7), pp. 671-5.

Schramm, S., Fraune, J., Naumann, R., Hernandez-Hernandez, A., Hoog, C., Cooke, H.J., Alsheimer, M. and Benavente, R. (2011) 'A novel mouse synaptonemal complex protein is essential for loading of central element proteins, recombination, and fertility', *PLoS Genet*, 7(5), p. e1002088.

Schucker, K., Holm, T., Franke, C., Sauer, M. and Benavente, R. (2015) 'Elucidation of synaptonemal complex organization by super-resolution imaging with isotropic resolution', *Proc Natl Acad Sci U S A*, 112(7), pp. 2029-33.

Sedlak, S.M., Bruetzel, L.K. and Lipfert, J. (2017) 'Quantitative evaluation of statistical errors in small-angle X-ray scattering measurements', *J Appl Crystallogr*, 50(Pt 2), pp. 621-630.

Selker, E.U. (1990) 'Premeiotic instability of repeated sequences in Neurospora crassa', *Annu Rev Genet*, 24, pp. 579-613.

Seo, E.K., Choi, J.Y., Jeong, J.H., Kim, Y.G. and Park, H.H. (2016) 'Crystal Structure of C-Terminal Coiled-Coil Domain of SYCP1 Reveals Non-Canonical Anti-Parallel Dimeric Structure of Transverse Filament at the Synaptonemal Complex', *PLoS One*, 11(8), p. e0161379.

Sheldrick, G.M. (2010) 'Experimental phasing with SHELXC/D/E: combining chain tracing with density modification', *Acta Crystallogr D Biol Crystallogr*, 66(Pt 4), pp. 479-85.

Shibuya, H., Hernandez-Hernandez, A., Morimoto, A., Negishi, L., Hoog, C. and Watanabe, Y. (2015) 'MAJIN Links Telomeric DNA to the Nuclear Membrane by Exchanging Telomere Cap', *Cell*, 163(5), pp. 1252-1266.

Shibuya, H., Ishiguro, K. and Watanabe, Y. (2014) 'The TRF1-binding protein TERB1 promotes chromosome movement and telomere rigidity in meiosis', *Nat Cell Biol*, 16(2), pp. 145-56.

Shibuya, H. and Watanabe, Y. (2014) 'The meiosis-specific modification of mammalian telomeres', *Cell Cycle*, 13(13), pp. 2024-8.

Singh, M.K., Nicolas, E., Gherraby, W., Dadke, D., Lessin, S. and Golemis, E.A. (2007) 'HEI10 negatively regulates cell invasion by inhibiting cyclin B/Cdk1 and other promotility proteins', *Oncogene*, 26(33), pp. 4825-32.

Smith, C.A. and Kortemme, T. (2011) 'Predicting the tolerated sequences for proteins and protein interfaces using RosettaBackrub flexible backbone design', *PLoS One*, 6(7), p. e20451.

Smith, P.A. and King, R.C. (1968) 'Genetic control of synaptonemal complexes in Drosophila melanogaster', *Genetics*, 60(2), pp. 335-51.

Snowden, T., Acharya, S., Butz, C., Berardini, M. and Fishel, R. (2004) 'hMSH4-hMSH5 recognizes Holliday Junctions and forms a meiosis-specific sliding clamp that embraces homologous chromosomes', *Mol Cell*, 15(3), pp. 437-51.

Solari, A.J. (1980) 'Synaptosomal complexes and associated structures in microspread human spermatocytes', *Chromosoma*, 81(3), pp. 315-37.

Solari, A.J. and Moses, M.J. (1973) 'The structure of the central region in the synaptonemal complexes of hamster and cricket spermatocytes', *J Cell Biol*, 56(1), pp. 145-52.

Solari, A.J. and Tres, L.L. (1970) 'The three-dimensional reconstruction of the XY chromosomal pair in human spermatocytes', *J Cell Biol*, 45(1), pp. 43-53.

Sosa, B.A., Rothballer, A., Kutay, U. and Schwartz, T.U. (2012) 'LINC complexes form by binding of three KASH peptides to domain interfaces of trimeric SUN proteins', *Cell*, 149(5), pp. 1035-47.

Sreerama, N. and Woody, R.W. (2000) 'Estimation of protein secondary structure from circular dichroism spectra: comparison of CONTIN, SELCON, and CDSSTR methods with an expanded reference set', *Anal Biochem*, 287(2), pp. 252-60.

Starr, D.A. (2011) 'KASH and SUN proteins', *Curr Biol*, 21(11), pp. R414-5.

Stellfox, M.E., Bailey, A.O. and Foltz, D.R. (2013) 'Putting CENP-A in its place', *Cell Mol Life Sci*, 70(3), pp. 387-406.

Stewart, M., Quinlan, R.A. and Moir, R.D. (1989) 'Molecular interactions in paracrystals of a fragment corresponding to the alpha-helical coiled-coil rod portion of glial fibrillary acidic protein: evidence for an antiparallel packing of molecules and polymorphism related to intermediate filament structure', *J Cell Biol*, 109(1), pp. 225-34.

Strong, M., Sawaya, M.R., Wang, S., Phillips, M., Cascio, D. and Eisenberg, D. (2006) 'Toward the structural genomics of complexes: crystal structure of a PE/PPE protein complex from Mycobacterium tuberculosis', *Proc Natl Acad Sci U S A*, 103(21), pp. 8060-5.

Sumara, I., Vorlaufer, E., Stukenberg, P.T., Kelm, O., Redemann, N., Nigg, E.A. and Peters, J.M. (2002) 'The dissociation of cohesin from chromosomes in prophase is regulated by Polo-like kinase', *Mol Cell*, 9(3), pp. 515-25.

Sumner, A.T. (1991) 'Scanning electron microscopy of mammalian chromosomes from prophase to telophase', *Chromosoma*, 100(6), pp. 410-8.

Suzuki, M. (1989) 'SPXX, a frequent sequence motif in gene regulatory proteins', *J Mol Biol*, 207(1), pp. 61-84.

Svergun, D., Barberato, C. and Koch, M.H.J. (1995) 'CRYSOL– a Program to Evaluate X-ray Solution Scattering of Biological Macromolecules from Atomic Coordinates', 28(6), pp. 768-773.

Svergun, D.I. (1999) 'Restoring low resolution structure of biological macromolecules from solution scattering using simulated annealing', *Biophys J*, 76(6), pp. 2879-86.

Svergun, D.I. and Koch, M.H.J. (2003) 'Small-angle scattering studies of biological macromolecules in solution', *Reports on Progress in Physics*, 66(10), pp. 1735-1782.

Sym, M., Engebrecht, J.A. and Roeder, G.S. (1993) 'ZIP1 is a synaptonemal complex protein required for meiotic chromosome synapsis', *Cell*, 72(3), pp. 365-78.

Sym, M. and Roeder, G.S. (1994) 'Crossover interference is abolished in the absence of a synaptonemal complex protein', *Cell*, 79(2), pp. 283-92.

Sym, M. and Roeder, G.S. (1995) 'Zip1-induced changes in synaptonemal complex structure and polycomplex assembly', *J Cell Biol*, 128(4), pp. 455-66.

Syrjanen, J.L., Heller, I., Candelli, A., Davies, O.R., Peterman, E.J., Wuite, G.J. and Pellegrini, L. (2017) 'Single-molecule observation of DNA compaction by meiotic protein SYCP3', *Elife*, 6.

Syrjanen, J.L., Pellegrini, L. and Davies, O.R. (2014) 'A molecular model for the role of SYCP3 in meiotic chromosome organisation', *Elife*, 3.

Tachiwana, H., Kagawa, W., Osakabe, A., Kawaguchi, K., Shiga, T., Hayashi-Takanaka, Y., Kimura, H. and Kurumizaka, H. (2010) 'Structural basis of instability of the nucleosome containing a testis-specific histone variant, human H3T', *Proc Natl Acad Sci U S A*, 107(23), pp. 10454-9.

Takemoto, A., Kawashima, S.A., Li, J.J., Jeffery, L., Yamatsugu, K., Elemento, O. and Nurse, P. (2016) 'Nuclear envelope expansion is crucial for proper chromosomal segregation during a closed mitosis', *J Cell Sci*, 129(6), pp. 1250-9.

Tarsounas, M., Morita, T., Pearlman, R.E. and Moens, P.B. (1999) 'RAD51 and DMC1 form mixed complexes associated with mouse meiotic chromosome cores and synaptonemal complexes', *J Cell Biol*, 147(2), pp. 207-20.

Tease, C. and Hulten, M.A. (2004) 'Inter-sex variation in synaptonemal complex lengths largely determine the different recombination rates in male and female germ cells', *Cytogenet Genome Res*, 107(3-4), pp. 208-15.

Terwilliger, T.C., Adams, P.D., Read, R.J., McCoy, A.J., Moriarty, N.W., Grosse-Kunstleve, R.W., Afonine, P.V., Zwart, P.H. and Hung, L.W. (2009) 'Decision-making in structure solution using Bayesian estimates of map quality: the PHENIX AutoSol wizard', *Acta Crystallogr D Biol Crystallogr*, 65(Pt 6), pp. 582-601.

Thorslund, T., Esashi, F. and West, S.C. (2007) 'Interactions between human BRCA2 protein and the meiosis-specific recombinase DMC1', *Embo j*, 26(12), pp. 2915-22.

Toby, G.G., Gherraby, W., Coleman, T.R. and Golemis, E.A. (2003) 'A novel RING finger protein, human enhancer of invasion 10, alters mitotic progression through regulation of cyclin B levels', *Mol Cell Biol*, 23(6), pp. 2109-22.

Todaro, G.J. and Green, H. (1963) 'Quantitative studies of the growth of mouse embryo cells in culture and their development into established lines', *J Cell Biol*, 17, pp. 299-313.

Truebestein, L. and Leonard, T.A. (2016) 'Coiled-coils: The long and short of it', *Bioessays*, 38(9), pp. 903-16.

Tsubouchi, T. and Roeder, G.S. (2005) 'A synaptonemal complex protein promotes homology-independent centromere coupling', *Science*, 308(5723), pp. 870-3.

Tung, K.S. and Roeder, G.S. (1998) 'Meiotic chromosome morphology and behavior in zip1 mutants of Saccharomyces cerevisiae', *Genetics*, 149(2), pp. 817-32.

Tureci, O., Sahin, U., Zwick, C., Koslowski, M., Seitz, G. and Pfreundschuh, M. (1998) 'Identification of a meiosis-specific protein as a member of the class of cancer/testis antigens', *Proc Natl Acad Sci U S A*, 95(9), pp. 5211-6.

Viera, A., Alsheimer, M., Gomez, R., Berenguer, I., Ortega, S., Symonds, C.E., Santamaria, D., Benavente, R. and Suja, J.A. (2015) 'CDK2 regulates nuclear envelope protein dynamics and telomere attachment in mouse meiotic prophase', *J Cell Sci*, 128(1), pp. 88-99.

von Wettstein, D., Rasmussen, S.W. and Holm, P.B. (1984) 'The synaptonemal complex in genetic segregation', *Annu Rev Genet*, 18, pp. 331-413.

Vonrhein, C., Flensburg, C., Keller, P., Sharff, A., Smart, O., Paciorek, W., Womack, T. and Bricogne, G. (2011) 'Data processing and analysis with the autoPROC toolbox', *Acta Crystallogr D Biol Crystallogr*, 67(Pt 4), pp. 293-302.

Vranis, N.M., van der Heijden, G.W., Malki, S. and Bortvin, A. (2010) 'Synaptonemal Complex Length Variation in Wild-Type Male Mice', in *Genes (Basel)*. pp. 505-20.

Wallace, B.M. and Wallace, H. (2003) 'Synaptonemal complex karyotype of zebrafish', *Heredity (Edinb)*, 90(2), pp. 136-40.

Wang, Y., Chen, Y., Chen, J., Wang, L., Nie, L., Long, J., Chang, H., Wu, J., Huang, C. and Lei, M. (2019) 'The meiotic TERB1-TERB2-MAJIN complex tethers telomeres to the nuclear envelope', *Nat Commun*, 10(1), p. 564.

Ward, J.O., Reinholdt, L.G., Motley, W.W., Niswander, L.M., Deacon, D.C., Griffin, L.B., Langlais, K.K., Backus, V.L., Schimenti, K.J., O'Brien, M.J., Eppig, J.J. and Schimenti, J.C. (2007) 'Mutation in mouse hei10, an e3 ubiquitin ligase, disrupts meiotic crossing over', *PLoS Genet*, 3(8), p. e139.

Watanabe, Y. (2004) 'Modifying sister chromatid cohesion for meiosis', *J Cell Sci*, 117(Pt 18), pp. 4017-23.

Waterhouse, A.M., Procter, J.B., Martin, D.M., Clamp, M. and Barton, G.J. (2009) 'Jalview Version 2--a multiple sequence alignment editor and analysis workbench', *Bioinformatics*, 25(9), pp. 1189-91.

Weiner, B.M. and Kleckner, N. (1994) 'Chromosome pairing via multiple interstitial interactions before and during meiosis in yeast', *Cell*, 77(7), pp. 977-91.

West, A.M., Rosenberg, S.C., Ur, S.N., Lehmer, M.K., Ye, Q., Hagemann, G., Caballero, I., Uson, I., MacQueen, A.J., Herzog, F. and Corbett, K.D. (2019) 'A conserved filamentous assembly underlies the structure of the meiotic chromosome axis', *Elife*, 8.

Westergaard, M. and von Wettstein, D. (1972) 'The synaptinemal complex', *Annu Rev Genet*, 6, pp. 71-110.

Whitman, W.B., Coleman, D.C. and Wiebe, W.J. (1998) 'Prokaryotes: the unseen majority', *Proc Natl Acad Sci U S A*, 95(12), pp. 6578-83.

Whitmore, L. and Wallace, B.A. (2004) 'DICHROWEB, an online server for protein secondary structure analyses from circular dichroism spectroscopic data', *Nucleic Acids Res*, 32(Web Server issue), pp. W668-73.

Whitmore, L. and Wallace, B.A. (2008) 'Protein secondary structure analyses from circular dichroism spectroscopy: methods and reference databases', *Biopolymers*, 89(5), pp. 392-400.

Wieser, S. and Pines, J. (2015) 'The biochemistry of mitosis', *Cold Spring Harb Perspect Biol*, 7(3), p. a015776.

Winkel, K., Alsheimer, M., Ollinger, R. and Benavente, R. (2009) 'Protein SYCP2 provides a link between transverse filaments and lateral elements of mammalian synaptonemal complexes', *Chromosoma*, 118(2), pp. 259-67.

Woglar, A. and Jantsch, V. (2014) 'Chromosome movement in meiosis I prophase of Caenorhabditis elegans', *Chromosoma*, 123(1-2), pp. 15-24.

Wu, X., Wu, D., Lu, Z., Chen, W., Hu, X. and Ding, Y. (2009) 'A novel method for high-level production of TEV protease by superfolder GFP tag', *J Biomed Biotechnol*, 2009, p. 591923.

Wu, Y.K. and Kengaku, M. (2018) 'Dynamic Interaction Between Microtubules and the Nucleus Regulates Nuclear Movement During Neuronal Migration', *J Exp Neurosci*, 12, p. 1179069518789151.

Xu, D. and Zhang, Y. (2012) 'Ab initio protein structure assembly using continuous structure fragments and optimized knowledge-based force field', *Proteins*, 80(7), pp. 1715-35.

Xu, H., Beasley, M.D., Warren, W.D., van der Horst, G.T. and McKay, M.J. (2005) 'Absence of mouse REC8 cohesin promotes synapsis of sister chromatids in meiosis', *Dev Cell*, 8(6), pp. 949-61.

Yang, F., De La Fuente, R., Leu, N.A., Baumann, C., McLaughlin, K.J. and Wang, P.J. (2006) 'Mouse SYCP2 is required for synaptonemal complex assembly and chromosomal synapsis during male meiosis', *J Cell Biol*, 173(4), pp. 497-507.

Yuan, L., Brundell, E. and Hoog, C. (1996) 'Expression of the meiosis-specific synaptonemal complex protein 1 in a heterologous system results in the formation of large protein structures', *Exp Cell Res*, 229(2), pp. 272-5.

Yuan, L., Liu, J.G., Zhao, J., Brundell, E., Daneholt, B. and Hoog, C. (2000) 'The murine SCP3 gene is required for synaptonemal complex assembly, chromosome synapsis, and male fertility', *Mol Cell*, 5(1), pp. 73-83.

Yuan, L., Pelttari, J., Brundell, E., Bjorkroth, B., Zhao, J., Liu, J.G., Brismar, H., Daneholt, B. and Hoog, C. (1998) 'The synaptonemal complex protein SCP3 can form multistranded, cross-striated fibers in vivo', *J Cell Biol*, 142(2), pp. 331-9.

Zerbino, D.R., Achuthan, P., Akanni, W., Amode, M.R., Barrell, D., Bhai, J., Billis, K., Cummins, C., Gall, A., Giron, C.G., Gil, L., Gordon, L., Haggerty, L., Haskell, E., Hourlier, T., Izuogu, O.G., Janacek, S.H., Juettemann, T., To, J.K., Laird, M.R., Lavidas, I., Liu, Z., Loveland, J.E., Maurel, T., McLaren, W., Moore, B., Mudge, J., Murphy, D.N., Newman, V., Nuhn, M., Ogeh, D., Ong, C.K., Parker, A., Patricio, M., Riat, H.S., Schuilenburg, H., Sheppard, D., Sparrow, H., Taylor, K., Thormann, A., Vullo, A., Walts, B., Zadissa, A., Frankish, A., Hunt, S.E., Kostadima, M., Langridge, N., Martin, F.J., Muffato, M., Perry, E., Ruffier, M., Staines, D.M., Trevanion, S.J., Aken, B.L., Cunningham, F., Yates, A. and Flicek, P. (2018) 'Ensembl 2018', *Nucleic Acids Res*, 46(D1), pp. D754-d761.

Zhang, J., Pawlowski, W.P. and Han, F. (2013) 'Centromere Pairing in Early Meiotic Prophase Requires Active Centromeres and Precedes Installation of the Synaptonemal Complex in Maize[W]', in *Plant Cell*. pp. 3900-9.

Zhang, J., Tu, Z., Watanabe, Y. and Shibuya, H. (2017) 'Distinct TERB1 Domains Regulate Different Protein Interactions in Meiotic Telomere Movement', *Cell Rep*, 21(7), pp. 1715-1726.

Zhang, X., Lei, K., Yuan, X., Wu, X., Zhuang, Y., Xu, T., Xu, R. and Han, M. (2009) 'SUN1/2 and Syne/Nesprin-1/2 complexes connect centrosome to the nucleus during neurogenesis and neuronal migration in mice', *Neuron*, 64(2), pp. 173-87.

Zhou, Z., Du, X., Cai, Z., Song, X., Zhang, H., Mizuno, T., Suzuki, E., Yee, M.R., Berezov, A., Murali, R., Wu, S.L., Karger, B.L., Greene, M.I. and Wang, Q. (2012) 'Structure of Sad1-UNC84 homology (SUN) domain defines features of molecular bridge in nuclear envelope', *J Biol Chem*, 287(8), pp. 5317-26.

Zhu, D., Dix, D.J. and Eddy, E.M. (1997) 'HSP70-2 is required for CDC2 kinase activity in meiosis I of mouse spermatocytes', *Development*, 124(15), pp. 3007-14.

Zhu, H., Ownby, D.W., Riggs, C.K., Nolasco, N.J., Stoops, J.K. and Riggs, A.F. (1996) 'Assembly of the gigantic hemoglobin of the earthworm Lumbricus terrestris. Roles of subunit equilibria, non-globin linker chains, and valence of the heme iron', *J Biol Chem*, 271(47), pp. 30007-21.

Zickler, D. and Kleckner, N. (1998) 'The leptotene-zygotene transition of meiosis', *Annu Rev Genet*, 32, pp. 619-97.

Zickler, D. and Kleckner, N. (1999) 'Meiotic chromosomes: integrating structure and function', *Annu Rev Genet*, 33, pp. 603-754.

Zickler, D. and Kleckner, N. (2015) 'Recombination, Pairing, and Synapsis of Homologs during Meiosis', *Cold Spring Harb Perspect Biol*, 7(6).

Appendix 1 – SYCP1 amino acid sequence alignment

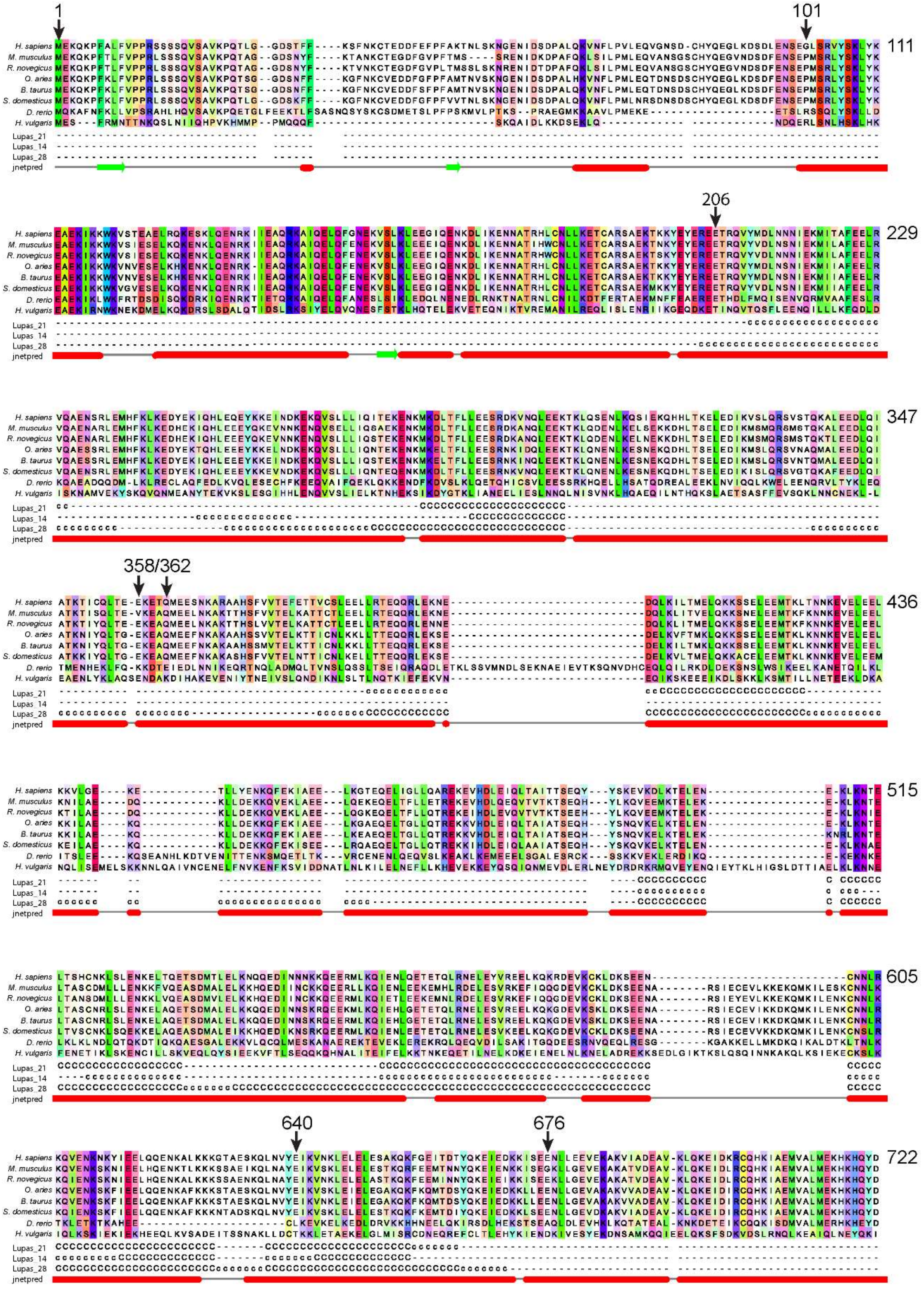
1
101
111
206
229
347
358/362
436
515
605
640
676
722
H. sapiens
M. musculus
R. novegicus
O. aries
B. taurus
S. domesticus
D. rerio
H. vulgaris
Lupas_21
Lupas_14
Lupas_28
jnetpred

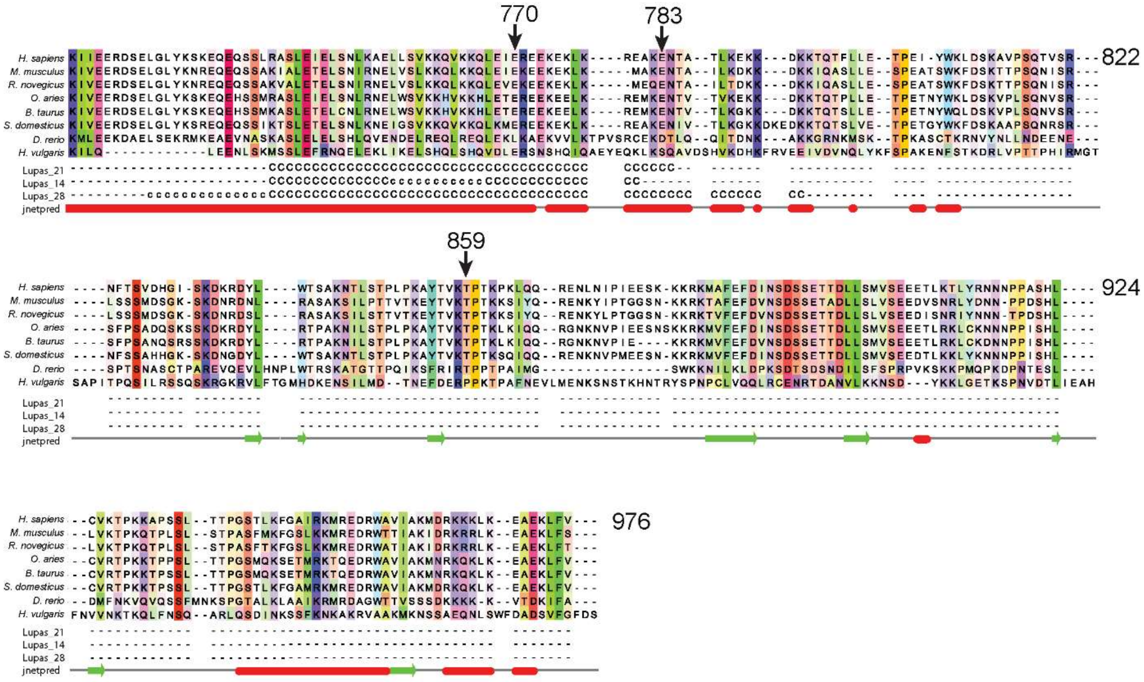
770
783
822
859
924
976
H. sapiens
M. musculus
R. novegicus
O. aries
B. taurus
S. domesticus
D. rerio
H. vulgaris
Lupas_21
Lupas_14
Lupas_28
jnetpred

Alignment of SYCP1 sequences. The amino acid sequences of human, mouse, rat, sheep, bovine, pig, zebra fish, and *hydra vulgaris* SYCP1 are aligned. Colour intensity is representative of conservation with white being non-conserved. Key residue numbers for this study are indicated. Lupas predictions for coiled-coil regions are shown above secondary structural predictions of JNet.

Appendix 2 – Purification and analysis of C-terminal SYCP1 constructs

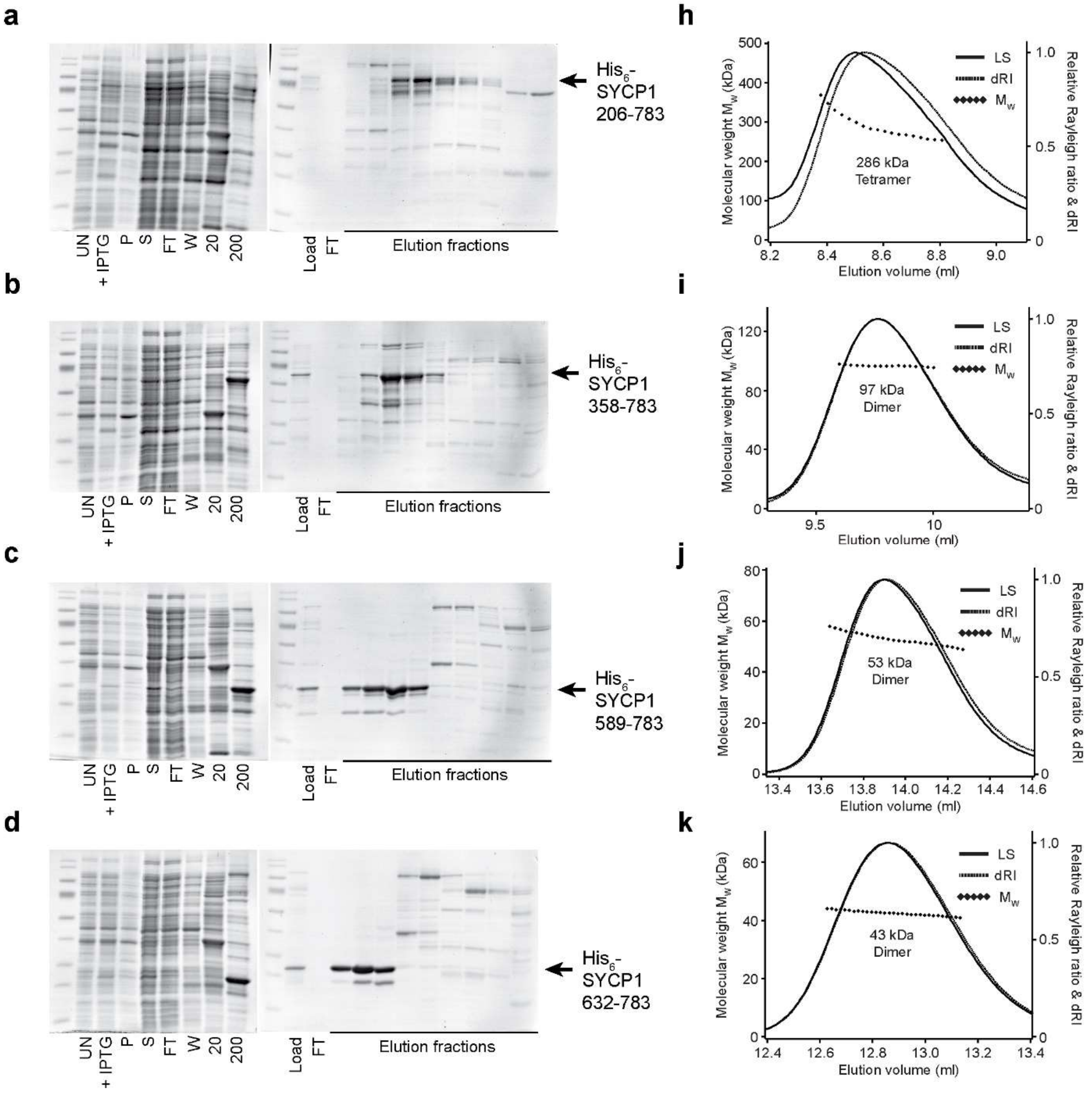

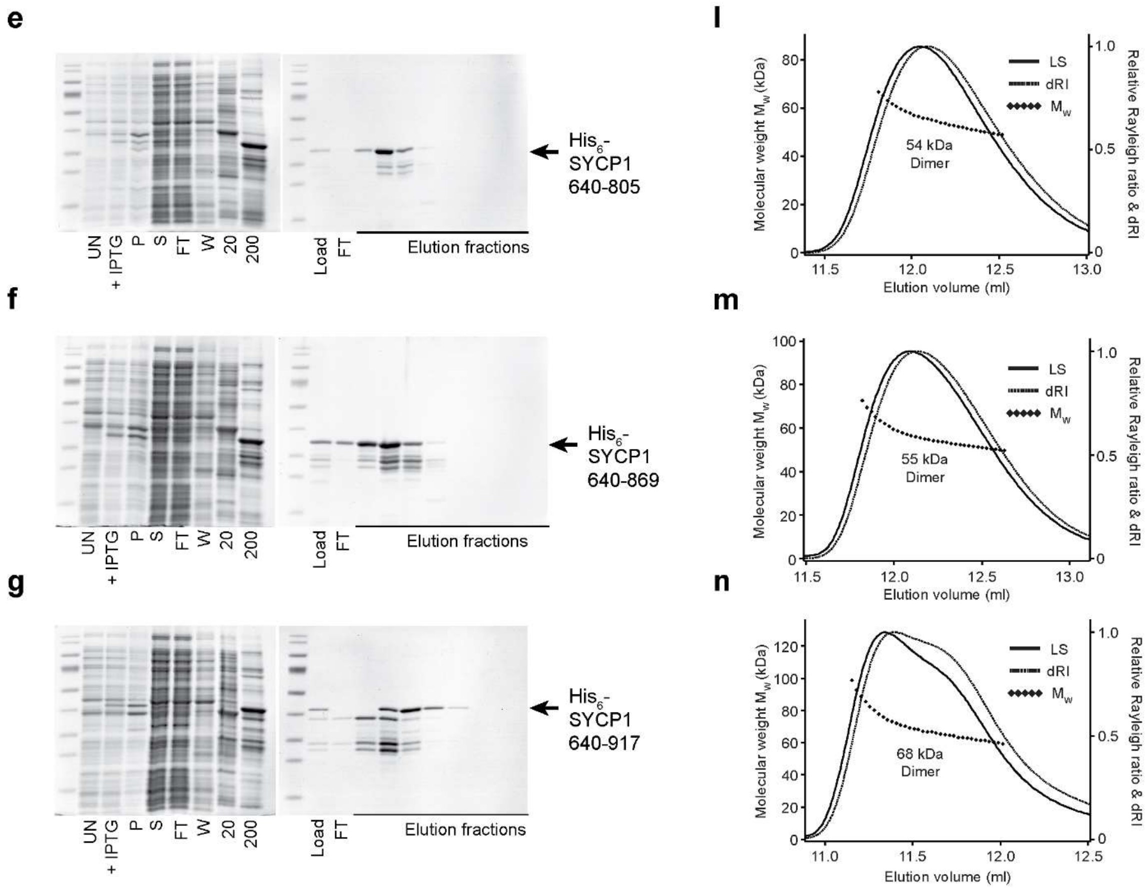

Purification and characterisation of SYCP1 C-terminal constructs. a-g) SDS-PAGE analysis showing the purification of His6-SYCP1 constructs by Ni-NTA affinity chromatography and anion exchange chromatography using the HiTrap Q. Constructs 640-805,640-869, and 640-917 had to be diluted to 50 mM KCl in order to bind the HiTrap Q column. **h-n)** SEC-MALS analysis of the corresponding SYCP1 constructs with the measured molecular weight indicated. All constructs were dimeric apart from SYCP1$_{206\text{-}783}$ which was tetramer. Light scattering (LS) and differential refractive index (dRI) are plotted as solid and dashed lines, respectively, with molecular weights (Mw) shown as diamonds across elution peaks.

Appendix 3 – SEC-MALS analysis of SYCP1 C-terminal constructs

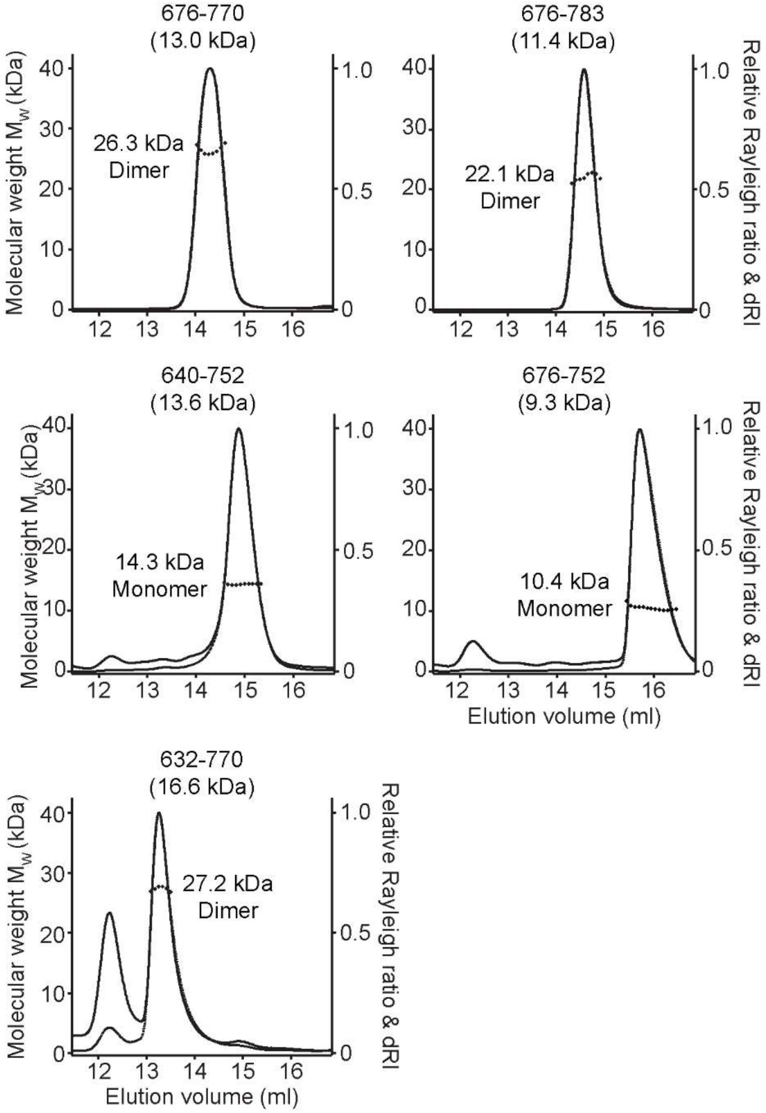

Optimisation of the construct SYCP1$_{640-783}$. SEC-MALS analysis of C-terminal constructs displaying the measured molecular weight and the determined oligomeric status of each construct.